On the Development and Application of Seeding Metrics to Improve River Flow Measurements Using Image Velocimetry

by

Martin James Jolley

A Thesis Presented in Partial Fulfillment
of the Requirements for the Degree
Doctor of Philosophy

Graduate Supervisory Committee:

Matthew Perks, Chair
Andrew Russell

School of HASS, Newcastle University
August 2024

Abstract

This thesis presents a novel approach to improving river flow measurement accuracy by optimising seeding metrics used in Particle Tracking Velocimetry (PTV), a non-contact method that estimates surface flow by tracking the movement of individual tracers—such as foam or debris—between frames of video footage. The study focuses on refining how seeding density, dispersion, and a combined metric known as the Seeding Density Index (SDI) are measured and applied under varying spatial and temporal conditions. SDI is developed as a post-processing tool that quantifies the quality of tracer conditions in each video frame by combining observed seeding density and dispersion values, and is shown to correlate with the accuracy of velocity measurements. Unlike traditional methods that rely on filtering input data, this research shifts the focus to post-analysis optimisation and error correction, improving the reliability of velocity estimates derived from video footage.

High-resolution video was captured at several UK river sites, alongside synthetic datasets with controlled tracer conditions. All data was processed using an adapted version of Kanade-Lucas-Tomasi Image Velocimetry (KLT-IV) software, developed to support new post-processing techniques. The synthetic simulations confirmed the effectiveness of the approach, while real-world footage validated the findings and demonstrated the practical benefits of applying SDI in routine flow monitoring. The first analysis uses synthetic videos to assess how different combinations of seeding density and dispersion affect flow measurement accuracy, and to define SDI values that can be used to estimate error in each video. The second analysis applies these findings to real-world case studies, recalculating discharge based on filtered results to test how well the metrics hold in natural conditions. The third analysis shifts focus to spatial effects, identifying where within a river cross-section measurements are most reliable based on seeding characteristics. These insights are then applied to site data to evaluate their practical value.

Together, these findings demonstrate how SDI can be used to improve the consistency and accuracy of river discharge estimation from video data, offering a practical tool for enhancing hydrological monitoring in a range of environmental settings. This research recommends the adoption of post-processed SDI as a standard component of image velocimetry workflows, particularly in operational monitoring contexts, where rapid, automated, and accurate flow estimation is increasingly essential.

Acknowledgements

A typical acknowledgements section usually spans no more than a single page, but this has been no typical PhD journey. With delays, extensions, setbacks, and daily battles with MATLAB, I have more to express than can be contained within one page. Therefore, I will focus this section on those I wish to formally thank, and extend my gratitude to others in Appendix C (Chapter 12).

First and foremost, my sincere thanks to the Engineering and Physical Sciences Research Council (EPSRC) for awarding Newcastle University, and subsequently myself, the PhD studentship (EP/R51309X/1). Without your funding, this work would not have been possible. Thanks also to the Environment Agency (EA) for being part of the PhD project, and to the team at SEPA who supported me during an internship. I am deeply grateful to my supervisors, Andy and Matt, who not only provided me with this opportunity but also showed immense patience throughout the years. Publishing a paper with me during lockdowns was no small feat. Your guidance through countless iterations and your ability to keep me grounded in my research were invaluable. Without your support, I might have ended up with twenty half-finished chapters on deadline day. Your expertise and patience have been truly crucial.

I also wish to extend my thanks to a few people who played a major role in my PhD life: Ethan, Holly, Becky, Sophie, and Francesco. Ethan and Holly, in the early years, you made the PhD journey enjoyable, even amidst the challenges of lockdown. Ethan, your friendship made the office bearable—even when I preferred working elsewhere. Francesco, although your time here was brief, it flew by, and it was refreshing to have someone working on a similar topic to share ideas with. Showing you around my home city of Newcastle and introducing you to the delights of jacket spuds with cheese, beans, and slaw was a pleasure. Becky and Sophie, your energy and positivity brightened the office and made it a place I looked forward to being. To all five of you, thank you.

A special thank you goes to my Mum and Dad, who, despite not fully understanding what a PhD entails, have supported me in every way possible. As I write this, sprawled across their kitchen table while Mum prepares tea, I am reminded of their unwavering support. I hope to make all their investments of time and money worthwhile... and yes, “Dr Jolley” does have a nice ring to it!

Lastly, I have dedicated space in Appendix 12 to express my heartfelt thanks to everyone who has been a significant part of my life over the past few years. Whether you directly helped me navigate this PhD or supported me in daily life, your contributions have brought me to where I am today.

Contents

Page

List of Abbreviations **19**

1 Introduction **2**

1.1 Chapter Overview . . . 2
1.2 The Importance of Flow Estimation in Rivers . . . 2
1.2.1 Rating Curves . . . 3
1.3 Common Techniques and Limitations of River Flow Estimation . . . 3
1.3.1 Use of ADCPs . . . 5
1.3.2 Salt Dilution Methods . . . 6
1.3.3 Radar . . . 6
1.3.4 Summary of Common Techniques . . . 6
1.4 Image Velocimetry Processes . . . 8
1.4.1 Introduction to Pre-Processed Seeding Density Index . . . 11
1.4.2 Introduction to Post-Processed Seeding Density Index . . . 11
1.5 Summary . . . 12
1.6 Aims and Objectives of the Thesis . . . 12
1.7 Thesis Structure . . . 13

2 Literature Review **17**

2.1 Chapter Overview . . . 17
2.2 Image Velocimetry Processes . . . 18
2.2.1 Capture Optimisation . . . 18
2.2.1.1 Ground Sampling Distance . . . 18
2.2.1.2 Capture Frame Rates . . . 22
2.2.1.3 Managing External Environmental Conditions . . . 23
2.2.1.4 Choice of platform . . . 24
2.2.1.5 Stabilisation . . . 25
2.2.1.6 Orthorectification . . . 27
2.2.1.7 Image Manipulation . . . 28
2.2.1.8 Flow State . . . 32

2.2.1.9 Feature Detection and Tracking Schemes . . . 33
2.2.2 Post-Processing . . . 36
2.2.2.1 Vector Correction . . . 36
2.2.2.2 Velocimetry Applications . . . 38
2.2.3 Tracers and Their Role in Image Velocimetry . . . 40
2.2.3.1 Significance of the Seeding Density Index . . . 41
2.2.3.2 Research Gaps and Motivation . . . 42
2.3 Chapter Summary . . . 42

3 Methodologies and Site Selection **44**
3.1 Chapter Overview . . . 44
3.2 Site Selection . . . 44
3.2.1 River Calder, Todmorden, Yorkshire . . . 44
3.2.2 River Sheaf, Sheffield, Yorkshire . . . 45
3.2.3 Image Capture . . . 45
3.2.4 Ground Control Point Coordinates . . . 47
3.2.4.1 GCPs . . . 47
3.2.4.2 Bathymetry . . . 48
3.3 Data Selection . . . 48
3.3.1 Synthetic Simulation Data . . . 49
3.3.2 Case-Study Site Data . . . 49
3.3.2.1 Filtering in KLT-IV . . . 49
3.3.2.2 Site-Study Data Results . . . 50
3.4 Video Processing using KLT-IV . . . 51
3.4.1 Pre-Processing . . . 51
3.4.1.1 Orthorectification . . . 52
3.4.1.2 Image Enhancement . . . 52
3.4.2 Processing . . . 53
3.4.2.1 Parameters . . . 53
3.4.2.2 Interpolation Methodology . . . 54
3.4.2.3 Discharge Calculations . . . 54
3.4.2.4 Tracer Availability . . . 54
3.5 Analytics . . . 54
3.5.1 Seeding Metrics . . . 54
3.5.1.1 Background on SDI Calculation . . . 55
3.5.1.2 Post-Processing SDI Calculation . . . 55
3.5.2 Synthetic Simulation Metrics and Observed Metric Results . . . 55
3.6 Data Validation and Calibration . . . 56

3.6.1 Camera and Software Calibration . . . 56
3.6.2 Validation of Velocity Measurements . . . 56
3.6.2.1 Synthetic Simulations . . . 56
3.6.2.2 Field Data . . . 56
3.7 Summary . . . 56

4 Seeding Density Indexing (SDI) for Improved Image Velocimetry Analysis: Using PTV Results to Optimise Tracer Metrics 59
4.1 Chapter Overview . . . 59
4.2 Introduction . . . 59
4.2.1 Research Questions . . . 60
4.3 Methods . . . 61
4.3.1 Synthetic Simulations . . . 61
4.3.2 Metrics for Analysis . . . 61
4.3.2.1 Seeding Density . . . 63
4.3.2.2 Dispersion . . . 65
4.3.2.3 Summary: Comparison of Seeding Density Index Approaches . . 66
4.3.3 Image Velocimetry Analysis . . . 67
4.3.3.1 Analysis using Particle Tracking Velocimetry . . . 67
4.4 Results . . . 68
4.4.1 Particle Trackig Velocimetry Results . . . 68
4.4.2 Metric Results . . . 68
4.4.2.1 Seeding Density . . . 68
4.4.2.2 Seeding Dispersion . . . 71
4.4.2.3 Summary of Seeding Density and Seeding Dispersion . . . 72
4.4.3 Formulating SDI . . . 74
4.4.3.1 Overview . . . 74
4.4.3.2 Generalised Equations . . . 74
4.4.3.3 Coefficient Fitting Results . . . 74
4.4.3.4 Summary of SDI Formulation . . . 76
4.5 Discussion . . . 76
4.5.1 Influence of Seeding Density on Velocimetry Accuracy . . . 77
4.5.2 Influence of Seeding Dispersion on Velocimetry Accuracy . . . 77
4.5.3 Comparison of Pre-Processed and Post-Processed SDI . . . 78
4.5.4 Zero-Velocity Vectors and Their Impact . . . 79
4.5.5 Influence of Video Duration on PTV Accuracy . . . 79
4.6 Conclusions . . . 80

5 Impacts of Seeding Density and Dispersion on Discharge Results of PTV Methods: A Case Study **82**
5.1 Chapter Overview . . . 82
5.2 Introduction . . . 82
5.2.1 Research Questions . . . 83
5.3 Methods . . . 84
5.3.1 Site Selection . . . 84
5.3.1.1 Overview . . . 84
5.3.2 Processing through PTV . . . 84
5.3.2.1 Data Preparation and Input . . . 84
5.3.2.2 Bulk Processing and Matching . . . 84
5.3.2.3 Modification for Data Storage . . . 84
5.3.2.4 Processing Outcome . . . 85
5.3.2.5 Initial Data Cleaning . . . 85
5.3.3 Filtering Data using SDI . . . 85
5.3.4 Stage-Discharge Relationship and Model Fitting . . . 88
5.3.4.1 Calibration Points and Model Adjustment . . . 88
5.3.4.2 Composite Modelling to Establish Baseline SDI Flow . . . 89
5.3.5 Error-Bound Estimation Using SDI . . . 90
5.3.6 Summary of Methods . . . 91
5.4 Results . . . 93
5.4.1 PTV Results . . . 93
5.4.1.1 Application of Composite Model . . . 94
5.4.1.2 Visual Representation . . . 94
5.4.2 SDI Data Analysis . . . 96
5.4.3 The Relationship Between Error and SDI . . . 97
5.4.4 Using SDI to Estimate Error in Observations . . . 100
5.4.5 Validating Error Bound Estimations . . . 101
5.5 Discussion . . . 104
5.5.1 Impacts of Depth and Error Change with SDI . . . 104
5.5.2 Impact of SDI Filtering on Flow Measurement Accuracy . . . 104
5.5.3 Error Analysis and SDI Correlation . . . 105
5.5.4 Using Asymmetric Error Bounds . . . 105
5.5.5 Generalisation and Application of Methodology . . . 106
5.6 Conclusions . . . 107

6 Using SDI to Optimise the Cross-Sectional Positioning for PTV Analysis - Numerical Study **109**

6.1 Chapter Overview . . . 109
6.2 Introduction . . . 109
6.3 Methods . . . 110
6.3.1 Synthetic Images . . . 110
6.3.2 Spatial Considerations . . . 111
6.3.2.1 Creation of Cross-Sections . . . 112
6.3.3 Velocimetry Considerations . . . 112
6.3.3.1 Interpolation and Data Averaging . . . 114
6.3.3.2 Impact of Interpolation on Results . . . 116
6.3.4 Error Analysis . . . 116
6.3.5 Calculating Density . . . 118
6.3.6 Calculating Dispersion . . . 118
6.3.7 Calculating SDI . . . 120
6.3.7.1 Spatial SDI Calculation . . . 120
6.3.8 Filtering Results . . . 121
6.3.9 Summary of Methods . . . 121
6.4 Results . . . 122
6.4.1 PTV Results . . . 122
6.4.1.1 Tracer Displacement . . . 122
6.4.1.2 Velocity Estimations . . . 123
6.4.1.3 Impact of Imposed Density on Velocity . . . 123
6.4.1.4 Impact of Spurious Velocity Vectors . . . 126
6.4.2 Cell Analysis . . . 128
6.4.3 Density Results . . . 129
6.4.3.1 Observed vs Imposed Density . . . 129
6.4.3.2 Relationship Between Relative Error and Observed Density . . . 131
6.4.4 Dispersion Results . . . 131
6.4.4.1 Imposed Dispersion Results . . . 131
6.4.4.2 Imposed Dispersion vs. Observed Dispersion . . . 132
6.4.4.3 Observed Dispersion Results . . . 135
6.4.5 Observations for SDI Calculations . . . 135
6.4.5.1 Formulating Spatial SDI Equations . . . 137
6.4.5.2 Spatial SDI Equation - Initial Study . . . 138
6.4.5.3 Spatial SDI - Average Equation . . . 139
6.4.5.4 Comparison to Non-Filtered Data . . . 142
6.4.5.5 Spatial SDI for Unfiltered Data . . . 143
6.5 Discussion . . . 146
6.5.1 PTV Analysis . . . 146

6.5.1.1 Spatial Variability and Tracer Detection . . . 146
6.5.1.2 Impact of Imposed Density and Dispersion . . . 146
6.5.1.3 Cross-Sectional Velocity Analysis . . . 147
6.5.2 Density . . . 147
6.5.3 Dispersion . . . 148
6.5.4 Spatial SDI Analysis . . . 149
6.5.4.1 Development of Spatial SDI Models . . . 149
6.5.4.2 Refining Spatial SDI Equations . . . 150
6.5.4.3 Strategic Cross-Section Placement . . . 150
6.6 Conclusions . . . 151

7 Synthesis: Post-processed SDI and its influence on PTV measurements 153
7.1 Chapter Overview . . . 153
7.2 Aims of this research . . . 153
7.3 Post-processed SDI and its influence on PTV measurements (Chapter 4) . . . 154
7.4 Impacts of Seeding Density and Seeding Dispersion on Discharge Results of PTV Methods - A Case Study (Chapter 5) . . . 155
7.5 Using SDI to Optimise the Cross-Sectional Positioning for PTV Analysis - Numerical Study (Chapter 6) . . . 156
7.6 Evaluation of Post-Processed SDI on PTV Methods . . . 157
7.6.1 Advantages . . . 158
7.6.1.1 Established Relationship between SDI and Velocity Error . . . 158
7.6.1.2 Independence from Input Data Quality . . . 158
7.6.1.3 Minimal Increased Complexity and Resource Requirements . . . 159
7.6.1.4 Enhanced Precision through Spatial Distribution Analysis . . . 160
7.6.1.5 Flexibility in Application of Cross-Sections . . . 160
7.6.1.6 Applications of Composite Models . . . 160
7.6.1.7 Impact of SDI on Error Variance with Discharge . . . 161
7.6.2 Limitations . . . 162
7.6.2.1 Challenges in Low-Densities . . . 162
7.6.2.2 Challenges in Low-Flow Conditions . . . 162
7.6.2.3 Complexities in Tracer Distribution and Data Interpretation . . . 162
7.7 Summary . . . 163
7.7.1 Established Relationship between SDI and Velocity Error . . . 163
7.7.2 Independence from Input Data Quality . . . 163
7.7.3 Spatial SDI Advantages . . . 163
7.7.4 Limitations . . . 164

8 Future Research **165**
8.1 Introduction . . . 165
8.2 Discussions . . . 166
8.2.1 Integration with Advanced Models . . . 166
8.2.2 Enhancing PTV Accuracy and Reliability . . . 170
8.2.2.1 Automation of PTV Filtering . . . 170
8.2.2.2 Addressing Environmental Challenges . . . 171
8.3 Conclusion . . . 172

9 Concluding Remarks **173**
9.1 Contributions to the Field . . . 173
9.2 Summary of Key Findings . . . 173

References **176**

10 Appendix A: KLT-IV Processing (Chapter 5) **190**
10.1 KLT Processing Videos Settings . . . 190

11 Appendix B: Publications and Co-Authorship **195**
11.1 Considerations When Applying Large-Scale PIV and PTV for Determining River Flow Velocity . . . 195
11.2 Image Velocimetry Handbook . . . 217
11.3 SEPA - DAT2203 Innovation in flow measurement report . . . 278

12 Appendix C: Further Acknowledgements **295**

List of Figures

Figure Page

1.1 An example of the hysteresis effect in the stage-discharge relationship during a flood event. The discharge for a given stage can be higher during the rising limb of a flood compared to the falling limb, illustrating the non-unique relationship between stage and discharge. 4

1.2 An insight into the number of publications over the past two decades into the research of large-scale Particle Image Velocimetry (PIV) and PTV, compared with those focused on the application of PIV and PTV on rivers. Data sourced via `www.webofscience.com`. The following refinements were applied to the search: Total papers, *topic* "Surface velocimetry PIV" OR *topic* "Surface velocimetry PTV" AND *all fields* "rivers". Application papers, *topic* "Surface velocimetry PIV application" OR *topic* "Surface velocimetry PTV application" AND *all fields* "rivers". Original image from Jolley et al. (2021). 9

1.3 A generalised system of the required processes for analysing river flow using image velocimetry methods. Pink sections represent the steps required for capture optimisation, blue represents pre-processing stages, yellow represents processing stages, and red shows post-processing stages (Harpold et al., 2006; Koutalakis et al., 2019; Perks, 2020). 10

1.4 Thesis structure and process for analysing data and producing results. The figure illustrates the flow of research following on from the findings of the literature review which overarches the rest of the thesis; from Chapter 3 Methodologies through to synthesis in Chapter 7. The figure highlights how each chapter builds on the findings of the previous chapter. 16

2.1 How Ground Sampling Distance (GSD) is described and can be altered using either an increase in resolution or decreasing the distance between the subject and the camera. 19

2.2 Schematic representation of GSD at a Nadir (directly downward viewing angle) (nadir) angle. In this configuration, the camera is oriented directly downward (perpendicular to the water surface), resulting in a uniform and evenly distributed ground sampling distance across the field of view. The overlaid grid illustrates how each pixel covers a consistent area on the water surface. (Jolley et al., 2021) . 20
2.3 Schematic representation of GSD at an oblique angle. Tilting the camera away from nadir introduces geometric distortion, resulting in a trapezoidal image footprint. This causes the ground sampling distance to vary across the field of view (Field of View (FOV)), with closer areas appearing more detailed and distant areas increasingly stretched and poorly resolved. The overlaid grid illustrates how uniform pixel spacing at the sensor translates to variable real-world pixel coverage. (Jolley et al., 2021) 21
2.4 Drone movement shown by overlapping stabilised frames onto original frames. The green mask seen on the processed row highlights where the stable image is within frame, with the final stabilised images cropping all unstable edges. (Jolley et al., 2021) 26
2.5 Example of an original image (bottom left) of a river surface in Todmorden, UK, highlighting in red the region of interest selected by the user, followed by the orthorectified image acquired while carrying out KLT-IV analysis (Perks, 2020). (Jolley et al., 2021) 29
2.6 A remodel of the Patalano et al. (2017) study, showing a flowchart for typical image processing sub-sequences with either PIVlab or PTVlab. This version has been adapted to include an additional stream addressing environmental challenges, such as glare, fog, rain, and snow, which may influence image quality and tracer visibility during pre-processing. (Jolley et al., 2021) 30
2.7 A series of image manipulation processes performed in Matlab using frames from the same video file. Note the amount of information in the binarised images if normalisation and histogram equalisation is performed prior. This shows that there are cases where more than one method of pre-processing can improve the amount of data that is traceable by programmes. (Jolley et al., 2021) 31
2.8 Schematics of general PIV (A) mechanics (Jolley et al., 2021). 33
2.9 Schematics of general PTV (B) mechanics (Jolley et al., 2021). 34
2.10 Examples of usable tracers highlighted from a study using a fixed camera with frames exactly 1 second apart. (Jolley et al., 2021) 41

3.1 The River Sheaf through the site at Highfield. 46
3.2 Raspberry Pi 3 Model B (Source: `https://www.raspberrypi.com/products/raspberry-pi-5/`) 47

3.3 River Calder level data for the selected study period between 1/11/2020 and 16/11/2020. 51
3.4 Sheaf river level data for the selected study period between 10/6/2019 and 12/10/2019. 52
3.5 Adapted workflow for Sections 1–3 of KLT-IV v1.0, demonstrating different scenarios based on camera orientation (Source: (Perks, 2020)). 53
3.6 The process to filter significant river level observations from the large dataset captured at each site. Automated selection of sections was performed using two pre-determined variables: Date-Time and River Level. The selected river level data was then used for further processing, with results stored and taken through to the SDI calculation stage, which then feeds into the comparisons of SDI Pre-Processed and Post-Processed results. 58

4.1 Examples of synthetic imagery used in this study. A and B show the minimum seeding density used (ρ = 4×10^{-4} Particles per Pixel (PPP)), while C and D show the maximum seeding density (ρ = 1.02×10^{-2} PPP). Dispersion extremes are also shown, with A and C highlighting the minimum μ = 0.5 (over-dispersed), and B and D showing the maximum μ = 200 (under-dispersed). 62
4.2 Example histogram plot for calculating seeding density. The x and y-axes represent the pixel coordinates of the Region of Interest (ROI). Each grid cell's area size is determined by the user-inputted block size. The total number of points detected and successfully tracked by PTV within each grid cell is shown on the z-axis. The seeding density result for each video processed is an average of the grid cell density values. 64
4.3 Examples of the *detectMSERFeatures* algorithm detecting low (a) and high (b) ν in tracer data. 65
4.4 PTV error results for the metric of seeding density. (A) Numerically imposed seeding density versus velocimetry error. (B) Velocimetry error as a function of actual seeding density. (C) Comparison between numerically imposed seeding density and actual seeding density obtained through PTV for each simulated video. 70
4.5 Seeding density plotted against error as in Figure 4.4B, using a MATLAB-created smoothing spline where p = 0.92913. The seeding density required to achieve an average error of 3% is 6.85×10^{-3} PPP. 71
4.6 The impact of numerically imposed and actual dispersion on error. (A) The relationship between numerically imposed dispersion and error. (B) The exponential relationship between actual dispersion and velocimetry error. (C) The comparison between numerically imposed dispersion and actual dispersion observed in the experiments. 73

4.7 (A) Observed vs. idealised SDI with derived power function. (B) Relationship between SDI and velocimetry error. (C) Comparison of calculated and observed error using the SDI–error function. 75

5.1 Standard deviation of the SDI for the frames processed through KLT-IV. The initial distribution (orange) represents the full dataset. Successive filters progressively reduce the dataset, with the third filter (black) showing a decrease in both the average SDI and the frequency of extreme values, indicating improved data quality and consistency. 87

5.2 Stage-discharge rating for the River Calder showing the measured data represented by its Stage-Discharge rating (blue), raw results (orange circles), and the filtered results (solid yellow) carried through to processing. The filtered results demonstrate improved accuracy and consistency by removing anomalous data points identified through systematic deviation methods. However, the data show a tendency to underestimate low flows and overestimate high flows, highlighting systematic biases that persist even after filtering. 93

5.3 **(A)** Composite model (Q_{comp}, orange line) created using the weighting function in Equation 5.7. The original model (Q_{eq1}, red line) from Equation 5.4, and the shifted model (Q_{eq2}, purple line) from Equation 5.5 are also shown. Blue points represent the SDI-filtered discharge data used for comparison. The three points used to calibrate the models, obtained from the measured data, are plotted as green crosses. **(B)** Composite model (Q_{comp}, orange line) plotted against SDI-filtered discharge data (blue points) and the stage-discharge results from the measured data rating curve (red points), modelled using the same depth values as the SDI-filtered results. 95

5.4 Stage-discharge rating for the River Calder showing the measured historical data (blue), filtered raw results (orange circles), the SDI Flow (solid red), and on the second axis, flow-change compared to depth (green dashed). 96

5.5 Initial comparison plots illustrating the relationship between depth, SDI, and error. **(A)** The composite model Q_{comp} and SDI Flow values plotted against depth. **(B)** The residuals of SDI Flow minus Q_{comp}, showing the error of the methodology used in this study, plotted against depth with a power fitting regression. **(C)** The SDI post-filtering values plotted against depth, with the relative error (SDI Flow - Q_{comp}) shown as a percentage on the secondary axis. **(D)** The relationship between the relative error (%) and SDI post-filtering values, with depths of less than 0.75 m removed to more clearly illustrate the relationship where systematic error is not assumed to play a significant role. 97

5.6 Graph showing the residual error between pre-filtered and post-filtered SDI data. Arrows indicate the magnitude of error change, with red representing a negative change (worse accuracy) and blue representing a positive change (better accuracy). 98
5.7 River Calder video frames taken where SDI is good (less than 3) on the left, and SDI is poor (greater than 30) on the right. The frame on the right, showcasing the poor SDI, highlights the study's finding that poor conditions affected the software's ability to process the video, resulting in erroneous outputs despite passing several filtering processes. 98
5.8 Graphs confirming the relationship between SDI and error. **(A)** The residuals of Q_{comp} and SDI-filtered flow against depth, with the moving average of SDI in relation to depth overlaid. **(B)** All data grouped onto one graph, with Q_{comp}, Observed Flow, SDI Flow, the model for SDI Flow, and the data used to validate Q_{comp}. 99
5.9 Histogram plots of the error change. Plots A and B show the error change in relation to limits to SDI of the pre-filtered data. Graph A shows results where SDI is less than 9.5, while graph B shows SDI greater than 9.5. Plots C and D show error change in relation to depth. Results are grouped where depth is greater than 0.7 m (graph C), and depths less than 0.7 m (graph D). 100
5.10 Composite model of SDI-based flow with asymmetric error bounds based on depth. The grey shaded region represents the asymmetric error bounds, and the red scatter points indicate the measured flow values. This plot illustrates the fitted model and the range of uncertainty in flow measurements. 101
5.11 Initial comparison plots for Sheaf results illustrating the results of plotting Q_{comp} model and SDI values against depth. **(A)** The composite model of Q_{comp} and SDI Flow points plotted against depth. **(B)** The residuals of SDI Flow minus Q_{comp}, showing the error of the methodology used in this study, plotted against depth with a power fitting regression. **(C)** The SDI post-filtering values plotted against depth with the relative error (SDI Flow - Q_{comp}) shown as a percentage on the secondary axis. **(D)** The relationship between the relative error (%) and SDI post-filtering values, with a single power fitting regression. 102
5.12 Modeled Q_{comp} with calculated error bounds compared with SDI Q values from PTV, and Measured Q values from manual Acoustic Doppler Current Profiler (ADCP) data. 103

6.1 Boundary and Cross Sections 111
6.2 Boundary limits (black solid lines), and cross sections (red dashed lines), with highlighted grids (cyan) used towards density and dispersion for each cross-section. 113

6.3 Displacement vectors overlaid on frames from a synthetic video at different time points: Frame 0, Frame 7, Frame 14, and Frame 20. 115
6.4 Displacement vectors for point tracers overlaid on the ROI. Vector lines connect start and end locations, with colour gradient indicating total displacement. Near-zero-velocity vectors are shown in red. 123
6.5 Scatter plots illustrating the distribution of successfully processed tracers across cross-sections for varying imposed densities and dispersions. 124
6.6 Plot of Cross-Section Velocity versus Imposed Density. Shows the average velocity for each cross-section with the true velocity marked, illustrating how velocities vary with imposed density across different cross-sections. 125
6.7 (A) Cross-Sectional Velocity versus Imposed Density with zero-velocities filtered out and their subsequent number of zero-velocity vectors against their respective imposed density (B) 127
6.8 Comparison of histograms illustrating the distribution of point tracer start locations under different imposed density and dispersion conditions. Cross-sections A–D are included for reference. 128
6.9 Observed density versus imposed density for all four cross-sections. The red line represents the line of equality ($y = x$), indicating where observed density matches the imposed density. 129
6.10 Filtered observed density versus imposed density after removing velocities less than 1 pixel (px)/s. The red line represents the line of equality ($y = x$), highlighting the improved alignment between observed and imposed densities for Cross-Sections A and D. 130
6.11 Comparison of unfiltered and filtered relative absolute error versus average density across different cross-sections. The green horizontal lines indicate the 3% error threshold, and the vertical blue line denotes the observed ideal density for each cross-section. 132
6.12 Comparison of relative absolute error versus imposed density, with imposed dispersion highlighted. The plot shows data before and after filtering out zero-velocity vectors. Maximum imposed dispersion ($\nu = 200$) is highlighted in red, and minimum imposed dispersion ($\nu = 0.5$) in green. 133
6.13 Comparison of imposed dispersion versus observed dispersion across different cross-sections, shown before and after filtering out zero-velocity vectors. The left column represents the "Before" data, and the right column represents the "After" filtering data, illustrating how filtering affects the range of observed dispersions. . 134

6.14 Comparison of observed dispersion values with relative absolute error, before and after filtering, across the four different cross-sections. The left column represents the unfiltered data, and the right column represents the filtered data. Power regression models highlight the relationship between dispersion and error, emphasising the impact of erroneous vectors. 136
6.15 Scatter plots of observed dispersion against observed density for each cross-section. Vertical and horizontal lines represent $x = 0.5$ and the corresponding density, respectively. 138
6.16 Scatter plots of observed dispersion against observed density for each filtered cross-section. Vertical and horizontal lines represent $x = 0.5$ and the corresponding density, respectively. 138
6.17 Model of error as a function of SDI and the subsequent calculated error against observed error. 139
6.18 Modelled using Cross-Section A's coefficients across the other cross-sections. . . . 140
6.19 Calculated Error vs Observed Error from Coefficients in Table 6.4 with RMSE. . . 141
6.20 Analysis of the relationship between SDI and error in Cross-Sections B and C. Subfigure (A) shows the calculated error against SDI and observed error, while subfigure (B) compares the calculated error directly with the observed error, highlighting any discrepancies between predicted and actual values. 143
6.21 Calculated Error vs Observed Error for non-filtered datasets. 144
6.22 Comparison of SDI and Error Calculations for Cross-Sections B and C. The figure includes SDI vs. Calculated Error (top row) and Observed Error vs. Calculated Error (bottom row) for both cross-sections, with RMSE values labelled. 145

8.1 Modelled workflow to incorporate temporal and spatial SDI into an automated PTV system. Part 1 looks at the standard features of PTV, with the added process of cloud processing of data. Part 2 looks at the analysis of the detected tracers using standard PTV filtering, as well as the newly established post-processed SDI metrics. Part 3 converts the measured results into discharge. Labels A–E correspond to the process seen in Figure 8.2. 167
8.2 An example of the suggested general process of PTV processing through to discharge estimations. 168
8.3 Modelled generalised stage–discharge relationship for continuous monitoring using automated PTV systems. Results are grouped via stage bins of 0.1 m (arbitrary to this generalisation), and shown as $t = n$. 169

10.1 River Calder at Todmorden Cross-Section Data 192
10.2 River Sheaf at Highfield Cross-Sectional Data 194

11.1 The impacts of using each image manipulation transformation onto a frame taken from drone footage, with a time-step between each for comparison. 241
11.2 Click the area highlighted here, select all, and copy to the code. Be sure to replace all back-slashes with double backslashes 243
11.3 Ensure that the ”opens with” is opening with Python IDE, here seen as Python 3.9. 244
11.4 Extracting images from a video 253
11.5 How to find the resolution of the video using VLC player 253
11.6 Importing the frames 254
11.7 Applying a ROI and a mask 255
11.8 The pre-processing parameters required for the tutorial video. Play with these values until tracers are as prevalent as possible. 256
11.9 Some typical values for the PIV settings used in the tutorial. These can be changed to include more passes and larger initial areas. 257
11.10 Post-processing considerations for the data, including vector validation and interpolation. Erroneous green vectors are removed and replaced with statistically valid orange vectors depending on the thresholds set at the menu on the left side of the pane. 258
11.11 This is the layout required from the GCP .xls file. From left to right, there is ID, X (real world), Y (real world), Z (real world), x (local pixel), y (local pixel). 259
11.12 How to easily find GRP local coordinates (x,y or i,j), from a still image using GIMP.260
11.13 The input file and the output ROI as seen in the RIVeR app. 261
11.14 The cross-section input data along with the defined cross-section image imposed onto the river, along with the velocity vectors that apply to the cross-section. . . . 262
11.15 This is the required data for inputting cross-sectional data and the parameters for calculating discharge for the tutorial. The alpha coefficient has been shown to average around the 0.85 mark, but is specific for each site. Be sure to define whether your cross-sectional data has either depths or elevations in the program (comes up as a text box during inputting). 263
11.16 KLT GUI with the full inputs shown. 268
11.17 To format a simple CSV file that contains the GCP data required for processing, then it needs to be laid out as X,Y,Z,x,y; where X,Y,Z are real-world coordinates and x,y are their pixel coordinate counterparts. 270
11.18 When setting out a ROI, be sure to only include areas of the river surface, and try to leave out any vegetation that may disturb surface velocity results. 271
11.19 Velocity results that have been tracked across the surface. Colour shows indication of speed, while the vector shows the vector trajectory and tracked distance. . . 272
11.20 The discharge results after running the full process are shown here. 272

11.21 A possible error code you can observe with numerous unexpected closures or shutdowns of Runtime. . . . 273
11.22 Transect and velocity map in FUDAA LSPIV, velocities increasing as they approach the weir just out of shot. . . . 278
11.23 Transect . . . 280
11.24 Velocity map. . . . 281
11.25 (A) View from the bridge at Cabrach and (B) Gauging Stage plot, showing numbers of gauging's and stage range covered. . . . 282
11.26 (A)All ADCP and Flow tracker gauging's since site creation 2017. (B) LSPIV Gauging deviations from existing rating. (C) Transect and velocity map in FUDAA LSPIV, velocities increasing as they approach the weir just out of shot. . . . 283
11.27 Overview of gauging data . . . 284
11.28 Headswood camera view. . . . 285
11.29 Part of Headswood rating and LSPIV/KLT gaugings plotted. . . . 286
11.30 KLT vectors. . . . 287
11.31 Processing and discharge results . . . 287
11.32 PIV Lab mask and vectors. . . . 288
11.33 Views showing different aspects: a bridge view and a transect with velocities. . . . 289
11.34 Orthorectification in RIVeR showing various stages and perspectives. . . . 290
11.35 Camera from the bank, using surveyed ground control points (A). Discharge Chart for Mill of Tore (B). . . . 291
11.36 KLT-PIV software (KLT) Q3.74 comparison to RIVeR software (LSPIV) Q3.61, M9 Stationary Q3.429 . . . 292
11.37 Results from STIV for Weisdale. No rated flow available at present, but this measurement may allow for a rating extension. . . . 292

List of Abbreviations

ADCP Acoustic Doppler Current Profiler. 3–5, 7, 10, 12, 15, 38, 54, 56, 84, 85, 102, 103, 158

AWS Amazon Web Services. 46

CCTV Closed-Circuit Television. 9

CLAHE Contrast Limited Adaptive Histogram Equalisation. 29, 32

EA Environment Agency. 3, 44

EPSRC Engineering and Physical Sciences Research Council. 3

FL Focal Length. 18, 19

FOV Field of View. 12, 19, 21, 23, 51

fps frames per second. 45, 61, 63, 67

GCP Ground Control Point. 28, 38, 44, 47, 48, 50–52, 56, 84

GPD Generalised Poisson Distribution. 49, 61

GSD Ground Sampling Distance. 11, 12, 18–21

GUI Graphical User Interface. 35

IP Internet Protocol. 18, 22, 23, 45

IwP Image Width in Pixels. 18, 19

KLT Kanade-Lucas-Tomasi. 50, 53

KLT-IV Kanade-Lucas-Tomasi Image Velocimetry. 2, 9, 12–14, 29, 48, 49, 51–54, 56, 84, 85, 87–89, 91, 93, 94, 102, 111, 113, 114, 123, 137, 159, 166, 169

LiDAR Light Detection and Ranging. 5

LSPIV Large Scale Particle Image Velocimetry. 34, 41

nadir Nadir (directly downward viewing angle). 12, 18, 20, 21, 27

NIR Near Infrared. 23, 50

PIV Particle Image Velocimetry. 8, 9, 11, 17, 23, 28, 29, 32, 33, 35–38, 42, 44, 78, 170, 171

PPP Particles per Pixel. 13, 61–63, 69, 71, 72, 74, 76, 77, 80, 110, 120, 131, 154, 174

PTV Particle Tracking Velocimetry. 2, 8, 9, 11–13, 15, 17, 29, 32–35, 37, 38, 42, 44, 45, 54, 55, 59–70, 72, 74, 76–85, 88–94, 97, 98, 101, 103–114, 116, 117, 120–123, 126, 129, 132, 137, 142, 146–174

px pixel. 16, 49, 56, 113, 114, 117, 121, 122, 126, 128–130, 146, 147

ROI Region of Interest. 13, 16, 31, 32, 45, 48, 52, 60, 63–68, 77, 78, 109, 111–113, 116–121, 123, 131, 135, 137, 141, 144, 146, 148–152, 156, 157, 160, 165, 171

SDI Seeding Density Index. 2, 11, 12, 14, 15, 17, 42, 43, 49, 54, 55, 57, 59–61, 63, 65, 66, 68, 69, 71–74, 76–87, 89–93, 95–110, 116, 120–122, 135, 137–139, 141–144, 147, 149–167, 169–174

SfM Structure-from-Motion. 26

SW Sensor Width. 18, 19

UAS Uncrewed Aerial System. 9

Chapter 1. Introduction

1.1 Chapter Overview

This chapter outlines the central themes and objectives of the thesis, emphasising the importance of accurate flow estimation in river systems for effective water resource management, environmental risk mitigation, and sustainable development. Current methodologies often lack the precision and reliability required in dynamic river environments, highlighting a significant research gap. Traditional flow measurement techniques, though valuable, are constrained by issues of accessibility, cost, and potential ecological impact.

This thesis addresses these limitations by exploring image velocimetry as a non-invasive, cost-effective alternative. Unlike previous research that focused primarily on technical processing aspects, this study places emphasis on optimising seeding metrics to enhance the accuracy of image velocimetry under diverse environmental conditions. The outcomes of this research have practical implications beyond academia, offering improved tools for flood prediction, climate change adaptation, and water resource management. By advancing flow measurement accuracy, this work aims to support policymakers and environmental managers in protecting and efficiently utilising water resources across a wide range of settings.

1.2 The Importance of Flow Estimation in Rivers

River flow monitoring is a fundamental aspect of hydrology, involving the measurement and analysis of water flow in rivers. Accurate estimation of river flows is crucial for sustainable water resource management, facilitating the allocation of water for agriculture, industry, and domestic use. It also plays a vital role in flood forecasting and management, helping to protect communities and infrastructure from the devastating impacts of floods (Merkuryeva et al., 2015). Moreover, river flow data is indispensable for ecological studies, providing insights into the health of river ecosystems (Bowes et al., 2018). The data derived from river flow monitoring is extensively utilised by hydrologists, environmental scientists, and policymakers. Hydrologists rely on this data to model river behaviour, predict future flows, and analyse water trends. Environmental scientists use it to assess the ecological health of rivers, while policymakers employ this information to develop effective water management strategies and policies (UKCEH, 2018).

The field of river flow monitoring is rapidly evolving due to technological advancements. The

integration of remote sensing (Cao et al., 2022), satellite data (Huang et al., 2018), and advanced modelling techniques (Merkuryeva et al., 2015) has significantly improved the ability to monitor river flows with greater precision. Furthermore, the application of machine learning and artificial intelligence is progressively enhancing the accuracy of flow predictions (Park and You, 2023). This data is becoming increasingly crucial in the broader context of climate change adaptation, particularly in understanding how rivers respond to shifting weather patterns. Such understanding is essential for ensuring water security, bolstering disaster resilience, and advancing environmental sustainability. Looking ahead, the significance of river flow monitoring in responsible water resource management and environmental conservation is set to grow. Continued technological advancements and our expanding knowledge of river systems are making flow estimation an indispensable tool in the sustainable management of water resources.

1.2.1 Rating Curves

Rating curves represent an empirical relationship between river stage (water level) and discharge (flow rate). These curves are crucial for converting continuous stage measurements into discharge values, enabling hydrologists to estimate river flow over time. Typically, rating curves are constructed by collecting flow measurements at various stages and fitting a mathematical model to the observed data. However, the accuracy of a rating curve is highly dependent on the quality and range of the data used, and this is where the limitations of traditional methods become apparent (Centre for Ecology and Hydrology, 2022).

One significant limitation associated with traditional rating curves is the assumption of a unique relationship between stage and discharge along a river reach. Natural floods often reveal that this relationship is not always unique; specifically, the discharge for a given stage during the rising limb of a flood can be significantly higher than for the same stage during the falling limb, a phenomenon known as hysteresis, as seen in Figure 1.1. This non-linear behaviour complicates the use of traditional rating curves during dynamic flood events. Furthermore, the practical limitations of methods that require manual data capture, such as traditional and current mainstream modern methods like ADCP, are exacerbated by the need to be on-site to capture the full range of stage rising and falling. This constraint highlights the potential advantage of automated methods, such as image velocimetry, which could continuously monitor river conditions without the need for constant human presence, thereby capturing the complete stage-discharge relationship more effectively.

1.3 Common Techniques and Limitations of River Flow Estimation

Advances in understanding hydrological processes and characterising river flows have been driven by the development of novel sensing instruments, data acquisition platforms, and new analytical techniques (Assem et al., 2017; Chen et al., 2007; Mishra et al., 2019). Among these advancements, the widespread adoption of ADCP technologies stands out (Kostaschuk et al., 2005). ADCPs have

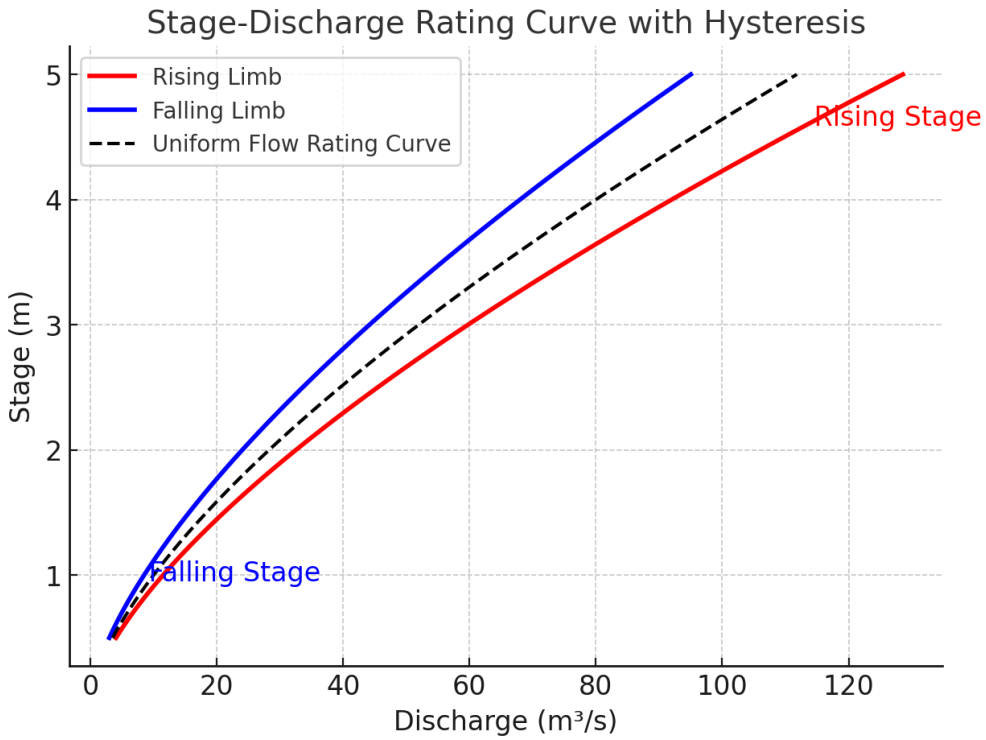


Figure 1.1: An example of the hysteresis effect in the stage-discharge relationship during a flood event. The discharge for a given stage can be higher during the rising limb of a flood compared to the falling limb, illustrating the non-unique relationship between stage and discharge.

significantly improved the ability to reliably collect data over large areas, including entire water columns, which is crucial for understanding the dynamic behaviour of rivers (Neill and Hashemi, 2018). However, while ADCPs offer advantages over traditional gauging techniques, such as ultrasonic sensors and electromagnetic current meters, they still face critical limitations. These devices require contact with the water body, which may not be feasible during high-flow conditions or in scenarios where physical access to the channel is restricted.

Traditional flow measurement methods, such as impellers and weirs, have long been used due to their simplicity and established history in hydrological studies. However, these methods are often challenged by high-flow conditions, where in-stream structures can be overwhelmed, leading to inaccurate measurements. Additionally, the necessity for physical contact with the water introduces hazards during floods or in remote areas, making these methods less reliable and more dangerous. High flows, turbulent conditions, and debris can impair the accuracy of these methods and pose a risk of damage to the equipment (Centre for Ecology and Hydrology, 2022). These challenges underscore the necessity for more innovative approaches, such as image velocimetry, which leverages video technology to capture surface flow patterns and compute velocity fields without physical contact.

In response to the limitations of traditional methods, modern techniques, including ADCPs, salt dilution methods, and radar technologies, have been developed to improve safety and applicability,

particularly in challenging environments. Despite these improvements, these modern techniques are not without their limitations. High costs, specific site requirements, and accuracy issues in dynamic or highly turbulent flows continue to hinder their effectiveness. For instance, the high cost of ADCPs limits their widespread adoption, especially in smaller rivers where depth is less significant. Furthermore, ADCPs and other methods like radar are often challenging to deploy in low-flow conditions or when physical access is difficult, further complicating their use (Muste et al., 2004; National Oceanic and Atmospheric Administration, 2024; Yorke and Oberg, 2002; Fulton et al., 2020).

The development of non-contact sensors for velocity measurements, such as surface velocity radar, and non-intrusive methods for acquiring bathymetric data, like bathymetric Light Detection and Ranging (LiDAR), radar, and photogrammetry, is facilitating the non-contact and autonomous monitoring of fluvial flows (Alimenti et al., 2020; Costa et al., 2006; Flener et al., 2013; Javernick et al., 2014). These methods provide data as reliable as conventional methods but can be costly to deploy, limiting their widespread adoption. Moreover, surface velocity radar is highly dependent on the surface roughness of the river and may be influenced by environmental noise, introducing uncertainties in the data (Fulton et al., 2020).

These persistent challenges justify the need for more versatile, non-invasive approaches like image velocimetry. Image velocimetry offers a promising solution by providing reliable flow measurements in diverse environmental settings, including those where traditional methods may fall short, thereby advancing the field of river flow monitoring and supporting better water resource management.

1.3.1 Use of ADCPs

ADCPs are extensively used in river flow monitoring and for constructing rating curves. ADCPs utilise the Doppler effect to measure water current speeds and directions by transmitting sound waves to particles in the water and detecting the frequency shifts as the waves are reflected back. These devices can be deployed on mobile platforms, such as boats and uncrewed vehicles, and are capable of measuring currents at various depths simultaneously, providing detailed flow profiles essential for understanding the dynamic behaviour of rivers. Despite their advanced capabilities, ADCPs have notable limitations. In smaller rivers, where depth is less significant, the high cost of the device can be prohibitive, limiting their use in some areas. Additionally, in low-flow conditions, ADCPs often face deployment challenges because the shallow water levels may prevent the effective use of boats or remote vehicles, reducing the accuracy and feasibility of flow measurements. Safety concerns for users, particularly in high-flow conditions, further complicate their deployment. Moreover, ADCPs lack remote sensing capabilities, which limits their effectiveness in inaccessible or hazardous environments (Muste et al., 2004; National Oceanic and Atmospheric Administration, 2024; Yorke and Oberg, 2002).

1.3.2 Salt Dilution Methods

The salt dilution method is another established technique for measuring river discharge, particularly effective in smaller streams where other methods may not be feasible. This method involves introducing a known quantity of salt into the river and measuring the increase in conductivity downstream, which correlates with the discharge rate. While this method is simple and cost-effective, making it a practical choice for many hydrological studies, it also has significant limitations. Accurate measurements require a well-mixed section of the river, which is not always achievable, particularly in larger rivers or during turbulent conditions. Additionally, environmental concerns, although typically minimal, must be considered, particularly in sensitive ecosystems (Wood and Dykes, 2002; Sentlinger et al., 2019). The limitations of the salt dilution method underscore the need for more reliable and non-invasive techniques that can be applied across various river conditions without risking environmental harm. Image velocimetry offers an environmentally neutral alternative that avoids introducing foreign substances into the river while still delivering precise flow measurements.

1.3.3 Radar

Radar technology represents a significant advancement in the non-contact measurement of surface velocity and river discharge, and it is increasingly used to develop rating curves in situations where traditional methods are impractical or unsafe. Radar systems, including coherent, continuous wave Doppler radars and pulsed radars, allow for remote sensing of river flow from fixed platforms, such as bridges or cable stays (Costa et al., 2006; Plant et al., 2005). The application of probabilistic algorithms in radar systems improves the reliability of measurements, particularly in developing rating curves.

However, radar systems also have limitations, such as high initial capital investment and specific site conditions that must be met for accurate measurement. Additionally, these systems can struggle with low-velocity flows, introducing uncertainties that can affect the accuracy of rating curves. These challenges highlight the ongoing need for alternative approaches like image velocimetry, which can overcome many of the limitations associated with radar and other non-contact methods. By capturing surface flow patterns through video technology, image velocimetry provides a robust and versatile method for river flow estimation, particularly in environments where other methods may fall short (Fulton et al., 2020).

1.3.4 Summary of Common Techniques

Given the significant limitations of both traditional and modern techniques, the need for a more versatile, non-invasive, and cost-effective approach is evident. Image velocimetry, as explored in this thesis, represents a promising solution by overcoming many of the challenges associated with

these methods. Through the use of video technology to capture and analyse surface flow patterns, this method offers the potential for more accurate and reliable flow measurements in diverse environmental settings, including those that are difficult to monitor using conventional techniques.

Table 1.1: Comparison of Common River Flow Estimation Techniques

Technique	**Advantages**	**Limitations**	**References**
ADCP	High accuracy; measures full velocity profile	Expensive; not suitable for low-flow conditions; requires on-site deployment	(Muste et al., 2004; National Oceanic and Atmospheric Administration, 2024; Yorke and Oberg, 2002)
Salt Dilution	Simple; cost-effective; works in small streams	Requires full mixing; accuracy affected by turbulence; environmental considerations	(Wood and Dykes, 2002; Sentlinger et al., 2019)
Radar	Non-contact; suitable for hazardous conditions	High cost; affected by surface roughness; limited in low-flow conditions	(Costa et al., 2006; Plant et al., 2005; Fulton et al., 2020)
Traditional Gauging (Weirs, Impellers)	Long-established method; widely used	Physical structures can be overwhelmed in high flows; requires manual operation	(Centre for Ecology and Hydrology, 2022)
Image Velocimetry	Non-contact; cost-effective; works in diverse environments	Requires sufficient tracer visibility; sensitive to lighting conditions	(Perks, 2020; Fulton et al., 2020; Jolley, 2021)

One important consideration is that while image velocimetry reduces many of the challenges associated with traditional techniques, it is still subject to certain environmental conditions. Specifically, seeding methods used in image velocimetry can face similar challenges to conventional methods under extreme conditions. In high-discharge scenarios, seeding tracers may be washed out too quickly or dispersed unevenly, impacting measurement accuracy. Conversely, in low-flow

conditions, tracer movement may be insufficient to generate a strong signal for velocity estimation. These challenges necessitate careful selection of seeding density and dispersal techniques to ensure robust flow estimations.

1.4 Image Velocimetry Processes

Image velocimetry represents an innovative approach to determining fluvial flows, particularly when combined with bathymetric data. Over the past two decades, research in large-scale image velocimetry has seen substantial growth, reflecting its increasing relevance and potential impact in hydrology (Figure 1.2). This technique builds upon the foundational principles of lab-based image velocimetry methods (Lindken et al., 2009), originally developed for controlled laboratory settings. These traditional methods involve seeding the flow with neutrally buoyant particles, illuminating them with laser light, and recording their movement with cameras, after which particle displacements are calculated using either PTV or PIV (Willert et al., 1996).

In transitioning from controlled lab environments to large-scale outdoor settings, image velocimetry adapts these principles to handle the complexities and variability of natural river systems. This shift has necessitated modifications in techniques and optimisation strategies to enhance the accuracy and reliability of measurements in uncontrolled environments. While lab-based image velocimetry has been widely adopted with established procedures (e.g. Cerqueira et al., 2018; Gollin et al., 2017), large-scale image velocimetry requires adaptable methodologies to accommodate varying environmental conditions and tracer availability (Perks, 2020). The flexibility of large-scale image velocimetry refers to its ability to be applied across different hydrological settings, accommodating variable lighting conditions, changing tracer characteristics, and differing river morphologies. However, this adaptability also makes standardisation more challenging.

The primary advantage of large-scale image velocimetry lies in its ability to provide non-invasive, accurate measurements of surface flow velocities in natural rivers, which are often challenging to monitor using traditional methods. This technique can be applied under a wide range of conditions, including extreme weather events and remote locations where conventional instruments might fail or pose safety risks. By capturing and analysing surface flow patterns, image velocimetry enables a detailed understanding of river dynamics, which is critical for both hydrological and hydraulic analyses.

The general workflow for image velocimetry can be summarised in four key stages: (i) capture optimisation, (ii) pre-processing, (iii) image processing, and (iv) post-processing (see Figure 1.3). Capture optimisation involves selecting and preparing equipment and parameters to ensure reliable image capture, such as maximising tracer visibility and minimising environmental noise. Pre-processing steps focus on stabilising footage and enhancing image quality to facilitate accurate analysis. Image processing applies algorithms to detect and track tracer displacements across the field of view, while post-processing seeks to validate and refine the data, ensuring that only reliable

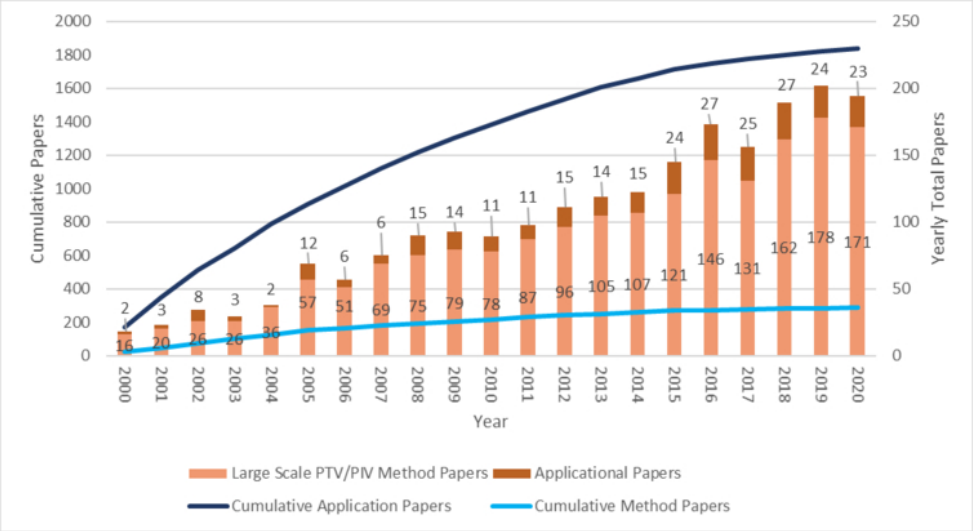


Figure 1.2: An insight into the number of publications over the past two decades into the research of large-scale PIV and PTV, compared with those focused on the application of PIV and PTV on rivers. Data sourced via `www.webofscience.com`. The following refinements were applied to the search: Total papers, *topic* "Surface velocimetry PIV" OR *topic* "Surface velocimetry PTV" AND *all fields* "rivers". Application papers, *topic* "Surface velocimetry PIV application" OR *topic* "Surface velocimetry PTV application" AND *all fields* "rivers". Original image from Jolley et al. (2021).

results are used in subsequent analyses, such as calculating discharge.

One of the key innovations of image velocimetry is its use of naturally occurring tracers, such as surface foam or floating debris, in contrast to lab-based methods that often rely on artificial seeding. This approach not only reduces the environmental impact but also allows for real-time monitoring in a variety of settings. The versatility of image velocimetry platforms—ranging from mobile methods like Uncrewed Aerial System (UAS) to fixed Closed-Circuit Television (CCTV) stations—further enhances its applicability. The choice of platform is typically determined by the specific requirements of the project, including the desired output, accessibility, and cost.

Within image velocimetry, there are two main methods of feature tracking: PTV (based on Lagrangian techniques), and PIV (based on Eulerian techniques). PIV generates gridded average surface velocities by tracking features across defined areas, while PTV tracks individual tracers, mapping their paths across the surface (Jolley, 2021). These two approaches also represent different observational frameworks: PIV adopts an Eulerian perspective, measuring flow velocity at fixed locations, whereas PTV uses a Lagrangian approach, tracking the movement of individual particles over time. The Lagrangian method can offer more detailed insights into transient and turbulent flow behaviours, especially in complex river systems. Each method has its own requirements and limitations. For instance, the selection of the frame rate and the optimisation of search areas are critical for ensuring accurate velocity measurements. PTV, particularly with algorithms like KLT-IV (Perks, 2020), has been shown to be less sensitive to user input parameters compared to PIV, allowing for more consistent and reproducible results across varied conditions.

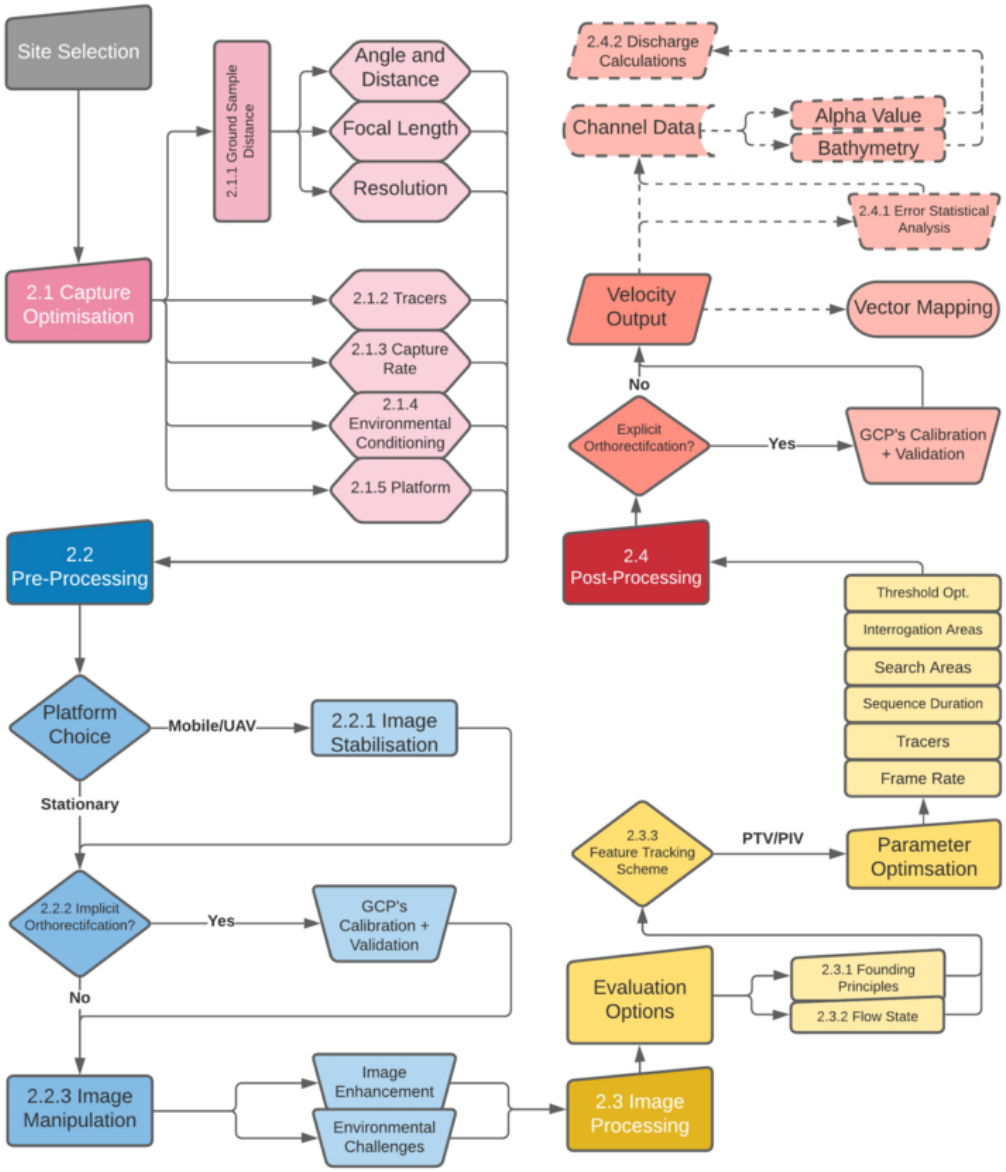


Figure 1.3: A generalised system of the required processes for analysing river flow using image velocimetry methods. Pink sections represent the steps required for capture optimisation, blue represents pre-processing stages, yellow represents processing stages, and red shows post-processing stages (Harpold et al., 2006; Koutalakis et al., 2019; Perks, 2020).

While the accuracy of image velocimetry is influenced by tracer availability and environmental conditions, it has shown strong agreement with traditional flow measurement methods. When supported by appropriate post-processing, such as the Seeding Density Index, image velocimetry can produce highly reliable flow estimates (Jolley, 2021; Boursicaud et al., 2016; Detert et al., 2017). Compared to contact-based instruments like ADCP, image velocimetry avoids depth-averaging biases and deployment constraints, and offers the advantage of producing spatially distributed surface

flow fields over entire river cross-sections (Fujita et al., 2007).

In conclusion, image velocimetry represents a significant advancement in river flow measurement. By overcoming key limitations of traditional methods, such as the need for physical contact with the water, high equipment costs, and reduced reliability in dynamic or hazardous conditions, it offers a safe, flexible, and non-invasive alternative for capturing surface flow data. The following chapters explore the specific methodologies and applications of image velocimetry, highlighting its potential to improve our understanding of river dynamics and support more effective water resource management.

1.4.1 Introduction to Pre-Processed Seeding Density Index

The SDI was initially developed as a metric to optimise frame selection in image velocimetry analysis, focusing on assessing seeding conditions—such as the density and dispersion of tracers—prior to actual image processing. The primary goal of Pre-Processed SDI is to identify frames with optimal seeding conditions to enhance the accuracy of velocity measurements derived from PTV and PIV techniques. Research, including studies by Pizarro et al. (2020b), has demonstrated that high seeding density and uniform dispersion significantly improve the reliability and accuracy of velocimetry algorithms. By filtering out frames with sub-optimal seeding conditions before analysis, Pre-Processed SDI helps reduce errors and improve the overall quality of flow measurements. While effective in controlled environments or in scenarios where seeding conditions are relatively stable and predictable, Pre-Processed SDI can face limitations in more complex and dynamic settings. In real-world river environments, seeding conditions can vary significantly over time and space, making it challenging to accurately assess them beforehand. If the initial estimates of SDI are inaccurate and unsuitable frames are selected for processing, errors may propagate through the analysis, ultimately affecting the accuracy of velocity and discharge estimations.

1.4.2 Introduction to Post-Processed Seeding Density Index

To overcome the challenges associated with Pre-Processed SDI, this thesis introduces Post-Processed SDI, which focuses on the seeding conditions observed and measured during the actual image velocimetry analysis. Unlike Pre-Processed SDI, Post-Processed SDI metrics are derived from the data as it is passed through PTV, allowing for a more accurate representation of the evolving seeding conditions throughout the measurement process. This approach not only captures the dynamic nature of seeding characteristics but also provides a mechanism to correct and refine PTV results based on the actual performance of the tracers during analysis. The motivation for developing Post-Processed SDI stems from the limitations of Pre-Processed methods, where reliance on estimated tracer characteristics can lead to inaccuracies that affect subsequent analysis. By focusing on actual results from PTV, Post-Processed SDI offers a feedback mechanism that enables adjustments during analysis, enhancing the robustness and reliability of PTV measurements.

This thesis develops Post-Processed SDI through a series of numerical experiments and validates it with case studies across diverse environmental settings. The aim is to demonstrate how this approach can optimise PTV processes, particularly in challenging river conditions where traditional methods may be less effective. The subsequent chapters will detail the methodologies used to develop Post-Processed SDI, its application in real-world scenarios, and its impact on the accuracy of river discharge estimations.

1.5 Summary

This chapter has reviewed key approaches to river flow monitoring, highlighting the limitations of traditional methods and the advancements brought by modern technologies such as ADCPs, salt dilution methods, and radar systems. Despite these innovations, challenges remain—particularly in dynamic and complex river environments. Image velocimetry has emerged as a promising alternative, offering a non-contact method for accurate flow measurement. We introduced the concept of the SDI as a key factor in enhancing the accuracy of image velocimetry, differentiating between Pre-Processed and Post-Processed SDI approaches. The Post-Processed SDI, developed and validated through this research, addresses the limitations of Pre-Processed methods by enabling real-time adjustments based on actual tracer performance during analysis. This approach improves the reliability of flow measurements, particularly in variable and challenging river conditions, setting the stage for the detailed methodologies and case studies presented in the following chapters.

Despite the progress made by existing techniques, a significant research gap remains in achieving consistently accurate and reliable flow measurements under varying seeding conditions. This thesis aims to bridge that gap by advancing the use of image velocimetry through the novel Post-Processed SDI approach, which offers real-time optimisation and enhanced precision across diverse hydrological contexts.Its novelty lies in evaluating tracer performance during the processing stage, allowing dynamic correction and filtering of velocity estimates based on actual tracer behaviour. The anticipated outcomes of this research are expected to contribute substantially to the field—improving the accuracy of river discharge estimations and supporting more effective water resource management strategies.

1.6 Aims and Objectives of the Thesis

The primary aim of this thesis is to enhance the accuracy and reliability of river flow measurements through the application of PTV techniques, with a particular focus on the development and implementation of the Post-Processed SDI. By refining the methodologies used to assess and optimise seeding metrics, this research seeks to improve the precision of flow estimations across diverse seeding conditions.

To achieve this aim, the thesis sets out the following specific objectives, each addressing a key

aspect of the research gap identified in the summary:

- **Objective 1: To assess the impact of resultant seeding density and dispersion on the accuracy of velocity measurements through both numerical experiments and real-world case studies.**
  - **Chapter 4:** This chapter explores how seeding density and dispersion influence the accuracy of image velocimetry results using synthetic data and numerical experiments.
- **Objective 2: To develop and validate the Post-Processed SDI as a tool for optimising frame selection in image velocimetry analysis.**
  - **Chapter 4:** This chapter focuses on the development of the Post-Processed SDI, detailing the methodology and validation processes through numerical experiments. It also examines how this approach differs from traditional Pre-Processed SDI methods.
  - **Chapter 5:** This chapter extends the analysis by applying the SDI to specific case studies, investigating the correlation between seeding metrics and PTV accuracy under different river conditions.
- **Objective 3: To integrate Post-Processed SDI metrics into existing image velocimetry workflows and evaluate their effectiveness in improving flow measurement accuracy.**
  - **Chapter 5:** This chapter assesses the practical integration of Post-Processed SDI into existing PTV workflows, demonstrating how these metrics can be used to enhance flow measurement accuracy in real-world scenarios.
  - **Chapter 6:** Focuses on using Post-Processed SDI metrics to optimise the cross-sectional positioning for PTV analysis, showcasing their role in refining measurement workflows.
- **Objective 4: To explore the application of SDI in different spatial settings, identifying best practices for its use in varying hydrological contexts.**
  - **Chapter 6:** This chapter explores the application of Post-Processed SDI in spatially diverse river cross-sections, identifying best practices for its implementation.
  - **Chapter 7:** Synthesises findings from the previous chapters and discusses the broader implications of Post-Processed SDI in diverse hydrological contexts, offering recommendations for future use.

1.7 Thesis Structure

This thesis is structured as follows, and can be seen graphically as represented by Figure 1.4:

- **Chapter 2: Literature Review** - This chapter offers a comprehensive review of image velocimetry techniques, such as PIV and PTV, and examines the role of seeding characteristics in PTV accuracy. It also reviews existing methods for assessing seeding density and dispersion, positioning the SDI within this broader context. The chapter identifies key gaps in the literature that this research aims to address, particularly the need for more robust and adaptable seeding metrics in dynamic river environments.

- **Chapter 3: Methodology** - This chapter details the experimental design, data collection methods, and analysis techniques used to develop and validate the SDI. It includes a description of the numerical simulations and real-world case studies that underpin the research. The chapter also discusses the rationale behind the chosen methodologies, ensuring that they are robust enough to address the identified research gaps.

- **Chapter 4: Seeding Density Index (SDI) for Improved Image Velocimetry Analysis** - This chapter explores the impact of SDI on PTV accuracy through numerical analyses, presenting findings related to seeding density, dispersion, and their correlation with PTV error. It aims to demonstrate how optimising these seeding metrics can lead to significant improvements in flow measurement accuracy, particularly in challenging environments.

- **Chapter 5: Impacts of Seeding Density and Dispersion on Discharge Results of PTV Methods - A Case Study** - This chapter applies Post-Processed SDI metrics to real-world scenarios, analysing the relationship between Post-Processed SDI and discharge accuracy in various river conditions. The findings serve to validate the practical relevance of Post-Processed SDI, highlighting its utility in diverse hydrological contexts and its potential for widespread adoption in river flow monitoring.

- **Chapter 6: Using SDI to Optimise the Cross-Sectional Positioning for PTV Analysis - Numerical Study** - This chapter investigates spatial variability in seeding metrics and their impact on PTV accuracy. It proposes strategies for optimal cross-sectional placement using Post-Processed SDI, contributing to the development of best practices for the application of image velocimetry in different hydrological settings.

- **Chapter 7: Synthesis: Post-Processed SDI and its Influence on PTV Measurements** - Summarises the key findings from the previous chapters and discusses the advantages and limitations of Post-Processed SDI in PTV workflows. This chapter provides a critical evaluation of the research outcomes, offering recommendations for the practical implementation of Post-Processed SDI in river flow monitoring and its integration into existing hydrological models.

- **Chapter 8: Future Research** - This chapter explores potential advancements in PTV and SDI research, suggesting directions for future studies. It identifies specific areas where fur-

ther exploration could enhance the accuracy and reliability of image velocimetry, including the integration of SDI with advanced hydrological models and the development of new techniques for assessing seeding conditions in real-time.

- **Chapter 9: Concluding Remarks** - The final chapter reflects on the research contributions and their implications for the field. It summarises the key achievements of the thesis and offers concluding thoughts on the significance of the work, particularly its potential impact on future research, policy, and practice in hydrology.

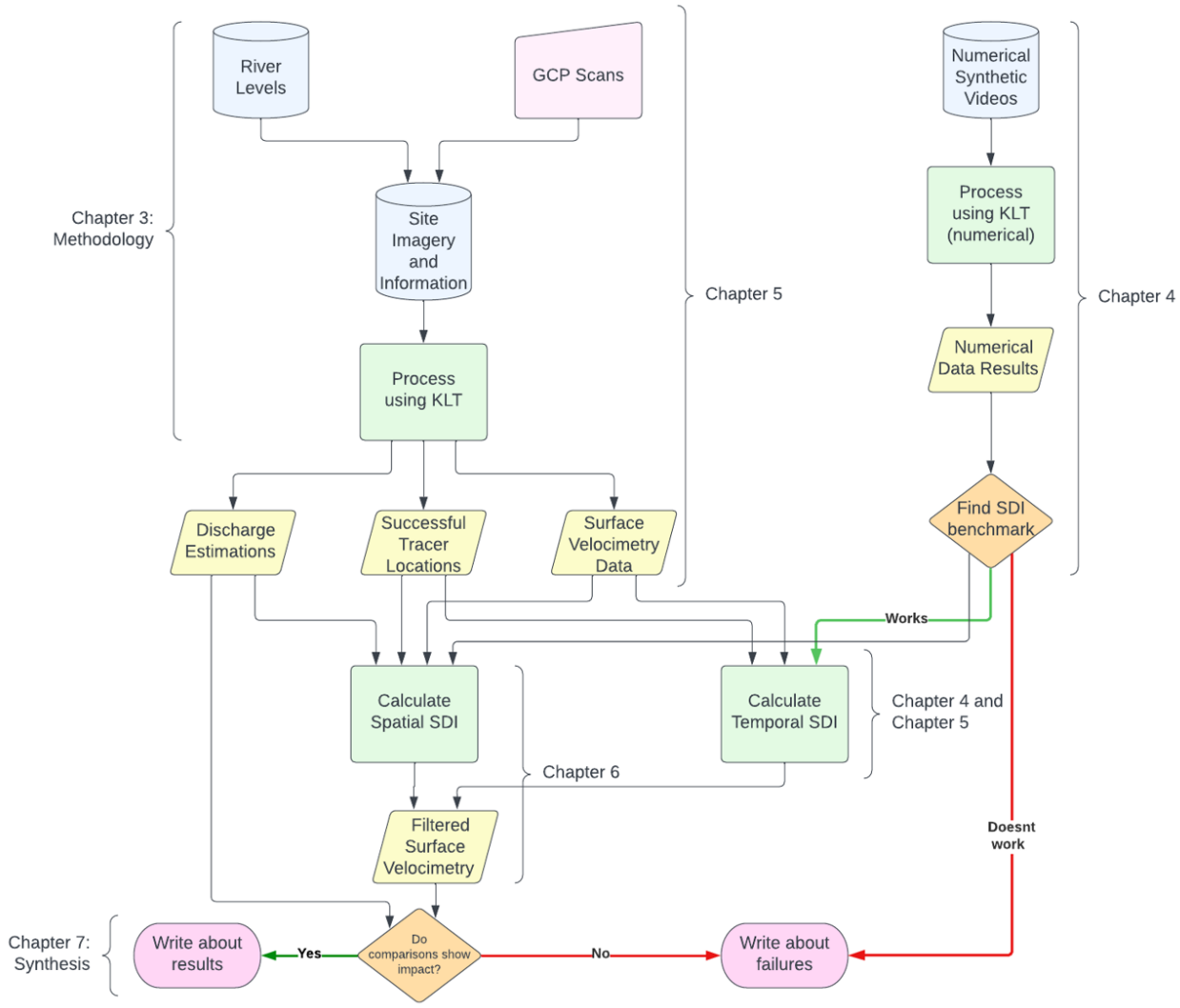


Figure 1.4: Thesis structure and process for analysing data and producing results. The figure illustrates the flow of research following on from the findings of the literature review which overarches the rest of the thesis; from Chapter 3 Methodologies through to synthesis in Chapter 7. The figure highlights how each chapter builds on the findings of the previous chapter.

Chapter 2. Literature Review

2.1 Chapter Overview

This chapter delves into the extensive body of research surrounding river flow monitoring and image velocimetry, providing a critical analysis of both historical and contemporary methodologies. River flow measurement is a cornerstone of hydrological science, playing a crucial role in global water management, climate change adaptation, and environmental protection. The accuracy of these measurements directly impacts the ability to predict floods, manage water resources, and protect ecosystems.

Despite significant advancements, challenges remain—particularly in the accurate and reliable estimation of river flows in complex and dynamic environments. This literature review situates image velocimetry within this broader context, examining how the progression from traditional methods to advanced techniques such as PIV and PTV has addressed—or failed to address—these challenges.

A central theme of this chapter is the SDI, which plays a pivotal role in enhancing the accuracy of image velocimetry. The chapter critically examines existing approaches to SDI, highlighting both their strengths and limitations, and identifies key gaps in the literature where further research is needed. By framing the discussion through the lens of SDI, this review not only evaluates the current state of the art but also proposes directions for future research that could further improve measurement accuracy.

This literature review aims not only to summarise the existing body of knowledge but also to identify areas where further research could significantly advance the field of river flow monitoring. By the end of this chapter, readers will have a comprehensive understanding of the current methodologies, the critical role of SDI in enhancing accuracy, and the potential future directions that could lead to even more reliable and precise river flow measurements. Several of these directions are explored in this thesis, particularly through the development and validation of Post-Processed SDI as a means of improving image velocimetry performance under variable seeding conditions.

2.2 Image Velocimetry Processes

2.2.1 Capture Optimisation

2.2.1.1 Ground Sampling Distance

The GSD of imagery is the distance between the centroid of two adjacent pixels (Figure 2.1). This value essentially defines the resolution of the image in real-world terms. A smaller GSD means each pixel represents a smaller area on the ground, allowing finer surface details to be resolved. The GSD of the imagery used in large-scale image velocimetry analysis is a critical consideration, with features smaller than the GSD being poorly resolved. For example, imagery with a GSD of 0.01 m/px may include features of 0.008 m length, but these would not be depicted as being any less than 0.01 m length in the imagery. Critically, if the GSD is significantly larger than the individual features present on the water surface, these features may not be visible in the imagery, and these features would therefore be unsuitable for image velocimetry purposes. Although there is no clear guidance on specific values relating to the point at which tracers are no longer visible, generally, a tracer would have to be significantly brighter than the background to dominate the overall contrast of the pixel. As a result of these factors, it is important that the image GSD (px/cm) for the proposed image acquisition settings is known in advance. This will ensure that features visible on the free surface will be adequately resolved by the camera system. In a scenario where the footage is acquired at nadir (i.e. with the camera pointing directly downward), this is governed by the focal length (Focal Length (FL); mm), sensor width (Sensor Width (SW); mm), and image width (Image Width in Pixels (IwP); pixels). These parameters determine how much ground area is projected onto each pixel, and therefore directly control the scale and clarity of the captured image. Using these characteristics of the camera sensor, and user knowledge of the desired GSD, the required height of image acquisition can be calculated (Equation 2.1; Pix4d, 2019), see Figure 2.2.

$$\text{Height (m)} = \frac{IwP \times GSD \times F}{SW \times 100} \tag{2.1}$$

The image sensor is the apparatus in the camera that converts optical imagery into an electric signal using a matrix of small potential wells (pixels) (Optics, 2021). The size of the image sensor relates to the amount of light a camera can capture, and typical security/Internet Protocol (IP) type cameras use a range between 1/4" (6.35 mm) to a 2/3" (16.9 mm) sensor (Caputo, 2010). Without a large enough image sensor, detail is lost due to a lack of capability to add detail through pixel colour/tone, or due to a low signal-to-noise ratio seen with smaller sensors (Morrow, 2021).

Subsequently, the GSD may be affected by the camera angle and the camera distance from the source. Introducing a non-nadir angle to the camera increases the length between the camera

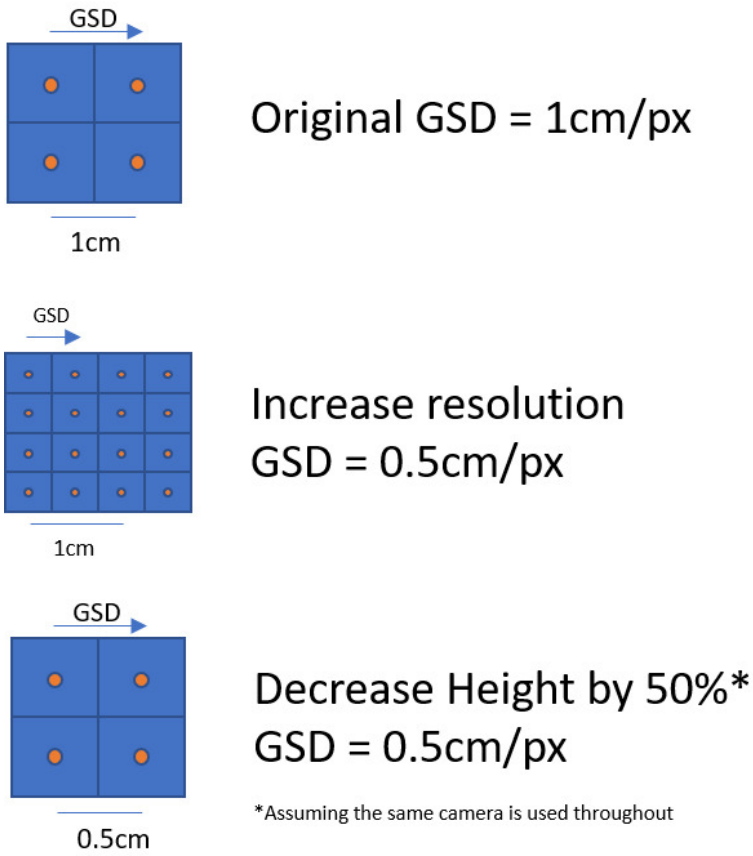


Figure 2.1: How GSD is described and can be altered using either an increase in resolution or decreasing the distance between the subject and the camera.

and the background of the image, in addition to increasing the width of the coverage. Effectively, with a shift in the pitch of the camera, it will create a trapezoidal-shaped image grid, where the background is scaled proportionally to the angle and distance from the source (Figure 2.3). This results in the GSD being variable across the FOV, and the image background being relatively poorly resolved. For this reason, the sensing of environments using oblique camera angles, particularly over long distances, may result in image acquisition where features on the water surface in the background cannot be easily detected. In instances of oblique image capture, the GSD (cm/px) can be determined using Equation 2.2, where L is a given length both horizontally (L_h; m) and vertically (L_v; m), IwP is the image width (px) (Equations 2.3–2.4), α_v is the angle of tilt seen in the roll axis (Equation 2.3), α_h is the angle of tilt seen in the pitch axis (Equation 2.4). Θ° is the angle of capture (Equation 2.5), calculated using the sensor width (SW) and the focal length (FL). These equations are implemented within *GSDCalc* (Jolley, 2021).

$$\text{GSD} = \frac{L \times 200}{IwP} \tag{2.2}$$

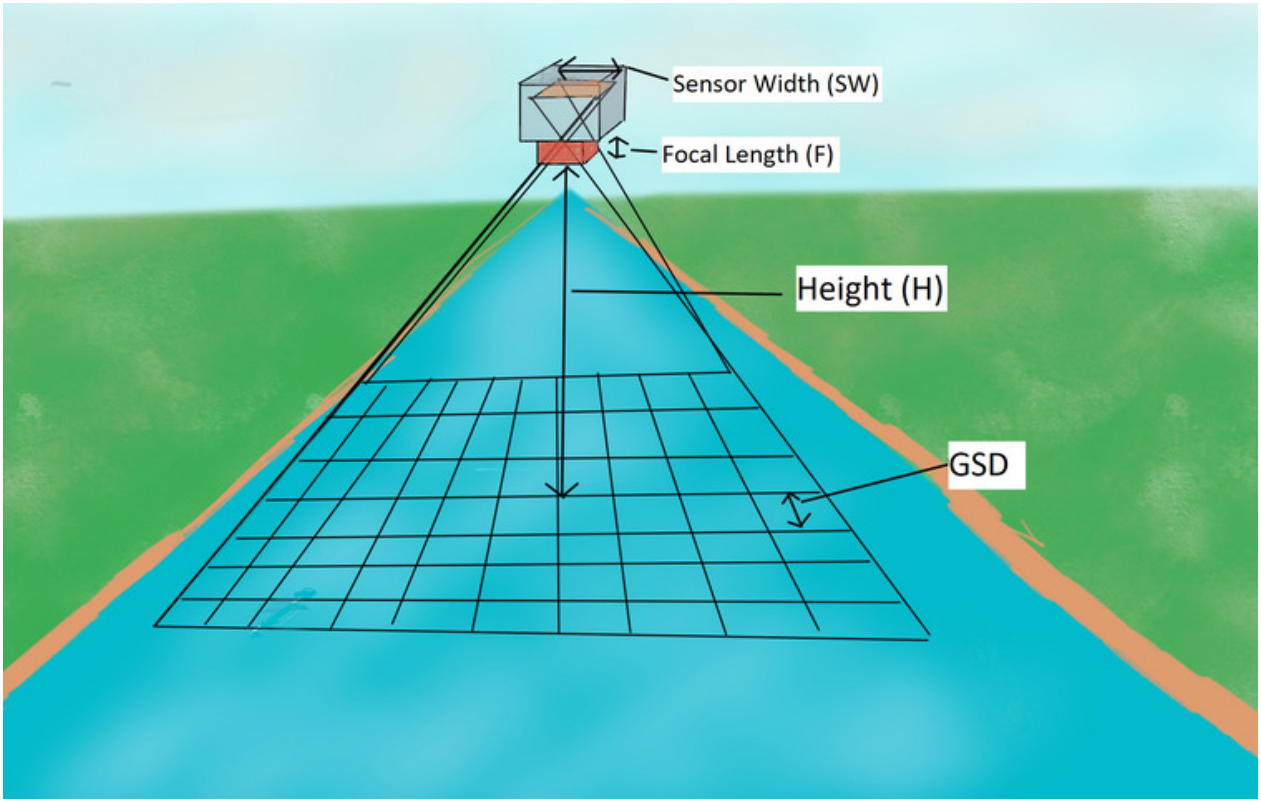


Figure 2.2: Schematic representation of GSD at a nadir angle. In this configuration, the camera is oriented directly downward (perpendicular to the water surface), resulting in a uniform and evenly distributed ground sampling distance across the field of view. The overlaid grid illustrates how each pixel covers a consistent area on the water surface. (Jolley et al., 2021)

$$L_v(m) = H \cdot \frac{\sin(\theta \pm \alpha_v)}{\sin(90 - (\theta \pm \alpha_v))} \tag{2.3}$$

$$L_h(m) = H \cdot \frac{\sin(\theta \pm \alpha_h)}{\sin(90 - (\theta \pm \alpha_h))} \tag{2.4}$$

$$\Theta^\circ = \tanh\left(\frac{SW}{F}\right) \tag{2.5}$$

When discussing camera angles, it is important to note the type of camera station in use. Camera stations are typically described as being either fixed or mobile platforms—these are discussed in Section 2.2.1.4. Due to the flexible nature of large-scale image velocimetry, a wide variety of camera angles are adopted. The fixed camera deployments described in Perks (2020) include camera angles up to 57 degrees from nadir. Alternatively, for mobile cameras, Eltner et al. (2020) suggests that a tilt angle more than 10° from nadir should be avoided where possible. Generally, for both fixed and mobile platforms, the closer the camera sensor is to nadir the better—provided that the region of interest is visible throughout, along with ground control points and static features

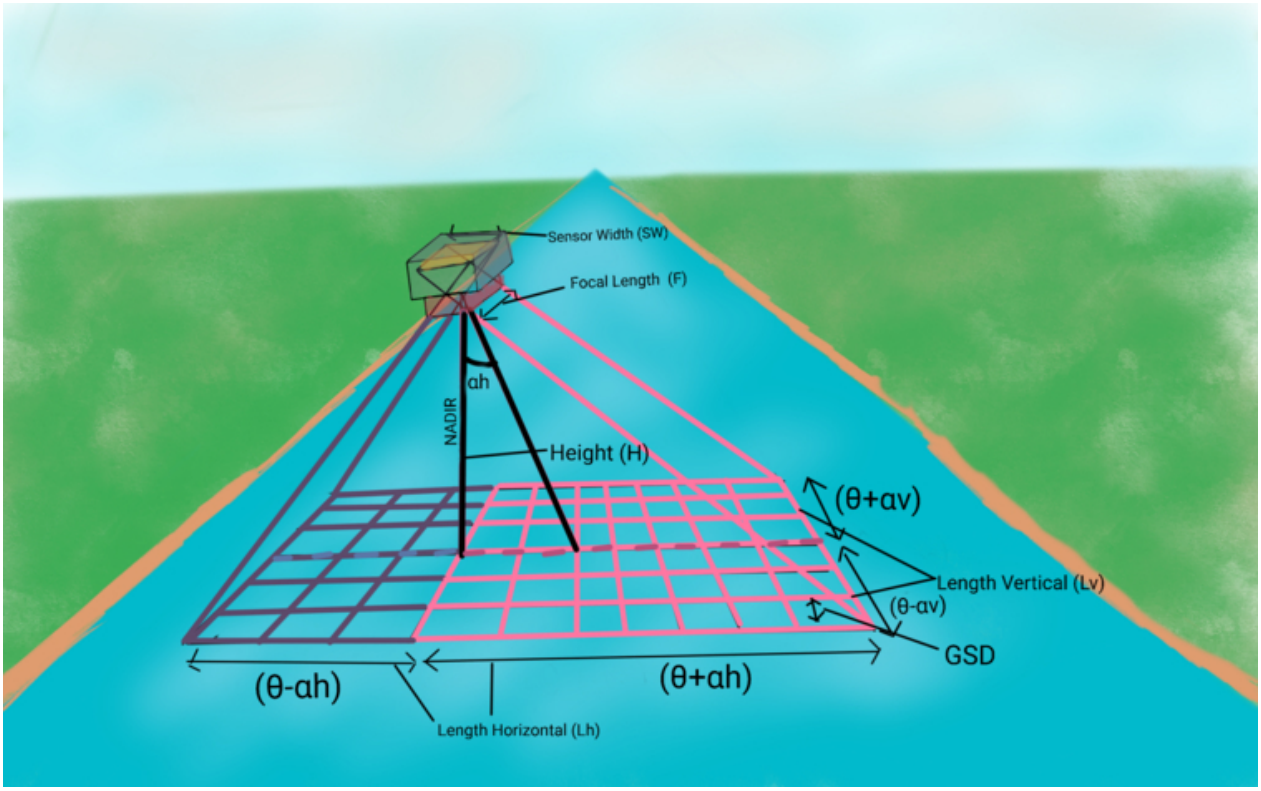


Figure 2.3: Schematic representation of GSD at an oblique angle. Tilting the camera away from nadir introduces geometric distortion, resulting in a trapezoidal image footprint. This causes the ground sampling distance to vary across the field of view (FOV), with closer areas appearing more detailed and distant areas increasingly stretched and poorly resolved. The overlaid grid illustrates how uniform pixel spacing at the sensor translates to variable real-world pixel coverage. (Jolley et al., 2021)

to enable stabilisation (when required). Finally, when installing fixed camera stations, a critical consideration is the effect of stage variation on the camera's FOV. As stage increases, the distance between the water surface and camera decreases, which can result in a reduction in the area sensed.

Camera focal length (usually given in mm) is the distance between the image sensor and the camera lens when the subject area is in focus. The smaller the focal length, the larger the area captured but at a smaller apparent size. Conversely, the larger the focal length, the smaller the area captured—but in higher detail. Generally, cameras have either prime (non-adjustable) or zoom (adjustable) lenses. It has been recommended that, independent of the lens used, the internal parameters of the camera should be established (Detert, 2020) and used to remove lens distortion effects prior to the extrinsic calibration stage (i.e. orthorectification; Section 2.2.1.6).

Finally, the GSD is greatly affected by the image resolution (i.e. number of pixels present within an image). Whilst it may seem intuitive to minimise the GSD by using the highest available image resolution, this comes at a time/power cost during image velocimetry analysis, with the benefits reaching an asymptote once the surface patterns and features in the image are adequately resolved. This has been demonstrated in lab-based studies. For example, Prasad et al. (1992) ob-

served that reducing image resolution by a factor of two resulted in only a small loss in the ability to detect tracers (equivalent to a 0.3% loss of 'good' features), while processing speed increased fourfold. Similar findings have also been observed in field settings. Analysis of low-resolution imagery (144p, 256×144) produced deviations in longitudinal velocity of only 5% relative to full-resolution imagery (1080p) (Boursicaud et al., 2016), with negligible changes in velocity results between 1280×720 and 256×144 (Leitão et al., 2018). Similarly, Tosi et al. (2020) observed that reducing the resolution of full HD images to 25% resulted in mean velocity outputs differing by less than 0.05 m/s (<10%), with a 23% reduction in computation time. Further to this research, it was demonstrated that reducing the resolution from full (1430×1080 px) to half (715×540 px) increased the number of cycles that can be performed on a single charge by 30% when using a 5000 mA/h battery (Livoroi et al., 2021). However, a formal evaluation of the influence of image resolution on accuracy across spatial scales is generally lacking. The absence of consensus regarding optimal resolution has led researchers to rely on intuition to define appropriate configurations (e.g. Dal Sasso et al., 2018). Ultra-HD and 4K videos could be used to enhance tracer visibility (e.g. when sensing over long distances or oblique angles), and to enable the detection of smaller tracers (Section 2.2.3). However, the processing power required to analyse higher definition videos remains a constraint. In instances where imagery has been acquired at very high resolution (e.g. Ultra-HD and 4K), it may be beneficial to sub-sample the imagery to a lower resolution to improve processing speeds, provided tracers remain clearly visible.

2.2.1.2 Capture Frame Rates

Commercially available cameras generally have default frame rates that are typically more than sufficient for capturing image sequences required for image velocimetry purposes (i.e. > 5 Hz). Given that the acquisition frame rate is not usually a constraint, the most important aspect is to ensure that the frame rate is consistent throughout the duration of acquisition (Detert, 2020; Perks, 2020), and that it matches the value present within the video metadata. This can be determined through analysis of the time stamps embedded within the on-screen display (Detert, 2020). This is generally configurable to be visible on footage acquired by IP camera systems.

IP cameras are digital cameras which use networked connections to transfer data and can allow the user to access live imagery remotely (Safesite, 2021). Often, these types of cameras are connected to a data logger which can receive, store, and send the imagery. A limitation with some data loggers can be their processing power. For instance, frames can be lost from sequences if using a logger and there is insufficient CPU power. This impacts the time consistency of frames, something that is vital to accurately using image velocimetry.

Complications with these methods can also arise from a lack of bandwidth. Increasing the frame rate has been shown to proportionally increase bandwidth usage (1 fps = 0.179 Mb/s, 10 fps = 4x more than 1 fps, 30 fps = 7x more than 1 fps) (Team, 2021). The relationship between frame

rate and bandwidth is not linear due to the way that IP cameras capture frames. IP cameras capture either an I-frame (*initial* / full frame) or a P-frame (*predictive* frame). I-frames capture the entirety of the FOV and are used as a reference frame, whereas P-frames only capture changes in an image in relation to the I-frame (Ace, 2013). The report by Ace (2013) also suggests that increasing the I-frame rate from 1 per second does not necessarily greatly improve image quality, but increasing the time between I-frames can significantly reduce image quality.

2.2.1.3 Managing External Environmental Conditions

The performance of image velocimetry analysis may be influenced by external environmental factors that cannot be easily controlled. These factors include the presence of wind, rain, varied lighting, fog, falling snow, and glare. The impacts of wind are most acutely seen during times of low flow, when wind shear may produce a surface expression that is independent of flow velocity (Coz et al., 2010). A recent development on the impact of wind demonstrated that, on average, surface velocity deviates by 3% and can reach a maximum of 8%, most typically when wind opposes flow direction and when its magnitude is significant relative to the flow (Peña-haro et al., 2020). The impacts of precipitation are not fully understood but have been reported to blur imagery, ultimately interrupting the processing of data (Fujita et al., 2007). Inhomogeneous lighting and glare on the river surface generate the false impression of colour gradients across the area of interest. This variation in brightness may cause blind spots and the loss of tracer visibility (Hauet et al., 2008; Zhang et al., 2013). Fog impacts velocity results by severely increasing the noise on the surface of the river, as it hinders the traceability of surface patterns; acquiring imagery during foggy conditions is generally to be avoided where possible (Zhang et al., 2013). Finally, for falling snow, there is little research on the true impact that it has on velocity results. However, in instances where large-scale PIV has been used on videos with falling snow present, authors tend to disregard data due to the scatter that it creates in results (Daigle et al., 2013).

The relative impact that these external environmental conditions have on the quality of image velocimetry results is currently unpredictable, and the overall impacts are still largely unknown. Where there are instances of noticeable snow or fog, due to the lack of evidence suggesting otherwise, such data should be disregarded. Secondly, the exposure of a monitoring location to variations in wind, precipitation, and glare should be minimised where possible through adjustments in the acquisition methods adopted. For example, in instances with high levels of glare, the use of a polarising filter may be beneficial. Alternatively, near infrared (Near Infrared (NIR)) cameras may act to reduce the severity of brightness differences and may visualise the tracers more prominently. However, it should be noted that the application of NIR sensors in some environments may lead to the loss of visible tracers due to attenuation of the NIR signal by the water (Zhang et al., 2013). Whilst future work will seek to provide correction factors for observable external environmental conditions (e.g. wind shear), these relationships have yet to be established, so where their effects

are visually influential, usage of the footage should be minimised where possible.

2.2.1.4 Choice of platform

Fixed stations allow a specific area of river to be analysed, providing a time-series of images that can be used to determine surface velocities. Usually, fixed stations are commissioned in order to monitor river flows, and to develop and extend discharge rating curves (e.g. Hauet et al., 2008). There are several ways that fixed stations can operate in regards to the capture and processing of data. The study from Tosi et al. (2020) evaluates methods of capturing and processing data in situ to reduce the amount of data that is required to be sent via external networks. This can be useful where stations are in remote locations and affordable networks (e.g. mobile networks), are scarce. Alternatively, as seen in the case studies of Perks (2020), networked cameras (as discussed in Section 2.2.1.2) can be used to stream imagery across a network to be processed either near real-time or at a later date.

Regardless of the proposed fixed station processing method, limitations include the inability to alter the field-of-view without recalculation of the coefficients for converting pixel space to real world distances (see Section 2.2.1.6). Resultantly, there is the potential for the site configurations being optimal under certain flow conditions, but unsuitable during others (e.g. during bypass flows, out-of-bank flows, etc.) Additionally, supplementary information is required in order to properly scale the imagery as a result of fluctuating water levels. This is typically in the form of river stage measurements which enable the distance between the water surface and the camera to be accounted for.

Alternatively, mobile platforms may be used to acquire footage for image velocimetry purposes. An example of this is the use of Uncrewed Airborne Vehicles/Systems (UAVs/UASs), or helicopters in fluvial environments that are hard to reach, dangerous to the operator, or where the inundated extent is greater than the field-of-view of the fixed monitoring station. These approaches have been particularly beneficial for understanding turbulent flows in rivers for sediment transport (e.g. Thumser et al., 2017), capturing flow data at ungauged sites (e.g. Kim et al., 2008), and determining river velocities during periods of high-flow (e.g. Perks et al., 2016). Additionally, this has opened up the possibility of large spatial extents being observed rapidly (e.g. Perks, 2020). Generally, using a mobile platform involves similar processes to those of fixed stations, but requires some extra stages in the pre-processing stage such as image stabilisation (see Section 2.2.1.5). A key advantage of using mobile platforms for image capture over fixed stations is that many of the optimisations listed in Section 2.2.1 could be met (e.g. camera angle being nadir, flexible fields of view, and spatially consistent GSD).

Although UAS is currently the main focus of mobile methods, it is important to note that there are other methods of mobile image velocimetry. Prior to UAS being reasonably attainable, mobile methods could be conducted using telescopic poles, as demonstrated in Dramais et al. (2011) and

Coz et al. (2010). Secondly, an important revelation of mobile image velocimetry is the use of software on mobile phones (Hain et al., 2016; Caldwell et al., 2019). Lab based studies on the use of mobile discharge apps (e.g. DischargeApp) show that the methods can reproduce discharges without the need of illumination within a 15% error 87% of the time (hand-held), and 100% of the time using a tripod (Carrel et al., 2019).

A more recent and promising advancement is the use of satellite imagery as a capture method, but is still in its infancy of development. There are limitations to using satellite data, such as the limitation of the GSD that is achievable by satellite imagery and whether it is capable of detecting and tracking features on a river surface. For reference on image quality, Kääb et al. (2019) uses satellite imagery to track river-ice and water velocities, and does so with a resolution of 3m using PlanetScope satellite imagery (Planet, 2021), capturing each frame at 90 s intervals. Satellite data stores (such as PlanetScope), are capable supplying high-resolution image sequences (as seen with Kääb et al. (2019)), and videos of less than or around 1m resolution (typically nadir). Video footage is usually only captured in the panchromatic band of the central detector and at a frame rate of between 30-120FPS. It is still yet to be seen how well these datasets can provide river flow gauging, and much more research is required into the feasibility of satellites before it can become a recommended method of remote sensing using image velocimetry.

2.2.1.5 Stabilisation

Image stabilisation is required due to the inevitable movement of mobile platforms (e.g. Bolognesi et al., 2017; Perks et al., 2016), and random movements of fixed cameras from vibrations due to influences such as wind or traffic (when fixed on a bridge) (Perks, 2020). Figure 2.4 demonstrates how images are impacted by stabilisation. Borders of the full initial image are cropped out by the algorithm in each frame (shown as the black boxes around the edges of the image) to only show the sections that are constant (shown in the green overlapping of imagery). Here we can see transformations in both shift and scale due to platform movement. Modern methods of stabilisation may use GPS locations of the camera and/or stable features in the region of interest to create a stable frame of reference for subsequent analysis (Ljubičić et al., 2021).

Stabilisation takes into account the effect of image translation, rotation, and scaling. Translation of the scene is a movement in the image within the xy plane (parallel to the ground). Rotation is a movement that causes a tilt in any direction of the camera (yaw, pitch, and roll). Scaling is impacted by change in platform elevation (z-direction), resulting in changes to the representation of pixel sizes in real-world units. When running feature detection algorithms, static points are used and are either detected corner points or clearly distinguishable stationary objects. For a full projective transformation, a minimum of four pairs (eight features) are required (Szeliski, 2006) to match the degrees of freedom (three pairs are required for affine transformations). Stabilised frames are often referenced to either the initial frame or a subsequently stabilised frame (every n^{th}

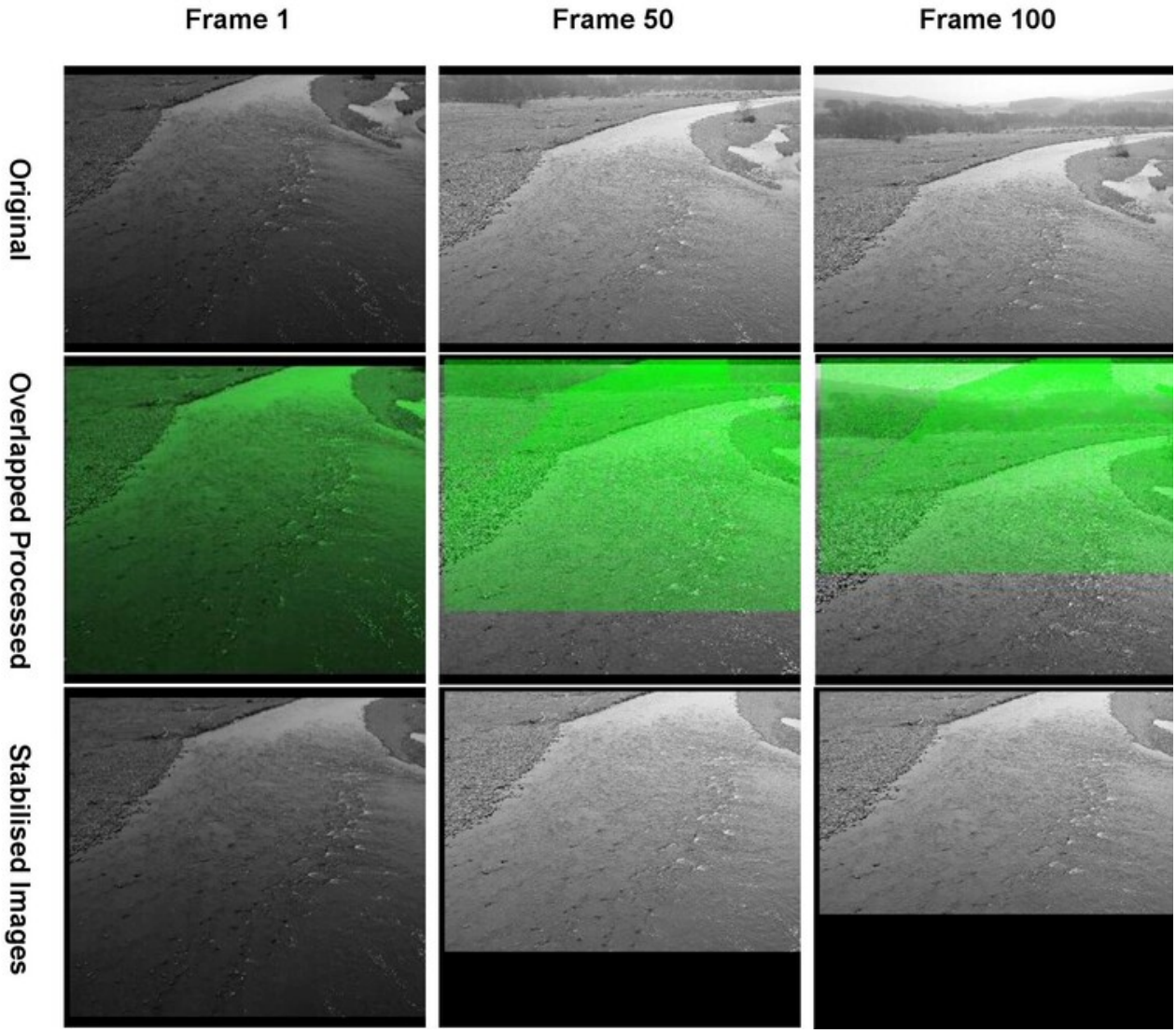


Figure 2.4: Drone movement shown by overlapping stabilised frames onto original frames. The green mask seen on the processed row highlights where the stable image is within frame, with the final stabilised images cropping all unstable edges. (Jolley et al., 2021)

frame of a series). This may be achieved using a 3D stabilisation technique (e.g. structure-from-motion; Structure-from-Motion (SfM)), or more commonly a 2D motion estimation technique (e.g. single-step discrete Fourier transform algorithm (Sicairos et al., 2008)), whereby it is assumed that the moving camera is perpendicular to the region of interest and undergoes only changes in the horizontal plane (movements in translation and yaw), and hence planar transformations are sufficient (Rodriguez-Padilla et al., 2019).

Stabilisation techniques can be manual or automatic. Manual methods rely on a selection of

static reference points which are then automatically processed to determine displacement between frames (Rodriguez-Padilla et al., 2019), while automatic methods select features and then track displacements using binary feature matching techniques (e.g. Harris Corner Detection and FAST) (Liu and Cheng, 2008; Mingkhwan and Khawsuk, 2017; Muja and Lowe, 2012). A general process for stabilisation techniques is: breaking down videos into sequential frames, selecting static features manually or automatically (i.e. feature detection), feature matching and outlier rejection, derivation of a transformation function, and image reconstruction and stitching (Tareen and Saleem, 2018). The coordinate grid can either be fixed or be updated throughout the process. Whilst fixed coordinate grids are typically used, the grid may need to be updated over time if there is excessive movement (e.g. translation of the platform). Grids may be altered through the use of similarity, affine, or projective transformations. Accurate transformation depends on the number of point pairs available in the image. Similarity transformations require shifts in the plane parallel to the ground and can result in translational, rotational, and scaling transformations. For these, a minimum of two point pairs are required. Affine transformation includes the same shift changes as similarity with the addition of shear transformations. This requires three point pairs. Finally, for a full projective transformation, which includes all of the above as well as perspective deformation, four point pairs are required (Ljubičić et al., 2021).

For fixed cameras, stabilisation is not necessarily required unless the camera experiences movement (e.g. oscillations generated by vibrations or wind). Detert and Weitbrecht (2015) observed that residual motion of 1 px/s caused by camera shake produced an apparent ground velocity of at least 0.02–0.03 m/s. More recently, Detert (2020) observed that the lack of stabilisation of image sequences acquired using a telescopic pole produced a shift in both image axes by up to ±4 pixels per time step (equivalent to 2 cm in this instance). This unaccounted-for movement may substantially impact velocity outputs, particularly under low-flow conditions, where the magnitude of camera movement is more significant relative to the actual flow velocity observed in the frame. When using mobile platforms to acquire footage for image velocimetry purposes, unstabilised image sequences may be a major contributor towards error. An example of this is presented in Detert (2020), where a re-analysis of previously published studies demonstrated that accounting for residual movement reduced errors by 20–30%.

2.2.1.6 Orthorectification

Following stabilisation of the image sequence (when required), orthorectification needs to be carried out, unless the image is being captured at nadir and image distortion has been removed. This seeks to remove perspective distortion and manipulate the image to represent accurate real-world distances. Orthorectification manipulates an image such that all pixels are of equal real-world length, so that when using a camera at an oblique angle, a pixel in the foreground is equivalent to a pixel in the background.

Orthorectification relies on Ground Control Point (GCP)s to calibrate known coordinate points in the field of view (Tauro et al., 2014). GCPs that have known real-world coordinates are established in the frame of view, and these are paired with the pixel location of these GCPs. 2D transformations can be made when the GCPs are located on a similar plane to the surface of the river. 2D transformations have an 8-parameter plan-to-plan perspective projection, which requires at least four GCPs at the river free-surface elevation (Detert, 2020; Detert et al., 2017; Detert and Weitbrecht, 2015; Fujita et al., 1998). 3D transformations are made where there are large variations in elevation between GCPs and the river surface. If this is the case, the orthorectification matrix will have 11 unknowns and can only be solved with six or more GCPs (Jodeau et al., 2008). It has been suggested that a minimum of four GCPs should be used in or immediately around the region of interest to best orthorectify 2D imagery captured orthogonally to the river surface (Detert, 2020; Detert et al., 2017; Detert and Weitbrecht, 2015). However, the reliability of orthorectification can only increase with the number of accurate GCPs used. An increase in GCPs increases the redundancy of the orthorectified system, improving the reliability of the results.

The process of orthorectification can either be explicit or implicit, i.e., transformations can either be applied to the raw footage (explicit) or to the vector fields (implicit). Higham and Brevis (2019) suggested that orthorectification of the velocity vector field, rather than the imagery, is more effective in most cases—more specifically with PIV examples. The smoothing of data is a process where the extremities of results are normalised and brought closer to the average. When footage undergoes PIV analysis, vectors are created using an average of the interrogation area surrounding them. This process of using average values for vectors inherently smooths data, reducing the impact that spurious/outlier tracer velocities have on the overall results. If orthorectification is applied after PIV analysis, then any spurious vectors that have been smoothed due to the averaging of the area will have less impact on error associated with converting pixel size to real-world lengths, and consequently, velocities. Alternatively, if this is done explicitly, then applying transformations to erroneous velocity values can exaggerate them, reducing accuracy. Conversely, explicit orthorectification has the advantage of ensuring each pixel has the same real-world dimensions prior to processing (Perks, 2020). An example of explicit orthorectification can be seen in Figure 2.5.

2.2.1.7 Image Manipulation

Image manipulation is the process of altering the properties of the acquired images with the aim of reducing interference (e.g. glare, visibility of the river bed, environmental impacts such as wind and rain) and enhancing the visibility of tracers. The first step in the image manipulation process is the conversion of multi-band imagery into single-band imagery (e.g. Dobson et al., 2014; Fujita et al., 2007). However, this is not required when footage is captured using a grayscale camera (e.g. Patalano et al., 2017), or thermal camera (e.g. Kinzel and Legleiter, 2019). The conversion of multi-band imagery to grey-scale is achieved by eliminating saturation levels and hue, keeping

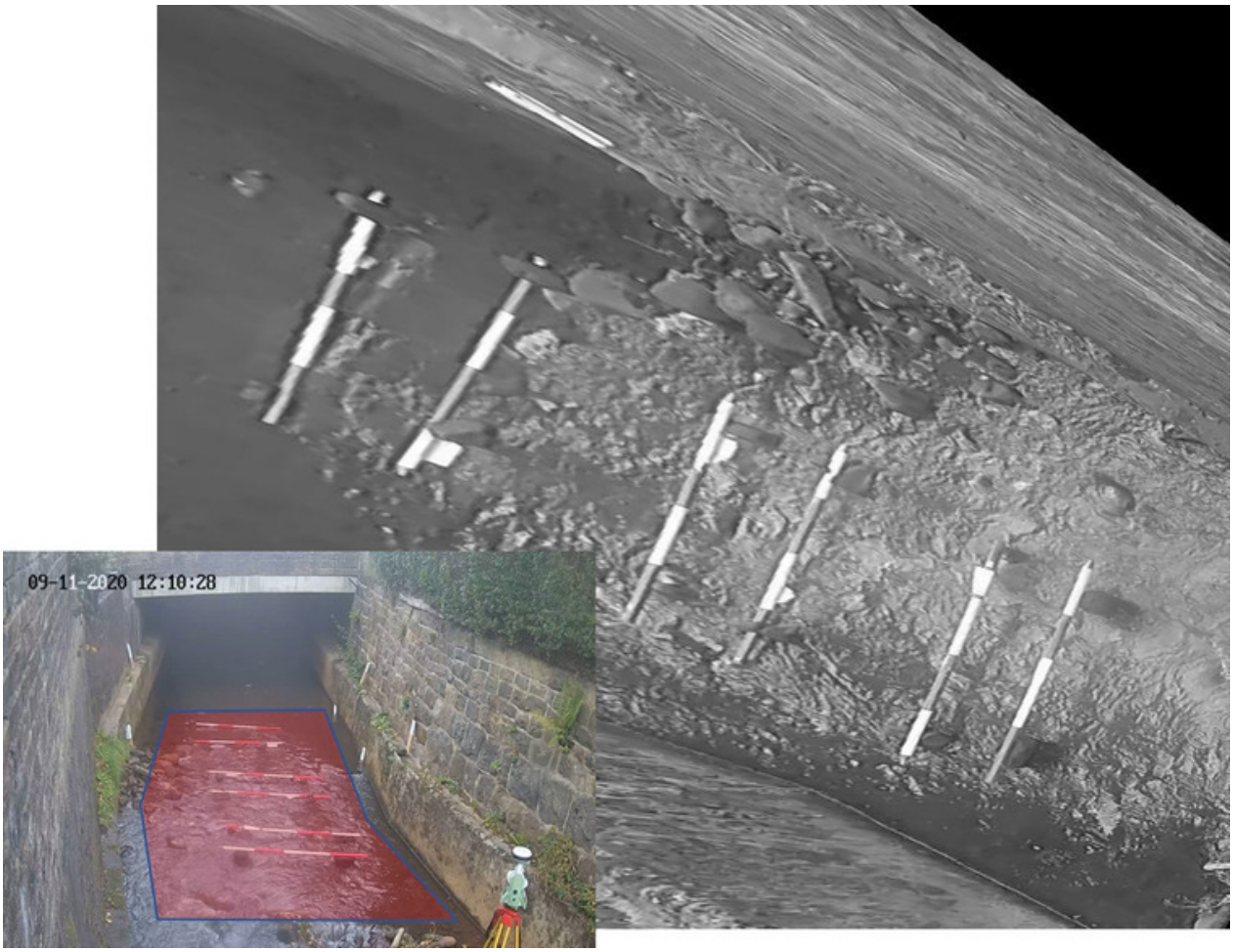


Figure 2.5: Example of an original image (bottom left) of a river surface in Todmorden, UK, highlighting in red the region of interest selected by the user, followed by the orthorectified image acquired while carrying out KLT-IV analysis (Perks, 2020). (Jolley et al., 2021)

only levels of luminance (Perks, 2020). Subsequent image manipulation is optional but may be beneficial.

Frequently used image enhancement techniques include: intensity normalisation, histogram equalisation, contrast-limited histogram equalisation (Contrast Limited Adaptive Histogram Equalisation (CLAHE)), and binarisation, which are all further explained below (Thielicke and Stamhuis, 2014; Inc., 2020). One of the most important processes for most image velocimetry techniques is to enhance imagery through contrast enhancement steps (Dellenback et al., 2000). Improving the contrast of images helps tracers stand out more in comparison to their environment, making tracking more effective and increasing displacement peak detectability, ultimately improving velocity fields (Deen et al., 2010). Figure 2.6 highlights the process of typical image processing carried out in PIV and PTV methods. Some of these methods were used in the examples seen in Figure 2.7.

Intensity normalisation spreads out the contrast histogram of an image such that a user-defined percent of the image is saturated in the high and low intensities. For footage where tracers are barely

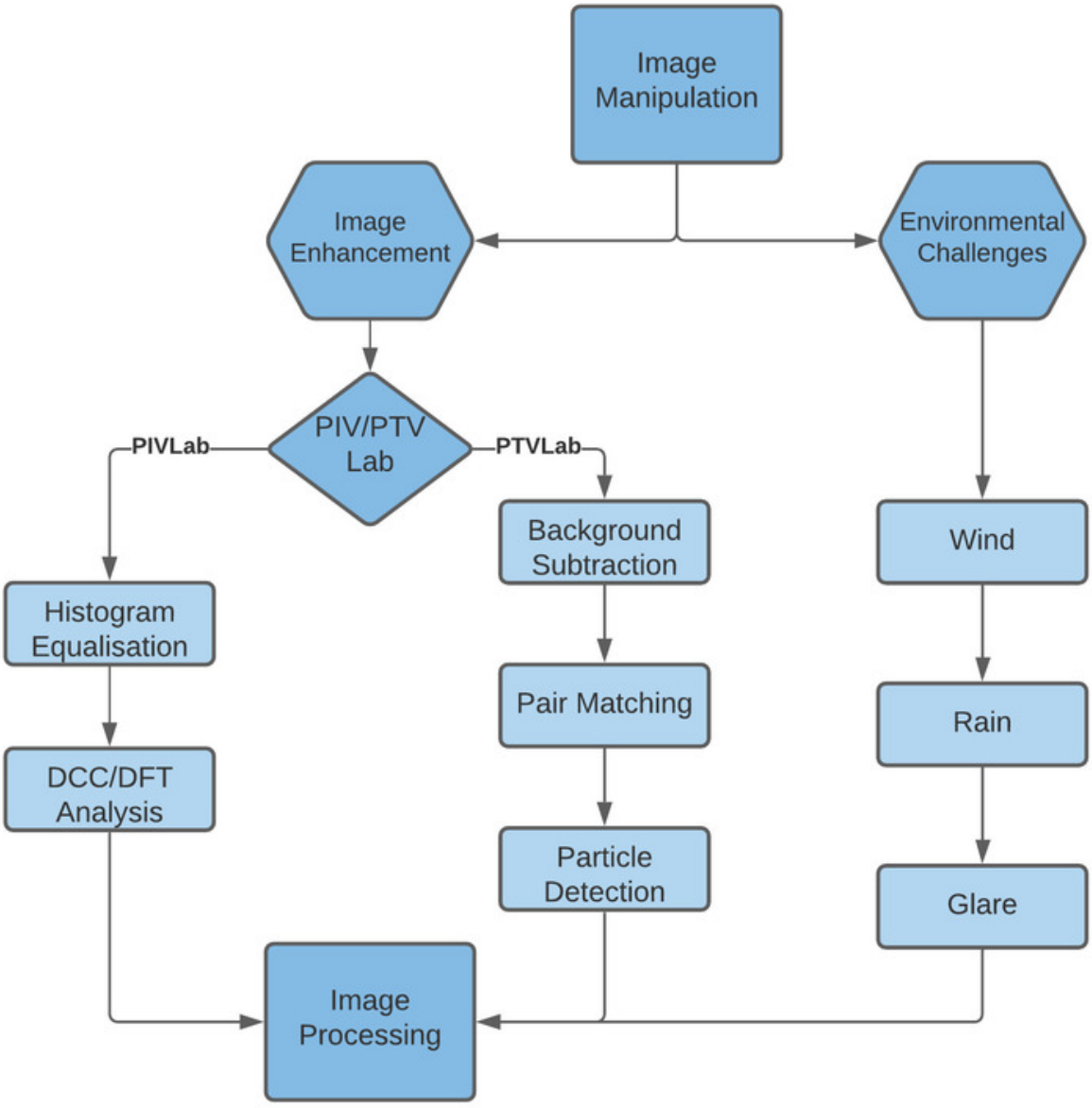


Figure 2.6: A remodel of the Patalano et al. (2017) study, showing a flowchart for typical image processing sub-sequences with either PIVlab or PTVlab. This version has been adapted to include an additional stream addressing environmental challenges, such as glare, fog, rain, and snow, which may influence image quality and tracer visibility during pre-processing. (Jolley et al., 2021)

distinguishable, normalisation may improve the contrast of the colours across the image. Histogram equalisation is the process of enhancing contrast by averaging out the brightness variation across the band. It increases the range and standard deviation of colour histograms and introduces a larger statistical range (Bora, 2017). This has been shown to be effective in situations where a colour band shows a cluster of contrast levels (Fujita and Aya, 2004).

Image binarisation typically uses threshold algorithms to split histograms into two, sometimes

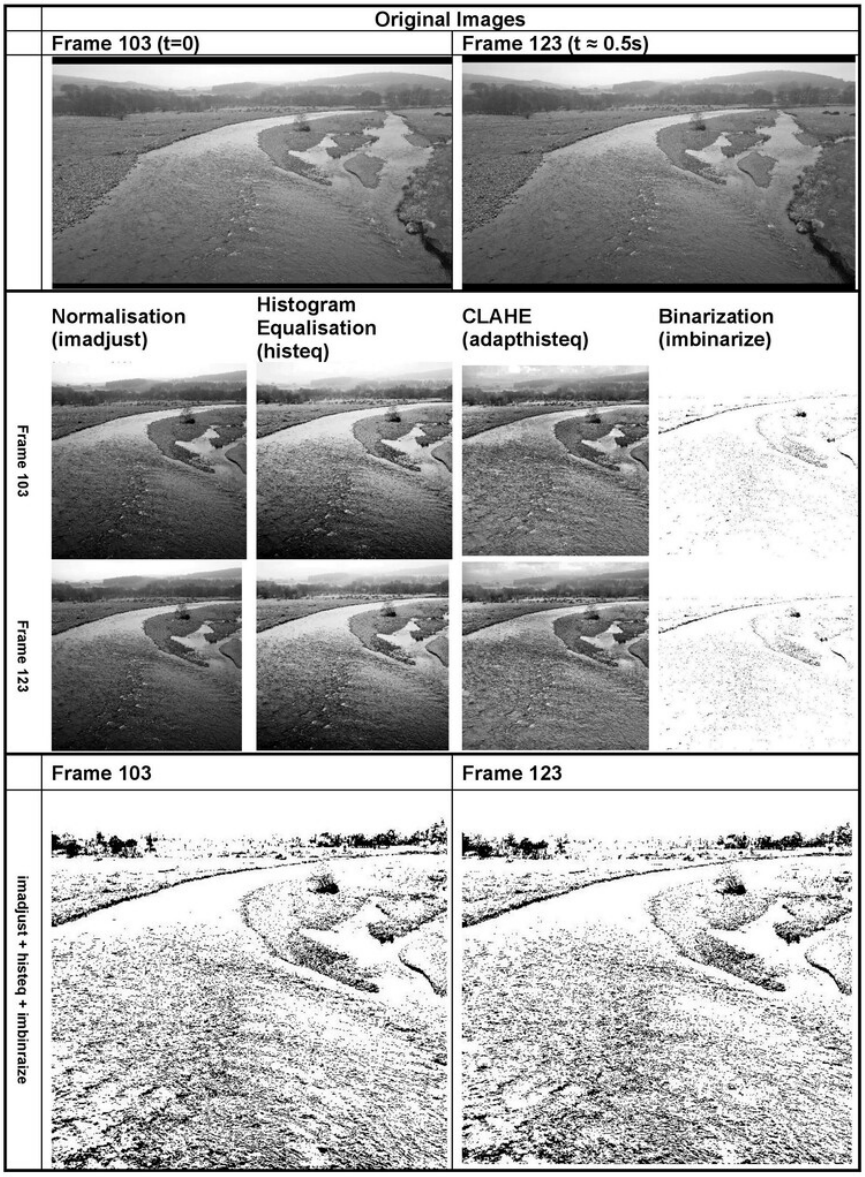


Figure 2.7: A series of image manipulation processes performed in Matlab using frames from the same video file. Note the amount of information in the binarised images if normalisation and histogram equalisation is performed prior. This shows that there are cases where more than one method of pre-processing can improve the amount of data that is traceable by programmes. (Jolley et al., 2021)

using several sub-processes such as background detection and edge detection (Malepati, 2010) to ensure foreground textures stand out as much as possible against their backgrounds (Tensmeyer and Martinez, 2020). This can be especially useful when, despite all previous efforts, tracers are still not clearly distinguishable from their background and surroundings. To improve the impact of all image manipulation processes, it is recommended that footage limits the amount of unnecessary imagery in frame and focuses on the ROI to ensure that the stretch of the normalisation process is applied primarily to tracers and the water surface, rather than surrounding vegetation.

Should the background of the image or river bed be too prevalent in imagery, and if there is a

bias error towards zero displacement, then it is advised that it is removed. To do this, it is possible to use the double-frame background removal process (Honkanen and Nobach, 2005; Patalano et al., 2017). Subsequent frames are analysed, and anything that remains stationary between the two frames is defined as background and noise, and therefore can be removed from the image. This will leave only the tracers that have been displaced. Detert and Weitbrecht (2015) makes a point of applying numerous methods of manipulation to achieve the clearest possible tracers. The study uses grey-scaling, applies a Gaussian filter to remove background noise (which helps sharpen edges), sets the intensity of pixels below a certain limit to zero, and finally performs CLAHE.

To summarise these findings, there is a clear generalisation of processes for image manipulation and pre-processing of videos for image velocimetry. As a minimum, images should be converted to a single-band image (e.g. grey-scaled) and cropped to the ROI to reduce unnecessary data processing and noise where possible. If tracers are not clearly distinguishable from the surface throughout the video, imagery should be normalised to highlight areas of most intense light and dark, and equalised to further distinguish the average levels of brightness seen across the image. Should this not be enough and the background or bed of the river is still overwhelming the tracking features, Gaussian filters can be applied to decrease image noise and sharpen edges, or background removal can be used to remove the background altogether, followed by a binarisation of the image in an attempt to isolate the tracers.

2.2.1.8 Flow State

Steady flow is used to describe fluid properties that remain constant with time, while unsteady flow does not. In the case of open channels where velocity is the property in question, we must look at the rate of change of velocity with respect to time, also known as acceleration. For steady flow, we require that $\frac{\delta v}{\delta t} = 0$, whereas for unsteady flows $\frac{\delta v}{\delta t} \neq 0$. One of the core assumptions of Euler's equation of motion is that of steady flow (Euler, 1756). Eulerian motion and PIV focus on a set of known locations of flow and represent an average of a body of fluid through a known location at a specific time (Durst et al., 1984). Although this average can potentially represent useful analysis of a body of fluid regarding average flow velocity for discharge estimation, challenges arise when sections experience multi-dimensional acceleration, as variation in velocity means the steady state assumption is not met.

Lagrangian motion and PTV do not encounter similar issues regarding flow steadiness because their foundations are built around calculating the particle's position at any given moment in time (Durst et al., 1984). These conditions are typically assumed as reasonable for many applications of PIV, as the technique tends to analyse two consecutive images with only a minor time-step.

2.2.1.9 Feature Detection and Tracking Schemes

PIV and PTV adopt differing principles for the determination of flow velocities. PIV uses an Eulerian understanding of flow motion, using dimensions of length along the river as search areas, utilising tracers or visible patterns that pass through or along these sections to calculate instantaneous velocity vectors for each area. Conversely, PTV uses the Lagrangian approach to calculate flow velocity, focusing on individual particles of flow visible on the surface and tracking their movement through space.

PIV utilises search and interrogation areas within an image to obtain particle displacements (Figure 2.8). Small window interrogation areas are tracked within larger search areas, and the centres of the interrogation areas are measured in terms of distance and divided by the time between frames to produce an average velocity over that search area (Muste et al., 2008). This approach has been shown to be capable of producing highly accurate results (e.g. Creutin et al., 2003; Muste et al., 2008). Given that a collection of individual tracers (surface patterns) is used to infer displacement, this approach is less sensitive to the transformation of individual features. However, inhomogeneity and discontinuity of tracers are critical issues that may negatively affect the quality of PIV analysis. In these instances, PTV techniques may perform better (Tauro et al., 2016).

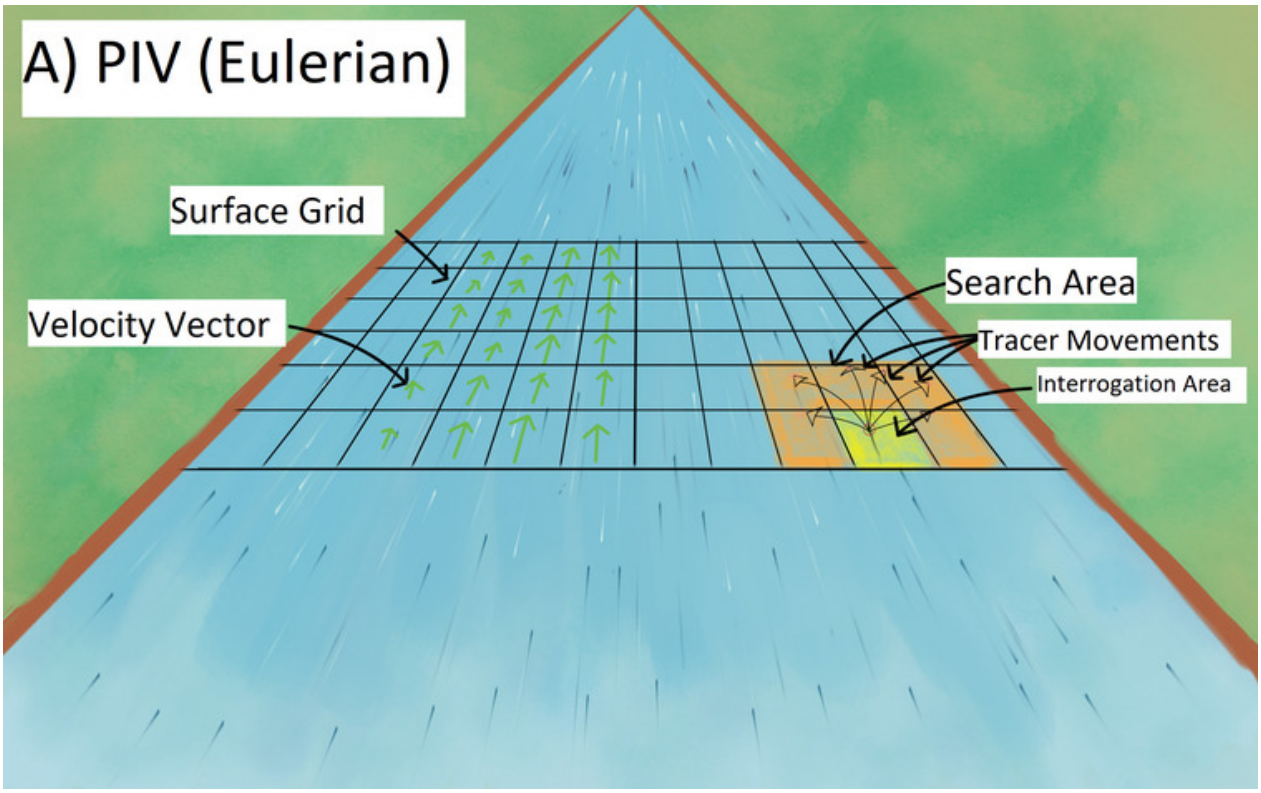


Figure 2.8: Schematics of general PIV (A) mechanics (Jolley et al., 2021).

PTV-based approaches (Figure 2.9), rely on tracking individual particles along a long-profile. This technique has been shown to perform well under low seeding density conditions (Lloyd et al.,

1995; Tauro et al., 2017). However, analysis may be adversely affected in instances where tracers change shape, size and from time-to-time disappear from frame. The greater number of tracers that are successfully tracked, the higher the probability of producing an accurate representation of the surface velocity. However, as the number of tracers increases, the required processing time/power also increases. The presence of very high tracer densities may also increase the ambiguity of the individual tracer detection and tracking process (Zhang et al., 1997). There are a range of particle detection and tracking algorithms available for PTV. For feature detection, Good Features to Track (GFTT) (Shi and Tomasi, 1994), FAST (Rosten and Drummond, 2006), and SIFT (Lowe, 1999). For tracking algorithms, cross-correlation can be used, but there are also others such as Kanade-Lucas-Tomasi (KLT) (Perks, 2020; Tomasi, 1991), and variations of the Nearest-Neighbour algorithm (e.g. Tauro et al., 2019).

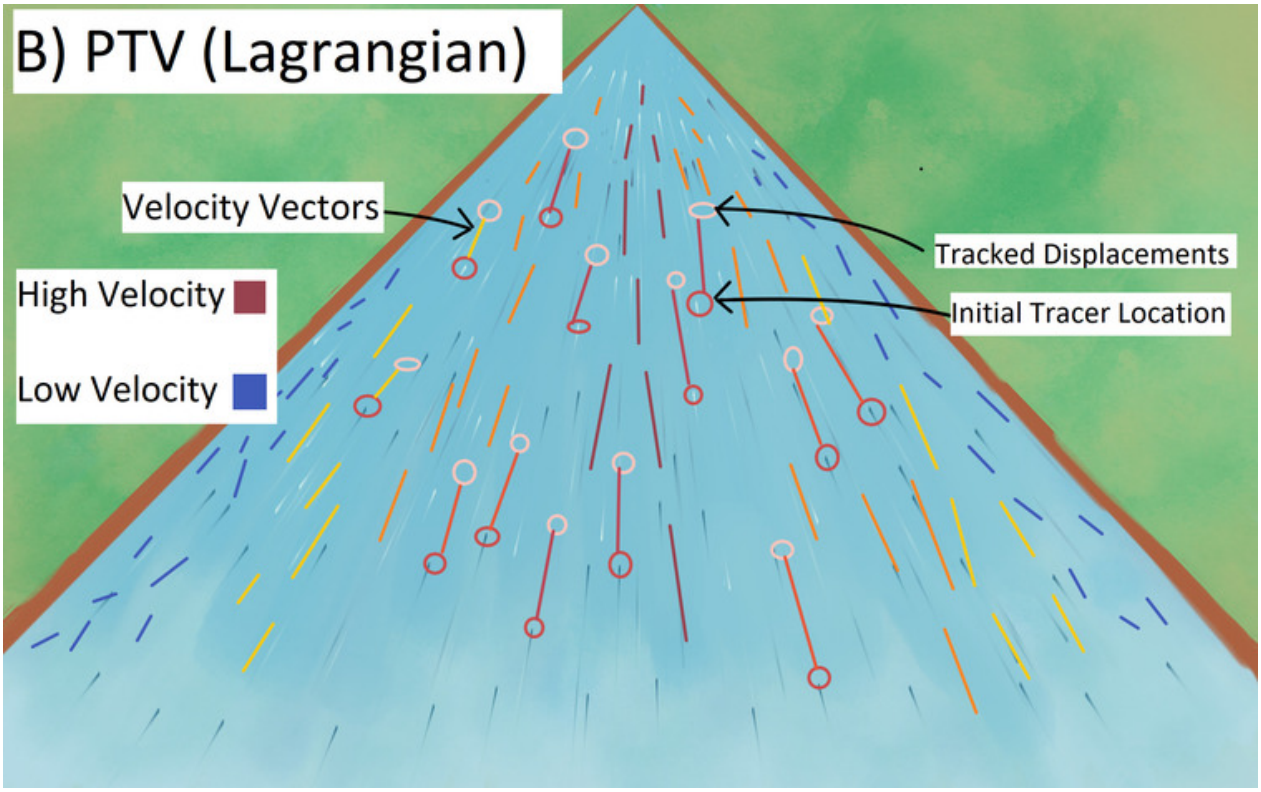


Figure 2.9: Schematics of general PTV (B) mechanics (Jolley et al., 2021).

Studies into the optimisation of processing using synthetic models have been highly successful in recent years in highlighting potential areas that are prone to causing errors in velocity results. The importance of these synthetic studies is to aid in selecting appropriate optimisations for differing scenarios (e.g. video length and frame rate). Both Pumo et al. (2021) for Large Scale Particle Image Velocimetry (LSPIV) and Dal Sasso et al. (2018) for PTV methods concur with the Pizarro et al. (2020a) study in that the concentration of particles is a crucial variable in relation to relative error. They also agree that, where seeding density is below optimal, longer durations of imagery

are required and that the contour region around the border of frames should not be included within analysis. These current pieces of synthetic research, however, acknowledge that the studies are not exhaustive in the variables considered, and more work is required to cover a broader range of associative error factors.

Table 2.1 summarises software suites that are available for users who wish to perform PIV or PTV analysis. Each software has its own feature detection and tracking scheme, along with varying methods of preparing and presenting data. Each software suite comes with a user-friendly Graphical User Interface (GUI) to load in imagery and perform various forms of analysis. The suites listed in this table are open-source or freely available to use.

Table 2.1: A non-exhaustive, generalised overview of software suites that are currently available, with some of their requirements and functions listed.

Software	Overview	Requirements and Functions
PTVlab (Brevis et al., 2011)	PTVlab is a MATLAB-based tool that uses particle identification to track movement. It enhances the images to better show particles and their centroids. With this data, it performs integrated cross-correlation and iterative relaxation labelling techniques to better represent varying seeding densities and track their trajectories.	Image enhancement is used to highlight the flowing particles and their centroids, which are then tracked by the software. This tracking requires the user to input interrogation area sizes.
Fudaa-LSPIV (Coz et al., 2014)	Fudaa-LSPIV is free software developed with a Java GUI. It begins with image pre-processing, converting video clips into PGM ASCII formats. It then sequentially performs orthorectification, PIV analysis, result processing, and discharge computation. It includes tools to visualise and export data in various formats.	For accurate results, users must input GCPs, water level estimations, and the position of the viewpoint. For discharge measurements, bathymetry profiles are required.
PIVlab (Thielicke and Stamhuis, 2014)	PIVlab is available as an open-source GUI within MATLAB, using several of MATLAB's built-in processes for image pre-processing, analysis, post-processing, and data exploration. It produces outputs in video, image, or vector map formats.	The software uses image enhancement, camera calibration, and orthorectification to improve imagery. It requires the user to define interrogation and search area sizes and performs direct cross-correlation and Fourier transformations.
RIVeR (Patalano et al., 2017)	RIVeR is a standalone MATLAB code that adopts PIV/PTV principles and is designed as a simple, user-friendly application. It extracts images from video footage, processes them using PIVlab/PTVlab algorithms, and uses GCPs to orthorectify the images to produce velocity and/or discharge results.	Video image extraction rates, frame rates, colour depths, and camera/lens parameters are required as initial input. GCPs must be referenced in the images for orthorectification. Cross-section bathymetry is needed for discharge calculations.
OTV (Tauro, Petroselli and Grimaldi, 2018)	OTV processes data using feature detection, Lucas-Kanade tracking, and trajectory-based filtering. This improves velocity accuracy by retaining only reliable trajectories to reduce error. The software produces an average surface velocity estimate.	OTV automatically detects features and does not require user-defined tracers. The user sets flow direction and trajectory quantity. Performance may be affected by low image resolution or low frame rates.

Photrak SSIV (Carrel et al., 2019; Leitão et al., 2018)	SSIV uses cross-correlation like most PIV methods, but filters rather than corrects erroneous vectors. Photrak provides two systems: DischargeKeeper (a fixed IP camera with local processing) and DischargeApp (for smartphones). It was initially designed for use with consumer-grade surveillance systems in urban environments.	SSIV requires full camera calibration and several reference points in the image for orthorectification. Search and interrogation areas must be defined by the user. Without water level input, only flow velocity (not discharge) is provided.
KLT-IV (Perks, 2020)	KLT-IV provides a step-by-step GUI to guide users through video processing, from fixed or mobile platforms, using GCPs to produce surface velocity and discharge data. It supports video stabilisation and orthorectification. KLT-IV uses GFTT and the Kanade-Lucas-Tomasi (KLT) pyramidal tracking scheme, discarding results with errors > 1px.	Accurate results require camera calibration, including lens model for distortion removal and image orthorectification. The software tracks tracer trajectories using user-defined extraction rates, block sizes, and reference points. Performance varies with extraction parameters.

2.2.2 Post-Processing

Post-processing has two main elements: error reduction (e.g. vector correction, Section 2.2.2.1) and velocimetry application (Section 2.2.2.2). Error reduction is the process of highlighting and filtering potentially erroneous datasets and velocity fields, while progressive calculations involve using the velocity data and applying it to secondary datasets — such as when surface velocities are used to calculate discharge through the incorporation of alpha values and bathymetry information.

2.2.2.1 Vector Correction

Post-processing may reduce errors through the application of statistical methodologies to highlight and filter erroneous outputs. For PIV, details of vector validation can be found in the study of Raffel et al. (2018), which implements several statistical methods of achieving data validation. Statistical validation methods perform similar techniques to distinguish outliers in PIV data, and do so typically by comparing vectors to their surrounding neighbours (Hart, 2000; Masullo and Theunissen, 2016). Alternatively, there is a bootstrapping technique available that does not generate statistics from its nearest neighbours, but instead, a statistic is generated for each component (Pun et al., 2007). Typically, the difference between each method is the type of statistical calculation applied to determine outliers. The basic statistical methods include, but are not limited to, vector difference tests, median tests (Westerweel, 1994), and normalized median tests (Westerweel and Scarano, 2005). Masullo and Theunissen (2016) suggests that overall, the most common detection techniques used in practice are the universal outlier detection scheme (adaptation of median test but normalises the median residual with respect to an estimate of local variation) (Westerweel and Scarano, 2005), and the distance-weighted universal outlier detection scheme for unstructured data (a generalisation of the universal outlier detection method, but with a variance in the definition and weighting to neighbouring vectors) (Duncan et al., 2010). These should be used in all studies where

spurious vectors are evident (especially with evident turbulence) (Westerweel, 1994), or results of velocimetry are being used for further applications (e.g. discharge).

Typically, corrective methods for spurious vectors will perform statistical analysis as seen above to detect outliers and determine if it falls under a set threshold as to whether or not it is likely a false reading or likely to be reliable. If it is determined to be erroneous, the vector should be removed and replaced using, most commonly, a 2D interpolation, or alternatively linear or polynomial interpolation (Stamhuis, 2006). Some common PIV statistical corrective methods are: Penalised Least-Squares Method (Tang et al., 2017), Kriging Regression (Baar et al., 2014), and Proper Orthogonal Decomposition Outlier Detection (POD-OC) (Wang et al., 2015). Replacing these vectors is important to ensure the results produce statistically meaningful velocities, and without it, can limit the accuracy, resolution, and usefulness of PIV (Hart, 2000).

For PTV data, detecting erroneous vectors is slightly more challenging due to its unstructured features (i.e. does not conform to a gridded system when processing, like seen with PIV methods). Many common PTV algorithms stem from techniques used by PIV regarding the way that it associates vectors with its nearest neighbours, but are altered to deal with the issue of identifying neighbouring vectors in PTV, and not being equally spaced. For PTV validation and correction, should there be more than 15% of outliers, automated programs could potentially fail to highlight them due to algorithms using neighbouring velocities to determine what classifies as an outlier, and should there be a high percentage of outliers, determining what is correct and what is not is challenging (Duncan et al., 2010).

Techniques for PTV error correcting typically involve a smoothing of displacement fields to use as a baseline to outliers (e.g. Akhmetbekov et al., 1996; Young et al., 2004). Duncan et al. (2010) constructed the Universal Outlier Detection Scheme (which can be used for both PIV and PTV), but it is a development of the algorithm from the Westerweel and Scarano (2005) study for PIV correctional algorithms. An alternative to these methods is a model-based technique (e.g. Young et al., 2004), which has been shown to validate up to 25% of outliers. In this study, the model is described as a 5-stage process. The first stage is initialisation, which involves displacement normalisation, the building of constraints, and then a regularised version of the displacement field is calculated. Secondly is relaxation, this stage produces a displacement field where invalid estimates are replaced with statistically more likely vectors. Third is point removal, which uses several statistical methods to determine validation scores (based on user-defined thresholds and a T value determined in the relaxation stage). The next stage is attraction, designed to iterate landmarks towards their associated termination landmarks. Finally, displacement interpolation, which can be used to estimate the displacement at any position in the image field.

2.2.2.2 Velocimetry Applications

The most common application for image velocimetry datasets is attempting to calculate discharge. Discharge can be calculated with the introduction of known, measured transects of the river within the camera field of view. These transects can be part of the geo-referencing local coordinate system and measured at the same time as the GCPs. For the discharge calculations to be as accurate as possible—when using PTV methods especially—the river surface needs to have a good spread of tracers. Where this is not the case, it is possible to interpolate or extrapolate measurements using polynomial, cubic, or the constant Froude method (Perks, 2020). Typically, discharge can be estimated using a velocity-area method, introducing typical fluid mechanics parameters (e.g. depth-average velocities, influenced by α) (Coz et al., 2010). The alpha coefficient (α) is a correction factor that relates surface velocity to the depth-averaged velocity of the flow. When calculating α values, vertical velocity profiles can be found using an ADCP, but Creutin et al. (2003) finds that using 0.85 is a reasonable assumption where this is not possible. Combining α with the calculated velocity, along with bathymetry, can give reasonable discharge calculations, as found with many studies on river discharge (e.g. Kim et al., 2008; Coz et al., 2010; Perks, 2020).

An issue to consider when studying river discharge via velocimetry is the variation of river channel cross-sectional area due to rising stage scour and waning stage fill, or due to the passage of sediment waves and bedforms even in more steady flows. It is suggested that after peaks of high flow, river bathymetry is remeasured to ensure that cross-sections remain as accurate as possible.

More recently, as an alternative to using estimated alpha values, mobile image velocimetry techniques have been used to derive the Gauckler-Manning-Strickler coefficient (K), for cross-sectional roughness in rivers (Bandini et al., 2021). The method simultaneously solves for K and discharge using both the linear form of Manning's equation and the mean-section method for computing discharge from depth-averaged vertical velocity. The uncertainty at the 95% confidence level resulted in most observations being within ±10% of the in situ discharge measurements. This method can be used to counter issues with streams that are non-ideal (e.g. highly meandering, non-uniform in slope, etc.).

For users who are looking to apply image velocimetry to analyse data for the first time, it can be difficult to understand which method (PIV or PTV) to use. The research presented throughout this study should provide some indication of what is the best method for the particular datasets. For further information to help aid decision-making regarding methodology choices and how to best apply PIV or PTV, see Table 2.2. These papers have been studied and briefly summarised regarding the background of the site, the hardware used, and the results discussed by the authors. This also includes the challenges that the authors faced, as well as the possible causes for such challenges. These papers have been selected as they provide similar but different methodologies using PIV or PTV (e.g. fixed platforms, mobile platforms, thermal cameras).

Table 2.2: A selection of application papers chosen due to their variation in hardware and software suites. Each has been briefly summarised for their backgrounds and results.

Details	Background	Results
Author: Creutin et al. (2003) Case Study: Iowa River, Iowa Software Application: In-house algorithm (PIV)	"Proof of concept" research paper. PIV was used without artificial tracers. GCPs used with a 70 m wide channel. Ten 10-minute recordings used for processing. Sony DCR-TRV320 camera used at an angle of 60° and 14 m above the river level. GSD was 6.4 pixels/m. Interrogation areas set at 64×64 pixels and search areas set at 24 pixels.	Discharges from the ten sequences ranged from 50–300 m^3/s. Results were compared to 215 current meter measurements, and PIV results agreed with the defined rating curve. Average velocities mostly agreed, except for two measurements. Disregarding these, error ranged between –11.6% and +4.2%. The study highlighted issues with results being sensitive to light, with reflections and shadows making movement detection difficult.
Author: Jodeau et al. (2008) Case Study: River Arc, France Software Application: LS-PIV	Dam flushing, discharge rate between 10–150 m^3/s. Survey area approximately 60×40 m. Tilt angle roughly 20° to the horizontal. Alpha calculated as 0.79 (default is 0.85). DEM used for bed elevations.	Bias thought to be due to friction coefficients used, especially in shallow areas; underestimation compared to a 2D model. Lack of tracer visibility on the right bank due to shadows. At lower discharges (e.g., 60 m^3/s), error compared to the rating curve was 30%. At higher discharges (77 m^3/s), the error reduced to 0–6%.
Author: Legleiter et al. (2017) Case Study: Alaska, USA Software Application: LS-PIV (Thermal)	Benchmarked using ADCP for velocity, discharge, and depths. Thermal camera (FLIR SC8340) used at 1280×720 px, 10 Hz, for 1 minute. Most cameras set to nadir; some used 13° off nadir. 25 mm lens provided a 41.2°×24.8° FOV. ROI of 512×512 px (approx. 6×3.5 m, GSD = 0.005 m).	Camera angle caused distortion in the FOV (2–9%) and reduced thermal signal in the near field. Thermal patterns, not discrete tracers, were tracked. Image edges were trimmed to minimise tilt-related distortion. Velocity ranged from 0.5–3 m/s across sites. Mean error across sites fell within one standard deviation (0.09–0.187 m/s), with ±1 SD of 0.132–0.247 m/s.
Author: Tauro, Petroselli and Grimaldi (2018) Case Study: Brenta River, Italy Software Application: OTV (PTV-based)	GoPro Hero 4 Black used at full HD (1920×1080) at 50 Hz. From a 4-minute video, twelve 20s clips were extracted at 1430×1080 px (7.1×5.3 m^2) and 25 Hz. Image manipulation included greyscaling and gamma correction.	Processing with OTV was 2 minutes on a basic PC, compared to 17±7 minutes using PIVLab/PTVLab. Benchmarking done against a current meter (3 cm below surface). FAST-based OTV had R^2 = 0.83; ORB-based = 0.74. PIVLab = 0.49; PTVLab = 0.6.
Author: Dal Sasso et al. (2018) Case Study: Noce River, Italy Software Application: PTVLab	Field study after numerical experimentation on optical PTV setups. Channel width: 28 m; slope: 1.1%. Benchmarked with current meter. DJI Phantom 3 with 4K UHD camera. 10 m nadir hover. HD capture at 24 FPS over 17.0×9.6 m^2. Artificial tracers used.	Bank areas showed high uncertainty due to fewer tracers. Frame rate needs to ensure particle displacement exceeds detection threshold — sub-sampling recommended. RMSE: 0.125 m/s overall; 0.04 m/s in well-seeded regions. Mid-reach error 1%, edge error 48%.
Author: Jin and Liao (2019) Case Study: Milwaukee River, USA Software Application: LS-PIV	Flow: 6–60 m^3/s. Nikon D7000 with HD 1080p and 50 mm lens. Oblique angle: 79°–86°. Orthorectified using 11 GCPs. ADV used for benchmarking. 25 FPS over 10 minutes. GSD = 0.02 m/px; area: 70×23 m.	Median filtering reduced outliers. Mean error: 29–36%. RMS velocities from ADV and PIV closely matched (0.12 vs. 0.14 m/s). Slight PIV overestimation likely due to ADV data being from 5 cm below the surface. Alpha set to 0.85.

Author: Pearce et al. (2020) Case Study: Kolubara River, Serbia Software Application: KLT-IV, LSPIV, LSPTV, OTV, SSIV	Low-flow experiments (3.4 m^3/s) benchmarked with ADCP. DJI Phantom 4 Pro with 1" CMOS 20MP camera. Artificial tracers. Six GCPs along channel. Resolution: 4096×2160 (4K), FPS: 23.98. Two 30s videos, sampled from 26 m (GSD = 0.77 cm/px) and 32 m (0.95 cm/px).	ADCP used on 3 cross-sections. KLT-IV and LSPIV had the best agreement (0–0.07 m/s error). Nash-Sutcliffe efficiency for first video: KLT-IV = 0.535; OTV = 0.3592; LSPIV = 0.4905; LSPTV = 0.1609; SSIV = 0.3875. KLT-IV showed low sensitivity to config changes. OTV most sensitive to trajectory thresholds.
Author: Perks (2020) Case Study: River Feshie, Scotland Software Application: KLT-IV (PTV-based)	Hikvision AcuSense 4MP IF network camera (20 Hz, 2688×1520), and DJI Phantom 4 (29.97 FPS, 4096×2160). High-flow stages: 0.785–1.762 m. GCPs used; images stabilised.	Mobile and fixed setups were evaluated. Deviations from the rating curve were 4% (mobile) and 1% (fixed) above 1.5 m stage. Vegetation blocked mobile camera edges; extrapolation used. Over 1 million trajectories captured; fixed camera had 7433 (from 10s of video). Both banks needed extrapolation.

2.2.3 Tracers and Their Role in Image Velocimetry

Tracers are thermally or optically distinct features on the water surface that are advected by the flow current. Under certain hydrological conditions, such as fast-flowing, turbulent streams, naturally occurring features (e.g., foam, turbulent structures) may be sufficient for successful image velocimetry analysis (see Figure 2.10). The spatial and temporal distribution of these tracers is crucial, as it significantly impacts the performance of image velocimetry methods. It is recommended that 10-30% of the water surface should be traceable throughout the analysis process (Meselhe et al., 2004). Recent studies underscore that not just the presence, but the density, dispersion index, and spatial variance of tracers are critical for optimising image velocimetry approaches (Dal Sasso et al., 2020). For instance, by selecting frames based on optimal tracer characteristics—such as dispersion and density, a reduction in surface velocity error by 16.1% to 39% can be achieved using PIV or PTV methods (Pizarro et al., 2020a; Dal Sasso et al., 2021). This frame selection process based on the SDI can reduce discharge errors to as low as 0.12-0.4% of the total error when not optimising frame selection in PIV methods (Pizarro et al., 2020a). In cases where natural tracers are insufficient, artificial tracers like environmentally friendly substances (e.g., bark, decomposing polymers) may be used. These tracers should be passive to the flow (e.g. meaning they should follow the movement of the water without introducing their own momentum or resisting flow direction), easily distinguishable, and non-disruptive to water quality (Detert and Weitbrecht, 2015). The size and shape of these tracers are also important. They should be larger than 1 pixel, ensuring stability over time and effective interaction with the flow (Tauro et al., 2017; Tsubaki et al., 2011). Research has shown that ellipsoidal particles of 2-5 pixels perform optimally, as they are less prone to internal forces and agglomeration compared to spherical tracers (Tang et al., 2008).

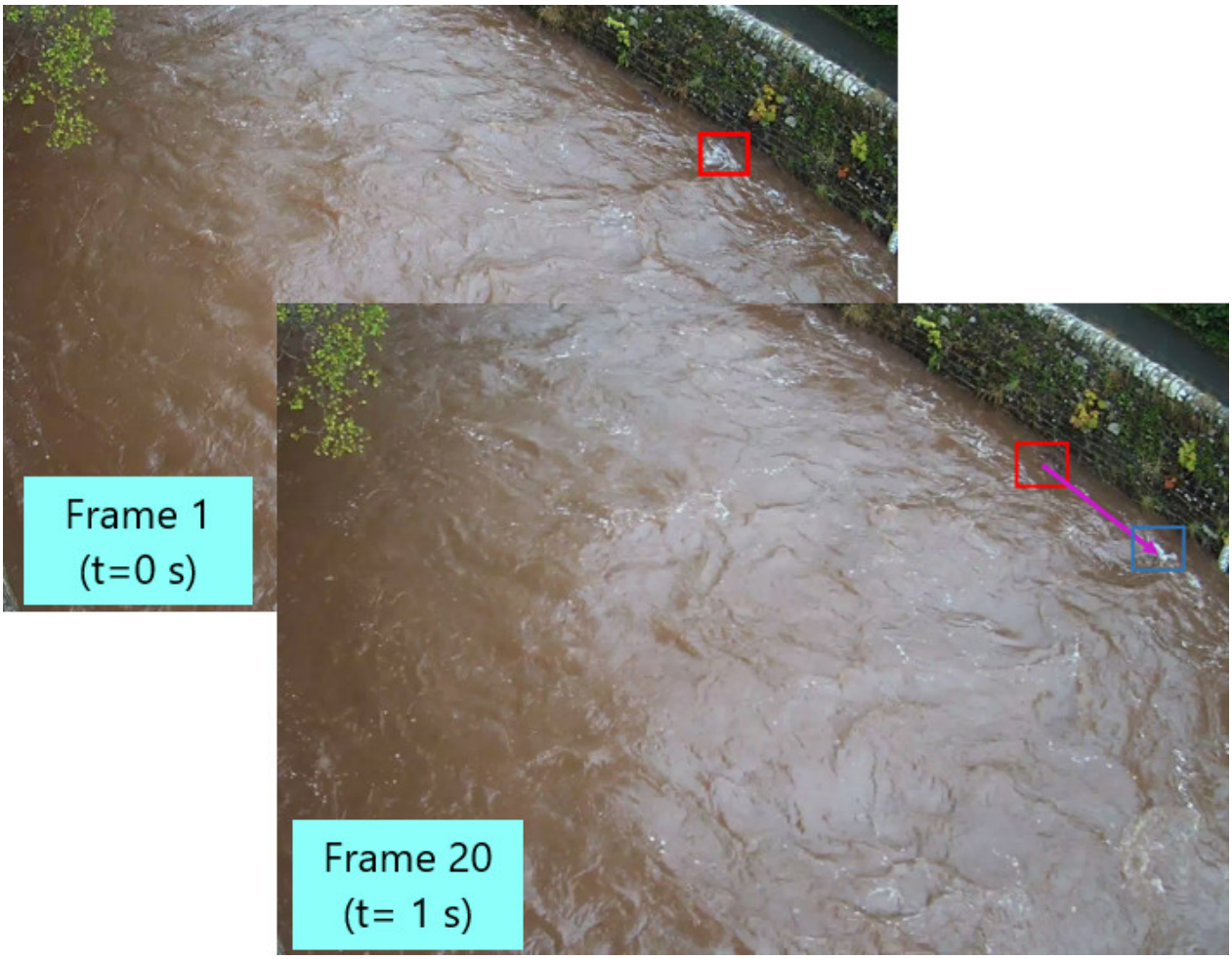


Figure 2.10: Examples of usable tracers highlighted from a study using a fixed camera with frames exactly 1 second apart. (Jolley et al., 2021)

2.2.3.1 Significance of the Seeding Density Index

The SDI is a critical metric in fluid flow imaging, particularly in techniques like LSPIV. It quantifies both the concentration and spatial distribution of tracers within the field of view, which are essential for accurate flow velocity measurements (Pizarro et al., 2020a). High concentration ensures that tracers are detectable, while an even spatial distribution avoids clustering, which can lead to inaccurate velocity readings. These factors underscore the importance of optimising the selection of the most informative frames for flow measurement. By focusing on time-averaged seeding metrics, SDI plays a pivotal role in significantly reducing measurement errors by identifying the optimal frames for analysis (Pizarro et al., 2020b). Studies have demonstrated the effectiveness of SDI in improving flow measurement accuracy across different hydraulic conditions. For example, in case studies by Dal Sasso et al. (2021) and Pizarro et al. (2020a), the use of optimised SDI parameters led to a 7 to 10 percent and 7 to 33 percent reduction, respectively, in velocity vector errors compared to processing all frames, significantly enhancing the precision of velocity measurements.

This improvement is particularly pronounced in complex and turbulent river environments, where traditional methods often struggle to maintain accuracy.

2.2.3.2 Research Gaps and Motivation

Despite the growing application of image velocimetry for surface flow monitoring, one of the most persistent challenges is maintaining measurement accuracy under varied and complex environmental conditions. Traditional approaches have primarily focused on refining image processing algorithms or improving hardware setups, yet they often overlook the fundamental importance of tracer quality in the captured imagery. In particular, the spatial and temporal distribution of tracers—while widely acknowledged as critical has lacked a standardised method for evaluation or integration into processing workflows.

The SDI addresses this limitation by offering a quantifiable metric for assessing tracer conditions. However, existing implementations of SDI have largely been limited to pre-processing, with relatively little focus on how tracer conditions evolve throughout the data collection process. Moreover, there is limited understanding of how SDI performs across a range of environmental scenarios, such as under poor seeding conditions or spatial variability in flow fields. These gaps suggest the need for a more dynamic and comprehensive approach to evaluating tracer distribution—one that can be applied both during and after data capture to inform the quality and reliability of velocity measurements.

This thesis aims to address these gaps by developing and applying a Post-Processed Seeding Density Index methodology, capable of evaluating seeding conditions directly from processed vector data. By doing so, it extends the utility of SDI beyond simple frame filtering and introduces a feedback mechanism for assessing measurement confidence. Through synthetic and real-world case studies, the thesis investigates the impact of SDI on measurement accuracy, highlighting its potential as both a quality control metric and a tool for optimising image velocimetry under diverse field conditions.

2.3 Chapter Summary

This literature review has provided a thorough analysis of the advancements and ongoing challenges in river flow monitoring through image velocimetry, with a particular focus on PIV and PTV techniques. As an evolving field, image velocimetry has seen significant progress in processing software and methodologies. However, the practical implementation of these techniques remains complex, especially for practitioners, due to the intricate interdependencies among critical factors such as orthorectification, seeding conditions, particle identification areas, frame rate, and video duration. Post-processing methods, such as vector correction, are also essential in enhancing the accuracy of results by filtering out spurious data.

The SDI has emerged as a pivotal metric for optimising tracer selection and improving measurement precision. Despite recent advancements, key challenges remain, particularly in making these techniques more accessible and reliable for widespread use. This review has highlighted the importance of addressing these challenges to improve the reliability and ease of use of image velocimetry techniques. These gaps form the basis for the work presented in this thesis, which aims to explore and refine SDI methodologies and develop practical workflows to support their application in real-world monitoring. By simplifying implementation and enhancing result accuracy, this research contributes to advancing the usability of image velocimetry across diverse hydrological contexts.

Chapter 3. Methodologies and Site Selection

3.1 Chapter Overview

This chapter presents the methodologies employed to acquire, process, and analyse image velocimetry data, with the aim of ensuring accurate and reliable river flow measurements. These methods are specifically designed to address the challenges identified in the literature, such as the need for improved accuracy in flow measurements under varying environmental conditions. The expected outcomes of these methodologies include not only enhanced precision in measuring flow velocities, but also a deeper understanding of the effectiveness of novel seeding metrics under real-world conditions. By applying advanced image velocimetry techniques (e.g. PIV and PTV), alongside newly developed approaches, this research seeks to fill critical gaps in current hydrological studies. The integration of auxiliary data, such as GCPs and bathymetry information, further enhances the spatial accuracy and depth-related insights that are crucial for precise flow measurement. This chapter provides a detailed understanding of the methodological framework that underpins the research, offering insights into the workflow and tools that ensure the robustness of the findings presented in the subsequent chapters.

3.2 Site Selection

This thesis focuses on two primary sites: the River Calder, Todmorden, and the River Sheaf, Sheffield, both located in the United Kingdom. These sites were chosen for their distinctive hydrological characteristics and the availability of historical data, making them ideal for studying river flow dynamics and image velocimetry techniques.

3.2.1 River Calder, Todmorden, Yorkshire

The River Calder at Todmorden is monitored by the Yorkshire department of the Environment Agency (EA). It is a tributary of the River Aire near Castleford, Yorkshire, with a catchment size of 28.974 km^2 (Environment Agency, 2023*a*). The River Calder site in Todmorden lies in the upper catchment of the River Calder. This heavily modified river predominantly runs through urbanised areas. The Calder catchment has historically been a high-risk area for property flooding. Normal stage levels are between 0.1 and 1.3 m, with property flood levels around 1.5 m, which was exceeded in 2015 when a level of 2.77 m was reached (Floodlist, 2023).

The image velocimetry site is an extension of the existing monitoring station at Todmorden. It is located within the town of Todmorden and is mains powered with mobile internet fully available. The section where the camera is located is a man-made U-shaped channel. This is useful when calculating high flows, as the cross-section's hydromorphology is less likely to change over time. Tracer availability is observably high in the ROI at both high and low flows. These tracers primarily consist of turbidity patterns caused by high flows, but the channel also contains a rough, uneven riverbed with several large obstacles upstream (Environment Agency, 2023*a*).

The site was chosen due to its historical data availability, high variability in flow conditions, and the presence of an existing monitoring station, making it ideal for studying the impacts of seeding density and dispersion on PTV methods. Data was collected continuously from 2018 to 2022.

3.2.2 River Sheaf, Sheffield, Yorkshire

The River Sheaf winds through the centre of Sheffield, South Yorkshire, flowing for approximately 9 kilometres. It has an average width of 10 metres and an average depth of about 1 metre (Britain's Rivers, 2023*a*). The river's catchment area is around 23 square kilometres (Britain's Rivers, 2023*b*; Environment Agency, 2023*b*). Located in a heavily urbanised area, this site offers straightforward access for maintenance and calibration. The camera setup, supported by mains power and mobile internet, allows for uninterrupted data collection and immediate data transmission. Typical water levels range from 0.12 to 1.10 m, with the highest recorded level at 3.26 m (River Levels UK, 2023). Abundant natural tracers, debris, and foliage enhance flow pattern visualisation.

This site was selected due to its urban setting, which allows for straightforward access and maintenance, and the availability of extensive historical data. Data was collected continuously from 2018 to 2022. Maintenance of the equipment in an urban setting required regular checks to ensure data quality and system functionality.

3.2.3 Image Capture

Data for analysis was acquired using fixed platform sites, each equipped with a Raspberry Pi unit powered by mains electricity at existing river gauging stations. This setup was selected for its ability to continuously capture high-quality data automatically and sequentially, effectively addressing the challenge of maintaining data continuity across varied river stages. The Raspberry Pi automates the processes of image capture, data storage, and transfer, and was chosen for its affordability, ease of coding, and strong Python support, making it an ideal solution for this application.

The Hikvision cameras, selected for their IP capabilities, affordability, and integration with Python, were configured to capture 20 to 30 seconds of video footage every 15 to 20 minutes at a resolution of 1080×1920 and a frame rate of 20 frames per second (fps). This combination of hardware ensures the collection of a substantial volume of data across different river stages and environmental conditions at multiple locations in the UK. The entire setup costs approximately £500



Figure 3.1: The River Sheaf through the site at Highfield.

per station, with ongoing expenses primarily arising from mobile internet data and cloud storage. Although alternative setups involving external hard drives for local storage could potentially reduce ongoing costs, they would require regular site accessibility, which was deemed less practical given the remote nature of many sites.

Data transfer from the Raspberry Pi units to Amazon Web Services (AWS) S3 cloud storage was managed via a Python script. AWS was selected for its cost-effectiveness, scalability, and ease of integration with other processing tools. Each video file was accompanied by metadata, including timestamps, site identifiers, and basic contextual information (e.g. weather, flow stage), which were logged into a centralised CSV for reference and indexing. Although not implemented in this study, AWS also offers the potential to automate the transfer of older data from the cloud to local devices, helping to reduce long-term storage costs. Processing costs were minimal, as video data was downloaded from AWS as needed and processed locally using standard computing resources. No cloud-based processing or high-performance computing infrastructure was required for this project.

Sites for the fixed platforms were strategically chosen based on their status as established monitoring locations with historical data, often featuring weirs that stabilise flow, thereby providing reliable conditions for analysis. The reliance on mains electricity at these sites eliminated the need for solar panels and batteries, simplifying the setup and reducing maintenance requirements. Given the high volume of video data captured at regular intervals across multiple monitoring sites, this approach provided a consistent and cost-effective solution for long-term data management and retrieval.

However, some challenges were encountered, including connectivity issues and occasional power shortages. To address these in future deployments, it is recommended to implement fail-safes for automatic rebooting when power is restored, potentially by employing a second Raspberry Pi as a controller to manage power-on code and other essential fail-safes. This approach would help ensure continuous operation and data collection, even in the event of temporary disruptions.



Figure 3.2: Raspberry Pi 3 Model B (Source: `https://www.raspberrypi.com/products/raspberry-pi-5/`)

3.2.4 Ground Control Point Coordinates

3.2.4.1 GCPs

For all sites that have cameras capturing data at an angle, it is vital that images are orthorectified. To orthorectify an image, at least eight GCPs are needed (see Section 2.2.1.6). Cameras are installed first and fixed in place so that the entirety of the river width can be seen. Once this has been established, it is possible to determine which GCPs can be used in the frame. It is possible to use naturally visible GCPs (such as corners of buildings, fence posts, etc.), however, for some sites in

this study, several points were manually placed in and around the ROI to ensure there is sufficient redundancy of points should more be needed.

Once the GCPs could be identified in the frame, a 3D laser scan of the ROI and surrounding area was taken using a Leica MS50. The data was then converted to point cloud data using Leica Infinity and CloudCompare software. From this, the coordinates of the visible GCPs were translated into their respective pixel coordinates, ready for input into KLT-IV. The GCPs used for this study for both the River Calder and the River Sheaf can be seen in Appendix 10.1.

3.2.4.2 Bathymetry

Bathymetry data is essential for understanding the cross-sectional profile of the river within the ROI, as it forms a critical input for accurate discharge calculations. For both the River Calder and the River Sheaf, bathymetry was captured using the same method involving the MS50, a multi-station instrument capable of high-precision scanning and detailed point measurements. A detail pole was used to take point readings at approximately 10 cm intervals along each cross-section. This high-resolution data provides a detailed and accurate representation of the riverbed's topography. The collected bathymetry data was then integrated into the KLT-IV software for discharge measurements. To ensure consistency and accuracy across all datasets, the bathymetry data was georeferenced to the same coordinate system as the GCPs. The depth measurements are relative to the true bed elevation, ensuring that all bathymetric data aligns correctly within the overall geospatial framework of the study. The bathymetry data used for this study for both the River Calder and the River Sheaf can be seen in Appendix 10.1.

While this study used high-resolution scanning to minimise uncertainty and support consistent comparative analysis, such detail is not essential for all image velocimetry applications. In many studies, simpler approaches, such as capturing the start and end points of a cross-section and measuring a series of depths manually, have proven sufficient for estimating discharge (Creutin et al., 2003; Jodeau et al., 2008). These more accessible methods are particularly useful in field environments where resources, time, or equipment are limited. For example, Dal Sasso et al. (2018) demonstrated that even under UAV-based approaches, basic bathymetric inputs can yield meaningful discharge estimates. The approach taken in this study was selected to maximise precision across diverse case study conditions, but the flexibility in bathymetry data collection methods reinforces the broad applicability and scalability of image velocimetry techniques.

3.3 Data Selection

The studies conducted in this thesis use two types of input data: synthetic imagery and site-study imagery. The synthetic dataset is used to establish controlled parameters, which in real-world case studies would often introduce variation and error. These controls include factors such as tracer velocity, tracer size and shape, and external influences such as environmental conditions. The

site-study imagery is then used to reintroduce these variables, allowing for a comparison between controlled and real-world results.

3.3.1 Synthetic Simulation Data

The methodology for generating synthetic videos was adapted from Pizarro et al. (2020b) to test and validate seeding metrics within a controlled environment for Pre-Processed SDI. This dataset consists of 1,680 videos created by stitching together 33,600 images for processing through KLT-IV. Each video varies in density (ρ) and dispersion (ν), covering 14 seeding densities and 12 spatial-clustering levels. Gaussian white noise was introduced to simulate environmental factors such as changes in luminosity, brightness, and shadows. Calibration ensured that these synthetic videos accurately reflected real-world scenarios by adjusting seeding densities and dispersion to align with field observations.

Tracers moved at a consistent velocity of 15 px/frame along the y-axis within a 500×500 px grid across 20 frames. This fixed velocity was later used for error calculations by comparing it with observed results. Tracers were randomly distributed, each with a uniform circular shape approximately 10 px in diameter and a consistent white colour. The spatial distribution was controlled using a Generalised Poisson Distribution (GPD), allowing for a range of seeding densities (λ) and spatial-clustering levels (ν).

3.3.2 Case-Study Site Data

3.3.2.1 Filtering in KLT-IV

Given the extensive volume of video data available for both the River Calder and River Sheaf sites, the KLT-IV system was adapted to include a video filtering mechanism designed to streamline data processing. This mechanism involves three key filtering stages: Date Selection, Time Selection, and Manual Selection—each aimed at refining the dataset to reduce the amount of data to be processed where it is not necessary, such as during low, baseline flows.

Date Selection The first filtering stage enables users to define specific date ranges for data extraction by setting start and end points. This step ensures that the dataset is concentrated on periods of hydrological interest, in this instance a mix of low, standard, and high flows, aligning the data with the study's temporal boundaries and allowing for efficient batch processing. While this method relies on the prior identification of periods of interest, it does not preclude its application for flood impact measurement or flood management planning. In those contexts, filtering could instead be based on real-time thresholds (e.g., stage level exceedance), enabling the same workflow to retrospectively or automatically focus on flood events without prior manual input.

Time Selection Following the Date Selection stage, the dataset is further refined based on the time of day the videos were captured. Recognising that videos captured at night may not provide sufficient visibility for accurate analysis, any videos recorded outside the predetermined daylight hours (10:00 AM to 4:00 PM) were excluded. This step ensures that only well-illuminated videos are retained, regardless of time of year, optimising the quality of the data for subsequent processing. The use of NIR cameras could be used to capture peaks in darkness, however, for the purpose of this study, it was not considered as to minimise variables.

Manual Selection In the final filtering stage, users are provided with direct oversight of the dataset. Through a review interface, users can manually deselect any unnecessary videos if required. The system also offers options for random or interval-based selection, such as selecting every second video, to manage the dataset size more effectively. This manual intervention ensures that the final dataset is precisely tailored to the specific requirements of the analysis.

3.3.2.2 Site-Study Data Results

Stage and video data were collected between 2019 and 2021 for both the River Calder and River Sheaf. Videos were captured every 15 minutes, resulting in a substantial dataset. River systems typically exhibit baseline flows with occasional peaks. The data selection process was tailored to capture both baseline and peak flow conditions using a two-stage filtering process: date filtering and time filtering, as detailed previously.

River Calder, Todmorden, Yorkshire Date filtering was employed to select periods with the highest stages throughout the year, including both rising and receding stages, along with at least two days of baseline flow. This approach ensured that the selected periods provided sufficient stage data corresponding to the video data, and that the quality of the videos was verified for Kanade-Lucas-Tomasi (KLT) tracking. Time filtering further excluded videos captured outside daylight hours (10:00 AM to 4:00 PM), avoiding analysis of videos recorded in low-light conditions. A new geolocation survey, used in GCP and orthorectification, was conducted at the River Calder site in 2020. This was followed by a period of no video data collection, limiting the available videos from that year. However, the new survey data is relevant for future use, making it significant for this study so that future research using the same dataset alongside new videos can be supported. Consequently, two main peaks of river stage were focused on, with the selected date range from 1 November to 16 November 2020. By applying the time filtering and the interval of every two videos, 531 videos were selected for processing, ensuring a comprehensive analysis across various flow conditions. The results of this process can be seen in Figure 3.3.

River Sheaf, Sheffield, Yorkshire To ensure that results in this thesis can be generalised, validation data is required. For the validation dataset, the River Sheaf was chosen. A total of 540

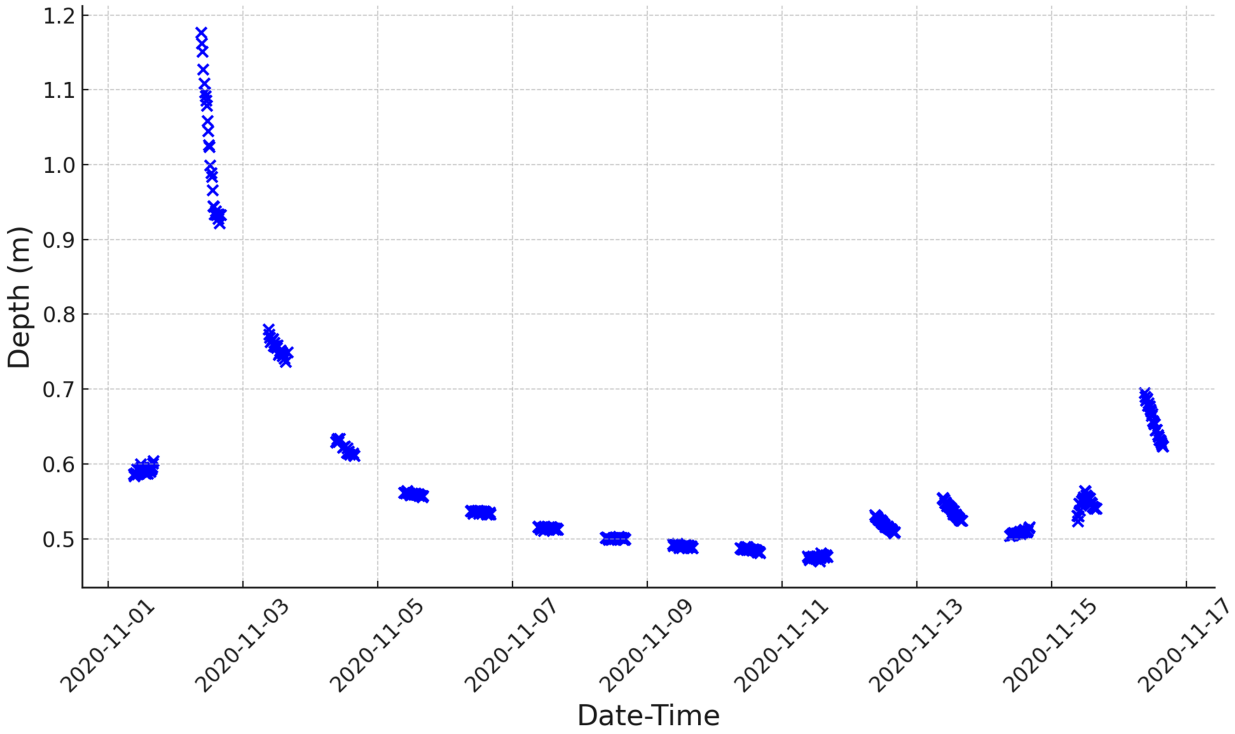


Figure 3.3: River Calder level data for the selected study period between 1/11/2020 and 16/11/2020.

raw videos were processed to ensure that at least two peaks in flow were captured and that the data encompassed a full range of rising and falling limbs across the flow regime. These videos were selected over two periods in 2019: from 10 June to 20 June, and from 30 September to 12 October. As with the River Calder site, all videos were filtered to include only those captured between 10:00 AM and 4:00 PM, ensuring good visibility. The videos and their corresponding levels are shown in Figure 3.4.

3.4 Video Processing using KLT-IV

3.4.1 Pre-Processing

The workflow for pre-processing, as depicted in Figure 3.5, illustrates the different scenarios based on camera orientation. This workflow, adapted from the KLT-IV v1.0 paper (Perks, 2020), shows the sequential steps categorised by video inputs, settings, and ground control sections. Grey, yellow, and green colours highlight the different stages, ensuring a clear understanding of the processes involved. It is important to note that either the GCP buffer or custom FOV should be provided to achieve accurate orthorectification.

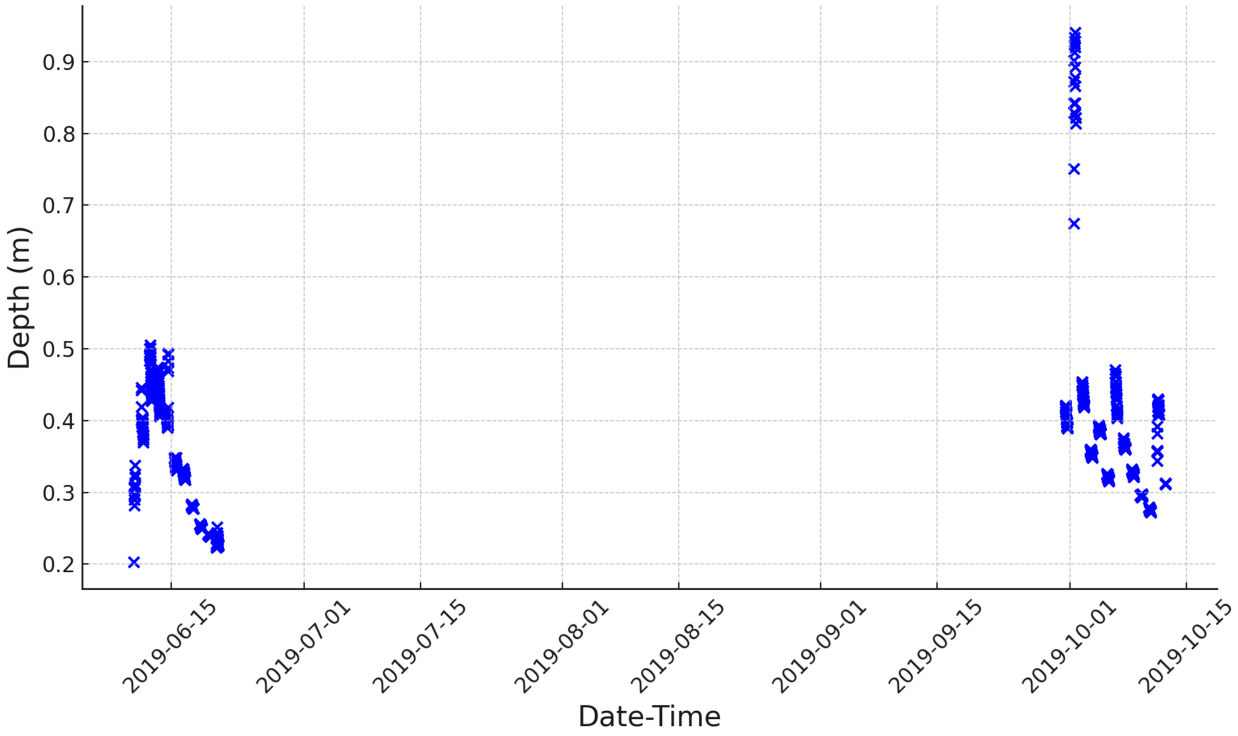


Figure 3.4: Sheaf river level data for the selected study period between 10/6/2019 and 12/10/2019.

3.4.1.1 Orthorectification

Orthorectification is a crucial pre-processing step that involves correcting the geometric distortions in video images to ensure they represent the river's actual geometry. In this study, orthorectification was performed using GCPs identified during site surveying. At least eight GCPs were required for accurate orthorectification. These were either naturally visible features (e.g., building corners or fence posts) or manually placed markers within the ROI. Manual markers were typically used, with reliance on natural points only in situations where placing markers was not feasible, such as at wide rivers like Kearsley (see Section 2.2.1.6).

A 3D laser scan of the ROI and surrounding area was conducted using the MS50. The resulting data was converted to point cloud format using Leica Infinity and CloudCompare software. The coordinates of visible GCPs were manually translated into their respective pixel locations using image software. These real-world XYZ coordinates were then matched with image XY coordinates. KLT-IV includes a validation tool that allows users to compare original and orthorectified points to verify alignment accuracy.

3.4.1.2 Image Enhancement

No additional enhancements beyond those built into KLT-IV were applied to the videos. KLT-IV automatically converts all frames to grayscale, simplifying processing by focusing on pixel luminosity. Although more advanced image enhancement techniques (see Section 2.2.1.7) could be

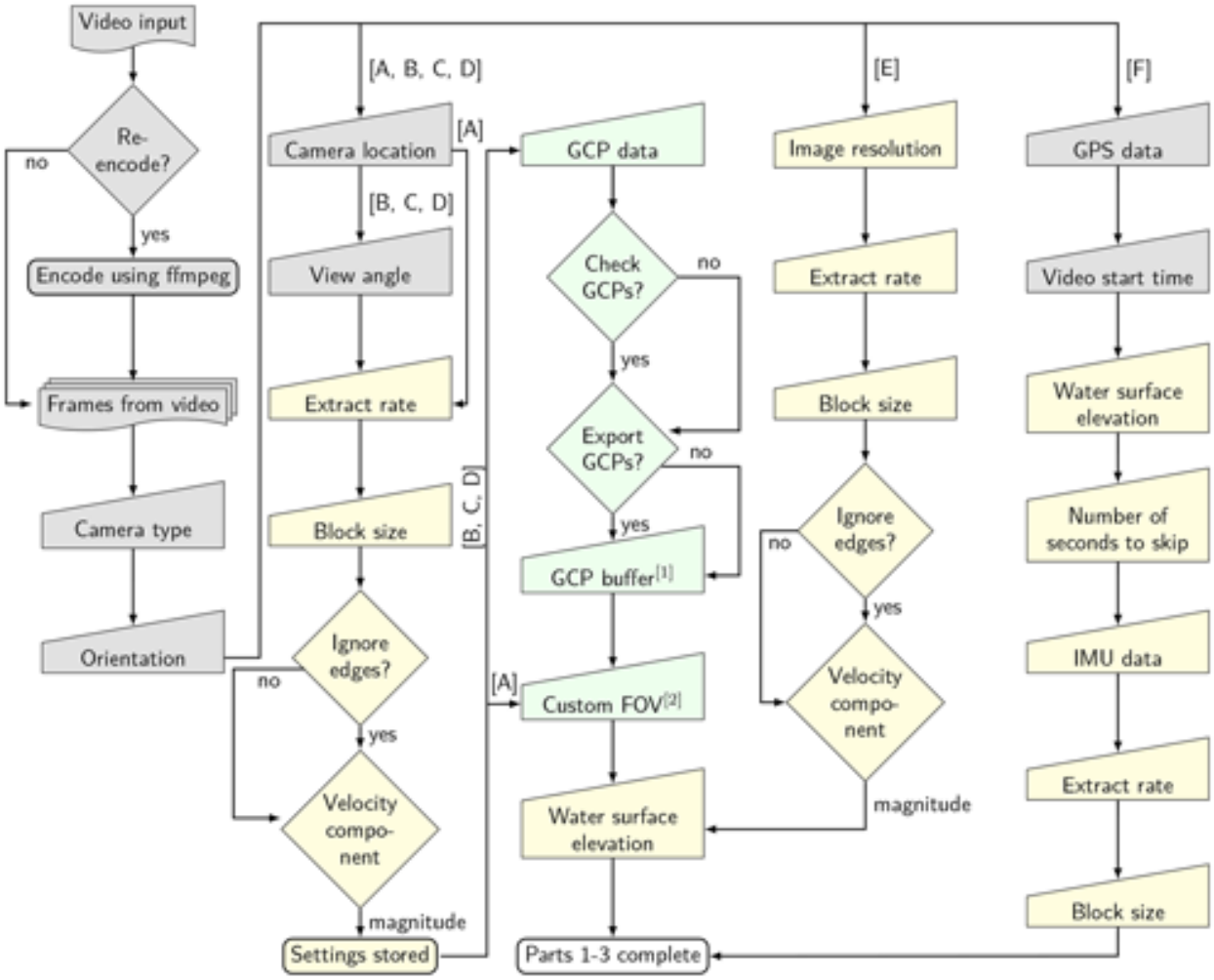


Figure 3.5: Adapted workflow for Sections 1–3 of KLT-IV v1.0, demonstrating different scenarios based on camera orientation (Source: (Perks, 2020)).

applied, they were excluded from this study to maintain consistency and minimise pre-processing, thereby supporting reproducibility in future work.

3.4.2 Processing

3.4.2.1 Parameters

Processing parameters in KLT-IV were configured to optimise tracer tracking accuracy—critical for reliable velocity results. These include block size and interrogation area definitions.

Block Size Block size defines the area around each tracer where the KLT algorithm searches for matching features between frames. A smaller block size offers higher precision but may increase sensitivity to noise, while a larger one improves stability but can reduce spatial resolution. The selected block sizes align with those used in Perks (2020), proven effective for similar river environments.

Interrogation Area The interrogation area determines the zone over which feature displacement is analysed. KLT-IV uses a pyramidal scheme that refines block size over three levels, halving the dimensions each time (Shi and Tomasi, 1994; Lucas and Kanade, 1981; Tomasi, 1991). Convergence is achieved over multiple iterations, with features exceeding 1 pixel bidirectional error being removed. This ensures robust tracking, especially in regions with low or inconsistent tracer presence (Raffel et al., 2018).

3.4.2.2 Interpolation Methodology

To fill gaps in velocity profiles, quadratic, cubic, and Froude-based interpolation methods were used. Each requires a minimum of four valid (non-NaN) data points. Quadratic and cubic methods fit second- and third-order polynomials, respectively, with negative velocities set to zero. The Froude method assumes a constant Froude number, estimating velocity from depth. All interpolation methods were implemented using KLT-IV's bulk processing functionality with CSV inputs.

3.4.2.3 Discharge Calculations

Discharge was estimated by converting surface velocities into depth-averaged velocities, using a coefficient of 0.85 based on the logarithmic velocity profile assumption (Creutin et al., 2003). This conversion, combined with bathymetry data, enabled unit discharge calculation across cross-sections, which were then aggregated to determine total river discharge. While no direct flow gauging was conducted alongside this study, discharge estimates were compared against historical rating curves and validated using independent ADCP measurements at selected sites.

3.4.2.4 Tracer Availability

Tracer availability is a key determinant of velocity measurement quality. PTV requires sufficient, well-distributed tracers—such as debris, foam, or surface features—for accurate tracking. Low density causes data gaps; high density can cause overlap and tracking errors (Tauro et al., 2017; Dal Sasso et al., 2020). This study evaluates tracer presence using post-processed metrics, which were shown to reduce velocity estimation error by up to 39% in previous work (Pizarro et al., 2020a). This aligns with findings that optimising tracer distribution significantly enhances velocity accuracy (Dal Sasso et al., 2021; Pizarro et al., 2020a).

3.5 Analytics

3.5.1 Seeding Metrics

This study focuses on three seeding metrics: seeding density, dispersion, and post-processed SDI. While Pizarro et al. (2020b) calculated SDI during pre-processing, this study introduces a novel

post-processing approach, evaluating only successfully tracked tracers. This improves assessment accuracy and ensures that metrics reflect real tracer behaviour during analysis.

3.5.1.1 Background on SDI Calculation

Pre-processed SDI begins with potential tracer identification using tools like `detectMSERFeatures` in MATLAB. Tracer density and dispersion are calculated, and integrated into a single index to determine frame suitability (Pizarro et al., 2020b).

3.5.1.2 Post-Processing SDI Calculation

Post-processed SDI focuses on actual tracked tracers. It reflects real tracer performance, offering a more reliable evaluation of data quality.

Seeding Density Seeding density (ρ) is calculated as:

$$\rho = \frac{\sum(N_i/G_{area})}{N_{gridcells}} \tag{3.1}$$

Where N_i is the number of tracked tracers in grid i, G_{area} is the grid cell area, and $N_{gridcells}$ is the total number of cells.

Dispersion Dispersion (D^*) reflects tracer clustering and is calculated as:

$$D^* = \overline{d^*} = \frac{var(N_{pg})}{mean(N_{pg})} \tag{3.2}$$

Where N_{pg} is the number of tracers per grid.

Seeding Density Index SDI is calculated as:

$$SDI = \nu^{k1} \left(\frac{\rho}{\rho_{ideal}} \right)^{k2} \tag{3.3}$$

Where ν is dispersion, ρ is seeding density, ρ_{ideal} is ideal density, and $k1$, $k2$ are calibration constants.

3.5.2 Synthetic Simulation Metrics and Observed Metric Results

This study uses both imposed (synthetic) and observed metrics. Synthetic densities range from $\rho = 4 \times 10^{-4}$ to 1.02×10^{-2} particles per pixel (PPP); dispersion from $\mu = 0.5$ to 200. Observed metrics are calculated post-analysis using only successfully tracked tracers, offering a realistic representation of PTV performance.

3.6 Data Validation and Calibration

3.6.1 Camera and Software Calibration

Camera and software calibration were critical to ensuring measurement accuracy. KLT-IV includes tools for stabilisation, orthorectification, and lens calibration. As camera movement was negligible, stabilisation was not required.

Camera Calibration: Camera model parameters were input into KLT-IV to ensure lens distortions were accounted for automatically.

Orthorectification Validation: Validation was conducted by overlaying known GCP coordinates with their positions in the orthorectified video. Visual checks confirmed sufficient alignment.

3.6.2 Validation of Velocity Measurements

3.6.2.1 Synthetic Simulations

Synthetic videos had a known particle velocity of 15 px/s. Measured values were compared using:

$$\text{Error}(\%) = \left(\frac{|\text{Measured Velocity} - \text{Known Velocity}|}{\text{Known Velocity}} \right) \times 100 \tag{3.4}$$

3.6.2.2 Field Data

Three validation methods were used:

1. **Stage-Discharge Curves:** Generated from KLT-IV outputs and compared to historical rating curves.
2. **Historical Comparison:** Results were benchmarked against long-term stage-discharge datasets at each site.
3. **ADCP Validation:** Independent ADCP measurements provided velocity data for ground-truthing video-based analysis.

3.7 Summary

This chapter has outlined the full methodology for acquiring, processing, and validating image velocimetry data. The research used fixed-site Raspberry Pi systems to capture high-resolution video, with GCPs and bathymetry data providing geospatial accuracy. Through KLT-IV, data were processed using established parameters, and tracer availability was assessed to ensure reliable flow estimation.

A novel post-processed SDI approach was introduced, focusing only on successful tracers to more accurately reflect measurement conditions. Validation was performed using both synthetic

and real-world benchmarks, and the system demonstrated strong agreement with known velocities and field data.

To conclude the chapter, Figure 3.6 provides a visual overview of the data reduction and analysis workflow employed throughout this research. It illustrates how river level observations were filtered using automated selection parameters, including date-time and stage level thresholds. These filtered observations then formed the basis for video processing and SDI calculation, ultimately enabling comparisons between pre-processed and post-processed results. This figure encapsulates the core methodological pipeline that underpins the analysis presented in the following chapters.

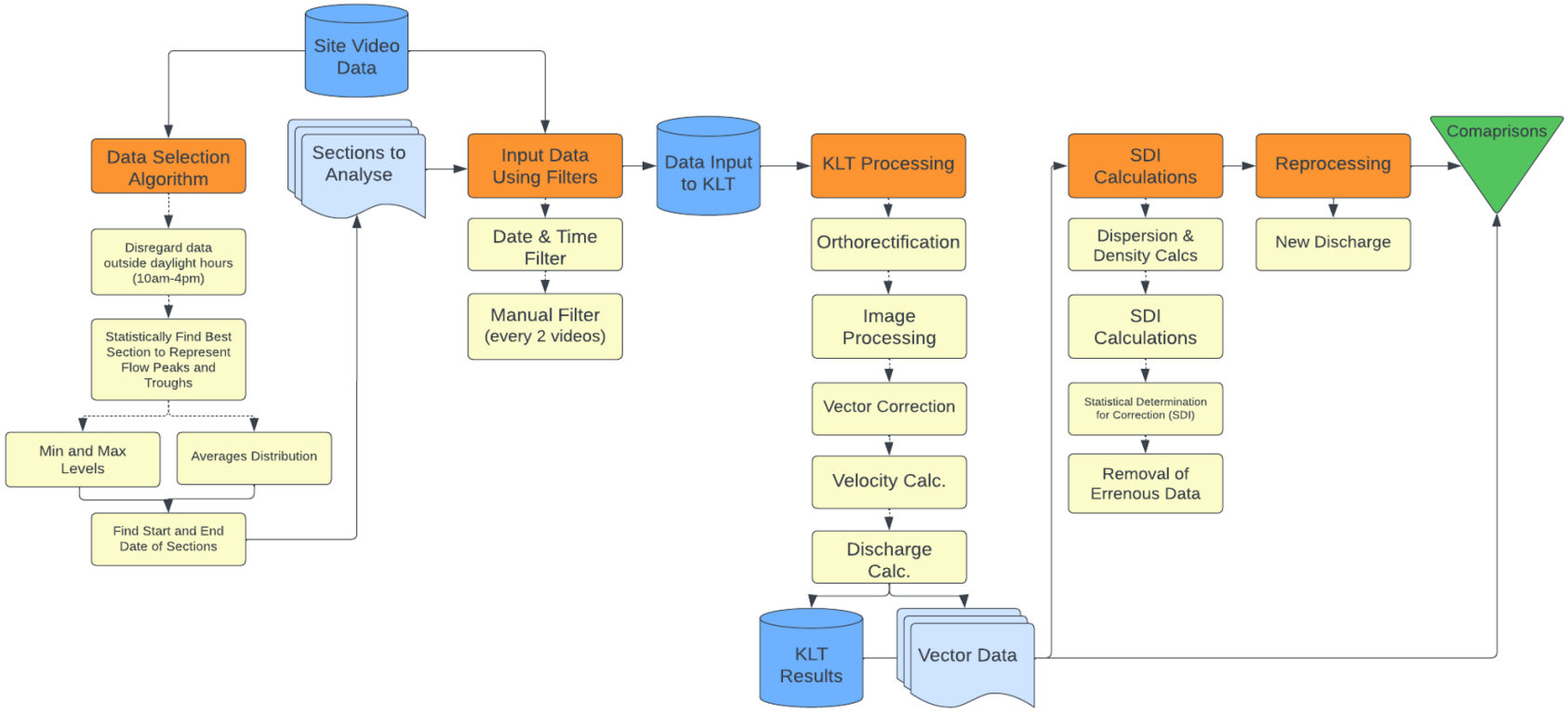


Figure 3.6: The process to filter significant river level observations from the large dataset captured at each site. Automated selection of sections was performed using two pre-determined variables: Date-Time and River Level. The selected river level data was then used for further processing, with results stored and taken through to the SDI calculation stage, which then feeds into the comparisons of SDI Pre-Processed and Post-Processed results.

Chapter 4. Seeding Density Indexing (SDI) for Improved Image Velocimetry Analysis: Using PTV Results to Optimise Tracer Metrics

4.1 Chapter Overview

This chapter addresses the challenges in achieving accurate river flow measurements using image velocimetry, focusing on the critical role of tracer characteristics such as density and spatial distribution, referred to as dispersion. Traditional methods rely on Pre-Processed SDI to evaluate image quality, but this approach may overlook the actual performance of tracers during analysis. To enhance the accuracy of PTV methods, this chapter introduces Post-Processed SDI, which assesses tracers based on output data from PTV. By focusing on the actual tracer metrics of density and dispersion obtained during tracking, this approach aims to refine SDI calculations and improve the precision of velocimetry estimates. The chapter details the methodology for calculating Post-Processed SDI and explores its potential benefits for optimising flow measurement.

4.2 Introduction

For non-contact estimates of river flows, image velocimetry combined with bathymetric data has emerged as a promising alternative approach. Over the past two decades, research has increasingly focused on the remote monitoring of river conditions using image velocimetry (Boursicaud et al., 2016; Perks et al., 2016; Tauro, Tosi, Mattoccia, Toth, Piscopia and Grimaldi, 2018). However, applying image velocimetry in uncontrolled outdoor environments—where conditions are often sub-optimal—presents several challenges. Accurate analysis relies heavily on the successful detection and tracking of features on the river surface (Dal Sasso et al., 2020; Pizarro et al., 2020a).

Researchers have identified three key metrics for assessing the quality of imagery in velocimetry analysis: seeding density, tracer dispersion, and the shape and size of tracers (Dal Sasso et al., 2018). Building on this foundation, Pizarro et al. (2020a) examined the impact of seeding density and dispersion on the reliability of velocimetry estimates and introduced the concept of the Seeding Density Index (SDI).

SDI is a technique that compares seeding density and spatial dispersion of tracers against idealised values derived from controlled numerical simulations, with the aim of reducing error in velocimetry analysis. This index has proven effective in filtering pre-processed frames, reducing velocimetry error by up to 39% in some cases (Pizarro et al., 2020a,b; Dal Sasso et al., 2021). To

compute the original SDI, the algorithm `detectMSERFeatures`, a built-in `MATLAB` function, is used. This algorithm assesses the stability of intensity across regions of an image and identifies distinctive shapes suitable for tracking (MathWorks, 2023). The size and distribution of these features are then used to calculate SDI metrics—specifically, seeding density and dispersion. However, this method estimates potential tracer conditions, rather than the actual tracers used by PTV software during analysis. As a result, frames containing usable data may be unnecessarily excluded, limiting analysis coverage and reducing the number of velocity vectors available for discharge estimation. Furthermore, because pre-processing thresholds are not aligned with real tracking behaviour of PTV, their relevance for accuracy validation is limited.

To address these limitations, this chapter introduces a new method: Post-Processed SDI. Unlike traditional approaches, Post-Processed SDI evaluates actual tracer performance by analysing the output from PTV. It reflects the real seeding density and dispersion within the ROI and is based solely on successfully tracked tracers. This approach provides a more accurate and flexible assessment of tracer conditions, enabling greater retention of data and enhancing overall precision in velocity estimation.

The overarching goal of this study is to identify the optimal values for seeding density and dispersion that minimise velocimetry error, and to propose a refined SDI model better aligned with real-world performance. This chapter introduces the theoretical framework behind Post-Processed SDI, outlines its practical implementation through controlled experiments, and demonstrates its potential to improve the accuracy of image velocimetry in natural environments.

4.2.1 Research Questions

These research questions are derived from, and directly support, the overarching aims and objectives outlined in Section 1.6. While Section 1.6 sets the broader motivation of improving non-contact river discharge measurement, particularly for real-world applications such as flood event quantification, the questions below focus on the specific analytical developments required to achieve that goal.

1. To what extent do actual seeding density and dispersion impact the accuracy of PTV in velocity analysis?

2. What is the optimal value for actual seeding density for developing a Post-Processed SDI equation tailored to PTV methods?

3. Can the new Post-Processed SDI be effectively used to estimate velocimetry errors in river flow analysis?

4.3 Methods

4.3.1 Synthetic Simulations

Previous studies have demonstrated that seeding density and dispersion play crucial roles in determining the accuracy of image velocimetry methods (Pizarro et al., 2020a,b; Dal Sasso et al., 2021). To investigate these factors, synthetic simulations offer an effective approach, providing complete control over external influences and minimising variability from uncontrolled or unmeasured factors. This allows key metrics such as density, dispersion, and velocity—each directly impacting error and SDI—to be precisely known and manipulated.

The synthetic videos used in this study were created by Pizarro et al. (2020a) to represent a series of realistic seeding scenarios. Fourteen total scenarios were used, each corresponding to a generated seeding density ranging from 0.4×10^{-4} PPP to 1×10^{-2} PPP. Within each of these density scenarios, dispersion values were varied and randomly generated using a generalised Poisson distribution (GPD), based on imposed seeding density (λ) and dispersion (υ). The study assumes a random distribution of tracers, with the mean number of points given by λS, where S is the considered area. The probability mass function used by Pizarro et al. (2020a) is shown in Equation 4.1. Simulations were constructed using a uniform background featuring both white and black regions, introducing variability and noise. Tracers varied in size and shape, with diameters ranging from 10–15 px and appearing as both circular and non-circular forms. Tracer movement was one-dimensional, with a known velocity of 15 px/s.

$$f_{GPD(\lambda s)}(\eta_i) = \frac{1}{C_{GPD}} \frac{\exp\left(-\frac{\lambda s}{\upsilon}\right)}{\sqrt{\upsilon}} \left(\frac{\exp(-\eta_i)\eta_i^{\eta_i}}{\eta_i!}\right)\left(\frac{\exp(1)\lambda s}{\eta_i}\right)^{\eta_i/\upsilon} \tag{4.1}$$

Here, λS and υ control the location and shape of $f_{GPD(\lambda S)}$, and C_{GPD} is an integration constant.

Dispersion values ranged from $\upsilon = 0.5$ (over-dispersed) to $\upsilon = 200$ (under-dispersed), with $\upsilon = 1$ representing an idealised GPD distribution. For each dispersion setting, 20 synthetic images were generated per density scenario. Each scenario was repeated 10 times, resulting in 14 seeding densities (λ), each with 12 levels of dispersion (υ), repeated 10 times, and composed of 20 frames each. In total, 33,600 images were produced and compiled into 1,680 synthetic videos, with each video containing 20 frames at 1 fps.

Examples of these synthetic outputs are presented in Figure 4.1.

4.3.2 Metrics for Analysis

This study focuses on two distinct sets of metrics: those imposed and generated within the synthetic imagery, and those observed through PTV analysis. The metrics generated within the synthetic images include numerically imposed seeding density and numerically imposed dispersion. These imposed values serve as the experimental controls, allowing for the manipulation of tracer

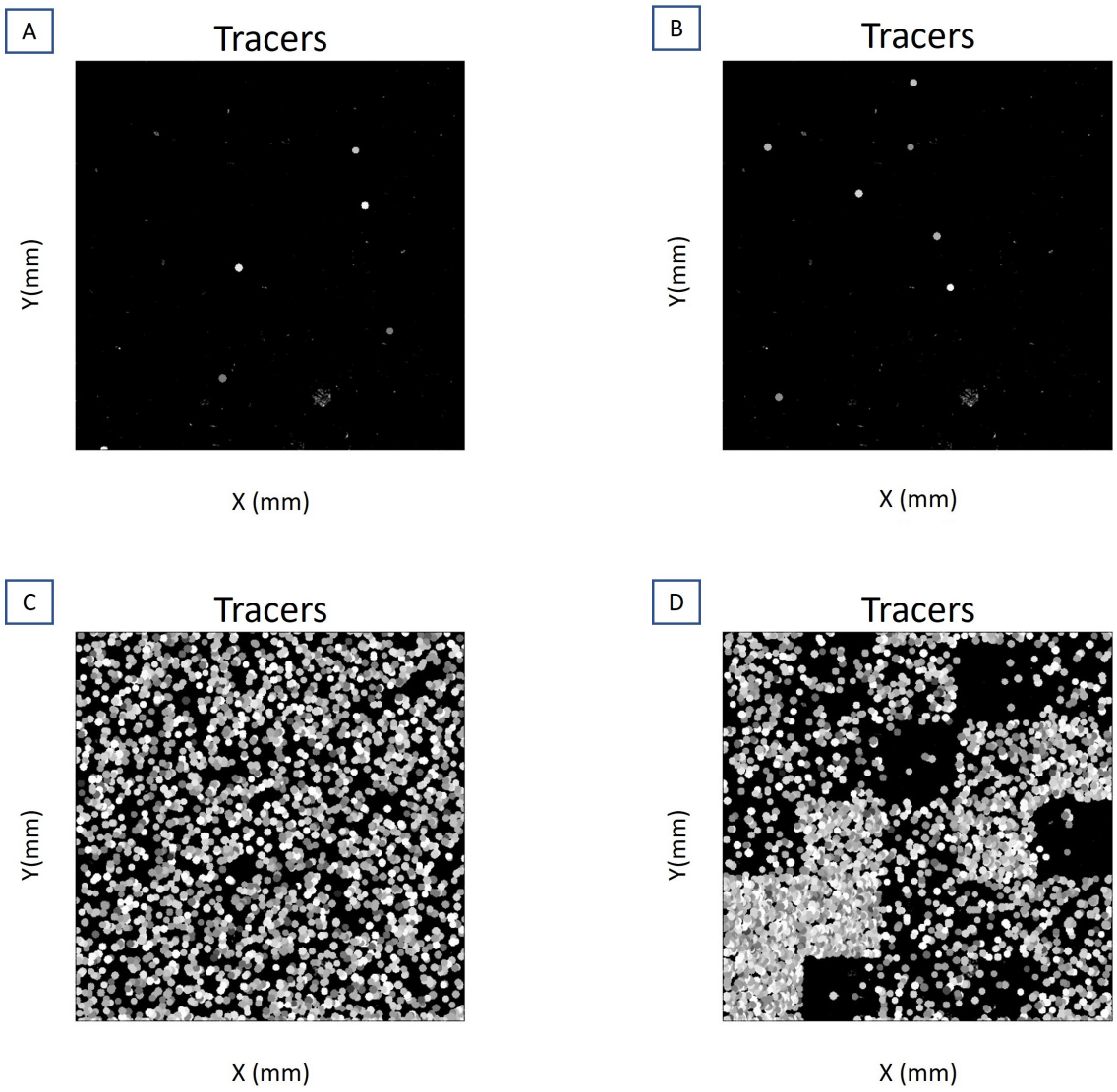


Figure 4.1: Examples of synthetic imagery used in this study. A and B show the minimum seeding density used (ρ = 4×10^{-4} PPP), while C and D show the maximum seeding density (ρ = 1.02×10^{-2} PPP). Dispersion extremes are also shown, with A and C highlighting the minimum μ = 0.5 (over-dispersed), and B and D showing the maximum μ = 200 (under-dispersed).

availability and dispersion.

As described in Section 3.3.1, the range of these values is set between $\rho = 4 \times 10^{-4}$ PPP and $\rho = 1.02 \times 10^{-2}$ PPP for imposed density, and $\mu = 0.5$ and $\mu = 200$ for imposed dispersion. The second set of metrics relates to actual density and actual dispersion, which are derived from the PTV analysis of the synthetic datasets. Both actual metrics are calculated using only successfully tracked tracers that have passed through PTV threshold algorithms, ensuring that only detectable and trackable features count towards density and dispersion metrics. These observed metrics will be further discussed in the following sections.

4.3.2.1 Seeding Density

Seeding density refers to the concentration of tracers within the ROI. The ROI refers to the specific area within an image or video frame selected for velocimetry analysis. It is typically delineated to exclude irrelevant parts of the image—such as banks, obstructions, or background features—and focuses solely on the portion of the river surface where flow measurements are intended. Seeding density is specifically defined as the average number of particles per pixel (PPP) within an image frame. This metric plays a significant role in determining the accuracy of PTV analysis by influencing the detection and tracking of particles across multiple frames.

Pre-Processed SDI Approach: In the pre-processed SDI approach, seeding density is calculated using the *detectMSERFeatures* algorithm during the pre-processing phase. The algorithm detects regions of consistent intensity, identifying potential features that can serve as tracers in the velocimetry analysis. The total area of these detected features within the ROI is summed and then divided by the total area of the ROI to calculate the seeding density. For instance, if four large features are detected with individual areas of $90\,\text{px}^2$, the total feature area would be $4 \times 90 = 360\,\text{px}^2$. Given an ROI size of $500 \times 500\,\text{px}$, resulting in an area of $250,000\,\text{px}^2$, the pre-processed seeding density would be calculated as $360/250,000 = 1.44 \times 10^{-3}$ PPP. This approach provides an estimate of potential tracers based on the detected features, which are used as input for further analysis in the PTV process.

Post-Processed SDI Approach: In contrast, the Post-Processed SDI approach shifts the focus from potential tracers to actual tracers that have been successfully tracked during PTV analysis. Instead of relying on pre-identified features, this method calculates seeding density based on the starting and ending positions of particles that are successfully tracked across frames. During PTV analysis, a specific particle is identified and tracked from one frame to the next. The positions of the particle in consecutive frames allow for the calculation of the distance travelled, and, by considering the frame rate (1 fps in this study), the velocity can be determined. Unlike pre-processed SDI, which considers the area of potential features, Post-Processed SDI focuses solely on the coordinates of the successfully tracked particles, providing a more accurate reflection of the actual tracer distribution within the ROI.

To calculate the post-processed seeding density, the ROI is divided into grid cells based on a user-defined block size at the start of the PTV analysis. Each grid cell has a known area. The seeding density for each grid cell is then calculated by dividing the number of successfully tracked particles within the cell by the cell's area. For instance, if a grid cell contains 20 successfully tracked particles and has an area of $31\,\text{px}^2$, the seeding density for that specific grid cell is $\frac{20}{31^2} = 2.08 \times 10^{-2}$ PPP. An example of this process and the outputs can be seen in Figure 4.2. This process is repeated across all grid cells within the ROI, and the results are averaged to obtain the overall

seeding density for each frame. The general equation for calculating post-processed seeding density is shown in Equation 4.2. This seeding density is calculated for each frame and averaged across the entire video to provide an overall seeding density for each synthetic video.

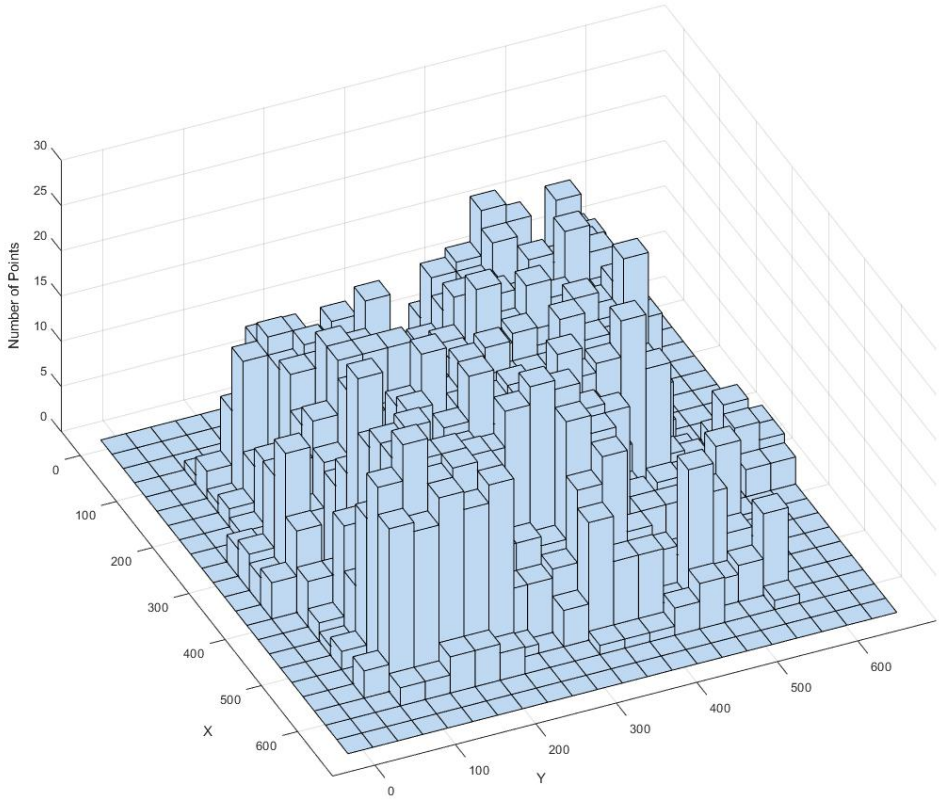


Figure 4.2: Example histogram plot for calculating seeding density. The x and y-axes represent the pixel coordinates of the ROI. Each grid cell's area size is determined by the user-inputted block size. The total number of points detected and successfully tracked by PTV within each grid cell is shown on the z-axis. The seeding density result for each video processed is an average of the grid cell density values.

$$\rho = \frac{\sum(N_i/G_{area})}{N_{gridcells}} \tag{4.2}$$

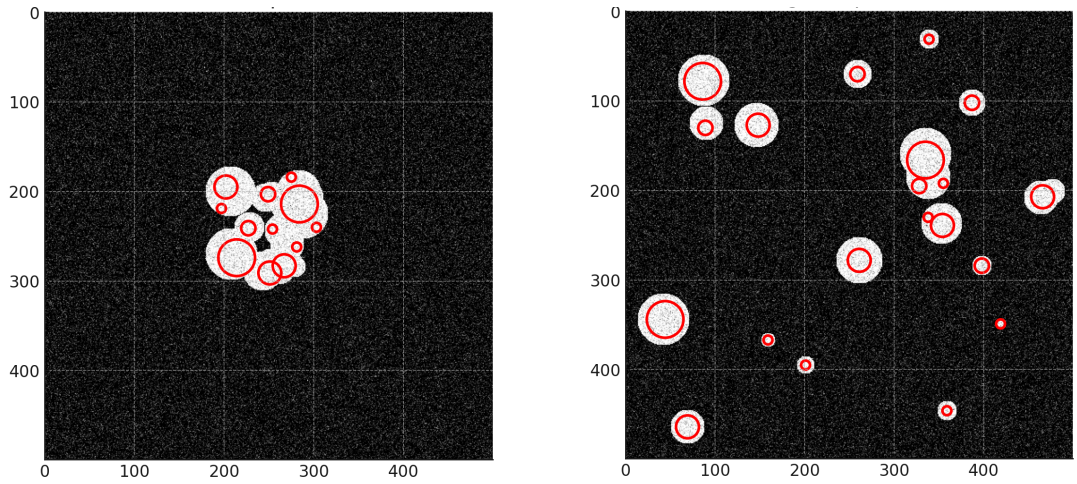
Where:

- ρ is the seeding density for the ROI.
- N_i is the total number of successfully tracked tracers in each grid cell i.
- G_{area} is the grid cell area (determined by the user-defined block size).
- $N_{gridcells}$ is the total number of grid cells in the ROI.

4.3.2.2 Dispersion

Dispersion (ν) quantifies the spatial clustering of tracers within the ROI, assessing how evenly or unevenly tracers are distributed. In the context of this study, it provides a measure of the variability in seeding density across different areas of the ROI, which is crucial for evaluating the quality of velocimetry data for flow estimations.

Pre-Processed SDI Approach: In the pre-processed SDI approach, dispersion is calculated before the PTV analysis. The *detectMSERFeatures* algorithm identifies potential features (tracers) within the ROI based on intensity stability. The algorithm detects regions of the image that exhibit consistent intensity across various thresholds, representing these as features or blobs. These features are then used to estimate seeding density across different grid cells within the ROI. Dispersion is computed by examining the standard deviation of the number of features within each grid cell relative to the average seeding density across all grid cells. For example, if the *detectMSERFeatures* algorithm detects a large number of features clustered in one area of the ROI, this clustering would result in a high dispersion value. Conversely, if the features are evenly distributed, the dispersion value would be lower, indicating a more uniform distribution of tracers. This process is repeated for each frame to calculate the overall dispersion for the pre-processed data. Figure 4.3 provides visual examples of how the *detectMSERFeatures* algorithm identifies and processes features.



(a) High ν **(b)** Low ν

Figure 4.3: Examples of the *detectMSERFeatures* algorithm detecting low (a) and high (b) ν in tracer data.

Post-Processed SDI Approach: In contrast, the Post-Processed SDI approach calculates dispersion based on the actual tracers that have been successfully tracked during PTV analysis, rather than relying on pre-identified potential features. An example of why this has been considered as an alternative is seen in Figure 4.3b: while the *detectMSERFeatures* algorithm generally does a good job of identifying tracers, variations in tracer shapes or close proximity between tracers can impair

density and dispersion metrics. This is because the algorithm might either generate multiple tracers from what would be classified as a single point tracer in PTV, or it could group several tracers into a single point.

The post-processed method, on the other hand, directly reflects the actual distribution of successfully tracked tracers within the ROI, providing a more accurate and relevant measure of dispersion. To calculate the dispersion in the Post-Processed SDI approach, the standard deviation (σ) of seeding density in each grid cell is first determined. This standard deviation is then divided by the average seeding density ($\overline{\rho_i}$) across all grid cells to obtain the dispersion (ν), as defined in Equation 4.3:

$$\nu = \frac{\sigma_\rho}{\overline{\rho_i}} \tag{4.3}$$

Where:

- ν represents the dispersion.
- σ_ρ is the standard deviation of seeding density across grid cells.
- ρ_i denotes the seeding density in each individual grid cell.
- $\overline{\rho_i}$ is the average seeding density over all grid cells in the ROI.

The standard deviation (σ) is calculated using the formula:

$$\sigma_\rho = \sqrt{\frac{\sum (\rho_i - \overline{\rho_i})^2}{N}} \tag{4.4}$$

Where:

- σ_ρ is the standard deviation.
- ρ_i represents the seeding density in each grid cell.
- $\overline{\rho_i}$ is the average seeding density over all grid cells.
- N is the total number of grid cells in the ROI.

4.3.2.3 Summary: Comparison of Seeding Density Index Approaches

The key difference between the pre-processed and post-processed SDI approaches lies in their treatment of seeding density and dispersion. In the pre-processed approach, both seeding density and dispersion are estimated based on potential tracers identified before the PTV analysis using the *detectMSERFeatures* algorithm. This method calculates seeding density by dividing the total area of detected features by the area of the ROI and estimates dispersion based on the standard deviation

of these features' areas relative to the overall ROI size. However, this approach only considers potential tracers and does not account for whether these features are successfully tracked during the analysis, which can limit its accuracy in reflecting the actual conditions during the velocimetry process.

In contrast, the post-processed approach calculates both seeding density and dispersion based on tracers that are actually tracked during the analysis. This method divides the ROI into grid cells, calculates the density and dispersion of tracers within each cell, and averages these values to obtain the overall metrics for each frame. The post-processed approach provides a more accurate and realistic measure of both seeding density and dispersion, as it directly links these metrics to the performance of the PTV software, leading to more reliable and precise flow measurements. A dispersion value (ν) of 1, for example, indicates perfect evenness in seeding density across all grid cells, signifying minimal spatial clustering. This comprehensive approach ensures that the calculated metrics reflect the actual behaviour of tracers within the ROI, enhancing the reliability of the velocimetry analysis.

4.3.3 Image Velocimetry Analysis

4.3.3.1 Analysis using Particle Tracking Velocimetry

The 1680 synthetic datasets were loaded into the software and processed using a simplified version of KLT-IV, which was customised for handling numerical data. The user-input parameters for this simplified version include the extract rate, block size, velocity component, and ROI. In this study, the extract rate was set to 1 to match the synthesised frame rate. This means that each frame was analysed in sequence with the subsequent frame because the synthetic videos were generated with a frame rate of 1 frame per second (fps). The velocity component remained as velocity magnitude since the tracers' movement direction was already unidirectional. This choice simplifies the analysis process. The block size parameter was kept at its default value of 31×31 pixels, deemed an acceptable size given the tracer diameter is controlled at 4 px. The ROI was set to cover the entire synthesised frame. These settings ensured that all relevant data were captured, and the results could be easily replicated.

To determine the accuracy of PTV results, successfully tracked tracer velocity was compared to the known velocity for tracers (15 px/s). This was calculated as a percentage error, as shown in Equation 4.5:

$$\epsilon = 100 \times \frac{u_o - u_r}{u_r} \tag{4.5}$$

Where u_o is the observed velocity and u_r is the numerically imposed velocity (15 px/s). Output data included the measured velocity for each tracer, as well as the start and end location (in pixel coordinates) of each successfully tracked particle. These locations were used to determine seeding

density and dispersion. The total time required to process all 1680 simulations for the full SDI analysis was 309 seconds using an Intel(R) Core(TM) i5-6400 CPU @ 2.70 GHz with 16 GB RAM.

4.4 Results

4.4.1 Particle Trackig Velocimetry Results

The performance of PTV was assessed by calculating the velocimetry error, as described in Section 4.3.3.1 and Equation 4.5, using the imposed numerical velocity of 15 pixels per second. The primary objective was to investigate how seeding density and spatial dispersion of tracers influenced the accuracy of the final velocity estimates. No post-processing methods were applied to filter the velocity results in this assessment. The ROI used for analysis was defined to match the original dimensions of the synthetic image generation process. This approach aligns with previous studies on image velocimetry and PTV methods.

Consistent with findings in the literature, the velocity results obtained in this study consistently underestimated the actual velocity, irrespective of seeding density and dispersion (Dal Sasso et al., 2018; Pizarro et al., 2020a). This underestimation may be attributed to the presence of sporadic zero-velocity vectors. Upon closer examination of the results presented in Table 4.1, it is evident that videos with fewer successfully tracked tracers tend to exhibit a higher proportion of zero-velocity vectors compared to those with more tracers.

Range (error %)	**Less than 10**	**Between 10 and 25**	**Greater than 25**
Average Total Tracers	30004	6183	3534
Average Successful Tracers	27801	4402	1550
Average Number Of Zero-Velocity Vectors	314	462	478
Average % of Successful Zero-Velocity Vectors	1.1%	10.5%	30.9%

Table 4.1: The PTV results indicate that videos with higher error percentages tend to have a greater proportion of zero-velocity vectors than those with lower errors. Note that all error percentages are originally negative but are shown as absolute values for clarity.

The observed relationship between velocity error and the number of successfully tracked tracers supports the hypothesis that lower tracer densities increase the visibility of static background features, leading to more frequent detection of zero-velocity vectors. This finding underscores the importance of understanding how seeding density and dispersion influence the accuracy of PTV-based velocimetry measurements.

4.4.2 Metric Results

4.4.2.1 Seeding Density

Previous studies, such as Pizarro et al. (2020a) and Dal Sasso et al. (2020), have explored the relationship between imposed seeding density and velocimetry error in PTV analysis. Their findings

revealed a significant correlation between the numerically imposed seeding density (the density of tracers introduced into the flow during the experiment) and the velocimetry error (the discrepancy between the estimated and actual velocities). In this study, a comparison is made between the observed error and the numerically imposed densities from the synthetic images. This relationship is visually represented in Figure 4.4A, where numerically imposed seeding densities are plotted on the x-axis and the corresponding velocimetry errors on the y-axis.

Upon examining Figure 4.4A, it is observed that, in the context of Post-Processed SDI studies, the relationship between imposed seeding density and error follows a pattern consistent with that seen in Pre-Processed SDI studies. However, in Pre-Processed SDI analyses, results were further segregated within their density bins by their imposed dispersion values. Specifically, the minimum (ν = 0.5) and maximum (ν = 200) dispersion values directly correlated with the minimum and maximum errors observed within each density group (Pizarro et al., 2020a). This pattern is not observed in the Post-Processed SDI study, as will be further explored in Section 4.4.2.2. Overall, Figure 4.4A shows a clear trend of decreasing velocimetry error with increasing imposed seeding densities.

Optimal Seeding Density To determine the ideal density required for the SDI equations, a similar approach to that used in Pre-Processed SDI studies is applied. This involves comparing observed error with actual seeding density obtained through PTV, as shown in Figure 4.4B. The results confirm the expected strong relationship between these two variables. However, since the data are not grouped by numerically imposed densities, it is challenging to identify a specific density that yields exactly 3% error.

Within the range of 4.895×10^{-3} PPP to 1.02×10^{-2} PPP, the error consistently ranges between 3.5% and 2.5%. To determine an optimised seeding density, a smoothing spline (p = 0.92913) was applied to the error-density dataset, as illustrated in Figure 4.5. This smoothing process highlights the value at which the average error drops below 3%. The optimal seeding density is identified as 6.85×10^{-3} PPP, which is approximately six times greater than the optimal density required for Pre-Processed SDI methods (1.02×10^{-3} PPP) (Pizarro et al., 2020a).

Imposed vs. Actual Seeding Density Figure 4.4C compares the numerically imposed seeding density with the actual seeding density acquired through PTV. The x-axis represents the imposed density, while the y-axis shows the actual density as determined through analysis.

This comparison reveals an interesting relationship: when the imposed density is low, the actual PTV-derived seeding density is approximately 10 times higher. For example, an imposed density of 4×10^{-5} PPP yields an actual density of 3.8×10^{-4} PPP. This difference may be largely attributed to the influence of zero-velocity vectors resulting from noise in the image sequences. Table 4.1 supports this observation, showing that when errors exceed 25%, approximately 31% of successfully tracked tracers correspond to zero-velocity vectors.

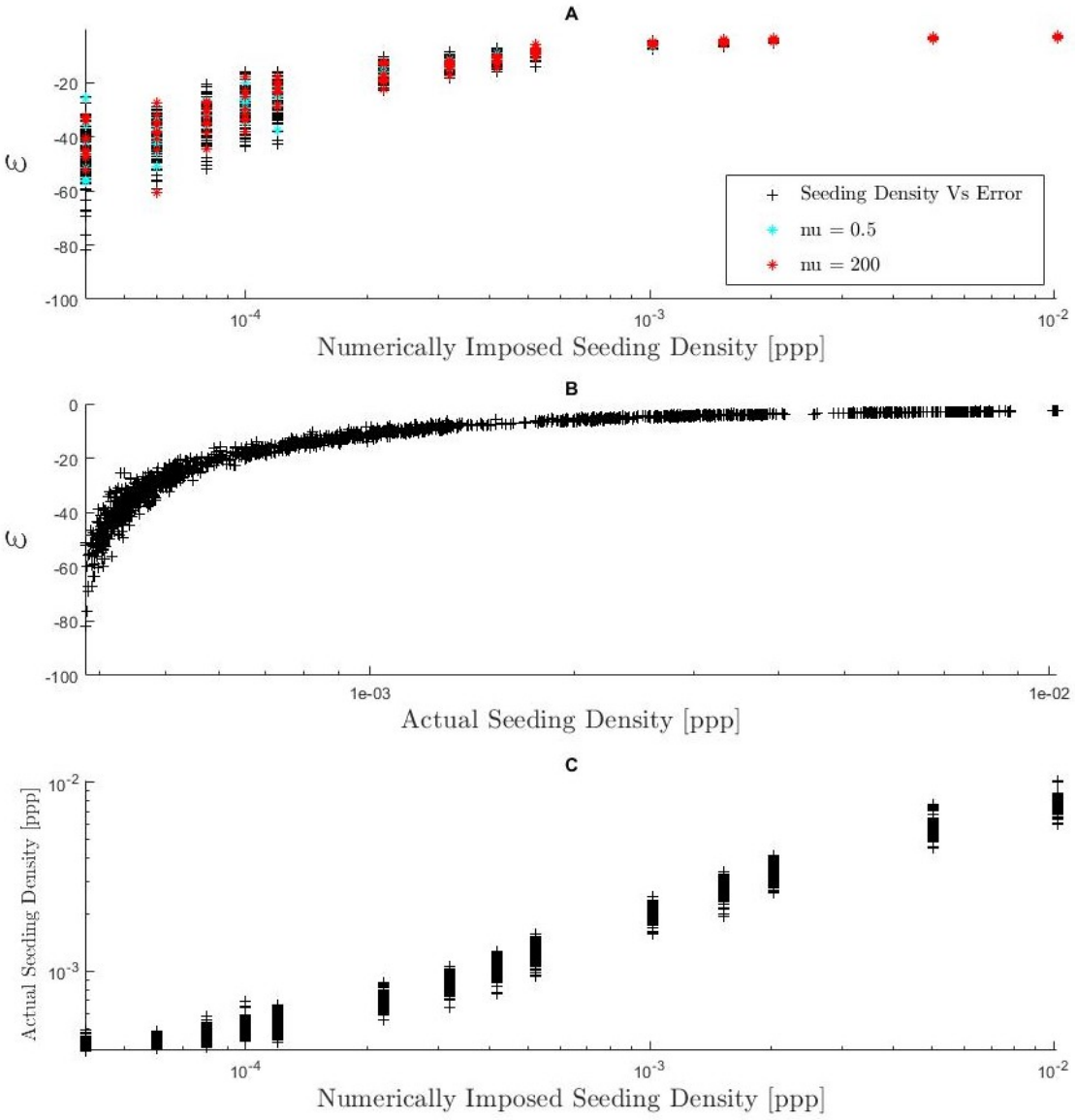


Figure 4.4: PTV error results for the metric of seeding density. (A) Numerically imposed seeding density versus velocimetry error. (B) Velocimetry error as a function of actual seeding density. (C) Comparison between numerically imposed seeding density and actual seeding density obtained through PTV for each simulated video.

In essence, this comparison highlights the substantial impact of noise and zero-velocity vectors on the relationship between imposed and actual seeding densities. While a clear correlation exists between higher errors, lower seeding densities, and a higher percentage of zero-velocity vectors, other contributing factors may also influence velocimetry error and should be explored further such as background motion, inconsistent tracer brightness, or occlusion by environmental elements may also contribute to the observed variability in velocimetry error.

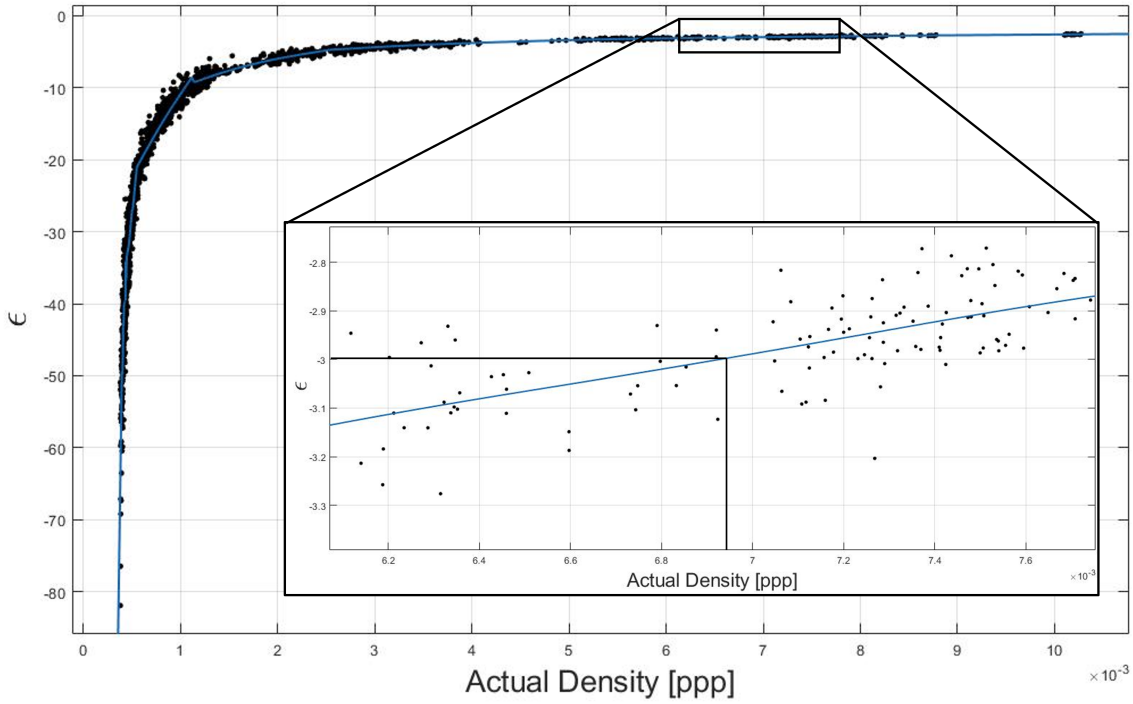


Figure 4.5: Seeding density plotted against error as in Figure 4.4B, using a MATLAB-created smoothing spline where $p = 0.92913$. The seeding density required to achieve an average error of 3% is 6.85×10^{-3} PPP.

4.4.2.2 Seeding Dispersion

Pre-Processed Dispersion Comparisons Seeding dispersion plays a critical role in determining the accuracy of velocimetry analyses, particularly in pre-processed metrics. Previous studies have demonstrated that the velocity error is minimised when using dispersion values around $\nu = 0.5$ and maximised for dispersion values near $\nu = 200$ (Pizarro et al., 2020a). This indicates that dispersion should significantly impact the resulting velocity error. In studies of Pre-Processed SDI, the range of error values observed between $\nu = 0.5$ and $\nu = 200$ serves as an envelope encompassing the error values within each density group.

In this study, however, a different trend emerges when comparing the actual dispersion observed in experiments with numerically imposed dispersion values. Figure 4.4A illustrates that synthetic videos created with specific numerically imposed dispersion values—such as $\nu = 0.5$ (blue) and $\nu = 200$ (red)—do not effectively constrain or bound the error within each density group. These values fail to show a clear correlation with the resulting error, suggesting that other factors, particularly seeding density, may play a more significant role in influencing velocimetry error.

Post-Processed Dispersion Observations The differences between Pre-Processed and Post-Processed SDI approaches are further supported by Figure 4.6A, which shows minimal changes in error across varying imposed dispersion values. This reinforces the idea that adjusting numerically imposed dispersion within a certain range does not substantially affect the resulting error.

Despite the absence of a strong relationship with imposed dispersion, an exponential relationship is observed between actual dispersion and velocimetry error, as shown in Figure 4.6B. This relationship is described by:

$$\epsilon = -0.5248(\exp^{1.311x}) \quad \text{(RMSE = 3.345\%)}, \tag{4.6}$$

where ϵ is the velocimetry error and x is the actual dispersion. This equation demonstrates that as actual dispersion approaches the ideal value of $\nu = 1$, the velocimetry error significantly decreases. The value $\nu = 1$ corresponds to a coefficient of variation derived from grid cell density averages, as outlined in Section 4.3.2.2, reinforcing the assumption that minimal clustering (i.e., uniform tracer distribution) improves accuracy.

Figure 4.6C highlights the lack of a relationship between observed dispersion and numerically imposed dispersion. Regardless of the imposed dispersion value, actual dispersion values tend to fall within a relatively narrow range, approximately 1 to 3.5. This discrepancy is likely due to the presence of zero-velocity vectors, which are introduced through image noise and not by the simulated motion of tracers (none of which are meant to be static). These zero-velocity vectors may substantially distort post-processed dispersion calculations, especially in scenarios with high or low tracer density.

Role of Zero-Velocity Vectors In Pre-Processed SDI calculations, efforts are made to remove spurious vectors prior to computing seeding metrics. In contrast, Post-Processed SDI in this study does not filter such vectors. This choice reflects the practical challenge of removing zero-velocity vectors in real-world PTV applications. Given their demonstrated influence on error, their presence must be considered when interpreting the relationship between imposed and observed dispersion. These vectors, typically introduced by noise, highlight the importance of refining dispersion calculation methods to improve measurement reliability.

Future studies should explore more robust approaches that address these discrepancies and reduce the influence of noise on dispersion metrics. Section 2.2.2.1 provides an overview of several vector correction methods that could be explored further to enhance the processing and validation of PTV outputs.

4.4.2.3 Summary of Seeding Density and Seeding Dispersion

The analysis of seeding density and dispersion reveals crucial insights into their roles in affecting velocimetry error. For seeding density, a significant correlation between the numerically imposed seeding density and velocimetry error was confirmed, consistent with previous studies (Pizarro et al., 2020a). The optimal seeding density for Post-Processed SDI was determined to be 6.85×10^{-3} PPP, which is substantially higher than the density required for Pre-Processed SDI methods. This optimal density was identified through a smoothing spline applied to the observed error and

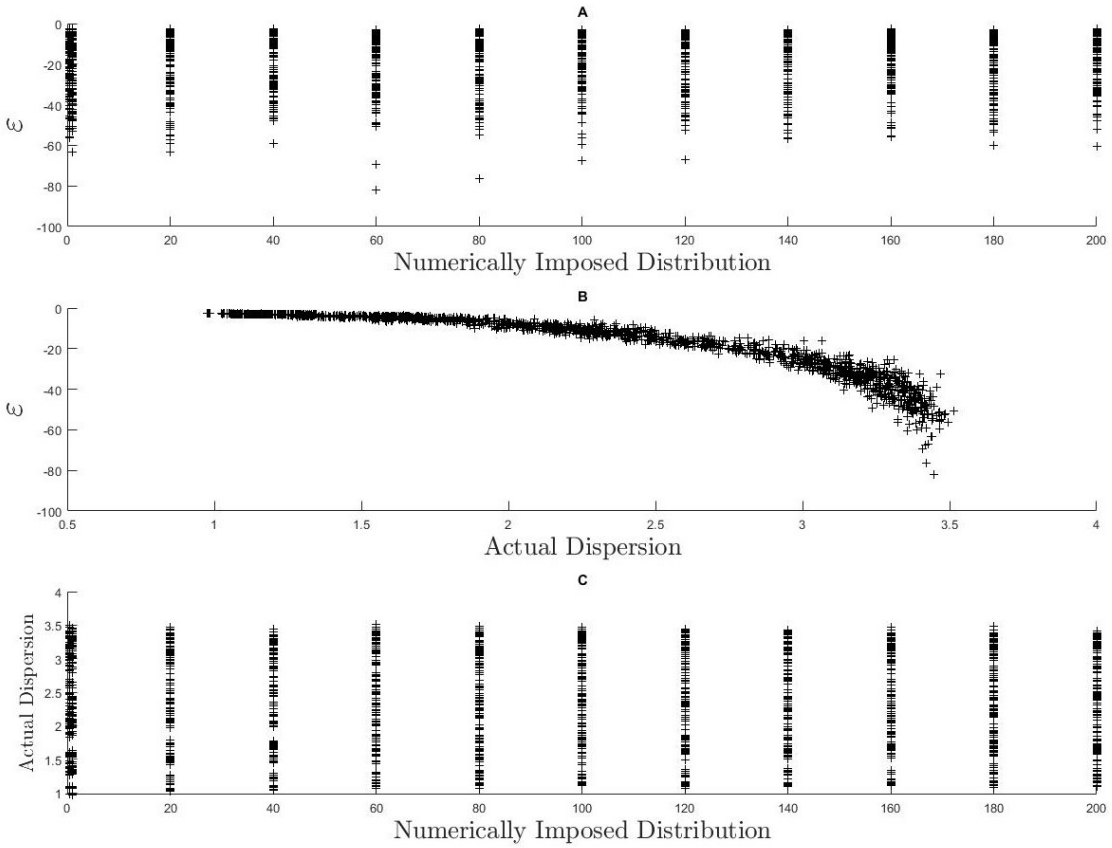


Figure 4.6: The impact of numerically imposed and actual dispersion on error. (A) The relationship between numerically imposed dispersion and error. (B) The exponential relationship between actual dispersion and velocimetry error. (C) The comparison between numerically imposed dispersion and actual dispersion observed in the experiments.

actual seeding density data, highlighting the importance of considering actual density rather than relying solely on numerically imposed values.

In terms of seeding dispersion, previous studies indicated that the error is minimised with dispersion values around $\nu = 0.5$ and maximised near $\nu = 200$ in Pre-Processed SDI (Pizarro et al., 2020a). However, in this study of Post-Processed SDI, numerically imposed dispersion values did not show a clear correlation with velocimetry error, suggesting that other factors, particularly seeding density, may have a more significant influence. Despite this, an exponential relationship between actual dispersion and velocimetry error was identified, indicating that as the dispersion approaches the ideal value of $\nu = 1$, the error decreases significantly. Moreover, the presence of zero-velocity vectors—often a result of noise and erroneous readings—was found to skew the calculation of observed dispersion during post-processing. This underscores the need for refined methods to account for such discrepancies and reduce the influence of noise on dispersion metrics.

4.4.3 Formulating SDI

4.4.3.1 Overview

Similar to the approach taken in Pizarro et al. (2020a), the analysis of the synthetic data for SDI primarily focuses on two key metrics: seeding density (ρ) and dispersion (ν). It is hypothesised that velocimetry errors depend solely on these two metrics. For the Pre-Processed optimised SDI metrics, the ideal values were determined to be $\nu = 1$ and $\rho_{\text{ideal}} = 1.02 \times 10^{-3}$ PPP (Pizarro et al., 2020a). However, upon analysing the results obtained from the Post-Processed SDI, new optimal values deviate slightly. The revised optimal values are $\nu = 1$ and $\rho_{\text{ideal}} = 6.85 \times 10^{-3}$ PPP, as observed from the analysis of the Post-Processed PTV data.

4.4.3.2 Generalised Equations

In Pizarro et al. (2020a), it was suggested that the relationship between the metrics can be represented by a function f as a multiplication of power laws, where the functional relationship of f is described by a two-parameter exponential function. Given the success of this approach in capturing the relationship for the Pre-Processed SDI, the same methodology is used for the analysis of the Post-Processed SDI.

$$\epsilon = c_1 \left(1 - \exp^{-c_2 \cdot \text{SDI}}\right) \tag{4.7}$$

$$\text{SDI} = \nu^{k_1} \left(\frac{\rho}{\rho_{\text{ideal}}}\right)^{k_2} \tag{4.8}$$

The coefficients c_1, c_2, k_1, and k_2 are crucial fitting parameters for the model. Figure 4.7A demonstrates the process of establishing the functional relationship between optimised SDI (idealised metric $\nu_{\text{ideal}} = 1$) and the observed SDI (using actual ν). This relationship is fundamental for determining the coefficients k_1 and k_2, used in Equation 4.8 by calculating the relationship between observed and idealised dispersion. Subsequently, these coefficients are important in creating the calculated SDI, forming the basis for estimating error. The calculated SDI is then correlated with its relative error, as illustrated in Figure 4.7B.

4.4.3.3 Coefficient Fitting Results

	c_1	c_2	k_1	k_2	RMSE (error %)
PTV	15.31	0.05789	0.9781	-0.7053	3.14

Table 4.2: Using the optimal density value of $\rho = 6.85 \times 10^{-03}$ PPP and optimal dispersion value of $\nu = 1$, the best-fit coefficients c_1, c_2, k_1, and k_2 were determined. No further calibration was required due to the low RMSE.

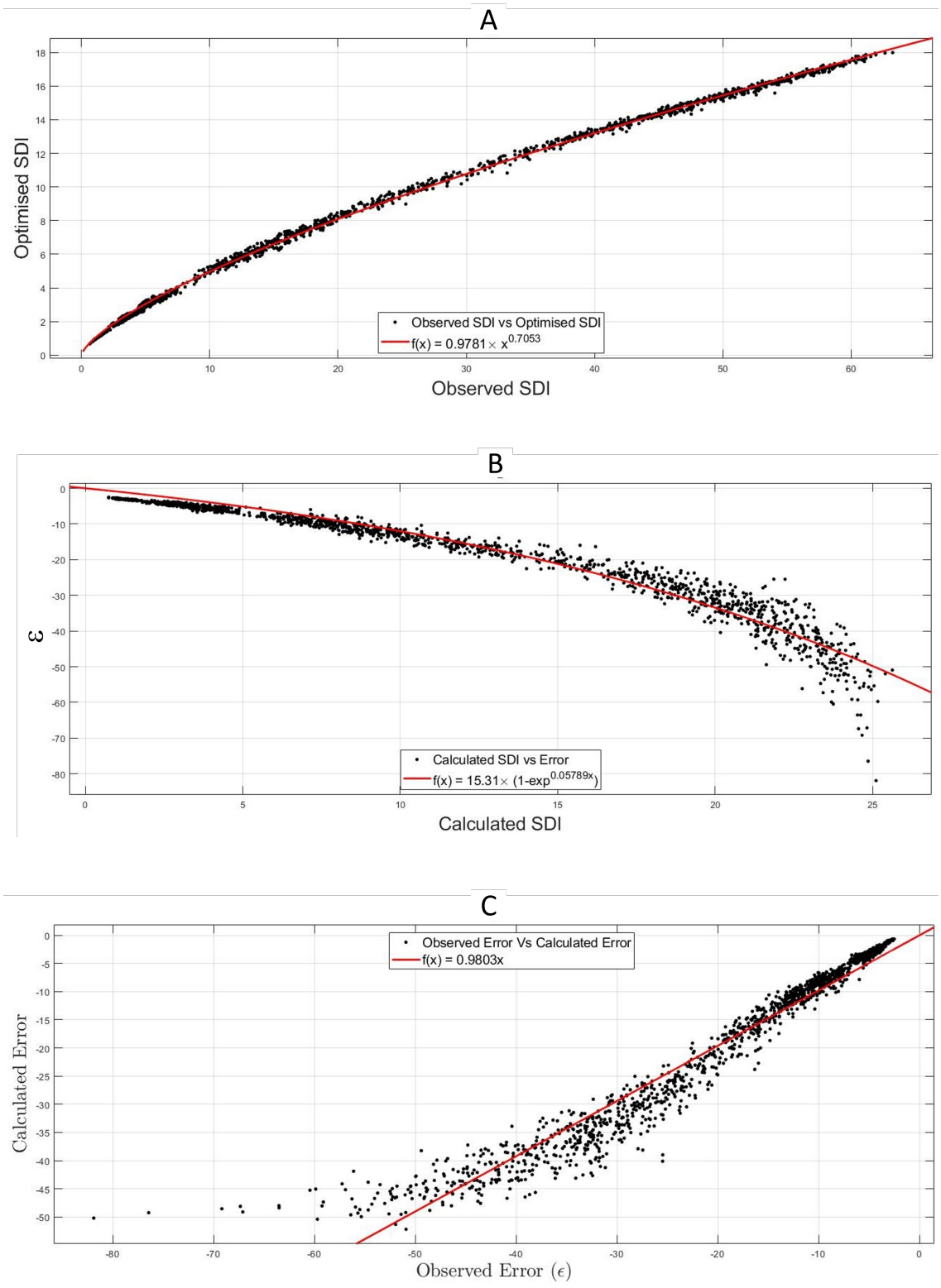


Figure 4.7: (A) Observed vs. idealised SDI with derived power function. (B) Relationship between SDI and velocimetry error. (C) Comparison of calculated and observed error using the SDI–error function.

Using the established relationships, we derive the fitting coefficients shown in Table 4.2. This yields a robust function for error estimation using Post-Processed SDI, as described in Equation 4.7. Using this relationship, error is computed based on the fitted SDI and plotted against observed error in Figure 4.7C. The outcomes reveal a strong linear correlation ($y = 0.9807x$) between observed and calculated errors using Post-Processed SDI, especially for lower error values ($\epsilon < 15\%$) with a coefficient of determination of $R^2 = 0.948$, indicating high model reliability.

Table 4.2 summarises the findings, with the calibration root mean square error (RMSE) reported at a notably low 3.14%. As a result, no additional coefficient tuning was deemed necessary. The fitted relationships allow for quick approximation of velocimetry error based on Post-Processed SDI, as shown in the following equations:

$$SDI_{\text{Post-Processed}} = \nu^{0.9781} \left(\frac{\rho}{\rho_{\text{ideal}}} \right)^{-0.7053} \tag{4.9}$$

$$\epsilon = 15.31 \left(1 - \exp^{-0.05789 \times SDI} \right) \tag{4.10}$$

4.4.3.4 Summary of SDI Formulation

This study formulated a Post-Processed SDI based on two core metrics: seeding density (ρ) and dispersion (ν). Adopting the methodology of Pizarro et al. (2020a), it was assumed that these two factors are the primary contributors to velocimetry error. The analysis revealed updated optimal values specific to the post-processed approach: $\rho_{\text{ideal}} = 6.85 \times 10^{-3}$ PPP, compared to 1.02×10^{-3} PPP for Pre-Processed SDI, while optimal dispersion remained $\nu = 1$.

To describe the relationship between these metrics and error, the study applied a function composed of exponential power laws. The final SDI formulation used fitted coefficients (c_1, c_2, k_1, and k_2), enabling the computation of velocimetry error as a function of SDI. This formulation showed a strong correlation with observed errors, particularly under low-error conditions. With an RMSE of just 3.14%, the model proved highly reliable and did not require further calibration, offering a robust method for error estimation in image velocimetry based on Post-Processed SDI.

4.5 Discussion

The aim of this research was to investigate the influence of seeding density and dispersion on the accuracy of PTV methods for estimating river discharge. This included three core objectives: (1) to quantify the impact of actual seeding density and dispersion on PTV velocity accuracy, (2) to identify optimal seeding conditions and use them to formulate a Post-Processed SDI metric, and (3) to evaluate the potential of SDI to estimate error bounds and improve the reliability of discharge results under real-world conditions.

4.5.1 Influence of Seeding Density on Velocimetry Accuracy

The influence of seeding density on the accuracy of velocimetry results was a central focus of this study. Seeding density is considered a critical parameter that directly affects the reliability and precision of PTV measurements (Pizarro et al., 2020b,a; Tsubaki et al., 2011). In this study, the optimal seeding density was determined to be 6.85×10^{-3} PPP. This value was identified through a series of synthetic simulations designed to mimic various seeding scenarios, ranging from relatively low to high densities. By using synthetic datasets, it was ensured that the results were not influenced by external environmental factors. The optimal seeding density found in this study is significantly higher than the previously established optimal density for pre-processed SDI methods of 1.02×10^{-3} PPP, as reported by Pizarro et al. (2020a). A strong relationship between seeding density and velocimetry error was revealed through the analysis of PTV results. As shown in Figure 4.4B, the error decreases as the seeding density increases, reaching a minimum at the optimal density of 6.85×10^{-3} PPP. Beyond this point, further increases in density do not significantly reduce the error, indicating a saturation point where the benefits of additional tracers are marginal. The observed error at the optimal density was consistently around 3%, which is considered an acceptable threshold given previous studies Pizarro et al., 2020a.

Previous methods that focused on seeding density primarily relied on pre-processed analysis, serving as a predictive tool for assessing the quality of image sequences before conducting PTV analysis. These pre-processed metrics, such as those obtained using the `detectMSERFeatures` algorithm (Figure 4.3), aimed to estimate potential seeding density and dispersion to identify suitable frames for analysis. While these predictive tools are valuable for initial assessments, they do not necessarily reflect the actual conditions during PTV analysis. In contrast, the approach taken in this study emphasised post-processed data, using the actual results obtained from PTV to validate and refine seeding density metrics. This post-processed methodology provided a more accurate representation of the conditions experienced during velocimetry analysis.

An important implication for PTV measurements that arises from the findings of this study is the need for adequate seeding density to ensure accurate velocity estimations. The results indicate that a higher seeding density than previously recommended is required to improve measurement accuracy using actual results. Such alignment would enhance the reliability of pre-processed metrics in predicting velocimetry error and improve overall measurement performance.

4.5.2 Influence of Seeding Dispersion on Velocimetry Accuracy

In this study, the relationship between actual seeding dispersion and velocimetry error was examined in detail. Dispersion (ν) was calculated as the coefficient of variation of seeding density, providing a measure of how evenly tracers are distributed across the ROI. An optimal dispersion value of $\nu = 1$ was identified, indicating minimal spatial clustering and a uniform distribution of tracers. The results demonstrated an exponential relationship between actual seeding dispersion

and velocimetry error, as shown in Figure 4.6B. The error decreased significantly as the dispersion approached the ideal value of $\nu = 1$, underscoring the importance of achieving even tracer distribution to minimise measurement errors. This relationship can be described by the equation $\epsilon = -0.5248(\exp^{1.311x})$, where ϵ represents velocimetry error and x represents dispersion.

Interestingly, no clear relationship was observed between the numerically imposed dispersion and the actual dispersion calculated from the synthetic datasets (Figure 4.6C). This discrepancy suggests that factors beyond the initial seeding configuration influence the final dispersion observed during PTV analysis. One such factor is the presence of zero-velocity vectors, often associated with image noise rather than true tracer movement. These vectors can distort calculated dispersion, contributing to mismatches between imposed and observed values.

By focusing on post-processed data, this study provides a more accurate assessment of dispersion's influence on velocimetry accuracy compared to pre-processed methods. Previous studies such as Pizarro et al. (2020a) used pre-processed metrics to estimate the suitability of image sequences for velocimetry. However, those approaches do not account for the actual conditions during PTV analysis. In contrast, the post-processed approach used here relies on real outcomes obtained from PTV, providing a more reliable validation of dispersion metrics.

Two important implications for PTV emerge from this study. First, achieving even tracer dispersion within the ROI is essential for minimising measurement error. Second, accounting for the influence of image noise and zero-velocity vectors is crucial, as these factors can significantly affect dispersion calculations and, in turn, the accuracy of velocity measurements.

4.5.3 Comparison of Pre-Processed and Post-Processed SDI

In Pre-Processed SDI, the primary aim is to predict the suitability of image sequences for velocimetry by highlighting the best segments based on their SDI values (Pizarro et al., 2020a; Dal Sasso et al., 2021). This method typically uses algorithms such as `detectMSERFeatures` in MATLAB to estimate potential tracer density and dispersion before processing the data with PTV or PIV algorithms. While helpful for preliminary assessments, this technique does not fully reflect the conditions experienced during actual analysis. As a result, discrepancies may occur between estimated and actual metrics, potentially compromising error prediction accuracy.

In contrast, the Post-Processed SDI method applied in this study relies on actual seeding density and dispersion values calculated directly from PTV results. This approach allows for a more accurate and reliable validation of SDI metrics, as it is based on the features that were actually tracked during analysis. By using real data rather than estimated metrics, the Post-Processed SDI approach enables a more precise estimation of velocimetry error. The results of this study clearly demonstrate that using post-processed metrics significantly enhances the accuracy and reliability of error estimation by eliminating the assumptions and uncertainties inherent in pre-processed methods.

Given the complementary strengths of both approaches, future research could explore their

combined application in challenging field environments. Pre-Processed SDI could be used to screen and select video segments with high tracer quality, while Post-Processed SDI could be used to evaluate how well those tracers were actually tracked throughout the sequence. In settings with poor visibility or limited tracer availability, this combined method could reduce data processing time and improve reliability by filtering out sub-optimal frames. This approach holds particular promise once Post-Processed SDI becomes more widely validated and adopted as this would provide a broader empirical basis for selecting appropriate SDI thresholds, increase user confidence in the method's accuracy, and support the development of standardised workflows that integrate both pre, and post, processing stages.

4.5.4 Zero-Velocity Vectors and Their Impact

Zero-velocity vectors occur when PTV software mistakenly identifies stationary features or noise as tracers. These vectors, which represent no movement, introduce significant inaccuracies into velocity calculations, leading to increased overall velocimetry error. Their impact is particularly pronounced in scenarios with low seeding densities, where the limited number of tracers makes the analysis more susceptible to noise. Consequently, the proportion of zero-velocity vectors tends to increase under such conditions.

This study revealed a clear correlation between the prevalence of zero-velocity vectors and elevated velocity estimation errors. For instance, videos with error rates exceeding 25% exhibited an average of 30.9% zero-velocity vectors among the successfully tracked tracers, compared to only 1.1% in videos with less than 10% error, as shown in Table 4.1. The presence of zero-velocity vectors also distorts dispersion calculations, as they are included in the count of tracers despite their lack of movement. This leads to inflated density and dispersion metrics, further compromising the accuracy of the analysis.

4.5.5 Influence of Video Duration on PTV Accuracy

The synthetic datasets used in this study consisted of video sequences composed of 20 frames, each captured at a rate of one frame per second. This consistent duration allowed for an in-depth analysis of the temporal changes in seeding density and dispersion, and their subsequent effects on velocimetry error.

The study found that the critical factor influencing accuracy is not video duration itself, but rather the number of reliable tracers successfully tracked by the software. Capturing longer video sequences can increase the likelihood of obtaining enough tracers for reliable data analysis, particularly when seeding density is low, although this comes with increased processing time (Tauro and Salvatori, 2017; Pizarro et al., 2020a).

Optimal video length may vary depending on the quality and availability of tracers on the river surface. It is recommended to capture footage with as many potential tracers as possible. When

tracer availability is limited, extending the capture duration can help improve the accuracy of the analysis. In real-world scenarios, where external noise and variability are present, longer video durations may be necessary to ensure reliable measurements—particularly in cases of low seeding density or non-optimal dispersion—where additional data points can help verify vector velocities and eliminate outliers.

4.6 Conclusions

This study aimed to enhance the accuracy of PTV methods for estimating river discharge by investigating the influence of seeding density and dispersion. Through detailed analysis of 1680 synthetically generated videos—each 20 frames long with tracers moving at 15 pixels per second—key findings were obtained regarding the optimal conditions for minimising velocimetry error. The research introduced a new Post-Processed SDI metric, tailored specifically for PTV, which provides more precise error estimation based on actual tracer metrics observed during analysis. The study addressed the following research questions:

1. **To what extent do actual seeding density and dispersion impact the accuracy of PTV in velocity analysis?**
   The findings revealed a strong and significant relationship between both seeding density and dispersion and the accuracy of PTV measurements. The analysis demonstrated that as seeding density increased, velocimetry error decreased, showing a clear inverse relationship. Similarly, achieving even tracer dispersion (optimal value of $\nu = 1$) was crucial in minimising measurement errors. These results underscore the importance of both factors in ensuring accurate velocity estimations in PTV.

2. **What is the optimal value for actual seeding density for developing a Post-Processed SDI equation tailored to PTV methods?**
   Through a series of controlled synthetic simulations, the study identified the optimal seeding density to be 6.85×10^{-3} PPP. This value is significantly higher than the previously recommended 1.02×10^{-3} PPP for Pre-Processed SDI methods, highlighting the need for higher actual seeding densities to achieve accurate velocity estimations in PTV. Additionally, an optimal dispersion value of $\nu = 1$ was confirmed, supporting the need for evenly distributed tracers to improve measurement accuracy.

3. **Can the new Post-Processed SDI be effectively used to estimate velocimetry errors in river flow analysis?**
   The study demonstrated that the new Post-Processed SDI metric significantly improves the accuracy and reliability of error estimation. By relying on actual data from PTV analysis, the Post-Processed SDI offers a robust method for predicting velocimetry errors based on

observed seeding density and dispersion. The relationship between SDI and error, defined by the equation $\epsilon = -0.5248(\exp^{1.311\,SDI})$ (RMSE = 3.345%), provides a practical and precise tool for estimating error in river discharge measurements.

The study also highlighted the impact of zero-velocity vectors—erroneous readings occurring when the software misidentifies stationary features as tracers. These vectors significantly skew dispersion calculations and inflate velocimetry error, particularly in scenarios with low seeding densities.

The comparison between Pre-Processed and Post-Processed SDI methods showed that Post-Processed metrics—based on actual PTV results—provide more accurate and reliable assessments of seeding density and dispersion. This approach eliminates potential discrepancies associated with estimated metrics and leads to more precise error prediction. Despite the strengths of the new metric, the study acknowledges the limitation of using synthetic imagery. While synthetic datasets offer controlled environments for detailed analysis, they do not fully capture the complexities of real-world river systems. Therefore, future research should focus on validating and refining the Post-Processed SDI using real-world data, to account for environmental variability and improve its practical applicability.

In summary, the new dimensionless Post-Processed SDI, calculated as:

$$\mathrm{SDI}_{\text{post-processed}} = \nu^{0.9596} \left(\frac{\rho}{\rho_{\text{ideal}}} \right)^{0.7053}, \tag{4.11}$$

where ν, ρ, and ρ_{ideal} represent the observed dispersion, actual density, and idealised density respectively, offers a robust tool for improving the accuracy of velocity measurements. While further validation in field conditions is necessary, the findings of this study provide a solid foundation for advancing PTV methodologies in river flow analysis.

Chapter 5. Impacts of Seeding Density and Dispersion on Discharge Results of PTV Methods: A Case Study

5.1 Chapter Overview

This chapter extends the findings from Chapter 4 by investigating how seeding density and dispersion affect discharge measurements derived from PTV in river flow analysis. By using Post-Processed SDI as a filtering tool, the study aims to enhance the accuracy and reliability of flow measurements. Discharge results from SDI-optimised datasets are compared against non-optimised datasets, with historical flow data serving as a benchmark. The comparison focuses on two key metrics: relative discharge error and the sensitivity of these errors to variations in SDI.

The chapter outlines the methodology for applying Post-Processed SDI filtering to PTV data and presents a comprehensive analysis of the outcomes. The findings demonstrate the practical benefits of incorporating SDI in non-invasive flow measurement techniques across diverse environmental conditions. These results contribute to improved water resource management and support the advancement of hydrological research by offering a more reliable approach to estimating river discharge using image velocimetry.

5.2 Introduction

Accurate flow measurement in natural water bodies presents significant challenges due to inherent variability and unpredictable environmental conditions. Factors such as fluctuating water levels, variable flow velocities, and physical obstructions like rocks and vegetation can substantially influence tracer movement in PTV analyses (Dal Sasso et al., 2018; Pizarro et al., 2020b,a). Additionally, external conditions, including weather patterns and seasonal changes, introduce further complexities, often leading to inconsistencies and errors in discharge measurements (Tauro, Petroselli and Grimaldi, 2018). Despite advancements in flow measurement techniques, discrepancies between observed and calculated discharge values persist, underscoring the need for more robust analytical frameworks.

Addressing this gap, the present study evaluates the effectiveness of the Post-Processed SDI framework, initially developed under controlled conditions in Chapter 4, within real-world environments. By comparing PTV, derived discharge results with direct flow measurements across various environmental contexts, this chapter assesses the ability of SDI metrics to enhance mea-

surement accuracy and identifies their limitations.

The analysis employs `KLT-IV` software to evaluate tracer dispersion (ν) and seeding density (ρ), examining their combined impact on discharge estimation accuracy. Post-Processed SDI metrics serve as critical evaluative tools, with predefined benchmarks guiding the selection and filtering of PTV results. These benchmarks, derived from prior numerical studies (see Section 4.4.3), specify optimal values for ρ and ν that aim to minimise velocimetry errors. Frames not meeting these thresholds are excluded from analysis, enabling a focused evaluation of how adherence to optimal seeding conditions influences discharge accuracy.

In addition, the study explores the potential for SDI to support uncertainty estimation in flow measurements. Where filtering fails to bring SDI values within ideal ranges, results are analysed to assess how SDI can indicate measurement reliability. A composite model is also developed, integrating SDI-filtered PTV outputs with observed flow data to correct systematic biases, especially those stemming from seeding limitations at lower flows. This integrated modelling approach seeks to improve stage–discharge relationships across varied flow conditions and account for the under-representation typical of PTV-based estimates.

The significance of this chapter lies in its application of Post-Processed SDI metrics under uncontrolled, natural conditions, providing critical insights into their robustness and adaptability. By validating the Post-Processed SDI framework in diverse environments, the study contributes to refining PTV methodologies and supports the development of more precise, reliable tools for river flow analysis, tools that are essential for effective water resource management and informed hydrological decision making.

5.2.1 Research Questions

1. To what extent does the application of Post-Processed SDI metrics influence the accuracy of discharge calculations in PTV methods, under real-world conditions?

2. Can the integration of Post-Processed SDI metrics into PTV methods, in combination with a composite model, consistently improve the reliability of discharge estimations across a range of river flow conditions?

3. Can Post-Processed SDI support users of PTV in evaluating the reliability and accuracy of their data?

5.3 Methods

5.3.1 Site Selection

This chapter's analysis focuses on two sites, which are discussed in detail in Section 3.3.2.2.

5.3.1.1 Overview

River Calder at Todmorden, Yorkshire This site was selected due to the availability of historical data, variability in flow conditions, and the presence of established monitoring stations. The River Calder offers a robust dataset, supported by its man-made U-shaped channel and high tracer availability, making it well-suited for studying the effects of seeding density and dispersion on PTV methods.

River Sheaf in Sheffield, Yorkshire The River Sheaf, located in an urban setting with typical water levels ranging from 0.12 m to 1.10 m, provides a contrasting environment for validating findings across diverse flow conditions. Data collected at this site between 2019 and 2021 were processed to analyse tracer dispersion (ν) and seeding density (ρ) for SDI estimation. Flow estimates derived from PTV were validated against established stage–discharge curves, as well as ADCP measurements provided by the Environment Agency.

5.3.2 Processing through PTV

5.3.2.1 Data Preparation and Input

The video data was processed using KLT-IV software, with the detailed settings used provided in Appendices 10.1. GCPs and vertices in the same coordinate system were inputted as CSV files for both sites. This ensured accurate spatial referencing during the analysis.

5.3.2.2 Bulk Processing and Matching

KLT-IV's inbuilt feature allowed for bulk processing, where stage data were matched to video files using a 10-minute buffer. This automation streamlined the data processing workflow, ensuring consistent and reliable analysis across all video files.

5.3.2.3 Modification for Data Storage

The KLT-IV script was modified to save workspace results to individual ".mat" files for each video file that was processed. This facilitated subsequent SDI filtering analysis by ensuring that key variables, including the start and finish coordinates of all successfully tracked points, were preserved for further processing. This modification allowed for reprocessing of data as needed, enhancing the flexibility and robustness of the analysis.

5.3.2.4 Processing Outcome

For the River Calder site, out of 531 possible videos, 463 were successfully processed. The analysis proceeded with these 463 videos, which were then used for further SDI filtering and error estimation studies as described in the subsequent sections. For the River Sheaf, a total of 540 videos were successfully processed through KLT-IV.

5.3.2.5 Initial Data Cleaning

An initial data cleansing process was conducted to ensure the accuracy of the data used in subsequent analyses. This step was particularly important because the primary focus of this study is on assessing the effectiveness of Post-Processed SDI in improving discharge estimates, rather than evaluating the accuracy of the KLT-IV software itself. Data points that could introduce unnecessary errors and skew the results were systematically identified and removed to ensure that any observed improvements could be attributed to SDI adjustments. The cleansing process began with the calculation of absolute differences between the observed flow data (collected from established sources such as stage-discharge curves or ADCP measurements) and the raw flow outputs generated by KLT-IV. Relative differences were then computed by normalising these absolute differences against the observed flow values, providing a clearer understanding of the proportional discrepancy between the observed and raw data.

To systematically identify outliers, the first quartile (Q1) and third quartile (Q3) of the absolute differences were calculated. The interquartile range (IQR), defined as the difference between Q3 and Q1, was used to establish thresholds for outlier detection. Specifically, data points with absolute differences that fell outside the range $[Q1 - 1.5 \times IQR, Q3 + 1.5 \times IQR]$ were classified as statistical outliers. These outliers were assumed to indicate either measurement errors or instances where the raw data did not align with the known behaviour of the river system. The identified outliers were subsequently removed from the dataset to prevent them from affecting the post-processed analysis. Out of the 463 results originally obtained from KLT-IV, 43 results were identified as outliers and removed through this cleansing process, leaving a total of 420 results for further analysis.

5.3.3 Filtering Data using SDI

After processing the raw videos through KLT-IV, the locations of tracers within the frames were stored and prepared for SDI analysis. This analysis follows the methodology outlined in Chapter 4, where the seeding density and dispersion are calculated based on a user-defined block size, serving as the grid for these calculations. The SDI for each frame was calculated as per Equation 4.9. Given that SDI has been shown to correlate with the accuracy of PTV methods, it was hypothesised that optimising SDI by removing frames with higher SDI levels could improve the accuracy of PTV-derived measurements. Therefore, a filtering process was applied to the dataset, involving the

removal of frames where the calculated SDI values fell outside acceptable thresholds, typically indicating potential issues with tracer density or distribution. The filtering process was carried out in three stages, each systematically eliminating data points (frames) with SDI values that deviated significantly from the mean. This was achieved by applying standard deviation thresholds. The goal was to reduce the average SDI value of the dataset, thereby improving the quality and consistency of the remaining data. The steps of this filtering process are visually represented in Figure 5.1 and detailed below:

Step 1: Initial Distribution

The initial dataset X represented the SDI values calculated for each frame in the processed video dataset, with n observations x_i.

$$X = \{x_1, x_2, \ldots, x_n\}$$

The mean μ and standard deviation σ of the SDI values were calculated as follows:

$$\mu = \frac{1}{n}\sum_{i=1}^{n} x_i$$

$$\sigma = \sqrt{\frac{1}{n}\sum_{i=1}^{n}(x_i - \mu)^2}$$

Step 2: First Filter (Removing data beyond $\mu + 3\sigma$)

In the first filtering step, frames with SDI values greater than $\mu + 3\sigma$ were removed from the dataset.

$$X' = \{x_i \in X \mid x_i \leq \mu + 3\sigma\}$$

The mean μ' and standard deviation σ' were then recalculated for the filtered dataset X'.

$$\mu' = \frac{1}{n'}\sum_{i=1}^{n'} x_i \quad \text{where } n' \text{ is the number of elements in } X'$$

$$\sigma' = \sqrt{\frac{1}{n'}\sum_{i=1}^{n'}(x_i - \mu')^2}$$

Step 3: Second Filter (Removing data beyond $\mu' + \sigma'$)

A second filter was applied, removing frames with SDI values greater than $\mu' + \sigma'$.

$$X'' = \{x_i \in X' \mid x_i \leq \mu' + \sigma'\}$$

The mean μ'' and standard deviation σ'' were then recalculated for the further filtered dataset X''.

$$\mu'' = \frac{1}{n''} \sum_{i=1}^{n''} x_i \quad \text{where } n'' \text{ is the number of elements in } X''$$

$$\sigma'' = \sqrt{\frac{1}{n''} \sum_{i=1}^{n''} (x_i - \mu'')^2}$$

Step 4: Third Filter (Removing data beyond $\mu'' + \sigma''$)

The third filter removed frames with SDI values greater than $\mu'' + \sigma''$.

$$X''' = \{x_i \in X'' \mid x_i \leq \mu'' + \sigma''\}$$

The final mean μ''' and standard deviation σ''' were calculated for the dataset X''', which represents the SDI values after all filtering stages have been applied.

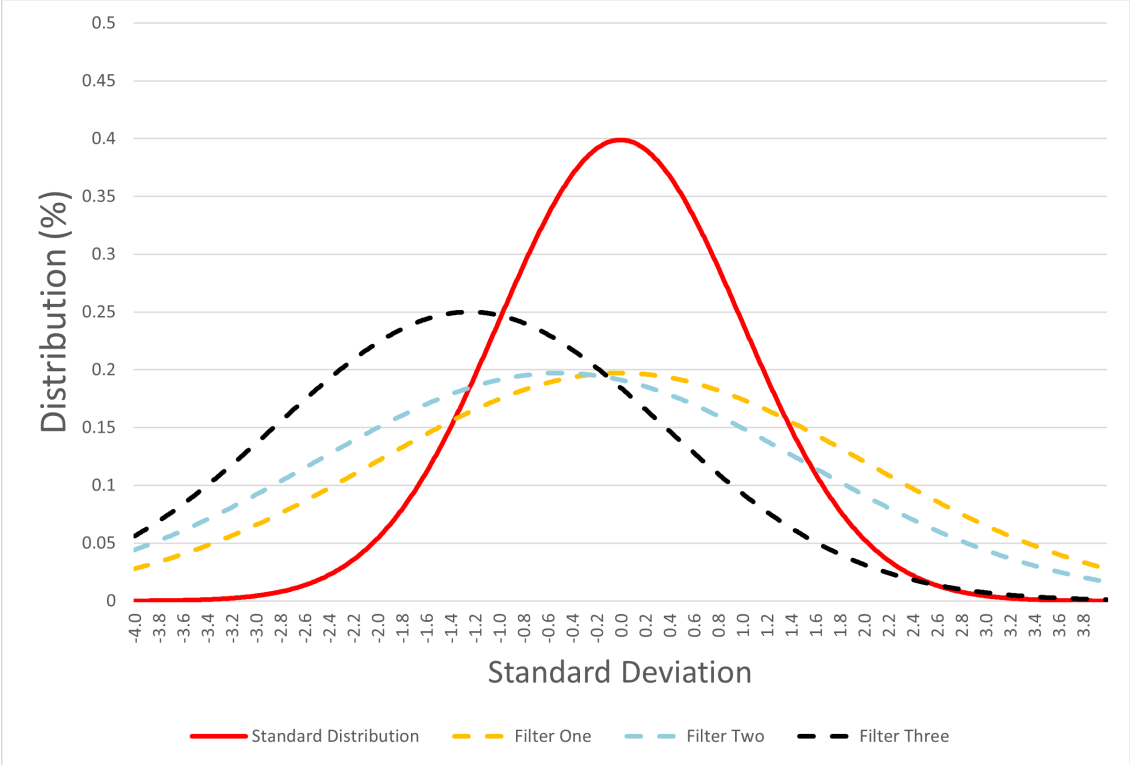


Figure 5.1: Standard deviation of the SDI for the frames processed through KLT-IV. The initial distribution (orange) represents the full dataset. Successive filters progressively reduce the dataset, with the third filter (black) showing a decrease in both the average SDI and the frequency of extreme values, indicating improved data quality and consistency.

5.3.4 Stage-Discharge Relationship and Model Fitting

Accurate stage-discharge relationships are essential for hydrological studies, as they provide a means to quantify river flow based on water stage data. However, one of the inherent challenges in applying image velocimetry methods, including PTV and the use of KLT-IV software, is the tendency to under-represent lower flows. This under-representation is a direct consequence of issues related to seeding characteristics, such as frame rates and extraction rates, and can be mitigated by sub-sampling data, reducing the frame rate, or changing the extraction rate (Dal Sasso et al., 2020; Pearce et al., 2020). These seeding-related challenges are common across all image velocimetry methods and must be addressed when developing models to fit stage-discharge data.

The general equation for stage-discharge relationships is expressed as:

$$Q(h) = a(h - h_0)^b \tag{5.1}$$

where:

- $Q(h)$ is the discharge (flow rate) as a function of the stage height h.
- a and b are empirical constants specific to the river or stream being studied.
- h_0 is the stage at which discharge is zero, often referred to as the "effective zero stage."

This equation assumes a power-law relationship between stage height and discharge, a common approximation in many open-channel flow scenarios. Constants a, b, and h_0 are typically determined through regression analysis of observed data, allowing for the estimation of discharge based on measured stage heights.

5.3.4.1 Calibration Points and Model Adjustment

To calibrate and adjust the stage-discharge model generated by PTV, data were randomly selected using three calibration points from the observed flow data. These points were typically selected during periods when the river was experiencing stable and representative flow conditions, rather than extreme events like floods or droughts. The calibration points used in this study were:

- Depth: 0.501 m, Observed Flow: 0.718 m³/s
- Depth: 0.470 m, Observed Flow: 0.613 m³/s
- Depth: 0.478 m, Observed Flow: 0.640 m³/s

5.3.4.2 Composite Modelling to Establish Baseline SDI Flow

The use of a composite model in this study was conceived as an innovative approach to address the systematic errors associated with PTV methods, particularly those stemming from seeding limitations at various flow stages. This approach involved blending two models: a baseline model derived from SDI-filtered discharge results and a shifted model calibrated with observed data, using a dynamic weighting function. The weighting function, which varies with depth, ensures a smooth transition between the models, thereby improving accuracy across the entire range of flow conditions. The decision to employ this weighting strategy was validated by the concept used in Beven and Freer (2001), where different model components are combined using weights that adjust based on hydrological conditions. By integrating these techniques, the composite model developed in this study addresses specific challenges of PTV methods while aligning with established practices in hydrological modelling.

Although this composite modelling approach was not the primary objective of this chapter, it became a necessary strategy to ensure that the errors measured could be attributed solely to the metrics assessed by SDI. By smoothing the model produced by PTV and integrating both observed data and SDI flow results, the aim was to create a more reliable stage-discharge relationship that effectively captures the role of SDI in reducing measurement error. The process began with the development of an initial model based on the SDI-filtered discharge results from KLT-IV, followed by calibrations to align the model more closely with observed data, especially at lower flows. The resulting composite model was designed to counteract the effects of seeding limitations, thereby providing a more accurate representation across the entire range of flow conditions. The composite equation was created by combining two models referred to as $Q_1(h)$ and $Q_2(h)$, using a modified weight function. This composite equation facilitates a smooth transition between the two models based on a relevant parameter, such as depth (h). The weight function, $w(h)$, is defined as:

$$w(h) = a\left(\frac{h - h_{\text{min}}}{h_{\text{max}} - h_{\text{min}}}\right)^2 + b\left(\frac{h - h_{\text{min}}}{h_{\text{max}} - h_{\text{min}}}\right) \tag{5.2}$$

where h_{min} and h_{max} represent the minimum and maximum values of the parameter h, respectively, and a and b are constants that shape the transition. The composite equation, $Q_{\text{comp}}(h)$, is then formulated as:

$$Q_{\text{comp}}(h) = (1 - w(h)) \cdot Q_1(h) + w(h) \cdot Q_2(h) \tag{5.3}$$

Parameter Justification

The choice of parameters $a = 1$ and $b = 0.5$ for the weight function is based on theoretical considerations and the desired behaviour of the transition between models. The rationale for these choices includes:

- **Smooth Transition**: The primary goal of the weight function is to ensure a smooth transition between the shifted model Q_{eq2} at lower depths and the original model Q_{eq1} at higher depths. Choosing a and b as 1 and 0.5 respectively helps achieve this smoothness.

- **Mid-Depth Emphasis**: The values $a = 1$ and $b = 0.5$ emphasise the transition around the mid-depth range. This is achieved by the quadratic term $a\left(\frac{h-h_{\text{min}}}{h_{\text{max}}-h_{\text{min}}}\right)^2$, which grows more quickly than the linear term, allowing a more pronounced weight shift in the middle of the depth range.

- **Balance Between Linear and Quadratic Components**: The linear component $b\left(\frac{h-h_{\text{min}}}{h_{\text{max}}-h_{\text{min}}}\right)$ ensures that the transition is not too rapid, complementing the quadratic component to create a balanced weight function. Choosing $b = 0.5$ provides a moderate influence of the linear term, which helps in achieving a gradual rather than a very steep transition.

- **Parameter Sensitivity**: The chosen values $a = 1$ and $b = 0.5$ represent an initial guess that can be fine-tuned based on further sensitivity analysis if necessary. Starting with these values allows for an evaluation of how changes in a and b impact the model's performance and adjustments as needed to better capture the expected behaviour of the system.

- **Robustness to Variability**: These values are chosen to ensure that the model remains robust across a range of depths. By using simple, moderate values for a and b, the model is less likely to 'over-fit' to specific depth ranges.

- **Mathematical Simplicity**: Starting with $a = 1$ and $b = 0.5$ simplifies the initial formulation and allows for easier interpretation and implementation. This simplicity helps in understanding the fundamental impact of each term in the weight function without the added complexity of more intricate parameters.

5.3.5 Error-Bound Estimation Using SDI

An approach was developed to estimate errors in scenarios where further filtering of frames could not reduce SDI values, based on the relationship between Post-Processed SDI calculations and measurement error. This method is particularly useful under sub-optimal capturing conditions, where poor SDI values might persist despite the application of filtering processes. Given the challenges of collecting comprehensive data across all depths, especially during high-flow events, error bounds based on SDI were calculated to provide a representation of the data's reliability.

The error estimation process began with a modelled composite flow curve, as seen in Section 5.3.4.2, which was fitted using PTV output data and measured validation points. Processed results, including SDI values and corresponding depth measurements, were used to calculate residual errors by subtracting the modelled flow values from the SDI-based flow values. These residual errors were then used to fit a Depth-Residual Error model and an SDI-Residual Error model. Power

fit regression was applied to both models to determine their coefficients of fit, resulting in the following error model parameterised by three variables, a, b, and c:

$$\text{Error} = a \cdot (\text{SDI}^b) \cdot (\text{Depth}^c)$$

This specific error equation was designed to capture the multiplicative nature of errors arising from both SDI and depth measurements. The power-law relationship allowed the model to account for varying sensitivities to SDI and depth, with a serving as a scaling factor, and b and c allowing for non-linear relationships. This model is particularly effective for estimating errors under different conditions, reflecting the physical realities of hydrological measurements where larger depths and higher SDI values can disproportionately increase errors. To address asymmetric error distribution, dynamic scaling factors were calculated based on the standard deviation of the residual errors. The upper and lower scaling factors were determined as follows:

$$SF_{\text{upper}} = 1 + \frac{\sigma_{\text{res}}}{\mu_{\text{res}}}$$

$$SF_{\text{lower}} = 1 - \frac{\sigma_{\text{res}}}{\mu_{\text{res}}}$$

Where: σ_{res} is the standard deviation of the residual errors and μ_{res} is the mean residual error.

These scaling factors were then used to adjust the modelled flow values to account for estimated errors, resulting in upper and lower error bounds:

$$Q_{\text{upper}} = Q_{\text{comp}} + SF_{\text{upper}} \cdot \text{Error}_{\text{estimated}}$$

$$Q_{\text{lower}} = Q_{\text{comp}} - SF_{\text{lower}} \cdot \text{Error}_{\text{estimated}}$$

This method created a range that better captured the potential for both overestimation and underestimation of flow values. Where no data was available to fit the error bounds, linear interpolation was employed.

5.3.6 Summary of Methods

This study focused on the analysis of two sites: the River Calder and the River Sheaf. Video data collected from these sites were processed using KLT-IV software. To ensure the accuracy of the results, an initial data cleaning process was conducted to remove outliers, focusing on eliminating erroneous data points that could distort the analysis. The central objective was to evaluate the effectiveness of SDI metrics in enhancing the accuracy of PTV-derived discharge measurements. A three-stage filtering process was implemented to remove frames with high SDI values, which are believed to introduce significant errors in flow estimation. When further filtering did not reduce SDI values sufficiently, an error estimation approach was developed based on the relationship between SDI metrics and measurement errors. This error estimation model utilised a power-law relationship

to account for the multiplicative nature of errors arising from both SDI and depth measurements. The model was parameterised by three variables and applied to estimate error bounds, incorporating dynamic scaling factors to address asymmetric error distributions. These scaling factors were used to adjust the modelled flow values, resulting in upper and lower error bounds that better captured the potential for both overestimation and underestimation of flow values.

Finally, the stage-discharge relationship was modelled, knowing that low-flows are typically under-represented, a known challenge in image velocimetry methods. To address this issue, a composite model was developed, combining SDI-filtered discharge results with observed data, using a dynamic weighting function. This composite approach aimed to smooth transitions between different flow conditions and provide a more accurate estimation of discharge across the full range of observed depths, thereby improving the reliability of stage-discharge relationships derived from PTV methods.

5.4 Results

5.4.1 PTV Results

The data obtained from KLT-IV was organised to display the video file name, corresponding depth, measured flow (based on the historical stage-discharge curve), and raw flow. The raw data, which had not yet been filtered or altered, were directly obtained from the software. Figure 5.2 illustrates this, where several anomalies in the results are clearly visible. A systematic deviation method, as discussed in Section 5.3.2.5, was applied to remove these anomalies. The data after applying this filtering process are shown in Figure 5.2. The data cleansing process (seen in Section 5.3.2.5) improved the reliability and consistency of the results, demonstrating the importance of initial data cleansing in achieving reliable flow measurements.

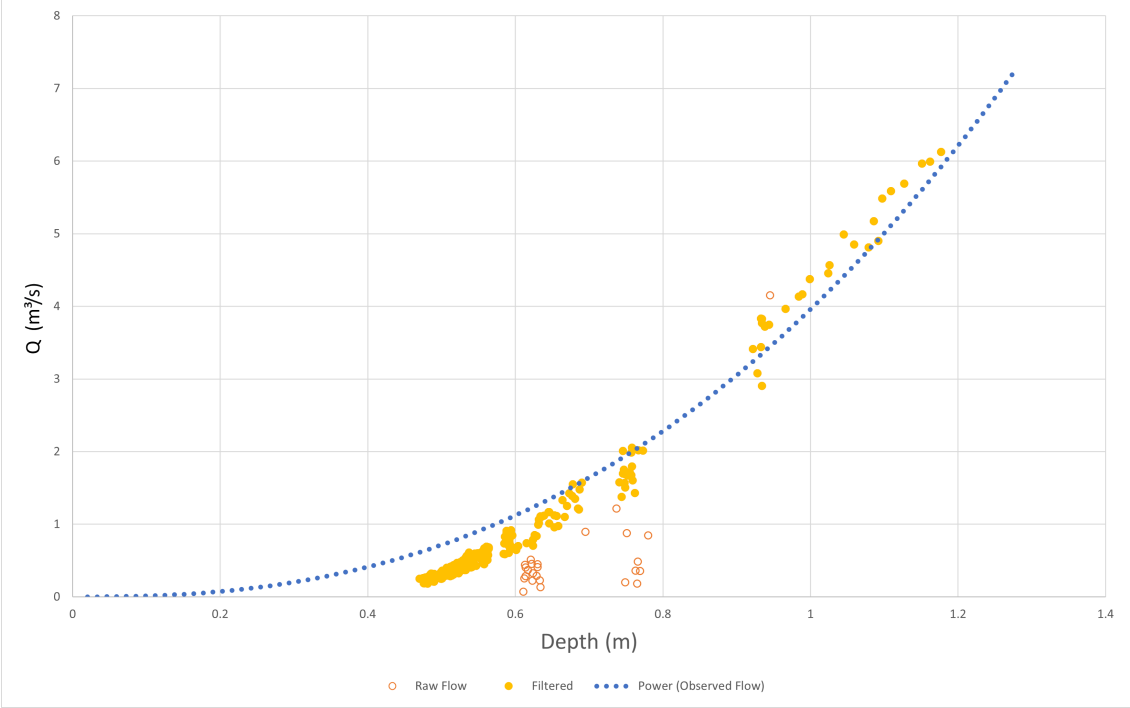


Figure 5.2: Stage-discharge rating for the River Calder showing the measured data represented by its Stage-Discharge rating (blue), raw results (orange circles), and the filtered results (solid yellow) carried through to processing. The filtered results demonstrate improved accuracy and consistency by removing anomalous data points identified through systematic deviation methods. However, the data show a tendency to underestimate low flows and overestimate high flows, highlighting systematic biases that persist even after filtering.

The initial model of SDI flow results was obtained from KLT-IV and is represented by Equation 5.4. To improve the model's accuracy, this fitted model was adjusted to best fit three validation points that were randomly selected from the observed data, as shown in Section 5.3.4.1. This adjustment resulted in Equation 5.5. While this shifted model accounts for discrepancies observed in the initial model by aligning it more closely with the actual measured data points at lower stages, it can exacerbate errors at higher stages, where PTV typically performs well. Therefore, a composite

model was developed to blend both the initial and shifted models, representing the entire range of results more accurately. This approach is discussed in the following section.

$$Q_{\text{eq1}}(h) = 8.651(h - 0.338)^{1.791} \tag{5.4}$$

$$Q_{\text{eq2}}(h) = 8.651(h - 0.338)^{1.791} + 0.338 \tag{5.5}$$

5.4.1.1 Application of Composite Model

To address the systematic error typically associated with the KLT-IV method, a combined equation from Equation 5.4 and Equation 5.5 was created using a modified weight function. This composite equation ensures a smooth transition between the shifted model (Q_{eq2}) and the initial model (Q_{eq1}), depending on the depth value. The weight function used for this transition is defined as:

$$w(h) = a\left(\frac{h - h_{\text{min}}}{h_{\text{max}} - h_{\text{min}}}\right)^2 + b\left(\frac{h - h_{\text{min}}}{h_{\text{max}} - h_{\text{min}}}\right) \tag{5.6}$$

where h_{min} and h_{max} represent the minimum and maximum depth values, respectively, and a and b are constants that shape the transition; in this instance, 1 and 0.5 respectively. The composite equation is then formulated as:

$$Q_{\text{composite}}(h) = (1 - w(h)) \cdot Q_{\text{eq2}}(h) + w(h) \cdot Q_{\text{eq1}}(h) \tag{5.7}$$

Where:

$$Q_{\text{eq1}}(h) = 8.651(h - 0.338)^{1.791}$$
$$Q_{\text{eq2}}(h) = 8.651(h - 0.338)^{1.791} + 0.338$$

The significance of the composite model lies in its ability to represent flow conditions more accurately across varying stages, addressing the limitations of both the initial and shifted models.

5.4.1.2 Visual Representation

Figure 5.3A and Figure 5.3B illustrate the observed data points, the original fitted model (Equation 5.4), the shifted model (Equation 5.5), and the new composite model. The new composite model demonstrates a smooth transition from the shifted model at lower depths to the original fitted model at higher depths, thereby enhancing the accuracy of our stage-discharge relationship analysis.

The visual representation in Figure 5.3 highlights the model's enhanced capability to capture flow variations more accurately, which is critical for improving the reliability of PTV-derived discharge measurements.

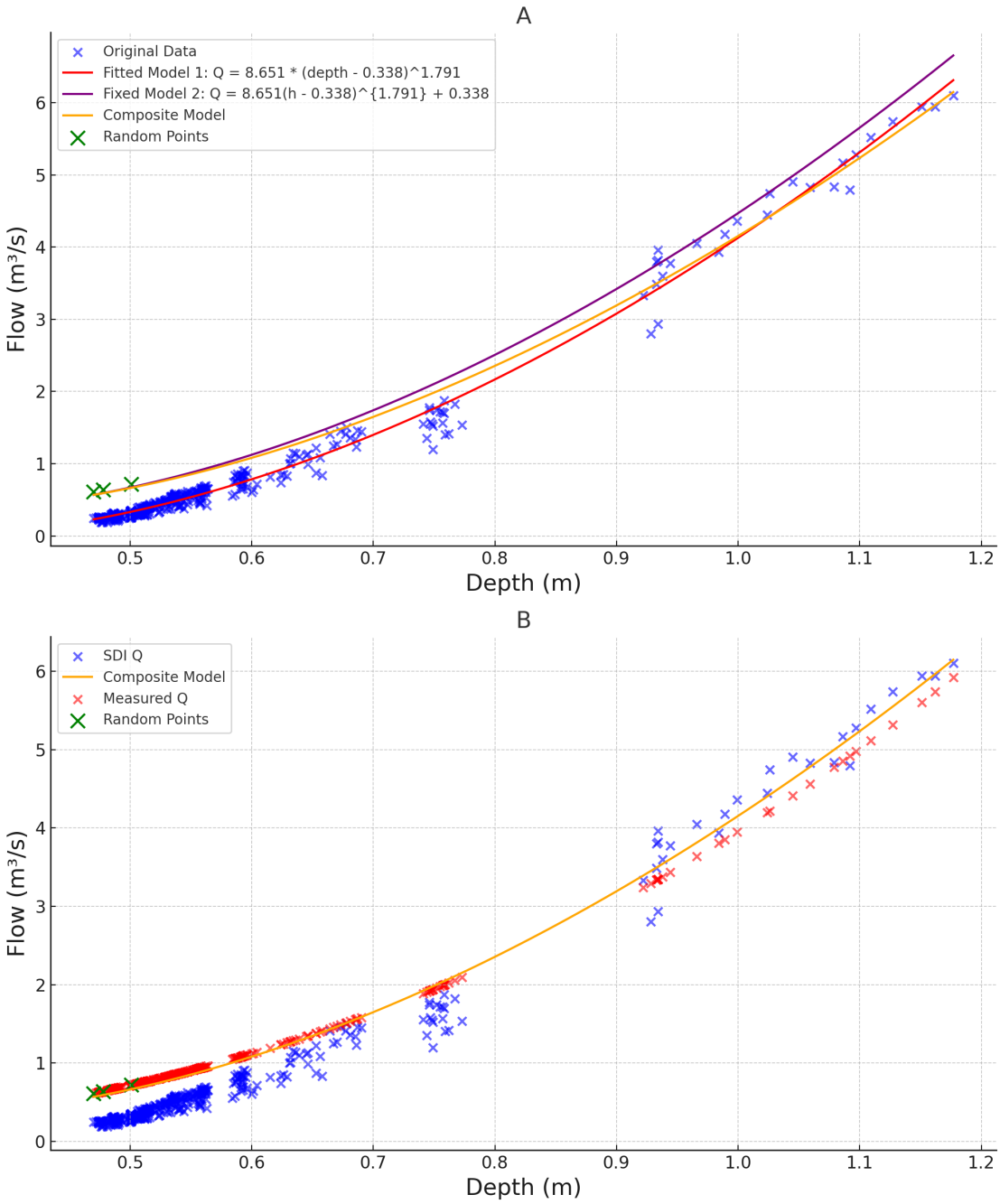


Figure 5.3: **(A)** Composite model (Q_{comp}, orange line) created using the weighting function in Equation 5.7. The original model (Q_{eq1}, red line) from Equation 5.4, and the shifted model (Q_{eq2}, purple line) from Equation 5.5 are also shown. Blue points represent the SDI-filtered discharge data used for comparison. The three points used to calibrate the models, obtained from the measured data, are plotted as green crosses. **(B)** Composite model (Q_{comp}, orange line) plotted against SDI-filtered discharge data (blue points) and the stage-discharge results from the measured data rating curve (red points), modelled using the same depth values as the SDI-filtered results.

5.4.2 SDI Data Analysis

In Figure 5.4, the relationship between the observed flow and the new SDI-filtered discharge is presented, with the raw, unfiltered, flow results mapped to show changes. This plot also includes the change of discharge on a secondary y-axis, highlighting the positive change in error from the SDI-filtered flow compared to the pre-filtered, raw, flow. The graph shows low variance in error change at lower river depths. However, greater variance is observed as depth increases, with both positive and negative error changes noted. Despite the variability, there is an overall trend of positive impact on the flow results, with a range of -0.2 m^3/s to +0.5 m^3/s across the dataset. A notable peak in error around a depth of 0.75 m is also observed, which warrants further analysis in relation to SDI to determine if it is a contributing factor. These findings suggest that SDI filtering has a generally positive impact on the accuracy of flow measurements, particularly at greater depths. However, the peak in error at 0.75 m depth indicates that additional factors may be influencing the accuracy at this specific depth. This suggests that videos exhibiting poor visibility (often associated with high SDI values), should be flagged during processing, either to assign higher uncertainty in the resulting flow estimates or to exclude them entirely if quality thresholds are not met.

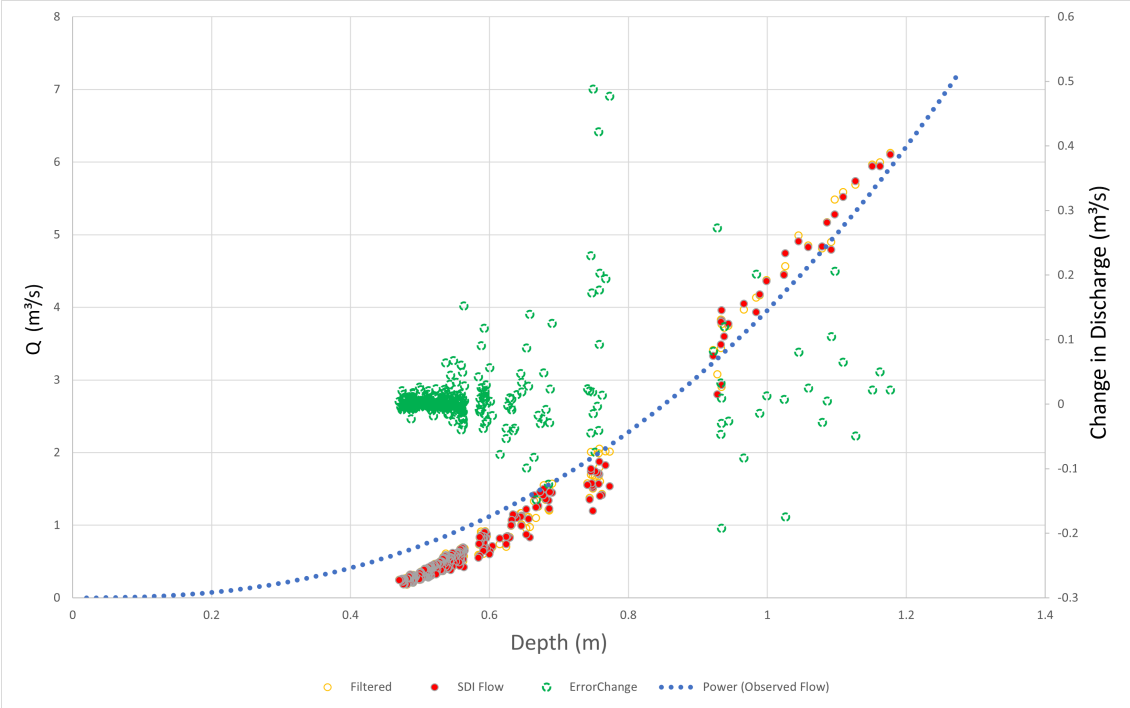


Figure 5.4: Stage-discharge rating for the River Calder showing the measured historical data (blue), filtered raw results (orange circles), the SDI Flow (solid red), and on the second axis, flow-change compared to depth (green dashed).

5.4.3 The Relationship Between Error and SDI

The relationship between SDI and error was further examined to understand its impact on PTV methods. The results indicate that SDI filtering enhances flow estimations, particularly at greater depths where a broad range of SDI values is encountered. However, an unexpected peak in error was observed at a depth of 0.75 m (Figure 5.5A-C), prompting further investigation. A significant increase in error variance was identified at this depth, coinciding with a peak in SDI values, suggesting that while SDI filtering is generally effective, it may not fully account for the complexities of flow dynamics at this depth.

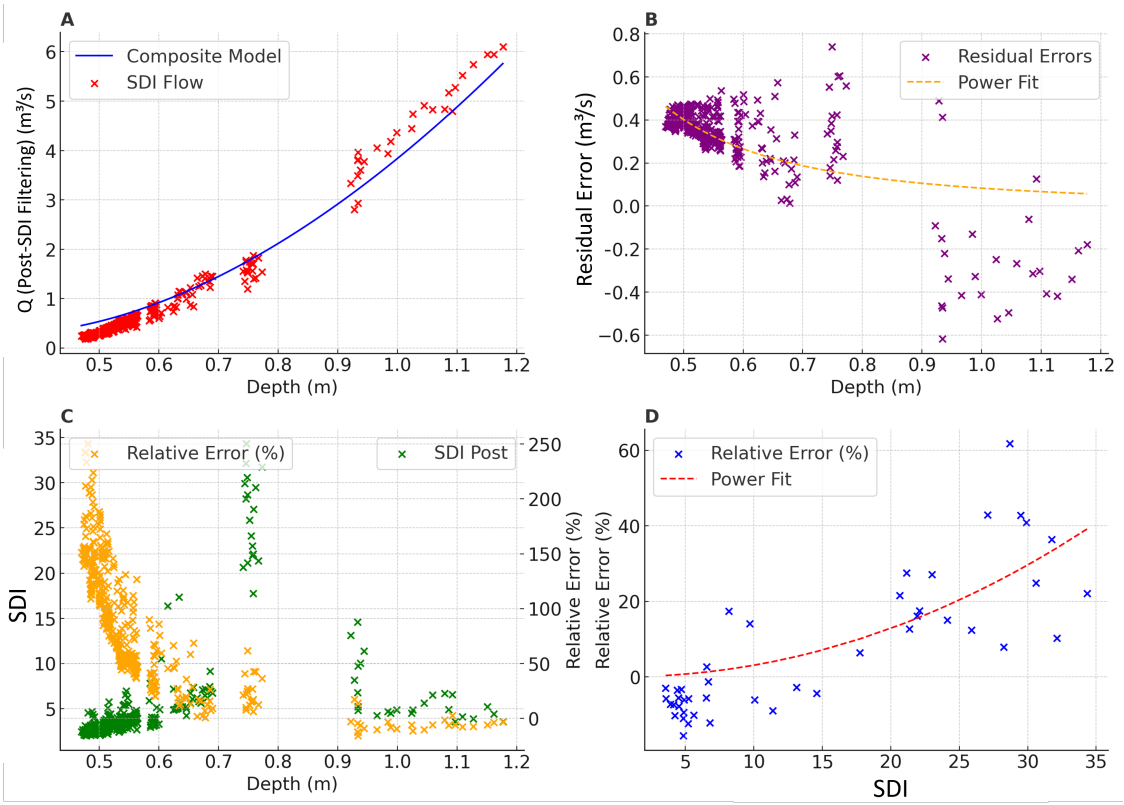


Figure 5.5: Initial comparison plots illustrating the relationship between depth, SDI, and error. **(A)** The composite model Q_{comp} and SDI Flow values plotted against depth. **(B)** The residuals of SDI Flow minus Q_{comp}, showing the error of the methodology used in this study, plotted against depth with a power fitting regression. **(C)** The SDI post-filtering values plotted against depth, with the relative error (SDI Flow - Q_{comp}) shown as a percentage on the secondary axis. **(D)** The relationship between the relative error (%) and SDI post-filtering values, with depths of less than 0.75 m removed to more clearly illustrate the relationship where systematic error is not assumed to play a significant role.

To further investigate this, a sub-sample with SDI values exceeding the third quartile (SDI = 4.29) was analysed. The residual errors for this subset were plotted, comparing pre-filtered and post-filtered results (Figure 5.6). The pronounced error around 0.75 m depth, where extreme SDI values exceeded the corrective capabilities of the SDI filter, was evident. However, the analysis also revealed that removing frames in high SDI scenarios led to deteriorating accuracy, indicating the

need for additional data capture in such conditions. Visual inspection of the footage (Figure 5.7) suggests that environmental factors like fog and mist contributed to unreliable outcomes. Although PTV performed reasonably well, with an average error of $0.5\,m^3/s$, the high variability in this section reduces confidence in the data. Notably, most data with high SDI values showed improved accuracy (blue arrows), with only minor increases in error (red arrows), supporting the general effectiveness of SDI filtering under these conditions (Figure 5.5D).

These observations underscore the complexity of applying SDI filtering across varying flow conditions, particularly when environmental factors introduce additional challenges. While SDI filtering is generally beneficial, its limitations at specific depths, such as 0.75 m, indicate that further refinement of the methodology may be necessary.

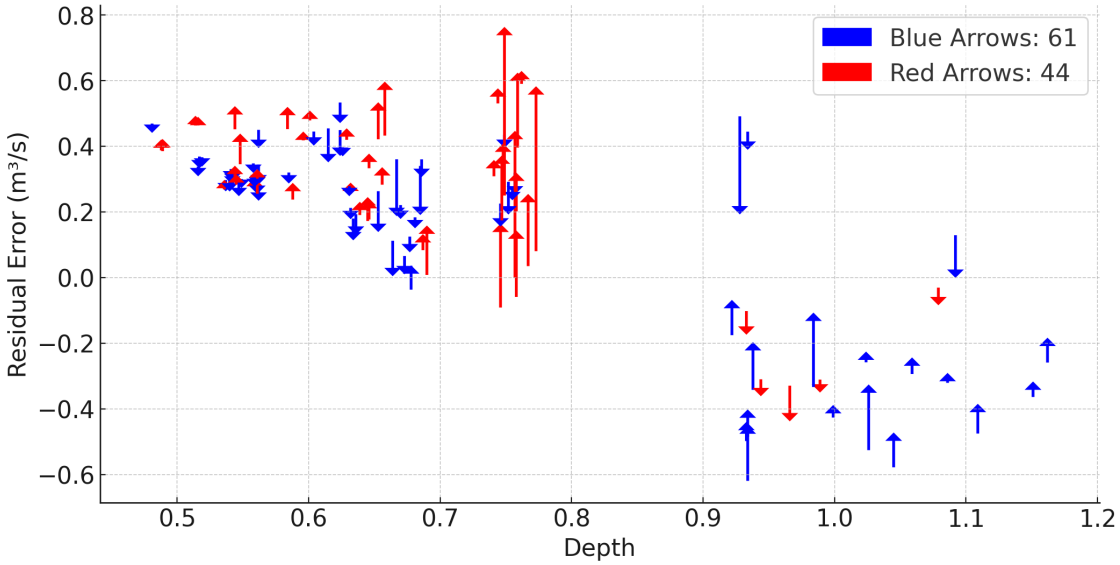


Figure 5.6: Graph showing the residual error between pre-filtered and post-filtered SDI data. Arrows indicate the magnitude of error change, with red representing a negative change (worse accuracy) and blue representing a positive change (better accuracy).



Figure 5.7: River Calder video frames taken where SDI is good (less than 3) on the left, and SDI is poor (greater than 30) on the right. The frame on the right, showcasing the poor SDI, highlights the study's finding that poor conditions affected the software's ability to process the video, resulting in erroneous outputs despite passing several filtering processes.

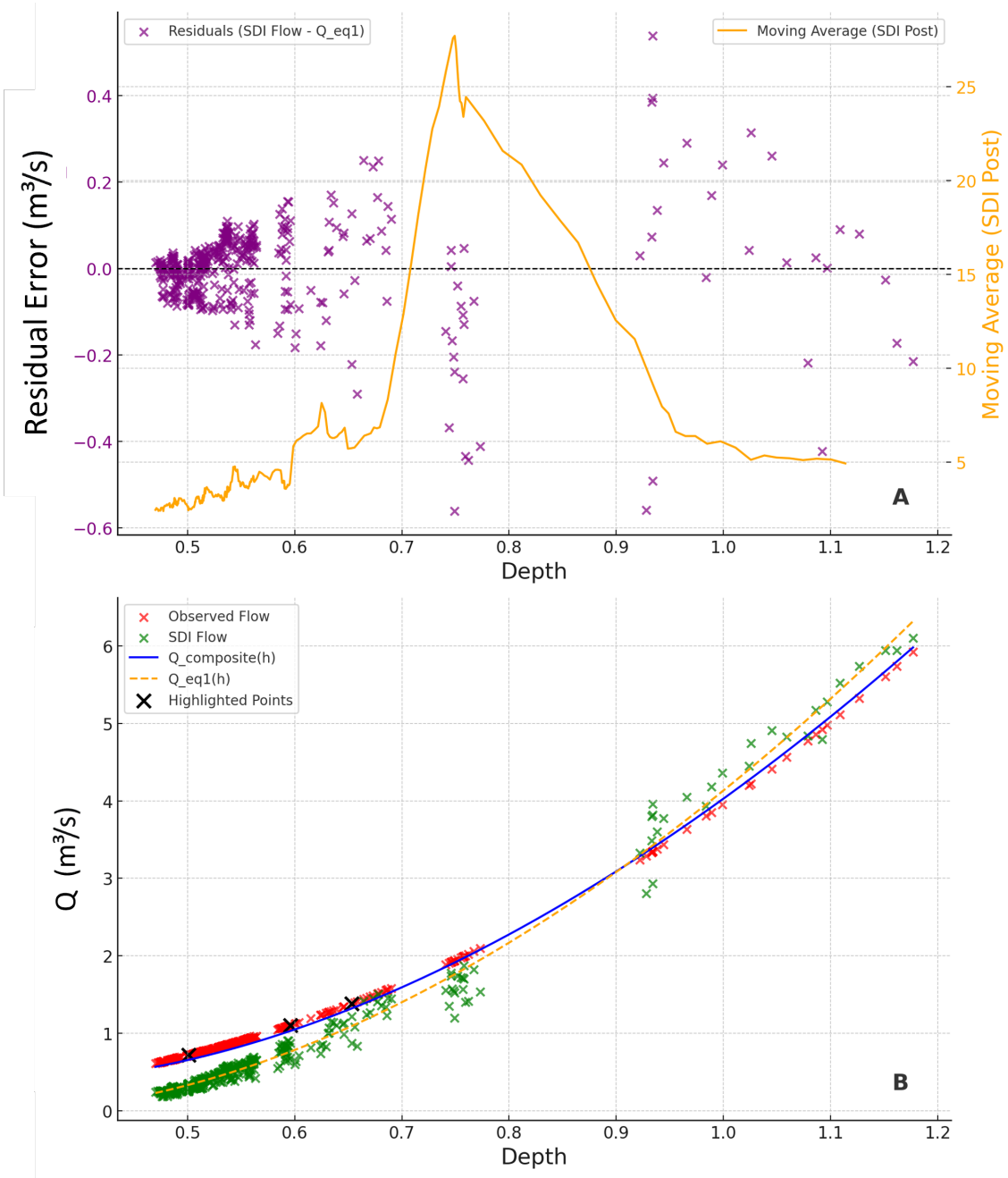


Figure 5.8: Graphs confirming the relationship between SDI and error. **(A)** The residuals of Q_{comp} and SDI-filtered flow against depth, with the moving average of SDI in relation to depth overlaid. **(B)** All data grouped onto one graph, with Q_{comp}, Observed Flow, SDI Flow, the model for SDI Flow, and the data used to validate Q_{comp}.

The relationship between SDI and error provides critical insights into the limitations of SDI filtering, particularly in challenging conditions. The analysis confirms that while SDI filtering generally improves flow measurement accuracy, certain depths and environmental conditions require additional considerations.

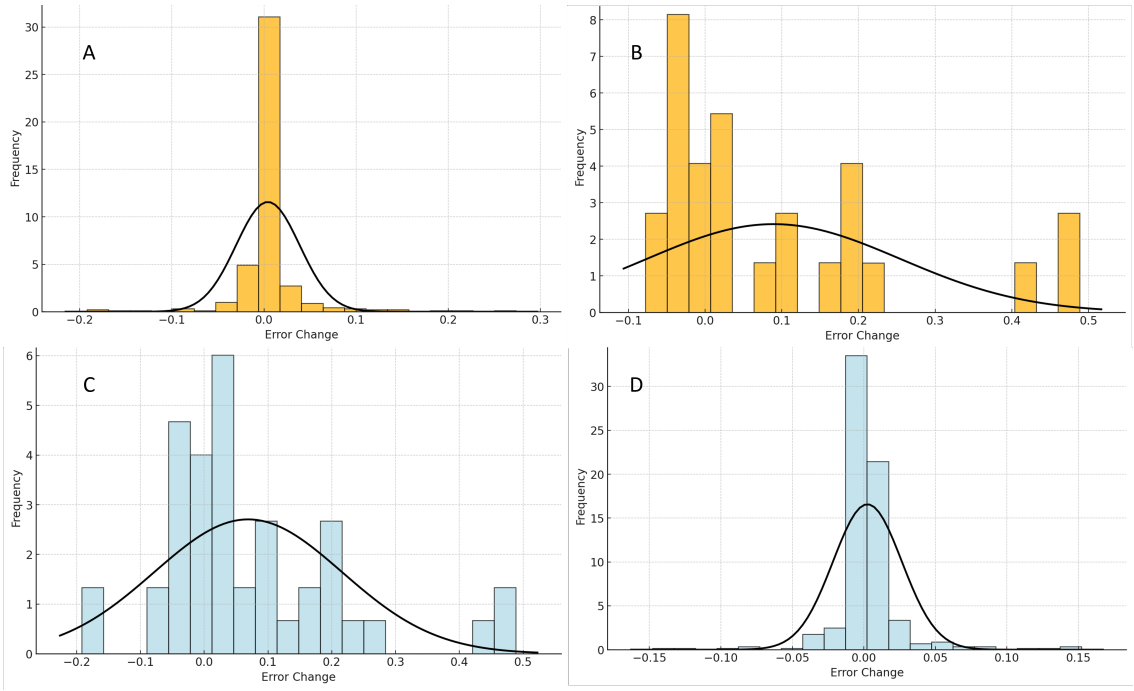


Figure 5.9: Histogram plots of the error change. Plots A and B show the error change in relation to limits to SDI of the pre-filtered data. Graph A shows results where SDI is less than 9.5, while graph B shows SDI greater than 9.5. Plots C and D show error change in relation to depth. Results are grouped where depth is greater than 0.7 m (graph C), and depths less than 0.7 m (graph D).

5.4.4 Using SDI to Estimate Error in Observations

With the relationship between error and Post-Processed SDI calculations established, SDI was used to estimate errors in cases where further filtering could not reduce SDI values sufficiently. This approach is particularly relevant in scenarios where capturing conditions are sub-optimal, leading to processed videos that still exhibit poor SDI results despite passing through the filtering processes, as seen in Figure 5.7. Such cases are crucial to identify as potentially unreliable, allowing for adjustments or a more cautious interpretation of the data.

The application of the error estimation model across a range of depths and SDI values revealed that while good SDI metrics generally corresponded to lower errors, there were notable exceptions, particularly under low-flow conditions. These findings suggest that even when SDI values are low, which typically indicates stable flow conditions, errors can still arise. This indicates that SDI alone may not fully capture the complexity of flow dynamics in all scenarios, particularly when the flow patterns are less dynamic or when the features being tracked are not fully representative of the actual flow velocities. In higher flow conditions, where SDI values tend to be higher due to increased turbulence and variability in flow, the error estimation model proved to be more effective. The model was able to quantify the errors associated with varying SDI and depth, allowing for the creation of asymmetric error bounds around the composite model of flow. These error bounds were crucial in providing a more accurate representation of the potential variability and uncertainty in

the flow measurements, especially under more challenging conditions.

The resulting analysis demonstrated the composite model of flow with its associated asymmetric error bounds, which were derived from the SDI-depth error relationship. The error bounds were visualised as confidence intervals for the predicted flow values across different depths, as shown in Figure 5.10. This method ensured that even when video data passed through various filtering processes, any residual errors could be identified and accounted for, thereby enhancing the reliability and robustness of the stage-discharge curves derived from PTV data. These findings highlight the utility of SDI in estimating error bounds, particularly in scenarios where other filtering processes may fail to adequately address the complexity of the data.

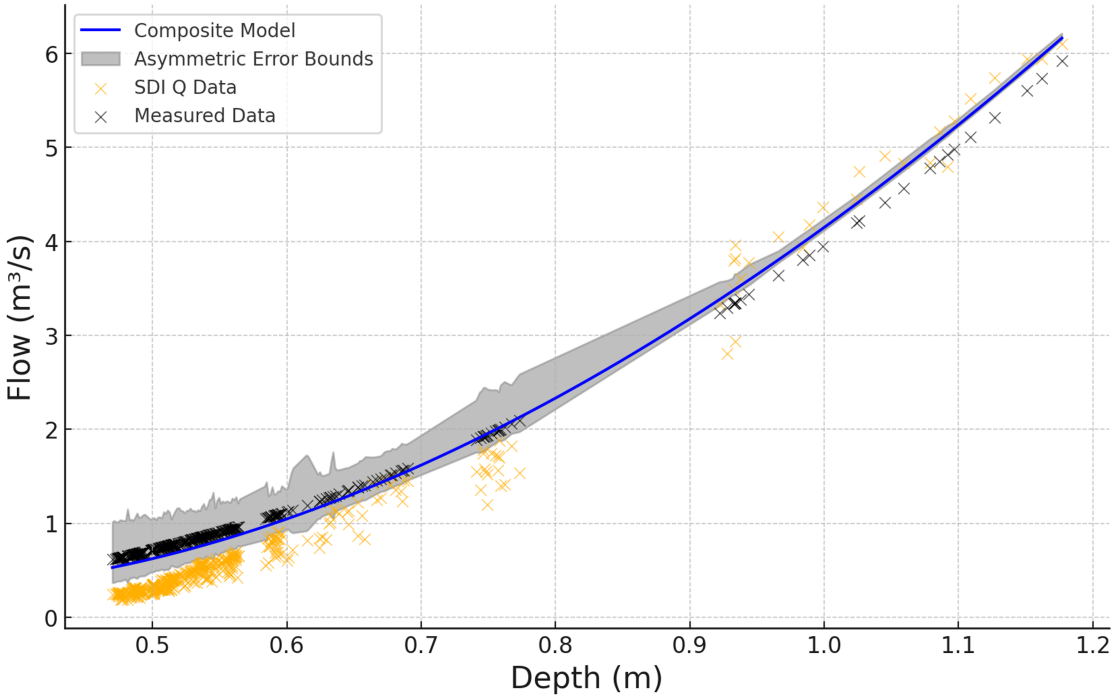


Figure 5.10: Composite model of SDI-based flow with asymmetric error bounds based on depth. The grey shaded region represents the asymmetric error bounds, and the red scatter points indicate the measured flow values. This plot illustrates the fitted model and the range of uncertainty in flow measurements.

5.4.5 Validating Error Bound Estimations

With the previous sections establishing the connection between SDI and error, a systematic error bound estimation process was developed to use SDI metrics to better estimate uncertainty in PTV results. The data processed were taken from the River Calder site, which included several data points across the flow regime of the river. The results showed that after a composite model for flow was created, it was possible to confidently encapsulate measured results within the error bounds for the study. To ensure that the approach is generalised and not biased towards the River Calder, a second site, the River Sheaf, was analysed to study the reliability of the approach.

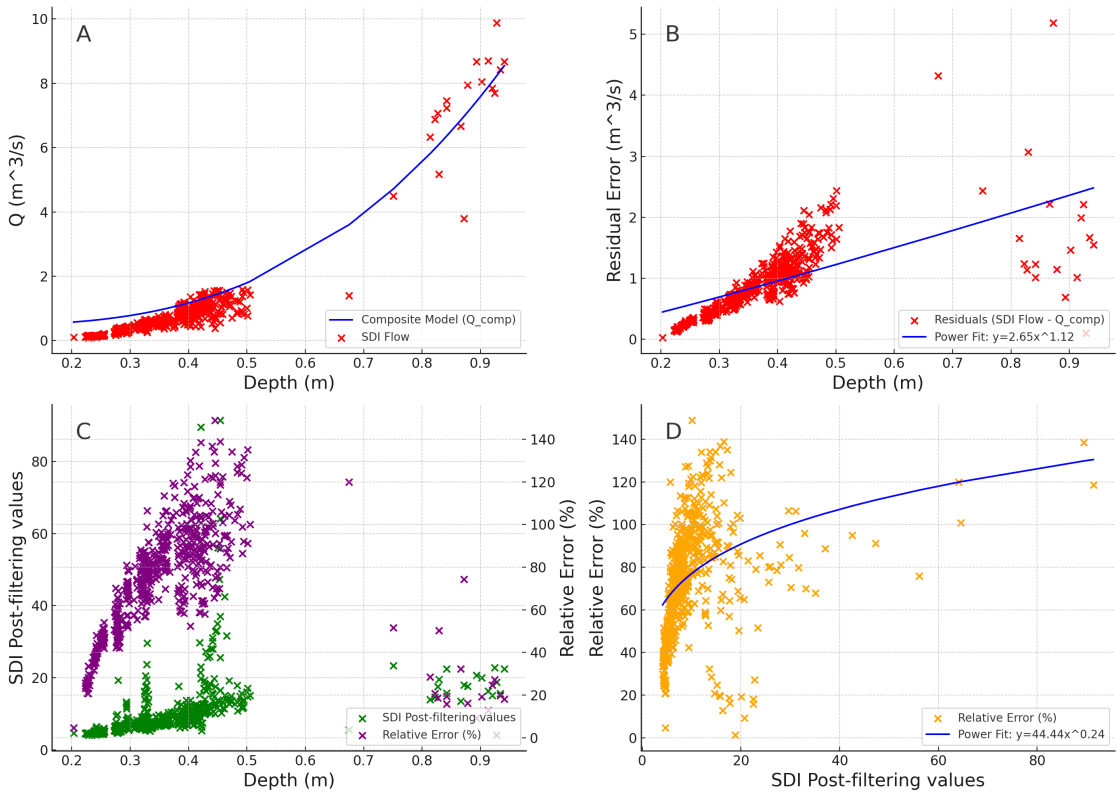


Figure 5.11: Initial comparison plots for Sheaf results illustrating the results of plotting Q_{comp} model and SDI values against depth. **(A)** The composite model of Q_{comp} and SDI Flow points plotted against depth. **(B)** The residuals of SDI Flow minus Q_{comp}, showing the error of the methodology used in this study, plotted against depth with a power fitting regression. **(C)** The SDI post-filtering values plotted against depth with the relative error (SDI Flow - Q_{comp}) shown as a percentage on the secondary axis. **(D)** The relationship between the relative error (%) and SDI post-filtering values, with a single power fitting regression.

Video data were again processed through KLT-IV, and SDI was used to filter frames to improve the SDI value for each individual video. The Post-Processed flow data were then plotted as SDI Flow, as seen in Figure 5.11A. From this data, a model fit was established as seen in Equation 5.8. Next, three randomly selected calibration points were selected from measured data points from ADCP measurements. These points were then used to fit a shifted model, seen as Equation 5.9. Finally, a composite model was created using the Equation 5.7 seen in Section 5.3.4.2.

$$Q_{\text{eq2}}(h) = 10.47(h)^{2.78} \tag{5.8}$$

$$Q_{\text{eq2}}(h) = 10.47(h)^{2.78} + 0.45 \tag{5.9}$$

The composite model developed for the River Sheaf was then validated against the residual error between Q_{comp} and SDI Flow, which was calculated and plotted against depth in Figure 5.11B. Figure 5.11C served as a visual check between SDI values, relative error, and their corresponding depth; it showed that as SDI increases, so too does the spread of relative error, which is consistent

with previous observations. To clarify this, SDI was plotted against Relative Error in Figure 5.11D. Both Figures 5.11B and 5.11D are shown with a modelled power regression to help later calculate the estimated error.

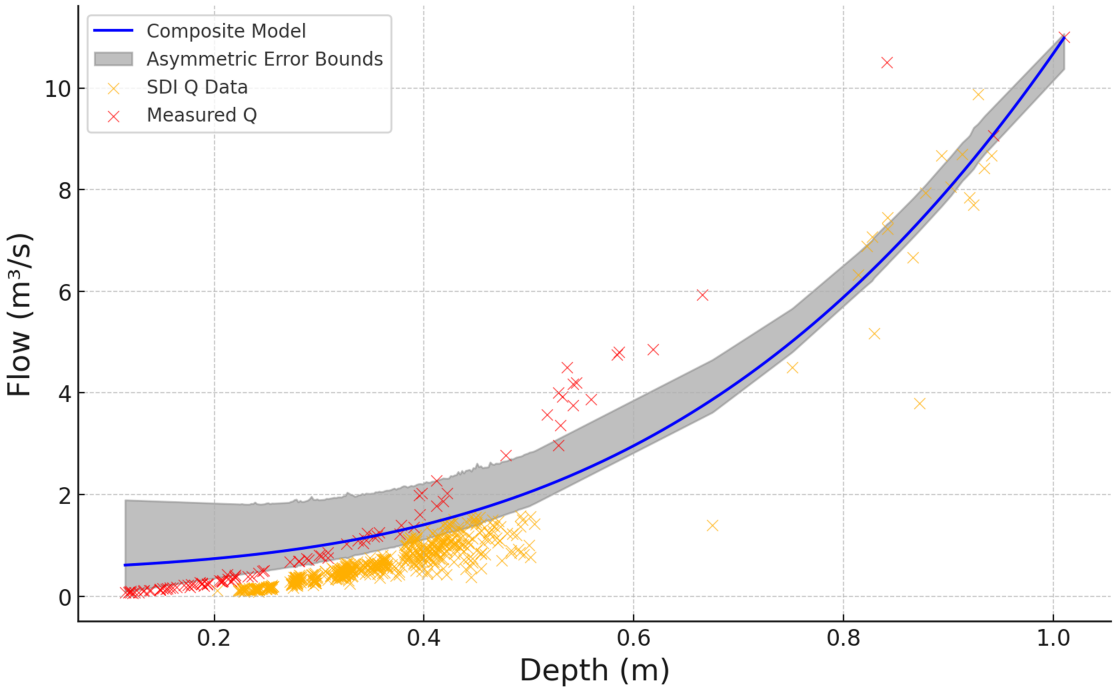


Figure 5.12: Modeled Q_{comp} with calculated error bounds compared with SDI Q values from PTV, and Measured Q values from manual ADCP data.

The error bounds for Q_{comp} were then determined using the same methods applied in Section 5.4.4. Figure 5.12 shows the computed higher and lower bounds in grey. These results indicate a strong confidence in the methods used to estimate error bounds through SDI. The composite model and its error bounds effectively encapsulate a wide range of measured data throughout the flow regime, despite using only three measured points for calibration, all of which were at the lower flow states of the rivers. However, the analysis revealed a potential issue around the depth of 0.6 m, where measured data suggested a step in the flow regime of the river that was not captured by the study data. While this could skew the validation data, the interpolated error bounds calculated from depth and SDI provide a reasonable indication of this error. The lower error bound was particularly effective in matching the measured Q data, suggesting that while the upper bound may overestimate at lower depths, the approach still provides valuable insights into the uncertainty of the measurements.

These findings underscore the importance of using a composite model with SDI-derived error bounds to capture the complexities and uncertainties inherent in river flow measurements. Despite some limitations, particularly at lower depths, the approach has demonstrated robustness across different sites and flow conditions.

5.5 Discussion

5.5.1 Impacts of Depth and Error Change with SDI

This study has highlighted two critical considerations regarding the relationship between depth and error changes associated with the SDI. Firstly, the collection of flow measurements over multiple days introduced variability due to changing environmental factors such as lighting, weather, and water clarity. These variations led to a range of SDI values and, consequently, a wide range of errors. This aligns with previous research that has noted the sensitivity of image velocimetry methods to environmental conditions (Tauro, Petroselli and Grimaldi, 2018). However, this study emphasises the extent of this variability, showing that fluctuations in environmental conditions can significantly impact SDI and measurement accuracy. These findings underline the importance of developing strategies to standardise SDI values across varying conditions or improve filtering techniques to mitigate the impact of environmental factors on measurement accuracy. Future studies could explore the development of adaptive filtering methods that adjust to specific environmental conditions in real-time, potentially improving the reliability of image-based flow measurements.

Secondly, the effectiveness of SDI filtering in consistently improving measurement accuracy is not straightforward to determine in the absence of a reliable benchmark flow for comparison. In flow conditions with depths below 0.7 m, the error changes post-SDI filtering were randomly distributed around zero. Approximately half of the cases showed improvements, while the other half exhibited deterioration. This randomness suggests that SDI filtering does not uniformly enhance accuracy at lower depths, likely due to the relatively stable flow conditions at these levels. This finding resonates with the research by Pizarro et al. (2020a), which suggests that lower SDI values, closer to 1, are indicative of better flow conditions with minimal error variation. However, the current study expands on this by indicating that the efficacy of SDI filtering may be highly dependent on specific flow conditions, particularly at lower depths where the benefits of filtering are less pronounced. Further investigation is necessary to determine the precise conditions under which SDI filtering is most effective and to develop guidelines for its application in various hydrological contexts.

5.5.2 Impact of SDI Filtering on Flow Measurement Accuracy

It was demonstrated that Post-Processed SDI filtering plays a critical role in improving the accuracy of flow measurements derived from PTV methods, particularly in higher depth conditions where SDI values are also elevated. This finding aligns with previous research by Dal Sasso et al. (2018) and Pizarro et al. (2020b), which similarly observed the utility of SDI metrics in complex flow environments. However, this study contributes further by quantifying the impact of SDI filtering across different flow conditions, revealing that its effectiveness is closely tied to the complexity of the flow environment. At lower flow conditions (depth < 0.7 m), SDI filtering impact on mea-

surement accuracy was minimal, despite the relatively large errors, reflecting the already stable and less complex flow conditions. In these scenarios, the SDI values were low, apparently indicating minimal need for correction. Consequently, the potential for improvement through filtering was limited.

In contrast, in higher flow conditions (depth > 0.7 m), where the flow dynamics are more complex, SDI filtering becomes essential. The increased variance in measurements at these depths necessitates more robust filtering to ensure accuracy, which this study has shown can lead to significant improvements in measurement accuracy. This suggests that SDI filtering is particularly effective in environments where flow conditions are less predictable and more variable. However, the reliance on SDI as the primary metric for improving measurement accuracy raises questions about the potential limitations of this approach, particularly in highly turbulent environments where SDI might not fully capture the complexity of the flow.

5.5.3 Error Analysis and SDI Correlation

The error analysis revealed a strong correlation between SDI values and measurement error, particularly at depths greater than 0.7 m. This relationship is crucial for understanding SDI filtering effectiveness and underscores the importance of using SDI as a key metric in assessing the reliability of PTV-derived measurements. The peak in error at approximately 0.75 m depth, identified in this study, highlights areas where inaccuracies are most pronounced, likely due to the witnessed video quality issues, as similarly noted by Dal Sasso et al. (2018). The results indicate that higher SDI values correspond to greater measurement errors, validating SDI as a reliable indicator of potential inaccuracies. While reducing SDI values through filtering led to error reductions, especially at greater depths, this study also identified limitations in this approach. The non-linear power-law relationship between SDI and error suggests that even small reductions in SDI can lead to considerable decreases in measurement errors. This finding is particularly significant, as it implies that efforts to improve video data quality or selectively increase SDI through strategic filtering could yield substantial benefits in flow measurement accuracy. Nevertheless, the observed peak in error at 0.75 m indicates that SDI filtering alone may not be sufficient to address all sources of error, particularly those related to environmental factors that affect video quality (see Figure 5.7). This highlights the need for continued refinement of SDI filtering techniques and the potential integration of other error-correction methods to enhance the accuracy of PTV-derived measurements.

5.5.4 Using Asymmetric Error Bounds

The filtering process using SDI metrics, while effective in some cases, has shown minimal error reduction in others. Despite this, the strong correlation between SDI values and measurement errors suggests that SDI remains a valuable indicator for assessing the reliability of flow measurements. To address the limitations observed in error reduction, this study introduces a novel approach that

utilises computed error bounds, incorporating both depth and SDI as key variables. These asymmetric error bounds account for the distribution of residual errors, providing a more precise estimation of uncertainty in the flow measurements. By considering both depth and SDI, this method offers a tailored approach to error estimation, adapting to the specific conditions of each measurement scenario. Validation using data from the River Sheaf has demonstrated the robustness of this approach, highlighting its potential to significantly enhance the reliability of stage-discharge curves derived from PTV data. The composite model, combined with dynamic scaling factors and the computed error bounds, effectively captured a high percentage of the measured flow data within the calculated error bounds for both the River Calder and the River Sheaf. This approach enhances the reliability of PTV-derived stage-discharge curves by ensuring that potential errors are identified and accounted for. However, it is important to recognise the limitations of this method, particularly at lower depths where the error bounds tended to overestimate uncertainty. This overestimation suggests that the model may require further refinement to more accurately reflect the variability in flow conditions at lower depths. Additionally, the reliance on SDI as a primary variable for error estimation may overlook other factors that contribute to measurement uncertainty, such as tracer distribution and flow turbulence.

Overall, while the use of asymmetric error bounds represents a significant advancement in the analysis of PTV-derived flow measurements, future research should aim to refine these models further. This could involve integrating additional variables or developing new filtering techniques that more effectively address the limitations identified in this study. Moreover, the findings underscore the need for continued exploration of the relationship between SDI, measurement error, and environmental conditions, with the goal of developing more robust methods for flow measurement in complex environments.

5.5.5 Generalisation and Application of Methodology

The successful application of the SDI-based error estimation methodology to the River Sheaf validation dataset demonstrates its potential for broader use. The methodology, which involves using SDI metrics to filter video frames, calculating composite flow models, and estimating error bounds, can be generalised to other river studies. This is particularly valuable in hydrological studies where traditional measurement methods may be impractical. The ability to dynamically estimate error bounds based on SDI and depth provides a flexible and scalable approach to flow measurement, potentially improving the accuracy and reliability of hydrological models. However, the generalisation of this methodology also requires careful consideration of its limitations. The study showed that while the methodology is robust across different sites, it may require adaptation to specific environmental conditions or flow regimes. For example, the model's tendency to overestimate uncertainty at lower depths suggests that additional calibration or alternative approaches may be necessary in such conditions. Additionally, the reliance on SDI as a central metric means that

the methodology's effectiveness may be limited in environments where SDI is a strong predictor of measurement error. Future research should focus on refining the methodology to account for these factors, potentially through the integration of additional metrics or the development of more sophisticated filtering techniques.

5.6 Conclusions

The accuracy of PTV for river flow analysis was enhanced through a systematic approach that addressed errors related to the SDI filtering process. This study aimed to assess the impact of Post-Processed SDI metrics on discharge calculations, and the findings provide valuable insights for refining non-invasive flow measurement techniques. The three research questions originally proposed at the start of this chapter were:

1. To what extent does the application of Post-Processed SDI metrics influence the accuracy of discharge calculations in PTV methods under real-world conditions?

2. Can the integration of Post-Processed SDI metrics into PTV methods, alongside a composite model, consistently enhance the reliability of discharge estimations across various river flow conditions?

3. Can Post-Processed SDI aid users of PTV in estimating the reliability and accuracy of data?

Key findings and their relationship to the research questions are as follows:

1. **Impact of SDI Filtering on Flow Accuracy:**
   The study demonstrated that applying SDI filtering can improve discharge accuracy, especially at higher depths and SDI values. This finding directly addresses **Research Question 1** by confirming the effectiveness of Post-Processed SDI metrics in enhancing the accuracy of PTV measurements under real-world conditions.

2. **Relationship Between Depth, SDI, and Error:**
   A non-linear relationship between SDI and error was observed, with a critical depth around 0.75 m where error variance peaked. This observation not only reinforces the importance of optimising SDI to reduce errors, as related to **Research Question 1**, but also supports **Research Question 2** by suggesting that integrating SDI metrics into a composite model can consistently enhance the reliability of discharge estimations across varying flow conditions.

3. **Development of a Composite Model:**
   The creation of a composite model that integrates original and shifted SDI flow models provided a more reliable stage-discharge relationship across different depths. This development is crucial for **Research Question 2**, as it demonstrates that a composite model can smooth

transitions between low and high flow estimations, thereby improving overall measurement reliability.

4. **Estimation of Error Bounds Using SDI:**
   A novel method was introduced to estimate error bounds based on SDI values and depth, establishing a direct link between SDI and measurement error. By incorporating a composite model and asymmetric error bounds, this approach offers a more precise estimation of uncertainty in flow measurements. This finding is relevant to **Research Question 3**, as it provides a practical tool for users to assess the reliability and accuracy of PTV data, enhancing the method's applicability in hydrological studies.

5. **Validation and Practical Applicability:**
   The effectiveness of the composite model was validated using observed flow data, confirming its utility in real-world scenarios. The successful application and adjustment of the model in various river environments demonstrate its generalisability and support its use as a standard method in hydrological research, addressing **Research Question 2** and **Research Question 3**.

The findings of this study make significant contributions to the field of hydrology by providing a refined methodology for using PTV in river flow analysis. The ability to accurately estimate flow under varying environmental conditions and flow regimes is crucial for effective water resource management, flood forecasting, and ecological studies. The composite model and error estimation methods developed offer a robust framework that can be adapted and applied in other hydrological contexts, potentially transforming flow measurement practices in complex environments. While this study has advanced the accuracy and reliability of PTV for river flow analysis, ongoing research and refinement are necessary to fully realise the potential of these techniques in diverse and challenging hydrological settings.

Chapter 6. Using SDI to Optimise the Cross-Sectional Positioning for PTV Analysis - Numerical Study

6.1 Chapter Overview

This chapter explores the application of SDI to optimise cross-sectional location for discharge estimations using PTV. Unlike previous research, seen in Chapters 4 and 5, and Pizarro et al. (2020b); Dal Sasso et al. (2021), which primarily focused on temporal analysis to enhance PTV accuracy, this chapter introduces a spatial analysis of SDI metrics. The study examines how seeding density and dispersion across various river cross-sections affect the precision of velocity estimations, which are crucial for accurate discharge measurements. By utilising a synthetic dataset originally developed for temporal analysis, the research assesses the impact of spatial variations in seeding characteristics by segmenting the ROI into multiple cross-sections and analysing a newly developed Spatial SDI. This approach aims to help PTV users optimise cross-section locations to maximise tracer reliability and minimise potential errors. The findings should highlight cross-sections with higher seeding densities and more uniform dispersion, and ultimately yield more reliable velocity measurements. Additionally, the chapter addresses challenges such as erroneous zero-velocity vectors that can distort SDI metrics and affect discharge accuracy. These insights contribute to the broader field of hydroinformatics, where precise discharge estimation is essential for effective environmental monitoring and management.

6.2 Introduction

Recent advancements in image velocimetry, particularly PTV, have greatly enhanced river discharge estimation under varied hydrological conditions. Historically, research has focused on specific contexts like high-flow monitoring (Tauro et al., 2017; Guillén et al., 2017) and fluvial dynamics (Lewis and Rhoads, 2018), but challenges remain in adapting these methods for diverse, uncontrolled environments where tracer visibility and distribution vary significantly. Accurate PTV application demands careful assessment of tracer characteristics—such as density, dispersion, and distribution—especially in natural river settings (Pizarro et al., 2020b; Alongi et al., 2023). SDI has emerged as a crucial metric, capable of reducing PTV error by up to 39% by optimising frame selection (Pizarro et al., 2020a; Dal Sasso et al., 2021). However, while SDI's role in temporal studies is well-documented, its application in spatially varying conditions, such as different river cross-

sections, is under-researched. Although extensive research exists on optimising cross-sections for hydrodynamic modelling (Chen and Liu, 2017; Montoya-Coronado et al., 2022), these studies do not specifically address PTV accuracy. For example, Eltner et al. (2020) investigated the effects of varying cross-sectional analysis on discharge estimations, highlighting the challenges posed by irregular cross-sections but not focusing on maximising PTV accuracy under different flow conditions. This study aims to fill that gap by exploring how different cross-sectional locations influence SDI metrics and velocity estimation.

When using PTV for river discharge estimation, factors like the velocity coefficient (Alpha value) (Creutin et al., 2003; Coz et al., 2010), riverbed variability (Gunawan et al., 2012), and local environmental conditions (Jolley, 2021) must be considered. Even with these factors accounted for, unsuitable cross-sections can lead to unreliable PTV analysis, as shown in the Headswood study (Appendix 11.3). Given the success of SDI in temporal studies (Chapter 4; Pizarro et al. (2020b)), this chapter shifts the focus from temporal to spatial analysis, investigating how different cross-sectional locations affect SDI metrics and velocity estimation. This approach could guide the optimal placement of cross-sections, enabling more accurate and reliable PTV analysis.

Research Questions

1. How can the spatial analysis of SDI metrics (seeding density and dispersion) be used to determine the optimal placement of cross-sections for discharge estimation using PTV, and does this optimisation effectively reduce velocity estimation errors?

2. Do the optimal seeding density and dispersion values, identified for minimising error in temporal velocity estimations, align with outcomes observed in spatially segmented synthetic models?

3. Can spatially-focused SDI metrics enhance the reliability of velocity estimations under various simulated river flow conditions?

6.3 Methods

6.3.1 Synthetic Images

The dataset utilised in this study is the synthetic dataset originally used in Chapter 4, and created by Pizarro et al. (2020a), for developing the new Post-Processed SDI equation. This dataset comprises 1680 videos with varying numerically imposed seeding densities and distributions, simulating diverse river surface tracking scenarios. These images are unaltered for this spatial analysis. Figure 4.1 displays the range of seeding densities (ρ = 4×10^{-4} PPP to ρ = 1.02×10^{-2} PPP) and distributions (υ = 0.5 to υ = 200). The synthetic images were generated to replicate real-world conditions

as closely as possible, allowing for controlled experiments on the effects of seeding density and dispersion on PTV accuracy.

6.3.2 Spatial Considerations

This study shifts the focus from temporal to spatial analysis, examining how seeding density and dispersion influence velocimetry error across different regions of the image. Instead of dividing the videos into epochs for frame-by-frame analysis, the ROI was segmented into four equal cross-sectional areas along the y-axis, covering the entire time frame. These four cross-sections were chosen to assess tracer behaviour at the entry and exit points of the ROI, as well as at two central locations, to determine whether it is more effective to place the cross-section closer to the entrance or the exit. Tracers processed by the PTV were analysed based on their positions relative to these cross-sections, as depicted in Figure 6.1. The complete numerical dataset was used to derive spatial metrics of density and dispersion, differing from the frame-by-frame approach used in previous studies.

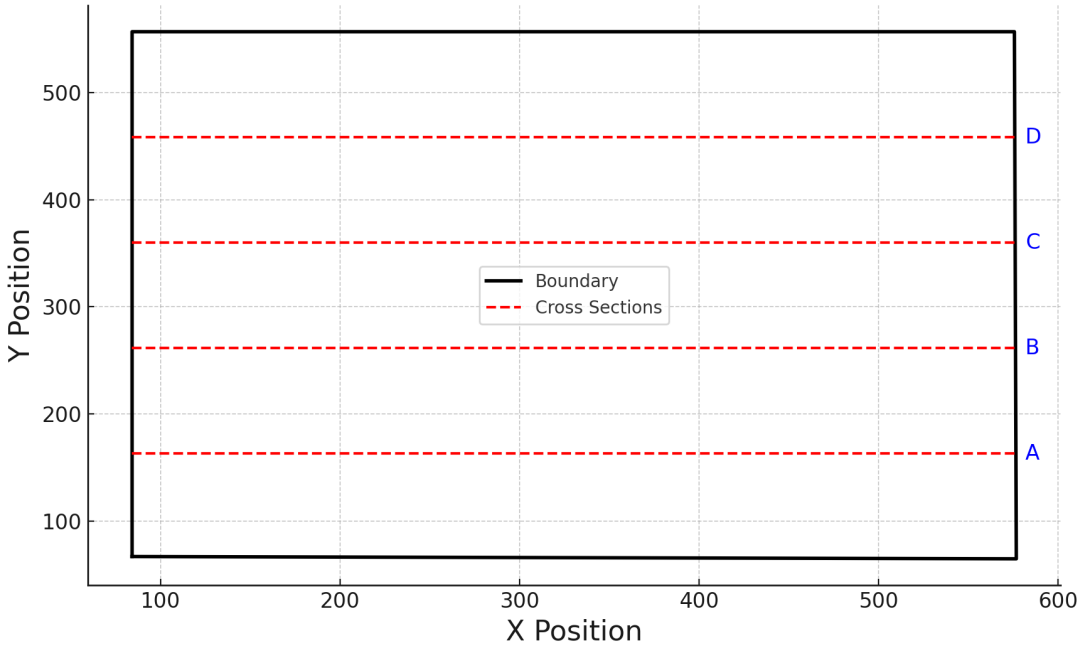


Figure 6.1: Boundary and Cross Sections

All successfully tracked tracers were recorded, and only those crossing the cross-section were considered. To determine relative dispersion for each cross-section, the image was also divided into a 22x22 grid using a user-set block size of 31x31 pixels initially inputted into KLT-IV. This segmentation allowed for a detailed examination of spatial variations in tracking performance, providing insights into localised errors and their correlation with seeding characteristics.

6.3.2.1 Creation of Cross-Sections

The creation of cross-sections allowed for a detailed spatial analysis of error, seeding density, and dispersion across the image. These cross-sections enable the examination of how these factors influence velocimetry error in specific regions of the ROI. To determine how to define the cross-sections within the ROI, the following steps were followed:

1. **Define Boundary Limits**: Boundary limits are established to define the ROI within the synthetic images. These boundaries determine the spatial extent of the analysis and ensure that all measurements are taken within a consistent area.

2. **Sectioning of the ROI**:
   The ROI is sectioned into five equal areas along the y-axis. This sectioning ensures that the spatial variability of seeding density and dispersion is captured effectively.

3. **Calculate Number of Cross-Sections**: The section edges are defined as the four cross-sections that are perpendicular to the y-axis.

4. **Determine Positions of Cross-Sections**: The co-ordinal positions of the cross-sections are calculated to ensure an even distribution across the ROI. Each cross-section represents a horizontal slice of the ROI, allowing for a detailed examination of the tracer distribution and velocity measurements in that specific segment.

5. **Grids used**: Figure 6.2 shows how cross-sections are located within the ROI, but also, how their density and dispersion is calculated by where they intercept with the grids that build the ROI. Where the cross-section slices through a grid, data from that grid is considered in spatial density and dispersion. However, only data-points that pass a cross-section (start before and end after), are used in velocity measurements. This is to mimic how PTV uses velocity measurements towards discharge measurements.

6.3.3 Velocimetry Considerations

The process for preparing velocimetry results involves several key steps to ensure precise and accurate analysis of seeding density, dispersion, and their respective impacts on velocity. The steps taken to prepare data for analysis were:

1. **Data Preparation**:
   To begin, tables were pre-allocated to store results for various metrics across different cross-sections. These tables were designed to capture data on seeding density and dispersion, providing a structured framework for subsequent analysis.

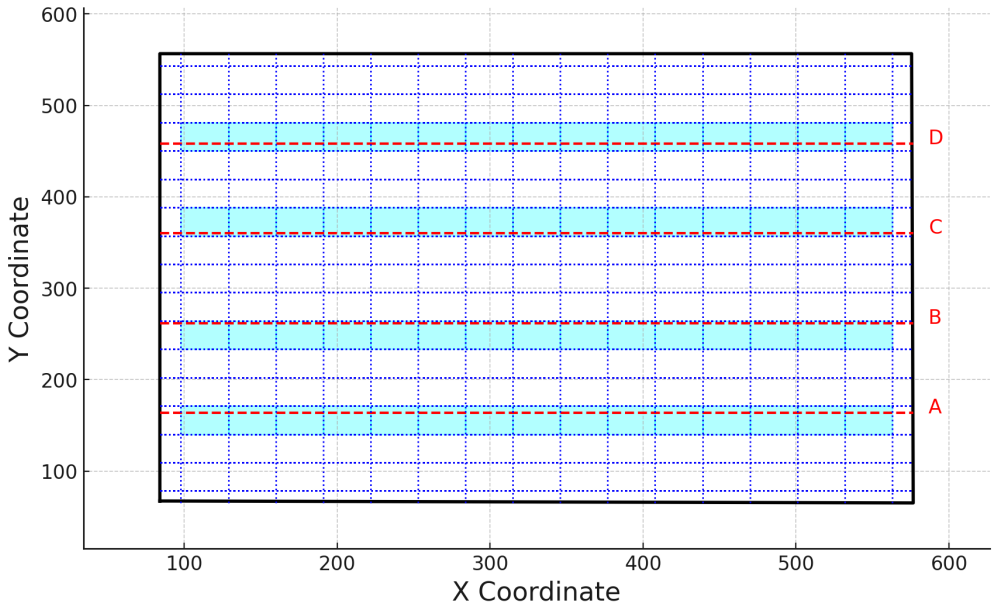


Figure 6.2: Boundary limits (black solid lines), and cross sections (red dashed lines), with highlighted grids (cyan) used towards density and dispersion for each cross-section.

2. **Data Loading and Cross-Section Calculation**:
   The data used in this study was the processed KLT-IV workspace from Chapter 4, where velocity results and tracer coordinates are stored in a ".mat" workspace. The number of cross-sections was decided as four to get a good representation of spatial variability, and their positions were systematically calculated to ensure an even distribution across the ROI; seen in Figure 6.1.

3. **Grid Position Calculation and Data Stacking**:
   The grid size was user-defined during the KLT-IV analysis stage as 31px. Subsequently, the number of grids within the transect was calculated. Temporal data from the PTV analysis was then stacked to facilitate further calculations towards the patterns of spatial impacts. The following step involved combining the positional data of tracers, to then compute the displacement and ultimately their velocities.

4. **Seeding Density and Dispersion Calculation**:
   Histograms were used to calculate seeding density, mean grid density, and variance grid density for the entire square area. These metrics are used to give the density, and the dispersion, which was calculated as the ratio of variance to mean grid density; this provided a measure of how evenly tracers were distributed across the ROI.

5. **Velocity, Density, and Dispersion Calculations for Cross-Sections**:
   For each cross-section, velocities, dispersion, and densities were calculated. This involved checking if points started within the grid boundaries and computing velocities for each point

that passed a cross-section.

6. **Interpolation and Data Averaging**:
   To ensure continuous and representative velocity profiles, interpolation was performed to fill in any missing data points along the cross-sections, replicating the process used in KLT-IV for discharge calculation. At least four data points were required for the interpolation to be valid. The interpolated velocities were then averaged for each cross-section and stored for further analysis. This is further explained in Section 6.3.3.1.

The point tracers for each processed synthetic video are to be stored in tables ready for analysis, and for each of these videos, the tracer location results are concatenated to calculate the full spatial variability across the entire video, as opposed to by frame as was done in the temporal studies. This analysis was conducted for all 1680 processed videos. Velocity was calculated from these point tracers using a simple displacement-time equation:

$$\text{Velocity (px/s)} = \frac{\text{end location (px)} - \text{start location (px)}}{\text{time (1 second)}} \tag{6.1}$$

.

6.3.3.1 Interpolation and Data Averaging

In typical PTV analyses, cross-sections are divided into cells, and the average velocity within each cell is calculated to estimate discharge. This method of creating cells along the cross-section is also integral to the calculation of seeding density and dispersion. However, in practice, some cells may lack sufficient velocity data, often due to low seeding density or high dispersion, making it impossible to calculate cross-sectional velocity directly. In these instances, PTV software will apply an interpolation method to the data to fill the missing gaps, typically quadratic, polynomial, or with KLT-IV, the option of Froude interpolation. In this study, quadratic (p2) interpolation, which fits a second-degree polynomial to the data, is used. This method is chosen for its ability to effectively model the curved nature of velocity profiles in fluid dynamics.

As illustrated in Figure 6.3, several sections along the cross-sections lack tracers representing flow, highlighting the challenge of obtaining representative velocity measurements. Calculating the average velocity for such a cross-section without addressing these gaps would produce a velocity profile that does not reflect how PTV programs typically calculate discharge. Therefore, to ensure that all cross-sections can be consistently and fairly analysed in this study, interpolation is used to estimate missing data points within these grid cells. This approach enables the generation of continuous velocity profiles that more accurately represent flow conditions. Without interpolation, the analysis would be incomplete, particularly in regions with sparse data, potentially leading to biased or unrepresentative results. Thus, interpolation is not merely a methodological choice but a necessary step to preserve the comparability and integrity of the analysis across all datasets.

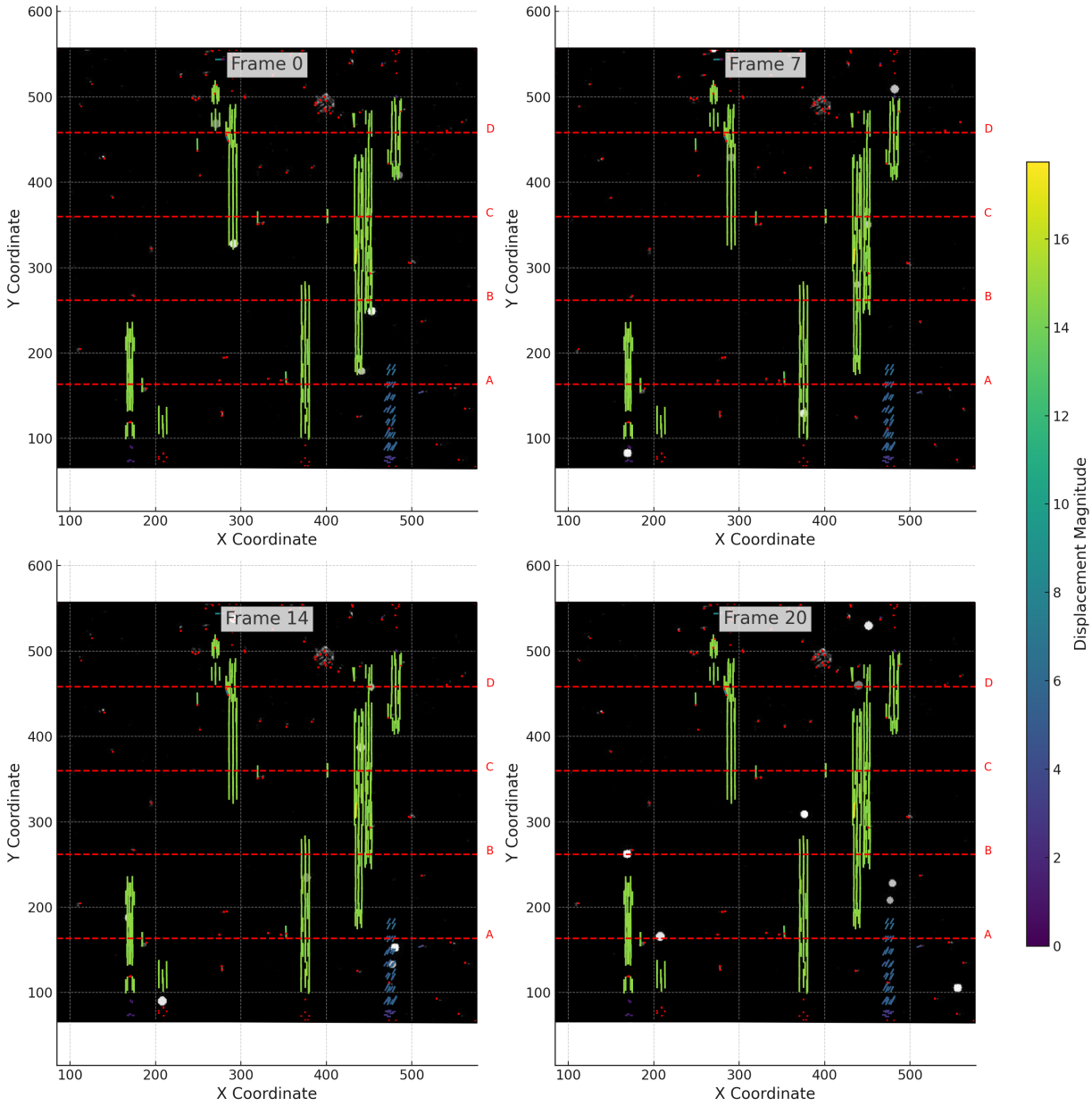


Figure 6.3: Displacement vectors overlaid on frames from a synthetic video at different time points: Frame 0, Frame 7, Frame 14, and Frame 20.

The interpolation process follows these steps:

1. **Identify Missing Data Points**: Detect gaps within the cross-sectional velocity data where direct measurements are absent.

2. **Quadratic Interpolation**: Apply a second-degree polynomial fit to the known data points surrounding each gap to establish a smooth curve.

3. **Estimate Missing Values**: Use the polynomial curve to estimate and fill in the missing velocity values, ensuring a continuous profile across the cross-section.

6.3.3.2 Impact of Interpolation on Results

Interpolating results can have several impacts on the overall analysis:

- **Continuity and Smoothness**: Interpolation helps in creating a continuous and smooth velocity profile. Discontinuous or erratic velocity data can lead to incorrect interpretations of the flow dynamics and can lead to large errors. However, without interpolation, results cannot be analysed, therefore making interpolation along the cross-section a critical step.

- **Accuracy of Estimates**: While interpolation provides a method to estimate missing values, it is important to note that these estimates are based on the existing data. If the surrounding data points are accurate and representative, the interpolated values will likely be reliable. However, if there are errors or biases in the original data, these can propagate through the interpolation process. This is where the spread of data (dispersion) also relates, as a good spread of reliable data points can help smooth an interpolation; if results are clustered to one side of the cross-section, then results on the far side can be unreliable.

- **Influence on Statistical Measures**: Interpolated values can affect the calculation of statistical measures such as mean velocity. The inclusion of interpolated data points can smooth out variability and potentially mask local variations in the flow.

- **Impact on SDI and Error Analysis**: The interpolation process can influence the SDI and error analysis results. By filling in gaps, interpolation ensures that these metrics are calculated based on a more complete dataset. However, it is crucial to consider that the interpolated values are estimates and may introduce some level of uncertainty when it comes to measuring the impact of SDI on error.

6.3.4 Error Analysis

Within the ROI

To quantify the impact of seeding density and dispersion on PTV accuracy, an error analysis was

conducted focusing on the average relative error in velocity measurements for each cross-section. This analysis helps us understand how variations in seeding density and dispersion affect the precision of PTV. The relative error in velocity measurements was calculated using Equation 6.2. In this study, the control velocity was set to a constant value of 15 pixels per second (px/s). For each cross-sectional segment, the tracked (measured) velocities were compared with this control velocity to determine the relative error. The steps involved in the error analysis are as follows:

1. **Data Collection**: Gather the measured velocities for each cross-section (A, B, C, D) from the PTV analysis for each video.

2. **Calculate Relative Error**: For each measured velocity, calculate the relative error using the formula provided in Equation 6.2. This involves:

    - Subtracting the control velocity (15 px/s) from the measured velocity.
    - Dividing by the control velocity.
    - Multiplying by 100 to express the error as a percentage.

3. **Average Relative Error**: Compute the average relative error for each cross-sectional segment to obtain a summary measure of the error distribution within that segment.

$$\text{Relative Error}(\%) = \left(\frac{\text{Measured Velocity} - \text{Control Velocity}}{\text{Control Velocity}} \right) \times 100 \tag{6.2}$$

$$\text{Average Relative Error}_{\text{segment}} = \text{mean} \left(\text{Relative Error}_{\text{cell}} \right) \tag{6.3}$$

Where $\text{Relative Error}_{\text{cell}}$ is the relative error for each individual cell within the cross-sectional segment.

This error analysis was conducted for all cross sections (A, B, C, D) to identify spatial patterns in error distribution and their correlation with seeding characteristics such as density and dispersion. By examining these patterns, an insight is gained into the following:

- **Impact of Seeding Density**: Understanding how variations in seeding density within different segments affect the accuracy of velocity measurements.
- **Effect of Dispersion**: Assessing the influence of dispersion on measurement precision, particularly how the heterogeneity in tracer distribution impacts error rates.
- **Spatial Error Patterns**: Identifying any spatial trends or patterns in the error distribution, which can highlight specific regions within the ROI that may require more analysis.

6.3.5 *Calculating Density*

Density calculation in spatial studies mirrors the approach used in temporal studies (Chapter 4). Each gridded cell's density is determined by dividing the total successful tracer points by the cell area. The average density for each segment is calculated using Equation 6.5.

$$\rho_{cell} = \frac{N_{sum_a}}{\text{Block Size}^2} \tag{6.4}$$

In this equation, ρ_{cell} represents the density within a single grid cell, N_{sum_a} is the total number of successful tracer points within the cell, and Block Size^2 is the area of the cell.

$$\rho_{segment} = \text{mean}(\rho_{cell}) \tag{6.5}$$

The density for each cell, ρ_{cell}, represents the concentration of tracers within that cell, while $\rho_{segment}$ provides an aggregate measure for the entire cross-section. This process provides a detailed view of how tracer points are distributed across different cross-sections within the image.

To summarise the method:

1. **Define the Grid**: The ROI is divided into a grid, with each cell having a specific area determined by the user-inputted Block Size.

2. **Count Tracers in Each Cell**: For each cell in the ROI segment, count the number of tracer points that fall within its boundaries; this gives N_{sum_a}.

3. **Calculate Cell Density**: The density of each cell, ρ_{cell}, is calculated by dividing the number of tracer points in the cell by the area of the cell, as shown in Equation 6.4.

4. **Average Density for Cross-Section**: The average density for a segmented cross-section, $\rho_{segment}$, is then calculated by taking the mean of the densities of all the cells within that segment, as shown in Equation 6.5.

6.3.6 *Calculating Dispersion*

As in Chapter 4, dispersion is calculated by dividing the standard deviation of density in each cell by the average density in the cross-sectional segment, as shown in Equation 6.6.

$$D_{segment} = \frac{\text{std}(\rho_{cell})}{\text{mean}(\rho_{cell})} \tag{6.6}$$

This measure of dispersion, $D_{segment}$, quantifies the heterogeneity of the tracer distribution within each segment. A higher dispersion indicates greater variability in seeding density, which can impact the precision of velocity measurements, especially when interpolation is applied. If there is a high density of points along one part of a cross-section, but a small density on others, then there

is a higher probability of interpolation misrepresenting the velocities along the cross-section. This measure of dispersion helps quantify the level of spatial clustering among the tracers. A dispersion value of 1 indicates a perfect evenness in seeding density across all grid cells, signifying minimal spatial clustering. Higher values of dispersion indicate greater variability and clustering of tracers within the ROI.

In this study, dispersion is calculated for specific cross-sections rather than for the entire ROI. This approach allows us to gain a more detailed and localised understanding of the variability in seeding density. Calculating dispersion for cross-sections provides insights into how the distribution of tracers varies across different parts of the ROI. In contrast, calculating dispersion for the entire ROI would provide a single value that might obscure local variations and hot-spots of tracer clustering or sparsity. This broader approach can mask critical details needed for precise velocity measurements for individual cross-sections.

By focusing on cross-sections:

- **Localised Analysis**: It is possible to identify areas within the ROI where the seeding density is highly variable, which might impact the accuracy of velocity measurements.
- **Enhanced Detail**: It provides a more granular view of the spatial distribution, revealing patterns that might be missed when considering the entire ROI.
- **Comparative Studies**: Allows for comparisons between different segments of the ROI to understand how tracer location varies spatially.

To summarise the method:

1. **Calculate Mean Seeding Density**: Determine the average seeding density, $\overline{\rho_i}$, across all grid cells within the ROI.
2. **Calculate Standard Deviation**: Compute the standard deviation of the seeding densities, σ, using the formula:

$$\sigma = \sqrt{\frac{\sum(\rho_i - \overline{\rho_i})^2}{N}} \tag{6.7}$$

   where σ is the standard deviation, ρ_i represents the seeding density of each individual grid cell, $\overline{\rho_i}$ is the average seeding density, and N is the total number of grid cells in the ROI.
3. **Calculate Dispersion**: Finally, calculate the dispersion, $D_{segment}$, by dividing the standard deviation by the mean seeding density, as shown in Equation 6.6.

$$D_{segment} = \frac{\sigma}{\overline{\rho_i}} \tag{6.8}$$

6.3.7 Calculating SDI

SDI is calculated using the methodology established in Chapter 4, considering seeding density (ρ) and dispersion (ν). Based on previous findings from Chapter 4, ideal values and coefficients were determined. The SDI equation, as outlined in Equation 6.9, approximates Post-Processed SDI from actual dispersion and seeding density values.

$$SDI = \nu^{k1} \left(\frac{\rho}{\rho_{ideal}} \right)^{k2} \tag{6.9}$$

In the context of this study, SDI serves as a metric for evaluating the quality of the seeding pattern spatially. The equation incorporates both density and dispersion to provide an assessment of seeding effectiveness. The coefficients k_1 and k_2, along with the ideal density value ρ_{ideal}, were derived from prior research and empirical data.

To elaborate further:

1. **Ideal Values and Coefficients**: In Chapter 4, the ideal values for dispersion (ν) and density (ρ_{ideal}) were found to be ν = 1 and ρ_{ideal} = 6.85×10^{-3} PPP, as observed from the analysis of post-processed PTV data. The coefficients k_1 and k_2 were determined to be k_1 = 0.9781 and k_2 = 0.7053, respectively.

2. **Seeding Density (ρ)**: Represents the concentration of tracers within each grid cell, calculated as described in Section 6.3.5.

3. **Dispersion (ν)**: Quantifies the variability of seeding density across the grid cells, calculated as described in Section 6.3.6.

The SDI equation combines these two metrics to give a single value that reflects the uniformity and effectiveness of the seeding pattern. A lower SDI indicates a more effective seeding pattern with less variability in error, which is crucial for accurate PTV measurements. By applying this SDI calculation across different segments, it is possible to identify regions with sub-optimal seeding and predict their impact on velocity error.

In this study, SDI is calculated for specific cross-sections rather than for the entire ROI as was the case in Chapter 4 and Chapter 5. This approach allows us to gain a more detailed and localised understanding of the variability in seeding density. Calculating SDI for cross-sections provides insights into how the distribution of tracers varies across different parts of the ROI, which can be critical for assessing the precision and accuracy of PTV measurements when trying to determine discharge.

6.3.7.1 Spatial SDI Calculation

As mentioned in Section 6.3.3.2, error analysis will be influenced by the interpolation of velocities along the cross-sections. Therefore, the impact that SDI has on cross-sectional analysis is also

likely to be impacted. In previous chapters, SDI and error were assumed proportional—where one goes up, so does the other. Where this was the case in Chapter 4, and was seen in some instances of Chapter 5, it may not be as obvious in this study. To study this, a breakdown of the SDI equation will be made for each cross-section individually and compared to the original (Equation 4.9), as well as computed relative error.

6.3.8 Filtering Results

Zero-velocity vectors have been shown to significantly impact results, particularly in scenarios where data points are sparse, leading to higher SDI values. To assess their influence, this study conducts two parallel analyses: one that includes the erroneous zero-velocity vectors in the calculation of error, SDI, and other metrics, and another that filters out all velocities below 1px/s, excluding them from average velocity measurements as well as from density and dispersion calculations. This dual analysis approach is employed because it is not always feasible to filter out all spurious vectors in practical applications. While this study can identify spurious tracers due to its synthetic nature and controlled velocity, in real-world scenarios, distinguishing true velocities across an entire ROI can be challenging, especially given localised conditions that impact velocity. By comparing the two sets of results, we can gain a deeper understanding of how the inclusion of zero-velocity vectors affects metrics and the coefficients of fit in related equations. The analysis aims to reveal the extent to which these vectors inflate density and dispersion values and contribute to increased error, providing valuable insights into their overall impact on the reliability of PTV measurements.

6.3.9 Summary of Methods

This study addresses three primary research questions related to the spatial analysis of SDI metrics in PTV-based discharge estimation. To investigate these, a synthetic dataset comprising 1680 videos was used, simulating various river surface conditions with differing seeding densities and dispersion. The study shifts from a temporal to a spatial focus, analysing how seeding density and dispersion influence velocimetry errors across different segments within a ROI. The synthetic videos were sectioned into four equal cross-sectional areas along the y-axis, each representing different parts of the flow to assess the impact of tracer positions on velocity measurements. The spatial analysis involved creating cross-sections within the ROI, where only tracers passing through these cross-sections were considered for velocity calculations. A 22x22 grid was applied to the ROI, facilitating detailed spatial metrics of density and dispersion, providing insights into localised errors and their correlation with seeding characteristics. The process involved several key steps:

1. **Data Preparation and Cross-Section Calculation**: Velocity data and tracer coordinates from the synthetic dataset were pre-processed, with cross-sections systematically calculated to ensure even distribution across the ROI.

2. **Seeding Density and Dispersion Calculation**: These metrics were computed using histograms to assess the distribution of tracers within each cross-sectional segment.

3. **Interpolation and Data Averaging**: Where data gaps existed, quadratic interpolation was employed to ensure continuous velocity profiles.

4. **Error Analysis**: The relative error of velocity measurements was calculated for each cross-section to understand how variations in seeding density and dispersion affect PTV accuracy.

5. **SDI Calculation**: The SDI was calculated for each cross-section, using a formula derived from previous studies, incorporating both seeding density and dispersion to assess seeding pattern quality.

Two parallel analyses were conducted to examine the impact of zero-velocity vectors, comparing results with and without these spurious data points to understand their effect on SDI and error metrics. This methodological approach enables a detailed spatial analysis of SDI metrics and their impact on the accuracy of PTV-based discharge measurements, providing insights that could inform better placement of cross-sections and improved error estimation techniques in real-world applications.

6.4 Results

6.4.1 PTV Results

6.4.1.1 Tracer Displacement

Figure 6.4 shows the displacement measurements for point tracers from a synthetic video with an imposed density of $\rho = 4.00 \times 10^{-5}$ and imposed dispersion $\nu = 0.5$, with start and end locations connected by vector lines. The colour gradient of these vectors represents the total displacement. Most detected tracers display a displacement of approximately 15px, which aligns with the expected velocity of 15 px/s. However, the figure also highlights several erroneous data points, represented by dark blue vectors and zero-velocity points highlighted in red. These erroneous data points are particularly prevalent at the intersections of cross-sections, notably around cross-sections A and D (top and bottom). Given that the displacement of these vectors are near-zero, it is highly unlikely that they are to pass through a cross-section and be counted towards velocity; however, notably at Cross-Section A, some of the erroneous data-points do cross through the cross-section, and will influence velocity measurements. Furthermore, regardless of their respective displacements, any points that lie within the grid that encompasses a cross-section are used to determine density and dispersion. Therefore, the zero-velocity vectors may not influence the average velocity, but they can still inflate the respective density and dispersion for those cross-sections.

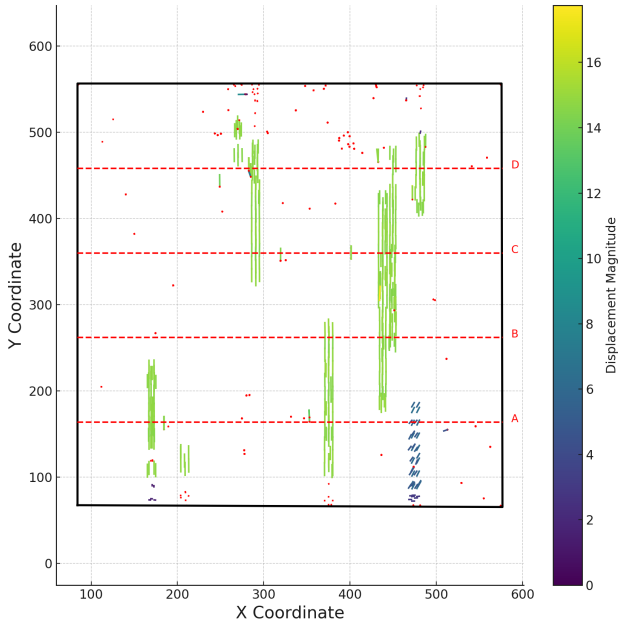


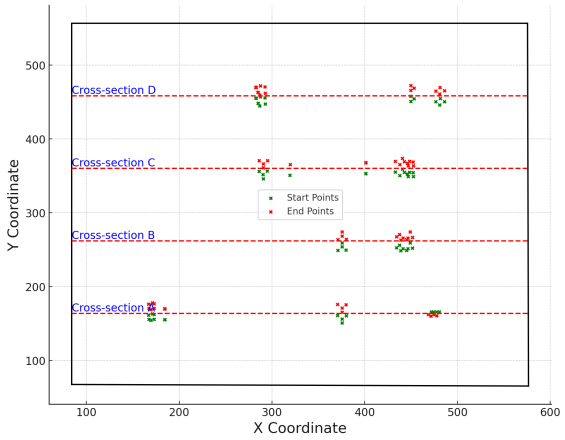
Figure 6.4: Displacement vectors for point tracers overlaid on the ROI. Vector lines connect start and end locations, with colour gradient indicating total displacement. Near-zero-velocity vectors are shown in red.

6.4.1.2 Velocity Estimations

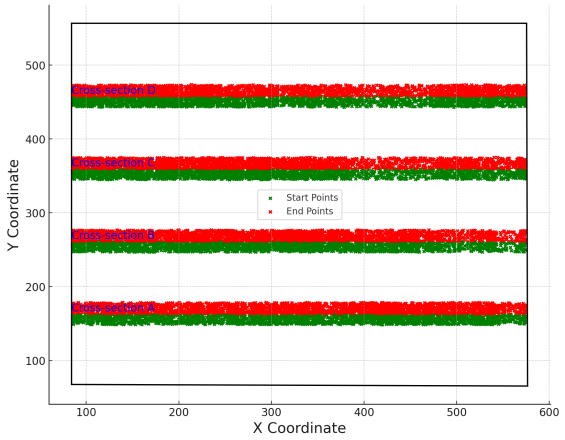
The velocities used to compute average cross-section velocities include only the detected point tracers that pass through a cross-section, consistent with standard PTV discharge calculation methods such as KLT-IV. Examples of such tracers are shown in Figure 6.5. Figure 6.5a demonstrates the scarcity of usable tracers from a video with an imposed density (that which is controlled and synthetically generated), of $\rho = 4 \times 10^{-5}$ and an imposed dispersion of $\nu = 0.5$. Conversely, Figure 6.5b shows an abundance of usable tracers with an imposed density of $\rho = 1.02 \times 10^{-2}$ and an imposed dispersion of $\nu = 200$. In the case of Figure 6.5a, interpolation along the cross-section is expected to be unreliable due to the sparsity of data points, whereas for Figure 6.5b, the minimal missing data points leave little room for interpolation to extrapolate to extreme erroneous values.

6.4.1.3 Impact of Imposed Density on Velocity

Assuming a correlation between the imposed density of the video and the actual tracers detected by the PTV algorithm (as consistent with Chapter 4), Figure 6.6 plots imposed density versus average cross-section velocity. At lower imposed densities, the spread of results is consistent with what is seen in Figure 6.5a, where there is clearly a lack of data along a cross-section, resulting in unreliable data and, in some cases, an average velocity of zero where not enough tracers are present to perform extrapolation. By averaging the velocity for each imposed density value and



(a) Scatter plot for a video with imposed density $\rho = 4 \times 10^{-5}$ and imposed dispersion $\nu = 0.5$. Shows a scarcity of usable tracers along cross-sections, leading to potential unreliability in interpolation.



(b) Scatter plot for a video with imposed density $\rho = 1.02 \times 10^{-2}$ and imposed dispersion $\nu = 200$. Shows an abundance of usable tracers along cross-sections, allowing for more reliable interpolation.

Figure 6.5: Scatter plots illustrating the distribution of successfully processed tracers across cross-sections for varying imposed densities and dispersions.

for each cross-section (see Table 6.1), it is evident that Cross-Sections B and C (the middle two cross-sections) generally outperform Cross-Sections A and D until the highest imposed densities, where the difference becomes negligible.

Imposed Density	Cross Section A	Cross Section B	Cross Section C	Cross Section D
4.00×10^{-5}	7.41	12.66	12.66	8.58
6.00×10^{-5}	9.33	13.69	12.79	10.11
8.00×10^{-5}	10.67	13.82	13.70	11.36
1.00×10^{-4}	11.59	14.18	13.88	11.73
1.20×10^{-4}	12.24	14.31	14.04	12.35
2.20×10^{-4}	13.95	14.67	14.56	13.71
3.20×10^{-4}	14.40	14.69	14.69	14.09
4.20×10^{-4}	14.55	14.70	14.71	14.29
5.20×10^{-4}	14.53	14.72	14.71	14.49
1.02×10^{-3}	14.70	14.72	14.72	14.66
1.52×10^{-3}	14.71	14.72	14.72	14.69
2.02×10^{-3}	14.72	14.72	14.72	14.71
5.02×10^{-3}	14.73	14.72	14.72	14.73
1.02×10^{-2}	14.73	14.73	14.73	14.73

Table 6.1: Average cross-section velocity for each imposed density value. This table provides a summary of velocities measured across different cross-sections under varying imposed densities.

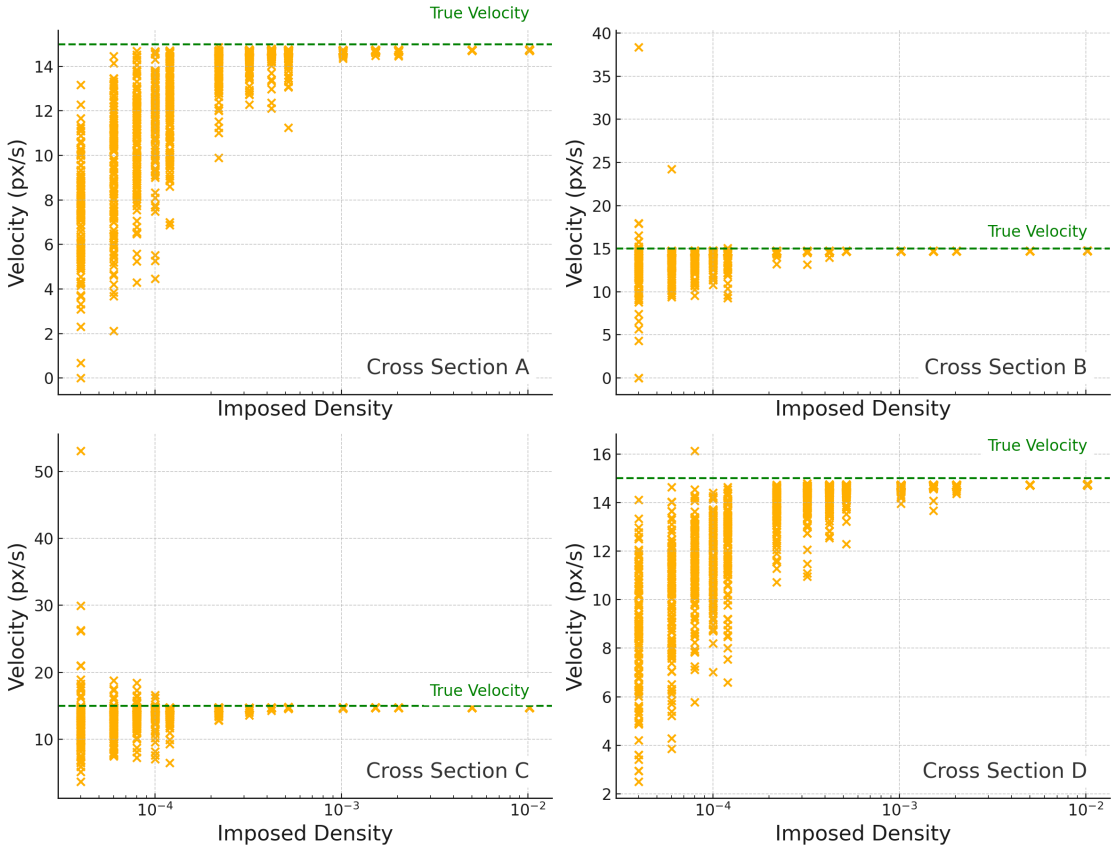


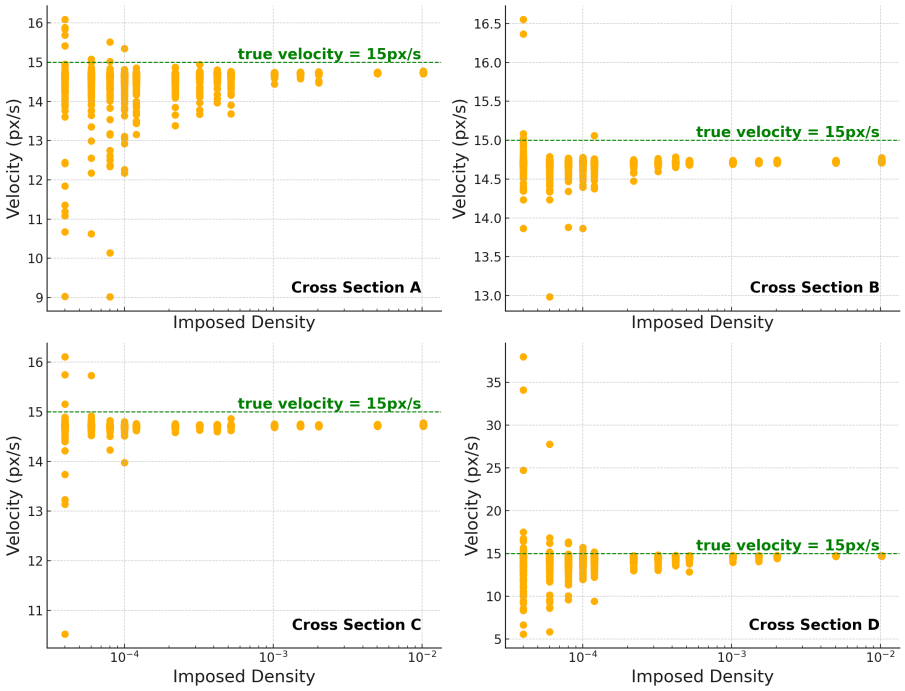
Figure 6.6: Plot of Cross-Section Velocity versus Imposed Density. Shows the average velocity for each cross-section with the true velocity marked, illustrating how velocities vary with imposed density across different cross-sections.

6.4.1.4 Impact of Spurious Velocity Vectors

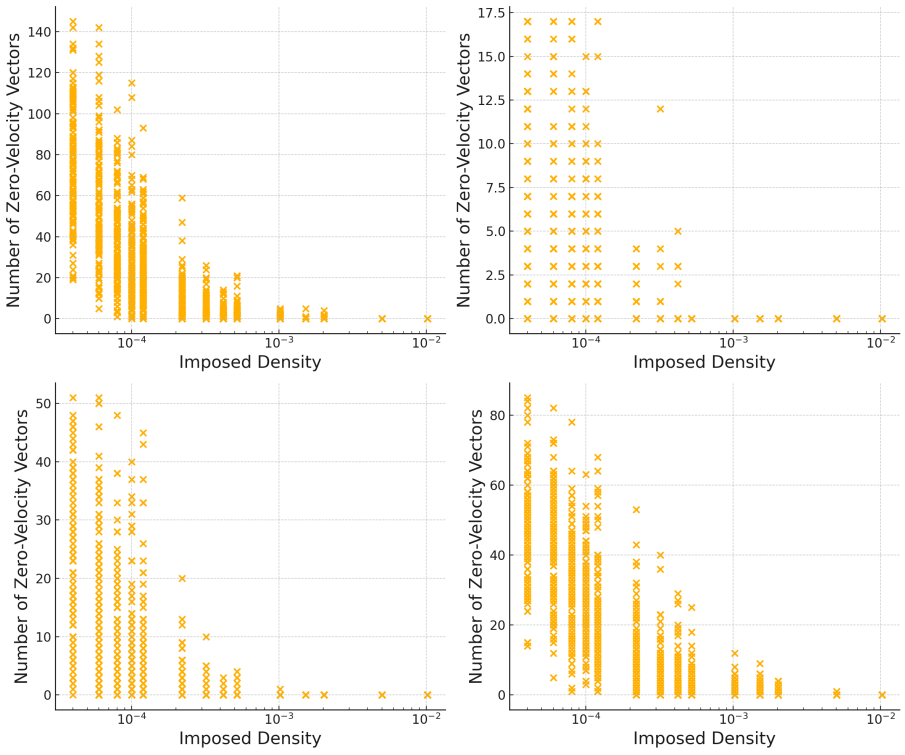
Figure 6.5a also shows some clearly erroneous zero-velocity vectors, particularly where they marginally interfere with the cross-sections, as seen in Cross-Section A. To assess the impact of these on the average velocity of the cross-sections, a filter was applied to remove all velocities $< 1px/s$ from the data, and velocities were recalculated. The results are shown in Figure 6.7a and Table 6.2. This filtering process shows a significant improvement in cross-sectional average velocity but also reinforces the accuracy disparity between Cross-Sections A and D compared to Cross-Sections B and C. The number of zero-velocity vectors for each imposed density is plotted in Figure 6.7b. There is a clear relationship between imposed density and the number of zero-velocity vectors filtered out. Overlaying frames from the synthetic videos with the velocity vectors (see Figure 6.3) indicates that many erroneous vectors are caused by background noise (small white dots designed to represent noise), tracers entering or exiting the frame, or inaccuracies in the PTV tracking. Given that zero-velocity vectors are often associated with background noise, the apparent influence decreases as imposed density increases, therefore suggesting that more features overlaying the background noise help the PTV algorithm filter out, and correct for, erroneous vectors.

Imposed Density	Cross Section A	Cross Section B	Cross Section C	Cross Section D
4.00×10^{-5}	14.34	14.71	14.65	13.84
6.00×10^{-5}	14.45	14.65	14.71	13.79
8.00×10^{-5}	14.35	14.68	14.70	13.84
1.00×10^{-4}	14.47	14.68	14.70	14.03
1.20×10^{-4}	14.51	14.69	14.71	14.11
2.20×10^{-4}	14.56	14.72	14.73	14.25
3.20×10^{-4}	14.60	14.74	14.75	14.32
4.20×10^{-4}	14.63	14.75	14.76	14.38
5.20×10^{-4}	14.65	14.76	14.77	14.42
1.02×10^{-3}	14.70	14.78	14.79	14.54
1.52×10^{-3}	14.73	14.79	14.80	14.60
2.02×10^{-3}	14.75	14.80	14.81	14.65
5.02×10^{-3}	14.80	14.82	14.83	14.75
1.02×10^{-2}	14.83	14.83	14.84	14.80

Table 6.2: Average velocity per cross-section and imposed density after filtering out zero-velocity vectors. This table shows the refined average velocities and their consistency across cross-sections once erroneous zero-velocity vectors are removed.



(a)

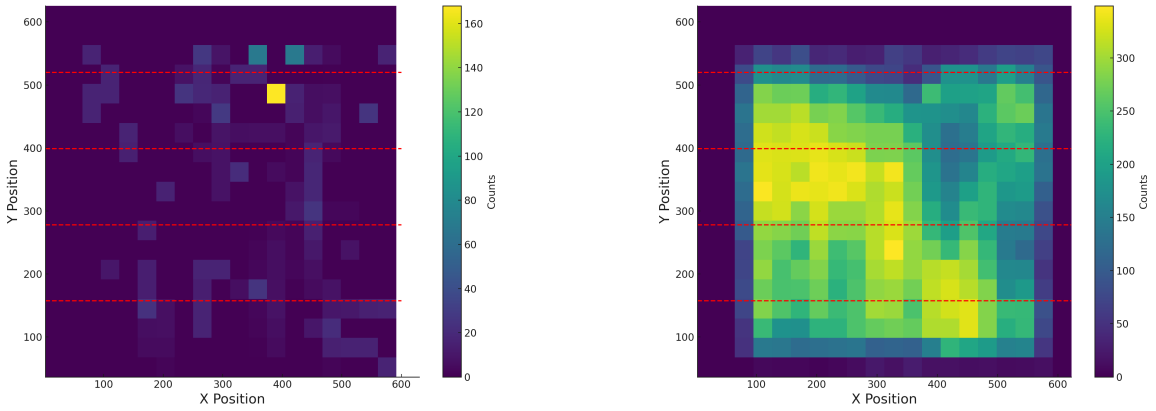


(b)

Figure 6.7: (A) Cross-Sectional Velocity versus Imposed Density with zero-velocities filtered out and their subsequent number of zero-velocity vectors against their respective imposed density (B)

6.4.2 Cell Analysis

To analyse the density and dispersion of the point tracer results, histograms with a grid size set at 31px were created. Each histogram plots the start locations of point tracers according to their coordinates and counts the number of tracers within each grid cell. Figures 6.8a and 6.8b illustrate histograms from two extremes of the dataset, representing different conditions of imposed density and dispersion. Figure 6.8a displays the histogram for a video with low imposed density (ρ = 4.00×10^{-5}) and low imposed dispersion (ν = 0.5). The high distribution of tracers across the grid cells reflects the low density and low dispersion value, resulting in a smaller density of tracers being located across the grid cells. Conversely, Figure 6.8b depicts the histogram for a video with high imposed density (ρ = 1.02×10^{-2}) and high imposed dispersion (ν = 200). The increased density and dispersion results in a more conglomerated distribution of tracers across the grid cells, but also showing a greater number of tracers in each cell and highlighting the effect of increased density and dispersion on the histogram.



(a) Histogram of point tracer start locations for a video with low imposed density (ρ = 4.00×10^{-5}) and low imposed dispersion value (ν = 0.5). The high distribution reflects the low density and dispersion conditions.

(b) Histogram of point tracer start locations for a video with high imposed density (ρ = 1.02×10^{-2}) and high imposed dispersion (ν = 200). The uneven distribution illustrates the effect of increased density and dispersion.

Figure 6.8: Comparison of histograms illustrating the distribution of point tracer start locations under different imposed density and dispersion conditions. Cross-sections A–D are included for reference.

6.4.3 *Density Results*

6.4.3.1 *Observed vs Imposed Density*

An essential part of the analysis is comparing the imposed density to the observed density derived from the PTV results. Figure 6.9 illustrates the relationship between imposed density and observed density across the four cross-sections. The observed density generally remains below the imposed density, consistent with previous temporal studies. However, at lower imposed densities, Cross-Sections A and D show a closer alignment between observed and imposed densities on average. The consistency across all four cross-sections suggests that the location of the cross-section does not significantly influence the observed density. Nevertheless, as noted in Section 6.4.1, the presence of erroneous zero-velocity vectors, particularly at lower imposed densities, can substantially affect the results. To address this, Figure 6.10 shows the data after filtering out velocities less than 1 px/s. The filtering decreases the observed density for Cross-Sections A and D, making their densities at lower imposed values more consistent with the patterns observed in Cross-Sections B and C, where the filtering had a minimal effect.

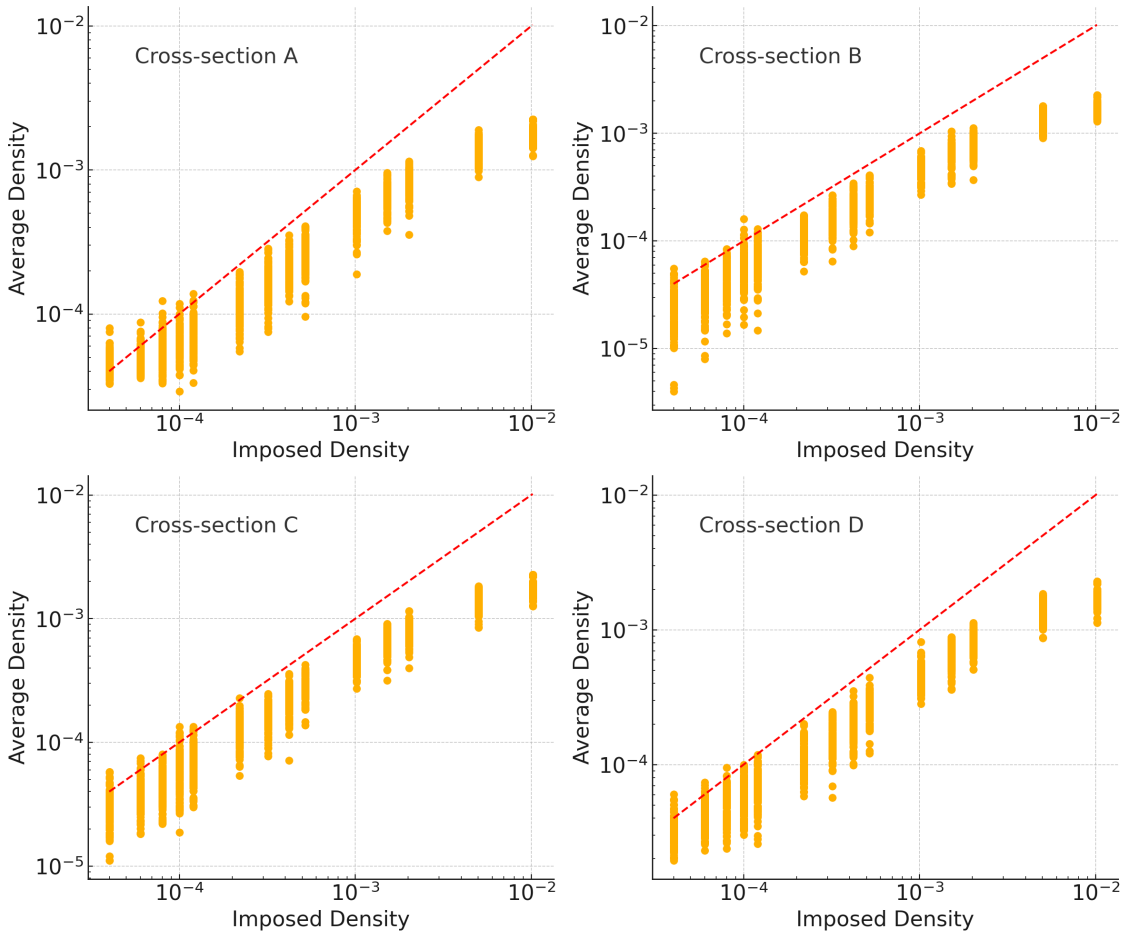


Figure 6.9: Observed density versus imposed density for all four cross-sections. The red line represents the line of equality ($y = x$), indicating where observed density matches the imposed density.

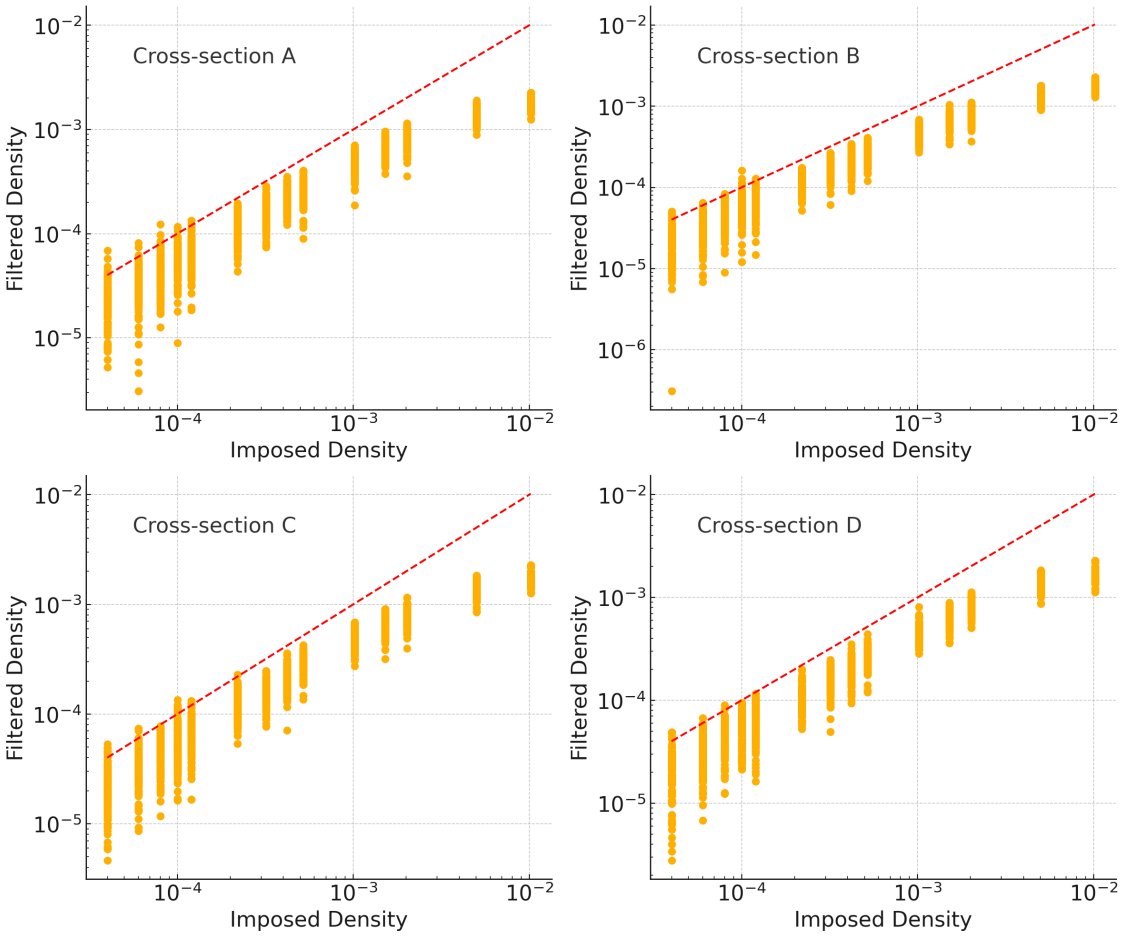


Figure 6.10: Filtered observed density versus imposed density after removing velocities less than 1 px/s. The red line represents the line of equality ($y = x$), highlighting the improved alignment between observed and imposed densities for Cross-Sections A and D.

6.4.3.2 Relationship Between Relative Error and Observed Density

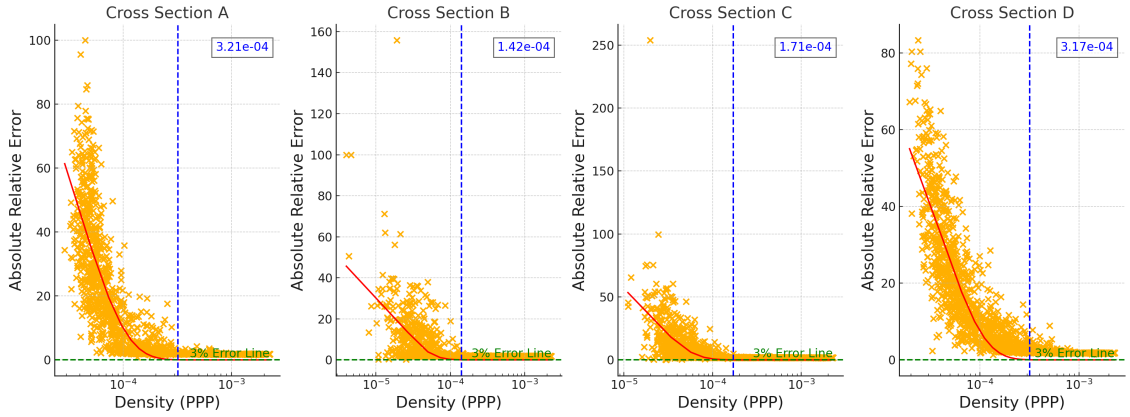
In this analysis, an investigation into the relationship between observed density and its corresponding error is made, following the approach used in Chapter 4. Figure 6.11a displays the pattern of relative error against average density for each cross-section. As anticipated, relative error decreases as density increases. Since the relative error in this study includes both positive and negative values (contrary to the negative-only errors in temporal studies), absolute error provides a clearer correlation. An exponential regression model was applied to facilitate comparison across different cross-sections. A horizontal line at 3% error (green) is included in the plots, representing the standard error threshold used in temporal studies. The intersection of each cross-section's model with this 3% error line indicates the density required to achieve this level of accuracy.

For pre-filtered data, Cross-Sections A and D require 2–3 times the density of Cross-Sections B and C to reach the 3% error threshold. To assess if this discrepancy is due to zero-velocity vectors, the data was recalculated and replotted with these vectors removed, as shown in Figure 6.11b. The filtered results reveal that densities across cross-sections trend closer together, though Cross-Sections A and D still show a broader range of relative errors compared to B and C, which consistently maintain less than 3% relative error. This indicates that filtering out zero-velocity vectors significantly improves the uniformity of error across different cross-sections in comparison to its corresponding density. Furthermore, the ideal density required to achieve a 3% error in spatial studies is three times lower than in temporal studies where the ideal density was 6.85×10^{-3} PPP. In contrast, the highest density achieved in the spatial analysis was 1.6×10^{-3} PPP. This discrepancy is likely due to spurious vectors that were not filtered out in temporal studies. Temporal studies counted all vectors, including erroneous ones, contributing to higher required densities for similar error results. In this spatial study, consistent spurious zero-velocity vectors, particularly near the ROI edges and background noise clusters, were identified and filtered out. Also, the interpolation applied to the cross-sectional velocities helps to smooth out the effects of erroneous vectors, leading to a more accurate average. This smoothing effect is evident in Figure 6.11b, where densities of 1.00×10^{-4} PPP achieve less than 3% relative error for Cross-Sections B, C, and D, while Cross-Section A is still close to this threshold.

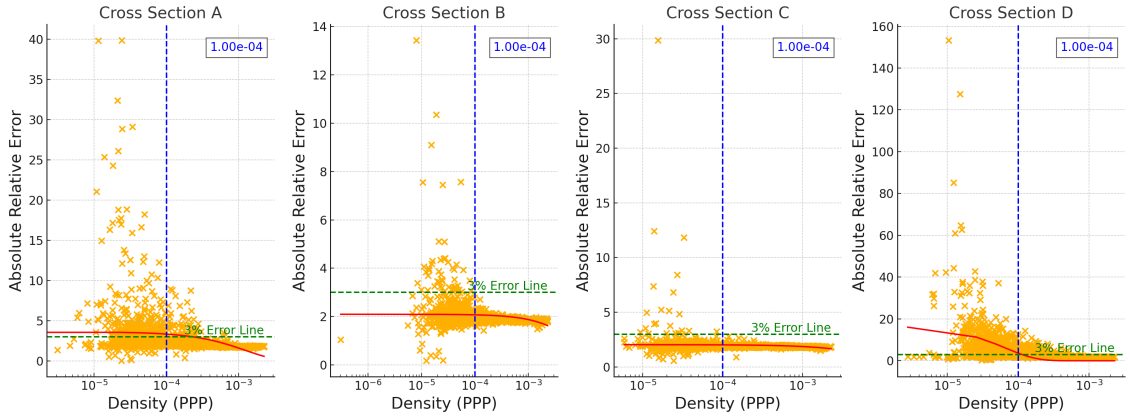
6.4.4 Dispersion Results

6.4.4.1 Imposed Dispersion Results

Variations in imposed dispersion are likely to introduce disparities and variations in these error results. To explore this, Figure 6.12 plots imposed density against relative error, highlighting the cases with maximum (ν = 200, red) and minimum (ν = 0.5, green) imposed dispersion. Given the results seen in Chapter 4 for imposed dispersion, the results once again indicate no clear pattern between imposed dispersion and relative error. Even after filtering out zero-velocity vectors, the



(a) Unfiltered relative absolute error vs. average density.



(b) Filtered zero-velocity vectors, relative absolute error vs. average density.

Figure 6.11: Comparison of unfiltered and filtered relative absolute error versus average density across different cross-sections. The green horizontal lines indicate the 3% error threshold, and the vertical blue line denotes the observed ideal density for each cross-section.

data shows that the higher error values at lower imposed densities are more common with maximum dispersion (red), but there is no significant overall relationship between imposed dispersion and error. This suggests that the imposed dispersion does not have a significant influence on the error results from PTV analysis.

6.4.4.2 Imposed Dispersion vs. Observed Dispersion

To further investigate the relationship between imposed dispersion and the resulting observed dispersion, observed dispersion was plotted against imposed dispersion, as depicted in Figure 6.13.

Although the dispersion units are dimensionless and the specific magnitude of the range is not directly comparable (due to differences in how pre-processed and post-processed dispersion are calculated), the key observation here is the lack of a clear trend where increased imposed dispersion correlates with increased observed average dispersion. An interesting pattern emerges when considering the role of zero-velocity vectors. The data reveals that these vectors significantly im-

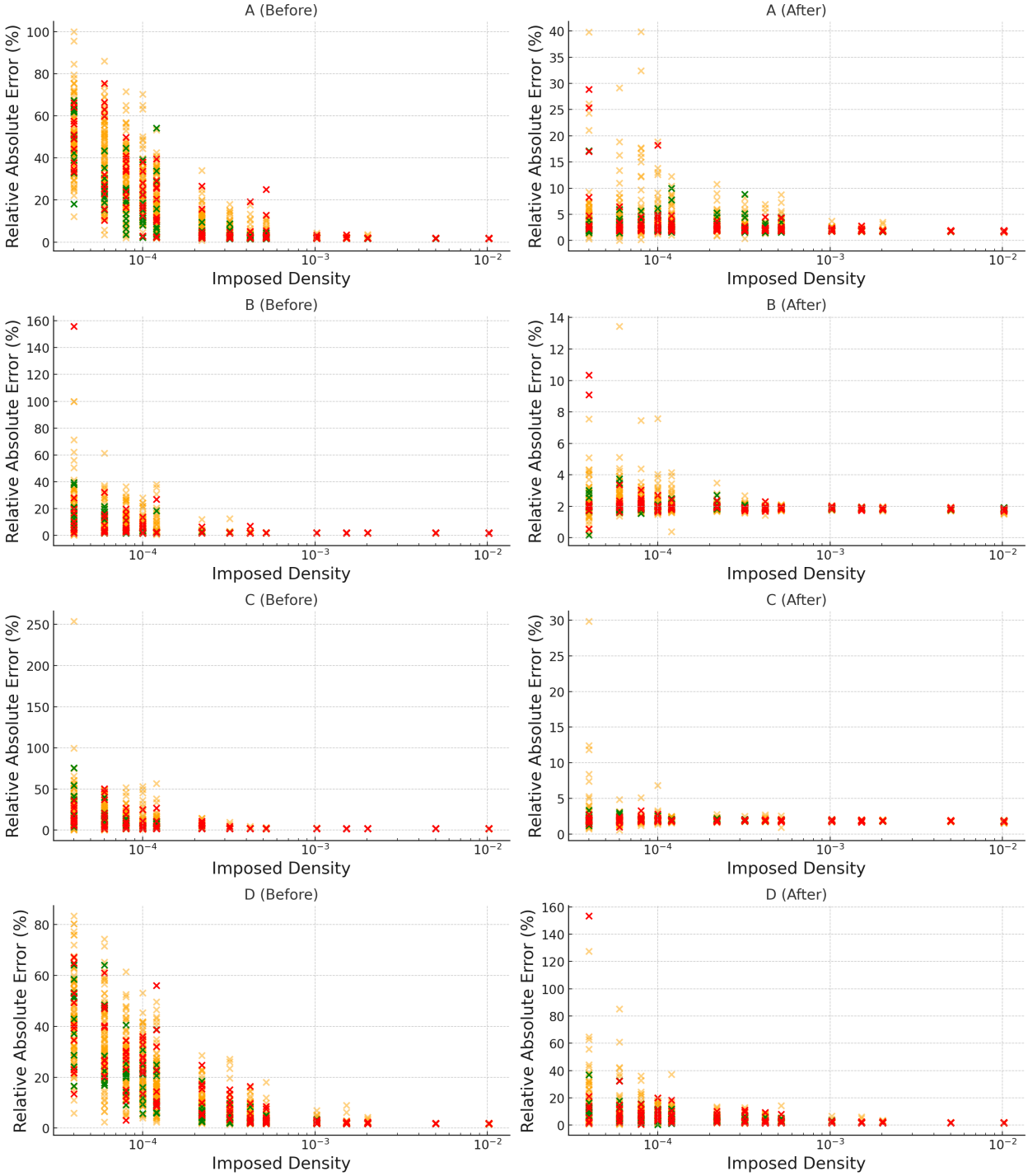


Figure 6.12: Comparison of relative absolute error versus imposed density, with imposed dispersion highlighted. The plot shows data before and after filtering out zero-velocity vectors. Maximum imposed dispersion (ν = 200) is highlighted in red, and minimum imposed dispersion (ν = 0.5) in green.

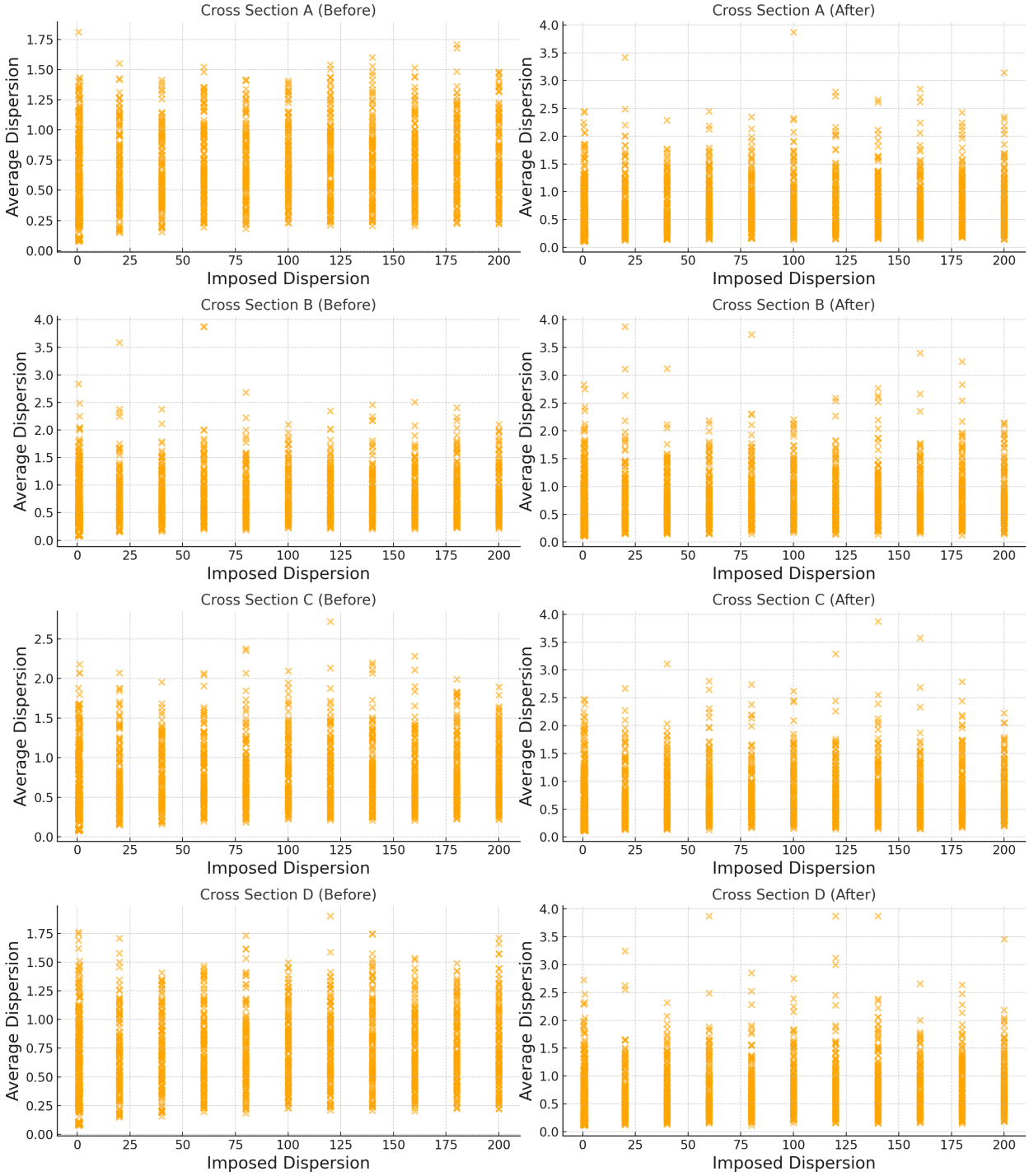


Figure 6.13: Comparison of imposed dispersion versus observed dispersion across different cross-sections, shown before and after filtering out zero-velocity vectors. The left column represents the ”Before” data, and the right column represents the ”After” filtering data, illustrating how filtering affects the range of observed dispersions.

pact the range of observed dispersion across all imposed dispersion datasets, as evidenced by the increased range after filtering. This finding suggests that zero-velocity vectors are not clustered but rather sporadically distributed throughout the ROI. If these zero-velocity vectors had been clustered, we would expect the dispersion to decrease after their removal, indicating a more evenly distributed set of tracers. However, the opposite trend is observed: the removal of these vectors uncovers a more clustered set of tracers within the ROI, implying that the zero-velocity vectors were contributing to an artificially inflated dispersion.

6.4.4.3 Observed Dispersion Results

Given the lack of a clear relationship between imposed dispersion and observed dispersion, it is essential to examine the relationship between observed dispersion and relative error. Figure 6.14 illustrates this relationship, and as anticipated from prior analyses, there is a strong correlation between increasing observed dispersion and absolute error, as represented by the power regression models in each subplot.

A critical observation from this figure is the difference between the filtered and unfiltered models, particularly in the range of dispersion values where the ideal dispersion $\nu = 1$ occurs. For unfiltered data in Cross-Sections B and C, a dispersion value of 1 or less typically results in an error close to the 3% threshold. As expected, when dispersion exceeds 1 in both filtered and unfiltered results, the variability in the results increases significantly. However, issues arise in Cross-Sections A and D, where erroneous vectors inflate both the observed dispersion and the corresponding error. This discrepancy is evident when comparing the before and after filtering results for these cross-sections. After removing the erroneous vectors, dispersion increases across the range, but error decreases significantly, with a dispersion value of 1 again corresponding to an error close to the 3% threshold.

These observations highlight a potential challenge when estimating error using the SDI. In cases where a cross-section is similar to A or D, particularly with low seeding density, relying on an ideal dispersion value of $\nu = 1$ could lead to an overestimation of reliability in the results. Therefore, it may be more prudent to adjust the SDI fit coefficients in spatial studies to place greater weight on dispersion when estimating error. A lower over-dispersion value of $\nu = 0.5$ is suggested. While this may lead to more conservative (higher) error estimates, it ensures that errors are not underestimated and can be appropriately accounted for.

6.4.5 Observations for SDI Calculations

In temporal studies, the relationship between density and dispersion was analysed, compared to their relative error, and then combined to derive the equation for the SDI (Equation 4.8). However, the results from the spatial studies indicate that the SDI equation derived from temporal studies is inadequate for spatial studies due to the significant variability in density and dispersion across the

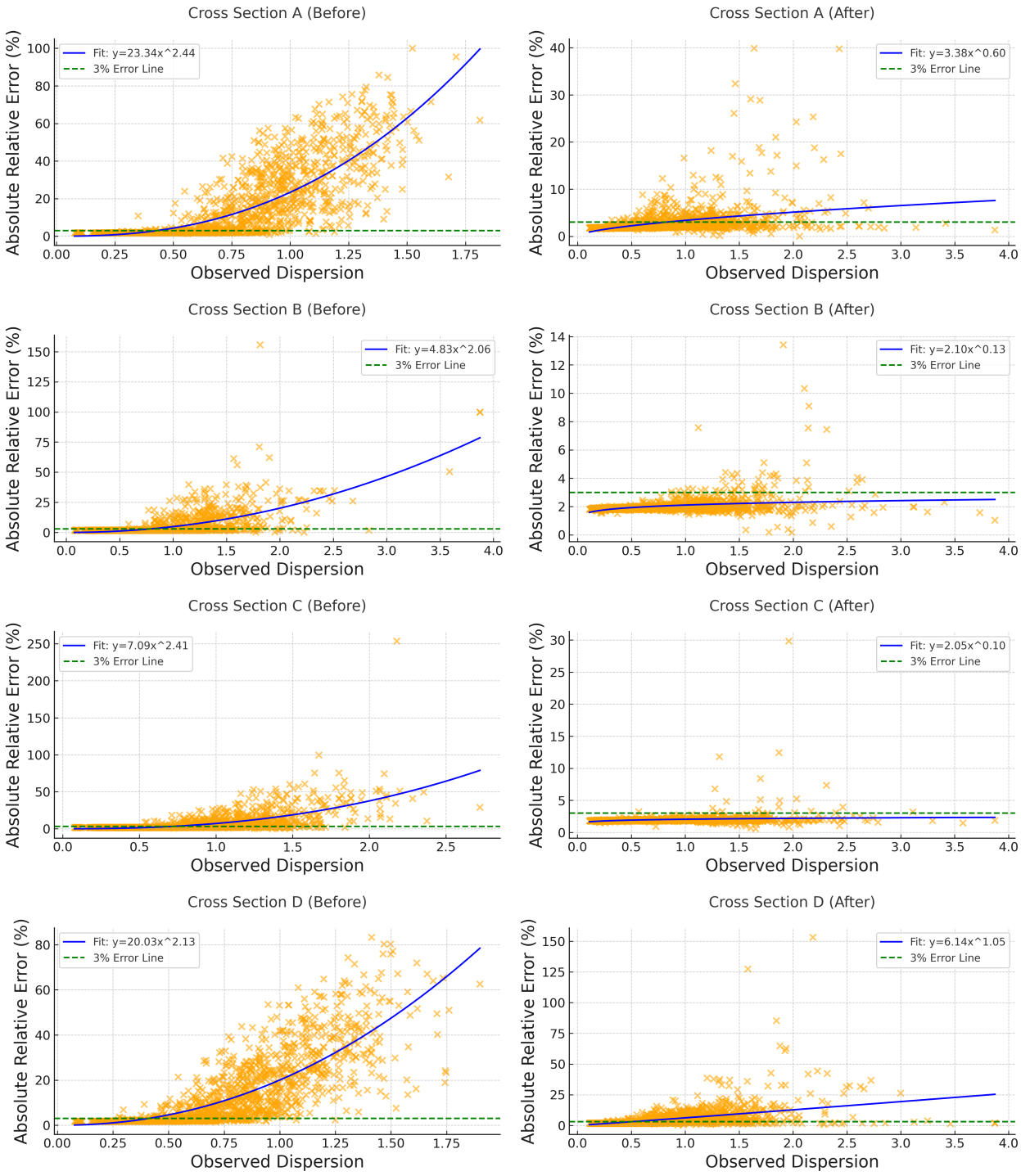


Figure 6.14: Comparison of observed dispersion values with relative absolute error, before and after filtering, across the four different cross-sections. The left column represents the unfiltered data, and the right column represents the filtered data. Power regression models highlight the relationship between dispersion and error, emphasising the impact of erroneous vectors.

frame. This variability undermines the reliability of general equations based on ideal density and dispersion values. Additionally, the impact of zero-velocity vectors in spatial studies is substantial and cannot be ignored. The location of these zero-velocity vectors within the ROI is critical, as they influence not only density and dispersion calculations but also average cross-sectional velocity results. Therefore, new SDI equations must be developed to more accurately represent spatial SDI analysis.

For spatial studies, the process of developing SDI equations should mirror that used in temporal studies. However, as evidenced by the density and dispersion results presented in this chapter, it is crucial to consider the location of the cross-section within the ROI. Each cross-section exhibits varying levels of reliability across different densities and dispersion, with Cross-Sections B and C demonstrating the most consistent reliability. Nonetheless, if SDI models were based solely on the most reliable cross-sections, it would be challenging to identify and account for less reliable sections. For example, as discussed in Section 6.4.4.3, dispersion values of $\nu = 1$ yield reliable results for Cross-Sections B and C but not for A and D. Therefore, the dispersion models used should be derived from the cross-section that produces the highest error estimation. Similarly, for density, the model should be based on the cross-section that presents the greatest challenge in achieving the ideal density, ensuring that areas below this density yield higher SDI values.

Moreover, it has been observed that filtering out erroneous zero-velocity vectors before calculations can lead to more accurate and reliable estimations. However, as discussed in Section 6.3.8, both datasets of filtered and non-filtered results will be used. This decision is intended to preserve a higher level of variability in SDI readings, as well as quantify the impact that these spurious vectors have on results, thereby hypothetically providing greater confidence in datasets that indicate good SDI results.

6.4.5.1 Formulating Spatial SDI Equations

Unfiltered SDI To formulate a new equation for Spatial SDI that addresses the issue of zero-velocity vectors, an over-dispersed value of $\nu = 0.5$ is employed to determine the ideal density for an objective error threshold of 3%, as suggested in Section 6.4.4.3. As shown in Figure 6.15, this results in a density of $\rho = 5.1 \times 10^{-4}$, with Cross-Section A representing the highest required density. This approach will lead to a conservative equation; however, given the potential influence of zero-velocity vectors, it is necessary to apply it.

Filtered SDI Some PTV systems, such as KLT-IV, allow the user to filter out known erroneous vectors. Therefore, a comparison Spatial SDI equation will also be formulated for cases where the user has actively removed all spurious vectors from the analysis. For this, the identified ideal densities and dispersion from the post-filter results will be utilised. Given that the filter has been applied, there is greater confidence in using the standard value of $\nu = 1$, as demonstrated by the analysis

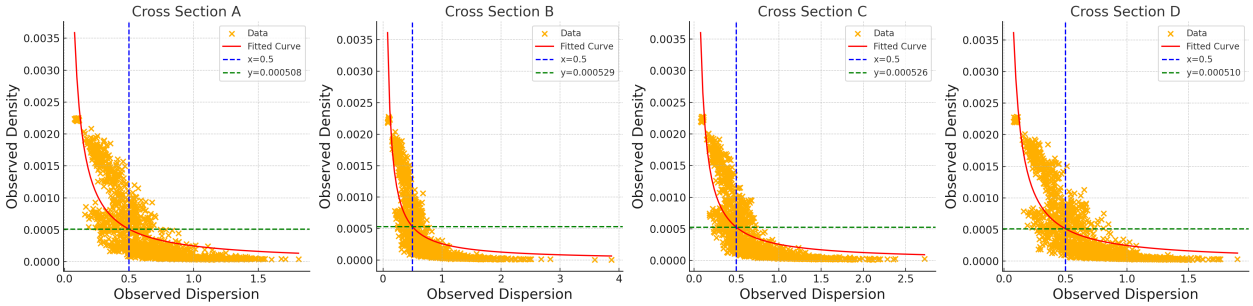


Figure 6.15: Scatter plots of observed dispersion against observed density for each cross-section. Vertical and horizontal lines represent $x = 0.5$ and the corresponding density, respectively.

in Figure 6.14. Figure 6.16 shows the post-filter analysis of density and dispersion relations, with $\nu = 1$ plotted, and an ideal density value of $\rho = 1.88 \times 10^{-4}$ from Cross-Section A, which can be applied in the formulation of the SDI.

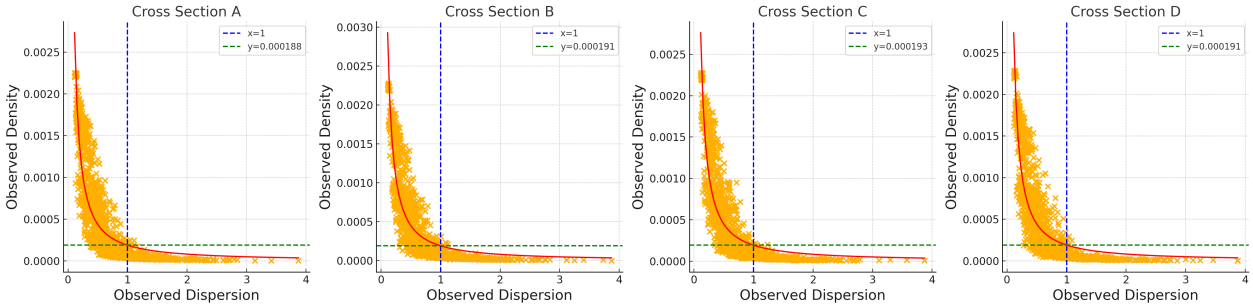


Figure 6.16: Scatter plots of observed dispersion against observed density for each filtered cross-section. Vertical and horizontal lines represent $x = 0.5$ and the corresponding density, respectively.

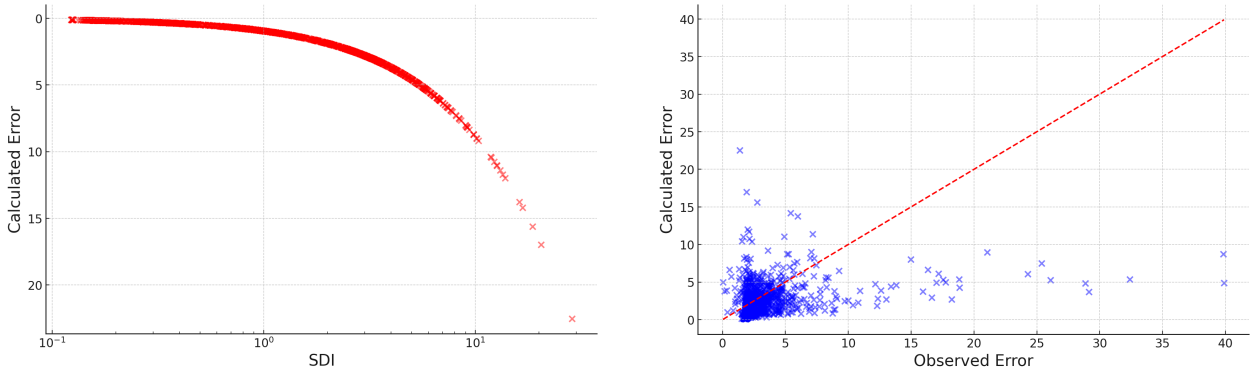
6.4.5.2 Spatial SDI Equation - Initial Study

To best represent the impact of SDI on error spatially, it is important to mitigate the influence of zero-velocity vectors on the average velocities, allowing for a more accurate representation of true density and dispersion. Therefore, in this initial study of Spatial SDI, filtered results are used to determine the coefficients c_1, c_2, k_1, and k_2. The ideal density used for model fitting is $\rho = 1.88 \times 10^{-4}$, corresponding to $\nu = 1$ from Cross-Section A, as consistent with Section 6.4.5.1. To study the impact of SDI on modelling, each cross-section will be analysed individually. As before (in Chapter 4), the first step is to define the general equations for SDI and error. This is done using Equations 6.10 and 6.11. Based on the relationship observed in Sections 6.4.3.2 and 6.4.4.3, it is expected that k_2 will be negative. The initial fitting parameters used for optimisation are the values from the Temporal SDI equation: $c_1 = 15.31$, $c_2 = 0.05789$, $k_1 = 0.9781$, and $k_2 = -0.7053$, with the optimisation focused on minimising the RMSE.

$$SpatialSDI = \nu^{k_1} \left(\frac{\rho}{\rho_{SpatialIdeal}} \right)^{k_2} \tag{6.10}$$

$$\epsilon = c_1 \left(1 - \exp^{-c_2 \times SpatialSDI}\right) \tag{6.11}$$

For the initial study, Cross-Section A is modelled first, given that it was used to determine the ideal density value of $\rho = 1.88 \times 10^{-4}$. This SDI and error relationship is then applied to the other cross-sections. Solving for c_1, c_2, k_1, and k_2, the SDI and relative calculated error (%) were modelled, with the results shown in Table 6.3 and plotted in Figure 6.17. Using these coefficients, results were found for the other cross-sections and plotted in Figure 6.18. The results show that for Cross-Sections A, B, and C, the coefficients produce reasonable fits, with RMSEs of 2.95, 2.4, and 1.95, respectively. However, for Cross-Section D, the coefficients do not model the error and SDI well, resulting in an RMSE of 7.58. Given this discrepancy, the coefficients for all cross-sections will be calculated individually and assessed for their sensitivity.



(a) Error as a function of SDI for Cross-Section A

(b) Observed vs Calculated Error for Cross-Section A

Figure 6.17: Model of error as a function of SDI and the subsequent calculated error against observed error.

Coefficient	k_1	k_2	c_1	c_2	**RMSE %**
Value	0.05	-0.8	70	0.0135	2.95

Table 6.3: Optimised coefficients and RMSE for Cross-Section A.

6.4.5.3 Spatial SDI - Average Equation

Given that the coefficients used to model Cross-Section A do not accurately represent all of the cross-sections, particularly Cross-Section D, a further study into the coefficients of fit and the subsequent SDI and error calculations is required. This study will average the coefficients across all the cross-sections to determine if an acceptable average RMSE (3 or less) can be maintained. The ideal density used for this study is the average filtered ideal density across all four cross-sections, given as $\rho = 1.91 \times 10^{-4}$.

Initially, coefficients were determined for each cross-section and averaged to attempt a general approach to the model fitting (as shown in Table 6.4). However, Cross-Section D still exhibited

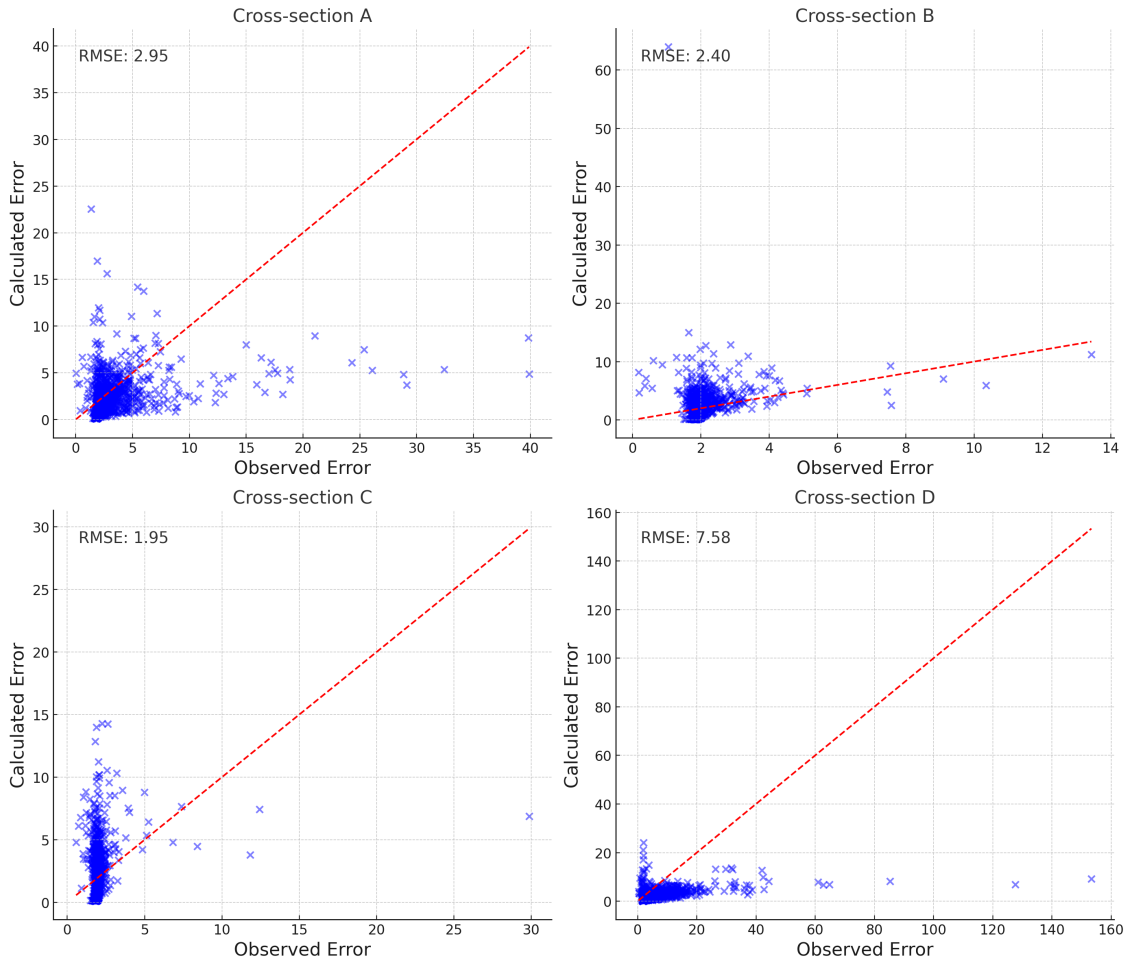


Figure 6.18: Modelled using Cross-Section A's coefficients across the other cross-sections.

the highest RMSE, as seen in Figure 6.19 and Table 6.5. While this does not support a general approach across the entire ROI, it does indicate that the top quarter of the image, where tracers exit the ROI, consistently represents the least accurate area for a cross-section. Returning to the approach of optimising each cross-section individually, as shown in Table 6.5, Cross-Sections B and C emerge as the most optimal, with Cross-Section C being the most consistent.

Coefficient	Value
$k1$	0.05
$k2$	-0.8
$c1$	59.8
$c2$	0.01595

Table 6.4: Averaged Coefficients

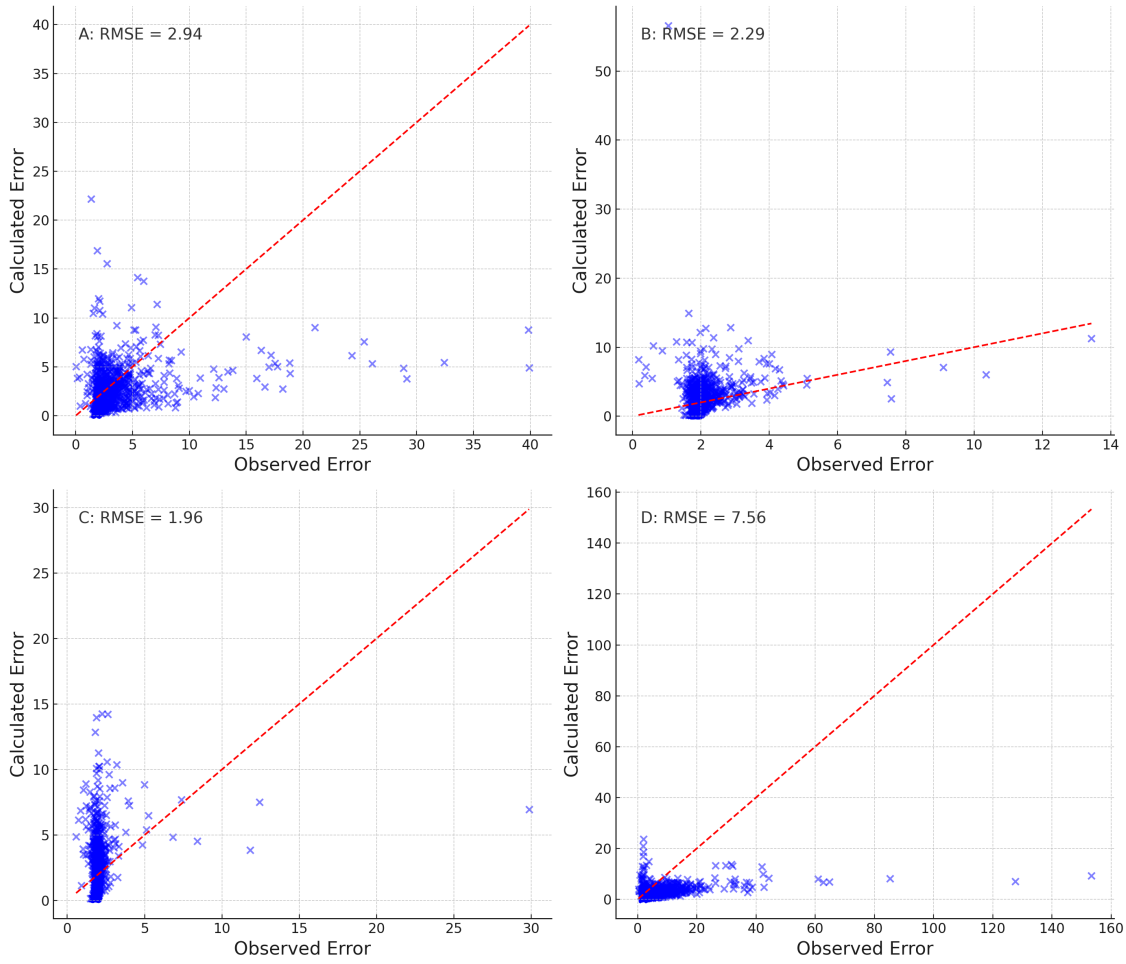


Figure 6.19: Calculated Error vs Observed Error from Coefficients in Table 6.4 with RMSE.

For Cross-Sections B and C, the fitting coefficients c_1, c_2, k_1, and k_2 are relatively the same, with only slight variations in c_2 and RMSE (Table 6.5). This suggests that for cross-sections in the central 50% of the ROI, a Spatial SDI formula, as given in Equations 6.12 and 6.13, can be used to

Cross-section	k_1	k_2	c_1	c_2	RMSE
A	0.05	-0.8	69.9999	0.0134	2.95
B	0.05	-0.8	50.00	0.0100	1.78
C	0.05	-0.8	50.00	0.0104	1.60
D	0.05	-0.8	69.2025	0.0300	6.90

Table 6.5: Coefficients for each cross-section and their corresponding RMSE values.

determine SDI and estimated error, as shown in Figure 6.20a, with the fit of calculated error against observed error depicted in Figure 6.20b.

As seen in Figure 6.20a, there appears to be a systematic error in the PTV measurements of velocity, with a consistent error of around 2–3% throughout the analysis. In Chapter 5, this was adjusted for using the composite model but is left unaccounted for in this study. To model this, a simple shift could be applied by implementing a constant; however, this falls outside the scope of this study, as the constant may vary with the dataset. The objective here is to find a general equation for spatial study. Given the RMSE results of the model, an error of 2% is considered acceptable for the remainder of the analysis.

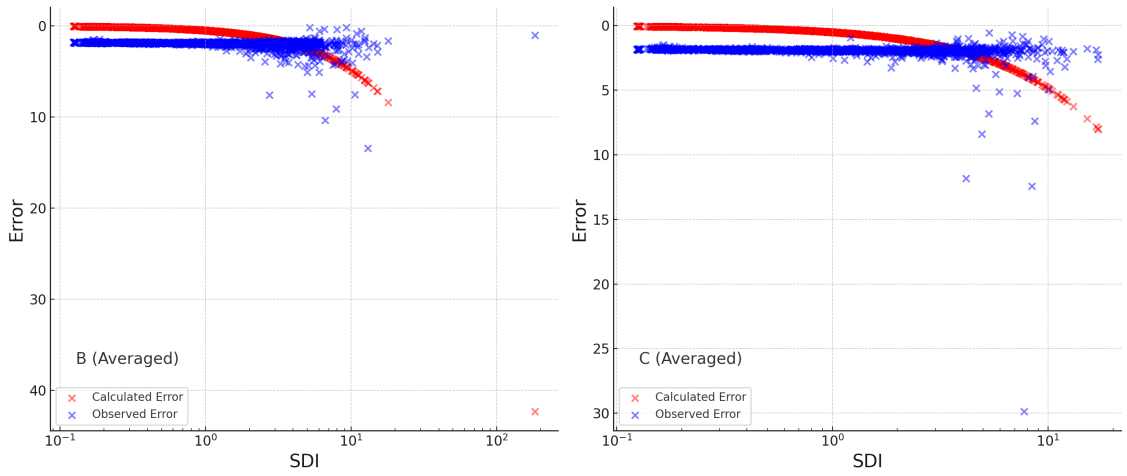
$$\epsilon = 50\left(1 - e^{-0.0102 \cdot \text{SDI}}\right) \tag{6.12}$$

$$\text{SDI} = \nu^{0.05}\left(\frac{\rho}{\rho_{cv1}}\right)^{-0.8} \tag{6.13}$$

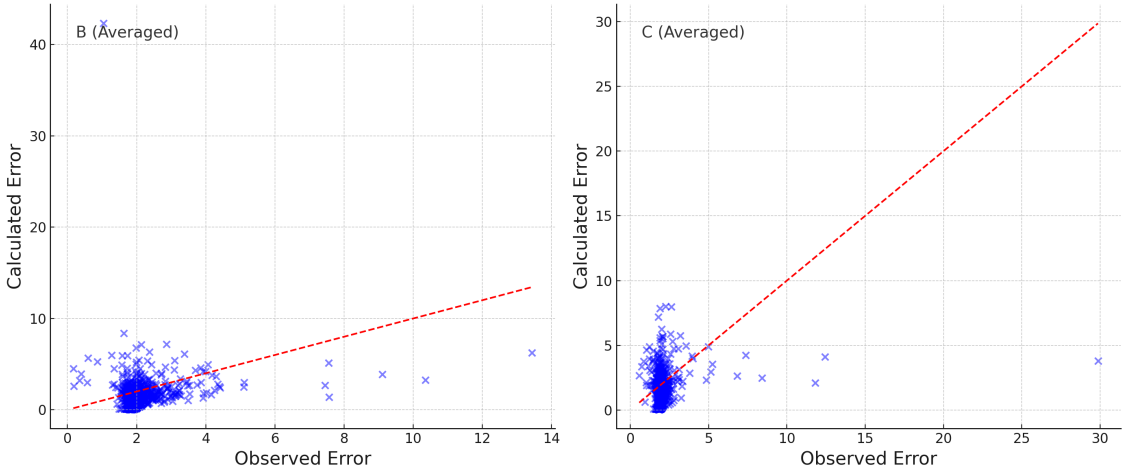
6.4.5.4 Comparison to Non-Filtered Data

This study examines how the general equation for Spatial SDI, with coefficients fitted for Cross-Sections B and C, performs when applied to non-filtered data containing zero-velocity vectors. These vectors, which may be present in the data before filtering, can significantly impact the accuracy of the model. To assess this, the equations presented in Equations 6.12 and 6.13 are applied to the non-filtered dataset, with $\rho_{cv1} = 5.1 \times 10^{-4}$.

The results, shown in Figure 6.21, demonstrate a lack of correlation between the general equation and the observed errors across all cross-sections. Cross-Section B shows the best correlation, with an RMSE of 7.8, yet it still fails to accurately represent the true velocities. The impact of zero-velocity vectors on the dataset is twofold. Firstly, these vectors significantly affect low-density cross-sectional velocities by decreasing the observed velocity, thereby increasing the error. Secondly, zero-velocity vectors are counted as data points, which affects SDI by increasing observed density and contributing to dispersion. These combined influences make it challenging to accurately determine error using SDI based on a cleaned version of the Spatial SDI equations.



(a) Calculated error (red) versus SDI for Cross-Sections B (left) and C (right). The observed error (blue) is also plotted for comparison, illustrating the relationship between SDI and error within these cross-sections.



(b) Comparison of calculated error versus observed error for Cross-Sections B and C. The red dashed line represents the ideal line of perfect agreement, where the calculated error would exactly match the observed error.

Figure 6.20: Analysis of the relationship between SDI and error in Cross-Sections B and C. Subfigure (A) shows the calculated error against SDI and observed error, while subfigure (B) compares the calculated error directly with the observed error, highlighting any discrepancies between predicted and actual values.

6.4.5.5 Spatial SDI for Unfiltered Data

This section examines the effectiveness of a general equation for Spatial SDI using unfiltered data. Given the poor model fit and high RMSE observed for Cross-Section D with filtered data, this section will exclude it from the analysis. Similarly, Cross-Section A has proven less effective than B and C. Therefore, to maximise the potential for a general equation to be effective with unfiltered data, only Cross-Sections B and C will be considered. By optimising for RMSE using data from Cross-Sections B and C, the coefficients of fit for the unfiltered data were determined, as shown in Equations 6.14 and 6.15. The results of these models are presented in Figure 6.22.

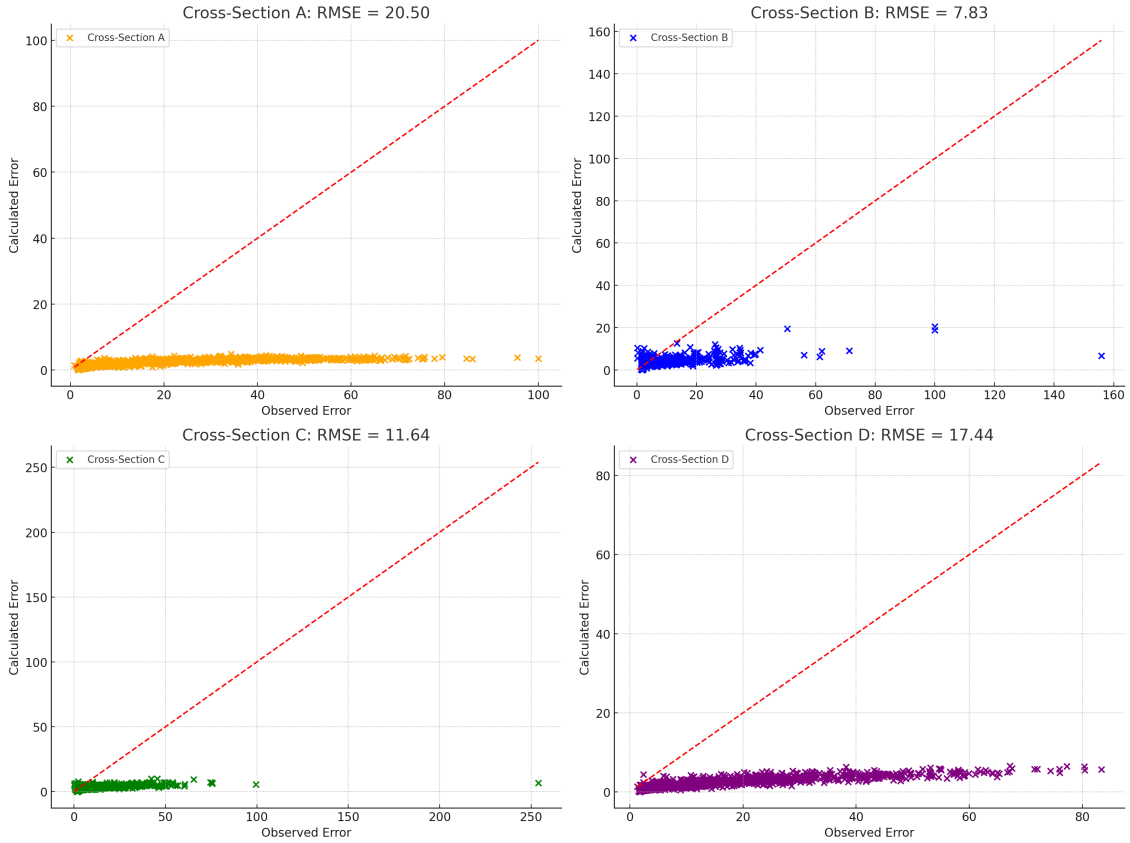


Figure 6.21: Calculated Error vs Observed Error for non-filtered datasets.

Given the impact of zero-velocity vectors on velocity errors, the RMSE results of 6.78 and 9.09 for Cross-Sections B and C, respectively, can be useful in modelling error bounds, as discussed in Chapter 5. Notably, the coefficient fits suggest that, with an increase in erroneous vectors, more weight is placed on dispersion in the SDI calculation. This could be due to the clustering of erroneous vectors in certain areas of the ROI, which are continuously measured throughout the video, as illustrated in Figure 6.3. The increase in the k_1 coefficient to a value above 1 is expected. In the filtered study and the temporal studies of SDI, dispersion was idealised at 1, implying that data was evenly dispersed across the ROI. However, in the unfiltered data, the situation is quite different. The presence of erroneous vectors leads to areas with high localised dispersion, which contributes disproportionately to the overall SDI. This increase in k_1 indicates that the dispersion now plays a more dominant role in influencing the SDI, reflecting the impact of these highly variable areas. As shown in Figure 6.14, using a dispersion value of 1 in unfiltered data can result in errors around 20%, highlighting the challenge of dealing with spurious vectors. In contrast, filtered data exhibits a clearer and more stable relationship between dispersion and error, as the effect of erroneous vectors is minimised.

$$\epsilon = 97.63\left(1 - e^{-0.0156 \cdot \mathrm{SDI}}\right) \tag{6.14}$$

$$\text{SDI} = \nu^{1.0346} \left(\frac{\rho}{5.1 \times 10^{-4}} \right)^{-0.6985} \tag{6.15}$$

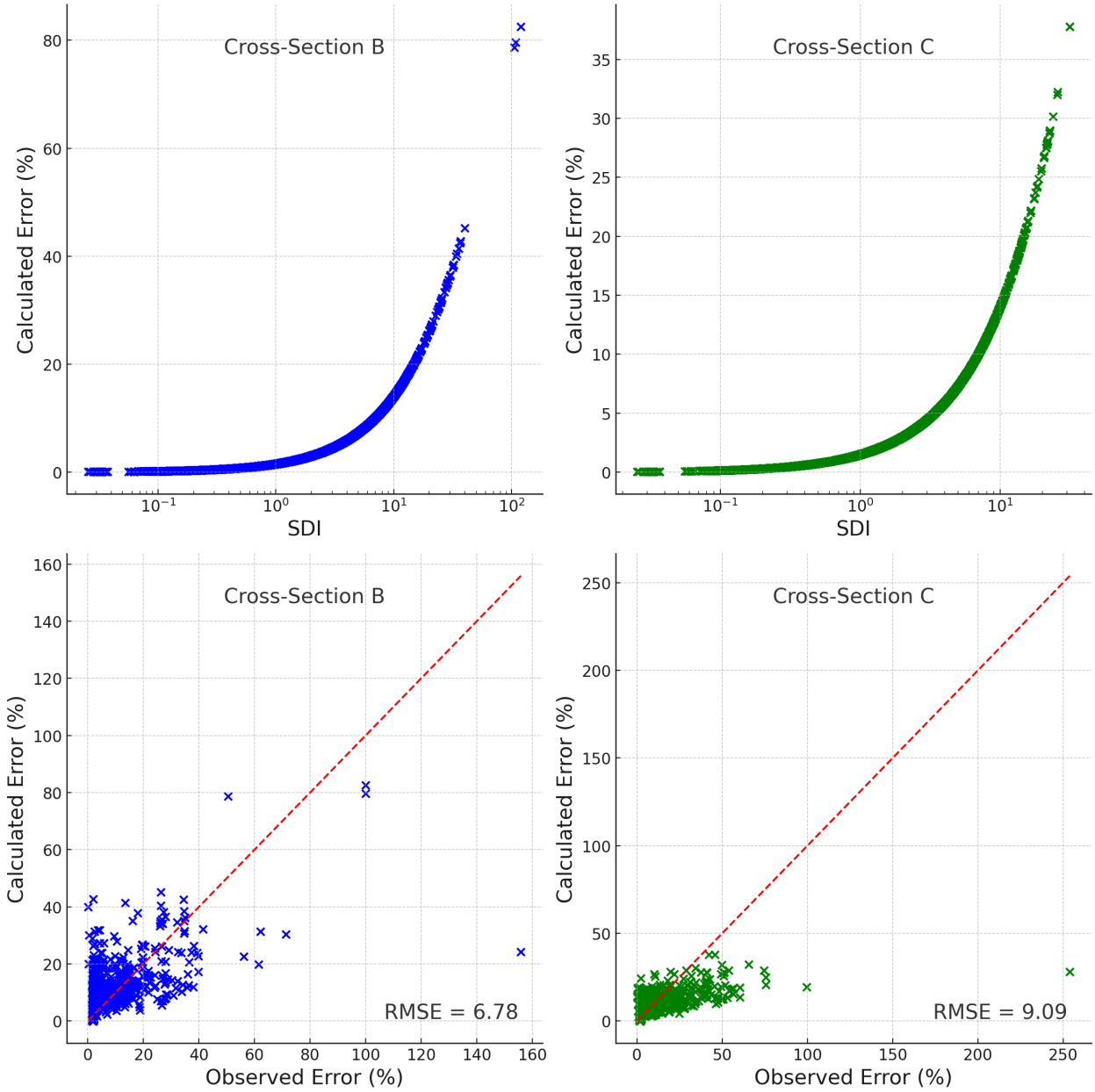


Figure 6.22: Comparison of SDI and Error Calculations for Cross-Sections B and C. The figure includes SDI vs. Calculated Error (top row) and Observed Error vs. Calculated Error (bottom row) for both cross-sections, with RMSE values labelled.

6.5 Discussion

6.5.1 PTV Analysis

The analysis of PTV results in this study highlights the challenges and potential strategies for improving flow measurement accuracy in river environments, particularly when varying seeding densities and dispersions are present.

6.5.1.1 Spatial Variability and Tracer Detection

The results show that the spatial location of tracers plays a critical role in the accuracy of velocity measurements. The successful analysis of point tracers from the synthetic videos indicates that spatial analysis, as opposed to frame-by-frame temporal analysis, can provide deeper insights into the distribution and behaviour of tracers across the ROI. The visual representation of vector locations (Figure 6.4) demonstrates how most tracers follow the expected flow velocity, but also highlights areas where erroneous data points occur, particularly around the intersections of cross-sections A and D. These erroneous data points, often identified as zero-velocity vectors, suggest that certain areas within the ROI may be prone to inaccuracies, likely due to insufficient tracer density or environmental factors affecting the PTV algorithm's ability to track particles accurately (in this instance, consistent background noise). The concentration of these errors near specific cross-sections points to the importance of careful cross-section placement, as incorrect positioning can exacerbate data inaccuracies.

6.5.1.2 Impact of Imposed Density and Dispersion

The imposed density and dispersion significantly influence the number and quality of usable tracers. As shown in Figures 6.5a and 6.5b, videos with higher imposed density and dispersion yield more data points along a cross-section, with fewer missing points and minimal need for interpolation. This finding aligns with previous research that emphasises the importance of maintaining an optimal seeding density for accurate PTV analysis (Pizarro et al., 2020b; Dal Sasso et al., 2021). In contrast, lower densities lead to sparse tracer distributions along cross-sections, making velocity interpolation unreliable. This is particularly evident in the analysis of Cross-Sections A and D, where the lack of sufficient tracers leads to significant deviations from expected velocity values. The filtered analysis, which removed zero-velocity vectors, underscores the improvement in data quality when erroneous vectors are excluded; in this case, filtering below an absolute minimum of 1 px/s was sufficient.

6.5.1.3 Cross-Sectional Velocity Analysis

The comparative analysis of cross-sectional velocities across different imposed densities reveals a consistent trend: Cross-Sections B and C generally provide more reliable velocity measurements than Cross-Sections A and D, particularly at lower densities. This suggests that middle cross-sections may be less susceptible to the edge effects and environmental noise that affect the outer sections. However, as imposed density increases, the difference in performance between the cross-sections becomes negligible, indicating that high seeding densities can compensate for less-than-ideal cross-section placement. The relationship between imposed density and the number of zero-velocity vectors further supports the need for adequate tracer seeding. As seen in Figure 6.7b, higher densities reduce the number of erroneous vectors, suggesting that a denser seeding environment helps the PTV algorithm differentiate between actual flow tracers and background noise.

6.5.2 Density

As illustrated in Figure 6.9, the observed density across all cross-sections generally remains below the imposed density, a trend consistent with previous temporal studies. Notably, at lower imposed densities, Cross-Sections A and D seem to exhibit closer alignment between observed and imposed densities, suggesting that these sections may be more sensitive to variations in seeding density. However, this apparent consistency across Cross-Sections A and D is contributed to by zero-velocity vectors. The presence of erroneous zero-velocity vectors, particularly at lower imposed densities, introduces substantial noise into the data. This is particularly evident in Cross-Sections A and D, where these erroneous vectors skew the observed density measurements. Filtering out velocities less than 1 px/s, as shown in Figure 6.10, reduces the observed density for these cross-sections, aligning their results more closely with those of Cross-Sections B and C. This suggests that proper filtering techniques are essential for mitigating the impact of erroneous data points and achieving more accurate density measurements.Although this blanket approach to removing zero-velocity vectors may introduce some bias—since it removes data without assessing whether a vector is truly erroneous—the presence of these vectors typically results in greater error than their exclusion. This is particularly true when using post-processed interpolation techniques, which rely on coherent flow structures and sufficient seeding coverage. Zero-velocity vectors, often caused by background noise or tracking artefacts, distort both the velocity field and the associated seeding metrics such as density and dispersion. Their presence can artificially inflate SDI values, leading to misleading error estimations. By removing these vectors, even at the cost of potentially discarding a small number of legitimate tracers, the analysis benefits from a more consistent and reliable representation of the underlying flow field. Consequently, this trade-off improves the robustness of spatial SDI calculations and error models. In exploring the relationship between observed density and relative error (Figure 6.11a), the results confirm the anticipated trend that relative error decreases as density increases. The exponential regression models applied to the data

reveal that Cross-Sections A and D require significantly higher densities to achieve the same level of accuracy as Cross-Sections B and C. This discrepancy underscores the importance of seeding density in achieving reliable PTV results, particularly in regions where cross-sectional data may be sparse. After filtering out zero-velocity vectors, the results show improved uniformity in error distribution across different cross-sections, as seen in Figure 6.11b. Cross-Sections B and C consistently maintain relative errors below 3%, while Cross-Section A, though improved, still exhibits a slightly broader range of errors. This indicates that while filtering improves overall accuracy, certain cross-sections may inherently require higher tracer densities to achieve optimal results.

The comparison between spatial and temporal studies further highlights the differences in required densities to achieve similar levels of accuracy. The ideal density needed to achieve a 3% error in spatial studies is notably lower than in temporal studies, where higher densities were necessary. This is likely due to the presence of spurious vectors in temporal analyses, which were less rigorously filtered. In contrast, the spatial analysis benefits from more effective filtering and interpolation techniques, leading to a more accurate representation of average velocities and a lower required density for similar error thresholds.

6.5.3 Dispersion

Initially, it was hypothesised that consistent imposed dispersion across all videos would correlate strongly with observed dispersion and relative error, leading to minimal variation in error for the same imposed densities. However, the results, as shown in Figure 6.12, indicate that imposed dispersion does not have a significant influence on relative error, even when zero-velocity vectors are filtered out. The lack of a clear pattern between imposed dispersion and relative error suggests that other factors, such as the interpolation and density of tracers within the ROI, may play a more critical role in determining the accuracy of PTV measurements. The absence of a trend between increased imposed dispersion and observed average dispersion, as illustrated in Figure 6.13, further supports this conclusion. Interestingly, the data show that zero-velocity vectors significantly impact the range of observed dispersion, with all imposed dispersion datasets exhibiting a broader range after filtering. This suggests that zero-velocity vectors are not clustered but rather sporadically distributed across the ROI, contributing to an artificial dispersion that distorts the results. The fact that removing these vectors reveals a more clustered set of tracers within the ROI indicates that the zero-velocity vectors were likely contributing to a misleading increase in observed dispersion.

The relationship between observed dispersion and relative error, depicted in Figure 6.14, highlights the strong correlation between increasing observed dispersion and absolute error. This relationship is consistent with the findings in earlier studies, where higher dispersion values generally correspond to higher error rates. The power regression models applied to the data show that, in Cross-Sections B and C, a dispersion value of 1 or less typically results in an error close to the 3% threshold. However, in Cross-Sections A and D, erroneous vectors inflate both observed dispersion

and corresponding error, underscoring the importance of accurate tracer tracking and filtering. The filtered results for Cross-Sections A and D reveal that while dispersion increases across the range after removing erroneous vectors, the corresponding error decreases significantly. This suggests that the observed dispersion value of 1 (indicating a perfect spread) can still serve as a reliable indicator for the 3% error threshold, provided that zero-velocity vectors are effectively filtered out. These observations raise important considerations for the application of SDI in estimating error within spatial studies. Specifically, in cases where cross-sections exhibit characteristics similar to Cross-Sections A or D—particularly when seeding density is low—relying on an ideal dispersion value of $\nu = 1$ may lead to an overestimation of the reliability of results. Therefore, it may be more prudent to adjust the SDI fit coefficients in spatial studies, placing greater emphasis on dispersion when estimating error. A suggested approach is to adopt a lower over-dispersion value of $\nu = 0.5$, which, although conservative, would ensure that errors are not underestimated, thereby allowing for a more accurate and reliable assessment of PTV data.

6.5.4 Spatial SDI Analysis

The relationship between density and dispersion in temporal studies, as encapsulated by the SDI equation, has proven inadequate when applied to spatial contexts. The spatial studies conducted reveal significant variability in density and dispersion across different cross-sections of the ROI, which undermines the generalisability of the SDI model originally developed for temporal analyses. This variability is further complicated by the substantial impact of zero-velocity vectors, which play a critical role in influencing both density and dispersion calculations, as well as average cross-sectional velocity measurements. Consequently, there is a clear need for the formulation of new SDI equations that more accurately reflect the complexities inherent in spatial studies.

6.5.4.1 Development of Spatial SDI Models

The process of developing SDI equations for spatial studies should align with the approach used in temporal studies, yet must incorporate adjustments that address the specific challenges of spatial analysis. As indicated by the results, the location of cross-sections within the ROI significantly affects data reliability, with Cross-Sections B and C consistently demonstrating the most reliable outcomes. Nevertheless, focusing SDI models solely on these reliable sections could obscure the challenges present in less reliable areas. For instance, Cross-Sections A and D exhibit significant discrepancies, particularly in dispersion values where a dispersion of $\nu = 1$ is reliable for Cross-Sections B and C but not for A and D. Therefore, dispersion models in spatial studies should be derived from the cross-section that exhibits the highest error estimation, while density models should consider cross-sections where achieving the ideal density is most challenging. This approach ensures that areas with lower density contribute to higher SDI values, providing a more robust measure of variability across the ROI. Moreover, while the results demonstrate that filtering

out erroneous zero-velocity vectors can improve the accuracy of SDI estimations, it is important to note that these models were developed without such filtering. This choice preserves a higher degree of variability in SDI readings, which enhances the confidence in datasets that exhibit low SDI values.

6.5.4.2 Refining Spatial SDI Equations

The development of spatial SDI equations must address the limitations identified in the application of temporal models. The coefficients used in temporal studies are not directly transferable to spatial studies due to the increased variability in density and dispersion across different cross-sections. The ideal density for spatial studies, for example, is lower than that required in temporal studies, reflecting the challenges posed by uneven tracer distribution and the presence of zero-velocity vectors.

In formulating these spatial SDI equations, the initial development should focus on the most reliable cross-sections, such as B and C. However, to ensure robustness across the entire ROI, it is essential to include data from less reliable cross-sections, such as A and D, to capture the full spectrum of potential errors. This comprehensive approach ensures that the resulting SDI models are not only accurate for the most reliable regions but also sensitive to the challenges presented by more problematic areas.

6.5.4.3 Strategic Cross-Section Placement

The location of cross-sections within the ROI plays a pivotal role in determining the accuracy of PTV measurements. Cross-Sections B and C, located centrally within the ROI, generally yield more reliable data, likely due to the uniformity of tracer density in these regions. In contrast, Cross-Sections A and D, situated near the edges of the ROI, are more prone to errors, likely due to lower density and a higher prevalence of zero-velocity vectors. For optimal results in river environment applications, cross-sections should be placed in areas where tracer density is maximised, and zero-velocity vectors are minimised. Additionally, further refinement of SDI models should incorporate a weighting factor for cross-section location, ensuring that sections with higher error potential are appropriately accounted for in the overall analysis. By acknowledging the spatial variability in tracer distribution and the critical role of cross-section location, the newly developed spatial SDI equations will provide a more accurate and reliable tool for assessing PTV data in complex river environments.

6.6 Conclusions

This study focused on enhancing the accuracy of discharge estimations using PTV by exploring the SDI and its application in spatially variable river environments. Through analysis of PTV data, key findings were obtained regarding the impact of spatial variability on velocity measurements and the development of tailored SDI equations.

The study addressed the following research questions:

1. **How does spatial analysis vary across a region of interest in determining the best placement of a cross-section for discharge estimation?** The research demonstrated that spatial analysis is crucial in identifying optimal cross-section locations for accurate discharge estimation. Cross-Sections B and C, located centrally within the ROI, consistently provided more reliable velocity measurements compared to edge cross-sections A and D. These findings highlight the importance of careful cross-sectional placement within the ROI, particularly in minimising the variability of error seen with differing levels of seeding density and dispersion.

2. **Do the optimal seeding density and dispersion values identified for minimising error in velocity estimations align with outcomes observed in spatially segmented synthetic river models?** The study confirmed that the optimal seeding density and dispersion values identified did not align with those observed in previous temporal studies. The spatial context introduced additional complexities, particularly for cross-sections located at the edges of the ROI. The ideal density and dispersion values derived for central cross-sections (B and C) were more consistent, whereas edge cross-sections (A and D) showed greater variability, necessitating adjustments to the SDI model to account for these spatial differences.

3. **Can spatially-focused SDI metrics enhance the reliability of velocity estimations under various simulated river flow conditions?** The research indicates that incorporating spatially-focused SDI metrics significantly enhances the reliability of velocity estimations. Tailored SDI equations for different cross-sectional locations within the ROI allow for more accurate error predictions and discharge calculations. However, the study also highlighted challenges posed by zero-velocity vectors, particularly in unfiltered data, suggesting that spatial SDI models must be carefully calibrated to account for these anomalies.

Additionally, the study emphasised the impact of zero-velocity vectors, which were found to significantly skew dispersion metrics and inflate velocity estimation errors, especially in scenarios with lower seeding densities. The research suggests that filtering out these erroneous vectors is critical to improving the accuracy of PTV-derived measurements.

The comparison between spatial and temporal SDI approaches revealed that while temporal models provide a baseline, spatial SDI models are better suited to account for the variability

within different sections of the ROI. This spatially-focused approach ensures more precise error predictions and better overall reliability of PTV measurements in river environments. Despite the strengths of the developed spatial SDI models, the study acknowledged limitations related to the reliance on synthetic datasets. While these datasets offer controlled conditions for detailed analysis, they do not fully capture the complexities of real-world river environments. Future research should aim to validate and refine these spatial SDI models using real-world data to account for environmental variability and improve their practical applicability.

With that said, two equations used to determine Spatial SDI, and subsequently Spatial Error, were created to help users of PTV understand the reliability of their data. Equation 6.16 and 6.17 can be used for cross-sections that have been filtered of their zero-velocity vectors and works best when cross-sections are present in the middle 50% of the ROI. Equation 6.18 and 6.18 can be used to determine error for unfiltered data, however, the RMSE of this model is not as accurate as the filtered model, and therefore should be used with caution. This model can be used to determine error bounds, as seen in Chapter 5.

Filtered SDI and Error Model

$$\epsilon = 50\left(1 - e^{-0.0102 \cdot \text{SDI}}\right) \tag{6.16}$$

$$\text{SDI} = \nu^{0.05}\left(\frac{\rho}{\rho_{c\nu 1}}\right)^{-0.8} \tag{6.17}$$

Unfiltered SDI and Error Model

$$\epsilon = 97.63\left(1 - e^{-0.0156 \cdot \text{SDI}}\right) \tag{6.18}$$

$$\text{SDI} = \nu^{1.0346}\left(\frac{\rho}{5.1 \times 10^{-4}}\right)^{-0.6985} \tag{6.19}$$

In summary, the spatial SDI models developed in this study provide a robust framework for optimising cross-sectional placement and enhancing the accuracy of PTV-based discharge estimations. Further research is needed to explore the application of these models in real-world scenarios, but the findings of this study lay a solid foundation for advancing PTV methodologies in river flow analysis.

Chapter 7. Synthesis: Post-processed SDI and its influence on PTV measurements

7.1 Chapter Overview

This chapter brings together the key findings from the research presented in this thesis, focusing on the development and application of SDI metrics within PTV processes for river discharge estimation. It provides an overall evaluation of the effectiveness and limitations of SDI-enhanced PTV techniques, including the impact of post-processing methods on measurement accuracy. The chapter also discusses the implications of applying SDI metrics under various environmental conditions, explores the spatial optimisation of cross-sectional data for more precise discharge calculations, and evaluates the pre- and post-processing techniques used in conjunction with SDI. The chapter concludes by addressing the limitations encountered during the research.

7.2 Aims of this research

The overarching aim of this thesis was to optimise the use of SDI metrics within PTV processes to enhance the accuracy of river discharge estimations. This research was driven by the need to further explore pre-processed SDI metrics, and validate the application of post-processed SDI metrics to enhance PTV techniques in diverse environmental conditions, ultimately assessing their potential advantages, limitations, and practical applications compared to traditional flow measurement methods.

Specifically, this thesis sought to:

- Investigate the impact of post-processed density and dispersion on the accuracy of PTV-derived surface flow velocities and discharge in both synthetic and real-world environments.
- Examine the role of post-processing techniques in improving the reliability of PTV results when enhanced by SDI metrics.
- Evaluate the effectiveness of SDI in optimising cross-sectional data for more accurate discharge calculations, particularly in spatially variable river conditions.
- Provide practical insights and recommendations for the implementation of PTV methods using SDI metrics in routine river monitoring, with a focus on improving the precision and efficiency of discharge estimations.

The following sections provide a summary of the key research findings (Chapters 4 to 6), demonstrating how each contributes to the overarching objectives of the thesis.

7.3 Post-processed SDI and its influence on PTV measurements (Chapter 4)

This chapter explores the development and application of SDI metrics to enhance the accuracy of PTV in estimating river discharge. The research focuses on the impact of seeding density and dispersion on the precision of PTV methods, specifically introducing a new post-processed SDI metric tailored to PTV. The findings reveal that seeding density plays a crucial role in minimising velocimetry error. Through synthetic simulations, an optimal seeding density of 6.85×10^{-3} PPP was identified. This value is significantly higher than the previously recommended 1.02×10^{-3} PPP for pre-processed SDI methods, as reported by Pizarro et al. (2020a). The results demonstrate a strong inverse relationship between seeding density and error, with additional tracers beyond the optimal density offering minimal improvements in accuracy.

The study also investigates the influence of seeding dispersion on velocimetry accuracy, uncovering a relationship between actual dispersion and error. As dispersion approaches an ideal value of $\nu = 1$, indicating minimal tracer clustering, the velocimetry error decreases significantly. This finding underscores the importance of achieving an even distribution of tracers to reduce measurement errors. However, the research highlights a lack of correlation between numerically imposed and actual dispersion, suggesting that factors such as zero-velocity vectors—errors introduced by stationary features or noise—may impact the dispersion calculations. These findings led to the development of a new dimensionless SDI metric, based on actual post-processed data rather than pre-processed estimates. This metric offers a more accurate tool for estimating velocimetry errors by considering the actual seeding density and dispersion observed during PTV analysis. The new SDI metric is formulated as $\mathrm{SDI}_{\text{post-processed}} = \nu^{0.9781} / \left(\frac{\rho}{\rho_{\text{ideal}}}\right)^{0.7053}$, where ν, ρ, and ρ_{ideal} represent the observed dispersion, density, and idealised density, respectively.

In addition to seeding density and dispersion, the study examines the impact of video duration on PTV accuracy. The research found that a video duration of 20 seconds was sufficient for capturing reliable PTV data in controlled synthetic environments. However, in real-world scenarios where external variables introduce more variability, longer video durations might be necessary to gather sufficient data points and mitigate noise-related errors. Another critical finding of this study is the effect of zero-velocity vectors on velocimetry results. These vectors, often caused by noise or the erroneous identification of stationary features as tracers, were found to significantly inflate velocimetry errors, particularly in cases of low seeding density. This highlights the importance of achieving an adequate seeding density and suggests that filtering out zero-velocity vectors could further enhance the accuracy of PTV measurements. While some zero-velocity vectors may reflect genuine stationary regions, their indistinguishability from spurious results in low-density conditions makes their removal the more reliable approach for minimising error and preserving data

integrity.

The implications of these findings are significant for both algorithm development and practical applications. The creation of a post-processed SDI metric tailored to PTV provides a robust method for improving the accuracy of river discharge measurements. By focusing on actual tracer data rather than estimates of the pre-processed imagery, this approach allows for users to either filter results dependent upon their SDI, or provide more reliable error predictions, enhancing the overall reliability of PTV methods. Practically, the study's results suggest that achieving optimal seeding density and ensuring even tracer dispersion are crucial for minimising velocimetry errors, guiding the design and implementation of future PTV studies, particularly in challenging or variable environments. Despite the strengths of this new SDI metric, the study acknowledges its limitations, particularly the reliance on synthetic datasets that do not fully capture the complexities of real-world conditions.

7.4 Impacts of Seeding Density and Seeding Dispersion on Discharge Results of PTV Methods - A Case Study (Chapter 5)

This chapter explores the critical role that seeding density and seeding dispersion play in the accuracy of discharge estimations using PTV methods, focusing on two river sites: the River Calder at Todmorden and the River Sheaf in Sheffield. By integrating SDI metrics into the PTV process, the chapter examines how variations in seeding conditions influence the reliability of flow measurements under different environmental conditions.

A key finding of the study is the effectiveness of SDI filtering in enhancing the precision of PTV-derived discharge measurements, especially in higher flow conditions where SDI values can vary significantly. It introduced a three-stage standard deviation filter that effectively removes outliers and enhances data quality. This approach is particularly useful in challenging environments where flow conditions and tracer distribution are unpredictable, leading to more reliable PTV measurements and, consequently, better hydrological models. For the River Calder, in relative low-flow conditions (depths less than 0.7 metres), the impact of SDI filtering on accuracy is minimal due to the already stable quality of SDI data. However, as depth increases beyond 0.7 metres, SDI filtering becomes increasingly beneficial, significantly reducing velocimetry errors. This underscores the importance of optimal seeding density and dispersion in ensuring accurate discharge estimations.

Additionally, the study identifies a critical depth of around 0.75 metres at the River Calder, where both error and SDI variance peak, suggesting that environmental factors like video quality and flow turbulence may introduce inaccuracies at specific depths. This finding highlights the need for careful consideration of environmental conditions when applying PTV methods, particularly in complex or variable flow regimes.

Moreover, the chapter introduces a novel method for estimating asymmetric error bounds using

SDI and depth as variables, providing a more refined tool for quantifying uncertainty in PTV-derived flow measurements. The method's validity is demonstrated through its application to data from the River Sheaf, confirming its generalisability across different river environments and marking a significant advancement in the field of hydrological measurement. The implications of these findings are substantial for both the development of PTV algorithms and their application in real-world hydrological studies. The research suggests that maintaining optimal seeding density and dispersion is crucial for minimising errors in discharge estimations. Furthermore, integrating SDI filtering into PTV processes can enhance the accuracy and reliability of non-invasive flow measurement techniques, particularly in higher flow conditions.

Finally, the successful application of the SDI-based error estimation process to the River Sheaf dataset validates the methodology and supports its broader applicability. The study shows that even with limited calibration data, the SDI-based approach can produce reliable stage-discharge curves, offering a practical solution for river monitoring where traditional measurement methods may be impractical.

7.5 Using SDI to Optimise the Cross-Sectional Positioning for PTV Analysis - Numerical Study (Chapter 6)

This chapter investigates the application of SDI to enhance the accuracy of discharge estimations using PTV by focusing on spatial analysis. Unlike previous chapters, which concentrated on the temporal aspects of PTV, this chapter shifts the emphasis to spatial variability, examining how seeding density and dispersion across different cross-sections of a river affect the precision of PTV measurements.

The study employs a synthetic dataset to simulate various river surface tracking scenarios, allowing for a controlled exploration of how spatial variations in seeding characteristics influence PTV accuracy. The methodology involves segmenting the ROI into multiple cross-sections and analysing the distribution of tracers within each section. This segmentation enables a detailed examination of the spatial dynamics within the river, providing insights into how different cross-sectional locations impact the reliability of velocity measurements and, consequently, discharge estimations.

Key findings from this spatial analysis highlight, once again, the critical role of both seeding density and dispersion in influencing PTV accuracy. The research demonstrates that cross-sections with higher seeding densities and more uniform dispersion patterns tend to produce more reliable velocity measurements. This is particularly evident when erroneous zero-velocity vectors, which can also distort seeding density and dispersion metrics, are filtered out. The presence of these zero-velocity vectors, often caused by background noise or stationary features mistakenly identified as tracers, can significantly skew the results, leading to inaccuracies in velocity estimations. By addressing these challenges, the study provides a clearer understanding of the spatial dynamics

involved in PTV and offers strategies for mitigating these issues to enhance measurement accuracy.

A significant contribution of this chapter is the introduction of a novel approach to formulating SDI equations tailored specifically for spatial analysis. Unlike the SDI metrics developed for temporal studies, these new equations account for the spatial variability of seeding characteristics across different cross-sections. The chapter explores the relationship between observed density, dispersion, and error across various cross-sectional segments, finding that higher densities and more even dispersion generally correlate with lower measurement errors. However, it also notes the impact that zero-velocity vectors have on error, suggesting that a one-size-fits-all approach may not be effective.

To address this, the chapter proposes customised SDI equations that consider whether data has been filtered or not. For instance, cross-sections at the edges of the ROI witness a higher degree of spurious vectors. The tailored approach allows for more adjustments to be made to give more reliable predictions of error, providing a more flexible framework for optimising PTV-based discharge estimations in spatially complex environments.

The implications of these findings are substantial for the development of more precise and reliable PTV methodologies. By incorporating spatial considerations into PTV analysis, this research advances the understanding of how local variations in seeding density and dispersion affect PTV accuracy. The study's results suggest that the application of spatially focused SDI metrics can significantly enhance the reliability of PTV measurements, particularly in rivers with complex flow dynamics or in regions where traditional flow measurement techniques may be less effective.

Moreover, the chapter addresses the practical challenges of implementing these findings in real-world applications. It emphasises the importance of filtering out zero-velocity vectors and other erroneous data points to improve the accuracy of SDI calculations and, by extension, velocity estimations. The research also highlights the need for further studies to validate the proposed SDI equations across different environmental conditions and river systems, ensuring their broad applicability and effectiveness.

In conclusion, Chapter 6 provides a comprehensive analysis of the spatial dynamics of PTV and introduces innovative methodologies for optimising discharge estimations using SDI metrics. The chapter's findings offer valuable insights for both researchers and practitioners in the field of hydroinformatics, contributing to the development of more accurate and reliable non-contact flow measurement techniques. By extending the application of SDI from temporal to spatial analysis, this research opens new avenues for improving the precision of PTV methods, ultimately enhancing the ability to monitor and manage river systems more effectively.

7.6 Evaluation of Post-Processed SDI on PTV Methods

This section provides an in-depth evaluation of the effectiveness of post-processed SDI applications on PTV results. The focus is on enhancing the reliability and accuracy of river discharge measure-

ments by exploring the comparative benefits and limitations of post-processed versus pre-processed SDI, as well as the role of spatial SDI in refining PTV-derived data. Insights from field applications and theoretical models are integrated to offer a comprehensive understanding of these techniques.

7.6.1 Advantages

7.6.1.1 Established Relationship between SDI and Velocity Error

Throughout each chapter (Chapters 4–6), SDI metrics consistently correlate with error. In many instances, this correlation is due to the presence of zero-velocity vectors, which not only skew velocity results but also inflate density and can influence dispersion. The results indicate that when density is low, the proportion of zero-velocity vectors to reliable tracers is high, leading to significant errors in the synthetic studies. The ideal density identified in these studies highlights the point at which density effectively averages out the errors caused by zero-velocity vectors, thus reducing their overall impact on the results. Additionally, the spatial synthetic study demonstrates how zero-velocity vectors can adversely affect cross-sectional analyses. While interpolation of results can be a useful tool where data is consistent along a cross-section, the introduction of zero-velocity vectors in regions with sub-optimal density or dispersion can further skew the results. If depths were assigned to these cross-sections, as would be done in real-world discharge studies, interpolating these unreliable cross-sections would yield highly inaccurate results, as observed in some instances in Chapter 5.

The difference between spatial and temporal studies of SDI is mostly insignificant. Although the ideal density for spatial studies is slightly lower than for temporal studies, and there are minor modifications to the coefficients of fit, SDI can still be modelled similarly across both types of analysis. This consistency across spatial and temporal studies indicates that SDI metrics are robust and reliable. These findings highlight two key insights. Firstly, users can automate temporal SDI analysis to filter out frames that may provide less reliable data through post-analysis of PTV results using temporal SDI equations. Secondly, using spatial SDI equations, users can identify segments that produce the best overall SDI values and use these segments for optimal placement of cross-sections when determining discharge. Together, these equations eliminate the ambiguity of where to best place cross-sections and, in some cases, can help PTV users optimise the location for their site.

7.6.1.2 Independence from Input Data Quality

All types of river analysis, whether using image velocimetry, ADCP, or other methods, rely on high-quality, reliable input data. However, data is sometimes processed under less-than-ideal conditions, as discussed in Chapter 5. Post-processed SDI analysis effectively highlights where these conditions are sub-optimal, as seen in Figure 5.5, where post-processed SDI spikes along with the associated error compared to model results. The post-processing using SDI consistently resulted in

more accurate flow measurements, with the SDI filtering showing significant improvements in error reduction, particularly when SDI values were above 9.5 (see Figure 5.9). Notably, post-processing, particularly at higher depths, resulted in an error reduction range of up to $0.5\,\mathrm{m}^3/\mathrm{s}$, representing a 10% improvement in flow accuracy in some cases. This indicates that post-processed SDI can significantly enhance the reliability of flow measurements, especially in challenging tracer density and dispersion conditions.

Stage-discharge ratings naturally smooth out these errors over time given more reliable data, but depend on this investment of more data for accuracy. If poor video quality, and consequently poor PTV analysis, occur during low flows, it is relatively easy to collect additional, reliable data points around the erroneous ones. However, correcting and extrapolating data for high flows under poor capture conditions can be challenging, making it difficult to achieve a good model fit without additional data for comparison. In pre-processed SDI analysis, quality data regarding SDI values must be available sequentially (frames strung together in a single video) for PTV processing, which may not always be feasible. SDI often fluctuates with peaks (high SDI) and troughs (low SDI), and filtering sequentially to maximise video length (thereby increasing the number of frames analysed) could leave the user with sub-optimal frames contributing to the results, or simply a lack of data to make reliable estimations. Post-processed SDI enables users to identify potential error hot-spots and either filter for frames captured with more reliable SDI metrics or collect additional data to correct modelled flows for increased accuracy. This advantage is particularly relevant in environments where obtaining high-quality imagery is difficult, such as in remote or inaccessible locations. The robustness of this approach was validated across two sites, the River Calder and River Sheaf, where post-processed SDI consistently improved alignment with observed data, demonstrating its generalisability.

7.6.1.3 Minimal Increased Complexity and Resource Requirements

The integration of post-processed SDI into existing PTV workflows does not significantly increase the complexity or resource requirements, which is a crucial advantage for many research settings. Post-processing can be incorporated into the existing PTV analytical pipeline without the need for substantial additional computational power or expertise. For instance, the KLT-IV software (used in this research) can be adapted to include post-processing routines with minimal modifications to the overall workflow. This is particularly important for new-to-PTV researchers with limited knowledge of methodologies, as it allows them to leverage the benefits of post-processed SDI without investing in new software and without the intense investment in time to manually filter data. This adaptability makes post-processed SDI a practical option for a wide range of research environments.

7.6.1.4 Enhanced Precision through Spatial Distribution Analysis

Spatial SDI represents a significant advancement in the precision of PTV methods for river discharge estimation. By focusing on the spatial distribution of tracers across different cross-sections of the river, spatial SDI allows for a more detailed and accurate analysis of flow patterns within the ROI. This method enables researchers to identify specific areas within the river cross-section where tracer density is inadequate or where dispersion patterns are sub-optimal, facilitating targeted adjustments to improve data accuracy by applying alternative cross-sections. In environments where flow conditions are highly variable or influenced by physical obstacles, spatial SDI can provide valuable insights into the distribution of flow velocities across different sections of the river.

7.6.1.5 Flexibility in Application of Cross-Sections

One of the key advantages of spatial SDI is the flexibility it offers in the application of cross-sections for river discharge estimation. While it is necessary to capture data from multiple cross-sections of the river, the decision on which cross-sections to apply for discharge analysis does not need to be made until after the post-processed SDI is analysed. This allows researchers to evaluate and select the most optimal cross-sections based on the results of the SDI analysis, thereby enhancing the accuracy of the discharge estimations. This approach provides users with the freedom to experiment with different cross-sections within the same dataset, choosing the ones that yield the best results according to the SDI metrics. Consequently, spatial SDI can significantly reduce the trial-and-error aspect of cross-sectional analysis, enabling more informed decisions that improve the precision of flow measurements. Additionally, this flexibility can lead to more efficient use of field data, as the same dataset can be leveraged in multiple ways, depending on the specific needs of the analysis. At the moment, this work has to be done manually, however, once applied to PTV software, the user could automate the process within the code, so that the software analyses the SDI for each segment and applies the cross-section with the best results for each video, making cross-section applicability more dynamic instead of assuming that one cross-section fits all.

7.6.1.6 Applications of Composite Models

In the study of SDI's impact on real-world case studies, it became apparent that modelling the effect of SDI on PTV discharge measurements is challenging due to the under-representation of flow at low stages. The consistency in PTV measurements, with minimal flow variation at low flows in both case studies, aligns with systematic errors, especially given the uniformity of SDI metrics at these flows. When compared to measured values, it is evident that SDI alone cannot correct these systematic errors, as expected. Therefore, to accurately assess SDI's impact at low flows, an error correction methodology was required before analysing SDI results. To achieve this, a composite model was developed using three calibration points randomly selected from observed data. The

use of random points was intended to prevent bias in the selection process, reflecting real-world scenarios where a new PTV site is established.

The composite model uses these three random points to adjust the PTV-modelled flow upwards at the lower end, addressing the under-representation of low flows that is systematically observed when using PTV. The assumption was made that PTV models flow accurately at higher stages, so the composite model was designed to gradually shift from 100% composite model influence at the lowest observed depth to 0% at the highest observed depth. Essentially, the composite model is a blend of the original PTV model with a shifted version, averaged over depth inputs. A significant advantage of this approach is evident in Figure 5.12, where the measured Q data shows high variance, particularly at higher depths. In some instances, discrepancies between observed and modelled flow can reach up to $3\,\mathrm{m}^3/\mathrm{s}$. However, at extreme depths (around 1 m), the composite model from PTV analysis aligns precisely with an observed measured point, providing greater confidence in the PTV-modelled results compared to the observed data.Since the composite model was designed to correct underestimation at low stages while preserving the accuracy of high-flow predictions, its convergence with the original PTV model at the highest observed depth reinforces its validity. This convergence indicates that the composite model retains the strengths of the original PTV formulation at high flows, while offering a more reliable representation of the full stage–discharge relationship by addressing systematic low-flow errors.

7.6.1.7 Impact of SDI on Error Variance with Discharge

PTV analysis is frequently used for establishing river discharge, which is influenced not only by the velocity of the river but also by its depth. While numerical studies and analyses of pre-processed SDI have focused on how SDI impacts velocity, the relationship between SDI, depth, and discharge has not been thoroughly established. Given the well-documented influence of SDI on velocity measurements, it was crucial to extend this understanding to discharge measurements. Since the relationship between depth and discharge is typically modelled using a power regression, it became possible to create error bounds related to SDI, as well as corrections using SDI.

After filtering data using SDI, a relative SDI value remains associated with each video, which can fluctuate between ideal (relatively low) and less-than-ideal (relatively high) values depending on the initial quality of the input data. By using these post-filtering SDI values, error bounds can be created alongside stage–discharge models to highlight areas where improvement is needed, or where data may be unreliable. For example, in Figure 5.10, error bounds increase around the composite model line at a depth of approximately 0.75 m, despite a cluster of available data, indicating that the SDI in this region was still less-than-ideal. This alerts the user to potential unreliability in the data and accounts for it by creating a larger error bound.

7.6.2 Limitations

7.6.2.1 Challenges in Low-Densities

In all three chapters of this thesis, as well as in studies on pre-processed SDI, seeding density has shown a strong correlation with error: the higher the seeding density, the smaller the error. However, the issue with post-processed SDI is that seeding density, as well as dispersion, can be inflated by spurious vectors, which, despite being clearly erroneous, are still counted towards both metrics. An increase in seeding density and dispersion due to inflation from zero-velocity vectors will subsequently decrease the SDI, giving a false sense of security regarding the error estimations. Without filtering for obvious errors (those closely around $0\,\mathrm{m/s}$), there is little that can be done to counter this limitation. In studies involving spatial SDI, clusters of zero-velocity vectors often occur where background noise has been detected by the PTV algorithm. These clusters can significantly influence SDI metrics, as the vectors are likely within the same user-defined grid, inflating both the seeding density and dispersion for that grid. In both temporal and spatial studies, this would negatively impact the SDI analysis results.

7.6.2.2 Challenges in Low-Flow Conditions

In low-flow conditions, the benefits of temporal-based post-processed SDI may be minimal given the relative error associated with the flow rates. Regardless of the movement of tracers in such conditions, when flow rates are low, there is a limit to how much SDI analytics can improve accuracy. In low flows, such as those observed in Chapter 5 for the River Calder and River Sheaf, SDI filtering typically results in improvements of around 0–$0.05\,\mathrm{m^3/s}$, which is negligible in most cases. This issue with low flows is further exacerbated by the systematic errors associated with PTV methods at low flows. To address this, the composite model was developed; however, without reliable calibration data, or if the calibration data is inaccurate, these modifications may not effectively distinguish poor results.

7.6.2.3 Complexities in Tracer Distribution and Data Interpretation

As discussed in Chapter 6, variability in tracer distribution posed a significant challenge, with unevenly distributed tracers leading to gaps in the data. These gaps often required extensive interpolation, which, in some cases, reduced the overall accuracy of the measurements. When applying spatial SDI metrics to real-world case studies, achieving a uniform distribution of tracers across different cross-sections can be challenging due to the inherent variability of natural systems. This variability can lead to inconsistencies in SDI calculations, potentially reducing the overall accuracy of PTV results. In heterogeneous environments, where flow conditions can change rapidly, maintaining consistent tracer distribution is particularly difficult, which may impact the reliability of measurements.

7.7 Summary

The primary objective of this research was to evaluate the effectiveness of post-processed SDI applications in enhancing the accuracy and reliability of PTV methods for river discharge measurements. By comparing post-processed and pre-processed SDI, as well as examining the role of spatial SDI in PTV estimations, this study sought to advance the precision of flow measurement techniques. Integrating both theoretical models and practical field applications, this research offers users of PTV an understanding of how these innovations can be applied to diverse and challenging riverine environments.

7.7.1 Established Relationship between SDI and Velocity Error

The research consistently demonstrated that SDI metrics are closely correlated with errors in velocity measurements for both temporal and spatial studies. The presence of zero-velocity vectors, which inflate both density and dispersion metrics, was found to be a significant source of error. Maintaining an optimal density was crucial in mitigating these errors, as evidenced by the synthetic studies. Furthermore, the impact of zero-velocity vectors on cross-sectional analyses was particularly pronounced in some circumstances of low seeding density, highlighting the need for careful consideration of SDI metrics in these contexts.

7.7.2 Independence from Input Data Quality

A key advantage of post-processed SDI is its ability to improve flow measurement accuracy even when input data quality is sub-optimal. In scenarios where SDI values exceeded 9.5 with high relative depths, the post-processing approach consistently reduced errors, with improvements of up to $0.5\,\mathrm{m}^3/\mathrm{s}$, which in some circumstances is greater than 10% of the witnessed flow. This was especially beneficial in challenging conditions with poor tracer density and dispersion, underscoring the robustness of post-processed SDI across various environments, including remote and inaccessible locations.

7.7.3 Spatial SDI Advantages

Spatial SDI significantly enhances the precision of PTV methods by focusing on the spatial distribution of tracers across different cross-sections. This approach allows for more informed selection of cross-sections after data processing, reducing the trial-and-error typically associated with discharge estimations. The ability to experiment with different cross-sections within the same dataset not only improves the accuracy of measurements but also optimises the use of field data, making spatial SDI an invaluable tool in complex flow environments.

7.7.4 Limitations

Despite the advantages of post-processed SDI, the research revealed several interrelated challenges. In low-density and low-flow conditions, post-processed SDI is particularly susceptible to inaccuracies. Low-density environments often result in spurious vectors, such as zero-velocity vectors, which can artificially inflate seeding density and dispersion metrics, leading to misleadingly low SDI values. This inflation can create a false sense of accuracy unless these erroneous vectors are effectively filtered out. Such issues are especially problematic in low-flow conditions, where the potential for improvement is minimal—typically yielding only slight accuracy gains. The systematic errors inherent in PTV methods during low-flow scenarios further compound these challenges, making it difficult to achieve reliable results without robust calibration data.

Furthermore, the variability in tracer distribution poses significant challenges, particularly in the application of spatial SDI. Achieving a uniform distribution of tracers across different cross-sections is complicated by the natural variability of riverine environments, which often leads to data gaps. These gaps necessitate extensive interpolation, sometimes reducing the overall accuracy of the measurements. This complexity is exacerbated in rapidly changing flow environments, where maintaining consistent tracer distribution is particularly difficult, further complicating the reliability of SDI calculations. As a result, these intertwined limitations highlight the need for more sophisticated data filtering, interpolation strategies, and careful consideration of environmental factors when applying SDI-enhanced PTV methods.

Chapter 8. Future Research

8.1 Introduction

This thesis has introduced innovative methods for analysing PTV techniques, with a primary focus on enhancing accuracy, reliability, and error estimation. The concept of using SDI for optimising PTV methodologies, as first proposed by Pizarro et al. (2020b), demonstrated that pre-filtering data to optimise SDI not only reduces the processing workload but also significantly improves the overall quality of results. Building upon this foundational concept, this research has investigated whether post-processed tracers, once subjected to PTV analysis, can be further utilised to refine results and provide deeper insights into the quality of the obtained data.

The research undertaken in this thesis has explored the temporal characteristics of SDI analysis within the context of PTV. The findings indicate a strong correlation between seeding density, dispersion, and error, all of which collectively contribute to the SDI. Moreover, the effectiveness of SDI in spatial analyses was demonstrated, allowing for the identification of ROI that are optimally suited for cross-sectional discharge assessments. The combined use of spatial and temporal SDI analysis offers a comprehensive evaluation of the data quality processed through PTV, thereby increasing confidence in the derived results. However, this thesis also recognises the limitations that have been encountered throughout these studies. Specifically, challenges in low-density environments, such as the influence of spurious zero-velocity vectors, and in low-flow conditions, where systematic errors are more pronounced, highlight the areas that require further refinement. Additionally, the complexities associated with achieving a uniform tracer distribution across cross-sections further emphasise the need for more sophisticated interpolation strategies to enhance the reliability of SDI calculations.

To address these challenges, several avenues for future research are proposed. These recommendations are aimed at further enhancing the precision, robustness, and applicability of PTV methodologies in hydrological studies. By integrating post-processed SDI with advanced computational models, broadening the scope of analysis to encompass a wider range of environmental scenarios, and refining data filtering techniques, future research can significantly elevate the quality and utility of PTV results. Additionally, addressing issues such as the management of zero-velocity vectors and incorporating a broader spectrum of environmental factors will be critical for developing more resilient and versatile models. These efforts will not only refine existing methodologies but also unlock new possibilities for predictive analysis and decision-making in complex and dy-

namic flow environments.

The subsequent sections outline specific recommendations for future research, with a focus on integrating advanced models, broadening the scope of analysis, enhancing data filtering techniques, addressing zero-velocity vectors, and incorporating environmental factors. These directions are intended to build upon the findings of this thesis and drive further advancements in the field of hydrology.

8.2 Discussions

8.2.1 Integration with Advanced Models

Post-processed SDI is ideally suited for integration with advanced computational models, including machine learning techniques and statistical analyses, which could significantly enhance the processing and precision of PTV software. Recent research has been conducted into the use of cloud processing and real-time continuous image velocimetry processing (Peña-Haro et al., 2021), which successfully employs SSIV techniques (an alternative image velocimetry technique to PTV) in real-world sites. A similar approach could be applied to PTV. With developments in machine learning and increased cloud processing power, the combination of image capture, PTV processing, and SDI filtering could be merged to develop a continuous data-stream of stage–discharge measurements for fixed sites.

One conceivable development could be the continuous capture and processing of data. PTV software, such as KLT-IV, has developed processes that allow for batch processing of large datasets with only initial parameters and settings being manually uploaded. With KLT-IV, stage data is the main limitation to automation, as it needs to be uploaded along with the input video data. To automate this process, data would have to be captured simultaneously with the video data, paired, and processed at the same time. This is not entirely unfeasible, as new research has demonstrated the use of calibrated cameras to determine river stage data (Vandaele et al., 2023). The study by Vandaele et al. (2023) presents a method for estimating river levels using convolutional neural networks (CNNs) to analyse images from river cameras. By segmenting water boundaries in the images and calibrating these with known reference points, the study managed to capture accurate river-level estimations, even under varying conditions. This research is invaluable for PTV methods, given that cameras are already in-situ to capture the video data required for PTV.

Figure 8.1 models a potential workflow that demonstrates how temporal and spatial SDI could be integrated into an automated PTV system. Cloud processing of image velocimetry (Peña-Haro et al., 2021), and automated river stage from cameras (Vandaele et al., 2023), have already been proven in concept. Therefore, to achieve automated continuous processing, three main processes require further research. The first is the incorporation of spatial and temporal SDI functions into PTV software. The second is machine learning and modelling of errors using spatial SDI metrics (seen in Figure 8.1 as the red dashed line in Part 2). Finally, further machine learning and modelling

could create composite models, such as the one discussed in Chapter 5.

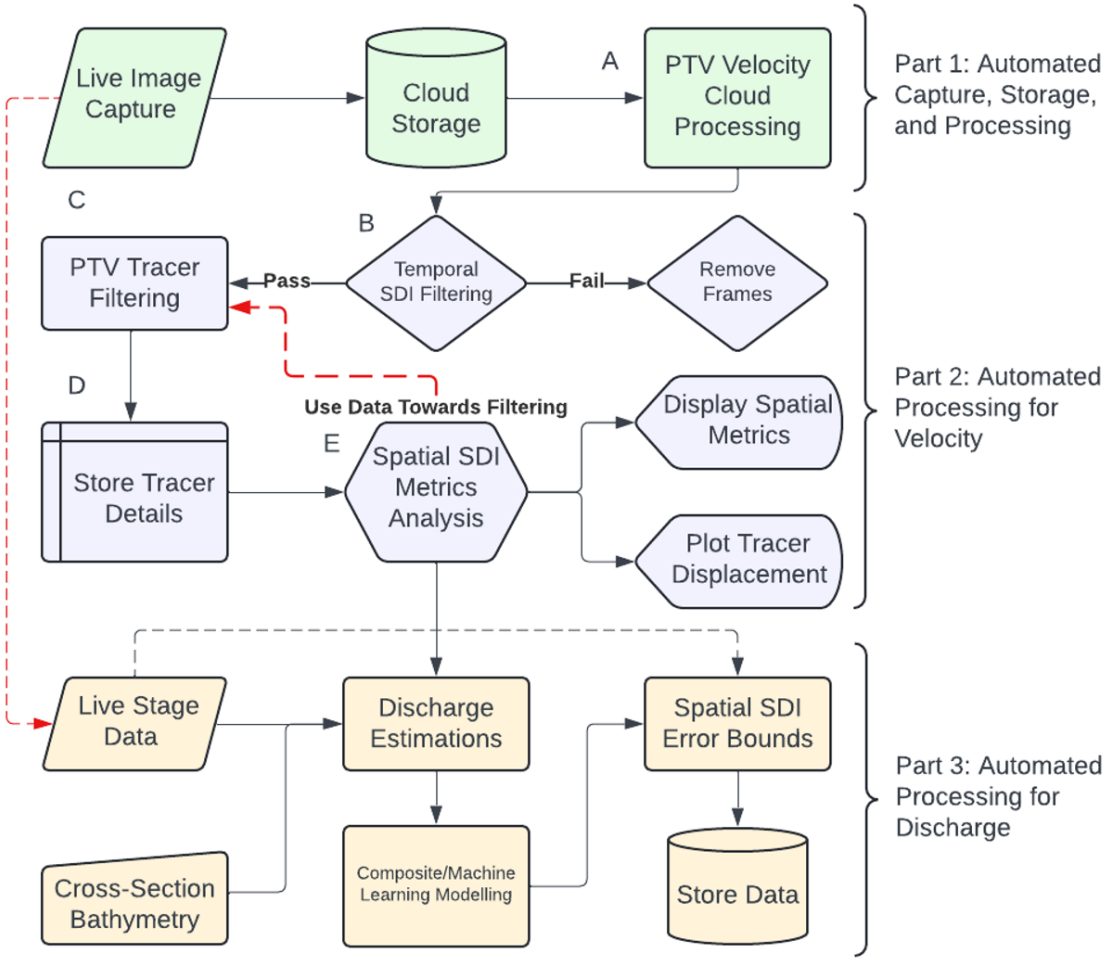


Figure 8.1: Modelled workflow to incorporate temporal and spatial SDI into an automated PTV system. Part 1 looks at the standard features of PTV, with the added process of cloud processing of data. Part 2 looks at the analysis of the detected tracers using standard PTV filtering, as well as the newly established post-processed SDI metrics. Part 3 converts the measured results into discharge. Labels A–E correspond to the process seen in Figure 8.2.

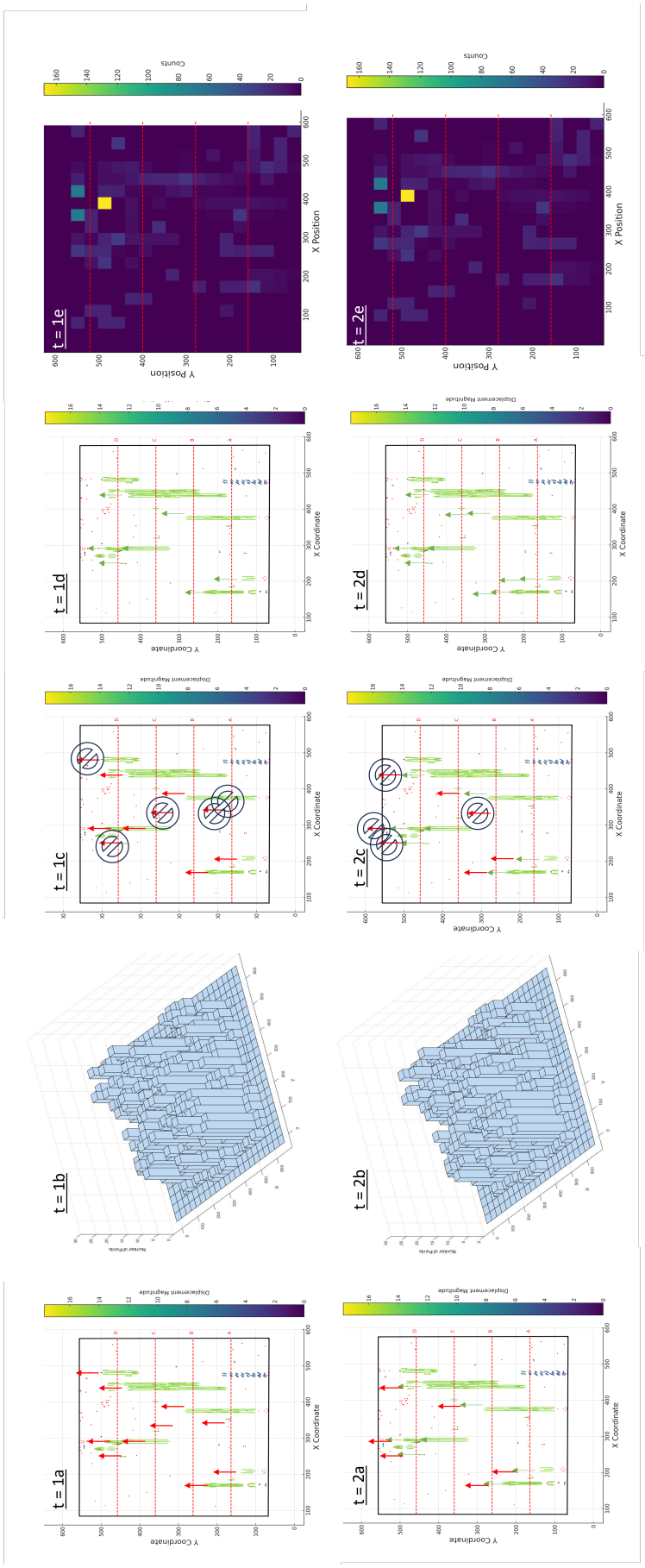


Figure 8.2: An example of the suggested general process of PTV processing through to discharge estimations.

The process of PTV velocity cloud processing through to discharge estimations, as seen in Figure 8.1, can be further modelled as illustrated in Figure 8.2. The concept behind this model is based on the input data required to build a stage–discharge model for a river. Where a full rating curve is required and a fixed PTV site is established, software could be automated to continuously monitor stage and add results to a model as stage varies, as suggested in Figure 8.3. Data is binned by stage so that SDI analytics can be grouped and only compared to stages of a similar level. This way, where data is continuously processed and stored, there can be an organised backlog of analytical data for temporal and spatial analysis for systems to benchmark to. This can also be beneficial as it is not often that a river stage will rapidly increase, meaning that as stage increases gradually, it can build a portfolio of SDI analytics for each grouped set of data. For the generalised model shown in Figure 8.3, data is grouped in bins of 0.1 m, but this could be any user-defined number based on the resolution of model desired.

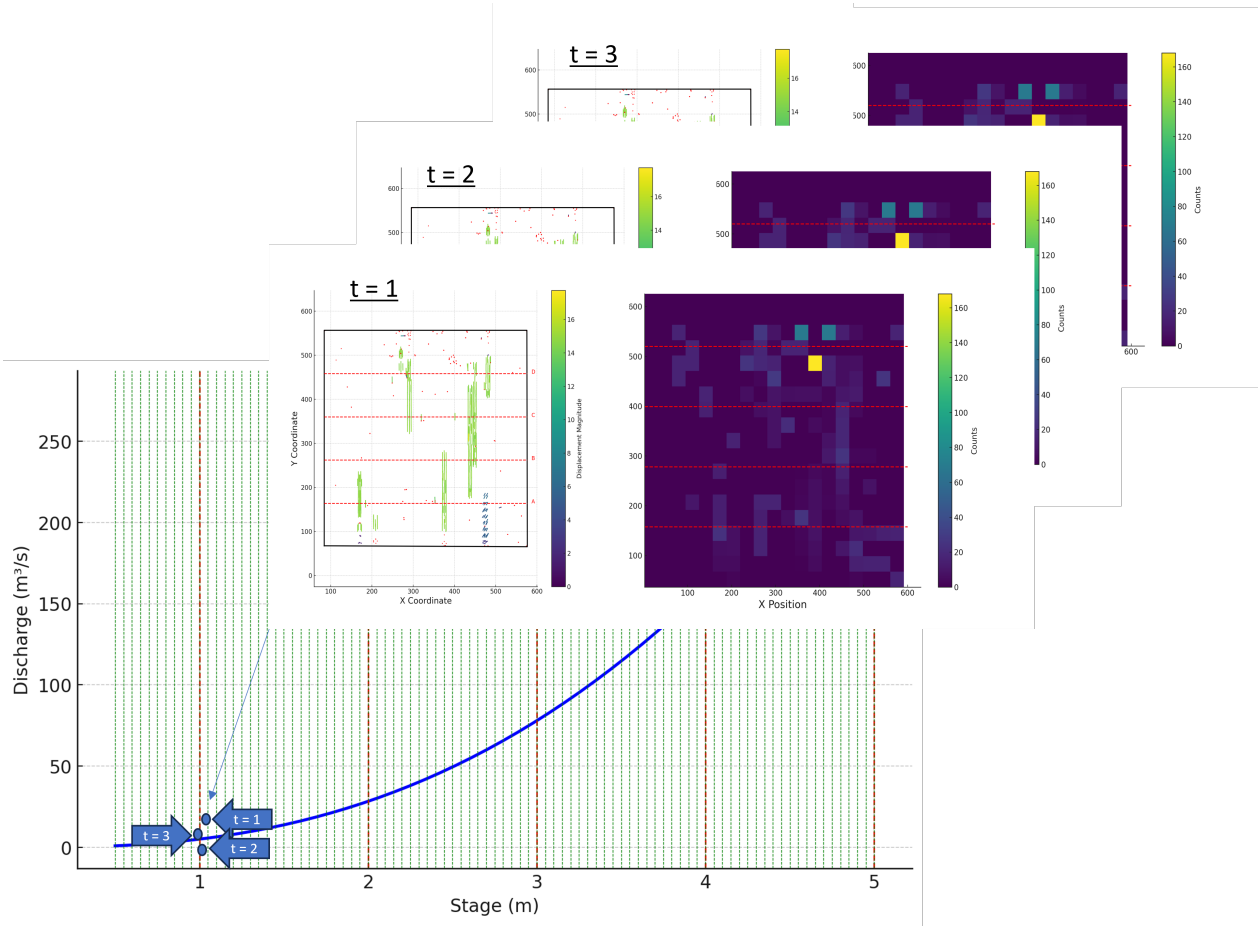


Figure 8.3: Modelled generalised stage–discharge relationship for continuous monitoring using automated PTV systems. Results are grouped via stage bins of 0.1 m (arbitrary to this generalisation), and shown as $t = n$.

In Figure 8.2, t represents the time period, which in KLT-IV methods is the interval rate set by the user. At $t = 1a$, the process of mapping the tracers is applied. At $t = 1b$, the temporal

SDI analysis is applied to the processed video, and can be used to filter frames and determine an estimated error given the depth and SDI. The $t = 1c$ stage is a PTV tracer filtering stage, and $t = 1d$ involves the data that has passed through the filtering, which is then stored for use in $t = 1e$. Stage $t = 1e$ is where spatial SDI is applied to the stored filtered data. Results from the spatial SDI analysis are then used to optimise discharge measurements and can also be incorporated into the PTV filtering models to help filter potentially erroneous vectors, improving the filters for PTV as more data is processed.

8.2.2 Enhancing PTV Accuracy and Reliability

Given the research presented in this thesis, it has been observed that to enhance the accuracy and reliability of PTV methods, future research should concentrate on two critical areas: advanced data filtering techniques and addressing zero-velocity vectors, and integrating environmental factors.

8.2.2.1 Automation of PTV Filtering

Given the crucial role of data filtering in determining the accuracy of PTV measurements, it is essential to develop and implement sophisticated filtering processes that can automatically and more effectively identify and mitigate erroneous vectors, and build it into PTV software. This is particularly important in operational environments where manual post-processing may not be feasible, and real-time analysis is desired. Additionally, addressing the limitations associated with zero-velocity vectors is essential for improving the precision of SDI calculations, as seen in Chapters 4–6.

Detecting erroneous vectors in PTV data is particularly challenging due to its unstructured nature, which contrasts with the gridded systems used in PIV methods. Many PTV algorithms are adaptations of PIV techniques, modified to address the challenge of identifying neighbouring vectors in a non-equally spaced system. However, if more than 15% of vectors are outliers, automated programs may struggle to identify them accurately, as these algorithms typically rely on neighbouring velocities to classify outliers. In cases with a high percentage of outliers, distinguishing between correct and incorrect vectors becomes increasingly difficult (Duncan et al., 2010). Duncan et al. (2010) developed the Universal Outlier Detection Scheme, specifically for PTV, which is based on the algorithm from Westerweel and Scarano (2005) originally designed for PIV correction. An alternative approach is the model-based technique (Young et al., 2004), which can validate up to 25% of outliers. This method involves a five-stage process:

1. Displacement normalisation, building constraints, and calculating a regularised displacement field.

2. Producing a displacement field where invalid estimates are replaced with statistically more likely vectors.

3. Using statistical methods to determine validation scores based on user-defined thresholds and a T-value from the relaxation stage.

4. Iterating landmarks toward their associated termination landmarks.

5. Estimating displacement at any position in the image field. This could be further enhanced if spatial SDI can be incorporated into the methodology.

Future research should explore automating methods that allow for the filtering of spurious and zero-velocity vectors from the analysis, without compromising the overall data quality. By developing the modelling techniques and filtering that removes these vectors, researchers can achieve more accurate and reliable assessments of flow conditions, ultimately enhancing the applicability of PTV in diverse environments.

8.2.2.2 Addressing Environmental Challenges

The initial concept of this thesis aimed to tackle the impact of environmental factors on PTV results. Through the research conducted on both PIV and PTV methods in Chapter 2, it became evident that environmental influences are a consistent issue in both research and practical applications. There have been some studies into the impacts of wind and rain on image velocimetry methods, such as Peña-haro et al. (2020), however, more is still needed. The challenge with straightforward studies of environmental impacts lies in their generalisation and limited applicability across diverse sites. Therefore, research into these impacts needed to focus on metrics beyond simple error results.

This is where SDI was hypothesised to play a crucial role in environmental studies, as it can highlight where data may be externally influenced. Consequently, temporal and spatial studies on SDI were conceived, focusing on post-processed data, which inherently targets tracers that have successfully passed through PTV methods. The studies conducted in this thesis aim to contribute towards measuring and quantifying environmental impacts on PTV results using both temporal and spatial SDI. Temporal SDI could be utilised to assess the overall environmental impact across the entire ROI, such as during heavy rain or fog that obscures the camera (as illustrated in Figure 5.7). On the other hand, spatial SDI could better address localised environmental issues, such as glare on the river surface or areas of a river that are sheltered from heavy rain and wind. The spatial SDI would signify high SDI where there are minimal data points given the glare and would therefore indicate to the system that it should associate a higher SDI with the side impacted, and subsequently, error. Using this in filtering would allow the system to only use areas of an image that are not externally influenced and therefore increase reliability.

By systematically incorporating SDI into future studies on environmental impacts, researchers can develop more comprehensive models that better reflect the complexities of natural river systems. This approach would lead to more accurate and reliable PTV applications, particularly in challenging and dynamic environments, thereby extending the utility of PTV for river discharge

measurements and other hydrodynamic studies that cannot rely on consistent environmental conditions.

8.3 Conclusion

The future research directions proposed in this thesis are intended to build upon the foundational integration of SDI into PTV analysis, with the goal of significantly enhancing the accuracy, reliability, and applicability of PTV methodologies within hydrological research. By focusing on the incorporation of advanced computational models, refining data filtering techniques, and systematically addressing environmental challenges, these studies aim to extend the capabilities and effectiveness of PTV. The integration of real-time processing and machine learning presents a promising opportunity to automate PTV systems, enabling continuous and adaptive analysis across a wide range of environmental conditions. Addressing the specific challenges posed by zero-velocity vectors and improving SDI calculations will be crucial steps toward increasing the precision and consistency of PTV measurements. Additionally, the systematic application of SDI to account for environmental impacts, such as wind, precipitation, and light variations (glare), will support the development of more robust and versatile models, ensuring reliable results across diverse scenarios.

By pursuing these research avenues, the proposed studies will not only refine existing methodologies but also expand the scope and utility of PTV, making it an increasingly valuable tool for hydrodynamic studies and environmental monitoring. These advancements are expected to contribute to a deeper understanding of complex flow environments and support more informed decision-making in the management of water resources.

Chapter 9. Concluding Remarks

9.1 Contributions to the Field

This thesis provides a comprehensive framework for the application of post-processed SDI metrics in optimising PTV processes for river discharge estimations. It highlights the critical influence of seeding density and dispersion on measurement accuracy and offers practical solutions for improving the reliability of PTV-based methods. The research contributes to the field by refining the methodologies for post-processed SDI optimisation, providing a robust tool for enhancing the precision of river flow measurements. Future research should focus on further refining post-processed SDI applications under extreme environmental conditions and exploring the integration of these metrics with advanced models to enhance the accuracy and applicability of river flow monitoring techniques. As the field of river discharge estimation continues to evolve, the insights gained from this thesis are poised to inform and inspire ongoing advancements, paving the way for more accurate and efficient monitoring of river systems using image velocimetry techniques in a practical, automated, and accessible manner.

9.2 Summary of Key Findings

In recent years, significant progress has been made in river discharge estimation through image velocimetry techniques such as PTV. However, optimising these techniques for diverse and dynamic field conditions remains a significant challenge. This research has addressed this challenge by focusing on the optimisation of post-processed SDI metrics, particularly in the context of seeding density and dispersion, to enhance the accuracy of PTV processes in river discharge estimations.

The key findings from each chapter are summarised as follows:

- **Chapter 2:** The literature review underscored the advancements and challenges in image velocimetry. While the field has seen substantial progress, practical implementation remains complex due to interdependencies among key factors such as orthorectification, seeding conditions, and post-processing methods. SDI emerged as a crucial metric for optimising tracer selection and improving measurement precision, yet challenges remain in making these techniques more accessible and reliable for widespread use.

- **Chapter 4:** Synthetic simulations were employed to explore the role of SDI in enhancing the accuracy of PTV measurements. The study identified optimal seeding density and dispersion

values, demonstrating that a post-processed SDI threshold of 6.85×10^{-3} PPP significantly reduces velocimetry errors. These findings provided a controlled environment to test the effectiveness of SDI optimisation, forming a solid foundation for subsequent real-world applications.

- **Chapter 5:** Building on insights from synthetic models, this chapter extended the analysis to real-world river conditions. It confirmed that variations in seeding density and dispersion significantly impact the accuracy of discharge results, with the post-processed SDI correlating well with real-world error measurements. The novel introduction of a composite model that integrates original and shifted SDI flow models enhanced the reliability of the stage–discharge relationship across different depths.

- **Chapter 6:** The analysis of post-processed SDI metrics was further refined by focusing on the spatial distribution of seeding across different river cross-sections. The research identified tools to allow users of PTV to optimise cross-sectional placements, guided by spatially focused SDI metrics, which improved flow measurement reliability. This chapter also addressed the challenges posed by zero-velocity vectors, particularly in scenarios with lower seeding densities.

However, this research also revealed several limitations, particularly in low-density seeding conditions where errors due to zero-velocity vectors were most pronounced. These vectors sometimes skewed the dispersion metric, inflating the perceived accuracy of measurements. Additionally, environmental factors such as wind and lighting conditions (e.g., glare and mist) further complicated the reliability of PTV measurements. These challenges underscore the need for careful calibration and validation against real-world datasets to ensure robustness across various conditions.

In the broader context of image velocimetry, this research aligns with and extends current advancements in PTV methodologies. The results, particularly regarding the post-processed SDI, represent a significant step forward by offering a more reliable error estimation framework compared to existing models. The improvements observed in both synthetic and real-world environments underscore the potential of this approach to enhance the precision and applicability of PTV techniques in hydrology.

Declaration of AI Assistance

Utilisation of AI Tools

During the development of this thesis, I have employed artificial intelligence (AI) technologies, including, but not limited to, OpenAI's ChatGPT. These AI tools have provided substantial support across a wide array of academic tasks. The applications of these tools have been as follows:

- Assisting in drafting and summarising key points on specific topics, which has significantly contributed to the coherent articulation of ideas within this work.
- Providing aid in the planning and structuring of written work, ensuring a logical and well-organised presentation of content.
- Facilitating exploration of various writing styles and approaches, enhancing the ability to communicate effectively across different sections of this thesis.
- Reviewing written materials to pinpoint and rectify stylistic, grammatical, and structural issues, thereby elevating the quality of academic writing.
- Offering assistance in debugging code relevant to the research, which has been crucial in the development and implementation of the computational components of this study.

The employment of AI tools was conducted with a commitment to uphold the principles of academic integrity and adhere to ethical standards of Newcastle University. Each use of AI was critically evaluated to ensure that the final output remained a product of my original thought, supplemented by AI-generated insights into structure and written content. This declaration affirms that while AI tools have been utilised for specific tasks, the intellectual rigor, analysis, and conclusions drawn in this thesis are fundamentally my own.

Bibliography

Ace, E. (2013), Internet protocol (ip) cameras: How do they work and what are the benefits, Technical report, IPVM.
URL: *https://ipvm.com/reports/frame-rate-surveillance-guide*

Akhmetbekov, Y. K., Markovich, D. M. and Tokarev, M. P. (1996), 'A novel correction algorithm for ptv', *HydroSenSoft, International Symposium and Exhibition on Hydro-Environment Sensors and Software* **8**, 3–4.
URL: *https://www.sciencedirect.com/science/article/pii/S0022169400000164*

Alimenti, F., Bonafoni, S., Gallo, E., Palazzi, V., Gatti, R. V., Mezzanotte, P., Roselli, L., Zito, D., Barbetta, S., Corradini, C., Termini, D. and Moramarco, T. (2020), 'Noncontact measurement of river surface velocity and discharge estimation with a low-cost doppler radar sensor', *IEEE Transactions on Geoscience and Remote Sensing* .

Alongi, F., Pumo, D., Nasello, C., Nizza, S., Ciraolo, G. and Noto, L. V. (2023), 'An automatic ann-based procedure for detecting optimal image sequences supporting ls-piv applications for river monitoring', *Journal of Hydrology* **626**, 130233.

Assem, H., Ghariba, S., Makrai, G., Johnston, P., Gill, L. and Pilla, F. (2017), Urban water flow and water level prediction based on deep learning, *in* 'Lecture Notes in Computer Science (including subseries Lecture Notes in Artificial Intelligence and Lecture Notes in Bioinformatics)'.

Baar, J. H. D., Percin, M., Dwight, R. P., Oudheusden, B. W. V. and Bijl, H. (2014), 'Kriging regression of piv data using a local error estimate', *Experiments in Fluids* .

Bandini, F., Lüthi, B., Peña-Haro, S., Borst, C., Liu, J., Karagkiolidou, S., Hu, X., Lemaire, G. G., Bjerg, P. L. and Bauer-Gottwein, P. (2021), 'A drone-borne method to jointly estimate discharge and manning's roughness of natural streams', *Water Resources Research* **57**.

Beven, K. and Freer, J. (2001), 'A dynamic topmodel', *Hydrological Processes* **15**.

Bolognesi, M., Farina, G., Alvisi, S., Franchini, M., Pellegrinelli, A. and Russo, P. (2017), 'Measurement of surface velocity in open channels using a lightweight remotely piloted aircraft system', *Geomatics, Natural Hazards and Risk* .

Bora, D. J. (2017), 'Importance of image enhancement techniques in color image segmentation: A comprehensive and comparative study', *Indian Journal of Science and Technology* **10**(1), 1–13.

Boursicaud, R. L., Pénard, L., Hauet, A., Thollet, F. and Coz, J. L. (2016), 'Gauging extreme floods on youtube: application of lspiv to home movies for the post-event determination of stream discharges', *Hydrological Processes* **30**(1), 90–105.
URL: *https://onlinelibrary.wiley.com/doi/10.1002/hyp.10532*

Bowes, M. J., Armstrong, L. K., Harman, S. A., Wickham, H. D., Nicholls, D. J., Scarlett, P. M., Roberts, C., Jarvie, H. P., Old, G. H., Gozzard, E., Bachiller-Jareno, N. and Read, D. S. (2018), 'Weekly water quality monitoring data for the river thames (uk) and its major tributaries (2009-2013): The thames initiative research platform', *Earth System Science Data* **10**(3), 1637–1653.

Brevis, W., Niño, Y. and Jirka, G. H. (2011), 'Integrating cross-correlation and relaxation algorithms for particle tracking velocimetry', *Experiments in Fluids* **51**(4), 977–989.

Britain's Rivers (2023*a*), 'River irwell', `https://www.britainsrivers.com/river-irwell`. Accessed: 17 May 2024.

Britain's Rivers (2023*b*), 'River sheaf', `https://www.britainsrivers.com/river-sheaf`. Accessed: 17 May 2024.

Caldwell, L., Armijo, D., Mukherjee, S., Minichiello, A., Truscott, T. and Kulyukin, V. (2019), Work in progress: Mobile instructional particle image velocimetry for stem outreach and undergraduate fluid mechanics education, *in* 'ASEE Annual Conference and Exposition, Conference Proceedings', pp. 1–11.

Cao, Q., Yu, G., Sun, S., Dou, Y., Li, H. and Qiao, Z. (2022), 'Monitoring water quality of the haihe river based on ground-based hyperspectral remote sensing', *Water (Switzerland)* **14**(1), 22.

Caputo, A. C. (2010), Digital video hardware, *in* 'Digital Video Surveillance and Security', Elsevier, pp. 39–88.

Carrel, M., Detert, M., Peña-Haro, S. and Lüthi, B. (2019), 'Evaluation of the dischargeapp: a smartphone application for discharge measurements', *HydroSenSoft, International Symposium and Exhibition on Hydro-Environment Sensors and Software* . Accessed: 17 May 2024.

Centre for Ecology and Hydrology (2022), 'Flood studies report - volume 3 - flood routing studies', `https://www.ceh.ac.uk/sites/default/files/2022-10/Flood%20Studies%20Report%20-%20Volume%203%20-%20Flood%20Routing%20Studies.pdf`. Accessed: 17 May 2024.

Cerqueira, R. F. L., Paladino, E. E., Ynumaru, B. K. and Maliska, C. R. (2018), 'Image processing techniques for the measurement of two-phase bubbly pipe flows using particle image and tracking velocimetry (piv/ptv)', *Chemical Engineering Science* .

Chen, Q., Zhang, Y. and Hallikainen, M. (2007), 'Water quality monitoring using remote sensing in support of the eu water framework directive (wfd): A case study in the gulf of finland', *Environmental Monitoring and Assessment* .

Chen, W. B. and Liu, W. C. (2017), 'Modeling the influence of river cross-section data on a river stage using a two-dimensional/ three-dimensional hydrodynamic model', *Water (Switzerland)* **9**(3).

Costa, J. E., Cheng, R. T., Haeni, F. P., Melcher, N., Spicer, K. R., Hayes, E., Plant, W., Hayes, K., Teague, C. and Barrick, D. (2006), 'Use of radars to monitor stream discharge by noncontact methods', *Water Resources Research* .

Coz, J. L., Hauet, A., Pierrefeu, G., Dramais, G. and Camenen, B. (2010), 'Performance of image-based velocimetry (lspiv) applied to flash-flood discharge measurements in mediterranean', *Journal of Hydrology* **394**(3-4), 245–254.

Coz, J. L., Jodeau, M., Hauet, A., Marchand, B. and Boursicaud, R. L. (2014), *Image-based velocity and discharge measurements in field and laboratory river engineering studies using the free Fudaa-LSPIV software*, CRC Press, pp. 1961–1967.
URL: *http://www.crcnetbase.com/doi/abs/10.1201/b17133-262*

Creutin, J. D., Muste, M., Bradley, A. A., Kim, S. C. and Kruger, A. (2003), 'River gauging using piv techniques: A proof of concept experiment on the iowa river', *Journal of Hydrology* **277**(1-2), 62–76.

Daigle, A., Bérubé, F., Bergeron, N. and Matte, P. (2013), 'A methodology based on particle image velocimetry for river ice velocity measurement', *Cold Regions Science and Technology* **89**, 36–47.

Dal Sasso, S. F., Pizarro, A. and Manfreda, S. (2020), 'Metrics for the quantification of seeding characteristics to enhance image velocimetry performance in rivers', *Remote Sensing* **12**(11), 1789.

Dal Sasso, S. F., Pizarro, A., Pearce, S., Maddock, I. and Manfreda, S. (2021), 'Increasing lspiv performances by exploiting the seeding distribution index at different spatial scales', *Journal of Hydrology* **601**, 126438.

Dal Sasso, S. F., Pizarro, A., Samela, C., Mita, L. and Manfreda, S. (2018), 'Exploring the optimal experimental setup for surface flow velocity measurements using ptv', *Environmental Monitoring and Assessment* **190**(2), 124.

Deen, N. G., Willems, P., Annaland, M. V. S., Kuipers, J. A. M., Lammertink, R. G. H., Kemperman, A. J. B., Wessling, M. and Meer, W. G. J. V. D. (2010), 'On image pre-processing for piv of single-and two-phase flows over reflecting objects', *Experiments in Fluids* .

Dellenback, P. A., Macharivilakathu, J. and Pierce, S. R. (2000), 'Contrast-enhancement techniques for particle-image velocimetry', *Applied Optics* **39**(32), 5978.
URL: *https://www.osapublishing.org/viewmedia.cfm?uri=ao-39-32-5978&seq=0&html=true*

Detert, M. (2020), 'How to avoid and correct biased riverine surface image velocimetry', *Water Resources Research* **n/a**(n/a), e2020WR027833. e2020WR027833.
URL: *https://agupubs.onlinelibrary.wiley.com/doi/abs/10.1029/2020WR027833*

Detert, M., Johnson, E. D. and Weitbrecht, V. (2017), 'Proof-of-concept for low-cost and non-contact synoptic airborne river flow measurements', *International Journal of Remote Sensing* **38**(22), 6391–6413.

Detert, M. and Weitbrecht, V. (2015), 'A low-cost airborne velocimetry system: Proof of concept', *Journal of Hydraulic Research* **53**(6), 767–776.

Dobson, D. W., Holland, T. and Calantoni, J. (2014), 'Fast, large-scale, particle image velocimetry-based estimations of river surface velocity', *Computers and Geosciences* .

Dramais, G., Coz, J. L., Camenen, B. and Hauet, A. (2011), 'Advantages of a mobile lspiv method for measuring flood discharges and improving stage-discharge curves', *Journal of Hydro-Environment Research* **5**(4), 301–312.
URL: *https://www.sciencedirect.com/science/article/abs/pii/S1570644311000049*

Duncan, J., Dabiri, D., Hove, J. and Gharib, M. (2010), 'Universal outlier detection for particle image velocimetry (piv) and particle tracking velocimetry (ptv) data', *Measurement Science and Technology* .

Durst, F., Miloievic, D. and Schönung, B. (1984), 'Eulerian and lagrangian predictions of particulate two-phase flows: a numerical study', *Applied Mathematical Modelling* **8**(6), 365–375.

Eltner, A., Sardemann, H. and Grundmann, J. (2020), 'Technical note: Flow velocity and discharge measurement in rivers using terrestrial and unmanned-aerial-vehicle imagery', *Hydrology and Earth System Sciences* .

Environment Agency (2023*a*), 'Calder catchment'. Accessed: 2024-05-17.
URL: *https://environment.data.gov.uk/catchment-planning/ManagementCatchment/4026*

Environment Agency (2023*b*), 'Don catchment'. Accessed: 2024-05-17.
URL: *https://environment.data.gov.uk/catchment-planning/ManagementCatchment/3042*

Euler, L. (1756), 'Principles of the motion of fluids', *Physica D: Nonlinear Phenomena* .

Flener, C., Vaaja, M., Jaakkola, A., Krooks, A., Kaartinen, H., Kukko, A., Kasvi, E., Hyyppä, H., Hyyppä, J. and Alho, P. (2013), 'Seamless mapping of river channels at high resolution using mobile lidar and uav photography', *Remote Sensing* .

Floodlist (2023), 'History of flooding in calderdale'. Accessed: 2024-05-17.
URL: *https://floodlist.com/analysis/calderdale-flood-history*

Fujita, I. and Aya, S. (2004), Refinement of lspiv technique for monitoring river surface flows, *in* 'Joint Conference on Water Resource Engineering and Water Resources Planning and Management 2000: Building Partnerships'.

Fujita, I., Muste, M. and Kruger, A. (1998), 'Large-scale particle image velocimetry for flow analysis in hydraulic engineering applications', *Journal of Hydraulic Research* .

Fujita, I., Notoya, Y., Tani, K. and Tateguchi, S. (2019), 'Efficient and accurate estimation of water surface velocity in stiv', *Environmental Fluid Mechanics* .

Fujita, I., Watanabe, H. and Tsubaki, R. (2007), 'Development of a non-intrusive and efficient flow monitoring technique: The space-time image velocimetry (stiv)', *International Journal of River Basin Management* **5**(2), 105–114.

Fulton, J. W., Mason, C. A., Eggleston, J. R., Nicotra, M. J., Chiu, C. L., Henneberg, M. F., Best, H. R., Cederberg, J. R., Holnbeck, S. R., Lotspeich, R. R., Laveau, C. D., Moramarco, T., Jones, M. E., Gourley, J. J. and Wasielewski, D. (2020), 'Near-field remote sensing of surface velocity and river discharge using radars and the probability concept at 10 u.s. geological survey streamgages', *Remote Sensing* **12**(8), 1296.
URL: *https://www.mdpi.com/2072-4292/12/8/1296/htm*

Gollin, D., Brevis, W., Bowman, E. T. and Shepley, P. (2017), 'Performance of piv and ptv for granular flow measurements', *Granular Matter* **19**(1), 18.

Guillén, N. F., Patalano, A., García, C. M. and Bertoni, J. C. (2017), 'Use of lspiv in assessing urban flash flood vulnerability', *Natural Hazards* **86**(2), 541–563.

Gunawan, B., Sun, X., Sterling, M., Shiono, K., Tsubaki, R., Rameshwaran, P., Knight, D. W., Chandler, J. H., Tang, X. and Fujita, I. (2012), 'The application of ls-piv to a small irregular river for inbank and overbank flows', *Flow Measurement and Instrumentation* **24**.

Hain, R., Buchmann, N. A. and Cierpka, C. (2016), 'On the possibility of using mobile phone cameras for quantitative flow visualization', *18th International Symposium on Applications of Laser Techniques to Fluid Mechanics* .

Harpold, A. A., Mostaghimi, S., Vlachos, P. P., Brannan, K. and Dillaha, T. (2006), 'Stream discharge measurement using a large-scale particle image velocimetry (lspiv) prototype', *Transactions of the ASABE* **49**(6), 1925–1935.

Hart, D. P. (2000), 'Piv error correction', *Laser Techniques Applied to Fluid Mechanics* pp. 19–35. **URL:** *https://link.springer.com/chapter/10.1007/978-3-642-56963-0_2*

Hauet, A., Kruger, A., Krajewski, W. F., Bradley, A., Muste, M., Creutin, J. D. and Wilson, M. (2008), 'Experimental system for real-time discharge estimation using an image-based method', *Journal of Hydrologic Engineering* **13**(2), 105–113.

Higham, J. E. and Brevis, W. (2019), 'When, what and how image transformation techniques should be used to reduce error in particle image velocimetry data?', *Flow Measurement and Instrumentation* .

Honkanen, M. and Nobach, H. (2005), 'Background extraction from double-frame piv images', *Experiments in Fluids* .

Huang, C., Chen, Y., Zhang, S. and Wu, J. (2018), 'Detecting, extracting, and monitoring surface water from space using optical sensors: A review', *Reviews of Geophysics* **56**(2), 333–360.

Inc., T. M. (2020), *Image Processing Toolbox™ Reference R 2020a*, The MathWorks Inc.

Ioli, F., Pinto, L., Passoni, D., Nova, V. and Detert, M. (2020), 'Evaluation of airborne image velocimetry approaches using low-cost uavs in riverine environments', *ISPRS - International Archives of the Photogrammetry, Remote Sensing and Spatial Information Sciences* **XLIII-B2**, 597–604.

Javernick, L., Brasington, J. and Caruso, B. (2014), 'Modeling the topography of shallow braided rivers using structure-from-motion photogrammetry', *Geomorphology* .

Jin, T. and Liao, Q. (2019), 'Application of large scale piv in river surface turbulence measurements and water depth estimation', *Flow Measurement and Instrumentation* **64**, 16–23.

Jodeau, M., Hauet, A., Paquier, A., Coz, J. L. and Dramais, G. (2008), 'Application and evaluation of ls-piv technique for the monitoring of river surface velocities in high flow conditions', *Flow Measurement and Instrumentation* .

Jolley, M. (2022), 'Handbook: Image velocimetry', https://github.com/MJolley1/LS-IV-Handbook/blob/main/Handbook___Image_Velocimetry%20(3).pdf. Accessed: 31 July 2024.

Jolley, M. J. (2021), 'Gsd camangle est', https://github.com/MJolley1/GSD{_}CamAngle{_}Est/blob/main/MJ{_}Oblique{_}CamAngle{_}Est.xlsx. Accessed: 31 July 2024.

Jolley, M. J., Russell, A. J., Quinn, P. F. and Perks, M. T. (2021), 'Considerations when applying large-scale piv and ptv for determining river flow velocity', *Frontiers in Water* **3**.
URL: *https://www.frontiersin.org/articles/10.3389/frwa.2021.709269/full*

Kääb, A., Altena, B. and Mascaro, J. (2019), 'River-ice and water velocities using the planet optical cubesat constellation', *Hydrology and Earth System Sciences* **23**(10), 4233–4247.

Kim, Y., Muste, M., Hauet, A., Krajewski, W. F., Kruger, A. and Bradley, A. (2008), 'Stream discharge using mobile large-scale particle image velocimetry: A proof of concept', *Water Resources Research* **44**(10), W10405.

Kinzel, P. J. and Legleiter, C. J. (2019), 'suas-based remote sensing of river discharge using thermal particle image velocimetry and bathymetric lidar', *Remote Sensing* .

Kostaschuk, R., Best, J., Villard, P., Peakall, J. and Franklin, M. (2005), 'Measuring flow velocity and sediment transport with an acoustic doppler current profiler', *Geomorphology* **68**(1-2), 25–37.

Koutalakis, P., Tzoraki, O. and Zaimes, G. (2019), 'Uavs for hydrologic scopes: Application of a low-cost uav to estimate surface water velocity by using three different image-based methods', *Drones* **3**(1), 14.

Le Coz, J., Jodeau, M., Hauet, A., Marchand, B. and Le Boursicaud, R. (2014), Image-based velocity and discharge measurements in field and laboratory river engineering studies using the free fudaa-lspiv software, *in* 'River Flow 2014: Proceedings of the International Conference on Fluvial Hydraulics', Lausanne, Switzerland, p. 7. 3–5 September 2014.

Lee, J., Shin, H., Ahn, J. and Jeong, C. (2016), 'Accuracy improvement of discharge measurement with modification of distance made good heading', *Advances in Meteorology* .

Legleiter, C. J., Kinzel, P. J. and Nelson, J. M. (2017), 'Remote measurement of river discharge using thermal particle image velocimetry (piv) and various sources of bathymetric information', *Journal of Hydrology* **554**, 490–506.

Leitão, J. P., Peña-Haro, S., Lüthi, B., Scheidegger, A. and de Vitry, M. M. (2018), 'Urban overland runoff velocity measurement with consumer-grade surveillance cameras and surface structure image velocimetry', *Journal of Hydrology* .

Lewis, Q. W. and Rhoads, B. L. (2018), 'Lspiv measurements of two-dimensional flow structure in streams using small unmanned aerial systems: 1. accuracy assessment based on comparison with stationary camera platforms and in-stream velocity measurements', *Water Resources Research* **54**.

Lindken, R., Rossi, M., Große, S. and Westerweel, J. (2009), 'Micro-particle image velocimetry (piv): Recent developments, applications, and guidelines', *Lab on a Chip* .

Liu, D. and Cheng, S. (2008), A brief introduction of feature matching, *in* 'Proceedings of the 2008 IEEE Region 5 Conference'.

Livoroi, A.-H., Conti, A., Foianesi, L., Tosi, F., Aleotti, F., Poggi, M., Tauro, F., Toth, E., Grimaldi, S. and Mattoccia, S. (2021), 'On the deployment of out-of-the-box embedded devices for self-powered river surface flow velocity monitoring at the edge', *Applied Sciences* **11**(15), 7027.

Ljubičić, R., Strelnikova, D., Perks, M. T., Eltner, A., Peña-Haro, S., Pizarro, A., Dal Sasso, S. F., Scherling, U., Vuono, P. and Manfreda, S. (2021), 'A comparison of tools and techniques for stabilising uas imagery for surface flow observations', *Hydrology and Earth System Sciences* **25**, 4769–4794.
URL: *https://hess.copernicus.org/articles/25/4769/2021/*

Lloyd, P. M., Stansby, P. K. and Ball, D. J. (1995), 'Unsteady surface-velocity field measurement using particle tracking velocimetry', *Journal of Hydraulic Research* **33**, 519–534.
URL: *https://www.tandfonline.com/doi/full/10.1080/00221689509498658*

Lowe, D. G. (1999), Object recognition from local scale-invariant features, *in* 'Proceedings of the Seventh IEEE International Conference on Computer Vision', Vol. 2, pp. 1150–1157.

Lucas, B. D. and Kanade, T. (1981), 'An iterative image registration technique with an application to stereo vision', *International Joint Conference on Artificial Intelligence (IJCAI)* .
URL: *https://www.researchgate.net/publication/215458777*

Malepati, H. (2010), Image processing tools, *in* H. Malepati, ed., 'Digital Media Processing', Elsevier, Oxford, pp. 153–186.

Masullo, A. and Theunissen, R. (2016), 'Adaptive vector validation in image velocimetry to minimise the influence of outlier clusters', *Experiments in Fluids* .

MathWorks (2023), 'detectmserfeatures', MATLAB documentation. Accessed: 17 May 2023.
URL: *https://uk.mathworks.com/help/vision/ref/detectmserfeatures.html*

Merkuryeva, G., Merkuryev, Y., Sokolov, B. V., Potryasaev, S., Zelentsov, V. A. and Lektauers, A. (2015), 'Advanced river flood monitoring, modelling and forecasting', *Journal of Computational Science* **10**, 77–85.

Meselhe, E. A., Peeva, T. and Muste, M. (2004), 'Large scale particle image velocimetry for low velocity and shallow water flows', *Journal of Hydraulic Engineering* **130**(9), 937–945.

Mingkhwan, E. and Khawsuk, W. (2017), Digital image stabilization technique for fixed camera on small size drone, *in* 'Proceedings of the 3rd Asian Conference on Defence Technology (ACDT 2017)'.

Mishra, M., Dugesar, V., Prudhviraju, K. N., Patel, S. B. and Mohan, K. (2019), 'Precision mapping of boundaries of flood plain river basins using high-resolution satellite imagery: A case study of the varuna river basin in uttar pradesh, india', *Journal of Earth System Science* .

Montoya-Coronado, V. A., Delenne, C., Finaud-Guyot, P. and Hostache, R. (2022), 'How to optimally represent riverbed geometry with a simplified cross-section shape in shallow water models', *Advances in Hydroinformatics* .

Morrow, D. (2021), 'Camera sensor size & image quality – photography guide'. Nikon - Understanding Focal Length.
URL: *https://www.davemorrowphotography.com/camera-sensor-size-guide*

Muja, M. and Lowe, D. G. (2012), 'Fast matching of binary features'.

Muste, M., Fujita, I. and Hauet, A. (2008), 'Large-scale particle image velocimetry for measurements in riverine environments', *Water Resources Research* **44**(6), W06413.

Muste, M., Yu, K. and Spasojevic, M. (2004), 'Practical aspects of adcp data use for quantification of mean river flow characteristics; part i: Moving-vessel measurements', *Flow Measurement and Instrumentation* **15**(1), 1–16.

National Oceanic and Atmospheric Administration (2024), 'Acoustic doppler current profiler (adcp)', `https://oceanexplorer.noaa.gov/technology/acoust-doppler/acoust-doppler.html`. Accessed: 20 July 2024.

Neill, S. P. and Hashemi, M. R. (2018), In situ and remote methods for resource characterization, *in* 'Fundamentals of Ocean Renewable Energy', Elsevier, Oxford.

Optics, E. (2021), 'Imaging electronics 101: Understanding camera sensors for machine vision applications', https://www.edmundoptics.co.uk/knowledge-center/application-notes/imaging/understanding-camera-sensors-for-machine-vision-applications/. Accessed: 30 March 2021.

Park, D. S. and You, H. (2023), 'A digital twin dam and watershed management platform', *Water (Switzerland)* **15**(11), 2106.

Patalano, A., García, C. M. and Rodríguez, A. (2017), 'Rectification of image velocity results (river): A simple and user-friendly toolbox for large scale water surface particle image velocimetry (piv) and particle tracking velocimetry (ptv)', *Computers and Geosciences* .

Pearce, S., Ljubičić, R., Peña-Haro, S., Perks, M., Tauro, F., Pizarro, A., Dal Sasso, S. F., Strelnikova, D., Grimaldi, S., Maddock, I., Paulus, G., Plavšić, J., Prodanović, D. and Manfreda, S. (2020), 'An evaluation of image velocimetry techniques under low flow conditions and high seeding densities using unmanned aerial systems', *Remote Sensing* **12**(2), 232.

Perks, M. T. (2020), 'Klt-iv v1.0: Image velocimetry software for use with fixed and mobile platforms', *Geoscientific Model Development Discussions* **13**(3), 1079–1096.

Perks, M. T., Russell, A. J. and Large, A. R. G. (2016), 'Technical note: Advances in flash flood monitoring using unmanned aerial vehicles (uavs)', *Hydrology and Earth System Sciences* **20**(10), 4005–4015.
URL: *https://hess.copernicus.org/articles/20/4005/2016/*

Peña-Haro, S., Carrel, M., Lüthi, B., Hansen, I. and Lukes, R. (2021), 'Robust image-based streamflow measurements for real-time continuous monitoring', *Frontiers in Water* **3**.

Peña-haro, S., Lüthi, B., Lukes, R. and Carrel, M. (2020), Wind effect on image-based river surface velocity measurements, Technical report, EGU General Assembly 2020.
URL: *https://presentations.copernicus.org/EGU2020/EGU2020-9943_presentation.pdf*

Pix4d (2019), 'What is absolute accuracy and relative accuracy?'.
URL: *https://www.pix4d.com/blog/accuracy-aerial-mapping#absolute-relative*

Pizarro, A., Sasso, S. D. and Manfreda, S. (2020b), 'Refining image-velocimetry performances for streamflow monitoring: Seeding metrics to errors minimization', *Hydrological Processes* **34**(25), 5167–5175.

Pizarro, A., Sasso, S. D., Perks, M. T. and Manfreda, S. (2020a), 'Identifying the optimal spatial distribution of tracers for optical sensing of stream surface flow', *Hydrology and Earth System Sciences* **24**, 5173–5189.

Planet (2021), ‘Planet satellite data’.

Plant, W. J., Keller, W. C., Hayes, K. and Spicer, K. R. (2005), ‘Streamflow measurements from air using doppler radar’, *Journal of Hydrology* **301**(1-4), 118–136.
URL: *https://doi.org/10.1016/j.jhydrol.2004.06.041*

Prasad, A. K., Adrian, R. J., Landreth, C. C. and Offutt, P. W. (1992), ‘Effect of resolution on the speed and accuracy of particle image velocimetry interrogation’, *Experiments in Fluids* **13**(2), 105–116.

Pumo, D., Alongi, F., Ciraolo, G. and Noto, L. V. (2021), ‘Optical methods for river monitoring: A simulation-based approach to explore optimal experimental setup for lspiv’, *Water (Switzerland)* **13**(3), 247.

Pun, C. S., Susanto, A. and Dabiri, D. (2007), ‘Mode-ratio bootstrapping method for piv outlier correction’, *Measurement Science and Technology* .

Raffel, M., Willert, C. E., Scarano, F., K”ahler, C. J., Wereley, S. T. and Kompenhans, J. (2018), *Particle Image Velocimetry: A Practical Guide*, Springer, Cham.

River Levels UK (2023), ‘River sheaf at highfield’. Accessed: 2024-05-17.
URL: *https://riverlevels.uk/river-sheaf-highfield*

Rodriguez-Padilla, I., Castelle, B., Marieu, V. and Morichon, D. (2019), ‘A simple and efficient image stabilization method for coastal monitoring video systems’, *Remote Sensing* **12**(1), 70.
URL: *https://www.mdpi.com/2072-4292/12/1/70*

Rosten, E. and Drummond, T. (2006), Machine learning for high-speed corner detection, *in* A. Leonardis, H. Bischof and A. Pinz, eds, ‘Computer Vision – ECCV 2006’, Springer Berlin Heidelberg, Berlin, Heidelberg, pp. 430–443.

Safesite (2021), ‘Internet protocol (ip) cameras – how do they work and what are the benefits?’.
URL: *https://www.safesitefacilities.co.uk/knowledge-base/internet-protocal-cameras-how-do-they-work*

Sentlinger, G., Fraser, J. and Baddock, E. (2019), Salt dilution flow measurement: Automation and uncertainty, *in* ‘Proceedings of the HydroSenSoft, International Symposium and Exhibition on Hydro-Environment Sensors and Software’, Vol. 8.

Shi, J. and Tomasi, C. (1994), Good features to track, *in* ‘Proceedings of the IEEE Computer Society Conference on Computer Vision and Pattern Recognition’, pp. 593–600.

Sicairos, M. G., Thurman, S. T. and Fienup, J. R. (2008), 'Efficient subpixel image registration algorithms', *Optics Letters* **33**(2), 156.
URL: *https://www.osapublishing.org/abstract.cfm?URI=ol-33-2-156*

Stamhuis, E. J. (2006), 'Basics and principles of particle image velocimetry (piv) for mapping biogenic and biologically relevant flows', *Aquatic Ecology* .

Szeliski, R. (2006), 'Image alignment and stitching: A tutorial', *Foundations and Trends in Computer Graphics and Vision* **2**(1), 1–104.
URL: *https://doi.org/10.1561/0600000009*

Tang, C., Sun, W., He, H., Li, H. and Li, E. (2017), 'Spurious piv vector detection and correction using a penalized least-squares method with adaptive order differentials', *Experiments in Fluids* **58**, 81.
URL: *http://link.springer.com/10.1007/s00348-017-2350-x*

Tang, H. W., Chen, C., Chen, H. and Huang, J. T. (2008), 'An improved ptv system for large-scale physical river model', *Journal of Hydrodynamics* **20**(2), 233–242.

Tareen, S. A. K. and Saleem, Z. (2018), A comparative analysis of sift, surf, kaze, akaze, orb, and brisk, *in* 'Proceedings of the 2018 International Conference on Computing, Mathematics and Engineering Technologies (iCoMET)', pp. 1–10.

Tauro, F., Petroselli, A. and Grimaldi, S. (2018), 'Optical sensing for stream flow observations: A review', *Journal of Agricultural Engineering* .

Tauro, F., Petroselli, A., Porfiri, M., Giandomenico, L., Bernardi, G., Mele, F., Spina, D. and Grimaldi, S. (2016), 'A novel permanent gauge-cam station for surface-flow observations on the tiber river', *Geoscientific Instrumentation, Methods and Data Systems* **5**, 241–250.

Tauro, F., Piscopia, R. and Grimaldi, S. (2017), 'Streamflow observations from cameras: Large-scale particle image velocimetry or particle tracking velocimetry?', *Water Resources Research* **53**(4), 3244–3257.

Tauro, F., Piscopia, R. and Grimaldi, S. (2019), 'Ptv-stream: A simplified particle tracking velocimetry framework for stream surface flow monitoring', *Catena* **172**, 378–386.

Tauro, F., Porfiri, M. and Grimaldi, S. (2014), 'Orienting the camera and firing lasers to enhance large scale particle image velocimetry for streamflow monitoring', *Water Resources Research* **50**(9), 7503–7516.

Tauro, F. and Salvatori, S. (2017), Surface flows from images: Ten days of observations from the tiber river gauge-cam station, *in* 'Hydrology Research'.

Tauro, F., Tosi, F., Mattoccia, S., Toth, E., Piscopia, R. and Grimaldi, S. (2018), 'Optical tracking velocimetry (otv): Leveraging optical flow and trajectory-based filtering for surface streamflow observations', *Remote Sensing* **10**(12), 2010.

Team, I. (2021), 'Frame rate guide for video surveillance'.
URL: *https://ipvm.com/reports/frame-rate-surveillance-guide*

Tensmeyer, C. and Martinez, T. (2020), 'Historical document image binarization: A review', *SN Computer Science* .

Thielicke, W. and Stamhuis, E. J. (2014), 'Pivlab – towards user-friendly, affordable and accurate digital particle image velocimetry in matlab', *Journal of Open Research Software* **2**.
URL: *http://openresearchsoftware.metajnl.com/articles/10.5334/jors.bl/*

Thumser, P., Haas, C., Tuhtan, J. A., Fuentes-Pérez, J. F. and Toming, G. (2017), Raptor-uav: Real-time particle tracking in rivers using an unmanned aerial vehicle, *in* 'Earth Surface Processes and Landforms', Vol. 42, John Wiley & Sons, Ltd, pp. 1894–1903.

Tomasi, C. (1991), 'Detection and tracking of point features', *School of Computer Science, Carnegie Mellon Univ.* **31**(2), 123–127.

Tosi, F., Rocca, M., Aleotti, F., Poggi, M., Mattoccia, S., Tauro, F., Toth, E. and Grimaldi, S. (2020), 'Enabling image-based streamflow monitoring at the edge', *Remote Sensing* **12**(12), 2047.

Tsubaki, R. (2017), 'On the texture angle detection used in space-time image velocimetry (stiv)', *Water Resources Research* .

Tsubaki, R., Fujita, I. and Tsutsumi, S. (2011), 'Measurement of the flood discharge of a small-sized river using an existing digital video recording system', *Journal of Hydro-Environment Research* **5**(1), 30–39.

UKCEH (2018), 'Need for river flow measurement'. Accessed: 2024-05-17.
URL: *https://nrfa.ceh.ac.uk/need-river-flow-measurement*

Vandaele, R., Dance, S. L. and Ojha, V. (2023), 'Calibrated river-level estimation from river cameras using convolutional neural networks', *Environmental Data Science* **2**.

Wang, H. P., Gao, Q., Feng, L. H., Wei, R. J. and Wang, J. J. (2015), 'Proper orthogonal decomposition based outlier correction for piv data', *Experiments in Fluids* .

Westerweel, J. (1994), 'Efficient detection of spurious vectors in particle image velocimetry data', *Experiments in Fluids* **16**(3-4), 236–247.

Westerweel, J. and Scarano, F. (2005), 'Universal outlier detection for piv data', *Experiments in Fluids* .

Willert, C., Raffel, M., Kompenhans, J., Stasicki, B. and Kähler, C. (1996), 'Recent applications of particle image velocimetry in aerodynamic research', *Flow Measurement and Instrumentation* **7**(2), 81–91.

Wood, P. J. and Dykes, A. P. (2002), 'The use of salt dilution gauging techniques: ecological considerations and insights', *Water Research* **36**, 3054–3062.

Yorke, T. H. and Oberg, K. A. (2002), 'Measuring river velocity and discharge with acoustic doppler profilers', *Flow Measurement and Instrumentation* **13**(5-6), 191–195.

Young, C. N., Johnson, D. A. and Weckman, E. J. (2004), 'A model-based validation framework for piv and ptv', *Experiments in Fluids* .

Zhang, X., Cox, C. S. and Wang, X. (1997), Further evaluation of feature correlation for piv and ptv, *in* S. S. Cha, J. D. Trolinger and M. Kawahashi, eds, 'Optical Technology in Fluid, Thermal, and Combustion Flow III', International Society for Optics and Photonics, SPIE, pp. 411–419. **URL:** *https://doi.org/10.1117/12.279750*

Zhang, Z., Wang, X., Fan, T. and Xu, L. (2013), 'River surface target enhancement and background suppression for unseeded lspiv', *Flow Measurement and Instrumentation* .

Chapter 10. Appendix A: KLT-IV Processing (Chapter 5)

10.1 KLT Processing Videos Settings

Todmorden, River Calder

KLT User Inputs

Attribute	Value	Attribute	Value
Mode	Multiple Videos	Extract Rate	0.5
Define Videos	Multiple Selected	Block Size (px)	31
Camera Type	Hikvision DS-2CD	Ignore Edges?	No
Camera (x)	999.62	Vel. Component	Normal Component
Camera (y)	1000.95		
Camera (z)	101.09		
Yaw	0		
Pitch	0.7		
Roll	0		

Table 10.1: KLT User Inputs and Settings for Todmorden, River Calder

GCP Data

Analysis and Discharge Settings

Vertices Data The vertices data used for the River Calder contains 2056 points along the cross-section. The data for the vertices can be in Figure 10.1.

X [meters]	Y [meters]	Z [meters]	X [px]	Y [px]
996.340	1009.380	97.555	987.080486	1115.002842
998.194	1010.047	97.568	1636.613288	1144.539720
996.157	1010.059	97.517	1028.297891	1040.110644
998.027	1010.724	97.534	1630.586170	1070.583380
995.372	1011.040	97.529	942.119053	910.148839
997.159	1011.892	97.497	1468.470982	930.859375
995.019	1011.710	97.554	935.613204	838.364644
996.864	1012.463	97.551	1440.522693	861.895461
994.021	1012.755	97.580	838.851404	726.869923
995.7255	1013.803	97.557	1284.820764	736.593192
993.525	1013.770	97.580	844.440908	663.301930
995.319	1014.650	97.538	1261.734528	683.397939
993.544	1011.571	98.089	601.350745	667.588588
992.284	1013.655	98.580	615.999183	428.500179
997.308	1013.669	97.765	1624.542859	755.271195
998.360	1011.859	98.570	1823.549543	705.288696

Table 10.2: Ground Control Points (GCPs) Data for Todmorden, River Calder

Parameter	Value
GCP Buffer (m)	5
Custom FOV	0, 0, 0, 0
WSE (m)	(See Stage Data)

Table 10.3: GCP and Water Surface Elevation (WSE) Parameters for Todmorden, River Calder

Analysis Parameter	**Value**	**Discharge Parameter**	**Value**
Output Location	User's Choice	Cross-section Input	Referenced Survey
Define ROI	User's Choice	Reference Height	True Bed Elevation
Export velocity?	On	Number of Cells	20
Orthophotos	Off	Interpolation Method	All
Resolution (m/px)	0.01	Alpha	0.85
Plot Movement?	N/A		
Plot Velocity?	No		
Export Settings	N/A		
Load Settings	N/A		

Table 10.4: Analysis and Discharge Settings for Todmorden, River Calder

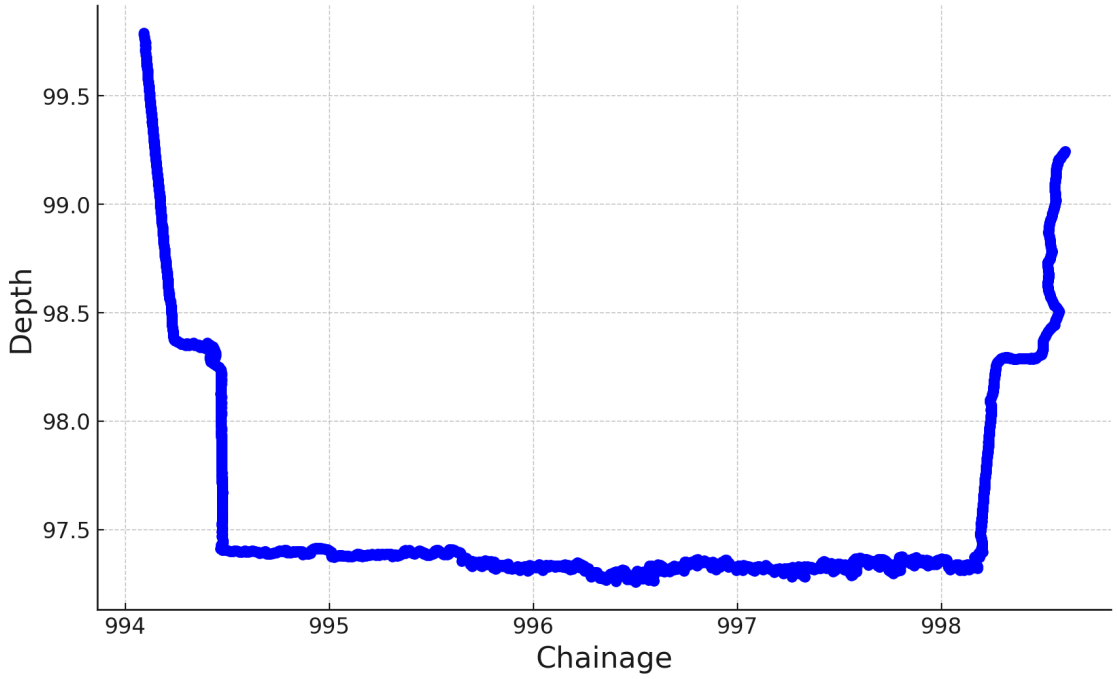


Figure 10.1: River Calder at Todmorden Cross-Section Data

Sheffield, River Sheaf

KLT User Inputs

Attribute	Value	Attribute	Value
Mode	Multiple Videos	Extract Rate	0.5
Define Videos	Multiple Selected	Block Size (px)	31
Camera Type	Hikvision DS-2CD	Ignore Edges?	No
Camera (x)	1000.81	Vel. Component	Normal Component
Camera (y)	1003.55		
Camera (z)	102.1		
Yaw	0		
Pitch	1		
Roll	0		

Table 10.5: KLT User Inputs and Settings for Sheffield, River Sheaf

GCP Data

Analysis and Discharge Settings

Vertices Data The vertices data used for the River Sheaf contains 580 points along the cross-section. The data for the vertices can be seen in Figure 10.2.

X [meters]	Y [meters]	Z [meters]	X [px]	Y [px]
1003.896	1012.511	97.328	332.2773804	731.7645311
1004.232	1012.014	97.302	430.4022875	772.4776206
1005.582	1011.990	97.278	699.9722007	734.8889321
1008.174	1010.336	97.327	1346.341979	780.8613052
1008.090	1012.070	97.312	1129.610925	652.5160542
1004.790	1017.038	97.400	304.2843127	404.4407393
1005.114	1015.504	97.337	406.8576833	492.5513954
1006.408	1016.891	97.315	537.1352324	399.4700824
1008.644	1015.365	97.270	928.8819724	446.6598929
1009.380	1017.379	97.414	890.8715226	331.6926438
1007.699	1019.656	97.476	578.4456689	260.2597982
1011.890	1014.372	97.336	1396.812864	436.1645134

Table 10.6: Ground Control Points (GCPs) Data for Sheffield, River Sheaf

Parameter	Value
GCP Buffer (m)	5
Custom FOV	0, 0, 0, 0
WSE (m)	(See Stage Data)

Table 10.7: GCP and Water Surface Elevation (WSE) Parameters for Sheffield, River Sheaf

Analysis Parameter	**Value**	**Discharge Parameter**	**Value**
Output Location	User's Choice	Cross-section Input	Referenced Survey
Define ROI	User's Choice	Reference Height	True Bed Elevation
Export velocity?	On	Number of Cells	20
Orthophotos	Off	Interpolation Method	All
Resolution (m/px)	0.01	Alpha	0.85
Plot Movement?	N/A		
Plot Velocity?	No		
Export Settings	N/A		
Load Settings	N/A		

Table 10.8: Analysis and Discharge Settings for Sheffield, River Sheaf

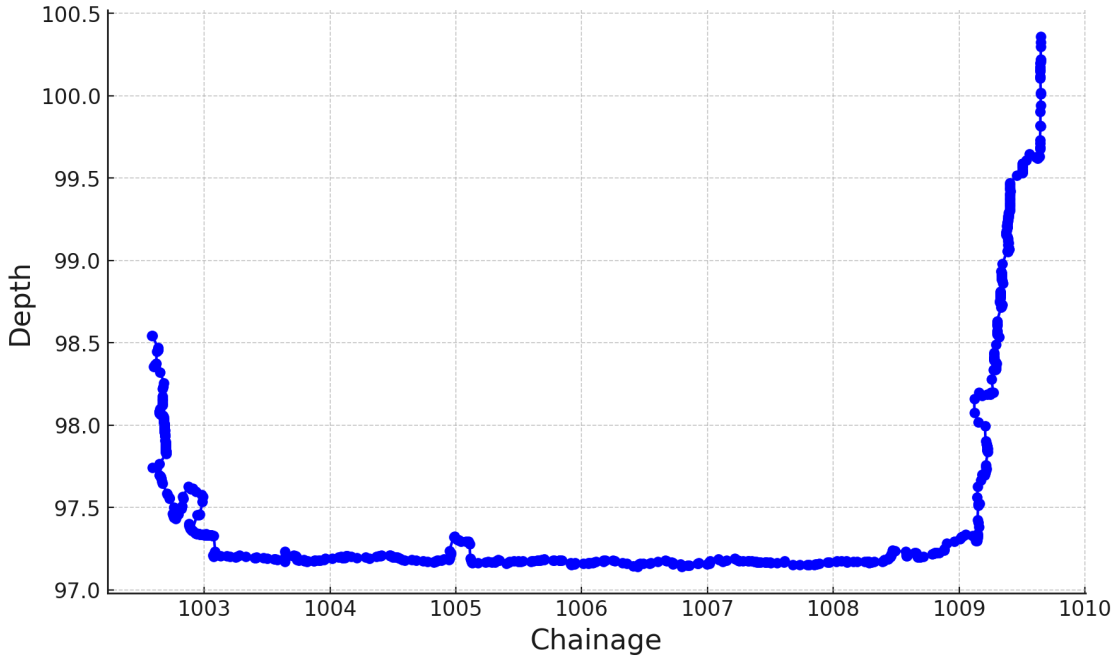


Figure 10.2: River Sheaf at Highfield Cross-Sectional Data

Chapter 11. Appendix B: Publications and Co-Authorship

Elements of thisthesis, particularly Chapters 1, 2, and 3, incorporate material from a peer-reviewed publication authored during the course of this research: Jolley MJ, Russell AJ, Quinn PF, and Perks MT (2021). "Considerations When Applying Large-Scale PIV and PTV for Determining River Flow Velocity." Frontiers in Water. 3:709269. The publication provided the foundation for the theoretical and methodological development of this work, especially in relation to image velocimetry techniques, seeding dynamics, and flow measurement accuracy. Relevant sections have been adapted and included within this work as mentioned above, and has been cited where direct material has been used.

11.1 Considerations When Applying Large-Scale PIV and PTV for Determining River Flow Velocity

frontiers in Water

REVIEW
published: 02 December 2021
doi: 10.3389/frwa.2021.709269

Considerations When Applying Large-Scale PIV and PTV for Determining River Flow Velocity

Martin J. Jolley[1]*, *Andrew J. Russell*[1], *Paul F. Quinn*[2] *and Matthew T. Perks*[1]

[1] School of Geography, Politics and Sociology, Newcastle University, Newcastle upon Tyne, United Kingdom, [2] School of Engineering, Newcastle University, Newcastle upon Tyne, United Kingdom

Large-scale image velocimetry is a novel approach for non-contact remote sensing of flow in rivers. Research within this topic has largely focussed on developing specific aspects of the image velocimetry work-flow, or alternatively, testing specific tools or software using case studies. This has resulted in the development of a multitude of techniques, with varying practice being employed between groups, and authorities. As such, for those new to image velocimetry, it may be hard to decipher which methods are suited for particular challenges. This research collates, synthesises, and presents current understanding related to the application of particle image velocimetry (PIV) and particle tracking velocimetry (PTV) approaches in a fluvial setting. The image velocimetry work-flow is compartmentalised into sub-systems of: capture optimisation, pre-processing, processing, and post-processing. The focus of each section is to provide examples from the wider literature for best practice, or where this is not possible, to provide an overview of the theoretical basis and provide examples to use as precedence and inform decision making. We present literature from a range of sources from across the hydrology and remote sensing literature to suggest circumstances in which specific approaches are best applied. For most sub-systems, there is clear research or precedence indicating how to best perform analysis. However, there are some stages in the process that are not conclusive with one set method and require user intuition or further research. For example, the role of external environmental conditions on the performance of image velocimetry being a key aspect that is currently lacking research. Further understanding in areas that are lacking, such as environmental challenges, is vital if image velocimetry is to be used as a method for the extraction of river flow information across the range of hydro-geomorphic conditions.

Keywords: review, PIV, river discharge, remote sensing, image velocimetry, surface velocity, river gauging, PTV

OPEN ACCESS

Edited by:
Giacomo Bertoldi,
Eurac Research, Italy

Reviewed by:
Alonso Pizarro,
Diego Portales University, Chile
Salvador Peña-Haro,
Independent Researcher, Zurich, Switzerland

***Correspondence:**
Martin J. Jolley
m.jolley1@newcastle.ac.uk

Specialty section:
This article was submitted to Water and Hydrocomplexity, a section of the journal Frontiers in Water

Received: *13 May 2021*
Accepted: *20 October 2021*
Published: *02 December 2021*

Citation:
Jolley MJ, Russell AJ, Quinn PF and Perks MT (2021) Considerations When Applying Large-Scale PIV and PTV for Determining River Flow Velocity. Front. Water 3:709269. doi: 10.3389/frwa.2021.709269

1. INTRODUCTION

Advances in understanding of hydrological processes and the characterisation of river flows have been driven by development of novel sensing instruments, data acquisition platforms, and new analytical techniques (e.g., Chen et al., 2007; Assem et al., 2017; Mishra et al., 2019). Of the recent advances in sensing river flows, arguably the most pronounced is the widespread adoption of acoustic Doppler current profiler (aDcp) technologies (Kostaschuk et al., 2005). This has led to advances in the ability to reliably collect data over large areas, most importantly, entire water

columns (Neill and Hashemi, 2018). Whilst this technology offers some advantages over traditional gauging techniques (e.g., ultrasonic sensors, electromagnetic current meters), they fail to overcome a critical limitation in that they require contact with the water-body, which may not be viable during high-flow conditions or where physical access to the channel is not possible.

In recognition of these challenges, the development of non-contact sensors for velocity measurements (e.g., surface velocity radar), and non-intrusive approaches for acquiring bathymetric data (e.g., bathymetric LiDAR, radar, photogrammetry) is now facilitating the non-contact and autonomous monitoring of fluvial flows (Costa et al., 2006; Flener et al., 2013; Javernick et al., 2014; Alimenti et al., 2020). These methods have been shown to provide data as reliable as conventional methods (Costa et al., 2006; Alimenti et al., 2020), but they may be costly to deploy, therefore limiting their widespread adoption of use. They are also subject to their own operational limitations. For example, surface velocity radar is highly dependent on the surface roughness of the river and may be influenced by environmental noise (Fulton, 2020).

An exciting, alternative approach which may be used to determine fluvial flows (when coupled with bathymetric data), is that of large-scale image velocimetry. Research into large-scale image velocimtery has been increasing year-on-year the past two decades, with more of an increasing emphasis on the application of software suites (**Figure 1**). This technique shares many principles to that of the lab-based image velocimetry method (Lindken et al., 2009), which was initially developed to conduct hydraulic analysis in controlled, laboratory settings. The fundamental principles of the lab-based approach include the seeding of the flow with neutrally buoyant particles, which are then illuminated with laser light and their movement recorded by camera before the particle displacements are determined using either Particle Tracking Velocimetry (PTV) or Particle Image Velocimetry (PIV) (Willert et al., 1996). Whilst large-scale image velocimetry often utilises these same tracking procedures in uncontrolled outdoor environments, certain elements are changed out of necessity and for optimisation of the outputs. Lab-based image velocimetry has been widely adopted with standardised procedures published (e.g., Gollin et al., 2017; Cerqueira et al., 2018). However, the flexible nature of large-scale image velocimetry has meant that techniques and approaches may vary based on the hydrological setting, environmental conditions, and platform of acquisition; this has ultimately made standardisation a more complex activity (Perks, 2020).

The aim of this review is to present and discuss the key challenges and considerations when seeking to acquire image velocimetry data within a fluvial setting (i.e., large-scale image velocimetry). The key stages in large-scale image velocimetry work-flows can be characterised as (i) capture optimisation (section 2.1); (ii) pre-processing (section 2.2); (iii) image processing (section 2.3); and (iv) post-processing steps (section 2.4), as outlined in **Figure 2**. Capture optimisation steps involve the appropriate selection of, and preparation of, equipment and its parameters for reliable image sequence capture (e.g., maximising tracer visibility, minimising environmental

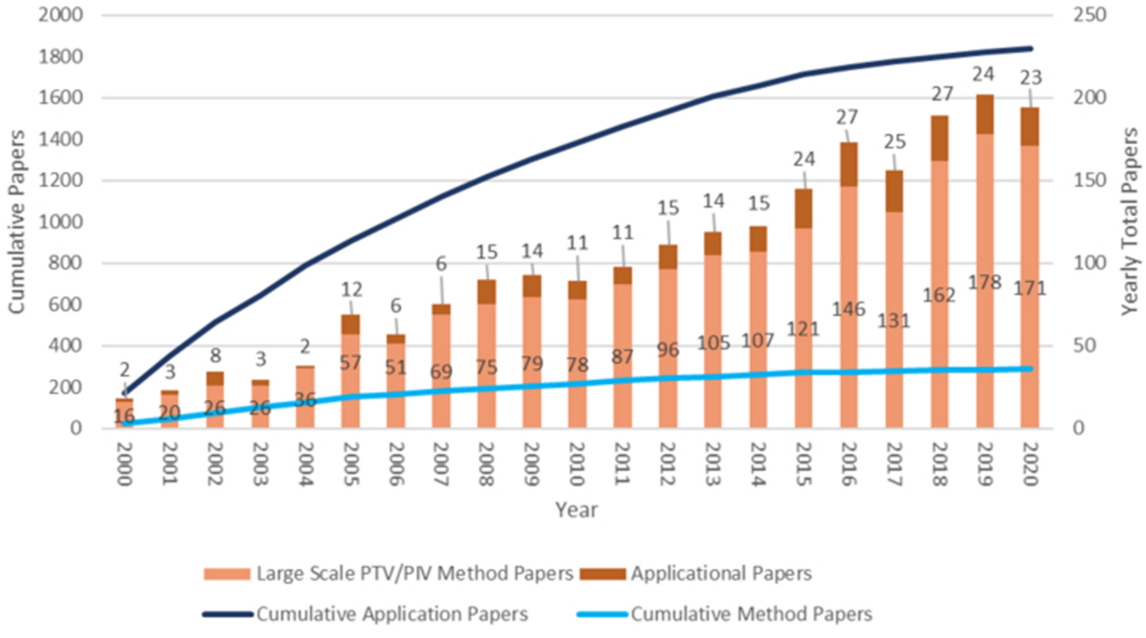


FIGURE 1 | An insight into the number of publications over the past two decades into the research of large scale PIV and PTV, compared with those focused on the application of PIV and PTV on rivers. Data found via www.webofscience.com. The following refinements were applied to the search: Total papers, *topic* "Surface velocimetry PIV" OR *topic* "Surface velocimetry PTV" AND *all fields* "rivers." Application papers, *topic* "Surface velocimetry PIV application" OR *topic* "Surface velocimetry PTV application" AND *all fields* "Rivers".

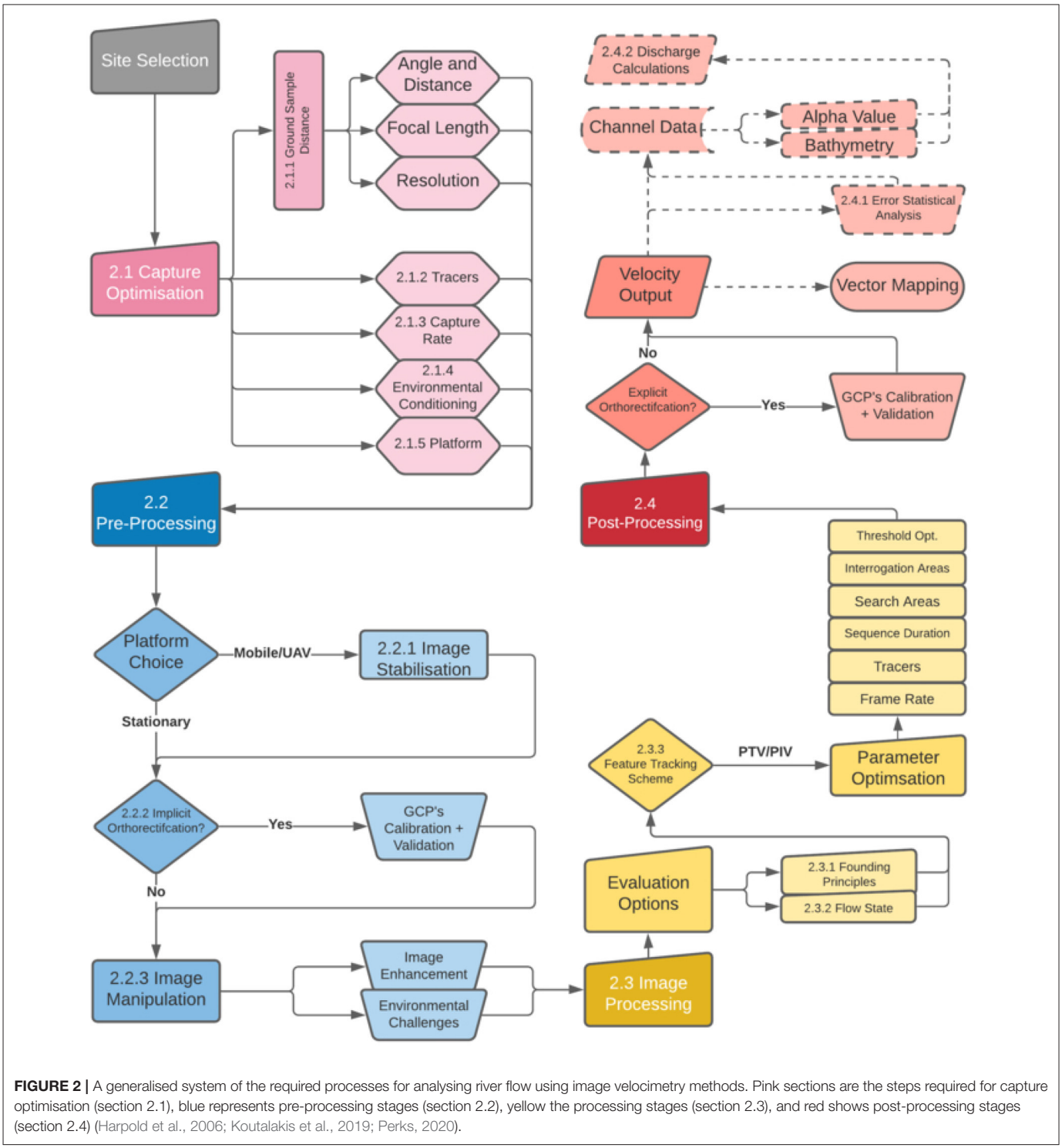


FIGURE 2 | A generalised system of the required processes for analysing river flow using image velocimetry methods. Pink sections are the steps required for capture optimisation (section 2.1), blue represents pre-processing stages (section 2.2), yellow the processing stages (section 2.3), and red shows post-processing stages (section 2.4) (Harpold et al., 2006; Koutalakis et al., 2019; Perks, 2020).

noise, and ensuring optimal ground sampling distance). Pre-processing steps may be described as those which ensure stable footage with a common spatial reference, with image properties being altered to minimise noise (e.g., removal of visible river bed), and to maximise the signal (e.g., visibility of surface tracers). Processing involves the application of 1D or 2D analysis of feature displacements across a defined field of view. Post-processing steps seek to validate the generated data and remove spurious results. The filtered dataset may then be used to generate secondary products (e.g., discharge) when combined with surrogate information (e.g., cross-section measurements).

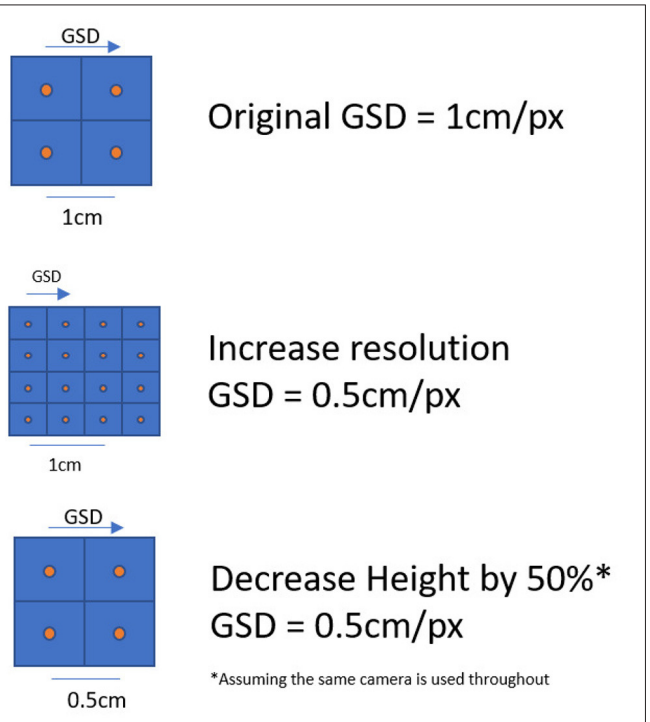


FIGURE 3 | How GSD is described and can be altered using either an increase in resolution, or decreasing the distance between the subject and the camera.

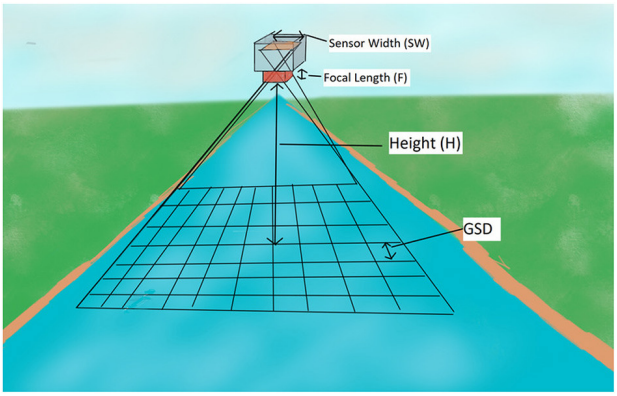


FIGURE 4 | Schematics of GSD of Nadir angle.

2. IMAGE VELOCIMETRY PROCESSES

2.1. Capture Optimisation

2.1.1. Ground Sampling Distance

The ground sampling distance (GSD) of imagery is the distance between the centroid of two adjacent pixels (**Figure 3**). The GSD of the imagery used in large-scale image velocimetry analysis is a critical consideration with features smaller than the GSD being poorly resolved. For example, imagery with a GSD of 1 cm/px may include features of 0.008 m length, but these would not be depicted as being any less than 0.01 m length in the imagery. Critically, if the GSD is significantly larger that the individual features present on the water surface, these features may not be visible in the imagery, and these features would therefore be unsuitable for image velocimetry purposes. Although there is no clear guidance on specific values relating to the point at which tracers are no longer visible, generally, a tracer would have to be significantly brighter than the background to dominate the overall contrast of the pixel. As a result of these factors, it is important that the image GSD (cm/px) for the proposed image acquisition settings is known in advance. This will ensure that features visible on the free-surface will be adequately resolved by the camera system. In a scenario where the footage is acquired at nadir, this is governed by the focal length (F; mm), sensor width (SW; mm) and image width (IwP; pixels). Using these characteristics of the camera sensor, and user knowledge of the desired GSD, the required height of image acquisition can be calculated (Equation 1; Pix4d, 2019), see **Figure 4**.

$$\text{Height (m)} = \frac{IwP \times GSD \times F}{SW \times 100} \tag{1}$$

The image sensor is the apparatus in the camera that converts optical imagery into an electric signal using a matrix of small potential wells (pixels) (Edmund Optics, 2021). The size of image sensor relates to the amount of light a camera can capture, and typical security/IP type cameras use a range between 1/4" (6.35 mm) to a 2/3" (16.9 mm) sensor (Caputo, 2010). Without a large enough image sensor, detail is lost due to a lack of capability to add detail through pixel colour/tone, or due to a high signal:noise ratio seen with smaller sensors (Morrow, 2021).

Subsequently, the GSD may be affected by the camera angle and the camera distance from the source. Introducing a non-nadir angle to the camera increases the length between the camera and the background of the image, in addition to increasing the width of the coverage. Effectively, with a shift in the pitch of the camera, it will create a trapezoidal shaped image grid, where the background is scaled proportionally to the angle and distance from source. This results in the GSD being variable across the field of view (FOV), and the image background being relatively poorly resolved. For this reason, the sensing of environments using oblique camera angles, particularly over long distances, may result in image acquisition where features on the water surface in the background cannot be easily detected. In instances of oblique image capture, the GSD (cm/px) can be determined using Equation (2), where L is a given length both horizontally (Lh;m) and vertically (Lv;m), IwP is the image width (px) (Equations 3–4), α_v is the angle of tilt seen in the roll axis (Equation 3), α_h is the angle of tilt seen in the pitch axis (Equation 4). Θ° is the angle of capture (Equation 5), calculated by using the Sensor Width (SW) and the Focal Length (F). These equations are implemented within GSDCalc (Jolley, 2021), **Figure 5**.

$$GSD = \frac{L \times 200}{IwP} \tag{2}$$

$$L_v\ (\text{m}) = H\frac{\sin(\theta \pm \alpha_v)}{\sin(90 - (\theta \pm \alpha_v))} \tag{3}$$

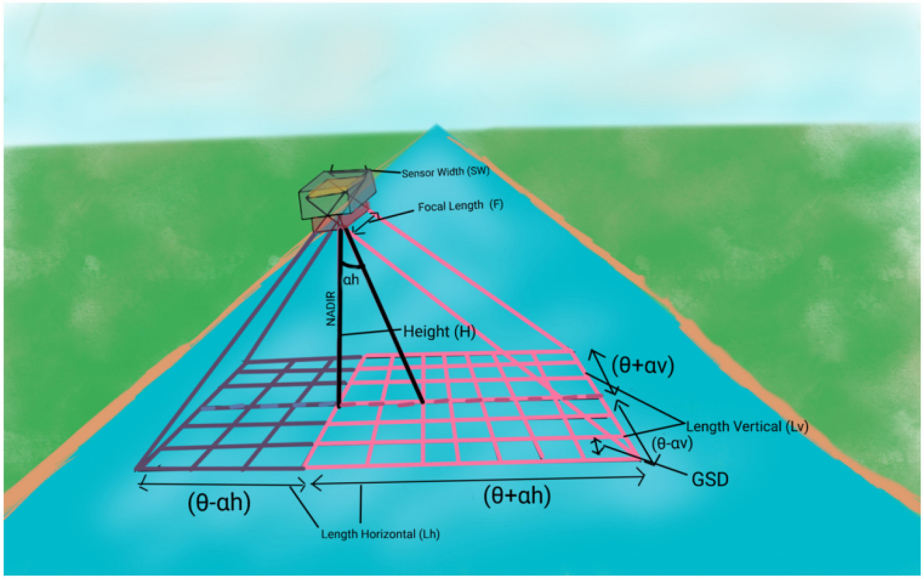


FIGURE 5 | Schematics of GSD at an oblique angle.

$$L_h\,(\mathrm{m}) = H\frac{\sin(\theta \pm \alpha_h)}{\sin(90 - (\theta \pm \alpha_h))} \tag{4}$$

$$\Theta^{\circ} = \tanh\frac{SW}{F} \tag{5}$$

When discussing camera angles, it is important to note the type of camera station in use. Camera stations are typically described as being either fixed or mobile platforms, these are discussed in section 2.1.5. Due to the flexible nature of large-scale image velocimetry, a wide variety of camera angles are adopted. The fixed camera deployments described in Perks et al. (2020) includes camera angles up to 57 degrees from nadir. Alternatively, for mobile cameras, Eltner et al. (2020) suggests that a tilt angle more than 10° from nadir should be avoided where possible. Generally, for both fixed and mobile platforms, the closer that the camera sensor is to nadir the better, providing that the region-of-interest is visible throughout, along with ground control points, and static features to enable stabilisation (when required). Finally, when installing fixed camera stations, a critical consideration is the effect of stage variation of the camera's FOV. As stage increases, the distance between the water surface and camera decreases, which can result in a reduction in the area sensed.

Camera focal length (usually given in mm), is the distance between the image sensor and the camera lens when the subject area is in focus. The smaller the focal length, the larger the area captured, but at a smaller apparent size. Subsequently, the larger the focal length, the smaller the area captured, but in higher detail. Generally, cameras have either prime (non-adjustable) or zoom (adjustable) lenses. It has been recommended that independent of the lens used, the internal parameters of the camera should be established (Detert, 2021), and used to removal lens distortion effects prior to the the extrinsic calibration stage (i.e., orthorectification; section 2.2.2).

Finally, the GSD is greatly affected by the image resolution (i.e., number of pixels present within an image). Whilst it may seem intuitive to seek to minimise the GSD by using the highest resolution of imagery available, this approach comes at a time/power cost when undertaking image velocimetry analysis, with the benefits reaching an asymptote once the surface patterns and features in the image can be adequately resolved. This has been demonstrated in lab-based studies. For example, Prasad et al. (1992) observed that when image resolution was reduced by a factor of two, this was accompanied with only a small loss in the ability to detect tracers (equivalent to a loss of 0.3% of "good" features). However, processing speed increased fourfold. Similar findings have also been observed within field settings. Analysis of low resolution imagery (144p, 256×144), produced deviations in longitudinal velocity of only 5% relative to full resolution imagery (1,080p) (Le Boursicaud et al., 2016), and negligible changes to velocity results between 1,280×720 and 256×144 (Leitão et al., 2018). Similarly, Tosi et al. (2020) observed that reducing the resolution of full HD images to 25%, resulted in mean velocity outputs differing by less than 0.05 m/s (<10%), with a reduction in computation time of roughly 23%. Further to this research, it is also demonstrated that reducing the resolution from full (1,430 × 1,080 px) to half (715×540 px) reduces power consumption enough to increase the number of cycles that can be performed on a single charge by 30% when using a 5,000 mA/h battery on a single charge (Livoroi et al., 2021). However, a formal analysis and evaluation of the influence of image resolution on resultant accuracy across spatial scales is generally lacking. The lack of consensus regarding the optimal resolution for image acquisition has led to researchers adopting intuition to define appropriate configurations (e.g., Dal Sasso et al., 2018). Ultra-HD

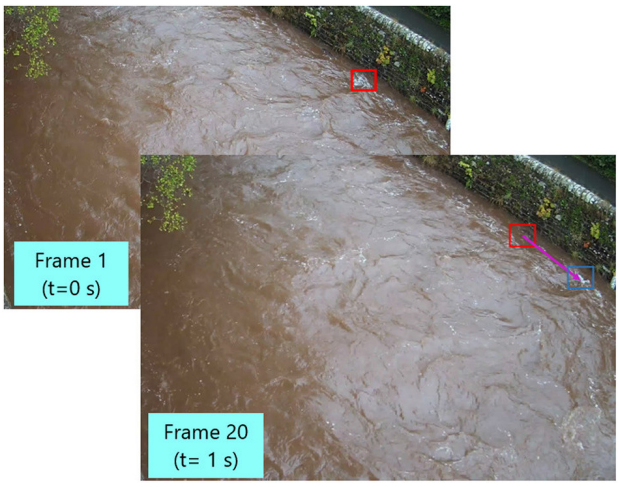


FIGURE 6 | Examples of usable tracers highlighted from a study using a fixed camera with frames exactly 1 s apart.

and 4K videos could be used to enhance tracer visibility (e.g., when sensing over long distances, or oblique angles), and to enable the sensing of smaller tracers (section 2.1.2). However, the processing power required to analyse higher definition videos is a constraint. In instances where imagery has been acquired at very high resolution (e.g., Ultra-HD and 4K), it may be beneficial to sub-sample the imagery to a lower resolution to improve processing speeds providing tracers are still visible.

2.1.2. Tracers

Tracers are thermally, or optically, distinct features present on the water surface that are advected by the current of the flow. Where hydrological conditions permit (e.g., fast-flowing, turbulent streams), sufficient naturally occurring features (e.g., foam, turbulent structures) may be present for successful image velocimetry analysis (see **Figure 6**). However, the spatial and temporal distribution of tracers can have a significant bearing on the performance of image velocimetry deployments with Meselhe et al. (2004) recommending that 10–30% of the surface should be traceable throughout the process. More recent work has strongly suggested that the density, dispersion index, and spatial variance of tracers are critical controls on the suitability and performance of image velocimetry approaches (Dal Sasso et al., 2020). Recent research into Seeding Density Indexing (SDI) shows that, by selecting frames to analyse based on optimum tracer characteristics (e.g., dispersion, density), then a reduction in surface velocity error of between 16.1 and 39% can be achieved using either PIV or PTV methods (Pizarro et al., 2020b; Dal Sasso et al., 2021). Consequently, by optimising frame selection based on SDI, discharge errors can be reduced to 0.12–0.4% of the total error seen when not optimising frame selection using PIV methods (Pizarro et al., 2020a). The most recent research into SDI has produced a threshold parameter (τ). τ sets a benchmark for frames and their subsequent SDI values, disregarding data that does not exceed the threshold SDI (Dal Sasso et al., 2021).

In instances where the spatial distribution of naturally occurring tracers is sub-optimal, with naturally occurring features that are either inhomogeneous in space and discontinuous in time, artificial tracers may be adopted. This is usually achieved by deploying an environmentally friendly substance such as bark or a decomposing polymer. They should be passive to flow, easily distinguishable, and have no effect on water quality (Detert and Weitbrecht, 2015). The size and the shape of the tracers is also important. As a minimum, tracers should be larger than 1px, which is a function of the ground sampling distance (see section 2.1.1; Dal Sasso et al., 2020), and their size/shape should be stable over time (Tsubaki et al., 2011; Tauro et al., 2017). Wu Tang et al. (2008) experimented with seeding sizes and shapes and determined that for artificially placed tracers, ellipsoidal particles of 2–5 pixels in size perform well. These are not large enough to be greatly affected by internal forces, and are less likely to form agglomerates compared to spherical tracers.

2.1.3. Capture Frame Rates

Commercially available cameras generally have default frame rates that are typically more than sufficient for capturing image sequences required for image velocimetry purposes (i.e., > 5 Hz). Given that the acquisition frame rate is not usually a constraint, the most important aspect is to ensure that the frame rate is consistent throughout the duration of acquisition (Perks, 2020; Detert, 2021), and that it matches the value present within the video metadata. This can be determined through analysis of the time stamps embedded within the on-screen display (Detert, 2021). This is generally configurable to be visible on footage acquired by Internet Protocol (IP) camera systems.

IP cameras are digital cameras which use networked connections to transfer data and can allow the user to access live imagery remotely (Safesite, 2021). Often, these types of cameras are connected to a data logger which can receive, store, and send the imagery. The limitation with some data loggers can be their processing power. For instance, frames can be lost from sequences if using a logger and there is insufficient CPU power. This impacts the time consistency of frames, something that is vital to accurately using image velocimetry.

Complications with these methods can also arise from a lack of bandwidth. Increasing the frame rate has been shown to proportionally increase bandwidth usage (1 fps = 0.179 Mb/s, 10 FPS = 4x more than 1FPS, 30 FPS = 7x more than 1FPS) (IPVM Team, 2021). The relationship between frame rate and bandwidth is not linear due to the way that IP cameras capture frames. IP cameras captures either an I-frame (*initial*/full frame or a P-frame (*predictive* frame). I-frames capture the entirety of the FOV and are used as a reference frame, whereas P-frames will only capture changes in an image in relation to the I-frame (Ace, 2013). The report by Ace (2013) also suggests that increasing the I-frame rate from 1 per second does not necessarily greatly improve image quality, but increasing the time between I-frames can significantly reduce image quality.

2.1.4. Managing External Environmental Conditions

The performance of image velocimetry analysis may be influenced by external environmental factors that cannot be easily controlled. These factors include the presence of wind, rain, varied lighting, fog, falling snow, and glare. The impacts of wind are most acutely seen during times of low flow when wind shear may produce a surface expression that is independent of flow velocity (Le Coz et al., 2010). A recent development on the impact of wind demonstrated that, on average, surface velocity deviates by 3% and can reach a maximum of 8%, most typically when wind opposes flow direction and when its magnitude is significant relative to the flow (Peña-haro et al., 2020). The impacts of precipitation are not fully understood but have been reported to blur imagery, ultimately interrupting the processing of data (Fujita et al., 2007). Inhomogeneous lighting and glare on the river surface generates the false impression of colour gradients across the area of interest. This variation in brightness may cause blind spots and the loss of tracer visibility (Hauet et al., 2008; Zhang et al., 2013). Fog impacts velocity results by severely increasing the noise on the surface of the river as it hinders the traceability of surface patterns; acquiring imagery during foggy conditions is generally to be avoided where possible (Zhang et al., 2013). Finally, for falling snow, there is little research in the true impact that it has on velocity results, however, in instances where large scale PIV has been used with falling snow present, authors tend to disregard data due to the scatter that it creates in results (Daigle et al., 2013).

The relative impact that these external environmental conditions have on the quality of image velocimetry results is currently unpredictable, and the overall impacts are currently unknown. Where there are instances of noticeable snow or fog, currently due to the lack of evidence saying otherwise, data should be disregarded. Secondly, the exposure of a monitoring location to variations in wind, precipitation, and glare should be minimised where possible through adjustments in the acquisition methods adopted. For example, in instances with high levels of glare the use of a polarising filter may be beneficial. Alternatively, near infrared (NIR) cameras may act to reduce the severity in brightness difference and may visualise the tracers more prominently. However, it should be noted that application of NIR sensors in some environments may lead to the loss of visible tracers due to attenuation of the NIR signal by the water (Zhang et al., 2013). Whilst future work will seek to provide correction factors for observable external environmental conditions (e.g., wind shear), these relations have yet to be established so their effects should be minimised where possible.

2.1.5. Choice of Platform

Fixed stations allow a specific area of river to be analysed, providing a time-series of images that can be used to determine surface velocities. Usually, fixed stations are commissioned in order to monitor river flows, and to develop and extend discharge rating curves (e.g., Hauet et al., 2008). There are several ways that fixed stations can operate in regards to the capture and processing of data. The study of Tosi et al. (2020) evaluates methods of capturing and processing data *in situ* to reduce the amount of data that is required to be sent via external networks. This can be useful where stations are in remote locations and affordable networks (e.g., mobile networks), are scarce. Alternatively, as seen in the case studies of Perks (2020), networked cameras (as discussed in section 2.1.3) can be used to stream imagery across a network to be processed either near real-time or at a later date.

Regardless of the proposed fixed station processing method, limitations include the inability to alter the field-of-view without recalculation of the coefficients for converting pixel space to real world distances (see section 2.2.2). Resultantly, there is the potential for the site configurations being optimal under certain flow conditions, but unsuitable during others (e.g., during bypass flows, out-of-bank flows, etc.) Additionally, supplementary information is required in order to properly scale the imagery as a result of fluctuating water levels. This is typically in the form of river stage measurements which enable the distance between the water surface and the camera to be accounted for.

Alternatively, mobile platforms may be used to acquire footage for image velocimetry purposes. An example of this is the use of Uncrewed Aerial Vehicles/Systems (UAVs/UASs), or helicopters in fluvial environments that are hard to reach, dangerous to the operator, or where the inundated extent is greater than the field-of-view of the fixed monitoring station. These approaches have been particularly beneficial for understanding turbulent flows in rivers for sediment transport (e.g., Thumser et al., 2017), capturing flow data at ungauged sites (e.g., Kim et al., 2008), and determining river velocities during periods of high-flow (e.g., Perks et al., 2016). Additionally, this has opened up the possibility of large spatial extents being observed rapidly (e.g., Perks, 2020). Generally, using a mobile platform involves similar processes to those of fixed stations, but requires some extra stages in the pre-processing stage such as image stabilisation (see section 2.2.1). A key advantage of using mobile platforms for image capture over fixed stations is that many of the optimisations listed in section 2.1 could be met (e.g., camera angle being nadir, flexible fields of view, and spatially consistent GSD).

Although UASs are currently the main focus of mobile methods, it is important to note that there are other methods of mobile image velocimetry. Prior to UAS being reasonably attainable, mobile methods could be conducted using telescopic poles, as demonstrated in Le Coz et al. (2010) and Dramais et al. (2011). Secondly, an important revelation of mobile image velocimetry is the use of software on mobile phones (Hain et al., 2016; Caldwell et al., 2019). Lab based studies on the use of mobile discharge apps (e.g., DischargeApp) show that the methods can reproduce discharges without the need of illumination within a 15% error 87% of the time (hand-held), and 100% of the time using a tripod (Carrel et al., 2019).

A more recent and promising advancement is the use of satellite imagery as a capture method, but is still in its infancy of development. There are limitations to using satellite data, such as the limitation of the GSD that is achievable by satellite imagery and whether it is capable of detecting and tracking features on a river surface. For reference on image quality, Kääb et al. (2019) uses satellite imagery to track river-ice and water velocities, and does so with a resolution of 3m using PlanetScope satellite imagery (Planet Labs Inc., 2021), capturing each frame

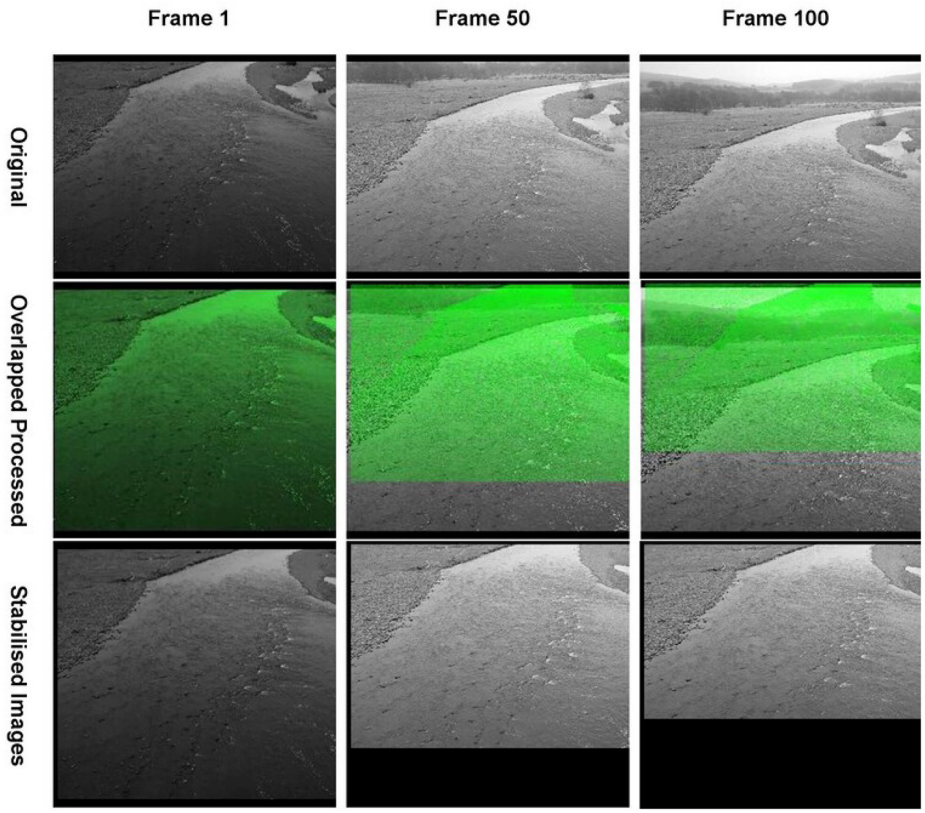


FIGURE 7 | Drone movement shown by overlapping stabilised frames onto original frames. The green mask seen on the processed row highlights where the stable image is within frame, with the final stabilised images cropping all unstable edges.

at 90 s intervals. Satellite data stores (such as PlanetScope), are capable supplying high-resolution image sequences (as seen with Kääb et al., 2019), and videos of less than or around 1m resolution (typically nadir). Video footage is usually only captured in the panchromatic band of the central detector and at a frame rate of between 30 and 120 FPS. It is still yet to be seen how well these datasets can provide river flow gauging, and much more research is required into the feasibility of satellites before it can become a recommended method of remote sensing using image velocimetry.

2.2. Pre-processing

2.2.1. Stabilisation

Image stabilisation is required due to the inevitable movement of mobile platforms (e.g., Perks et al., 2016; Bolognesi et al., 2017), and random movements of fixed cameras from vibrations due to influences such as wind or traffic (when fixed on a bridge) (Perks, 2020). **Figure 7** demonstrates how images are impacted by stabilisation. Borders of the full initial image are cropped out by the algorithm in each frame (shown as the black boxes around the edges of the image) to only show the sections that are constant (shown in the green overlapping of imagery). Here we can see transformations in both shift and scale due to platform movement. Modern methods of stabilisation may use GPS locations of the camera and/or stable features in the region of interest to create a stable frame of reference for subsequent analysis (Ljubičić et al., 2021).

Stabilisation takes into account the effect of image translation, rotation, and scaling. Translation of the scene is a movement in the image within the xy plane (parallel to the ground). Rotation is a movement that causes a tilt in any direction of the camera (yaw, pitch, and roll). Scaling is impacted by change in platform elevation (z-direction) resulting in changes to the representation of pixel sizes in real world units. When running feature detection algorithms, static points are used and are either detected corner points or clearly distinguishable stationary objects. For a full projective transformation, a minimum of four pairs (eight features), are required (Szeliski, 2006) to match the degrees of freedom (three pairs are required for affine transformations). Stabilised frames are often referenced to either the initial frame, or a subsequently stabilised frame (every *nth* frame of a series). This may be achieved using a 3D stabilisation technique (e.g., structure-from-motion; SfM), or more commonly a 2D motion estimation technique e.g., single-step discrete Fourier transform algorithm (Guizar-Sicairos et al., 2008), whereby it is assumed that the moving camera is perpendicular to the region of interest and undergoes only changes in the horizontal plane (movements in translation and yaw), and hence, planar transformations are sufficient (Rodriguez-Padilla et al., 2019).

Stabilisation techniques can be manual or automatic. Manual methods rely on a selection of static reference points which are then automatically processed to determine displacement between frames (Rodriguez-Padilla et al., 2019), while automatic methods select features and then track displacements using binary feature matching techniques (e.g., Harris Corner Detection and FAST) (Liu and Cheng, 2008; Muja and Lowe, 2012; Mingkhwan and Khawsuk, 2017). A general process for stabilisation techniques is: breaking down videos into sequential frames, selecting of static features manually or automatically (i.e., feature detection), feature matching and outlier rejection, derivation of transformation function, and image reconstruction and stitching (Tareen and Saleem, 2018). The coordinate grid can either be fixed or be updated throughout the process. Whilst fixed coordinate grids are typically used, the grid may need to be updated over time if there is excessive movement (e.g., translation of the platform). Grids may be altered through the use of similarity, affine, or projective transformations. Accurate transformation depends on the number of point pairs available in the image. Similarity transformations require shifts in the plane parallel to the ground and can result in translational, rotational, and scaling transformations. For these, a minimum of two point pairs are required. Affine transformation includes the same shift changes as similarity with the addition of shear transformations. This requires three point pairs. Finally, for a full projective transformation which includes all of the above as well as perspective deformation, four point pairs are required (Ljubičić et al., 2021).

For fixed cameras, stabilisation is not necessarily required, unless the camera experience movement (e.g., oscillations generated by vibrations, or wind). Detert and Weitbrecht (2015) observed that residual motion of 1 px/s caused by camera shake produced an apparent ground velocity of at least 0.02–0.03 m/s. More recently, Detert (2021) observed that the lack of stabilisation of image sequences acquired using a telescopic pole produced a shift in both image axes by upto ± 4 pixels per time step (equivalent to 2 cm in this instance). This unaccounted for movement may substantially impact velocity outputs, especially under flow velocity conditions, relative to the amount of movement seen in frame. When using mobile platforms to acquire footage for image velocimetry purposes, unstabilised image sequences may be a major contributor toward error. An example of this is presented in Detert (2021), where a re-analysis of previously published studies demonstrated that accounting for residual movement reduced errors by 20–30%.

2.2.2. Orthorectification

Following stabilisation of the image sequence (when required), orthorectification needs to be carried out, unless the image is being captured at nadir and image distortion has been removed. This seeks to remove perspective distortion and manipulate the image to represent accurate real-world distances. Orthorectification manipulates an image such that all pixels are of equal real world length, such that when using a camera at an oblique angle, a pixel in the foreground is equivalent to a pixel in the background.

Orthorectification relies on Ground Control Points (GCPs) to calibrate known coordinate points in the field of view (Tauro et al., 2014). GCPs that have known real-world coordinates are established in the frame of view and these are paired with the pixel location of these GCPs. 2D transformations can be made when the GCPs are located on a similar plane to the surface of the river. 2D transformations have an 8-parameter plan-to-plan perspective projection, which requires at least four GCPs at the river free-surface elevation (Fujita et al., 1998; Detert and Weitbrecht, 2015; Detert et al., 2017; Detert, 2021). 3D transformations are made where there are large variations of elevation seen between GCPs and the river surface. If this is the case then the orthorectification matrix will have 11 unknowns and therefore can only be solved with six or more GCPs (Jodeau et al., 2008). It has been suggested that a minimum of 4 GCPs should be used in or immediately around the region of interest to best orthorectify 2D imagery captured orthogonally to the river surface (Detert and Weitbrecht, 2015; Detert et al., 2017; Detert, 2021), however, reliability of orthorectification can only increase with the number of accurate GCPs used. An increase in GCPs used increases the redundancy of the orthorectified system improving the reliability of the results.

The process of orthorectification can either be explicit or implicit i.e., transformations can either be applied to the raw footage (explicit), or to the vector fields (implicit). Higham and Brevis (2019) suggested that orthorectification of the velocity vector field, rather than the imagery, is more effective in most cases, more specifically with PIV examples. The smoothing of data is a process where the extremities of results are normalised and brought closer to the average. When footage undergoes PIV analysis, vectors are created using an average of the interrogation area surrounding it. This process of using the average values for vectors inherently smooths data, reducing the impact that spurious/outlier tracer velocities has on the overall results. If orthorectification is applied after PIV analysis, then any spurious vectors which have been smoothed due to the averaging of the area will have less of an impact on error associated with converting pixel size to real world lengths and consequently velocities. Alternatively, if this is done explicitly, then applying transformations to erroneous velocity values can exaggerate them, reducing accuracy. Conversely, explicit orthorectification has the advantage of ensuring each pixel has the same real-world dimensions prior to processing (Perks, 2020). An example of explicit orthorectification can be seen in **Figure 8**.

2.2.3. Image Manipulation

Image manipulation is the process of altering the properties of the acquired images with the aim of reducing interference (e.g., glare, visibility of the river bed, environmental impacts such as wind and rain), and enhancing the visibility of tracers. The first step in the image manipulation process is the conversion of multi-band imagery into single-band imagery (e.g Fujita et al., 2007; Dobson et al., 2014). However, this is not required when footage is captured using a —scale camera (e.g., Patalano et al., 2017), or thermal camera (e.g., Kinzel and Legleiter, 2019). The conversion of multi-band imagery to grey-scale is achieved by eliminating saturation levels and hue, keeping only levels of luminance

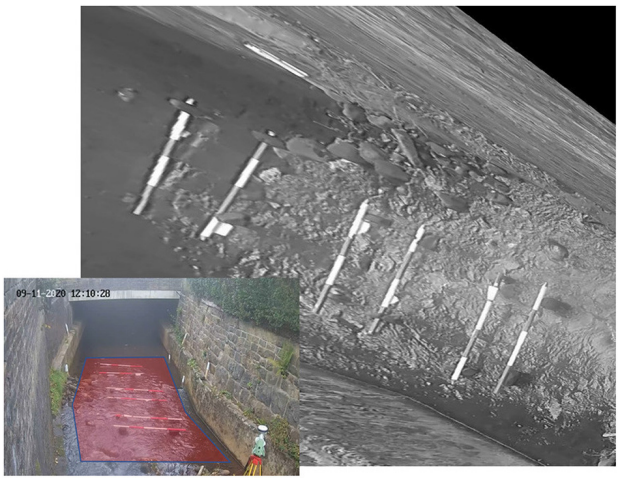


FIGURE 8 | Example of a river surface acquired at Todmorden, UK (bottom left). The red region indicates the region of interest selected by the user. The greyscale image is the orthorectified product produced using KLT-IV.

(Perks, 2020). Subsequent image manipulation is optional but may be beneficial.

Frequently used image enhancement techniques include: intensity normalisation, histogram equalisation, contrast limited histogram equalisation, and binarisation, which are all further explained below (Thielicke and Stamhuis, 2014; The Mathworks Inc., 2020). One of the most important processes for most image velocimetry techniques is to enhance imagery through contrast enhancement steps (Dellenback et al., 2000). Improving the contrast of images helps tracers stand out more in comparison to their environment, making tracking more effective and increasing displacement peak detectability, ultimately improving velocity fields (Deen et al., 2010). **Figure 9** highlights the process of typical image processing carried out in PIV and PTV methods. Some of these methods were used in the examples seen in **Figure 10**.

Intensity normalisation spreads out the contrast histogram of an image such that a user defined percent of the image is saturated in the high and low intensities. For footage where tracers are barely distinguishable, normalisation may improve the contrast of the colours across the image. Histogram equalisation is the process of enhancing contrast by averaging out the brightness variation across the band. It increases the range and standard deviation of colour histograms and introduces a larger statistical range (Jyoti Bora, 2017). This has been shown to be effective in situations where a colour band shows a cluster of contrast level (Fujita and Aya, 2004). Image binarisation typically uses threshold algorithms to split histograms into two, sometimes using several sub-processes such as background detection and edge detection (Malepati, 2010) to ensure foreground textures stand out as much as possible against their backgrounds (Tensmeyer and Martinez, 2020). This can be especially useful when, despite all previous efforts, tracers are still not prevalent to their background and surroundings. To improve the impact of all image manipulation processes, it would be recommended that footage limits the amount of unnecessary image in frame, and focuses on the area of interest to ensure that the stretch of the normalisation is altering tracers and the water surface, as opposed to surrounding vegetation.

Should the background of the image or river bed be too prevalent in imagery and there is a bias error toward zero displacement, then it is advised that it is removed. To do this, it is possible to use the double-frame background removal process (Honkanen and Nobach, 2005; Patalano et al., 2017). Subsequent frames are analysed and anything that remains stationary between the two frames is defined as background and noise, and therefore can be removed from the image. This will leave only the tracers that have been displaced. Detert and Weitbrecht (2015) makes a point of applying numerous methods of manipulation to achieve the clearest possible tracers. The study uses grey-scaling but also uses a Gaussian filter to remove noise in the background (which helps sharpen edges), then it sets the intensity of pixels below a certain limit to zero and finally performs CLAHE.

To summarise these findings, there is a clear generalisation of processes for image manipulation and pre-processing of videos for image velocimetry. As a minimum, images should be converted to a single-band image (e.g., grey-scaled) and cropped to the area of interest to reduce unnecessary data processing and noise where possible. If tracers are not clearly distinguishable from the surface throughout the video, imagery should be normalised to highlight areas of most intense light and dark, and equalised to further distinguish the average levels of brightness seen across the image. Should this not be enough and the background or bed of the river is still overwhelming the tracking features, Gaussian filters can be applied to decrease image noise and sharpen edges or background removal can be used to remove the background altogether, followed by a binarisation of the image in an attempt to isolate the tracers.

2.3. Image Processing

2.3.1. Founding Principles

The founding principles upon which image velocimetry algorithms are based, stem from either Eulerian or Lagrangian techniques, which are used to describe inter-dimensional flows (Hirt et al., 1974). These techniques are then applied to image velocimetry methodology. Lagrangian is the basis of PTV methods, and Eulerian is the foundation of PIV methods (Amelinckx, 1971; Euler, 2008). These principles alter the way that we perceive and record velocimetry data such that, if we were to record an identical point at the same instant using both methods, similar results are not guaranteed (Durst et al., 1984). With Lagrangian/PTV motion, the particle's velocity vector can be described at any given point in space-time. It provides a complete assessment of the dynamics of a fluid particle, knowing where the particle is in any given moment and what velocity it possess, making it a function of time in respect to an initial position (Price, 2006). Conversely, the Eulerian/PIV approach is the movement of a fluid past a control volume of known coordinates, making the velocity a function of a fixed space and time.

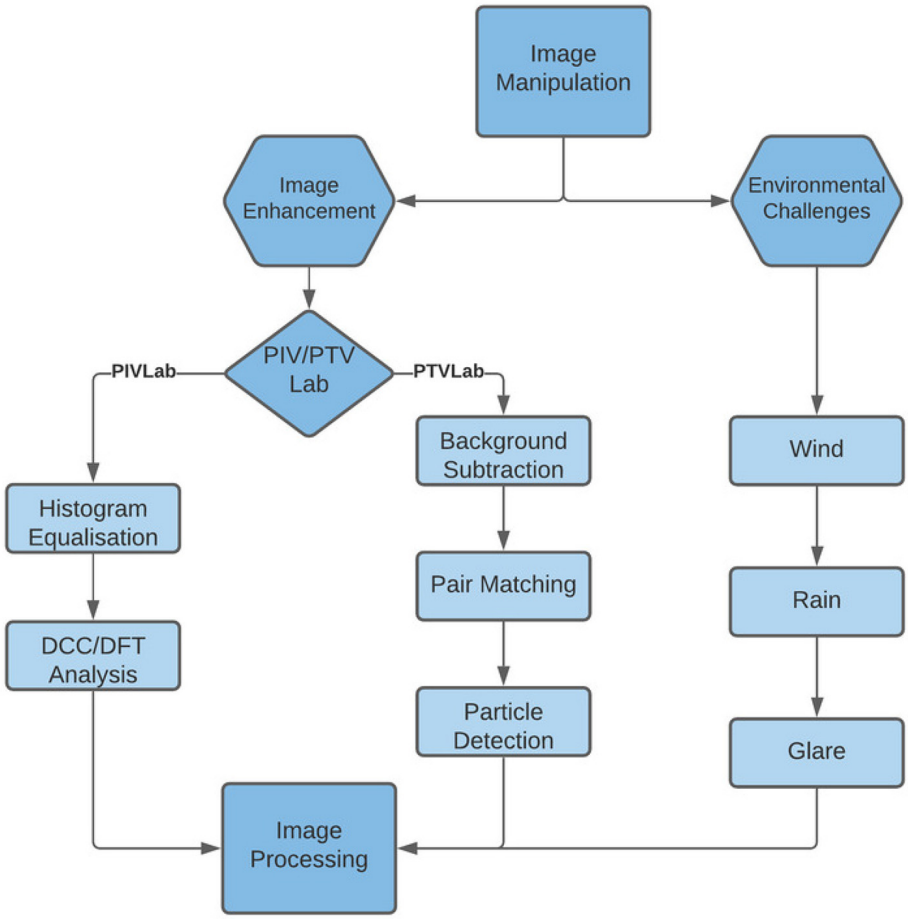


FIGURE 9 | A remodel of the Patalano et al. (2017) study, showing a flowchart for typical image processing sub-sequences with either PIVlab or PTVlab.

Problems can occur with Lagrangian/PTV motion when using natural tracers, as natural tracers are not entirely stable in structure and are capable of deformation, breaking-up, agglomerating, and interacting with one-another. Deformation of tracers also impacts upon the tracking of a centre of mass which, if a tracer deforms, can change position and ultimately impact the assessment of the tracers dynamics. For Eulerian/PIV, cross-correlation methods are used to determine patterns on the river surface and does allow for some transformations in tracers, so long as the 2D patterns are broadly consistent between the interrogation and search areas (Keane and Adrian, 1992).

2.3.2. Flow State

Steady flow is used to describe fluid properties that remain constant with time, while unsteady flow does not. In the case of open channels where velocity is the property in question, we must look at the rate of change of velocity in respect to time, also known as acceleration. For steady flow, we require that $\frac{\delta v}{\delta t} = 0$, whereas for unsteady flows $\frac{\delta v}{\delta t} \neq 0$. One of the core assumptions of Eulers equation of motion is that of steady flow (Euler, 2008). Eulerian motion and PIV focuses on set of known locations of flow and represents an average of a body of fluid through a known location at a specific time (Durst et al., 1984). Although this average can potentially represent useful analysis of a body of fluid regarding an average of flow velocity for use in discharge estimation, challenges arise when sections experience multi-dimensional acceleration, as a variation of velocity as the steady state assumption is not met. Lagrangian and PTV does not encounter similar issues regarding flow steadiness because its foundations are built around calculating the particles position at any given moment in time (Durst et al., 1984). These conditions are typically assumed as reasonable for many applications of PIV as the technique tends to analyse two consecutive images with only a minor time-step.

2.3.3. Feature Detection and Tracking Schemes

PIV and PTV adopt differing principles for the determination of flow velocities. PIV uses an Eulerian understanding of flow motion, using dimensions of length along the river as search areas, utilising tracers or visible patterns that pass through or along these sections to calculate instantaneous velocity vectors for each area. Conversely, PTV uses the Lagrangian approach to calculate flow velocity, focusing on individual particles

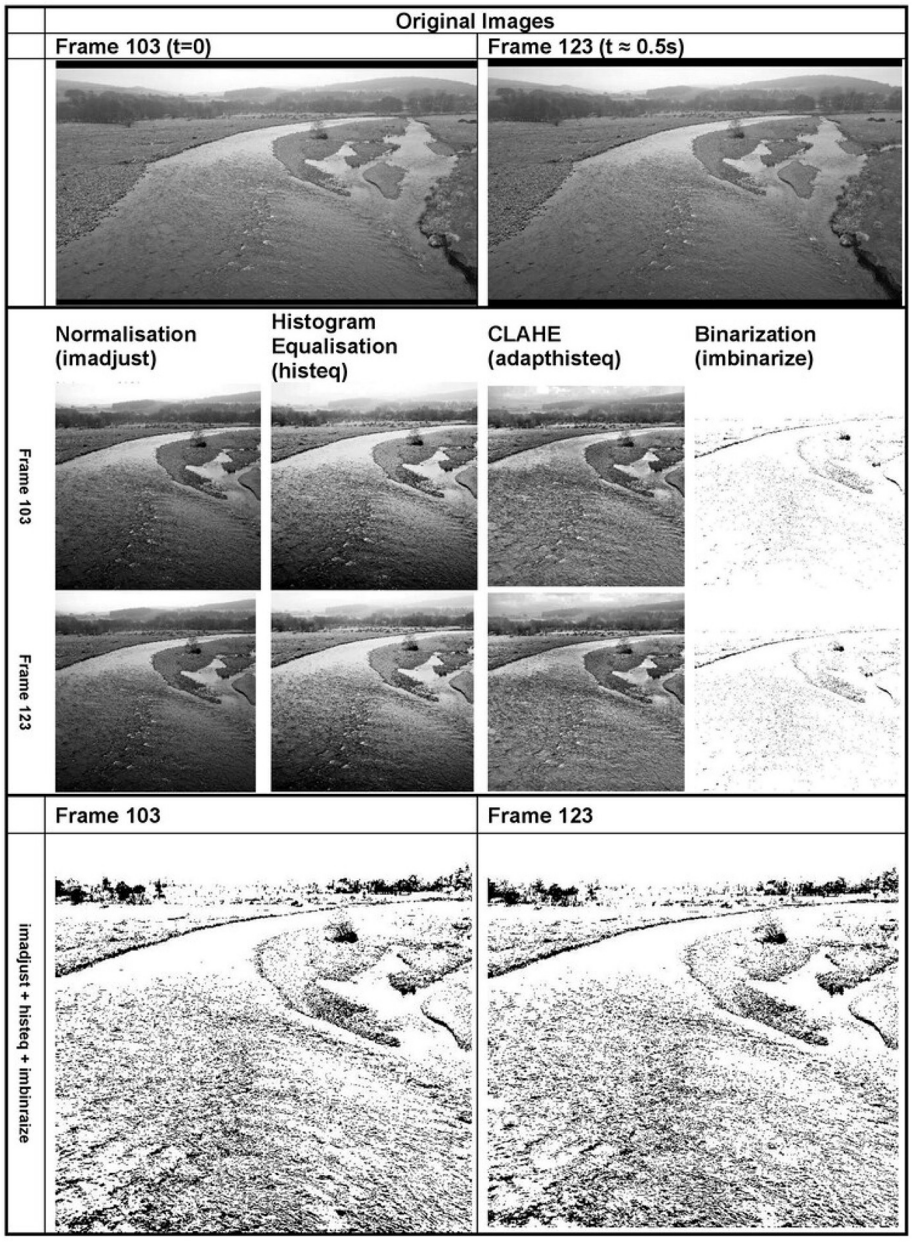


FIGURE 10 | A series of image manipulation processes performed in Matlab using frames from the same video file. Note the amount of information in the binarized images if normalisation and histogram equalisation is performed prior. This shows that there are cases where more than one method of pre processing can improve the amount of data that is traceable by programmes.

of flow visible on the surface and tracking their movement through space.

PIV utilises search and interrogation areas within an image to obtain particle displacements (**Figure 11**). Small window interrogation areas are tracked within larger search areas, and the centres of the interrogation areas are measured regarding distance and divided by the time between frames to produce an average velocity over that search area (Muste et al., 2008). This approach has been shown to be capable of producing highly accurate results (e.g., Creutin et al., 2003; Muste et al., 2008). Given that a collection of individual tracers (surface patterns) are used to infer displacement, this approach is less sensitive to the transformation of individual features. However, inhomogeneity and discontinuity of tracers are critical issues that may negatively affect the quality of PIV analysis. In these instances, PTV techniques may perform better over PIV techniques (Tauro et al., 2016).

PTV-based approaches (**Figure 12**), rely on tracking individual particles along a long-profile. This technique has been shown to perform well under low seeding density conditions

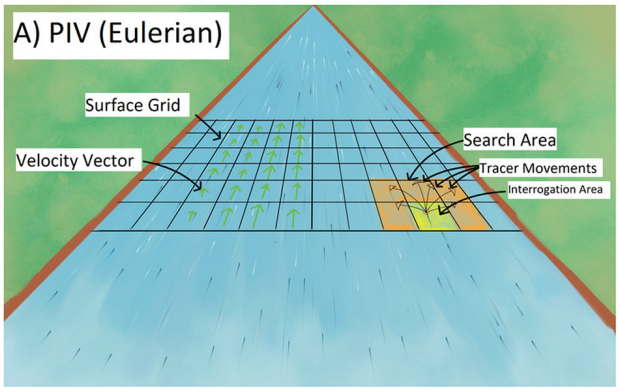


FIGURE 11 | Schematics of general PIV **(A)** mechanics.

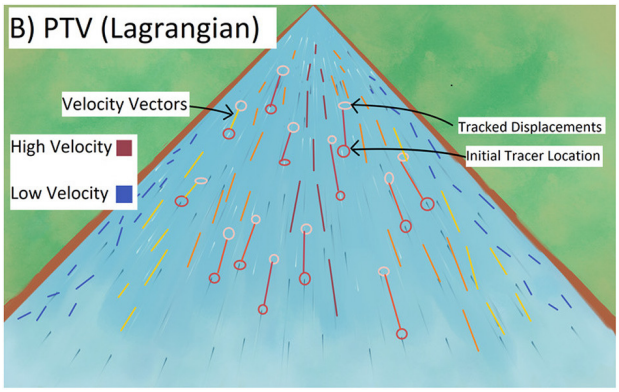


FIGURE 12 | Schematics of general PTV **(B)** mechanics.

(Lloyd et al., 1995; Tauro et al., 2017). However, analysis may be adversely affected in instances where tracers change shape, size and from time-to-time disappear from frame. The greater number of tracers that are successfully tracked, the higher the probability of producing an accurate representation of the surface velocity. However, as the number of tracers increases, the required processing time/power also increases. The presence of very high tracer densities may also increase the ambiguity of the individual tracer detection and tracking process (Zhang et al., 1997). There are a range of particle detection and tracking algorithms available for PTV. For feature detection, Good Features to Track (GFTT) (Shi and Tomasi, 1994), FAST (Rosten and Drummond, 2006), and SIFT (Lowe, 1999). For tracking algorithms, cross-correlation can be used, but there are also others such as Kanade-Lucas-Tomasi (KLT) (Tomasi, 1991; Perks, 2020), and variations of the Nearest-Neighbour algorithm (e.g., Tauro et al., 2019).

Studies into the optimisation of processing using synthetic models have been highly successful in recent years in highlighting potential areas that are prone to causing errors in velocity results. The importance of the synthetic studies is to aid in selecting appropriate optimisations for differing scenarios (e.g., video length and frame rate). Both Pumo et al. (2021) for LSPIV and Dal Sasso et al. (2018) for PTV methods concur with the Pizarro et al. (2020a) study in that the concentration of particles are a crucial variable in relation to relative error. They also agree that, where seeding density is below-optimal, longer durations of imagery are required and that the contour region around the border of frames should not be included within analysis. These current pieces of synthetic research, however, acknowledge the studies are not exhaustive in variables considered, and more is required to cover more areas of associative error.

Table 1 summarises software suites that are available for users that wish to perform PIV or PTV analysis. Each software will have its own feature detection and tracking scheme, along with varying methods of preparing and presenting data. Each software suite comes with a user-friendly GUI to load in imagery and perform several pieces of analysis on. The suites listed in this table are open-source or freely available to use.

2.4. Post-processing

Post-processing has two main elements; error reduction (e.g., vector correction, section 2.4.1), and velocimetry application (section 2.4.2). Error reduction is the process of highlighting and filtering possible erroneous datasets and velocity fields, while progressive calculations can use the velocity data and apply it to secondary datasets, such as when using the surface velocities to calculate discharge (through the incorporation of alpha values and bathymetry information).

2.4.1. Vector Correction

Post-processing may reduce errors through the application of statistical methodologies to highlight and filter erroneous outputs. For PIV, details of vector validation can be found in the study of Raffel et al. (2018), which implements several statistical methods of achieving data validation. Statistical validation methods perform similar techniques to distinguish outliers in PIV data, and do so typically by comparing vectors to its surrounding neighbours (Hart, 2000; Masullo and Theunissen, 2016). Alternatively, there is a bootstrapping technique available that does not generate statistics from its nearest neighbours, but instead, a statistic is generated for each component (Pun et al., 2007). Typically, the difference between each method is the type of statistical calculation applied to determine outliers. The basic statistical methods include, but are not limited to, vector difference tests, median tests (Westerweel, 1994), and normalised median tests (Westerweel and Scarano, 2005). Masullo and Theunissen (2016) suggests that overall, the most common detection techniques used in practice are the universal outlier detection scheme (adaptation of median test but normalises the median residual with respect to an estimate of local variation) (Westerweel and Scarano, 2005), and the distance-weighted universal outlier detection scheme for unstructured data (a generalisation of the universal outlier detection method, but with a variance in the definition and weighting to neighbouring vectors) (Duncan et al., 2010). These should be used in all studies where spurious vectors are evident (especially with evident turbulence) (Westerweel, 1994), or results of velocimetry are being used for further applications (e.g., discharge).

TABLE 1 | A non-exhaustive, generalised, overview of software suites that are currently available with some of their requirements and functions listed.

Software	Overview	Requirements and functions
PTVlab (Brevis et al., 2011)	PTVlab is also a MATLAB code, using particle identification to track movement. PTVlab enhances the images to better show particles and their centroids. With this data, it performs integrated cross-correlation and iterative relaxation labelling techniques to better represent varying seeding densities and track their trajectories.	Image enhancement is performed to highlight the flowing particles and their centroids which are tracked by the software. This tracking requires the user to input interrogation area sizes.
Fudaa-LSPIV (Le Coz et al., 2014)	Fudaa-LSPIV is a free software created using a Java GUI. It begins with image pre-processing taking video clips and converting image sequences into PGM ASCII formats. It then sequentially performs orthorectification, PIV analysis, result processing, and discharge computation. Within the software is the ability to visualise and export the data in different formats.	For accurate results, users will need to input GCPs, water level estimations and the positioning of the viewpoint. For discharge measurements, bathymetry profiles area required.
PIVlab (Thielicke and Stamhuis, 2014)	PIVlab is available as an open source GUI within MATLAB, using several of the built-in processes that MATLAB has to offer regarding image pre-processing, image analysis, post-processing and data exploration, producing outputs in video, image, or vector map forms.	The software uses image enhancement, camera calibration and orthorectification improve the images. It relies on the user to choose interrogation and search area sizes to perform direct cross-correlation and direct Frourier transformations.
RIVeR (Patalano et al., 2017)	RIVeR is a standalone MATLAB code that uses the theories behind PIV/PTV software but has been designed to provide a simple user-friendly application. It extracts images from video footage, processes them using PIVlab/PTVlab algorithms, then uses GCPs to orthorectify the images and produce velocity and/or discharge results.	Video image extraction rates, frame rates, colour depths, and camera and lens parameterisation is required as an initial input to the software. GCPs also need to be referenced in the images for orthorectification. For discharges, section bathymetry is required.
OTV (Tauro et al., 2018)	OTV processes data through feature detection, feature tracking (using the Lucas-Kanade algorithm), and trajectory-based filtering. This improves the reliability of the velocities as it only retains what are believed to be reliable feature trajectories to reduce error. This produces an average surface velocity estimation.	The software automatically detects features and does not rely on inputting tracers. The direction and length of the flow is determined by the user, who can also determine the quantity of trajectories. Can be mildly affected by lower resolutions and image frequency.
Photrak. SSIV (Leitão et al., 2018; Carrel et al., 2019)	SSIV uses cross-correlation like most other PIV methods, but unlike other PIV methods, SSIV filters erroneous vectors rather than attempting to correct them. Photrak has two systems available for use: DischargeKeeper which is a fixed IP camera with local processing for continuous measurements, and the DischargeApp for smartphone compatibility. Initially designed for use with consumer-grade surveillance equipment in urban environments.	SSIV requires full camera calibration to take place, with several reference points in the frame of view for orthorectification of the images. Search and interrogation areas need to be defined by the user. Without water level information, SSIV cannot provide discharge but only flow velocity.
KLT-IV (Perks, 2020)	KLT-IV is a user friendly interface that aids users with a step by step process, taking video sequences from fixed or mobile platforms and GCP data and producing surface velocity results and discharges (with the addition of alpha values and cross-sectional data). The software allows users to stabilise videos and orthorectify frames. KLT-IV uses GFTT and subsequently the Kanade-Lucas-Tomasi tracking scheme for tracking. This is a pyramidal tracking scheme that searches 30 iterations within interrogation areas to find the new location of each point until it reaches convergence, discarding any results that produce an error of 1px or more.	For accurate results, camera calibration is required. This relies on knowing the model of the camera for removal of lens distortion and orthorectification of images. This software then tracks individual trajectories through a known "extraction rate," block sizes, and known reference points. Variations occur dependant upon extraction rates.

Typically, corrective methods for spurious vector will perform statistical analysis as seen above to detect outliers and determine if it falls under a set threshold as to whether or not it is likely a false reading or likely to be reliable. If it is determined to be erroneous, the vector should be removed and replaced using most commonly, a 2D interpolation, or alternatively linear or polynomial interpolation (Stamhuis, 2006). Some common PIV statistical corrective methods are: Penalised Least-Squares Method (Tang et al., 2017), Kriging Regression (De Baar et al., 2014), and Proper Orthogonal Decomposition Outlier Detection (POD-OC) (Wang et al., 2015). Replacing these vectors is important to ensure the results produce statistically meaningful velocities, and without it, can limit the accuracy, resolution, and usefulness of PIV (Hart, 2000).

For PTV data, detecting erroneous vectors is slightly more challenging due to its unstructured features (i.e., does not conform to a gridded system when processing, like seen with PIV methods). Many common PTV algorithms stem from techniques used by PIV regarding the way that it associates vectors with its nearest neighbours, but are altered to deal with the issue of identifying neighbouring vectors in PTV, and not being equally spaced. For PTV validation and correction, should there be more

than 15% of outliers, automated programmes could potentially fail to highlight them due to algorithms using neighbouring velocities to determine what classifies as an outlier and should there be a high percentage of outliers, determining what is correct, and what is not, is challenging (Duncan et al., 2010).

Techniques for PTV error correction typically involve a smoothing of displacement fields to use as a baseline to outliers (e.g., Akhmetbekov et al., 1996; Young et al., 2004). Duncan et al. (2010) constructed the Universal Outlier Detection Scheme (which can be used for both PIV and PTV), but it is a development of the algorithm from the Westerweel and Scarano (2005) study for PIV correctional algorithms. An alternative to these methods, is a model based technique (e.g., Young et al., 2004), which has been shown to validate upto 25% of outliers. In this study, the model is described as a 5-stage process. The first stage is initialisation, which involves displacement normalisation, the building of constraints, and then a regularised version of the displacement field is calculated. Secondly is relaxation, this stage produces a displacement field where invalid estimates are replaced with statistically more likely vectors. Third is point removal which uses several statistical methods to determine validation scores (based on user defined thresholds and a T value determined in the relaxation stage). The next stage is attraction designed to iterate landmarks toward their associated termination landmarks. Finally, displacement interpolation which can be used to estimate the displacement at any position in the image field.

2.4.2. Velocimetry Applications

The most common application for image velocimetry datasets is attempting to calculate discharge. Discharge can be calculated with the introduction of known, measured, transects of the river within the camera field of view. These transects can be part of the geo-referencing local coordinate system and measured at the same time as the GCPs. For the discharge calculations to be as accurate as possible, when using PTV methods especially, the river surface needs to have a good spread of tracers, and where this is not the case, it is possible to interpolate or extrapolate measurements using polynomial, cubic, or the constant Froude method (Perks, 2020). Typically, discharge can be estimated using a velocity-area method, introducing typical fluid mechanics parameters [e.g., depth-average velocities, influenced by α (Le Coz et al., 2010)]. When calculating α values, vertical velocity profiles can be found using an aDcp, but Creutin et al. (2003) finds that using 0.85 is a reasonable assumption where this is not possible. Combining α with the calculated velocity, along with bathymetry can give reasonable discharge calculations as found with many studies on river discharge (e.g., Kim et al., 2008; Le Coz et al., 2010; Perks, 2020).

An issue to consider when studying river discharge via velocimetry is the variation of river channel cross-sectional area due to rising stage scour and waning stage fill, or due to passage of sediment waves and bed forms even in more steady flows. It is suggested that after peaks of high flow that river bathymetry is remeasured to ensure that cross-sections are as accurate as possible.

More recently, as an alternative to using estimated alpha values, mobile image velocimetry techniques have been used to derive Gauckler-Manning-Strickler coefficient (K), for cross-sectional roughness in rivers (Bandini et al., 2021). The method simultaneously solves for K and discharge using both linear equations of Manning's and the mean-section method for computing discharge from depth-average vertical velocity. The uncertainty at the 95% confidence level resulted in most of the observations to be near $\pm$10% of the *in situ* discharge measurements. This method can be used to counter issues with streams that are non-ideal (e.g., highly meandering, non-uniform in slope, etc.).

For users who are looking to apply image velcoimetry to analyse data for the first time, it can be difficult to understand which method (PIV or PTV), to use. The research presented throughout this study should provide some indication on what is the best method for the particular datasets. For further information to help aid decision making regarding methodology choices and how to best apply PIV or PTV, see **Table 2**. These papers have been studied and briefly summarised regarding the background of the site, the hardware that the method uses, and the results that are discussed by the author. This also includes the challenges that the author faced, as well as the possible causes for such challenges. These papers have been selected as they provide similar but different methodologies using PIV or PTV (e.g., fixed platforms, mobile platforms, thermal cameras).

3. CONCLUSION

Over the last two decades researchers have created numerous techniques for both PIV and PTV methods. Algorithms have been shown to be capable of estimating surface velocity accurately (compared to that of aDcp's), however, the onus is on the user to decipher the ideal methodology. The aim of this research was to present and discuss instances of best practice for image velocimetry processes based on existing papers and case studies, summarised by **Figure 2**. Where this study has stated it was not viable to suggest an optimal setting due to the lack of information surrounding the topic, example case studies were provided in an attempt to suggest precedence as an alternative.

Research was categorised into four main topics: capture optimisation, pre-processing, processing, and post processing. For capture optimisation, GSD should be as small as possible without having to rely on high resolutions. Adding an angle to the camera can skew GSD in the background of images and this should be accounted for where the region of interest overlaps foregrounds and backgrounds. Tracers are a critical part of image velocimetry techniques and it is important that they remain stable and cover at least 10-30% of the region of interest consistently. It is important that frame rates remain constant throughout the process and this can be checked against time stamps provided by most video cameras. The choice of platform used to capture data depends on the event that is to be captured. For capturing single events or for short term studies, UAS can be used but needs additional steps such as stabilisation. For longer

TABLE 2 | A selection of application papers chosen due to their variation of hardware and software suites.

Details	Background	Results
Author: Creutin et al. (2003) Case Study: Iowa River, Iowa Software Application: In-house algorithm (PIV)	"Proof of concept" research paper. PIV was used without artificial tracers. GCPs used with a 70 m wide channel. Ten, 10 min, recordings used for processing. Sony DCR-TRV320 camera used at an angle of 60° and 14 m above the river level. GSD was 6.4 pixel/m. Interrogation areas set at 64 × 64 pixels and search areas set at 24 pixels.	Discharges from the 10 sequences ranged from 50 to 300 m^3s^{-1}. Results were compared to 215 current meter measurements and PIV results agree with the defined rating curve. Average velocities mostly agreed, except for two measurements. Disregarding these two results, error ranged between −11.6 and +4.2%. The study highlighted the issue of results being sensitive to light, with reflections and shadows making it hard to detect movement.
Author: Jodeau et al. (2008) Case Study: River Arc, France Software Application: LS-PIV	Dam flushing, discharge rate between 10 and 150 m^3/s. Survey area roughly 60 × 40 m. Tilt angle roughly 20° to the horizontal. Calculated alpha to be 0.79 (0.85 is default). DEM used for bed elevations.	Bias (thought to be due to friction coefficients used), toward the shallow areas of the river; under-estimated compared to a 2D-model. Lack of tracer visibility on right bank due to tree shadow and lack of tracers. At smaller levels of discharge (60 m^3/s), calculated error (compared to a rating curve) was large (30%), however, at higher estimated discharges (77 m^3/s), estimated discharge was within 0–6% of the rating curve.
Author: Legleiter et al. (2017) Case Study: Alaska, USA Software Application: LS-PIV (Thermal)	Benchmarked using aDcp (velocity, discharge, depths). Thermal camera (FLIR SC8340) used to capture data (1,280 × 720px). Frame rate at 10 Hz captured for 1min. Cameras were fixed, with most angles set to nadir, however, some instances 13 degrees off nadir was used. 25mm focal lens used (provided a view of 41.2° x 24.8°). ROI of 512 × 512px used (roughly 6 × 3.5 m, GSD 0.005 m).	Angling the cameras resulted in issues; the distortion of the FOV (between 2 and 9%), but also reduced the near-field thermal energy received. The paper does not track "tracers" per se, but instead thermally distinct patterns. Results skewed from not accounting for camera distortions (e.g., camera tilts), however, the edges of the frames were trimmed when processing (where most of the distortion would occur). Velocities (from both aDcp's and PIV), ranged between 0.5 and 3 m/s for all the sites. The mean error for all sites was within one standard deviation (range of error between 0.09 and 0.187 m/s with a ±1 standard deviation of between 0.132 and 0.247 m/s)
Author: Tauro et al. (2018) Case Study: Brenta River, Italy Software Application: OTV (PTV based)	Camera used was a GoPro Hero 4 Black, set to capture at full HD (1,920 × 1,080 pixels) at a capture rate of 50 Hz. Out of a 4 min video, twelve 20s clips were extracted with a resolution of 1,430×1,080 pixels (equalling a field size of 7.1 × 5.3 m^2) at a rate of 25 Hz. Image manipulation was used, including greyscaling and gamma correction to darken mid-tones.	Processing time was measured using OTV and compared against PTVLab and PIVLab and was shown to be two magnitudes quicker using a simple personal computer (2 min for OTV and 17 ± 7 min for PIVLab/PTVLab). RMSE and R^2 values were used for comparisons with results. These results were compared against a benchmark from a deployed current meter (3 cm below the surface). FAST-based OTV produced a R^2 value of 0.83 compared to reference data, with ORB-based OTV 2nd best with 0.74. For comparison, PIVLab produced a R^2 value of 0.49 and PTVLab 0.6 compared to the reference data.
Author: Dal Sasso et al. (2018) Case Study: Noce Rivers, Italy Software Application: PTV-Lab	Field study after numerical experimentation on optical settings for PTV solutions. Average channel width 28 m, slope gradient 1.1%. Waded current meter benchmarking. DJI Phantom 3 Quadcopter with a 4k UHD mounted camera with 3 axis stabilisation system. 10m hover above surface with orthogonal angle to surface (nadir). Captured in HD (1,920 × 1,080px) at 24 FPS. Surface captured was 17.0 × 9.6 m^2. Artificial tracers were used.	Reconstruction of velocities at banks show higher uncertainty due to bank effects, and a lack of tracer movement; produces significant underestimation. Emphasis on frame rate being such that a particles displacement is larger than that of the particle being tracked, and if not, to subsample frames (reduce framerate to increase displacement). Results compared to benchmark show a good comparison in the middle of the reach (1% error), compared to that of the edges which are much less reliable (48% error). Benchmark velocities show a median of 0.437 m/s, and a max of 0.48 m/s, whereas PTV-Lab produced a RMSE of 0.125 m/s for the full width, and 0.04 m/s when considering only the areas with good seeding concentration.
Author: Tauro et al. (2019) Case Study: Brenta River, Italy Software Application: PTV-Stream	Telescopic pole used with a GoPro Hero 4 Black. Nadir angle to surface to remove need for orthorectification. FOV was 9.5 × 5.3 m. HD (1,920 × 1,080px) used with 50 Hz capture rate. Split into 12 20s videos and edges removed to crop image to 1,430 × 1,080px. Mask used to cover vegetation visible. Distortion removed from camera. Artificial tracers were used.	Results agree with widely used PTV-Lab, but PTV-Stream significantly reduced computational requirements (reported to be around 10% of the total time usually required to process a video). Sampled at 25, 12, and 8 Hz and all results overlap (showing robustness). Mean velocity was above average compared to current meter benchmark (0.46 m/s compared to 0.38 m/s), attributed to the difference in depth of the readings (surface vs. few centimetres below water surface. Results show that PTV-Stream capture the fluctuation in shape of velocity across the river cross-section (higher in middle).
Author: Jin and Liao (2019) Case Study: Milwaukee River, USA	Flow ranged between 6-60m^3/s. Camera used was a NikonD7000 with HD 1080p imaging and a distortion free lens (50 mm F1.4). Oblique angle used (between 79° and	Median tests used, average error between 29 and 36% over the whole study. The RMS of the velocity agrees well with the ADV benchmarking after the median tests were performed to remove

(Continued)

TABLE 2 | Continued

Details	Background	Results
Software Application: LS-PIV	86°). Images were orthorectified using 11 GCPs. Water level found by marking extra GCP just above water level. ADV used for benchmarking along cross-section. 25FPS used over a 10min period. Images used have GSD of 0.02 m/px over an area of 70 × 23 m.	outliers. Good correlation between the ADV and the PIV magnitude (0.12 and 0.14m/s from the ADV and PIV, respectively). Typically, results were larger than that of the ADV and it is thought to be due to the ADV measurements coming from 5cm under the surface of the river, resulting in less turbulence compared to that of the surface velocity. Velocity index for depth average calculations set at 0.85.
Author: Pearce et al. (2020) Case Study: Kolubara River, Serbia Software Application: KLT-IV, LSPIV, LSPTV, OTV, SSIV	Comparison paper between software suites. Low flow experiments (approx. 3.4 m^3s^{-1}, benchmarked with aDcp. Mobile platform used (DJI Phantom 4 Pro) with a standard fitted camera sensor (1" CMOS 20MP). Artificial tracers used. Six GCPs were used along the channel. Resolution of 4k (4096 × 2160 pixels) and a FPS of 23.98. Two videos of 30s were sub-sampled captured from 26 m elevation (GSD of 0.77 cm/px), and 32 m (GSD of 0.95 cm/px).	The aDcp was used across three cross-sections. KLT-IV and LSPIV provided the best correlation with the results from the aDcp averaging a range between 0 and 0.07 ms^{-1}. On average, KLT-IV, LSPIV, OTV and SSIV software suites are in better agreement with the aDcp than LSPTV. The Nash-Sutcliffe results for the softwares compared to the aDcp are for video one: 0.535 (KLT-IV), 0.3592 (OTV), 0.4905 (LSPIV), 0.1609 (LSPTV), and 0.3875 (SSIV). A sensitivity study was also produced. The results show that KLT-IV is generally insensitive to changes in configurations. OTV had the lowest sensitivity scores across software suites, however, can be sensitive to the particle trajectory length threshold.
Author: Perks (2020) Case Study: River Feshie, Scotland Software Application: KLT-IV (PTV based)	Hikvision AcuSense 4mMP IF network camera (20 Hz, 2,688 × 1,520px), and DJI phantom 4 (29.97 fps, 4,096 × 2,160px). High flow conditions (stage range between 0.785 and 1.762 m). GCPs were used throughout detection and the images were stabilised to negate platform movement.	A range of stage was used to reconstruct the flow (between 0.785 and 1.762 m). Mobile and fixed cameras produced deviations from a rating curve at 4 and 1% at stages above 1.5m. Vegetation obstructed mobile imaging, had to extrapolate edge, but had over one-million trajectories. Fixed camera had 7433 trajectories (10s of video), mostly in centre, both banks needed extrapolating.

Each has been briefly summarised for their backgrounds and their results.

studies such as monitoring river flows and developing discharge rating curves, fixed stations can be used to provide a time-series of images.

For mobile stations, stabilisation is a critical component to the process, sometimes the same is true for fixed cameras that witness oscillations or vibrations due to external influences. For the best results, it is suggested that at least four pairs are used for a full projective transformation to be available and can be selected either manually or automatically. It is also possible to use GPS tracking to detect movement of the camera. The best features to use are static points such as corners of structures. Orthorectification is also required where the camera angle is not nadir. An absolute minimum of six GCPs is required, however, it is the case of the more the better. At least four GCPs should be in the immediate area of the region of interest. If tracers are not prevalent throughout the imagery, it is suggested that imagery is manipulated using contrast enhancement steps. After enhancement, should tracers still not be defined against the background, further image enhancement steps can be applied such as binarisations. As a minimum, images need to be greyscaled and cropped where possible.

Lagrangian and Eulerian algorithms are the basis for PTV and PIV respectively. Each mechanic of motion has its own assumptions and limitations, but also their own advantages. Where tracers are dense and interact with one another consistently or deform and break up, Lagrangian motion is difficult to define. Conversely, for Eulerian, a steady state of flow and tracer availability is required for reliable results. Steadiness of flow is not as much of an issue for Lagrangian techniques as it defines the particles energy and location at any moment of time. PIV methods can be used with more confidence if there are a steady amount of tracers throughout the whole time of processing, providing an output of average velocity across a gridded system on the surface of the river. PTV methods are more detailed, in that they trace an individual particles movement along the longitude of the river surface and can work well where seeding is more scarce.

After calculating surface velocities, general practice should include the detection of outliers and either the removal or the replacement of said outliers. There are numerous statistical algorithms available to the user to aid in achieving corrected velocity vectors, mostly using a statistical means (e.g., median tests), and the nearest neighbouring vector; errors are then replaced using interpolation methods. This is achievable for both PIV and PTV data, however, more research has been done into PIV corrective techniques because of its results being gridded and structured, making the nearest neighbours easier to identify computationally. From this research it is suggested that any datasets being used in further calculations or designs (e.g., discharge), should undergo statistical validations and corrections. Discharge calculations rely on an alpha value being used (typically around 0.85), which estimates the average depth velocity. The alpha value coupled with the bathymetry of a known transect of the river can be used in an area-velocity method of calculating discharge. Where surface velocity is not constant (due to lack of tracers or anything else), velocity can be interpolated or extrapolated using the data readily available from the rest of the river. This can then be used in calculating discharges.

Image velocimetry is a process upon which each stage is ultimately dependant on the previous. Without adequate

consideration in prior steps, subsequent stages cannot be relied upon to accurately convey flow data. This research has depicted many of the aspects that require careful planning regarding the best practice for PIV and PTV methods. There are many studies currently available, cited in this research, that allow a user to deduce how to optimally capture and process imagery, either through experimental evidence or through applied precedence. Some stages are less evidenced than others, and require the users intuition to best determine methodology; one of the most important of these, arguably, is GSD. GSD is a complex balance between detail and resources, it is a mix of physical characteristics such as distances and angles, coupled with resolutions and hardware (sensors and lenses). Without optimising GSD to be small enough for a specific site, detail is lost and can hinder the processing capability of PIV/PTV through the lack of ability to detect and track good features. Alternatively, too small of a GSD could critically increase the processing power, storage, and bandwidth requirements to a point that they are unjustifiable. With that being said, it is also vital that stabilisation is competently applied. Stabilisation, where platform movement is detected, can be just as critical as GSD, as research shows that large positional errors can be removed with a good, accurate stabilisation being applied to the imagery. Decisively, however, as previously stated, PIV and PTV are processes with each stage as important as its predecessor and that one of the main limitations with the ideal settings suggested throughout this research, is that it conforms to a generalised process. This means that, despite there being sufficient evidence for the optimal practices suggested, there is always a need for discretion from the user to best meet the requirements for their brief; such as challenging terrains or budget limitations.

To conclude, image velocimetry is a well researched field. The algorithms that are currently available to users tend to prove effective for remote sensing of river surface velocities. As there are currently many software suites available for processing of imagery (e.g., PIVlab, PTVlab, KLT-IV, etc.), a shift of emphasis should be made from focusing on the use of a single algorithm and stating its error bounds, to optimising the methodology of a study to suggest best practice and choice of algorithm and its corresponding variables. With that said, areas such as environmental conditions and the errors associated with them require further study to determine the overall impact that they can have on results, and if possible, quantifying so that further optimisation to the processing system can be suggested, depending on the conditions of time of image capture.

AUTHOR CONTRIBUTIONS

MJ, MP, and AR contributed to conception and design of the study. This paper was researched and written by MJ. All figures were created by MJ. All authors contributed to editing and reviewing of the manuscript.

ACKNOWLEDGMENTS

MJ is in receipt of an EPSRC PhD studentship awarded to Newcastle University (EP/R51309X/1).

REFERENCES

Ace, E. (2013). *Test: H.264 I vs P Frame Impact*. Technical report. IPVM.

Akhmetbekov, Y. K., Markovich, D. M., and Tokarev, M. P. (1996). *A Novel Correction Algorithm for PTV*. 3–4. Available online at: http://tokarevmp.narod.ru/site/articles/myarticles/piv07.pdf

Alimenti, F., Bonafoni, S., Gallo, E., Palazzi, V., Vincenti Gatti, R., Mezzanotte, P., et al. (2020). Noncontact measurement of river surface velocity and discharge estimation with a low-cost Doppler Radar sensor. *IEEE Trans. Geosci. Remote Sens*. 58, 5195–5207. doi: 10.1109/TGRS.2020.2974185

Amelinckx, S. (1971). Classical dynamics of particles and systems. *Phys. Bull*. 22:157–8. doi: 10.1088/0031-9112/22/3/020

Assem, H., Ghariba, S., Makrai, G., Johnston, P., Gill, L., and Pilla, F. (2017). "Urban water flow and water level prediction based on deep learning," in *Lecture Notes in Computer Science*. ed LNCS (Springer), 317–329. doi: 10.1007/978-3-319-71273-4_26

Bandini, F., Lüthi, B., Peña-Haro, S., Borst, C., Liu, J., Karagkiolidou, S., et al. (2021). A Drone-Borne method to jointly estimate discharge and manning's roughness of natural streams. *Water Resour. Res*. 57. doi: 10.1029/2020WR028266

Bolognesi, M., Farina, G., Alvisi, S., Franchini, M., Pellegrinelli, A., and Russo, P. (2017). Measurement of surface velocity in open channels using a lightweight remotely piloted aircraft system. *Geomat Nat Hazards Risk* 8, 73–86. doi: 10.1080/19475705.2016.1184717

Brevis, W., Nino, Y., and Jirka, G. H. (2011). Integrating cross-correlation and relaxation algorithms for particle tracking velocimetry. *Exp. Fluids*. 50, 135–147. doi: 10.1007/s00348-010-0907-z

Caldwell, L., Armijo, D., Mukherjee, S., Minichiello, A., Truscott, T., and Kulyukin, V. (2019). "Work in progress: mobile instructional particle image velocimetry for stem outreach and undergraduate fluid mechanics education," in *ASEE Annual Conference and Exposition, Conference Proceedings* (Tampa, Florida).

Caputo, A. C. (2010). "Digital video hardware," in *Digital Video Surveillance and Security*, ed Anthony C. Caputo (Elsevier), 39–88. doi: 10.1016/B978-1-85617-747-4.00003-2

Carrel, M., Detert, M., Pena-Haro, S., and Luethi, B. (2019). "Evaluation of the DischargeApp: a smartphone application for discharge measurements," in *HydroSenSoft, International Symposium and Exhibition on Hydro-Environment Sensors and Software* (Madrid).

Cerqueira, R. F., Paladino, E. E., Ynumaru, B. K., and Maliska, C. R.(2018). Image processing techniques for the measurement of two-phase bubbly pipe flows using particle image and tracking velocimetry (PIV/PTV). *Chem. Eng. Sci*. 189, 1–23. doi: 10.1016/j.ces.2018.05.029

Chen, Q., Zhang, Y., and Hallikainen, M. (2007). Water quality monitoring using remote sensing in support of the EU water framework directive (WFD): a case study in the Gulf of Finland. *Environ. Monitor. Assess*. 124, 157–166. doi: 10.1007/s10661-006-9215-8

Costa, J. E., Cheng, R. T., Haeni, F. P., Melcher, N., Spicer, K. R., Hayes, E., et al. (2006). Use of radars to monitor stream discharge by noncontact methods. *Water Resour. Res*. 42. doi: 10.1029/2005WR004430

Creutin, J. D., Muste, M., Bradley, A. A., Kim, S. C., and Kruger, A. (2003). River gauging using PIV techniques: a proof of concept experiment on the Iowa River. *J. Hydrol*. 277, 182–194. doi: 10.1016/S0022-1694(03)00081-7

Daigle, A., Bérubé, F., Bergeron, N., and Matte, P. (2013). A methodology based on particle image velocimetry for river ice velocity measurement. *Cold Regions Sci. Technol*. 89, 36–47. doi: 10.1016/j.coldregions.2013.01.006

Dal Sasso, S. F., Pizarro, A., and Manfreda, S. (2020). Metrics for the quantification of seeding characteristics to enhance image velocimetry performance in rivers. *Remote Sensing*. 12. doi: 10.5194/egusphere-egu21-9229

Dal Sasso, S. F., Pizarro, A., Pearce, S., Maddock, I., and Manfreda, S. (2021). Increasing LSPIV performances by exploiting the seeding distribution index at different spatial scales. *J. Hydrol*. 598. doi: 10.1016/j.jhydrol.2021.126438

Dal Sasso, S. F., Pizarro, A., Samela, C., Mita, L., and Manfreda, S. (2018). Exploring the optimal experimental setup for surface flow velocity measurements using PTV. *Environ. Monitor. Assess*. 190:460. doi: 10.1007/s10661-018-6848-3

De Baar, J. H., Percin, M., Dwight, R. P., Van Oudheusden, B. W., and Bijl, H. (2014). Kriging regression of PIV data using a local error estimate. *Exp. Fluids*. 55. doi: 10.1007/s00348-013-1650-z

Deen, N. G., Willems, P., Sint Annaland, M. V., Kuipers, J. A., Lammertink, R. G., Kemperman, A. J., et al. (2010). On image pre-processing for PIV of single-and two-phase flows over reflecting objects. *Exp. Fluids*. 49, 525–530. doi: 10.1007/s00348-010-0827-y

Dellenback, P. A., Macharivilakathu, J., and Pierce, S. R. (2000). Contrast-enhancement techniques for particle-image velocimetry. *Appl. Optics* 39:5978. doi: 10.1364/AO.39.005978

Detert, M. (2021). How to avoid and correct biased riverine surface image velocimetry. *Water Resour. Res*. 57. doi: 10.1029/2020WR027833

Detert, M., Johnson, E. D., and Weitbrecht, V. (2017). Proof-of-concept for low-cost and non-contact synoptic airborne river flow measurements. *Int. J. Remote Sens*. 38, 2780–2807. doi: 10.1080/01431161.2017.1294782

Detert, M., and Weitbrecht, V. (2015). A low-cost airborne velocimetry system: proof of concept. *J. Hydraul. Res*. 23, 532–539. doi: 10.1080/00221686.2015.1054322

Dobson, D. W., Todd Holland, K., and Calantoni, J. (2014). Fast, large-scale, particle image velocimetry-based estimations of river surface velocity. *Comput. Geosci*. 70, 35–43. doi: 10.1016/j.cageo.2014.05.007

Dramais, G., Le Coz, J., Camenen, B., and Hauet, A. (2011). Advantages of a mobile LSPIV method for measuring flood discharges and improving stage-discharge curves. *J. Hydroenviron. Res*. 5, 301–312. doi: 10.1016/j.jher.2010.12.005

Duncan, J., Dabiri, D., Hove, J., and Gharib, M. (2010). Universal outlier detection for particle image velocimetry (PIV) and particle tracking velocimetry (PTV) data. *Measure. Sci. Technol*. 21. doi: 10.1088/0957-0233/21/5/057002

Durst, F., Miloievic, D., and Schönung, B. (1984). Eulerian and Lagrangian predictions of particulate two-phase flows: a numerical study. *Appl. Math. Modell*. 8, 101–115. doi: 10.1016/0307-904X(84)90062-3

Edmund Optics (2021). *Imaging Electronics 101: Understanding Camera Sensors for Machine Vision Applications*.

Eltner, A., Sardemann, H., and Grundmann, J. (2020). Technical Note: flow velocity and discharge measurement in rivers using terrestrial and unmanned-aerial-vehicle imagery. *Hydrol. Earth Syst. Sci*. 24, 1429–1445. doi: 10.5194/hess-24-1429-2020

Euler, L. (2008). Principles of the motion of fluids. *Phys. D Nonlinear Phenomena*. 237, 1840–1854. doi: 10.1016/j.physd.2008.04.019

Flener, C., Vaaja, M., Jaakkola, A., Krooks, A., Kaartinen, H., Kukko, A., et al. (2013). Seamless mapping of river channels at high resolution using mobile liDAR and UAV-photography. *Remote Sensing*. 5, 6382–6407. doi: 10.3390/rs5126382

Fujita, I., and Aya, S. (2004). "Refinement of LSPIV technique for monitoring river surface flows," in *Joint Conference on Water Resource Engineering and Water Resources Planning and Management 2000: Building Partnerships*. (Reston, VA). doi: 10.1061/40517(2000)312

Fujita, I., Muste, M., and Kruger, A. (1998). Large-scale particle image velocimetry for flow analysis in hydraulic engineering applications. *J. Hydraul. Res*. doi: 10.1080/00221689809498626

Fujita, I., Watanabe, H., and Tsubaki, R. (2007). Development of a non-intrusive and efficient flow monitoring technique: the space-time image velocimetry (STIV). *Int. J. River Basin Manage*. 5, 105–114. doi: 10.1080/15715124.2007.9635310

Fulton, J. W. (2020). *Guidelines for Siting and Operating Surface-Water Velocity Radars*. Technical report, USGS.

Gollin, D., Brevis, W., Bowman, E. T., and Shepley, P. (2017). Performance of PIV and PTV for granular flow measurements. *Granular Matter*. 19. doi: 10.1007/s10035-017-0730-9

Guizar-Sicairos, M., Thurman, S. T., and Fienup, J. R. (2008). Efficient subpixel image registration algorithms. *Opt. Lett*. 33:156. doi: 10.1364/OL.33.000156

Hain, R., Buchmann, N. A., and Cierpka, C. (2016). "On the possibility of using mobile phone cameras for quantitative flow visualization," in *18th International Symposium on Applications of Laser Techniques to Fluid Mechanics* (Lisbon).

Harpold, A. A., Mostaghimi, S., Vlachos, P. P., Brannan, K., and Dillaha, T. (2006). Stream discharge measurement using a large-scale particle image velocimetry (LSPIV) prototype. *Trans. ASABE*. 49, 1791–1805. doi: 10.13031/2013.22300

Hart, D. P. (2000). "PIV error correction," in *Laser Techniques Applied to Fluid Mechanics* (Berlin; Heidelberg: Springer), 19–35. doi: 10.1007/978-3-642-56963-0_2

Hauet, A., Kruger, A., Krajewski, W. F., Bradley, A., Muste, M., Creutin, J. D., et al. (2008). Experimental system for real-time discharge estimation using an image-based method. *J. Hydrol. Eng*. 13, 105–110. doi: 10.1061/(ASCE)1084-0699(2008)13:2(105)

Higham, J. E., and Brevis, W. (2019). When, what and how image transformation techniques should be used to reduce error in Particle Image Velocimetry data? *Flow Meas. Instrument*. 66, 79–85. doi: 10.1016/j.flowmeasinst.2019.02.005

Hirt, C. W., Amsden, A. A., and Cook, J. L. (1974). An arbitrary Lagrangian-Eulerian computing method for all flow speeds. *J. Comput. Phys*. doi: 10.1016/0021-9991(74)90051-5

Honkanen, M., and Nobach, H. (2005). Background extraction from double-frame PIV images. *Exp. Fluids*. 38, 348–362. doi: 10.1007/s00348-004-0916-x,

IPVM Team (2021). *Frame Rate Guide for Video Surveillance*. Technical report.

Javernick, L., Brasington, J., and Caruso, B. (2014). Modeling the topography of shallow braided rivers using Structure-from-Motion photogrammetry. *Geomorphology*. 213, 166–182. doi: 10.1016/j.geomorph.2014.01.006

Jin, T., and Liao, Q. (2019). Application of large scale PIV in river surface turbulence measurements and water depth estimation. *Flow Meas. Instrument*. 67, 142–152. doi: 10.1016/j.flowmeasinst.2019.03.001

Jodeau, M., Hauet, A., Paquier, A., Le Coz, J., and Dramais, G. (2008). Application and evaluation of LS-PIV technique for the monitoring of river surface velocities in high flow conditions. *Flow Meas. Instrument*. doi: 10.1016/j.flowmeasinst.2007.11.004

Jolley, M. (2021). GSD *camangle EST*. Available online at: https://github.com/MJolley1/GSDCalc

Jyoti Bora, D. (2017). Importance of image enhancement techniques in color image segmentation: a comprehensive and comparative study. *Indian J. Sci. Res*. 15, 115–131. doi: 10.6084/m9.figshare.5280799

Kääb, A., Altena, B., and Mascaro, J. (2019). River-ice and water velocities using the Planet optical cubesat constellation. *Hydrol. Earth Syst. Sci*. 23, 4233–4247. doi: 10.5194/hess-23-4233-2019

Keane, R. D., and Adrian, R. J. (1992). Theory of cross-correlation analysis of PIV images. *Appl. Sci. Res*. 49, 191–215. doi: 10.1007/BF00384623

Kim, Y., Muste, M., Hauet, A., Krajewski, W. F., Kruger, A., and Bradley, A. (2008). Stream discharge using mobile large-scale particle image velocimetry: a proof of concept. *Water Resour. Res*. 44. doi: 10.1029/2006WR005441

Kinzel, P. J., and Legleiter, C. J. (2019). sUAS-based remote sensing of river discharge using thermal particle image velocimetry and bathymetric lidar. *Remote Sensing*. 11. doi: 10.3390/rs11192317

Kostaschuk, R., Best, J., Villard, P., Peakall, J., and Franklin, M. (2005). Measuring flow velocity and sediment transport with an acoustic Doppler current profiler. *Geomorphology* 68, 25–37. doi: 10.1016/j.geomorph.2004.07.012

Koutalakis, P., Tzoraki, O., and Zaimes, G. (2019). Uavs for hydrologic scopes: application of a low-cost UAV to estimate surface water velocity by using three different image-based methods. *Drones*. 3:14. doi: 10.3390/drones3010014

Le Boursicaud, R., Pénard, L., Hauet, A., Thollet, F., and Le Coz, J. (2016). Gauging extreme floods on YouTube: application of LSPIV to home movies for the post-event determination of stream discharges. *Hydrol. Process*. 30, 90–105. doi: 10.1002/hyp.10532

Le Coz, J., Hauet, A., Pierrefeu, G., Dramais, G., and Camenen, B. (2010). Performance of image-based velocimetry (LSPIV) applied to flash-flood discharge measurements in Mediterranean rivers. *J. Hydrol*. 394, 42–52. doi: 10.1016/j.jhydrol.2010.05.049

Le Coz, J., Jodeau, M., Hauet, A., Marchand, B., and Le Boursicaud, R. (2014). "Image-based velocity and discharge measurements in field and laboratory river engineering studies using the free FUDAA-LSPIV software," in *Proceedings of*

the International Conference on Fluvial Hydraulics, River Flow 2014 (Lausanne). doi: 10.1201/b17133-262

Legleiter, C. J., Kinzel, P. J., and Nelson, J. M. (2017). Remote measurement of river discharge using thermal particle image velocimetry (PIV) and various sources of bathymetric information. *J. Hydrol.* 554, 490–506. doi: 10.1016/j.jhydrol.2017.09.004

Leitão, J. P., Peña-Haro, S., Lüthi, B., Scheidegger, A., and Moy de Vitry, M. (2018). Urban overland runoff velocity measurement with consumer-grade surveillance cameras and surface structure image velocimetry. *J. Hydrol.* 565, 791–804. doi: 10.1016/j.jhydrol.2018.09.001

Lindken, R., Rossi, M., Große, S., and Westerweel, J. (2009). Micro-Particle Image Velocimetry (PIV): Recent developments, applications, and guidelines. *Lab Chip* 9, 2551–2567. doi: 10.1039/b906558j

Liu, D., and Cheng, S. (2008). "A brief introduction of feature matching," in *2008 IEEE Region 5 Conference* (Kansas City, MO), 1–4. doi: 10.1109/TPSD.2008.4562728

Livoroi, A.-H., Conti, A., Foianesi, L., Tosi, F., Aleotti, F., Poggi, M., et al. (2021). On the deployment of out-of-the-box embedded devices for self-powered river surface flow velocity monitoring at the edge. *Appl. Sci.* 11:7027. doi: 10.3390/app11157027

Ljubičić, R., Strelnikova, D., Perks, M. T., Eltner, A., Pena Haro, S., Pizarro, A., et al. (2021). A comparison of tools and techniques for stabilising uas imagery for surface flow observations. *Hydrol. Earth Syst. Sci. Discuss.* 2021, 1–42. doi: 10.5194/hess-2021-112

Lloyd, P. M., Stansby, P. K., and Ball, D. J. (1995). Unsteady surface-velocity field measurement using particle tracking velocimetry. *J. Hydraul. Res.* 33, 519–534. doi: 10.1080/00221689509498658

Lowe, D. G. (1999). "Object recognition from local scale-invariant features," in *Proceedings of the Seventh IEEE International Conference on Computer Vision* (Kerkyra). doi: 10.1109/ICCV.1999.790410

Malepati, H. (2010). "Image processing tools," in *Digital Media Processing*. (Elsevier), 509–552. doi: 10.1016/B978-1-85617-678-1.00010-7

Masullo, A., and Theunissen, R. (2016). Adaptive vector validation in image velocimetry to minimise the influence of outlier clusters. *Experiments in Fluids*. doi: 10.1007/s00348-015-2110-8

Meselhe, E. A., Peeva, T., and Muste, M. (2004). Large scale particle image velocimetry for low velocity and shallow water flows. *J. Hydraul. Eng.* 130, 937–940. doi: 10.1061/(ASCE)0733-9429(2004)130:9(937)

Mingkhwan, E., and Khawsuk, W. (2017). "Digital image stabilization technique for fixed camera on small size drone," in *2017 Third Asian Conference on Defence Technology (ACDT)* (Phuket). doi: 10.1109/ACDT.2017.7886149

Mishra, M., Dugesar, V., Prudhviraju, K. N., Patel, S. B., and Mohan, K. (2019). Precision mapping of boundaries of flood plain river basins using high-resolution satellite imagery: a case study of the Varuna river basin in Uttar Pradesh, India. *J. Earth Syst. Sci.* 128:105. doi: 10.1007/s12040-019-1146-1

Morrow, D. (2021). "Camera sensor size & image quality-photography guide", in *Dave Morrow Photography LLC*. Available online at: https://www.davemorrowphotography.com/camera-sensor-size-guide (accessed Mar 12, 2021).

Muja, M., and Lowe, D. G. (2012). "Fast matching of binary features," in *2012 Ninth Conference on Computer and Robot Vision* (Toronto, ON). doi: 10.1109/CRV.2012.60

Muste, M., Fujita, I., and Hauet, A. (2008). Large-scale particle image velocimetry for measurements in riverine environments. *Water Resour. Res.* doi: 10.1029/2008WR006950

Neill, S. P., and Hashemi, M. R. (2018). "*In situ* and remote methods for resource characterization," in *Fundamentals of Ocean Renewable Energy* (Elsevier), 157–191. doi: 10.1016/B978-0-12-810448-4.00007-0

Patalano, A., García, C. M., and Rodríguez, A. (2017). Rectification of Image Velocity Results (RIVeR): a simple and user-friendly toolbox for large scale water surface Particle Image Velocimetry (PIV) and Particle Tracking Velocimetry (PTV). *Comput. Geosci.* 107, 323–330. doi: 10.1016/j.cageo.2017.07.009

Pearce, S., Ljubičić, R., Peña-Haro, S., Perks, M., Tauro, F., Pizarro, A., et al. (2020). An evaluation of image velocimetry techniques under low flow conditions and high seeding densities using unmanned aerial systems. *Remote Sensing* 12:232. doi: 10.3390/rs12020232

Peña-haro, S., Lüthi, B., Lukes, R., and Carrel, M. (2020). *Wind Effect on Image-Based River Surface Velocity Measurements*. Technical report, EGU General Assembly 2020. doi: 10.5194/egusphere-egu2020-9943

Perks, M. T. (2020). KLT-IV v1.0: image velocimetry software for use with fixed and mobile platforms. *Geosci. Model Dev. Discuss.* 13, 6111–6130. doi: 10.5194/gmd-2020-187

Perks, M. T., Dal Sasso, S. F., Hauet, A., Jamieson, E., Le Coz, J., Pearce, S., et al. (2020). Towards harmonisation of image velocimetry techniques for river surface velocity observations. *Earth Syst. Sci. Data* 12, 1545–1559. doi: 10.5194/essd-12-1545-2020

Perks, M. T., Russell, A. J., and Large, A. R. (2016). Technical note: advances in flash flood monitoring using unmanned aerial vehicles (UAVs). *Hydrol. Earth Syst. Sci.* 20, 4005–4015. doi: 10.5194/hess-20-4005-2016

Pix4d (2019). *What is Absolute Accuracy and Relative Accuracy*?

Pizarro, A., Dal Sasso, S. F., and Manfreda, S. (2020a). Refining image-velocimetry performances for streamflow monitoring: seeding metrics to errors minimization. *Hydrol. Process.* 34, 5167–5175. doi: 10.1002/hyp.13919

Pizarro, A., Dal Sasso, S. F., Perks, M. T., and Manfreda, S. (2020b). Identifying the optimal spatial distribution of tracers for optical sensing of stream surface flow. *Hydrol. Earth Syst. Sci.* 24, 5173–5185. doi: 10.5194/hess-2020-188

Planet Labs Inc. (2021). "Planet satellite data," in *Global Monitoring, Daily Insight*. Available online at: https://www.planet.com/products/planet-imagery/ (accessed April 1, 2021).

Prasad, A. K., Adrian, R. J., Landreth, C. C., and Offutt, P. W. (1992). Effect of resolution on the speed and accuracy of particle image velocimetry interrogation. *Experiments in Fluids*. doi: 10.1007/BF00218156

Price, J. F. (2006). "Lagrangian and Eulerian representations of fluid flow: kinematics and the equations of motion", in *Online Publication*, *Fluid Dynamics* (Falmouth, MA: Woods Hole Oceanographic Institution). Available online at: http://www.whoi.edu/science/PO/people/jprice

Pumo, D., Alongi, F., Ciraolo, G., and Noto, L. V. (2021). Optical methods for river monitoring: a simulation-based approach to explore optimal experimental setup for LSPIV. *Water*. 13:247. doi: 10.3390/w13030247

Pun, C. S., Susanto, A., and Dabiri, D. (2007). Mode-ratio bootstrapping method for PIV outlier correction. *Meas. Sci. Technol.* 18, 3511–3522. doi: 10.1088/0957-0233/18/11/035

Raffel, M., Willert, C. E., Scarano, F., Kähler, C. J., Wereley, S. T., and Kompenhans, J. (2018). *Particle Image Velocimetry: A Practical Guide*. (Springer). doi: 10.1007/978-3-319-68852-7

Rodriguez-Padilla, I., Castelle, B., Marieu, V., and Morichon, D. (2019). A simple and efficient image stabilization method for coastal monitoring video systems. *Remote Sensing* 12:70. doi: 10.3390/rs12010070

Rosten, E., and Drummond, T. (2006). Machine learning for high-speed corner detection," in *Computer Vision–ECCV 2006*, eds A. Leonardis, H. Bischof, and A. Pinz (Berlin; Heidelberg: Springer) 430–443. doi: 10.1007/11744023_34

Safesite (2021). *Internet Protocol (IP) Cameras–How do They Work & What are the Benefits*?

Shi, J., and Tomasi, C. (1994). "Good features to track," in *Proceedings of the IEEE Computer Society Conference on Computer Vision and Pattern Recognition*. (Seattle, WA).

Stamhuis, E. J. (2006). Basics and principles of particle image velocimetry (PIV) for mapping biogenic and biologically relevant flows. *Aquat. Ecol.* 40, 463–479. doi: 10.1007/s10452-005-6567-z

Szeliski, R. (2006). Image alignment and stitching: a tutorial. *Found. Trends. Comput. Graph. Vis.* 2, 1–104. doi: 10.1561/0600000009

Tang, C., Sun, W., He, H., Li, H., and Li, E. (2017). Spurious PIV vector detection and correction using a penalized least-squares method with adaptive order differentials. *Exp. Fluids.* 58:81. doi: 10.1007/s00348-017-2350-x

Tareen, S. A. K., and Saleem, Z. (2018). "A comparative analysis of SIFT, SURF, KAZE, AKAZE, ORB, and BRISK," in *2018 International Conference on Computing, Mathematics and Engineering Technologies (iCoMET)* (Sukkur), 1–10. doi: 10.1109/ICOMET.2018.8346440

Tauro, F., Petroselli, A., Porfiri, M., Giandomenico, L., Bernardi, G., Mele, F., et al. (2016). A novel permanent gauge-cam station for surface-flow observations on the Tiber River. *Geosci. Instrument. Methods Data Syst.* 30, 1114–1130. doi: 10.5194/gi-5-241-2016

Tauro, F., Piscopia, R., and Grimaldi, S. (2017). Streamflow observations from cameras: large-scale particle image velocimetry or particle tracking velocimetry? *Water Resour. Res.* 53, 10374–10394. doi: 10.1002/2017WR020848

Tauro, F., Piscopia, R., and Grimaldi, S. (2019). PTV-Stream: a simplified particle tracking velocimetry framework for stream surface flow monitoring. *Catena*. 172, 378–386. doi: 10.1016/j.catena.2018.09.009

Tauro, F., Porfiri, M., and Grimaldi, S. (2014). Orienting the camera and firing lasers to enhance large scale particle image velocimetry for streamflow monitoring. *Water Resour. Res.* 50, 7470–7483. doi: 10.1002/2014WR015952

Tauro, F., Tosi, F., Mattoccia, S., Toth, E., Piscopia, R., and Grimaldi, S. (2018). Optical tracking velocimetry (OTV): Leveraging optical flow and trajectory-based filtering for surface streamflow observations. *Remote Sensing*. 49, 199–206. doi: 10.3390/rs10122010

Tensmeyer, C., and Martinez, T. (2020). Historical document image binarization: a review. *SN Comput. Sci*. 1:173. doi: 10.1007/s42979-020-00176-1

The Mathworks Inc. (2020). *Image Processing Toolbox–Reference R 2020a*.

Thielicke, W., and Stamhuis, E. J. (2014). PIVlab–towards user-friendly, affordable and accurate digital particle image velocimetry in MATLAB. *J. Open Res. Softw*. 2. doi: 10.5334/jors.bl

Thumser, P., Haas, C., Tuhtan, J. A., Fuentes-Pérez, J. F., and Toming, G. (2017). RAPTOR-UAV: real-time particle tracking in rivers using an unmanned aerial vehicle. *Earth Surface Proc. Landforms* 42, 2439–2446. doi: 10.1002/esp.4199

Tomasi, C. (1991). *Detection and Tracking of Point Features*. School of Computer Science, Carnegie Mellon University.

Tosi, F., Rocca, M., Aleotti, F., Poggi, M., Mattoccia, S., Tauro, F., et al. (2020). Enabling image-based streamflow monitoring at the edge. *Remote Sensing*. 12:2047. doi: 10.3390/rs12122047

Tsubaki, R., Fujita, I., and Tsutsumi, S. (2011). Measurement of the flood discharge of a small-sized river using an existing digital video recording system. *J. Hydroenviron. Res.* 5, 313–321. doi: 10.1016/j.jher.2010.12.004

Wang, H. P., Gao, Q., Feng, L. H., Wei, R. J., and Wang, J. J. (2015). Proper orthogonal decomposition based outlier correction for PIV data. *Exp. Fluids*. doi: 10.1007/s00348-015-1894-x

Westerweel, J. (1994). Efficient detection of spurious vectors in particle image velocimetry data. *Exp. Fluids* 16, 236–247. doi: 10.1007/BF00206543

Westerweel, J., and Scarano, F. (2005). Universal outlier detection for PIV data. *Exp. Fluids*. 39, 1096–1100. doi: 10.1007/s00348-005-0016-6

Willert, C., Raffel, M., Kompenhans, J., Stasicki, B., and Kähler, C. (1996). Recent applications of particle image velocimetry in aerodynamic research. *Flow Meas. Instrument*. 7, 247–256. doi: 10.1016/S0955-5986(97)00012-5

Wu Tang, H., Chen, C., Chen, H., and tong Huang, J. (2008). An improved PTV system for large-scale physical river model. *J. Hydrodyn*. 20, 669–678. doi: 10.1016/S1001-6058(09)60001-9

Young, C. N., Johnson, D. A., and Weckman, E. J. (2004). A model-based validation framework for PIV and PTV. *Exp. Fluids* 36, 23–35. doi: 10.1007/s00348-003-0602-4

Zhang, X., Cox, C. S., and Wang, X. (1997). "Further evaluation of feature correlation for PIV and PTV," in *Optical Technology in Fluid, Thermal, and Combustion Flow III* (San Diego, CA), 411–419. doi: 10.1117/12.279750

Zhang, Z., Wang, X., Fan, T., and Xu, L. (2013). River surface target enhancement and background suppression for unseeded LSPIV. *Flow Measure. Instrument*. 30, 99–111. doi: 10.1016/j.flowmeasinst.2012.12.002/

Conflict of Interest: The authors declare that the research was conducted in the absence of any commercial or financial relationships that could be construed as a potential conflict of interest.

Publisher's Note: All claims expressed in this article are solely those of the authors and do not necessarily represent those of their affiliated organizations, or those of the publisher, the editors and the reviewers. Any product that may be evaluated in this article, or claim that may be made by its manufacturer, is not guaranteed or endorsed by the publisher.

Copyright © 2021 Jolley, Russell, Quinn and Perks. This is an open-access article distributed under the terms of the Creative Commons Attribution License (CC BY). The use, distribution or reproduction in other forums is permitted, provided the original author(s) and the copyright owner(s) are credited and that the original publication in this journal is cited, in accordance with accepted academic practice. No use, distribution or reproduction is permitted which does not comply with these terms.

11.2 Image Velocimetry Handbook

Introduction

More frequent, high intensity storms and flooding means that the understanding of flow regimes is as important as ever, and advances in the technology that we use has been seen with the use of novel introduction of new methods and techniques (e.g. deep learning models Assem et al. (2017), satellite mapping Mishra et al. (2019)). One of the most widely adopted new technologies is the introduction of acoustic Doppler current profiler's (aDcp)Kostaschuk et al. (2005). Although this method allows users to accurately capture entire water columns along a profile Neill and Hashemi (2018), the issue is that it requires contact with the water surface, which can be problematic in areas witnessing high flows which are inaccessible due to safety concerns for either the user or the equipment. An alternative approach to this is to capture flow data in a non-contact manor. A technique that allows the user to do this is image velocimetry and in particular, large scale image velocimetry Creutin et al. (2003); Jodeau et al. (2008); Dal Sasso et al. (2018); Perks et al. (2016). Large-scale image velocimetry can be an autonomous method of flow gauging a site using surface velocities captured via a camera, and processed using feature detection and tracking software Brevis et al. (2011); Coz et al. (2014); Perks (2020). Consequently, discharge can be calculated from the surface velocity using estimates of alpha values (depth-average velocity values), and cross-sectional data Kim et al. (2008); Coz et al. (2010).

This book is designed to be of use to those wishing to create large-scale image velocimetry sites. There are many methods to use to apply image velocimetry with (e.g. hardware used, software suites used, system settings). To ensure best-practice, it is important to fully understand which methods are best for a particular site, as well fully defining what it is you wish to capture (e.g. high flows, low flows, continuous flows, surface flow patterns).

Each section of this book adds a level of depth to the discussions around the best-practice for image velocimetry using a combination of experience, available literature, and study-based precedence. We begin in section 11.2 by looking at some of the key pieces of terminology that relates back to image velocimetry and the basics of what they mean, and how they are typically applied in a general sense. section 11.2 is a summary of a literature review paper produced by Jolley et al. (2021). This section is dedicated to the more technical aspects of using PIV/PTV software and will expand on some of the terms introduced from section 11.2.

The subsequent three sections (sections 11.2, 11.2, 11.2), consider some more practical elements that are vital to the use of image velocimetry, including hardware considerations, software considerations, and the code requirements respectively. Finally, section 11.2 looks at providing an overall recommendation on how to best set-up a site depending on three key-factors: overall aim, budget, size of site. The key-factors identified have been chosen as they influence the main decisions around how to best capture data using either: fixed or mobile stations (aim & budget), software suite used (aim & budget), camera calibration settings (budget & size of site), processing

and storage requirements (aim, budget & size of site), etc.

There are, of course, many variations of methods that can be used to acquire and process image velocimetry data, however, for years this list of methods has been expanding which does not help those looking to find the best solution to their individual needs. The aim of this handbook is to narrow down the methodology and decisions required to begin using image velocimetry. The methods seen in this handbook is non-exhaustive and it could be argued that there are better methods for particular sites/challenges. Despite this, the need for a generalised 'best-practice' is great, and with the information presented throughout this handbook, it should be much clearer for those new to the topic to understand what is required for them to undergo reliable gauging using PIV or PTV.

Introducing Terminology

It is important to first establish a base understanding of some of the terminology that is to be used throughout this handbook. To do this, a list below has been created that summarises some of the key terms, abbreviations, and methods associated with the processing of image velocimetry data. Although this list is non-exhaustive, it includes the key parameters that users will need when first installing sites, how they can be used, and why they are important.

aDcp - *acoustic Doppler current profiler* An aDcp is typically used to determine the flow across a cross-section in rivers, but also presents cross-sectional areas and vertical velocity columns. The aDcp's use sound waves by bouncing frequencies off of neutrally buoyant particles in the water and produce instantaneous current velocity Lee et al. (2016).

Alpha Coefficient/Value The alpha coefficient is a depth-average velocity value that is associated with bed friction. Alpha coefficients are specific to each site and should be calculated where possible. It is possible to calculate alpha values using aDcp's, but it has been shown that an average of 0.85 can be used with a good level of confidence, as research typically shows values between 0.79-0.91 Coz et al. (2010).

Nadir Nadir is a direction of which a camera is typically described should it be plum. This means that it is perfectly perpendicular to the plane and follows the line of gravity (towards the centre of the earth); essentially, pointing directly down.

Flow State The flow state of a river can either be steady or unsteady. Steady flow has little acceleration across the area of interest, which is important for PIV methods. The fundamentals of PIV means that steady flow across the search areas is assumed, and localised areas of acceleration (and hence, velocity change), are ignored and an average is outputted. Unsteady flow has pockets of acceleration across the river, and can be more accurately represented using PTV methods that can track tracers throughout their whole movement.

GCP - *Ground Control Point* GCP's are used for orthorectification of images. These are stationary referencing points that are visible throughout image sequences and have known coordinates, either in a localised or global grid. Typically, it is advised that there are more than at least 6 GCP's

available to orthorectify to.

GSD - *Ground Sampling Distance* GSD is a combination of several factors including: resolution, height of camera, angle of camera, and camera properties (sensor size, lens). GSD is the dimension that each pixel in frame is associated with, typically described as *"cm/px"*. Where a camera is at nadir and has been calibrated to remove lens distortion (often seen with most cameras), GSD is equal across the image. However, any imagery that has introduced an angle will experience an altering GSD across the image, with a stretch of pixels in the further distances from the camera (background). This is usually associated with orthorectification.

Image Manipulation Image manipulation is a more advanced feature associated with image velocimetry. Where imagery may not be ideal, or where tracers are not as prevalent as they could be, then there are several steps that can be taken to edit the image sequences. The basics of image manipulation is to grey-scale imagery, usually done by software suites automatically. Other applications can be normalisation and equalisation, both manipulate the brightness variations across an image to make dark areas darker, so that light areas (typically tracers), can stand out more. For more information, see the image manipulation section in Jolley et al. Jolley (2021).

IP - Internet Protocol IP is a term used for uniquely identifying devices that are connected via a network. It acts as an address for the devices. Typical use of IP's day to day is your computer or your phones connected to the internet, but can also be used to connect IP cameras to networks or directly to computers.

module For this research, any computing unit that can receive, process or transmit data will be referred to as a module . This includes RPI's, data loggers, and computers.

Orthorectification Orthorectification is the process of georeferencing GCP's in frame and associating them with pixels so that each pixel is given a real-world length dimension. It is vital that orthorectification is done as accurately as possible, as it is these lengths associated with pixels that are used to determine how far a tracer moves between frames and its corresponding velocity. It is suggested that a minimum of six GCP's are used around the area of interest.

PIV - *Particle Image Velocimetry* PIV is a method of which image velocimetry follows to calculate surface velocities. It is an alternative method to PTV. It essentially follows a time-average velocity approach, which means tracers are not tracked for the entirety, but are located and then searched for after a period of time (a certain number of frames). This method relies on search and interrogation areas to track tracers across the image. Outputs are direction-magnitude vectors, usually of equal space along the stretch of the river. The method has been used to provide highly accurate results compared with aDcp's and is less sensitive to tracer disfigurement than its PTV counterpart. However, discontinuity and inhomogeneity of tracers severely hinder PIV processing. When choosing between PIV or PTV, it is important to consider the average tracer availability and stability in various flows.

Platforms (Fixed or Mobile) Platform choice depends on the type of study required from a site. For discharge rating curves over a long period of time, fixed stations are required. A fixed

station is a permanent/semi-permanent set-up where cameras are installed and secured to not move over the period of time. Mobile platforms are more temporary set-ups, usually for capturing peak flows or areas of interest where fixed platforms are not an option. Mobile platforms are typically drones or UAS's, but can be any temporary platform (e.g. telescopic poles, mounting poles etc.).

PTV - *Particle Tracking Velocimetry* PTV is a method of which image velocimetry follows to calculate surface velocities. It is an alternative method to PIV. PTV identifies and tracks a tracer for the entirety of its movement in frame. This method has been known to perform well even without a high seeding density, however, the more tracers present the more accurate that PTV can be. On the other hand, as each tracer is tracked throughout the entirety of its progression along the river, the processing required for high volumes of tracers may be more of a hindrance than it helps. Issues arise from PTV when tracers deform through the process of tracking. When choosing between PIV or PTV, it is important to consider the average tracer availability and stability in various flows.

RPi - Raspberry Pi Raspberry Pi's are small computing modules that are known for being relatively cheap and powerful. They run off of a Linux system and can be used as a simple shell or can be connected to and used with a Graphical User Interface (GUI).

Stabilisation All mobile platforms and some fixed stations will require stabilisation. Stabilisation is a process where all frames are referenced to a previous frame (usually the 1st frame), and the edges are cropped so that the image in the middle (where the area of interest usually is), looks to remain steady. There are several ways to perform stabilisation (e.g. pre-built programs, MATLAB code), most of which use types of detection and tracking software with consistently visible and stable features (e.g. corner points of walls or buildings etc.).

Tracers Tracers are the fundamentals to PIV and PTV methods. These are any trackable features on the surface of the river. These can be either artificially placed for specific studies (using wood chippings or decomposing materials), or where possible, naturally occurring. Natural tracers can be foam, or strong ripples seen on the surface caused by turbidity. The more tracers visible in the area of interest the better any algorithm can perform. There are recent studies on the density of tracers required for the best results, focused on Seeding Density Indexing (SDI). SDI is a benchmark system that disregards frames that do not meet the required SDI requirements (Pizarro et al., 2020b).

UAS - Unoccupied Aerial System UAS systems mostly used with image velocimetry are drone units. These systems allow a user to remote control a flying unit, most likely propeller based. This mobile method of image capture can be used where either fixed stations are not present and there are flows of interest, or where flows are too treacherous to obtain manually.

Technical Considerations for Image Velocimetry Practices

Pre-Processing

Prior to capturing and analysing any velocimetry data, users should look to optimise the set-up of the station to ensure that any imagery captured has the best possible chance of being usable. To do this, there are several considerations to be made. Tracers, average environmental conditions, Ground Sampling Distances (GSD), lighting, and orthorectification are all vital components to consider when setting up a station. Here, we will break down each of these and explain how and why they need to be optimised. This is a condensed down version of what to consider, and mostly taken from research previously carried out in Jolley et al. Jolley (2021).

Site Selection

When choosing where to place velocimetry systems or perform analysis, one must consider how the site characteristics match those needs that velocimetry has. Tracers and environmental conditions are two considerations that can be crucial to how well a system can perform, whereas the infrastructure of a site is something which is less crucial, but still needs consideration. If unsure on the availability of tracers, it is possible to take a short video clip (around 20-30 seconds), to initially run through RIVeR to check for compatibility; if successful, vectors will be prevalent on a majority of the surface.

Tracer Availability Tracers are any artificial or naturally occurring feature that is free-flowing on the surface of the river, capable of being tracked by automated systems. Artificial tracers can be used (e.g. wood-chips or decomposing materials), in individual studies of particular flows, typically seen with low-flow scenarios where the flow can be laminar and without substantial flow patterns. Ideally, we would look for areas of high natural tracers which can include foam from turbidity, or prevalent surface patterns. As a rule of thumb, look to have at least 10-30% coverage of trackable features. Advance users of image velocimetry should look at the Seeding Density Indexing (SDI) of sequences, as it shows to reduce velocity error by between 16-39% with both PIV and PTV methods (Pizarro et al., 2020b; Dal Sasso et al., 2021).

Environmental Conditions Adverse environmental conditions can disrupt either the capture of imagery, or the analyses of sequences. Fog, snow, rain and wind are currently the conditions that have been highlighted as problematic, with the addition of the glare across image also being questioned on its ability to impact results. Rainfall can disrupt tracers, as well as create false tracers where rainfall is heavy and flow is slow. Wind shears on the surface of the river and can also disrupt true paths of tracers, and in some cases, create more false tracers. Fog and snow can simply obscure the cameras view and the level of tracers that it can detect. There are no clearly defined ways of error correcting the environmental impacts, but it has been shown that strong headwinds

relative to the direction of flow can cause up to 8% of error to surface velocities. More research is being carried out in this field. For now, it is best to limit situations where strong headwinds and adverse conditions are seen. This means ideal sites would be somewhat sheltered from many of the elements and brightness is consistent across the river for a majority of the day. Where this is not always possible, be more cynical with results gathered, and in some cases, disregard where extremities are witnessed (thick fog, heavy snowfall).

Infrastructure When discussing the infrastructure for fixed image velocimetry, it can vary depending on what requirements the user has regarding the power requirements, networking, and structures that can be used for housing. Typically, it is easier for velocimetry stations to be set up at existing monitoring stations that have mains electricity, and are usually not too isolated to receive a mobile signal for networking. However, this does not limit where stations can be set up. Depending on the module used and the power requirements it has, solar panels and 12v batteries can be connected to create a completely in-dependant site. These may require more maintenance (battery changes and cleaning of solar panels), but are viable options, especially with low-power modules such as RPi's and simple data loggers.

Where networking is not viable from mobile networks or landlines, satellite broadband is usually available in most areas and can be used to upload data. Alternatively, data can be stored in-situ and manually collected routinely. This is not the ideal way of using the remote methods that image velocimetry can provide and should only be done as a final option. For the housing on structures, there are many viable options. Depending on the remoteness of the site, there are a few key things that need to be considered: the height that the camera can reach and its subsequent angle and GSD (see section 11.2), the security from both environmental conditions and vandalism, and the issues with legality concerning capturing imagery in general public areas. All of these are issues that are site specific, and cannot be generalised.

Camera Setup

Ensuring that the camera has been properly calibrated and ideally situated greatly increases the chances of accurately representing surface velocities. There are three main areas to consider prior to setting up your camera and housing: GSD, orthorectification , and lighting.

GSD GSD is a vital consideration to a majority of image velocimetry approaches. Often, this can be overlooked and the GSD is an afterthought. However, should GSD be properly considered prior to station set-up, that it could improve the probabilities of capturing more useful data (e.g. detect more tracers, track tracers more effectively). GSD is a mix of a few elements, but effectively, it is the distance associated with each pixel. For example, a 200×200 pixel image capturing an area of 20×20m will have a GSD of 0.01m/px (1cm/px). The main elements you need to consider for GSD when capturing at nadir are: image resolution, height of camera, camera focal length, camera

sensor width. However, where angles are introduced, GSD can be harder to estimate. Introducing an angle in any direction will skew GSD in the distance of imagery. This can get complicated, and does not need to be a perfect science. To help better understand how GSD is impacted, please see the excel spreadsheet created and readily available on GitHub Jolley et al. (2021). This spreadsheet allows the user to input the camera properties (sensor and focal parameters), heights and angles of the camera, and resolutions. From this information, it can estimate the average GSD across the image.

As a general rule of thumb, you want to be aiming for as small of a GSD as possible, around 1-3cm/px, to match the size of the tracers that you typically see in the imagery (ideally a tracer would be slightly larger than 1 pixel so that it is clearly defined). It is best to begin by limiting the resolution that you use, as research shows that using high resolutions does not always significantly increase the accuracy of models, but does significantly increase the power and processing requirements Jolley (2021). This gets complicated when you have to consider the size of the area that is required to be covered and how you are able to get tracers clearly defined. For smaller channels (¡10m) and capturing at nadir, it is a good idea to begin by using a resolution of around half full-HD (960×540), although it has been shown that lesser resolutions can obtain data just as well (something to consider depending on site limitations). For wider/larger channels, half full-HD can also be used initially for angles up to about 30°, for angles larger than this (previous studies use angles up to around 60°), perhaps consider using higher resolutions (up to full-HD). At larger angles, it may be hard to capture meaningful data in the far bank, but post-processing tools can help extrapolate this data where it may be missing/unreliable.

To set up the camera optimally, it is advisable to bare in mind that the closer to nadir a camera is the better. This means that the height of the camera can play a relatively large part in impacting GSD. However, large camera heights can be challenging in regards to maintenance and safely setting up the station. Therefore, it is advised to use a camera that has a variable focal length (zoom capability), and set up the camera in a safe and efficient manner at the highest possible height, with the smallest possible angle. It is possible to get focal lenses that provide 180° of view with a high level of resolution which can be used where heights cannot be reached accessibly.

Orthorectification Orthorectification is a process of associating a real-world length with pixels by georeferencing stationary points (GCPs) in frame using either a localised coordinate grid, or a globalised grid. It requires a stable image frame throughout, which can be achieved from a secure fixed station (although can sometimes undergo small oscillations), or through stabilisation for mobile platforms, see section 11.2. There is much research on the best ways of implementing orthorectification, but for simplicity, users should look to implement an absolute minimum of six GCPs in the frame, with at least four immediately around the area of interest Jolley (2021). It is, however, advised to use more than six GCPs, as an increase in GCPs increases reliability. Where data is captured perfectly at nadir, orthorectification is not a necessity. Alternatively, it is vital

that the user accounts for lens distortion and manipulates the imagery data to remove these by calibrating the camera. Often, cameras come with the parameters it uses when distorting images and this can be accounted for relatively simply (some models of camera come with software that allows them to be modified to remove lens distortion).

Lighting A major issue with image velocimetry is its capability of working at night where channels are not illuminated. Infra-red cameras can be used and some studies show that image velocimetry can be applicable in these conditions, however, it is unclear on how effective it is at accurately representing surface velocity. This is something to be monitored at sites and evaluated at the time. Where it is not a viable option and results are not coming through, illumination can be used during the times that image captured is required. For example, if the user sets capture time to be 30s of capture every 15 minutes, then lights can be programmed to illuminate the surface for the 30s that are captured and then turn off.

Stabilisation Stabilisation is a process that references each frame to a reference frame (usually the 1st or a previous frame), and crops out edges to give the appearance of a stationary frame. This is mostly used for mobile platforms, where stabilisation is a critical component. However, it is sometimes important for fixed platforms that witness some forms of movement through vibrations from traffic (when close to a road e.g. on a bridge), wind, or any other oscillations. To perform video stabilisation, some cameras have built in stabilisation (e.g. GoPro's), but pre-programmed software can be used, as well as MATLAB coding, as seen with this example available on GitHub.

Processing

There are two main ways of processing data, either remotely through uploads and downloads, or in-situ. Studies have looked at the amount of power required to process sequences in-situ using RPi's "at the edge" and have manipulated software to better suit these requirements Livoroi et al. (2021). This study concludes that a RPi 4 uses the least amount of energy, and can perform 160 full cycles of of Optical Tracking Velocimetry (OTV) on a single 12v battery charge (715×540, monochrome). This methodology of in-situ processing, along with those that are similar, is incredibly useful where network connections are not reliable or upload speeds do not allow vast amounts of data transfer. However, where networking is efficient and can be done with relative ease, it is currently advised to not use in-situ processing. The reason being, with images being networked and stored online, it is available to be viewed and re-analysed in alternative methods where reliability is questioned.

Remote processing is currently the most common method of using image velocimetry. This typically involves capturing footage and uploading it to a cloud storage solution. Footage can be temporarily stored onto the module ready for uploading. This data is then downloaded to a computer for processing and a software suite can be used to produce the velocity outputs. This

results in the module at the site not requiring large amounts of processing power and can be cheaper module units.

Post-Processing

Post-processing can be a generic term for anything that the surface velocity results are used for; most notably being calculating discharges. However, there are also some other processes that can be applied to the output data, including those that look to validate and correct the velocities calculated.

Calculating Discharge

Many software suites have the built in capability of producing discharges from the velocimetry data. For this, bathymetry (cross-sections), is usually required. The simplest method to use is a velocity-area method, which introduces typical fluid dynamics parameters, such as α. α is a depth-average value obtained from finding vertical velocity profiles (typically with aDcp's). Where it is not possible to obtain site specific α values, it is reasonable to assume a value of 0.85 Creutin et al. (2003); Coz et al. (2010).

Error Correction

There are methods that can filter erroneous vectors for both PIV and PTV results. For PIV, vector validation is an option, which uses several statistical methods and referencing each cell to its nearest neighbour for comparison Raffel et al. (2018); Hart (2000). These methods include vector difference tests, median tests, and normalized median tests Westerweel (1994); Westerweel and Scarano (2005). For PTV methods, validating data can be more challenging due to the unstructured layout of its vectors. The algorithms used for PTV validation stem from those that were created for PIV, however, will struggle to validate data that has more than 15% of outliers. For both PIV and PTV, validation and correction can be done using the Universal Outlier Detection Scheme which is available as a MATLAB code online Duncan et al. (2010). For a majority of studies, it would be hoped that corrective methods need not be used, however, where more detail is required or where it is obvious that errors are occurring (often in more turbulent areas), then it may be advised to run corrective measures. RIVeR (one of the pieces of software we look at in section 11.2, has built in post-processing features that can easily be used by users to validate and replace vectors).

Hardware Considerations

In this section, we will begin to discuss some of the pieces of hardware that can be used to set-up image velocimetry stations. These will be advisories, and lists will not be exhaustive, however,

each piece of hardware will be chosen because of its capabilities to perform the type of analysis and optimal parameters listed in section 11.2.

Platform Type

As previously mentioned, platforms can be either fixed and more permanent features, or mobile platforms can be used for capturing individual flows (usually extremes). Each method is fully capable of providing reliable image velocimetry data, but each has its own limitations and advantages. Fixed platforms are generally used for long-time studies such as discharge-rating curves, and are typically CCTV cameras attached to a structure such as a pillbox monitoring station or scaffolding poles. Mobile cameras are more flexible and have their own criteria that needs to be met to ensure reliable data is captured. The most popular way of using mobile platforms currently, is with the aid of UAS's (drones). Here, we will discuss some of the popular methods that can be used for both fixed and mobile platforms, and begin to look at the considerations needed to produce reliable results.

Fixed Platforms As previously stated, fixed platforms are stationary cameras, more permanently fixed to structures that will not undergo movement. These stations are capable of capturing a time-series of imagery that can either be processed in-situ or alternatively, networked and processed after. The issue with fixed stations is that once they have been established, you cannot alter the field of view without having to recalculate coefficients used for converting pixels to real world coordinates Jolley (2021). During this form of analysis, often it is important to know the stage of the river to understand the distance between the camera and the surface of the river. This can be done with pre-existing stage meters, or ultrasonic level sensors that are also recording the stage alongside the camera data. When using fixed stations, there are a couple of key parts that are required to be considered, namely the source of power for the module and camera, as well as the networking of the module should it be needed.

Power Considerations The easiest way to provide power to fixed stations is through the use of mains that are connected up to a previously installed monitoring station. However, how often will it be required to get further information at stations that are already monitored? There may be occasions that it is needed to extend discharge rating curves or validate them, however, a majority of the time we will be looking to capture data in either more remote locations not previously monitored, or in areas where mains is simply not viable. For this, it should be noted that systems can be battery operated depending upon the module and camera model used. Without going into detail on the module used (as this will be discussed later in section 11.2), a typical method of providing power to monitoring stations is using a 12v battery (such as a car battery), and a solar panel. This method may require some regular maintenance (e.g. swapping out batteries, cleaning solar panels), however, the time spent maintaining these sites could outweigh the time

usually spent monitoring the site manually. The key to using batteries for this is to ensure they are raised off the ground and are fairly well insulated to prevent the cold from draining them. Solar panels may be enough at times to fully recharge the batteries, however, there may be circumstances where foliage and the time of year prevent the panels from sufficiently keeping the battery charged, it is in these instances that they will likely need replacement and manually recharging. ***Something to think about?...*** Alternatively, depending on the state of the site, it may be possible to install a small hydro-power charging unit to supplement or replace the solar panels. Hydro-power will be relatively consistent throughout the year, more-so that solar power. However, this has not been a tried and tested method in regards to image velocimetry, so there is no precedence. With that said, there is no reason why it could not be a viable option for some sites, as technology advances have been able to create portable hydro-chargers that are no larger than a car battery themselves. A perfect example of such a contraption could be the Blue Freedom portable charger seen here. As previously stated, this is not a tried and tested method of charging stations, but with a little more research and in comparison with site studies, there is no reason as to why something like this could not be implemented.

Networking Considerations Where stations are not going to be visited to manually collect data, data will need to be networked via some method from the module to off-site storage for remote processing. The most common method here can be mobile networking where it is possible. For many locations that are not completely remote, there can be stable mobile network connections that can be used via a networking module hat (addition to modules e.g. RPi hats), a sim card, and a suitable antenna. The usual cost of this per month for the internet connection is around £20-30 for unlimited internet. This could be adjusted depending on several factors such as data size, type of processing (in-situ or off-site), and frequency of monitoring. However, there will be some cases where mobile networks are not sufficient. For these areas, a majority of the time satellite internet will be available and can be used. This is more expensive than mobile internet, usually around double the price per month, but is available in even the most remote of places. Where satellite broadband is used, if cost minimisation is a priority, it may be worth looking at in-situ processing and only communicating results rather than uploading full videos, especially where videos are a high-resolution and hence require a large bandwidth. However, if budget is not a major concern, it could be advisable to still communicate full videos so that data can be checked and alternatively processed.

Mobile Platforms Mobile platforms are ever more present in the modern era, and are becoming increasingly affordable. Historically, mobile methods of image velocimetry would include using tools such as telescopic poles, but modern methods allow users to implement drones and UAS's. Mobile methods are predominately used to capture specific flows such as extremely high flows where it is too dangerous to deploy aDcp's or other contact methods. The advantage it has over

other non-contact methods is that it still provides a full area of velocimetry data rather than point specific data. The reason for using drones or telescopic poles instead of simply setting up a camera say on a tripod, is to prevent the need for orthorectification by capturing at nadir angles. Using a temporary setup on a tripod will still require the user to orthorectify the images. This can be done at a later time if the camera is geo-referenced to a global grid (using GPS), and surveys are later carried out using the same system. This would be done if storm chasing flows and it is not safe to perform a GCP survey during the high flow.

UAS UAS systems such as DJI Phantom drones now cost less than £1500 per unit. These come installed with gimbals and cameras that are able to capture high-definition footage for periods of around 30 minutes of flying time. The main issue with using UAS systems is the need for accurate and reliable stabilisation to remove apparent movement (see section 11.2). As stated, orthorectification is not required when capturing data at nadir , however, it will not always be the case, and where cameras are required to be angled (height of the drone is outside that of which you are comfortable flying it needed for capturing the full width of the river), orthorectification is still required. This can be accomplished by laying out several GCPsalong the bank of the river, such as simple checked board sheets. Many UAS systems have the capability of automatically storing their location using GPS for determining camera location. A good example of using UAS systems for capturing image velocimetry data is seen in Perks et al. (2016) Perks et al. (2016) and Ioli et al. (2020) Ioli et al. (2020).

Telescopic Pole Telescopic poles have been used several times in previous studies Dramais et al. (2011); Coz et al. (2010). They often include a remote controlled platform at the end of the mast, and can use a majority of cameras, however, a GoPro is usually the preferred choice due to its cost, weight, and capture capabilities, (see section 11.2). The use of a telescopic pole allows a user to elevate the camera to an advantageous height that reduces the angle of capture and subsequently the distortion of GSD in far field zones. Much like that of UAS based captured, stabilisation will need to be applied to the images and orthorectification where angles are non-nadir.

Out of Bank Flows At times of substantially high flows, where rivers burst their banks, analysis may be wanted to be carried out. Issues with out of bank flow measurements is, that with fixed cameras, the out of bank flow must already be within frame as it is not possible to change the Field Of View (FOV) without having to re-calibrate imagery. An alternative that has been soft-trialed is the use of fish-eye lenses that capture 360° views, so that should a river burst its banks, it has some chance of being captured. This still, however, requires further research. It may be possible to capture and process the out of bank flows with mobile platforms, but the challenge would be understanding how flow traverses the landscape. Alpha valuesmay be well established for in-bank flows, however, there is a lot less research around depth-average velocities for out of bank flows.

Where surface velocities have successfully been captured, it could still be possible to estimate the discharge, but note there may be substantial error bounds.

Surveying Requirements

As previously mentioned, image velocimetry requires a series of GCPs for orthorectification. For post-processing discharges, cross-sections of the river are also usually required. Therefore, the best way to navigate this is to do a full site survey at the initial time of setting up. Once the camera has been installed, lay out your 8+ GCPs within frame and ensure they will not move during your survey. Once set-up, capture these GCPs in a video that can later be used for analysis, or simply capture an image so you can clearly see each GCP. Next, do a full site survey that includes capturing all of the GCPs, the camera location, and 2 or 3 cross-sections along with water level. Using a base-station as a reference point could also mean that you can locate your local coordinate grid to a global grid using GPS. This process needs to be only done occasionally, namely when the camera undergoes any sort of movement (tilts, shifts, rotations), or after a large event (as large events can disrupt river beds, through scour and other processes). For advanced users, 3D laser scans can be used to capture the full channel in frame, along with camera locations and cross sections. This gives a much more dynamic range of locations that can be used for orthorectification, and if captured in low flows, can give more accurate cross-sections. Cross-sections can also be captured using an aDcp if also geo-referenced to the same grid.

Camera When it comes to image velocimetry, the type of camera used could simply be personal preference, or limited by budget. The important factors when it comes to the camera choice are its lens lengths, max resolution, sensor size, and cost. There are also other limiting factors that could be problematic depending on the type of site being developed such as weight, power consumption, and size. Where a site has ideal conditions (i.e. has no limiting factors), within reason, most cameras could be used and still obtain usable data. The key to selecting the camera is deciding what the limiting factors are, how they are to be used, and ensuring there is not a large amount of redundancy in terms of the capabilities of the camera and what is required from it. For example, using a 4k camera to capture imagery that is going to be no higher than 720p. For mobile image velocimetery methods, where cameras are not already provided, the weight, size and compatibility are also important considerations.

Camera Types The parameters of a camera are the main variants between camera models (e.g. lenses, resolutions, etc.), however, the type of camera also extends to the way that the camera runs and how it communicates to a module. For years, cameras have been able to run off of low-power connections, such as USB's (such as webcams). Alternatively, larger cameras such as security cameras still require a higher voltage input. The availability of power will be a major consideration in the type of camera to be used. The following cameras could all be used for fixed platforms,

but not all are also compatible with mobile platforms. With that being said, although they may be compatible with both, they may not be the best solution for both, and some cameras better lend themselves to the flexibility that fixed stations may need.

USB Many modern webcams are cheap, reliable and capable of capturing high resolution imagery, typically to at least HD (1080p). Webcams connect via USB for their means of communication and power, which can be an efficient way of capturing data as it minimises the number of connections required. USB based cameras, however, are not typically built to withstand outside conditions and will need to be protected via casing. With that said, the cost of the these cameras means that they are easily replaceable should they be broken or damaged. Other issues with using USB methods are that they are typically not very flexible in what they can offer regarding range, FOV, and ultimately GSD. Previously, GSD was mentioned that it is one of the most important considerations regarding image velocimetry practice. A camera that provides a flexible GSD means that it can be optimised on site with minimal effort to capture tracers in the highest possible detail. There are a number of case studies that implement USB based cameras, with some options available listed here:

Table 11.1: Examples of small, USB cameras that are readily available and could be effectively used in the field for both mobile and fixed platforms.

Camera	Max resolution	Focal Length /FOV	Sensor Size	Features	Estimated Cost (£)
Olympus Tough TG-6	4K	4.5-18mm	12MP 1/2.3 inch	USB Connection, Weatherproof	369.00
GoPro Hero10	5.3K	SuperView, Wide, Linear, Linear + Horizon-Leveling, Narrow	23MP 1/2.3 inch	Lightweight, weatherproof, USB connection	380.00
Arducam B020201	1945x1109 pixels	160 degree	2MP 1/2.8 inch	Not weatherproof, very lightweight, vast compatibility, USB connection, 0.0011ux	46.00
raspberry pi HQ Camera	1080p30, 720p60 and 640 × 480p60/90	Depends on lens	12MP 6.287mm x 4.712mm	Multiple lenses available, vast compatibility, USB connection, very compact	47.27 + lens

Network Cameras Network cameras are digital cameras that operate over network connections, rather than relying on local storage for capturing imagery. Network cameras (or IP cameras), can be connected to and viewed live, via computer or even mobile methods. IP cameras can be connected via wireless, Ethernet and even USB. These cameras provide high quality imagery that can be used for velocimetry, but are typically larger and heavier than the more mobile methods listed in Table 11.1. Some possible IP cameras that can be used are listed in table 11.2, and are picked for their flexibility and capabilities of being used for image velocimetry.

Analogue Cameras Analogue cameras are the typical type of camera used for CCTV. They require power and data cables and feed data to modules. They have a history of being reliable and cheap sources of video surveillance, but have recently became second best to IP cameras in most fields regarding quality, reliability, and in some cases, price. There are instances, however, where this is not true. Some analogue cameras provide good quality imagery in low-light conditions, for a reasonable price.

Table 11.2: Examples of network cameras that are readily available and could be effectively used in the field for fixed platforms.

Camera	Max resolution	Focal Length /FOV	Sensor Size	Features	Estimated Cost (£)
HIKVISION DS-2CD2647G2-LZS	2688×1520	3.6 to 9 mm	1/1.8 inch	0.0005 Lux, 60m illumination, colourised low light imagery, weatherproof	370.00
Wisenet QNP-6230H	1920x1080	4.44-102.2mm	1/2.8 inch	colour: 0.2 lux (F1.6), b/w: 0.01 lux, 360 degree pan, 23x optical zoom, weatherproof	950.40
Vivotek FD9368-HTV	1920x1080	2.8-12mm	1/2.9 inch	IR capabilities (30m), <0.005 lux b/w, weatherproof	200.40
LILIN ZHR8182EX2	4K	3.6mm–10mm	1/1.8 inch	IR capabilities (35m), colour: 0.4 lux, b/w 0.08 lux, weatherproof	776.40
ReoLink RLC-523WA	2560x1920	2.7-13.5mm	1/2.7"	Wifi connection, IR capabilities (60m), weatherproof, 360 degree pan	205.59
Reolink Go	1080p HD	110 degree diagonal	-	Wire-free, battery, solar compatible, 5V power, IR capabilities (10m), fixed lens (digital zoom), sim network	173.73
Hikvision EXIR Fixed Bullet Solar Power 4G Network Camera	1920×1080	2.8mm,4mm,8mm	1/2.8"	IR capabilities (30m), wire-free, battery, solar included, colour: 0.004 Lux, b/w: 0.002 Lux, fixed lens, sim network	1,800.00 + VAT

Table 11.3: Examples of analogue cameras that are readily available and could be effectively used in the field for fixed platforms.

Camera	Max resolution	Focal Length /FOV	Sensor Size	Features	Estimated Cost (£)
RS PRO Analogue Camera	1312 x 1069	5-50mm	2.12 MP	IR capabilities (40m), colour: 0.08 Lux, B/W: 0.008 Lux, small in size	335.20
Vicon Analogue Outdoor IR CCTV Camera	1080p	2.8-12mm	1/2.8 inch	IR capabilities (30m), colour: 0.03 Lux, B/W: 0.01 Lux, 360 degree view	230.77
Twilight Pro CAM HD VFC 2 G	1080P	2.8-12mm	1/2.9 inch	IR capabilities (30-50m)	63.65

Processing Raw Data

Video data capture is the start of image velocimetry, and whatever methods you use to capture that data, feeds into the second step; processing. There are two main ways of performing analysis of the raw data, either in-situ or off-site. In-situ processing can be done primarily where network connections are not available for data transfer, or where it is limited in such it may only be able to transfer output data (e.g. text files of results, where the size of the files may be relatively small).

Modules

Modules are systems that are capable of communicating with the camera, and are used to capture, store and transfer data. There are many different methods that could be used to capture, store and transfer data, and sometimes multiple devices can be used in tandem. The main module systems to use are one-board processors (such as RPi's), simple data loggers (such as the Iris wireless logger), or full systems which can be complete computer set-ups.

Raspberry Pi

RPi's have several models, the latest being the RPi 4B. RPi's are single board computers that have a good amount of processing power in relation to their cost. Typically, depending on model, a RPi unit costs between £5 and £60 for the basics, with additional costs for SD cards and alternative hats. All RPi's can be used as a controller to capture data, most can be used to store some data, and some can be wired to provide a data transfer and sometimes even process some image velocimetry data.

The advantage of using a RPi is the cost effectiveness of them. RPi's are Linux based operators, and can be coded to run any script. If connected to a mobile network, it is also possible to remotely control them, which can be significant if setting up a full network of modules. raspberry pi Pico's are the cheapest models at £3.60, and is specifically designed as a controlling module . With this, it should be possible to use it to control cameras and other hardware, however, it is not possible to do many more advanced pieces of processing such as running programs or uploading data. For a more flexible and complete station, it is advised that the modules used when using an RPi is a raspberry pi 4, or whatever the latest model is. Pi4's have the capability of being fully remote accessed, programmable to run code and software, and have the capability to be added to in terms of different hat modules (for mobile networking, power capabilities and other connections). Pi4's have also been trialled at running a PIV software (OTV), relatively successfully. In addition to this, it is also possible to purchase and apply camera modules to the RPi4 which have the potential to be used for image velocimetry analysis. RPi4's cost around £34, with power hats costing around £20, and sixfab mobile networking hats around £30.

High-Performance Methods

The running definition for a full system is one that is able to compute and transmit data as one unit, simply a laptop or desktop computer. If processing in-situ is required and the conditions are hospital (e.g. power supply, dry housing), then it may be best to set up a laptop with sufficient RAM to capture, record, and process the data. USB mobile network dongles are available to connect the laptops to mobile networks if possible so that they can transfer results, or hard-drives can be connected to increase internal storage so that all data is captured, processed and stored on-site ready for retrieval. Alternatively, single board computer alternatives to the RPi are available that provide desktop computer results. These can be the equivalent of a super-computer that processes up to 3.6 GHz, such as the UDOO Bolt V8, capable of running windows 10 and the software suites used for image velocimetry, with the need to adapt the programs for running on lower-power modules.

Trigger Sensitive Systems

Trigger sensitive systems can prevent modules and systems from drawing too much power from being active despite not being needed. Examples of this would be to use a trip linking the camera and the stage of the river so that there is only data captured for particular flows. This can be done using ultrasonic level meters or equivalent. Alternatively, Iris data-loggers, if used, have a 5V power out switch that can be triggered to deliver power to a 5V camera unit. There are several other methods that can perform the same task and should be explored by the user.

Networking

Networking data from the site can be a challenge, especially in remote locations where mobile networks are inconsistent or non-existent. The type of networking done will depend upon the type of module used and the type of data needed to be transferred. A major advantage of networking to a module is the capability of remote accessing fully. Not only can you remotely and automatically transfer data from the site to places such as online storage, but it is also possible to log in to some modules and control them without being on site, should code or software need updating.

Mobile Networking

The simplest of methods for connecting modules to the internet for networking would be to use mobile internet. Mobile internet for modules works very much the same way as a mobile phone, with typically a networking adapter (either a USB stick or module hat), a sim card, and an antenna. To use mobile networks, the sim card needs to be registered to a mobile network and activated with some allowance for mobile roaming included. The amount of data required depends on the characteristics of the site and what output you want from it. Large rivers that require higher resolution images will need more data to upload the videos, however, if you process the imagery in-situ and only send across the results of the analysis, then you would not need as much. It is best to decide what you want to accomplish at the site and adjust for that where budgets are not large, otherwise, sim cards that come with unlimited data are the best way forward, mainly to avoid a data loss should it run out. The main issue with mobile networking, however, is the signal strength. Image velocimetry is a very useful technique for sections of river that are isolated, where remote working is a major benefit. In these areas, especially those that are hilly or mountainous, there may be very little to no signal. In these areas, alternative solutions are required.

Satellite Networking

Satellite networks work similarly to those of mobile networks, but instead of connecting to the nearest mobile network mast, satellite connections are used for the transfer of data. Historically, satellite connections were relatively slow to that of wired and mobile networks, however, the advances in technology have pushed up the speeds that are capable from satellite networking tremendously. The major benefit of using satellite networking is its capability to connect virtually anywhere. Where locations are remote, and mobile networking is not available, satellite networking is the only alternative for connecting to the station. The main disadvantage of using satellite networking is the sheer cost of running. The set-up usually requires a satellite dish, which can be portable, but are still fairly substantial in size and set-up. The cost of running satellite internet is also nearly double that of mobile internet, and is still capped on monthly usage (there are, however, large data packages available that could still meet requirements).

Bandwidth

The bandwidth of a site usually is not a major consideration, as uploads are done automatically and can be done in their own time. Problems with bandwidth occur where a backlog of data begins, should it not be uploading at a speed that is quicker than the time between capturing data. Also, issues may persist where sites require remote working, and streaming the camera through the mobile network for any reason. Typically, HD streaming requires 2.8Mbps. Anything close to 2.8Mbps should not result in any uploading issues for the videos, but could perhaps impact any streaming via remote connection that may be required. With that said, it is not very often a remote connection to live stream the camera will be required, and therefore should not impact the decision significantly. Where the bandwidth is not sufficient, the interval between cameras should be lengthened to allow for a full upload of the previous video before the next is stored. If this is impacts the study significantly, there alternative solutions should be found.

Storage

Storage is a significant part of the image velocimetry cycle. Decisions should be made from the start on what data should be stored, how it should be stored, and who has access to that storage. When storing video imagery, there are particular problems that may persist legally. Where there are images of people, permission is needed from those people to store the data, unless there are measures in place which already accounts for this. Secondly, the amount of storage required for some sites is substantial, and will ultimately determine what solution to storage is used.

Hard Storage

Hard storage is defined as a physical location for the data, e.g. on hardrives or portable storage units. Portable storage units now have the capability to store terabytes of data on them, which can be more than enough to store over a years worth of HD videos to, and results. Hard storage can be used either in-situ, or data can be sent across a network to a hard storage solution off-site. The advantage of a hard storage solution is that there is a non-networked copy of the data, which could mean limited access to people, as well as having the data in one physical place. However, should that hard storage device become corrupt, lost, or damaged, then it can result in all of the data being lost instantly. Many camera units have the capability of storing data on them as a hard copy on micro-SD which is placed directly inside the unit. This could be a valuable asset where hard storage is used, as it can allow for some data to be retrieved should the original hard storage unit become damaged. With that being said, it is also possible to make multiple copies of the data (back-up copies), however, this instantly doubles the demand for storage and also creates issues of where to store data, and who may get access to the data.

Cloud Storage

Cloud storage is a relatively new piece of technology, and has seemingly endless amounts of storage space. Personal services such as Googledrive, Dropbox, and OneDrive have flourished over the past decade, as it allows users to store all of their data off of a single device (away from hard storage), and into a cloud, where it is accessible from anywhere and can be shared instantly. There are now various cloud services available for business users, that boast about the quality of the security that they have, which can be essential for such things as risk assessments for capturing and storing video data. Cloud services can be uploaded to directly from a module , and once uploaded, accessible from anywhere. This could be a major benefit for automated systems where code is used to upload/download data remotely, and then results re-uploaded to either storage or websites for up to date data. Previous studies conducted at Newcastle University uses Amazon Web Services, S3, for all of the cloud storage requirements. Modules can automatically connect to S3 services and create 'buckets' (folders) for data to be routinely dumped directly via mobile networking.

Software Considerations

Introduction to Software

In this section, we are to discuss the analysis processes that turns raw video data into image velocimetry outputs. The main focus of this work will focus on PIV and PTV methods, such as LSPIV and LSPTV. A little bit of detail will be provided on how these schemes work, as it provides the fundamentals on which method is best to use for the specific site, as each has its own advantages and disadvantages. We will also begin to look at some of the software suites that are currently available, and begin narrowing them down for practical uses.

Detection and Tracking Schemes

Detection and tracking schemes are fundamentally what builds a PIV or PTV algorithm. Tracers are initially detected by the algorithm, which can range from patterns on the surface that are stable across the timeline, or individual particles such as pieces of foam (for more, see tracers at section 11.2). Tracking schemes are what allows algorithms to follow the detected tracers between frames, and there are numerous way to both detect and track said tracers. The way algorithms work is explained in Jolley et al. (2021) Jolley (2021), but is outside the scope of this handbook. What is required, is to understand that software varies in the way that they detect and track tracers, and this is the main difference between many.

PIV PIV is a method of image velocimetry that basically breaks down a frame into search and interrogation areas. Once established, each search area detects and tracks tracers independently to the next using the interrogation areas to find particle displacement. This results in each search

area producing a time-average velocity, usually provided in the form of a direction and magnitude velocity vector. There are a few key areas that must be considered when using PIV methods, mainly that the search areas must be large enough to successfully detect and track tracers without losing them (e.g. if tracers are moving too fast they can fall outside a search area and not be successfully tracked). PIV is a method that works well and can be highly accurate (compared to aDcp measurements), where tracers are prevalent throughout the timeline, and can be less sensitive to the deformity of the tracers Muste et al. (2008). Problems arise, however, where tracers are inhomogeneous or are discontinuous, and can negatively affect the quality of the analysis. Where this is the case, PTV methods may be better suited.

PTV PTV methods are known for being a little more complex in the way that algorithms perform. Instead of focusing on areas of a river, PTV methods detect and track individual particles for the entirety of the video (where they are not lost). PTV methods tend to work better than PIV methods where there are low seeding densities. However, the more tracers that are successfully tracked, the higher the probability of producing a reliable surface velocity profile. With that said, the main disadvantage of using PTV methods is the processing power required, especially when tracking large amounts of tracers of a long period of time, as the amount of tracers and processing time are somewhat proportional. At times, large amounts of tracers can also impact the tracking capabilities of the algorithms, as it can make tracers much more ambiguous Zhang et al. (1997).

Available Software

There are many different variations of software that use either PIV or PTV methods, many are free or open source. As these methods have developed, they have began to become much more user friendly, with easy to operate GUI's and more advance features that allow the user to do more with them. It is not proven currently proven that commercial software provide better results from imagery, however, they may be developed to be more user friendly and intuitive. With that said, the cost of commercial licences can be very expensive (around the £10,000 mark per licence), for what usually is a cheap system (around £1000 per system depending on set-up). This section will begin to explore those software suites and look at some of the requirements for each.

Open Source

Free and/or open source software allows for rapid development to drive the advances of a software. The main benefits of open source software is the community support that surrounds the piece. Many of the pieces of software that are open source are used in many varying pieces of literature. Suites such as LSPIV that have been around for years, have been a focus method of image velocimetry for pieces of work that do not just focus on outcomes, but also parameters such as the impact of tracer densities, mobile platforms, and other papers that compare one piece of software to another. This

sort of development and critique of software is not always readily available to pieces of software that have been commercialised, and the general community of those that are knowledgeable in using the free software will greatly outnumber those using the commercialised. A list of some free software can be seen in table

Table 11.4: A non-exhaustive, generalised, overview of software suites that are currently available with some of their requirements and functions listed. Taken from Jolley et al. 2021 Jolley (2021)

Software	**Overview**	**Requirements and Functions**
PTVlab Brevis et al. (2011)	PTVlab is a MATLAB code, using particle identification to track movement. PTVlab enhances the images to better show particles and their centroids. With this data, it performs integrated cross-correlation and iterative relaxation labelling techniques to better represent varying seeding densities and track their trajectories.	Image enhancement is performed to highlight the flowing particles and their centroids which are tracked by the software. This tracking requires the user to input interrogation area sizes.
Fudaa-LSPIV Coz et al. (2014)	Fudaa-LSPIV is a free software created using a Java GUI. It begins with image preprocessing, taking video clips and converting image sequences into PGM ASCII formats. It then sequentially performs orthorectification, PIV analysis, result processing, and discharge computation. Within the software is the ability to visualise and export the data in different formats.	For accurate results, users will need to input GCPs, water level estimations and the positioning of the viewpoint. For discharge measurements, bathymetry profiles are required.
PIVLab Thielicke and Stamhuis (2014)	PIVLab is available as an open source GUI within MATLAB, using several of the built-in processes that MATLAB has to offer regarding image pre-processing, image analysis, post-processing and data exploration, producing outputs in video, image or vector map forms.	The software uses image enhancement, camera calibration and orthorectification to improve the images. It relies on the user to choose interrogation and search area sizes to perform direct cross-correlation and direct Fourier transformations.

Table 11.4: (continued)

Software	Overview	Requirements and Functions
RIVeR Patalano et al. (2017)	RIVeR is a standalone MATLAB code that uses the theories behind PIV/PTV software but has been designed to provide a simple user-friendly application. It extracts images from video footage, processes them using PIVLab/PTVlab algorithms, then uses GCPs to orthorectify the images and produce velocity and/or discharge results.	Video image extraction rates, frame rates, colour depths, and camera and lens parameterisation is required as an initial input to the software. GCPs also need to be referenced in the images for orthorectification. For discharges, section bathymetry is required.
OTV Tauro, Petroselli and Grimaldi (2018)	OTV processes data through feature detection, feature tracking (using the Lucas-Kanade algorithm), and trajectory-based filtering. This improves the reliability of the velocities as it only retains what are believed to be reliable feature trajectories to reduce error. This produces an average surface velocity estimation.	The software automatically detects features and does not rely on inputting tracers. The direction and length of the flow is determined by the user, who can also determine the quantity of trajectories. Can be mildly affected by lower resolutions and image frequency.
Photrak SSIV Carrel et al. (2019); Leitão et al. (2018)	SSIV uses cross-correlation like most other PIV methods, but unlike other PIV methods, SSIV filters erroneous vectors rather than attempting to correct them. Photrak has two systems available for use: DischargeKeeper which is a fixed IP camera with local processing for continuous measurements, and the DischargeApp for smartphone compatibility. Initially designed for use with consumer-grade surveillance equipment in urban environments.	SSIV requires full camera calibration to take place, with several reference points in the frame of view for orthorectification of the images. Search and interrogation areas need to be defined by the user. Without water level information, SSIV cannot provide discharge but only flow velocity.

Table 11.4: (continued)

Software	Overview	Requirements and Functions
KLT-IV Perks (2020)	KLT-IV is a user friendly interface that aids users with a step by step process, taking video sequences from fixed or mobile platforms and GCP data and producing surface velocity results and discharges (with the addition of alpha values and cross-sectional data). The software allows users to stabilise videos and orthorectify frames. KLT-IV uses GFTT and subsequently the Kanade-Lucas-Tomasi tracking scheme for tracking. This is a pyramidal tracking scheme that searches 30 iterations within interrogation areas to find the new location of each point until it reaches convergence, discarding any results that produce an error of 1px or more.	For accurate results, camera calibration is required. This relies on knowing the model of the camera for removal of lens distortion and orthorectification of images. This software then tracks individual trajectories through a known 'extraction rate', block sizes, and known reference points. Variations occur depending upon extraction rates.

Commercial

The majority of software currently available for PIV and PTV methods have been developed and published for free use under general public licence. However, there is one piece of software called Hydro-STIV that is currently being sold for commercial use. This software does not use the typical PIV or PTV method, but instead, uses what is known as Surface-Time Image Velocity (STIV). This is different to PIV and PTV, and uses brightness variation across frames to determine flow. Instead of tracking particles, it follows a particular search line and measures its change in brightness to produce what is known as a 'gradient'. This gradient produced by each search line gives the space-time average velocity along the river, the steeper the gradient, the slower the velocity and vice-versa. The brochure for this software can be found here, which gives a good breakdown on how the software works. There is also several pieces of research surrounding the use and development of STIV and similar software Fujita et al. (2007, 2019); Tsubaki (2017). For the initial phases of development of techniques that this handbook focuses on, STIV is not a consideration for use. The free software suites currently available that uses PIV and PTV methods can more than aptly represent surface velocity fields, as has been shown in numerous pieces of research over the past 20 years. Perhaps, once stations have been successfully created and stabilised, other software suites can be trialled and compared to aDcp and PIV/PTV data to determine which is more user friendly

and requires less training/validation.

Image Pre-Processing

In some cases, video imagery needs to be manipulated so that tracers are as prevalent as possible on the river surface. All software suites require imagery to be captured or converted in gray-scale, which can then be further enhanced using several different methods. The overall aim of image pre-processing is to reduce the noise around the area of interest, reduce the probabilities of erroneous vectors, and enhance the chances of a tracer being detected and successfully tracked.

Image Manipulation

There are several methods that can be used to enhance tracer visibility ready for tracer detection and tracking. These methods all effectively darken the areas that are not required, and brighten the visibility of tracers to make them more prevalent on the surface. Code can be written for these methods to automatically apply manipulation to raw data ready for analysis where it is needed. In many cases, it can be advised to use image manipulation to enhance tracer visibility, so long as the module that is being used for analysis is capable of processing the raw images and applying said transformations. The transformations that have previously been studied are: intensity normalisation, histogram equalisation, contrast limited adaptive histogram equalisation (CLAHE), and image binarisation. It is stated that the most important application of manipulation would be the enhancement of contrast by using intensity normalisation, histogram equalisation, and CLHE. To do this, scripts can be used to take a video, break it down into frames, apply the transformation, and stitch together the frames to recreate the video. Examples of how these manipulations impact imagery once applied can be seen in figure 11.1. It is worth noting, that in some software suites (especially those created in MATLAB), image pre-processing comes as standard (e.g. RIVeR and CLAHE).

Image Post-Processing

Post-processing of data can generally mean anything that is done with the data after it has been analysed for surface velocity. Typically, discharges are wanted from the surface velocity, so we would apply depth-average flow analysis to the data to get out our discharge. This will be the case for a majority of studies, therefore, this section will not focus on this too much, as it is typically a main part of most PIV and PTV software suites and comes as standard. This section will focus on the validation and correction of velocity vectors, prior to the analysis of discharge.

Corrective Software

Typically, when an image output of surface velocity is provided, it is easy to spot where spurious vectors may have appeared. These vectors go against the general direction of flow, or completely

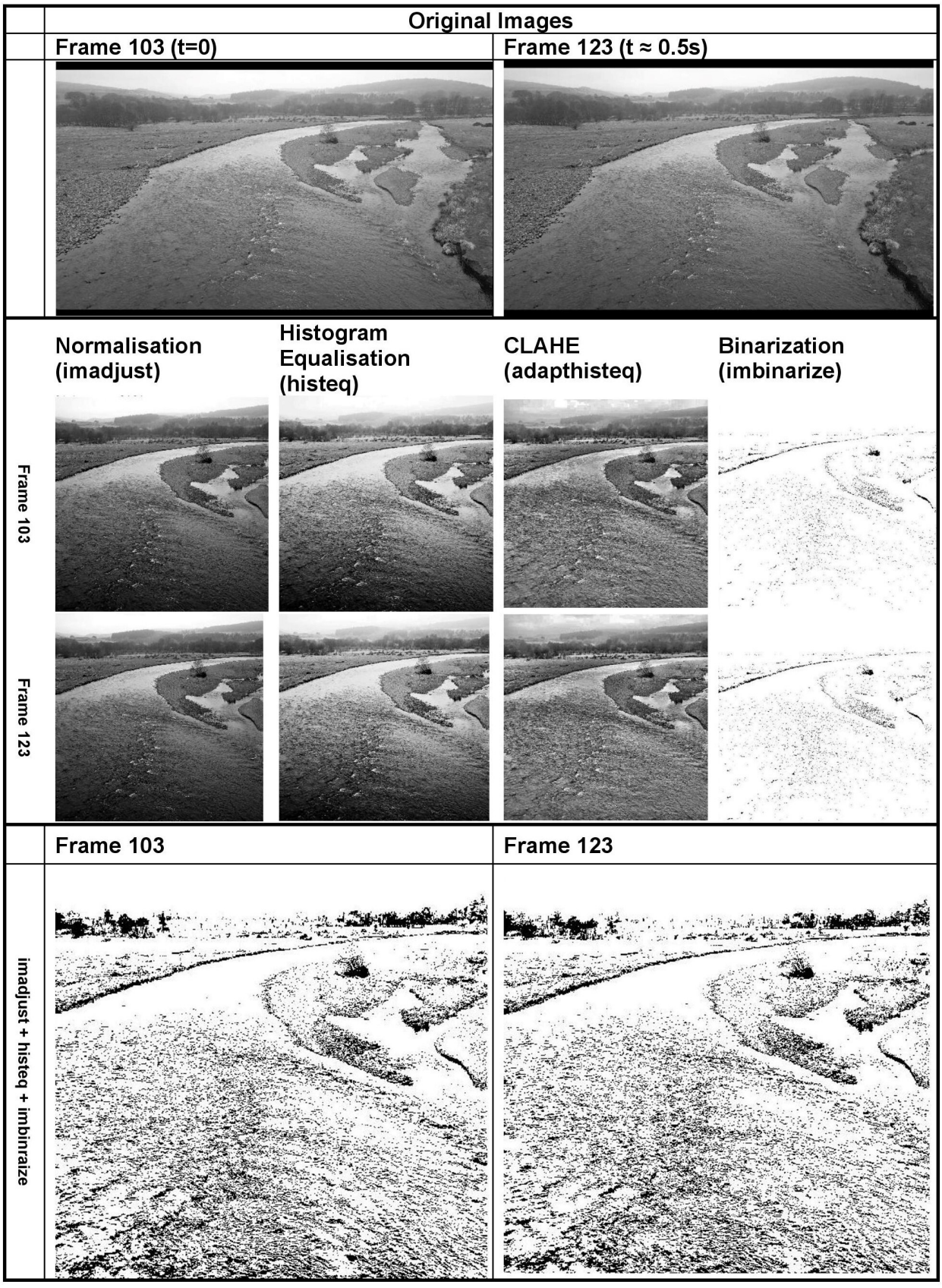


Figure 11.1: The impacts of using each image manipulation transformation onto a frame taken from drone footage, with a time-step between each for comparison.

misidentify the velocity of the surface compared to its nearest neighbours. Where this is the case, it is vital to post-process the analysis using corrective methods. There are several algorithms available that can undergo these transformations, however, some software include post-processing steps as standard. PIVLab and Fudaa-LSPIV (to name a couple), allow users to apply vector validation automatically, and remove any spurious vectors from the field. PTVlab (similarly a MATLAB PTV add-on), can also apply vector validation methods at the users digression. In general, post-processing techniques are usually available as a built-in script that can be applied where the user wants. This step is not always necessary, but is useful to apply where confidence in producing accurate flow patterns is low, or where errors continuously occur, particularly at highly turbid sites where vectors can be more often seen.

Code and Module Setup

The Code Explained

Introduction

A code is required so that the automation of capture and upload is automated and does not require a user input at any stage. A code has been created using python script that does just this. It begins by creating new folders that store back up data and new data. The code then begins to capture the data using the camera IP address, and finishes by uploading the data and deleting anything that has been uploaded. The code requires users to input several pieces of information before it can be used, including the IP camera address, destination folder, and site name; the code should do the rest. Begin by downloading the code created for windows devices here.

Installing the code

Begin by downloading both the ”Code” file and the ”S3cmd” files and saving them to a folder in your documents. Open both of these python scripts by right clicking the files and ”open with” Notepad.

Setting up ”Code”

Once you have opened the code in notepad, scroll down to a section listed ”User input”. As you can see, the whole script is commented throughout to describe what each line does, and where things are needed editing. We begin with the save destination. Go on to your documents, find an area that you wish to save all the new data, and highlight the destination at the top, seen highlighted in figure 11.2. Copy this text to the code within the quotation marks and be sure to double backslash all the backslashes.

Set up the next part of the code by setting ”zz” (the time between captures), to what you wish. It is advised to not make it much more regular than 15 minutes (reduce the chance of a backlog).

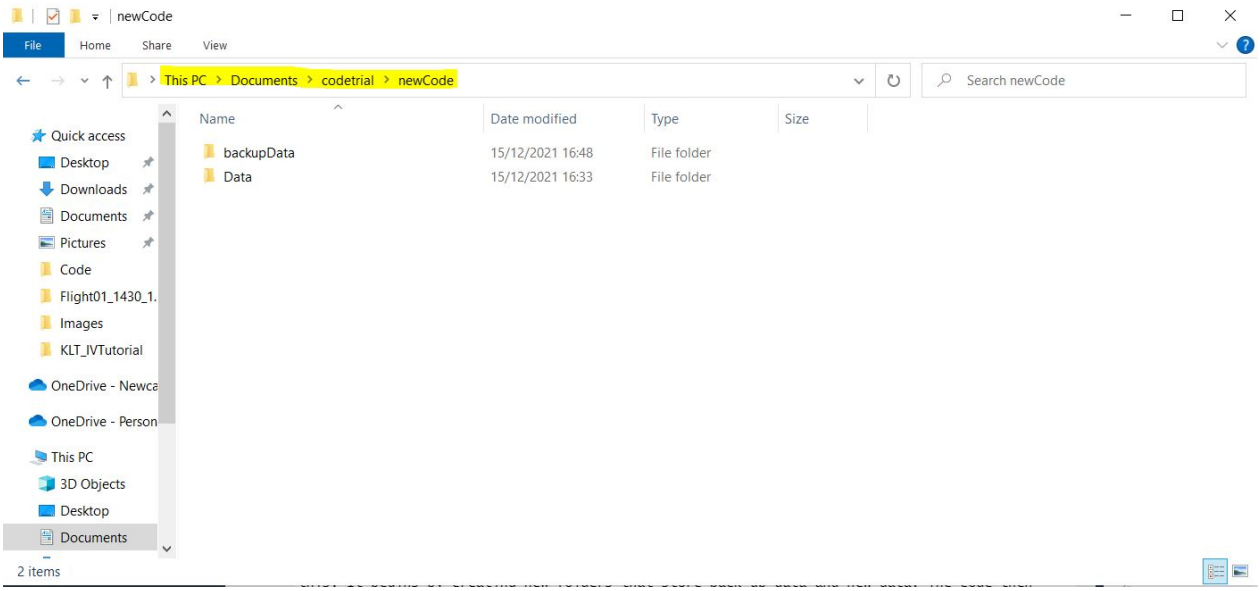


Figure 11.2: Click the area highlighted here, select all, and copy to the code. Be sure to replace all backslashes with double backslashes

Set the FPS to what you desire also, 20-30fps is recommended as default. Next, you need to set the IP camera address. This should be a default value of 192.168.1.64:554 if you are using a Hikvision and have set up using the ”Hikvision camera setup” instructions. If not, you can find the IP of your camera and enter that there instead.

Finally, we have to set up the file containing our AWS keys. Open the file ”S3cmd” in notepad by right-clicking and ’open with’. Within the code, you will see 6 lines that contain multiple ”#’s”, these need removing and replacing with your access key and secret access key. To find these, go onto AWS S3, go on to your account, and find ”My security credentials”. Find the ”Access keys” section, and click on ”Create new access key”. Download the key files so that you can use them again in the future for other stations, but be sure they are secure. Click on ”Show access keys” and you will be shown the two keys you need to copy and paste into the S3cmd script. Be sure to save both scripts and these can now be closed. Right click on either of the files, click on ’properties’ and look on the ’general’ tab. Where it says ”opens with”, ensure it is ”Python IDE”, typically Python 3.9 (see figure 11.3).

Using the Code

Once the code has been set up, we can place it into the windows OS start up folder so that when the module boots, the code automatically begins to run. This is needed for a multitude of reasons, but the most important being, if the power drops out then the module picks up where it left off without any interaction. To do this, select and copy the two files that you edited from before and navigate to the following path: ”C:\Users\”USER”\AppData\Roaming\Microsoft\Windows\Start Menu\Programs\Startup” Paste the two files ”S3cmd” and ”Code” to this folder. To run the code

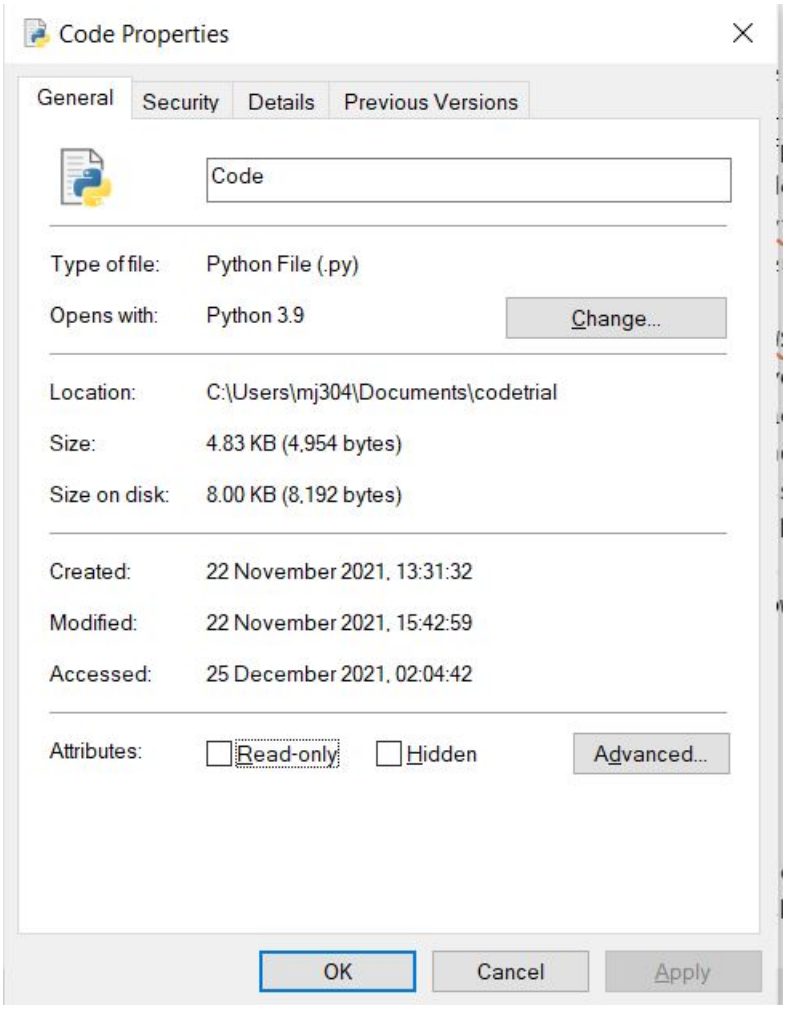


Figure 11.3: Ensure that the ”opens with” is opening with Python IDE, here seen as Python 3.9.

manually, double click the Code file. Close the file explorer and everything should now be ready to work.

Site Design

Overview

Now that we have explored many of the different aspects that must be considered when designing an image velocimetry site, we are better poised to begin determining what is best for new sites. To do this, we will explore some of the already developed studies and sites that are currently or previously created, and look at the hardware/software used for those, as well as some of the challenges and limitations that they faced. I will also draw from some of the experience that I have had out in the field, and what equipment we use at Newcastle University to acquire and process imagery.

Existing Case Studies

A general list of PIV and PTV experiments was explored in Jolley et al. (2021) Jolley (2021) and displayed in the table seen below (table 11.5). When new to setting up image velocimetry stations, it is advised that you familiarise yourself with some of the previous studies and how they extracted data from the videos, also note the type of hardware that they used and what worked/did not work with the software choice.

Table 11.5: A selection of application papers chosen due to their variation of hardware and software suites. Each has been briefly summarised for their backgrounds and their results. Originally published in Jolley et al. (2021) Jolley (2021)

Details	Background	Results
Author: Creutin et al. (2003) Case Study: Iowa River, Iowa Software Application: In-house algorithm (PIV)	"Proof of concept" research paper. PIV was used without artificial tracers. GCPs used with a 70m wide channel. Ten, 10 minute, recordings used for processing. Sony DCR-TRV320 camera used at an angle of 60° and 14m above the river level. GSD was 6.4 pixel/m. Interrogation areas set at 64×64 pixels and search areas set at 24 pixels.	Discharges from the ten sequences ranged from 50-300m^3s^{-1}. Results were compared to 215 current meter measurements and PIV results agree with the defined rating curve. Average velocities mostly agreed, except for two measurements. Disregarding these two results, error ranged between -11.6% and +4.2%. The study highlighted the issue of results being sensitive to light, with reflections and shadows making it hard to detect movement.
Author: Jodeau et al. (2008) Case Study: River Arc, France Software Application: LS-PIV	Dam flushing, discharge rate between 10m^3/s to 150m^3/s. Survey area roughly 60×40m. Tilt angle roughly 20° to the horizontal. Calculated alphato be 0.79 (0.85 is default). DEM used for bed elevations.	Bias (thought to be due to friction coefficients used), towards the shallow areas of the river; under-estimated compared to a 2D-model. Lack of tracer visibility on right bank due to tree shadow and lack of tracers. At smaller levels of discharge (60m^3/s), calculated error (compared to a rating curve) was large (30%), however, at higher estimated discharges (77m^3/s), estimated discharge was within 0-6% of the rating curve.

Author: Legleiter et al. (2017) Case Study: Alaska, USA Software Application: LS-PIV (Thermal)	Benchmarked using aDcp(velocity, discharge, depths). Thermal camera (FLIR SC8340) used to capture data (1280×720px). Frame rate at 10Hz captured for 1min. Cameras were fixed, with most angles set to nadir, however, some instances 13 degrees off nadir was used. 25mm focal lens used (provided a view of 41.2°x24.8°). ROI of 512×512px used (roughly 6×3.5m, GSD 0.005m).	Angling the cameras resulted in issues; the distortion of the FOV (between 2% and 9%), but also reduced the near-field thermal energy received. The paper does not track 'tracers' per se, but instead thermally distinct patterns. Results skewed from not accounting for camera distortions (e.g. camera tilts), however, the edges of the frames were trimmed when processing (where most of the distortion would occur). Velocities (from both aDcp's and PIV), ranged between 0.5m/s and 3m/s for all the sites. The mean error for all sites was within one standard deviation (range of error between 0.09-0.187m/s with a ± 1 standard deviation of between 0.132-0.247m/s)
Author: Tauro, Petroselli and Grimaldi (2018) Case Study: Brenta River, Italy Software Application: OTV (PTV based)	Camera used was a GoPro Hero 4 Black, set to capture at full HD (1920×1080 pixels) at a capture rate of 50 Hz. Out of a 4 minute video, twelve 20s clips were extracted with a resolution of 1430×1080 pixels (equalling a field size of 7.1×5.3 m^2) at a rate of 25 Hz. Image manipulation was used, including grayscaling and gamma correction to darken mid-tones.	Processing time was measured using OTV and compared against PTVLab and PIVLab and was shown to be two magnitudes quicker using a simple personal computer (2 minutes for OTV and 17±7 minutes for PIVLab/PTVLab). RMSE and R^2 values were used for comparisons with results. These results were compared against a benchmark from a deployed current meter (3cm below the surface). FAST-based OTV produced a R^2 value of 0.83 compared to reference data, with ORB-based OTV 2nd best with 0.74. For comparison, PIVLab produced a R^2 value of 0.49 and PTVLab 0.6 compared to the reference data.

Author: Dal Sasso et al. (2018) Case Study: Noce Rivers, Italy Software Application: PTV-Lab	Field study after numerical experimentation on optical settings for PTV solutions. Average channel width 28m, slope gradient 1.1%. Waded current meter benchmarking. DJI Phantom 3 Quadcopter with a 4k UHD mounted camerawith 3 axis stabilisation system. 10m hover above surface with orthogonal angle to surface (nadir). Captured in HD (1920×1080px) at 24 FPS. Surface captured was 17.0×9.6 m^2. Artificial tracers were used.	Reconstruction of velocities at banks show higher uncertainty due to bank effects, and a lack of tracer movement; produces significant underestimation. Emphasis on frame rate being such that a particles displacement is larger than that of the particle being tracked, and if not, to subsample frames (reduce framerate to increase displacement). Results compared to benchmark show a good comparison in the middle of the reach (1% error), compared to that of the edges which are much less reliable (48% error). Benchmark velocities show a median of 0.437m/s, and a max of 0.48m/s, whereas PTV-Lab produced a RMSE of 0.125m/s for the full width, and 0.04m/s when considering only the areas with good seeding concentration.
Author: Perks (2020) Case Study: River Feshie, Scotland Software Application: KLT-IV (PTV based)	Hikvision AcuSense 4mMP IF network camera (20Hz, 2688 × 1520px), and DJI phantom 4 (29.97fps, 4096×2160px). High flow conditions (stage range between 0.785m-1.762m). GCPs were used throughout detection and the images were stabilised to negate platform movement.	A range of stage was used to reconstruct the flow (between 0.785m-1.762m). Mobile and fixed cameras produced deviations from a rating curve at 4% and 1% at stages above 1.5m. Vegetation obstructed mobile imaging, had to extrapolate edge, but had over one-million trajectories. Fixed camera had 7433 trajectories (10s of video), mostly in centre, both banks needed extrapolating.

Author: Jin and Liao (2019) Case Study: Milwaukee River, USA Software Application: LS-PIV	Flow ranged between 6-60m^3/s. Camera used was a NikonD7000 with HD 1080p imaging and a distortion free lens (50mm F1.4). Oblique angle used (between 79° and 86°). Images were orthorectified using 11 GCPs . Water level found by marking extra GCP just above water level. ADV used for benchmarking along cross-section. 25FPS used over a 10min period. Images used have GSD of 0.02m/px over an area of 70×23m.	Median tests used, average error between 29% and 36% over the whole study. The RMS of the velocity agrees well with the ADV benchmarking after the median tests were performed to remove outliers. Good correlation between the ADV and the PIV magnitude (0.12m/s and 0.14m/s from the ADV and PIV respectively). Typically, results were larger than that of the ADV and it is thought to be due to the ADV measurements coming from 5cm under the surface of the river, resulting in less turbulence compared to that of the surface velocity. Velocity index for depth average calculations set at 0.85.
Author: Pearce et al. (2020) Case Study: Kolubara River, Serbia Software Application: KLT-IV, LSPIV, LSPTV, OTV, SSIV	Comparison paper between software suites. Low flow experiments (approx. 3.4 m^{3}s^{-1}, benchmarked with aDcp. Mobile platform used (DJI Phantom 4 Pro) with a standard fitted camera sensor (1" CMOS 20MP). Artificial tracers used. Six GCPs were used along the channel. Resolution of 4k (4096×2160 pixels) and a FPS of 23.98. Two videos of 30s were sub-sampled captured from 26m elevation (GSD of 0.77 cm/px), and 32m (GSD of 0.95 cm/px).	The aDcp was used across three cross-sections. KLT-IV and LSPIV provided the best correlation with the results from the aDcp averaging a range between 0–0.07 ms^{-1}. On average, KLT-IV, LSPIV, OTV and SSIV software suites are in better agreement with the aDcp than LSPTV. The Nash-Sutcliffe results for the softwares compared to the aDcp are for video one: 0.535 (KLT-IV), 0.3592 (OTV), 0.4905 (LSPIV), 0.1609 (LSPTV), and 0.3875 (SSIV). A sensitivity study was also produced. The results show that KLT-IV is generally insensitive to changes in configurations. OTV had the lowest sensitivity scores across software suites, however, can be sensitive to the particle trajectory length threshold.

Equipment Recommendations

This section will begin to look at a very generalised example of what can be achieved via image velocimetry methods, and what sort of considerations can be made. The ultimate aim of this section is to come away with a decision tree that can be followed to allow the user to decipher the best possible way to capture and process data, in the most efficient way. The preferred pathway will be highlighted where limitations of the site are minimal, and generally conditions are met. For this specific section, the assumption that a fixed platform is required for analysis, as mobile platforms are much more simplistic in the overall needs, as they are temporary structures.

Design Aspects

The main considerations for designing image velocimetry sites has been broken down into 6 variables: power supply, mobile network availability, accessibility to site, type of monitoring, channel width, and in-situ processing. These variables influence the equipment that is likely to feature on a site, and the way that data collection will work. These variables have been chosen because they are the most influential impacts on the set-ups. The suggestions made through this handbook have been selected for ideal circumstances, and cannot always be applied to every site. With that in mind, it is sometimes a requirement to use personal judgement on developing a site because of site specific limitations or specific output requirements. For example, in the handbook, an ultrasonic level is suggested where only high flows are required, however, it may be possible to use existing level meters, or optically observe the river level using the camera footage and deep-learning algorithms.

Costs

On average, the cost of a suggested set-up in this handbook is £999.32. This is an estimated cost that does not take into consideration some of the smaller items (e.g. wiring needs, securing cameras, securing modules etc.). It does, however, include a years worth of networking (mobile or satellite), which does take up a significant amount of the budget. The items used in the suggestions to follow are listed in table 11.6.

Table 11.6: Equipment list, prices, and URL's

Item Name	Estimated Price	URL
ReoLink RLC-523WA	£205.59	https://reolink.com/product/rlc-523wa/
Vivotek FD9368-HTV	£200.40	https://www.vivotek.com/fd9368-htv
Reolink Go	£173.73	https://reolink.com/product/reolink-go/
HIKVISION DS-2CD2647G2-LZS	£370.00	https://www.hikvision.com/en/products/IP-Products/Network-Cameras/colorvu-series/ds-2cd2647g2-lzs/
RSPi 4B	£54.00	https://thepihut.com/products/raspberry-pi-4-model-b
UDOO Bolt V8	£339.91	https://shop.udoo.org/en_eu/udoo-bolt-v8.html
LattePanda Delta	£181.93	https://www.mouser.co.uk/ProductDetail/DFRobot/DFR0543?qs=sGAEpiMZZMtTz4c6chlxkDfAvxRwNyzNMFfwzYMkEuIUBveNfvwNkA%3D%3D
Konnect Sat. Lmt	£408.88	https://europe.konnect.com/en-GB?gclid=CjwKCAjwkvWKBhB4EiwA-GHjFqxVR88Az0LSV1P8g94lXu1b4rN-dGDzBR5uOYmV4_trD-cqA_dRkRoCl4MQAvD_BwE
Konnect Sat. Unl	£840.00	https://europe.konnect.com/en-GB?gclid=CjwKCAjwkvWKBhB4EiwA-GHjFqxVR88Az0LSV1P8g94lXu1b4rN-dGDzBR5uOYmV4_trD-cqA_dRkRoCl4MQAvD_BwE
Mob_Vodafone_USB (Including data costs)	£360	www.vodafone.co.uk/mobile-broadband-deals?icmp=uk 1_consumer topnav 1_shop 3_broadband 5_mobile_wi-fi&linkpos=topnav 1 1 3 5
Mob_Vodafone_PiHat (Including data costs)	£380.37	https://sixfab.com/product/raspberry-pi-4g-lte-modem-kit/
RSPi 4B_SSDUnit (Including data costs)	£43.00	https://thepihut.com/collections/raspberry-pi-ssd-storage/products/wd-green-240gb-2-5-ssd https://thepihut.com/collections/raspberry-pi-ssd-storage/products/ssd-to-usb-3-0-cable-for-raspberry-pi
12V_Battery_and_Case	£200.00	User Specific
RS Solar Panel Unit	£100.00	RS PRO 20W Polycrystalline solar panel — RS Components (rs-online.com)
MaxSonar	£222.00	https://www.maxbotix.com/Ultrasonic_Sensors/MB7586.htm

Decision Tree

A decision tree helps make decisions based on typically yes or no questions. For the purpose of this handbook, the 6 variables listed in section 11.2 are used as questions, and have two options given for each to try and determine the needs for specific sites. The equipment listed in table 11.6 has been suggested because it provides a flexible approach to working. This does mean, however, that there may be better, more specific set-ups for each site, but in general can be used efficiently. This section looks at the match-ups with the questions and the site requirements. A spreadsheet has been created and is available on GitHub. A manual version of the tool can be seen in table 11.7 and table 11.8. Both of these require the user to select one of two options for each of the six variables to create a 6-string binary output number which can be matched to its subsequent set-up equipment list. An equipment list for setting up a site using a latte panda is available, also on GitHub. These are the items required for setting up most of a site that uses either battery or mains. This is a basic set-up and should be altered to better represent the needs of the site at hand. A mounting pole (diameter around 80mm), is also required to be secured at site to situate the camera.

Table 11.7: Variables listed as questions, find your binary output (111111, 000000, 110010 etc.) and compare it to the results table. Option 1 binary result is a 1, whereas option 2 produces a 0. For example: mains, no, low, high only, <10m, no, is 111111, whereas battery, yes, high, any, 10m+, yes, is 000000 and any variation of this.

Question	Subject	Option 1	Option 2
1	Power supply available	Mains	Battery
2	Mobile internet available?	No	Yes
3	Accessibility to site	Low	High
4	Flow to monitor	High Only	Any
5	Channel width (approx.)	<10m	10m+
6	Process the data on-site?	No	Yes

Using PIV and PTV

In this section, we will look at three of the pieces of software freely available for use. Two of the three methods are user-friendly GUI's designed primarily for PIV use, while the final one is also a user-friendly GUI, but uses PTV methods. Before you go to site and capture any data, it is highly advised that you familiarise yourself with the following bits of software so it is completely clear on what information is required for each one so that once captured, the process can run smoothly and accurately. Pieces of information such as GCP coordinates and cross-sections can be used multiple times so long as the camera position and river bed stays constant throughout the processing period, so it is important that these are done carefully and accurately to ensure the best possible chance of producing reliable data.

RIVeR (PIV)

Introduction RIVeR is a Matlab compiled app that uses the fundamental calculation algorithm of PIVLab, and has a user-friendly GUI to walk through the process of extracting images from video, through to computing discharge from a cross-section. To use RIVeR, Matlab runtime (2015b) is required, as well as the RIVeR application file. For the purpose of this walk-through, we will be using RIVeR version 2.5. An example will also be provided for use as a tutorial that can be used to experiment with. For the tutorial files, please visit here. If using the tutorial file, then you can find a copy of RIVeR2.5 in the folder, simply extract this and use this copy after downloading and installing Matlab Runtime.

There are two main ways to process the data; automatically or manually. The automatic feature of RIVeR uses some default values and the suggested settings for the video after entering some of the basic information such as resolution, region of interest, and masks. The manual method of processing data is not any more complicated than using the automated feature, but allows much more of a variation and control over the processing of the data. In this section, manual processing will be broken down into each of its features and discussed on how best to process data that you may have. The following sections provide a more in-depth look at how to use the app so it is easier to process your own data. There is a section at the end designed to run through the tutorial "in a nutshell", as it gives you every click and input you need to process the data the same way that was initially done. Use this tutorial to get a feel for the software, and play about with the features of RIVeR that this walk-through does not cover.

Image Extraction The process starts with opening the software. Once Matlab Runtime (2015b) has been installed, extract the RIVeR folder from the .Zip File, and open the application file using administrative permissions (right click on the file), if possible (this is not vital, but is suggested). Once RIVeR is open, the first job is to extract frames from the video that you are processing (tutorial named "TutorialVideo1"), see figure 11.4. To do this, the resolution of the video is required. If this information is not readily available from the properties of the video, or known prior to the capture of the video, then it is possible to find out using VLC player (usually comes with windows computers but is freely available online). Simply open the video in the app, and press CTRL+J to open the "codec data", this is where the resolution data is available (see figure 11.5). Enter this resolution and apply a gray scale to the video as standard. Finally, go to "file - PIVLab - PIVLab GUI" to open up the processing segment of the software.

Once open, the first step is to load and import the images that we have just extracted from the video file. Click on "Load Images", followed by "Browse" to find the **folder** that the images are stored in, usually named the same as the video file; click on it and then click "Select Folder" to bring up a side menu of all the images located in the folder. Here you can select the images that you wish to load, but by default, click on any of the images on the left hand menu, select all by pressing

CTRL+A, and press the ”Import” button to move them to the right menu (see figure 11.6). Delete from the right menu any images that do not belong and ensure that the sequences of the images are in order (usually numbered at the end of the stringed name). Once loaded, it should bring up an image of the river which can now begin to be processed.

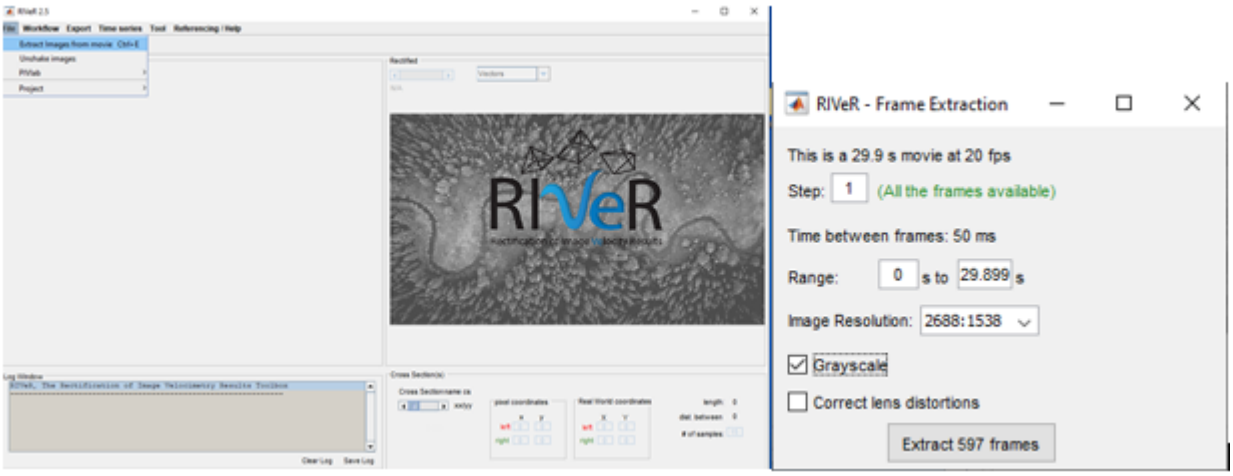


Figure 11.4: Extracting images from a video

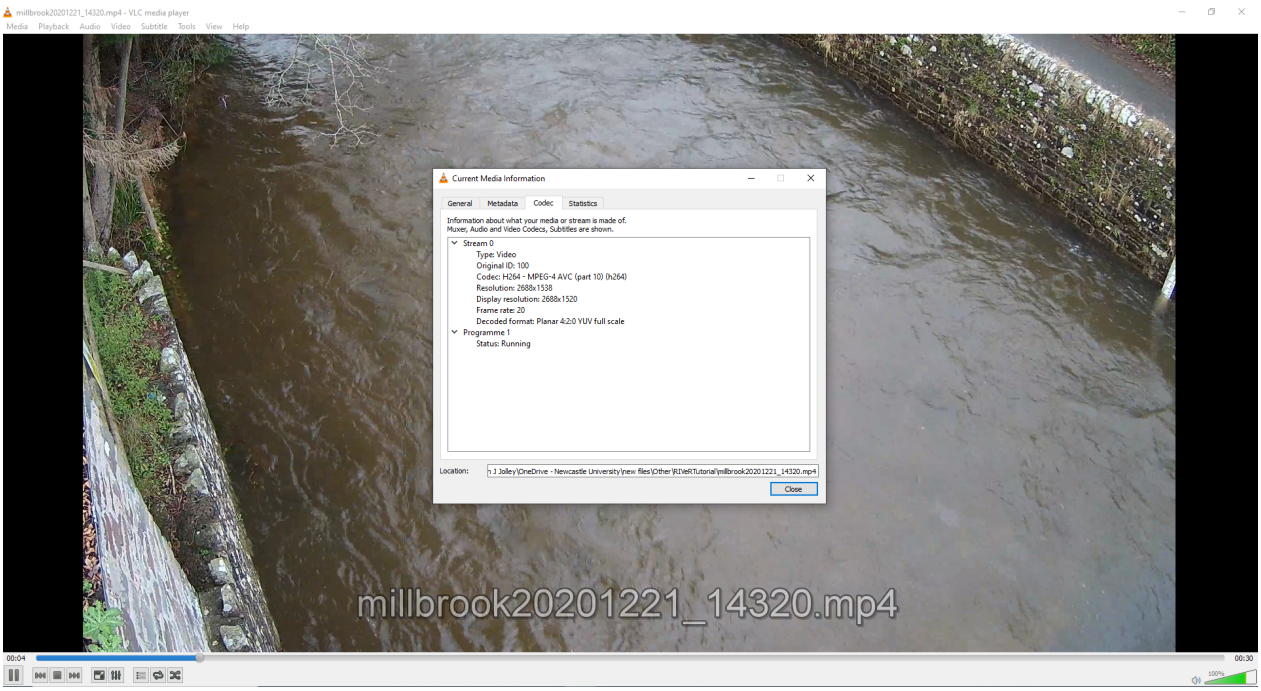


Figure 11.5: How to find the resolution of the video using VLC player

Selecting the region of interest To start, a region of interest (ROI) is required along with any masks that are used to hide objects that may impact results (e.g. any structures or foliage that falls into the region of interest). A ROI is an area that highlights the section of surface of the river to be

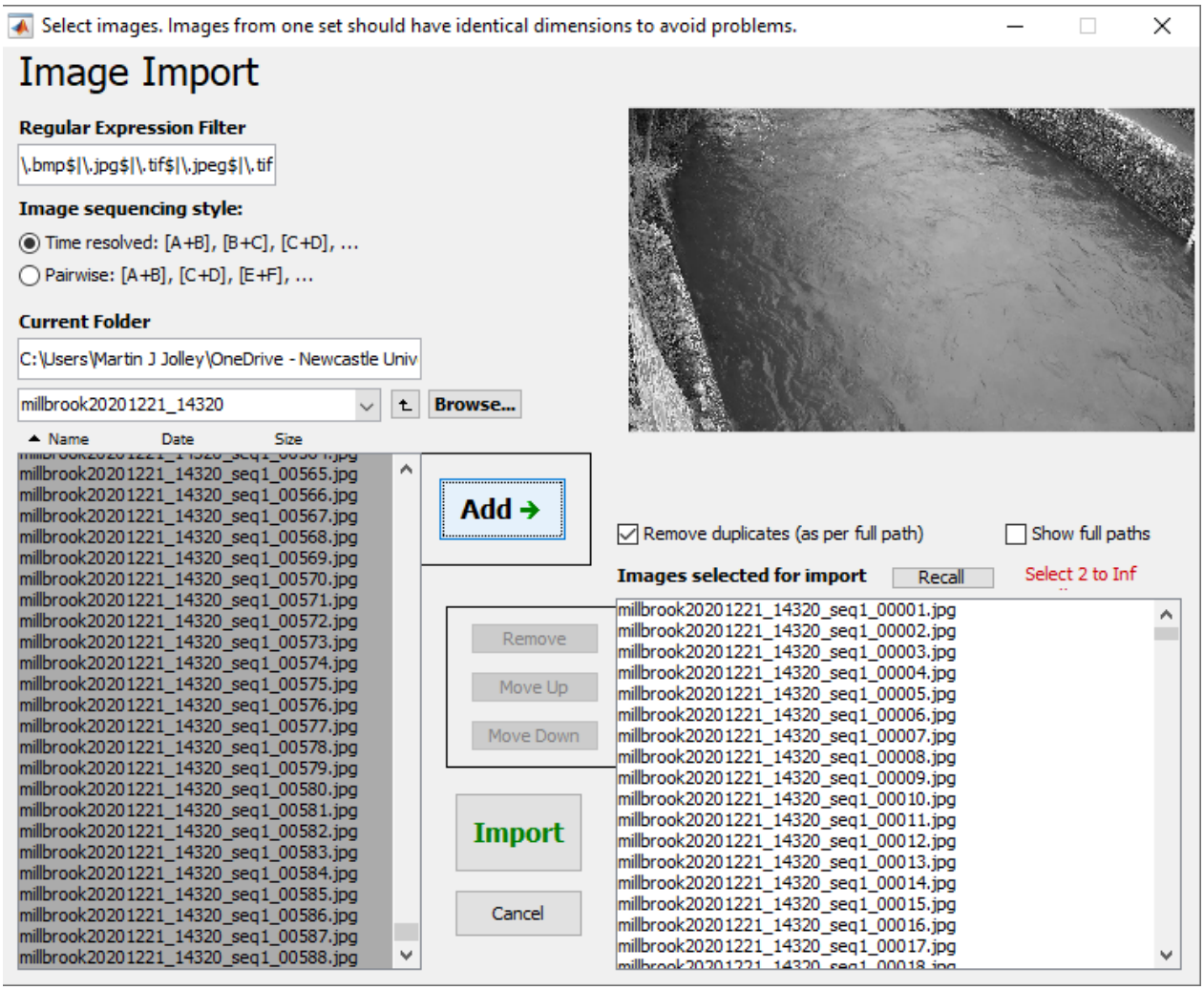


Figure 11.6: Importing the frames

processed by the software. The ROI should encompass at least one area that has a cross-section, and should have at least four GCPs in or immediately around it (see section 11.2). To begin, click on ”Image Settings - Exclusions (ROI, Masks)”. If it is the first time processing the data, select manually the area that you wish to process by clicking ”Select ROI” and note down the ”x,y, width, height” values that it produces so that you can use them again later (alternatively, we are going to save the PIVLab settings at the end which will store most of the input data for ease). Once selected, click on ”Draw masks for current frame”, which allows you to create a polygon shape around instances of obstruction to flow. It is import to cover any foliage or structures that are in the ROI that are not to be processed. Once you have covered them, save the masks for use at a later time. When you are happy with the region of interest and the masks that have been applied, be sure to click the ”apply current masks to frames” and have ”1:end” selected, this will simply apply the masks that you have selected to each frame, otherwise it will only be applied to the reference frame.

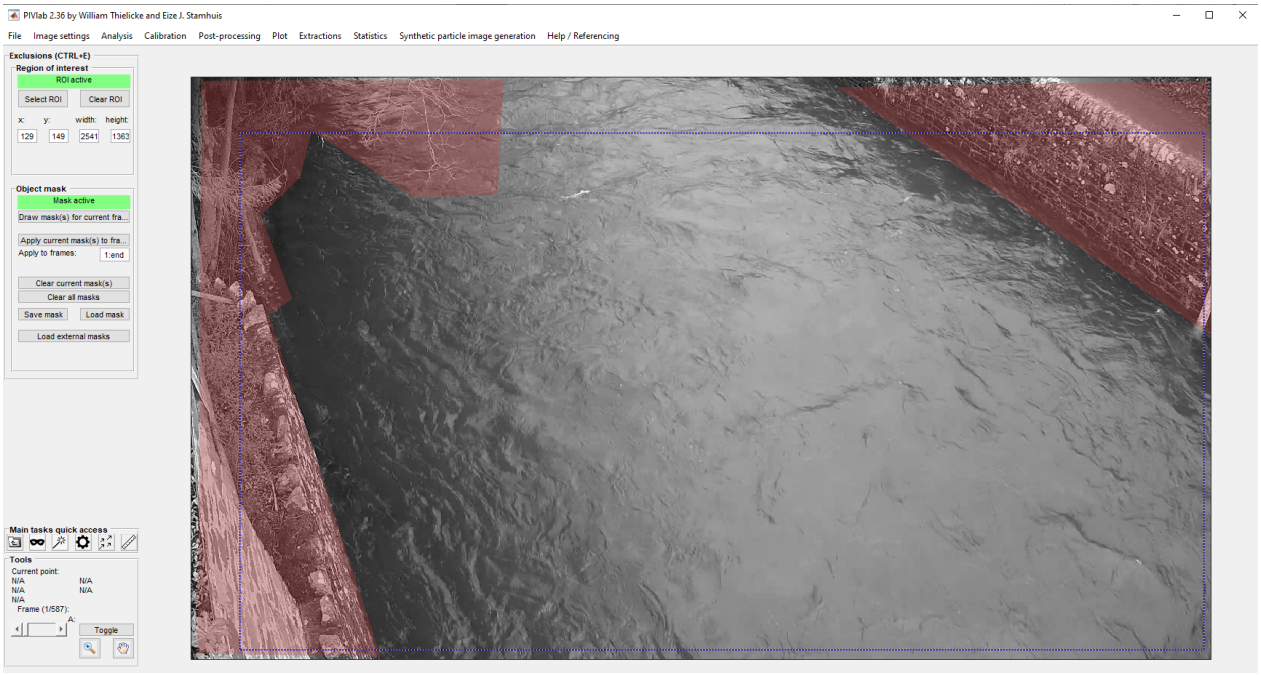


Figure 11.7: Applying a ROI and a mask

Image pre-processing Next up on ”Image settings”, is the pre-processing settings found at ”Image settings - Image pre-processing”. In this menu, it is possible to apply a number of pre-processing steps to the imagery, and the type of filters needed depends on the quality of raw data collected, see figure 11.8. If there are plenty of visible to the eye tracers and the background (e.g. riverbed), is not prevalent, then not much is typically needed and CLAHE can be applied. Where tracers are not so prevalent, then applying the kernal high pass filter and the other available options may make it easier, but this will be dependant upon the type of footage captured and should be experimented with. For images that feature a highly visible background, background subtraction (the available GUI listed on image pre-processing), can be used. This compares two sequential frames and removes any pixels that may be constant between the two, leaving only the changes (which could typically be the tracer information that we are trying to capture). Again, the effectiveness of this will vary depending on the input data, as most videos captured from fixed stations will hopefully not need this level of pre-processing.

PIV settings Now is time to choose the PIV processing settings, go to ”Analysis - PIV settings”. From here, we are able to choose the PIV algorithm to be used (suggested FFT window deformation as default), the interrogation and search area sizes, the number of passes to be completed, and the correlation parameters. As a general rule of thumb, a search area about 50% the size of the interrogation area is usually suggested, but for simplicity, the app comes with a ”suggest settings” feature. Generally, it is easiest to use this feature to decide on your starting pass sizes, as it will vary from site to site, and ultimately depends on the average size of the tracers that the software

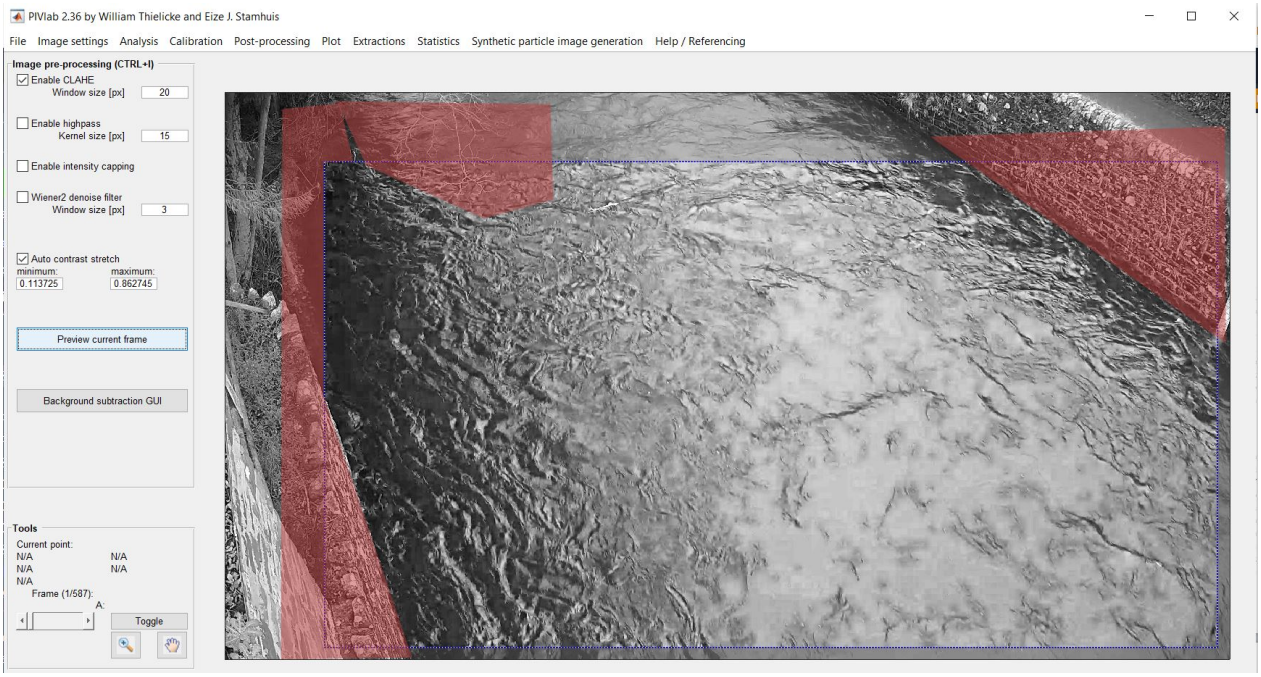


Figure 11.8: The pre-processing parameters required for the tutorial video. Play with these values until tracers are as prevalent as possible.

will use to produce the surface velocity. With each ”pass”, data is carried through and recalculated to increase the accuracy of results, but this also can substantially increase the processing time required. Typically, the idea is to start big and get smaller as you pass through the steps (e.g. 164 for pass 1, 82 for pass 2, and so on). With this in mind, although smaller interrogation areas may increase the resolution, it can also increase the noise.

Now the fun begins, go to ”Analysis - ANALYZE!”, followed by ”Analyze all frames” to begin watching the magic happen. The time for processing to complete ultimately depends on the computer processing power you have at your disposal, the length of the video to be analysed, and the processing steps previously mentioned (e.g. interrogation areas, number of passes, etc.). Typically, with the computer used to analyse the tutorial data, processing time lasted between 35-40 minutes.

Post-processing Once complete, you should be left with a vector map that shows the direction of the flow for each area, as well as a magnitude depicted by the size of the arrow vector. You could just leave it as that if you are happy and confident in the typical direction that is shown on the map. However, if you want to calculate discharges, it is vital to remove as much erroneous information as possible. To do this, PIVLab has some built in features that can be used, found in ”Post-processing - Vector validation”, see figure 11.10. Usually, for flows that are not greatly turbulent, it is quite evident which direction the vectors should be heading, and any that look obviously wrong can be corrected easily. To do so, it is initially recommended that a correlation filter should be used and I believe that for any flows that are not relatively largely turbulent, 3 standard deviations should be

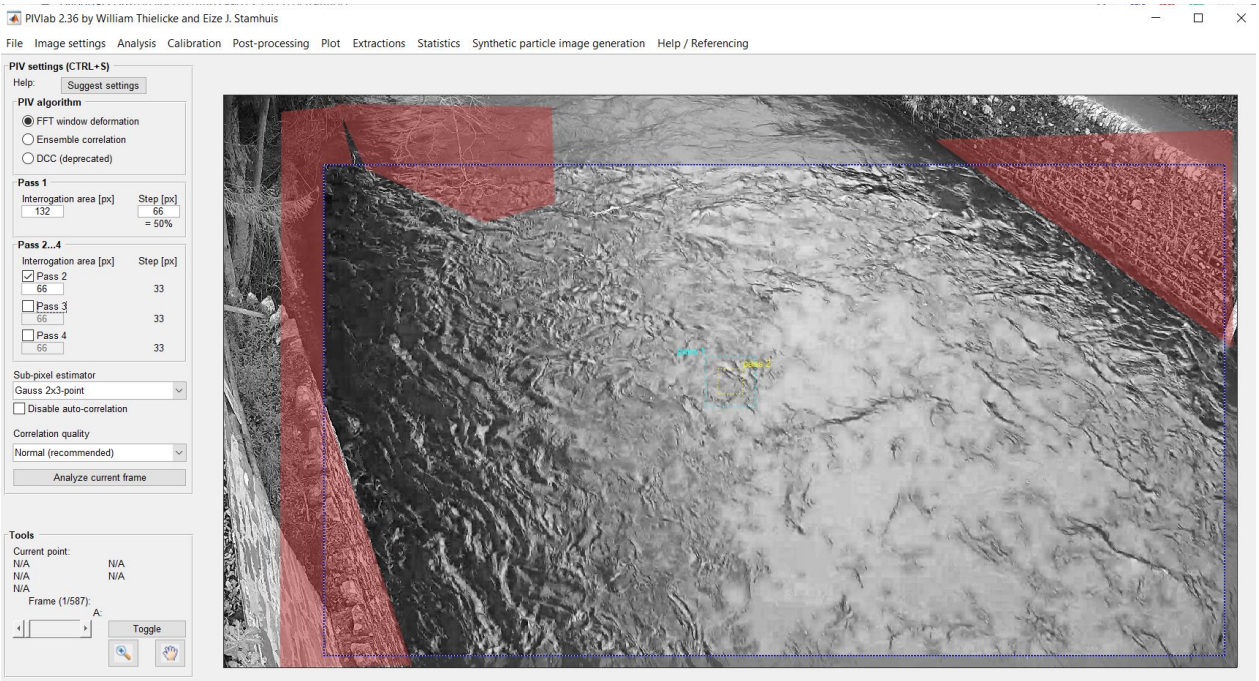


Figure 11.9: Some typical values for the PIV settings used in the tutorial. These can be changed to include more passes and larger initial areas.

used to encompass 99.7% of all values, and it is reasonable to assume the 0.3% are outliers. Even if this assumption is incorrect, any missing values for velocity can be filled using interpolation techniques. A wrong value could produce a larger deviation from the true discharge than using an interpolated value as the calculated value is done so using average velocities surrounding the missing area. As general good practice, it is advised to use the ”standard deviation filter threshold”, set to 3, and the ”local median filter threshold” set to default (5 and 0.1), and then finish by clicking ”interpolate missing data” and ”apply to current frame” to check the new vectors highlighted as orange. You could also ”refine velocity limits” manually by selecting an area of the velocities believed to be most credible, however I would advise this to only be used once users are fully comfortable with how everything works. When happy with the post-processing applied to the frame, be sure to apply the changes to all the frames.

Saving data Now it is time to save your settings and your session. Saving your settings means that next time you want to analyse a video from the same camera (e.g. when you have a fixed site and you want to process multiple videos). Saving the session means that you can reopen the analysis of that video with all the settings previously set so that you can change and re-analyse the footage. To do this, simply go to ”file - save” and do so for both. From here, there are other pieces that can be done in PIVLab, however, for the purpose of this walk-through, they are not required as we want to simply calculate our discharges. Feel free to explore the other menus and features once you have saved your session and can revert back to it if needed. You can now close the PIVLab

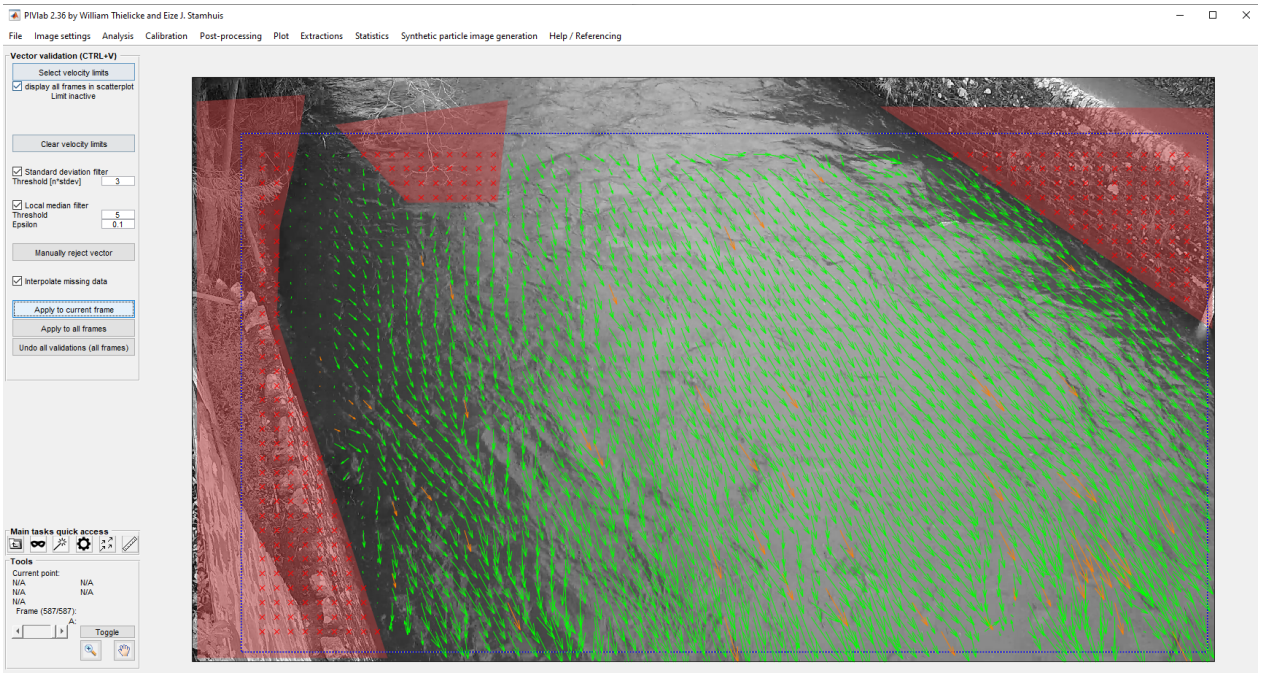
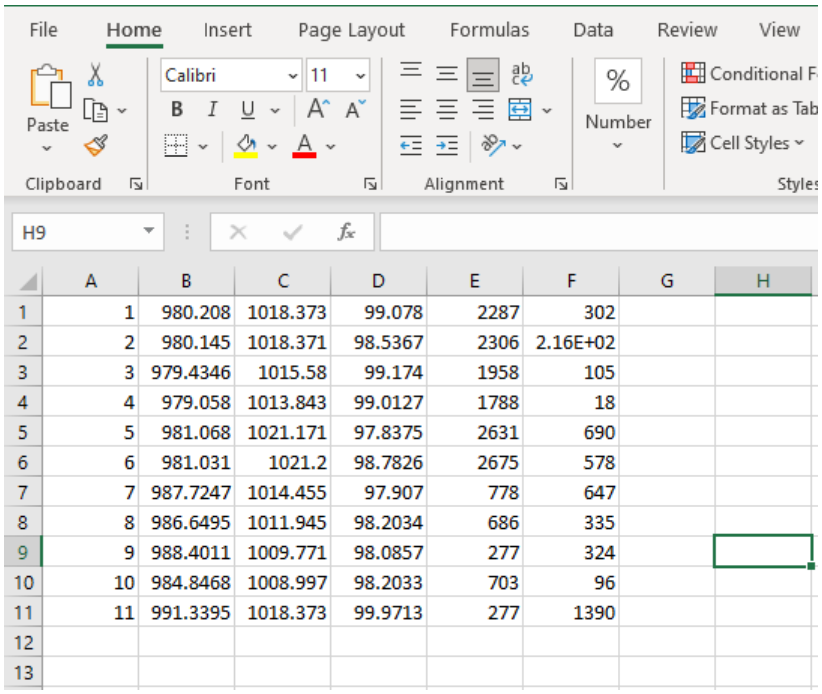


Figure 11.10: Post-processing considerations for the data, including vector validation and interpolation. Erroneous green vectors are removed and replaced with statistically valid orange vectors depending on the thresholds set at the menu on the left side of the pane.

GUI window (not RIVeR).

Orthorectification Back in RIVeR, we are now ready to calculate our surface velocity values (not just their magnitudes and directions), as well as our discharge. To begin, go to ”workflow - load PIV analysis - load PIVLab session” and browse to where you saved your PIVLab session from the PIVLab GUI. Each time you successfully complete a step, the step turns green in the drop-down menu. Next, go to ”workflow - load background image” and let it automatically choose the image. Similarly, go to ”workflow - load CP’s image” and browse to a frame from the video used to capture the GCPs .

It is now time to rectify the images. Go to ”workflow - define CPs/ region of interest” and we are going to be redefining it in 3D as hopefully we have more than 8 GCPs located in the frame; so go to ”define in 3D - import ID,X,Y,Z,x,y file” and find the GCP file for the site. This file should be a .xls file that contains, in order, ID, the real-world X,Y,Z coordinates of the GCPs, and the local coordinates x,y of each in frame too, see figure 11.11. To find the pixel coordinates of the GRPs, simply isolate a frame of the video that has the GRPs in frame and use the open source ”GIMP” image processor, to find the pixel location in frame (see figure 11.12. If the GCP video you collected has been processed in RIVeR, then it will already be broken down into frames, and any of these frames can be used to find local coordinates. If the GCP video has not been broken down, open the video using VLC media player (free application, usually comes with windows PCs), and save a snapshot by going to ”Video - Take Snapshot”; open this screenshot in GIMP and find the



	A	B	C	D	E	F	G	H
1	1	980.208	1018.373	99.078	2287	302		
2	2	980.145	1018.371	98.5367	2306	2.16E+02		
3	3	979.4346	1015.58	99.174	1958	105		
4	4	979.058	1013.843	99.0127	1788	18		
5	5	981.068	1021.171	97.8375	2631	690		
6	6	981.031	1021.2	98.7826	2675	578		
7	7	987.7247	1014.455	97.907	778	647		
8	8	986.6495	1011.945	98.2034	686	335		
9	9	988.4011	1009.771	98.0857	277	324		
10	10	984.8468	1008.997	98.2033	703	96		
11	11	991.3395	1018.373	99.9713	277	1390		
12								
13								

Figure 11.11: This is the layout required from the GCP .xls file. From left to right, there is ID, X (real world), Y (real world), Z (real world), x (local pixel), y (local pixel).

GCP coordinates that you need.

The next two definitions of the plane of interest is the water level (real world coordinates), and the region of interest (real world coordinates). Go to ”workflow - define CPs/ region of interest - Define in 3D”, and for the water level ”Define gage”, and for the region of interest ” Define real world region of interest”. The tutorial images were defined using a cloud point, meaning there is more than enough coordinate data to cover a range of regions of interests and water levels. For the purpose of the tutorial, the water level is showing 5m on the gauge on the video, which in coordinates is around the 98.15 mark, so this is our gauge. The region of interest, much like the GCPs, can be input as a .xls file. The layout for this is X,Y,Z (all real-world coordinates), and in the order of point 1 being a corner of a rectangle, with point 2 being the next corner of the rectangle going clockwise (see figure 11.13. The next step is simply defining the time-step of the video, which is usually detected automatically; but if it is not, then it is simply the time between frames (e.g. 20fps would be 50ms). Finally, go to ”workflow - rectify results” to process the orthorectification.

Cross-sections To calculate the discharge, we need to define a known cross-section. To do this, a definition is needed either in the form of drawing on to the image (workflow - cross-section - add new - define cross section), or defining a known cross-section (workflow - cross-section - add new - define coordinates). For the tutorial, the file CS1 holds the location data for the cross-section we are to calculate for using real-world coordinates on the surface of the water (X and Y), see figure .

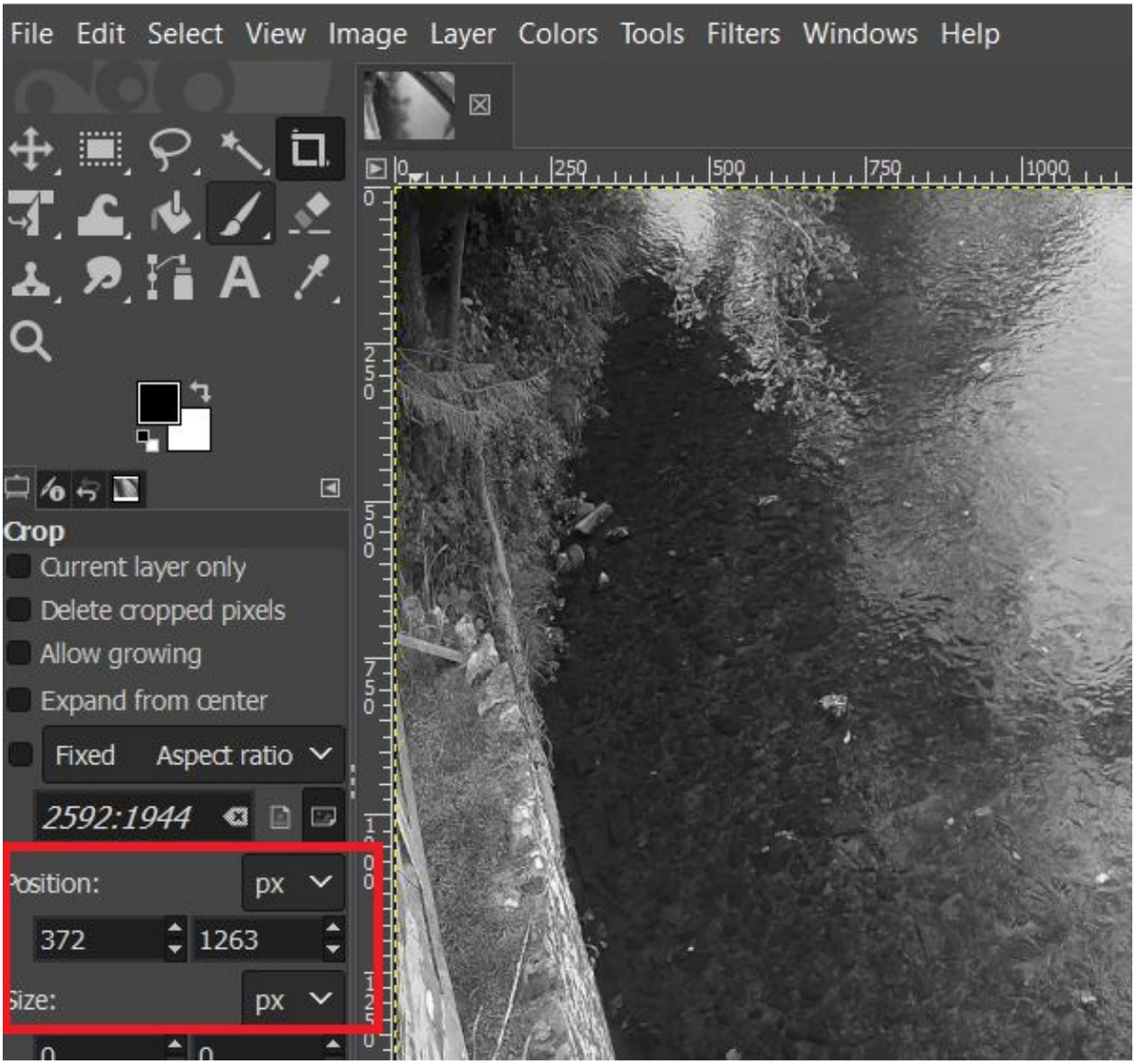


Figure 11.12: How to easily find GRP local coordinates (x,y or i,j), from a still image using GIMP.

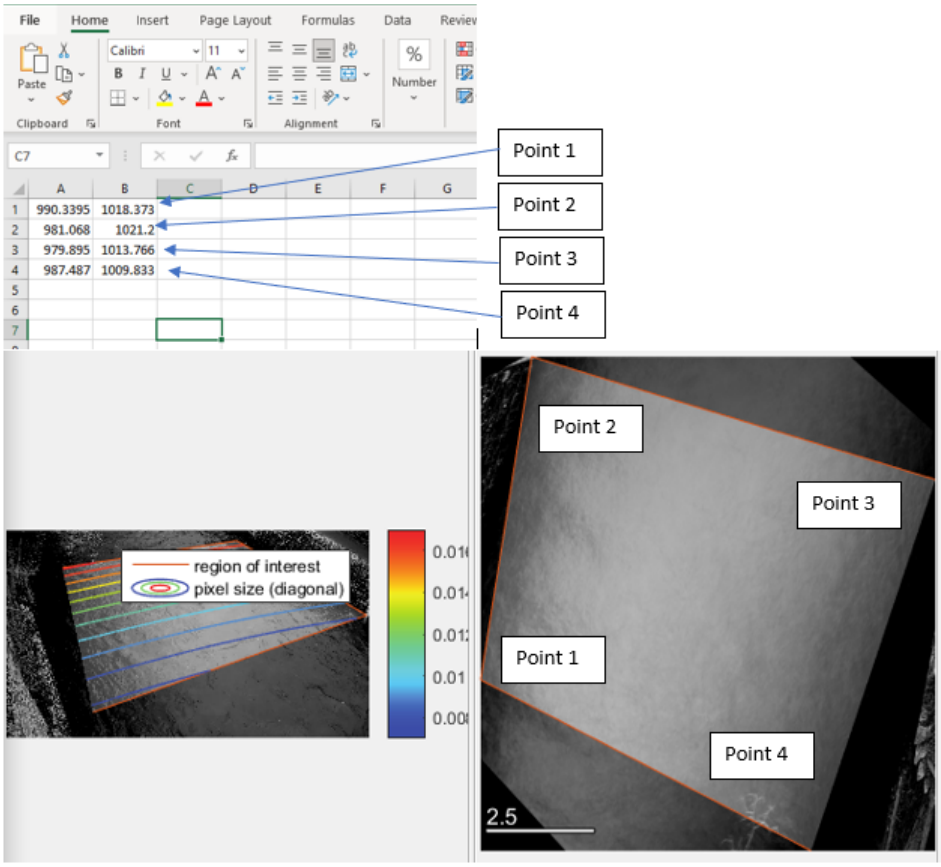


Figure 11.13: The input file and the output ROI as seen in the RIVeR app.

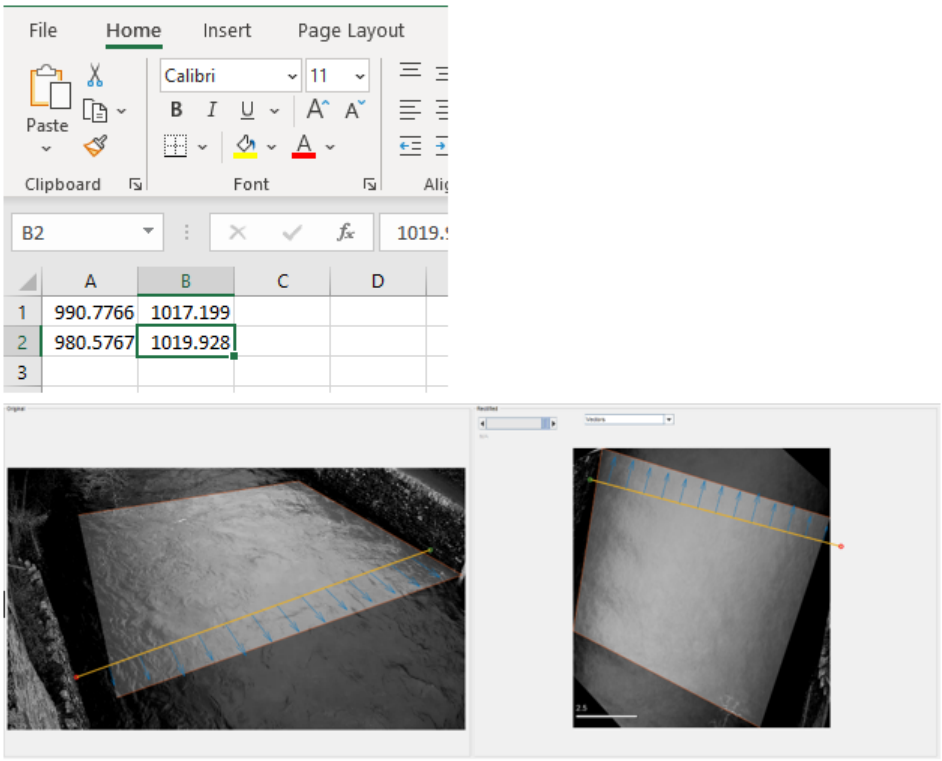


Figure 11.14: The cross-section input data along with the defined cross-section image imposed onto the river, along with the velocity vectors that apply to the cross-section.

Calculating Discharge If everything is completed, you will be able to open the discharge menu found at ”Workflow - add cross section - compute discharge”. From this menu, we enter our cross-sectional depth values along the cross-section previously defined. To do this, it is advised you have the bathymetry in a .CSV file format as seen in figure 11.15. Go to ”File - import - CSV file” and find the bathymetry file (named bathy for the tutorial), and select ”Depths” so that the software can plot the cross-section along with its estimated velocity values. Next up, enter the stage value and velocity coefficient (alpha value) parameters. With the tutorial cross-sectional depths, all values were referenced to the local zero plane, so the stage is now directly taken from the rule and does not have to be in the real-world coordinate grid. For simplicity, you could calculate everything to the real-world coordinates captured at the time of the rest of the data (such as GCPs), and use the real coordinates for depths and stage. Either way is fine so long as you are sure on the location of the cross-section and the consistency of coordinate grids. The velocity coefficient (alpha value, see section 11.2), can be assumed to be a default value of 0.85, but can be calculated precisely by using an aDcp. You could also associate an error bar with results by calculating the discharge with the range of alpha coefficients between 0.79-0.91, as these are the typical values for alpha. For the purpose of this tutorial, the edges of the river have purposely been left out of calculation so that the program can interpolate these values and you can see what it does. When calculating this for yourself, you should really try and calculate velocity across the whole river and only interpolate

where sections are not available. So, with that said, tick the box that says ”inter. NaNs” and look at the difference in velocity profiles. Now click the all important ”Compute” button to see the estimated discharge. Once you are happy with everything, save it as the AreaComp file, close it up and save the project.

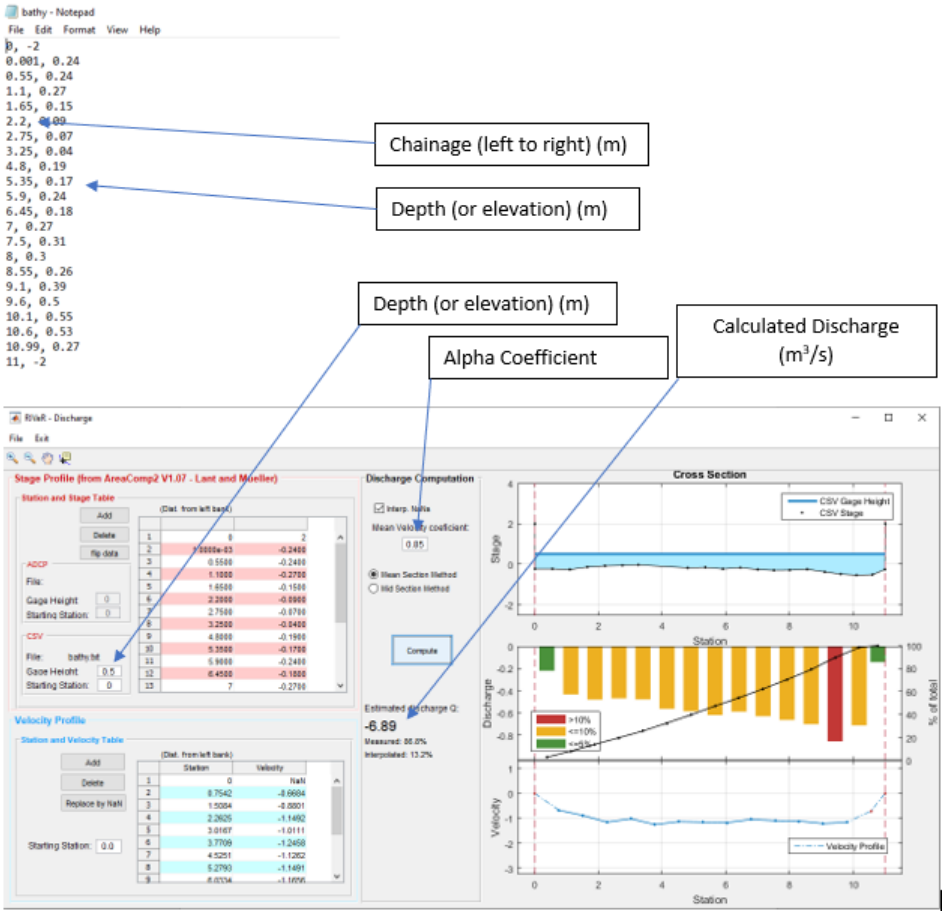


Figure 11.15: This is the required data for inputting cross-sectional data and the parameters for calculating discharge for the tutorial. The alpha coefficient has been shown to average around the 0.85 mark, but is specific for each site. Be sure to define whether your cross-sectional data has either depths or elevations in the program (comes up as a text box during inputting).

Summary RIVeR is a very simple tool to use once you have understood what the program needs for raw data. It is heavily advised that you take a full 3d laser scan of channels so you have more than enough data to use for referencing. Ideally, you should capture all coordinate data in one go so that everything is referenced to the same grid. This includes the GCPs, of which you should capture AT LEAST 8, but ideally around 12 or more with 4 or more directly around the ROI. You need to capture the ROI coordinates, but this could be later calculated using the 3D cloud if captured, if not, capture these at the time of the GCPs. Cross-sections are also required in real-world coordinates, so be sure to capture these at the same too (XYZ data). Capture at least 1 cross-section but ideally 3 so they can be compared and validated between one another. The number of data points along

the cross-section is up to the user and depends on the method used. They can be manually captured or captured using an aDcp, so long as the coordinate grids can be matched accurately. It is also important that you capture a video that encompasses all of the GCPs. The GCPs could be stationary objects that are clearly visible in the images, or can be temporary points that you have placed, but is still captured in the video; this is the method used for the tutorial. The stage is also required for calculation, therefore, either a stage capturing device is required and some points along the water surface (e.g. when capturing a cross-section, capture a few points of the water surface along the same cross-section so the stage can be converted to the real-world coordinate grid), or if there is a stage rule already at the site, this can be captured within the video and used (the same as the tutorial). It is still important to know the coordinate value of the water surface, so it is still advised to capture some points so that it can be calculated. For example, within the tuturial, the rule gives an indication of the water level and each level is associated with a Z coordinate such as 0.5m = 98.15, 0.6m = 98.25, 0.7m = 98.35 and so on (this was captured during a 3d laser scan of the channel).

There are several other features of RIVeR such as exporting data in different formats, but this can be up to the user on how they use these, and can be played about with at your own discretion. For the purpose of this walk-through and tutorial, we will end with calculating discharges, but if you wish to know more, there is some more information on some other bits in the handbook that is found in the folder containing the GUI, which is automatically downloaded with RIVeR 2.5.

Tutorial in a nutshell To make things simpler and save some time, the following points will walk you through the tutorial files to come up with a full process using given values. Simply follow these steps carefully to fully extract images and process the data to find an estimated discharge.

1. Download the files required for RIVeR including the software and the tutorial files, found here (available until Sunday May 8 2022).

2. Download and install Matlab Runtime (2015b), available here.

3. Extract and open the file containing the the tutorial files, and extract the copy of RIVeR2.5 found inside ready for use.

4. Open the extracted folder for RIVeR2.5, right click on ”RIVeR_GUI” and open with administrative permissions (if possible), if not possible, just open by double clicking. This should open up the RIVeR2.5 GUI.

5. Click ”File” and ”Extract images from movie”. Find the tutorial folder and double click on the file named ”TutorialVideo1” to bring up the extraction menu. We want to step each frame (so keep at 1), the time between frames should be automatically detected at 50ms, the range is the full video (just under 30s), the image resolution needs set to (2688:1520), and the frames need gray-scaling. Then click ”Extract frames”

6. Go to ”File - PIVLab - PIVLab GUI” to open up the PIVLab GUI.

7. Click ”Load Images” and then ”Browse”. Go to the folder that contains the tutorial data, and click on the newly created folder containing the images ”TutorialVideo1” followed by ”Select folder” to load up the image sequences.

8. Click on the left hand side menu of one of the images, press ”Ctrl + A” to select all and then ”Add” to move the frames to the right hand side menu. Now click ”Import”.

9. Click ”Image settings - Exclusions” to bring up the ROI and Masking settings.

10. Enter the following details for the ROI: x=149, y=141, width=2460, height= 1346. This will create the rectangle for the ROI over the river.

11. Click on ”Load mask” and select the file in the tutorial folder named ”PIVlab_mask_Tutorial” to bring in the masks that have already been preset. These mask the stationary/ moving areas that we do not want processed. Finally, click on ”apply current masks to all frames”.

12. Go back onto ”Image settings” and click ”pre-processing”. Check that ”Enable CLAHE” is selected and at a size of 20px, as well as ”Auto contrast stretch”. Preview this effect to ensure it works.

13. Go to ”Analysis” and click on ”PIV settings”. From the top down, ensure that ”FFT window deformation” is selected, Pass 1 is set to 136 and 68 for interrogation and step respectively, Pass 2 is on and is set to 68 and 34, ”Gauss 2x3-point is selected, and the correlation quality is normal. Analyse the current frame to see the impact.

14. Click back on ”Analyse”, and go to ”ANALYSE!”. Press on ”Analyse all frames” to begin the processing. Depending on processing power, this can take between 20-50 minutes.

15. Once complete, go to ”Post-processing” and select ”Standard deviation filter threshold” and set it to 3. Click on the ”Local median filter” and set it to 5 and 0.1. Also ensure that ”Interpolate missing data” is selected. Apply to all frames.

16. Go onto ”File” and save the PIVLab session to the tutorial folder. Close the PIVLab GUI and go back onto RIVeR.

17. Go onto ”Workflow” and ensure that ”Load PIV/PTV session” is green, meaning it has the session you just processed loaded.

18. Click on ”Workflow” and go onto ”Load background image” and let it automatically select a frame. Open ”Workflow” again and select the ”Load CPs image” option and select any of the frames (the CP image is not provided so is not needed, any image will do here).

19. Next up, go onto ”define CPs/ region of interest” and ”Define in 3D”, followed by ”Import CPs file”, select the ”MillbrookGCPs” file. Select ”OK” to the pop up. Go back to the same menu, only this time ”Define Gage”. Set the water surface plane to ”98.15” (this is the Z coordinate location of the water surface relating to a gauge reading of 0.5m).

20. Next up is the ”Define real world region of interest”. Find the ROI file in the tutorial folder and select it and click ”OK”.

21. On ”Workflow”, next step is defining the time step. This should be set to 50ms, but should automatically be detected.

22. Rectify the results by clicking on ”Workflow” and ”Rectify results”.

23. Next is defining a cross-section. This has been supplied as a excel file. Go to ”Workflow” and go down to ”Cross-section - add new - define coordinates” to open the browsing menu. ”Import from excel” and go to the tutorial folder. On the drop down menu at the bottom right which says ”(*.xls), click on it and select ”(*xlsx)”, this should bring up the ”CS1” file. Double click, followed by ”OK” and name it CS_1. This will bring up the cross-section and the results associated with them.

24. Next up, we need to calculate the discharges associated with the cross-section. Go to ”Workflow - Cross-section - compute discharge”. This will bring up the discharge GUI.

25. Go to ”File” and ”Import” and ”CSV File” to bring up the bathymetry associated with the cross-section; it is ok to clear the data already entered (click yes ot a pop up window). The file is in the tutorial folder and named ”Bathy”. Double click this to open it, it has 0 headers and contains ”Depths”.

26. Back on the discharge GUI, the gauge height associated with the video is 0.5m. We also want it to interpolate data, so click on the checkbox named ”Inter. NaNs”. The mean velocity coefficient we default to is 0.85 as suggested in literature (so change the 1 to 0.85).

27. Finally, click on ”Compute” to bring up the estimated discharge, which should hopefully be -6.89 (the negative can be ignored).

28. Save everything if you want to keep them all for a later date. RIVeR can now be closed.

KLT-IV (PTV)

Introduction KLT-IV has been created as a stand-alone program created in MATLAB and packaged using ffmpeg. The installation of the software requires MATLAB2019 Runtime, and will be installed during the download if not already present on the device. The version 1.0 of the software is available here (accessed Oct 2021), with the corresponding paper defining its background and application Perks (2020). For the latest version (V1.01), please contact us (m.jolley1@newcastle.ac.uk), and I can forward it on to the creator (Matthew Perks). For the purpose of this tutorial and walkthrough, we will be using the files found here (available until June 2022). These are from the paper that comes with KLT-IV (V1.0) and is an example from the River Feshie, using a fixed camera at an oblique angle to the river. A disclaimer here: it is not a perfect example of a video we would usually look to run through KLT, we are simply using it as an example for simplicity. Usually we would look to capture more GCPs, at a less oblique camera angle, and for a longer duration.

To use KLT-IV, it is required to know the following parameters:

1. GCP coordinates (real or local, but must be consistent with the rest of the coordinates)
2. Camera location (coordinates, see above)
3. Camera angles (tilt, yaw, pitch)
4. Water level (WSE)
5. Camera model (if listed), to remove distortion

KLT-IV has been shown to be a reliable method of capturing surface velocity and calculating discharges, but also is less sensitive than other methods to user inputs such as defining interrogation parameters. The most important parameters to get as accurate as possible are the GCP coordinates, camera location, and the WSE, as these define the transformation applied to the images during orthorectification. The camera model and angles are somewhat corrected during the orthorectification stages and are not vital for accurate results, but are preferable to have, especially on long-term periodic data. Where imagery is not steady, stabilisation can be carried out automatically in-app by the software, done by defining the orientation and setting it as one of the ”dynamic” settings (usually ”GCPs + stabilisation”).

Video Inputs Once MATLAB2019 Runtime is installed, then you are able to open and run KLT-IV 1.01. There are several parameters to define in the video inputs section including the video/s to be processed and the camera data. The first job to complete is to select the mode (usually a single file, but multiple can be selected to process a batch of videos). For the purpose of this walkthrough, we will be processing a single file. Select Mode - Single Video, and then go to Define Video(s) and browse to your file (the tutorial file is called ”KLTIVTutorialVid”. It will ask if you want to

re-encode your video, but usually the file format videos come in are compatible with Matlab, so default is 'No'. Next you need to select your camera type if it is known and listed; if not, select "Not listed" (select not listed for the sake of this example). The orientation of your camera depends on the type of the platform you are using (mobile or fixed), and the angle of capture (nadir or angled). Where a platform is fixed but undergoes movement (e.g. wind oscillations etc.), then stabilisation should still be selected and dynamic should be selected. This can sometimes greatly increase the processing time. For the purpose of the tutorial, we should selected stationary and GCP.

Next we need to define some of the coordinates and angles that we are capturing from. For the tutorial, these have been provided as follows: 284954, 804757, 238.47 (X,Y,Z), and can be seen in the GCP spreadsheet "GCPS and camera location". For the angle of the camera, it does not have to be exact as these will be nullified by the orthorectification process if there are enough tracers, but does help the process if given accurately. For the purpose of this study, we will set our values (given in radians), to 0, 0.43, and 0, see figure 11.16 below.

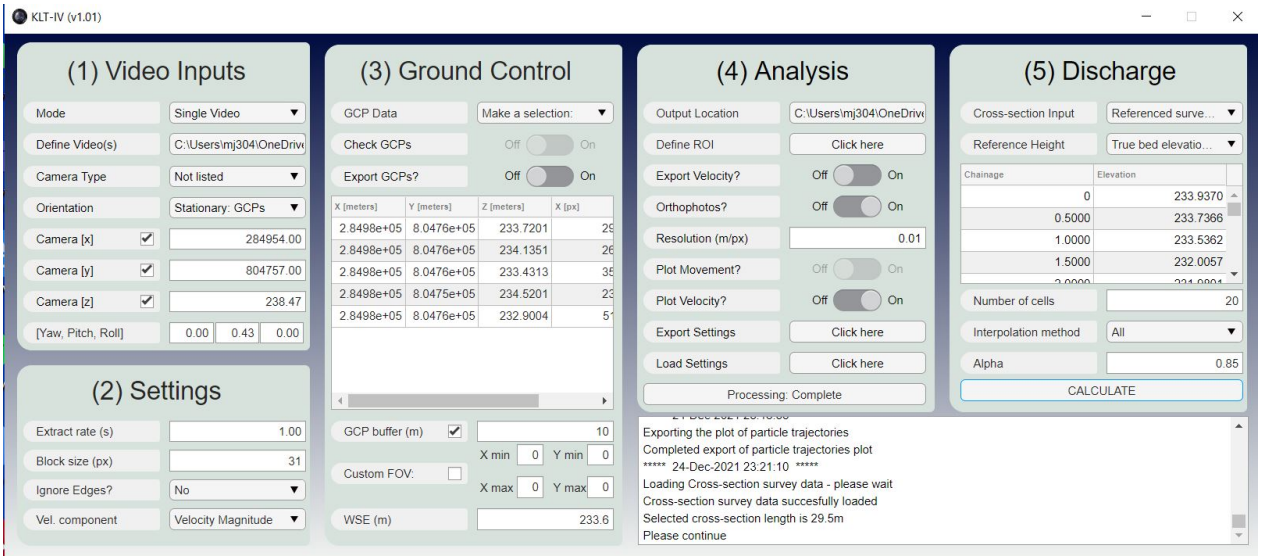


Figure 11.16: KLT GUI with the full inputs shown.

KLT Settings Settings in KLT define how you want to go about processing the data, and includes the extract rates, block sizes (in pixels), including or ignoring the edges of the videos, and what component you want to measure (velocity or normal). To understand more on how to use these settings, see the paper Perks (2020) which explains them all in detail, but I will briefly summarise them here too. The extract rate is the time between tracking features and displaying their displacement, where flows are fast, it will be more advisable to decrease the time between capturing displacements, as the smaller the number the greater the number of trajectories. Alternatively, the larger the extract rate, the smoother the trajectories will be and possibly the more robust. Anything between 0.5s and 2s is advised. Due to the nature of KLT, the block size input for settings is insensitive to input, and can be anything larger than the minimum (5px), but the default which

is recommended most of the time is 31px. Ignoring the edges usually is advised where camera parameters such as lens distortion are not confidently removed. It simply ignores the outer 10% of the frame so that these trajectories do not influence the overall accuracy of the output. The software provides velocity magnitudes in metres per second and in X and Y components. You can decide how to input these settings, play about with them but for the sake of the tutorial, let's leave them as default (1.00, 31, No, Velocity Magnitude).

Ground Control The GCP input for KLT is an important aspect of the processing. Data can be input in three different ways: Manually (as a table format), from a CSV file (X,Y,Z,x,y format like with RIVeR, see figure 11.11), or selected from the image. Manually means you have to enter the known coordinate points along with the corresponding pixel coordinates if known. From CSV requires you to have the GCPs in a format of XYZ (real world coordinates) and xy (pixel coordinates). The software then loads in these values as if they were manually inputted. The "From image" option is a useful tool that KLT has over RIVeR. It opens up an image from the sequence that allows a user to click on a pixel and define its real world coordinates one at a time. Once finished, it will load the values into the table, again, as if done manually. These can then be exported by selecting "export GCPs?". Where "Dynamic: GCPs" was selected earlier in case of mobile platforms, then GCPs are tracked between frames iteratively. It is advised to select "Check GCPs" where they are hard to visually see (and therefore hard to track).

The GCP buffer option allows the user to extend the FOV around the GCPs for the defined distance (e.g. the default of 10m extends the FOV out by 10m past the GCP network). However, if a specified FOV is defined, then the software will only extend to this field of view. Finally we need to define the WSE. This means working in the same coordinate grid as the camera and the GCPs. It is simply the Z coordinate of the camera, minus the difference between the camera and the water level, e.g. camera Z coordinate of 100m and the water surface is 6m below that, then the WSE is 94m. For the tutorial, the GCP CSV is provided (separate to the one with the camera location), this is named "GCP_input" in the tutorial files; let us set our buffer area to 4m.

Analysis The analysis section is the final section we need to edit before extracting velocity data. Firstly, simply select a destination that you wish to store all of your data by pressing on the "Output Location" and finding the folder you want to save to. Next, the ROI needs defining, and this is a simple process in KLT. Click on "Define ROI" and right click a polygon area that you wish to process. This is not a necessity (unless running stabilisation, in which case, it is), and the program will simply revert back to the area defined by the GCP buffer instead. Choose whether or not you wish to export velocity outputs and orthophotos, for the purpose of the tutorial, draw an ROI along the river (as seen in figure 11.18 and check both "Export velocity" and "Orthophotos" so you can see how it outputs this data; these can be played about with after if you wish. For resolution, there are maximum values, but the software sorts this for you if it is ever exceeded; anything around

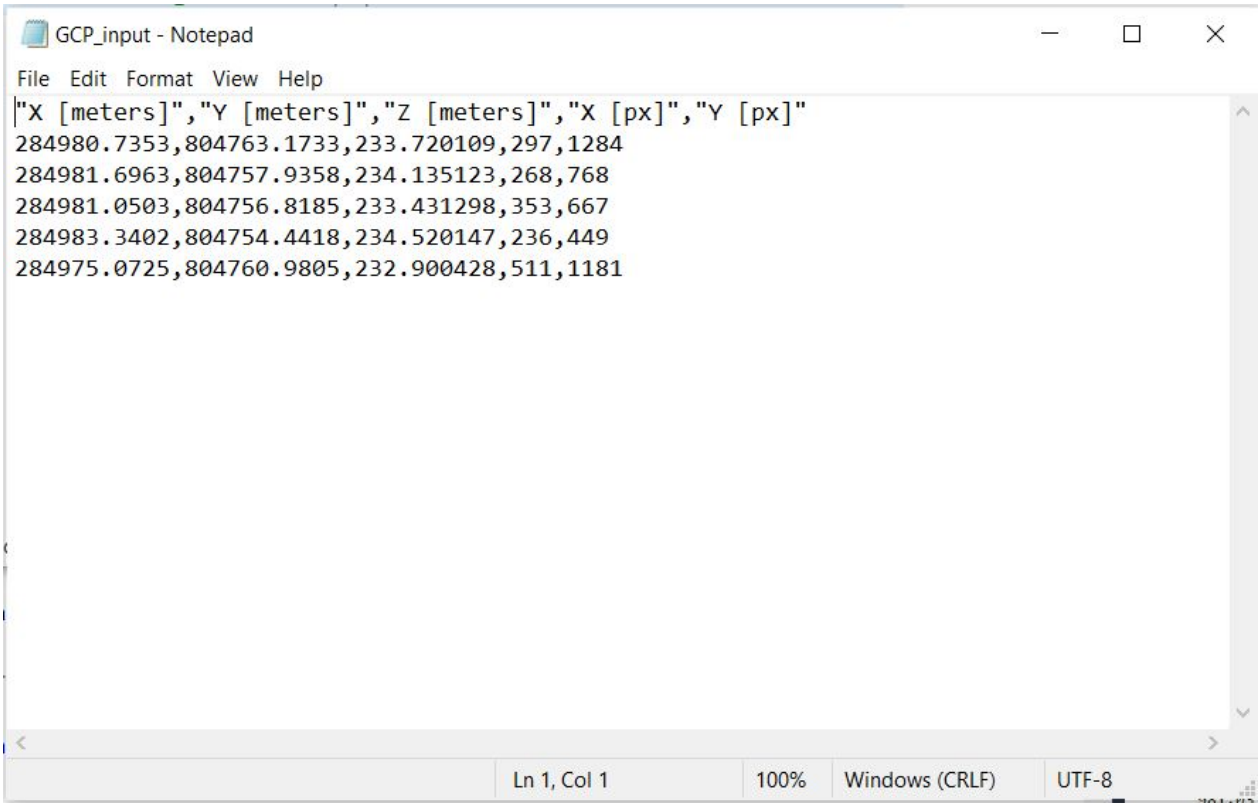


Figure 11.17: To format a simple CSV file that contains the GCP data required for processing, then it needs to be laid out as X,Y,Z,x,y; where X,Y,Z are real-world coordinates and x,y are their pixel coordinate counterparts.

0.01 is usually fine. The ”Plot movement” function is used for dynamic platforms and tracks the movement of the camera through time, for the tutorial, this is not needed. Finally, lets plot the velocities and click ”RUN” to begin the program tracking. The results that you get can be exported to a spreadsheet, but can also be plotted on the orthorectified image as seen in figure 11.19. For this tutorial, we are more interested in the discharge outputs.

Discharge Within KLT is the built in ability to apply cross-sectional data to the velocimetry results either using a ’referenced survey’ (in the same coordinate grid as the GCPs), or as ’relative distances’ where two points can be identified in frame to work from. For a referenced survey, your CSV file needs to have a heading in the first row in the order of X,Y,Z(depth). For relative distances, after picking the start and finish point of the cross-section, you need to define the chainage (distance along the line e.g. 0m,0.5m,1m,1.5m etc. for a cross-section with a reading every 50cm), and the Z(depth). Regarding the depth, you need to tell the software if you are defining a bed elevation, or the water depth.

A search distance is used here for pairing velocity data ready to find the median around each ”node” (a measurement along the transect). This is followed by the type of interpolation you wish to do where tracers are not present. For channels that are fairly uniform, in that the velocity is



Figure 11.18: When setting out a ROI, be sure to only include areas of the river surface, and try to leave out any vegetation that may disturb surface velocity results.

fastest in the middle and slowest at the edges, quadratic can be used. For flows that are asymmetric or have secondary peak flows, polynomial may work best. For any other type of flow, try using the constant Froude method. Finally, you need to define the depth-average velocity constant (or Alpha value), which studies show can default at 0.85 but if you have specific data for the cross-section then use that. For the purpose of this tutorial, a csv file is prepared ready for use regarding a referenced survey cross-section that shows bed elevation, this is named "XS_input". For the number of cells, keep it at 20, set the interpolation to 'all', and the alpha value to 0.85. Finally, hit "Calculate". You should get around 16-17m $^3/s$ for flow depending on how you play about with any of the numbers (see figure 11.20.

Summary The main pieces of information required to process videos in KLT-IV are a full survey of the site, including water levels, camera locations, and a minimum of 8 GCPs. Cross-sections are also required if the user wishes to calculate discharges from the velocity data. Optional inputs are the camera type if it is listed in the program, and a more specific alpha value (if obtained using means such as an aDcp). Stabilisation is done automatically for the user if they have defined that the platform is dynamic (not stationary).

KLT-IV is a standalone piece of software created on MATLAB by Matt Perks at Newcastle University. The aim of the software was to provide a user-friendly PTV software that can be used

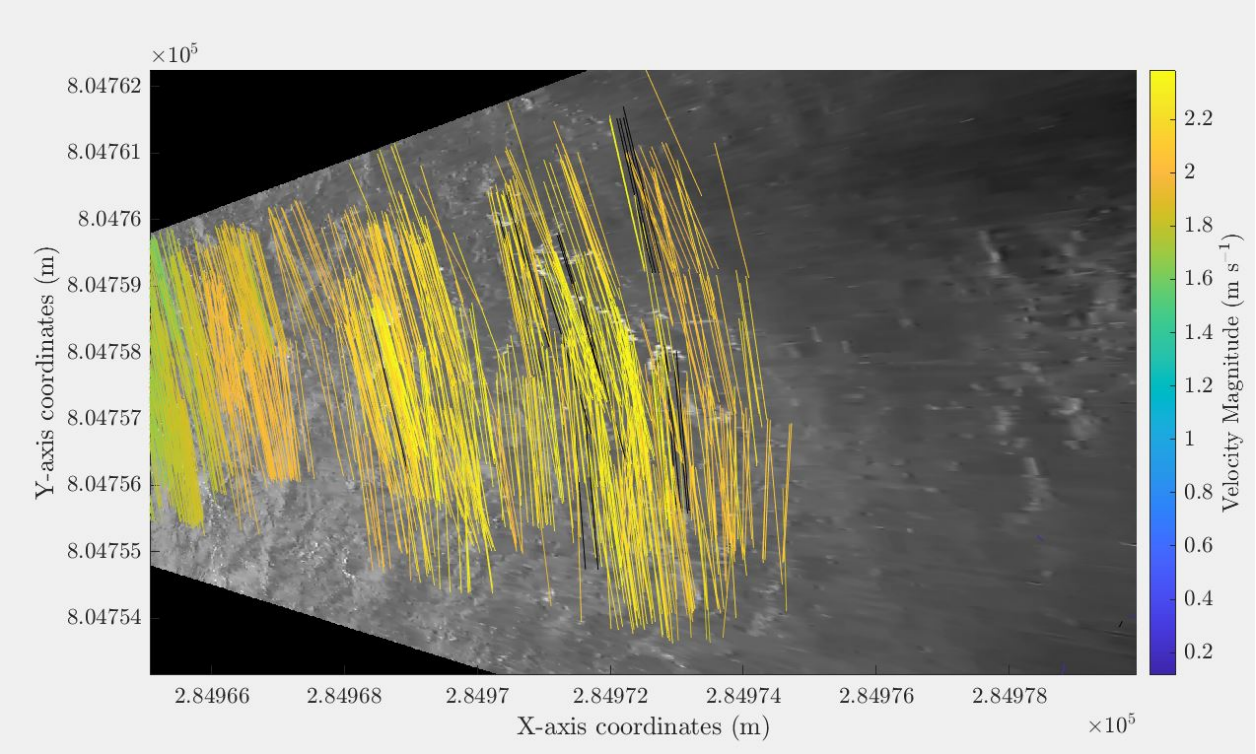


Figure 11.19: Velocity results that have been tracked across the surface. Colour shows indication of speed, while the vector shows the vector trajectory and tracked distance.

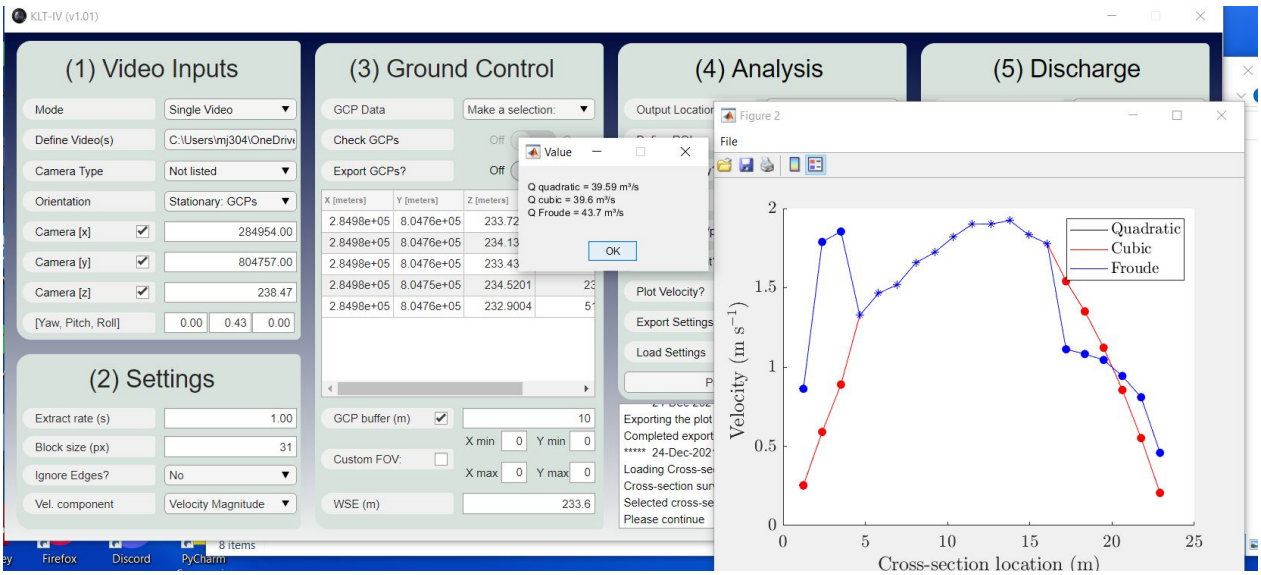


Figure 11.20: The discharge results after running the full process are shown here.

for mobile and fixed platforms alike. The user-friendly GUI walks the user through each of the steps required for processing, from pre-processing of the video, to processing, and finally, through to post-processing and discharges. The simple simplicity of KLT-IV makes it a very useful tool for processing of videos to achieve discharges.

If you want to trial more datasets and have a go at processing either multiple videos at once,

or using dynamic platforms, then there is a repository found here: `https://zenodo.org/record/3882254#.YcW3cGjP1Pb` that was created with the original KLT-IV that contains dozens of files ready to run through the software for training.

Troubleshooting

Sometimes with an unexpected crash or closure of the program, it can cause some of the MATLAB Runtime paths to corrupt. An error that can be common with unexpected/forced shutdowns is a ”ctfroot” error (see figure 11.21). To resolve this error, we need to remove some temporary files that have not been cleaned up from the previous run. To do this, open ”My documents” and find the temp folder for KLT-IV. The path for this is something along these lines:
”C:\Users\”USER”\AppData\Local\Temp\”USER”\mcrCache9.7”
Next, once you have found this folder, highlight all the files inside the mrCache9.7 folder, and delete them. Run the software again and hopefully these temp files come back and the program starts as usual. For Mac and Linux operators, the process will be the same but the path may be different.

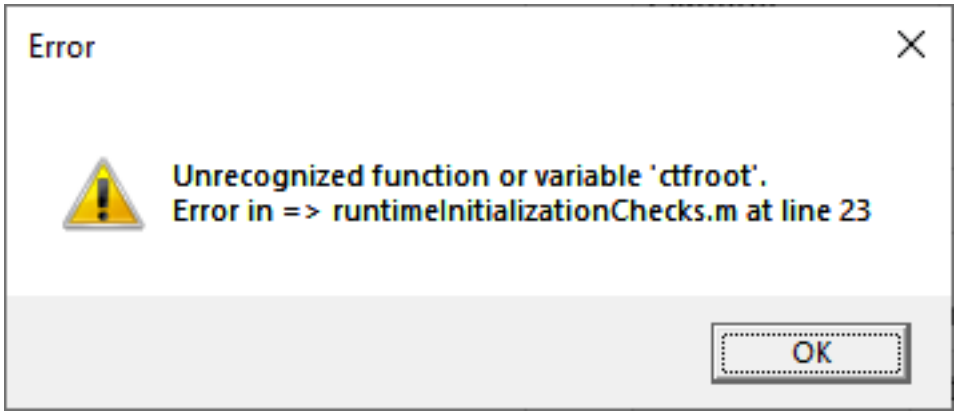


Figure 11.21: A possible error code you can observe with numerous unexpected closures or shutdowns of Runtime.

Tutorial in a nutshell To make things simpler and save some time, the following points will walk you through the tutorial files to come up with a full process using given values. Simply follow these steps carefully to fully extract images and process the data to find an estimated discharge.

1. Download the files required for KLT-IV including the software and the tutorial files, found here (available until June 2022).

2. Open KLT and wait for the program to fully boot. Select ”single file”, then define the video by finding it in the tutorial folder.

3. Select ”not listed” from the camera list. Although the camera may be defined in the list, and it is usually the best way to proceed, we are just going through as default.

4. Enter the camera location coordinates as follows: 284954, 804757, 238.47 (X,Y,Z respectively). The camera angles to be entered are 0, 0.43, and 0 (Yaw, Pitch, Roll).

5. For the settings, we will be leaving them as default (1, 31, no, velocity magnitude)

6. The GCP data has been provided as the CSV file named "GCP_input". Import this data, and set the buffer to 10m, leaving the custom FOV, and setting the WSE to 233.6m.

7. Next, define where you want to save your output files, followed by defining the ROI as seen in figure 11.18. Export the velocities and orthophotos if you wish.

8. Leave the resolution to 0.01 for the first run but feel free to play about with this, or any other value to see how it impacts results. Finally, plot the velocity and analyse the data.

9. Once finished, lets find the discharge. Import the cross-section input using the file XS_input. This has True bed elevations in it, so set the reference height to that.

10. Lets set the number of cells to 20, and look at how all of the interpolation methods change the data. Leave the alpha value at 0.85 as default, but play with this too to see how it impacts results. Press calculate when this is done.

Conclusions

This handbook provides an insight into how image velocimetry operates, including the overarching theory as well as the practical exercise required to set-up stations. The initial sections break down image velocimetry into its key stages and what practically is needed to be considered at each of the stages. By doing it this way, the hope is that a process is formed for when users arrive at a site, and begin to go through a sort of checklist for determining whether or not a site is compatible with the methods. The checklist should run through the order of the contents; note, that it always begins with tracer availability. Environmental conditions and infrastructure available are smaller considerations, as it is possible to work around these by creating new structures, using battery packs, and protecting the camera from external conditions (e.g. placing a hood over the camera to keep away rain). Once a site is determined feasible, the specifics of the set-up need to be considered, such as the camera to be used and at what height it needs to be set to get an optimum GSD. Good surveys of the site need to be taken at some stage prior to processing the data. This can be done after the site set-up if the conditions on the day are too challenging, and data can be captured and later adapted with orthorectification. Where movement is detected in these captured images, it is also to consider performing stabilisation to remove any spurious movements and vectors. Where errors are still evident, post-processing correction methods should be used, and are often available within software suites. This all needs to be done prior to calculating any discharges.

The type of hardware used can be user defined; there is no single best way of creating a site as it fully depends on the conditions and the desired outputs. This handbook has looked into some typically used pieces of hardware and methods to acquire footage and get them to the stage of processing. It is always up to the user to see if there are more specific ways of achieving results, as this research provides a generic set-up that can be used in a majority of cases. The important steps are capturing the footage (camera), and delivering that data to a place it can be processed either using in-situ processing (module), or remotely (network). The advantage of using a network connection to a site, as well as using an IP camera as suggested in the handbooks methods, is that it is possible to control the site fully remotely as well as view and capture data live.

The software used by the user, again, is user defined. Both PIV and PTV have their own advantages and disadvantages as listed throughout this handbook. For highly seeded flows, PIV may be the better option because of the relatively smaller processing required. But for other flows, it may be better to consider a PTV method. RIVeR and KLT-IV are the respective PIV and PTV methods suggested for using at sites because of their availability and performance track record. For the purpose of initial stages of implementing these sites, it is advised to use RIVeR to begin with, and where outputs are not reliable, then try other methods (KLT-IV).

The modal set-up considered in this handbook is the use of a Reolink RLC camera which provides a great amount of freedom of movement, good IR capabilities, illumination built in if needed, and the ability to connect to a router wirelessly which is ideal where satellite routers have been installed at a site and mains power is available. Typically, a LattePanda Delta has been advised where in-situ processing is not required. This is because of its simplicity, with windows capabilities, it should be relatively easy to plug and go. It is typically only used to control the camera and convey the data from site to cloud storage, which means something as powerful as the UDOO Bolt V8 is not needed and would be mostly redundant, whereas it is easier to configure on average than a RPi4B. In terms of networking, mobile internet is always the best method of connectivity because of its reliability, availability, and price. Where sites are not covered by mobile internet, it may be best to reconsider where you place the site. If it is not possible to do so, consider if it is more feasible to process the data on site or simply just store the image data on site, and manually collect it routinely for bulk processing. The alternative to this is to install satellite internet at the site to be used for connectivity and data transfer. This process can be more complicated and costly, but once installed, could be useful for a number of things regarding image velocimetry methods (e.g. wireless cameras like the Reolink GO and RLC). This process also suggests the use of an ultrasonic level meter where only high flows are required, but cameras and deep learning algorithms can be used to determine stage where depth boards are already in place. Alterations like this are the bits that are down to the user and are mostly site specific.

What Next?

Version 1 of this handbook has been written in line with the first phase of several in the effort to develop a systematic way of using image velocimetry in everyday hydrometry. The methods described here are for beginners in the field, and provide only the basics of how to produce reliable results using imaging methods. There are more advanced features that can be used in conjunction (e.g. dual camera systems for 3D modelling of flow), but these are still being developed in research, and will not feature in any of the immediate phases.

The second phase of the roll-out of image velocimetry should begin to think about how to mass produce sites based on the results that come from this initial stage. The use of image velocimetry on sites can massively benefit the automated capture of larger flows, usually missed by other methods. Sites across the country that require the capturing of these higher flows should immediately be considered for installation of a site, especially as the cost of implementing a site costs on average £1000, which is relatively cheap compared to alternative hydrometry methods. A second benefit that could come from the second phase would be introducing some more smart technology, such as using deep learning on all of the cameras to detect the water stage without the need of any other implements. Not just this, but anything along the lines of it that can begin to reduce the need of secondary items and increase the automated efficiency of sites. A review of the use of RIVeR/KLT-IV should also be made. This software was recommended because of its wide availability and ability to produce reliable results. However, it is noted that specialist software like these can be hard to understand and use efficiently. Although these two pieces of software have been developed to be user-friendly with accessible GUI's, there may be alternatives that are better suited, and hence, a review could benefit. Further studies should also begin to include mobile methods (e.g. drones), ready for use in the field. Many of the methods for mobile platforms are the same as fixed, with the addition for a few extra steps such as stabilisation.

Two model sites are to be created in January 2022, using Hikvision cameras and latte pandas. Once these sites are set up and fully operational, this handbook should be edited to include all of the details and pictures that came from these set-ups, as well as any insights into issues we run into.

Equipment Lists

This section is in reference to the spreadsheet tool available on GitHub. Use it to generally decide the sort of equipment you would need to set up an image velocimtery site at several locations, depending on 6 given variables seen in table 11.7. The full list of results can be seen in the table below for a manual method (see table 11.8).

Table 11.8: The full results table for the binary output collected from the variable list table. Choose one of the two options for each of the 6 variables to produce your binary result (between 000000-1111111), and match it to the corresponding equipment suggestion in this table.

000000	Hikvision DS-+-RSPi 4B-+-Mob_Vodafone_PiHat-+–+-12V_Battery_and_Case-+-RS Solar Panel Unit-+–+–+-	1104.37
000001	Hikvision DS-+-RSPi 4B-+-Mob_Vodafone_PiHat-+–+-12V_Battery_and_Case-+-RS Solar Panel Unit-+–+–+-	1104.37
000010	Hikvision DS-+-RSPi 4B-+-Mob_Vodafone_PiHat-+–+-12V_Battery_and_Case-+-RS Solar Panel Unit-+–+–+-	1104.37
000011	Hikvision DS-+-RSPi 4B-+-Mob_Vodafone_PiHat-+–+-12V_Battery_and_Case-+-RS Solar Panel Unit-+–+–+-	1104.37
000100	Hikvision DS-+-RSPi 4B-+-Mob_Vodafone_PiHat-+–+-12V_Battery_and_Case-+-RS Solar Panel Unit-+-MaxSonar-+–+-	1326.37
000101	Hikvision DS-+-RSPi 4B-+-Mob_Vodafone_PiHat-+–+-12V_Battery_and_Case-+-RS Solar Panel Unit-+-MaxSonar-+–+-	1326.37
000110	Reolink Go-+-RSPi 4B-+-Mob_Vodafone_PiHat-+–+-12V_Battery_and_Case-+-RS Solar Panel Unit-+-MaxSonar-+–+-	1130.1
000111	Reolink Go-+-RSPi 4B-+-Mob_Vodafone_PiHat-+–+-12V_Battery_and_Case-+-RS Solar Panel Unit-+-MaxSonar-+–+-	1130.1
001000	Hikvision DS-+-RSPi 4B-+-Mob_Vodafone_PiHat-+–+-12V_Battery_and_Case-+-RS Solar Panel Unit-+–+–+-	1104.37
001001	Hikvision DS-+-RSPi 4B-+-Mob_Vodafone_PiHat-+–+-12V_Battery_and_Case-+-RS Solar Panel Unit-+–+–+-	1104.37
001010	Hikvision DS-+-RSPi 4B-+-Mob_Vodafone_PiHat-+–+-12V_Battery_and_Case-+-RS Solar Panel Unit-+–+–+-	1104.37
001011	Hikvision DS-+-RSPi 4B-+-Mob_Vodafone_PiHat-+–+-12V_Battery_and_Case-+-RS Solar Panel Unit-+–+–+-	1104.37
001100	Hikvision DS-+-RSPi 4B-+-Mob_Vodafone_PiHat-+–+-12V_Battery_and_Case-+-RS Solar Panel Unit-+-MaxSonar-+–+-	1326.37
001101	Hikvision DS-+-RSPi 4B-+-Mob_Vodafone_PiHat-+–+-12V_Battery_and_Case-+-RS Solar Panel Unit-+-MaxSonar-+–+-	1326.37
001110	Reolink Go-+-RSPi 4B-+-Mob_Vodafone_PiHat-+–+-12V_Battery_and_Case-+-RS Solar Panel Unit-+-MaxSonar-+–+-	1130.1
001111	Reolink Go-+-RSPi 4B-+-Mob_Vodafone_PiHat-+–+-12V_Battery_and_Case-+-RS Solar Panel Unit-+-MaxSonar-+–+-	1130.1
010000	Vivotek HTV-+-RSPi 4B-+–+-RSPi 4B_SSDUnit-+-12V_Battery_and_Case-+-RS Solar Panel Unit-+–+–+-	597.4
010001	Vivotek HTV-+-RSPi 4B-+–+-RSPi 4B_SSDUnit-+-12V_Battery_and_Case-+-RS Solar Panel Unit-+–+–+-	597.4
010010	Vivotek HTV-+-RSPi 4B-+–+-RSPi 4B_SSDUnit-+-12V_Battery_and_Case-+-RS Solar Panel Unit-+–+–+-	597.4
010011	Vivotek HTV-+-RSPi 4B-+–+-RSPi 4B_SSDUnit-+-12V_Battery_and_Case-+-RS Solar Panel Unit-+–+–+-	597.4
010100	Vivotek HTV-+-RSPi 4B-+–+-RSPi 4B_SSDUnit-+-12V_Battery_and_Case-+-RS Solar Panel Unit-+-MaxSonar-+–+-	819.4
010101	Vivotek HTV-+-RSPi 4B-+–+-RSPi 4B_SSDUnit-+-12V_Battery_and_Case-+-RS Solar Panel Unit-+-MaxSonar-+–+-	819.4
010110	Reolink Go-+-RSPi 4B-+–+-RSPi 4B_SSDUnit-+-12V_Battery_and_Case-+-RS Solar Panel Unit-+-MaxSonar-+–+-	792.73
010111	Reolink Go-+-RSPi 4B-+–+-RSPi 4B_SSDUnit-+-12V_Battery_and_Case-+-RS Solar Panel Unit-+-MaxSonar-+–+-	792.73
011000	Vivotek HTV-+-RSPi 4B-+–+-RSPi 4B_SSDUnit-+-12V_Battery_and_Case-+-RS Solar Panel Unit-+–+–+-	597.4
011001	Vivotek HTV-+-RSPi 4B-+–+-RSPi 4B_SSDUnit-+-12V_Battery_and_Case-+-RS Solar Panel Unit-+–+–+-	597.4
011011	Reolink Go-+-RSPi 4B-+–+-RSPi 4B_SSDUnit-+-12V_Battery_and_Case-+-RS Solar Panel Unit-+–+–+-	570.73
011100	Vivotek HTV-+-RSPi 4B-+–+-RSPi 4B_SSDUnit-+-12V_Battery_and_Case-+-RS Solar Panel Unit-+-MaxSonar-+–+-	819.4
011101	Vivotek HTV-+-RSPi 4B-+–+-RSPi 4B_SSDUnit-+-12V_Battery_and_Case-+-RS Solar Panel Unit-+-MaxSonar-+–+-	819.4
011110	Reolink Go-+-RSPi 4B-+–+-RSPi 4B_SSDUnit-+-12V_Battery_and_Case-+-RS Solar Panel Unit-+-MaxSonar-+–+-	792.73
011111	Reolink Go-+-RSPi 4B-+–+-RSPi 4B_SSDUnit-+-12V_Battery_and_Case-+-RS Solar Panel Unit-+-MaxSonar-+–+-	792.73
100000	Hikvision DS-+-UDOO Bolt-+-Mob_Vodafone_USB-+–+–+–+–+-	1066.11
100001	Vivotek HTV-+-LattePanda-+-Mob_Vodafone_USB-+–+–+–+–+-	738.53
100010	Hikvision DS-+-UDOO Bolt-+-Mob_Vodafone_USB-+–+–+–+–+-	1066.11
100011	Vivotek HTV-+-LattePanda-+-Mob_Vodafone_USB-+–+–+–+–+-	738.53
100100	Hikvision DS-+-UDOO Bolt-+-Mob_Vodafone_USB-+–+–+–+-MaxSonar-+–+-	1288.11
100101	Vivotek HTV-+-LattePanda-+-Mob_Vodafone_USB-+–+–+–+-MaxSonar-+–+-	960.53
100110	Hikvision DS-+-UDOO Bolt-+-Mob_Vodafone_USB-+–+–+–+-MaxSonar-+–+-	1288.11
100111	Vivotek HTV-+-LattePanda-+-Mob_Vodafone_USB-+–+–+–+-MaxSonar-+–+-	960.53
101000	Vivotek HTV-+-UDOO Bolt-+-Mob_Vodafone_USB-+–+–+–+–+-	896.51
101001	Vivotek HTV-+-LattePanda-+-Mob_Vodafone_USB-+–+–+–+–+-	738.53
101010	Vivotek HTV-+-UDOO Bolt-+-Mob_Vodafone_USB-+–+–+–+–+-	896.51
101011	Vivotek HTV-+-UDOO Bolt-+-Mob_Vodafone_USB-+–+–+–+–+-	896.51
101100	Hikvision DS-+-UDOO Bolt-+-Mob_Vodafone_USB-+–+–+–+-MaxSonar-+–+-	1288.11
101101	Vivotek HTV-+-LattePanda-+-Mob_Vodafone_USB-+–+–+–+-MaxSonar-+–+-	960.53
101110	Hikvision DS-+-UDOO Bolt-+-Mob_Vodafone_USB-+–+–+–+-MaxSonar-+–+-	1288.11
101111	Vivotek HTV-+-LattePanda-+-Mob_Vodafone_USB-+–+–+–+-MaxSonar-+–+-	960.53
110000	Hikvision DS-+-UDOO Bolt-+-Konnect Sat. Lmt-+–+–+–+–+-	1118.79
110001	Vivotek HTV-+-UDOO Bolt-+-Konnect Sat. Lmt-+–+–+–+–+-	949.19
110010	Reolink RLC-+-LattePanda-+-Konnect Sat. Unl-+–+–+–+–+-	1227.52
110011	Reolink RLC-+-LattePanda-+-Konnect Sat. Unl-+–+–+–+–+-	1227.52
110100	Vivotek HTV-+-UDOO Bolt-+-Konnect Sat. Lmt-+–+–+–+-MaxSonar-+–+-	1171.19
110101	Reolink RLC-+-LattePanda-+-Konnect Sat. Lmt-+–+–+–+-MaxSonar-+–+-	1018.4
110110	Reolink RLC-+-UDOO Bolt-+-Konnect Sat. Lmt-+–+–+–+-MaxSonar-+–+-	1176.38
110111	Reolink RLC-+-LattePanda-+-Konnect Sat. Lmt-+–+–+–+-MaxSonar-+–+-	1018.4
111000	Reolink RLC-+-UDOO Bolt-+-Konnect Sat. Lmt-+–+–+–+–+-	954.38
111001	Reolink RLC-+-LattePanda-+-Konnect Sat. Unl-+–+–+–+–+-	1227.52
111010	Reolink RLC-+-LattePanda-+-Konnect Sat. Lmt-+–+–+–+–+-	796.4
111011	Reolink RLC-+-UDOO Bolt-+-Konnect Sat. Unl-+–+–+–+–+-	1385.5
111100	Reolink RLC-+-UDOO Bolt-+-Konnect Sat. Lmt-+–+–+–+-MaxSonar-+–+-	1176.38
111101	Reolink RLC-+-LattePanda-+-Konnect Sat. Lmt-+–+–+–+-MaxSonar-+–+-	1018.4
111110	Reolink RLC-+-UDOO Bolt-+-Konnect Sat. Lmt-+–+–+–+-MaxSonar-+–+-	1176.38
111111	Reolink RLC-+-LattePanda-+-Konnect Sat. Lmt-+–+–+–+-MaxSonar-+–+-	1018.4

11.3 SEPA - DAT2203 Innovation in flow measurement report

Written by Andrew Revill (SEPA)
Publshed internally at SEPA

Transect and Velocity Map

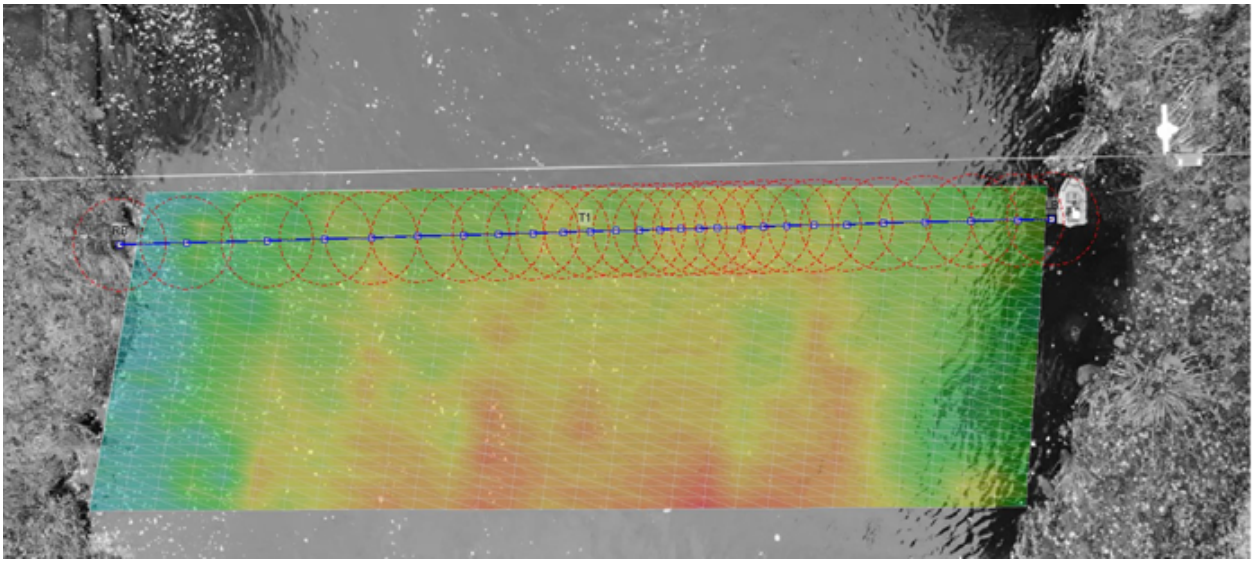


Figure 11.22: Transect and velocity map in FUDAA LSPIV, velocities increasing as they approach the weir just out of shot.

Project Scope

One of the key AOP activities under the area of Warn is the publication and initiation of delivery of the Flood Warning Development Framework 2022-27. This framework has 3 key aims, one of which is to enhance capabilities through innovation and development. Well-calibrated flood flow measurements are crucial for underpinning our flood warning service and flood forecasting capabilities but measuring and calibrating these flows is challenging. This project will evaluate emerging, low-cost, and rapidly developing technologies for continuous river flow measurement. Techniques such as Large Scale Particulate Imaging Velocimetry (LSPIV) applied using a range of technologies including cameras, UAVs, and satellites will be considered. The outcomes of the project are:

- Embed the first generation of LSPIV sites in SEPA's Hydrometric Network. This includes developing our understanding of the requirements of these sites in terms of equipment, maintenance, power, staff resource, training requirements, and environmental factors. This project will inform the business case for the future installation of a small network of LSPIV sites

nationally and will ultimately improve the information underpinning SEPA's flood warning service.

- Work with partners such as the Centre for Ecology and Hydrology to support UK-wide research and development focused on the application of image velocimetry techniques (e.g., use of UAVs and satellite imagery).

Introduction

"Since the late 1990s, image sequence analysis velocimetry techniques (such as PIV – Particle Image Velocimetry) developed in the laboratory have been gradually applied to outdoor geophysical flows, particularly watercourses (Fujita et al. 1998; Hauet 2006). The movement of tracers (natural or added) visible on the surface of the flow is detected by autocorrelation of patterns from one image to the next, after orthorectification of the images; the surface velocity fields thus obtained can be filtered and averaged over a series of image pairs to establish the average velocity field; using one or more bathymetric transects and coefficients linking surface velocity and depth-average velocity, one or more discharge estimates can be calculated." Le Coz et al. (2014)

Two fixed IP cameras were installed in the SW area at Headswood and Sterling Mills. The cameras were connected to low-powered single-board PCs, a Latte Panda and Raspberry Pi 4 (RPi) respectively. Additional solar panels and batteries power the equipment. The videos can be captured at scheduled intervals (15 min to 4 hours) and video lengths (10-30 seconds) usually suffice, with the resulting video transferred to AWS S3 storage via Vodafone mobile data. Videos can be accessed in a timestamped data structure for velocity processing.

A survey was undertaken at each site to create a point cloud of x, y, z coordinates to allow for orthorectifying the camera view and tying in bathymetric profiles to generate flow results. The videos could then be processed when required, optimizing for stage or on-site conditions to generate flows from a variety of available software packages. These software packages use methods detailed in ISO 748, the current standard of SEPA flow measurement. A new ISO standard 24577, Hydrometry – Use of non-contact methods for measuring water surface velocity and discharge, is in development and will focus on these methods. RIVeR (LSPIV algorithm) was chosen as the primary processing software for its relative ease of use and being free. Other processing packages were also tested.

A handbook covering equipment selection, site establishment, and processing is available here: Jolley (2022)

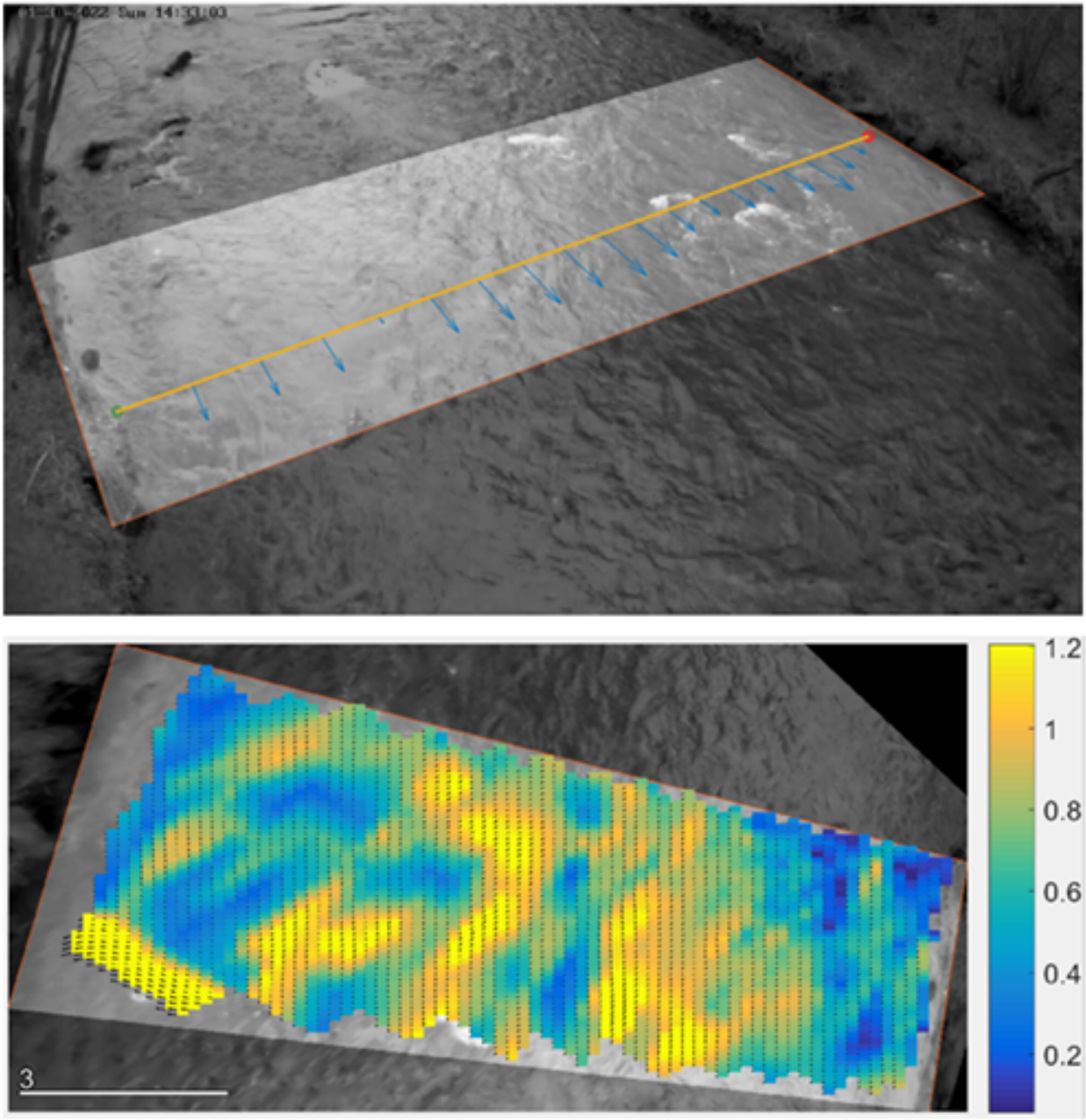


Figure 11.23: Transect

Sterling Mills

Site Setup

Raspberry Pi 4 linked via Ethernet to an IP camera mounted on a downstream bridge. The camera is located at a more desirable higher angle than Headswood and looks more directly upstream as opposed to across the stream.

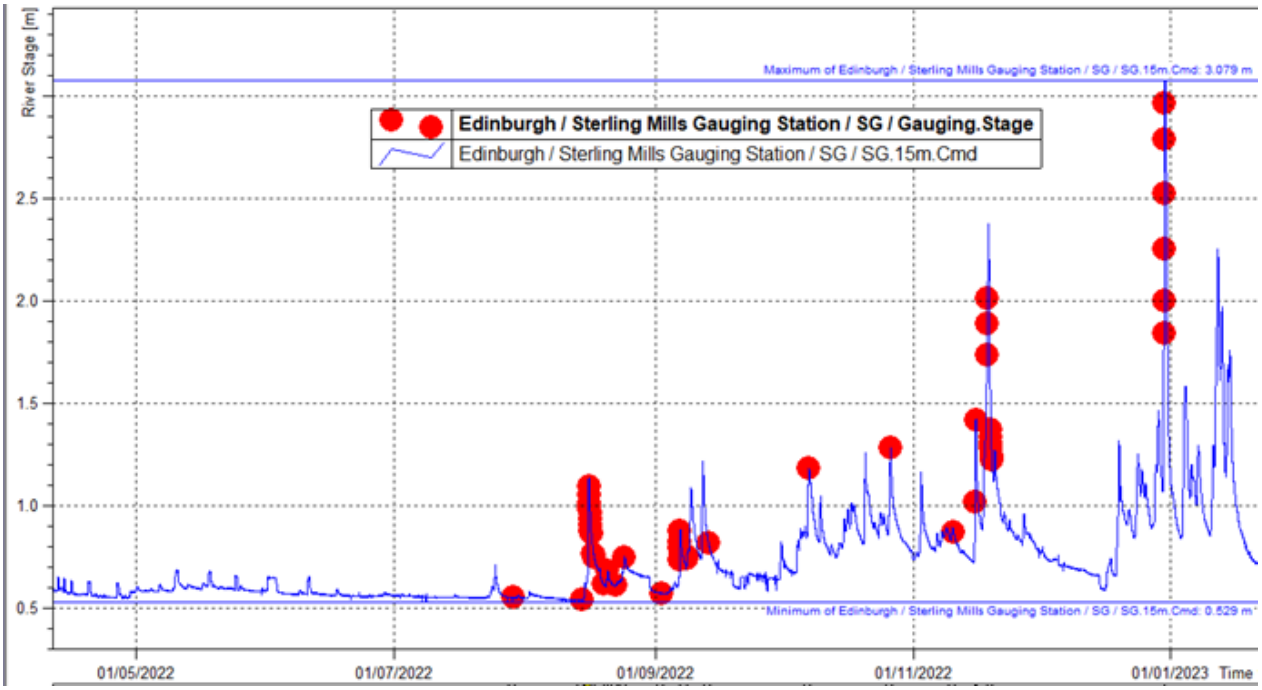


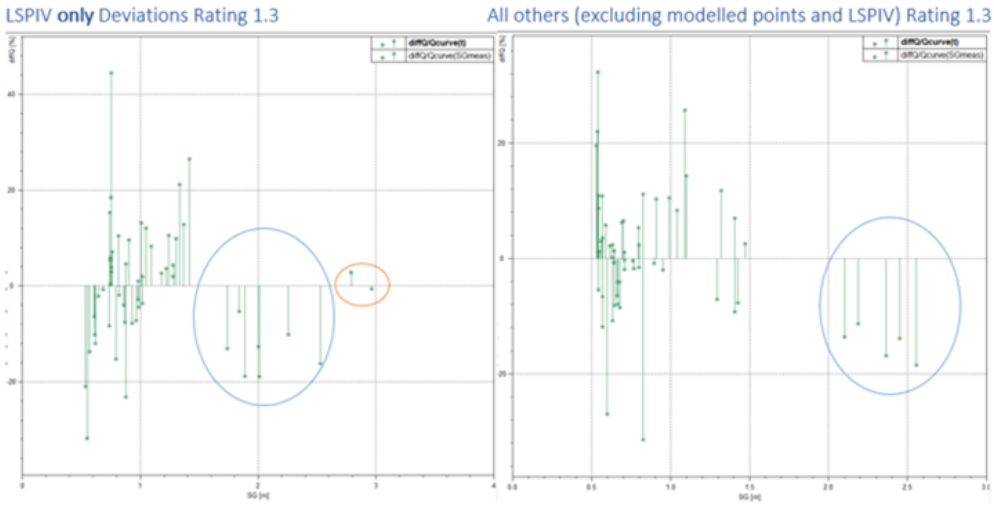
Figure 11.24: Velocity map.

Site Challenges

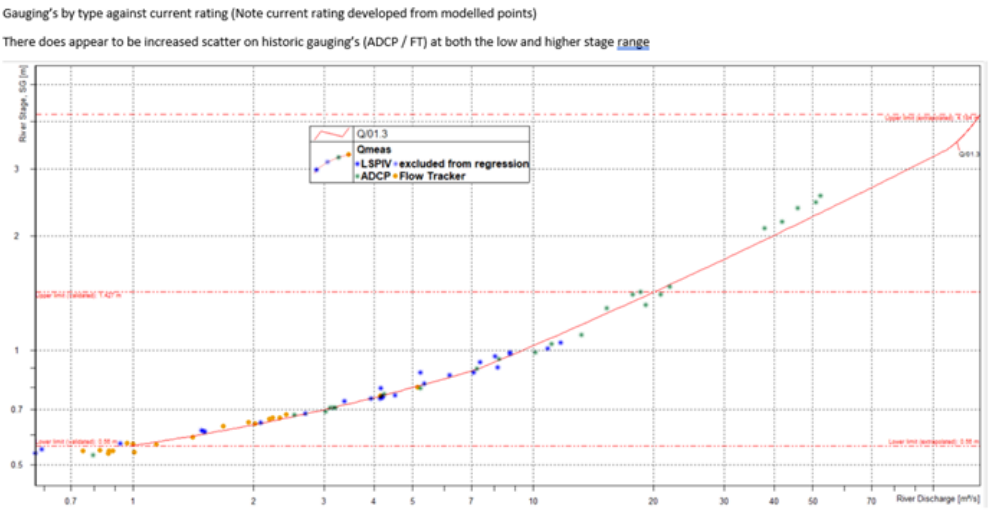
- OS running from SD card, which may be subject to corruption over time. This was partially resolved by remotely copying the OS to a bootable USB thumb drive, which was tested on another RPi and worked.
- Initially not set up to GMT. This issue has been resolved.
- Code did not start automatically on reboot. Initially required VNC to the Raspberry Pi to start manually. This was partially resolved with a CRON task on boot, though it has not been fully implemented.
- The cross-section is not ideal, but the benefits from the camera location likely outweigh this limitation.
- The traditional ADCP gauging section is in a pool upstream, and alpha values of 0.85 were assumed, corresponding to a standard 1/6th power law extrapolation of velocity in the vertical.
- The streetlights on the bridge above the camera were hoped to provide illumination for night video collection. However, reflections from the lights have hindered the use of the videos.

Site Results

Multiple events were processed at this station. Despite constraints such as daylight recording and recording intervals, intensive gauging of the site was possible in a short period of time. Since July 2022, 53 individual gauging events have been recorded. This is approximately five times the number carried out at most sites in the network annually, all done remotely without site visits.



(a) View from the bridge at Cabrach.



(b) Gauging Stage plot, showing numbers of gauging's and stage range covered.

Figure 11.25: (A) View from the bridge at Cabrach and (B) Gauging Stage plot, showing numbers of gauging's and stage range covered.

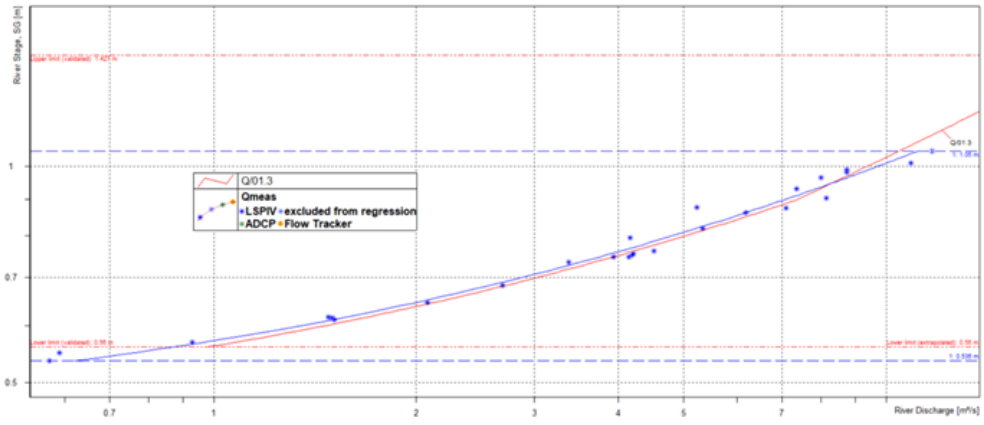
In terms of deviations over 20%, there is little difference (1x LSPIV ¿40%). Overall deviations for traditional methods are lower, but it should be noted they are carried out in a better location upstream. ADCP and LSPIV gaugings from 1.8m to 2.6m have very similar deviations (blue). LSPIV gaugings over the year are within 5mm of the lowest historic gauged stage to 409mm above the highest historic gauged stage. The 2 highest LSPIV gaugings align well with the modeled high

flow rating (orange).

It is interesting that the rough distribution ± deviations across the stage range seem to follow the same trend regardless of the method, except for the low flows where there is a negative bias apparent in LSPIV. The channel conditions are not ideal at low flows for LSPIV, but there is consistency, so it could potentially indicate a rating shift this year.

Lower Flows

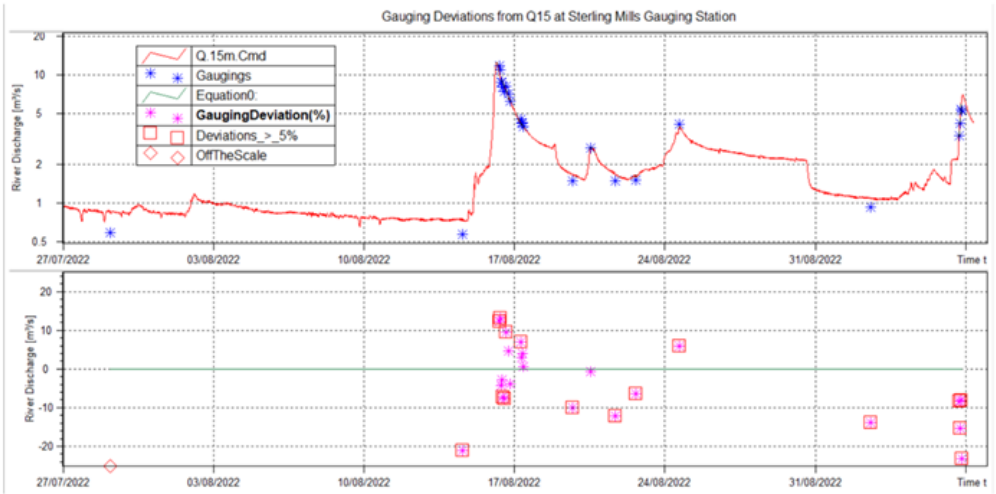
LSPIV gauging only and regression. There does appear to be good correlation between the LSPIV gauging's when compared like for like. Would be hard to say there is obvious bias?



(a) All ADCP and Flow tracker gauging's since site creation 2017.

LSPIV Deviations from existing rating. Poorer performance noted at low flows and significantly on the rising stage (this may be due to a offset between stage reading 15min and video recording) Or site conditions..... Camera located downstream out with gauging pool?

There does seem a trend towards negative deviations overall. Is the 0.85 Alpha value representitve? Accuracy of the cross-section?



(b)

	Gaugings Total	+ Deviations to rating	- Deviations to rating	2SE%	2SMR
ADCP + Flowtracker	43	18	25	21.24	3.31
LSPIV	54	27	27	26.9	3.64
Combined	97	45	52	24.3	2.48

(c) Transect and velocity map in FUDAA LSPIV, velocities increasing as they approach the weir just out of shot.

Figure 11.26: (A)All ADCP and Flow tracker gauging's since site creation 2017. (B) LSPIV Gauging deviations from existing rating. (C) Transect and velocity map in FUDAA LSPIV, velocities increasing as they approach the weir just out of shot.

	Size:	Unit	Total	Section 1	Section 2	Section 3
Total number of gaugings	N	-	114	83	19	21
Count of real measurements	-	-	114	83	19	21
Number of artificial datapoints	-	-	0	0	0	0
Number of auxiliary points	-	-	0	0	0	0
Min. SG of Regression	min SG	m	1	1	1	3
Max. SG of Regression	max SG	m	4	1	3	4
Min. Q of Regression	min Q	m³/s	0.66	0.66	18.71	49.57
Max. Q of Regression	max Q	m³/s	130.48	23.08	50.30	130.48
Min. SG of measurements	min SG	m	1	1	1	3
Mean value SG of measurements	mean SG	m	1	1	2	3
Max. SG of measurements	max SG	m	4	1	3	4
Min. Q of measurements	min Q	m³/s	0.57	0.57	17.71	52.11
Mean value Q of measurements	mean Q	m³/s	26.46	7.05	32.95	97.91
Max. Q of measurements	max Q	m³/s	128.65	25.04	52.47	128.65
Student t Test						
Degree of freedom	N-2	-	112	81	17	19
Student t(95%)	t*	-	1.96	1.96	2.10	2.10
Standard error (1 level of confidence)	Se	%	10.24	11.72	9.53	2.36
Student t-test on absence of bias (signs)						
Number of positive signs	N+	-	54	37	10	12
Number of negative signs	N-	-	60	46	9	9
Probability for positive signs	p	-	0.50	0.50	0.50	0.50
Probability for negative signs	q	-	0.50	0.50	0.50	0.50
Expected Number of positive signs	Np	-	57.00	41.50	9.50	10.50
Standard deviation	sqrt(Npq)	-	5.34	4.56	2.18	2.29
Empirical t	t	-	0.66	1.10	0.00	0.44
Result	-	-	Accept	Accept	Accept	Accept
Absence from bias (values)						
mean percentage deviation	P	%	-0.29	-0.30	-0.53	0.59
Standard error	Se(P)	%	0.96	1.28	2.09	0.49
SMR (2 levels of confidence)	2SMR	-	1.92	2.58	4.30	1.05
Quality of rating curve						
Correlation coefficient	R	-	---	0.992838	0.971743	0.996955
R square	R²	-	---	0.985727	0.944284	0.993920

Figure 11.27: Overview of gauging data

Rating LSPIV 1 would provide a statistical improvement, utilising all gaugings and modeled points ¿ 2.6m. 3 segments, although not strictly following the JBA modeled point top end of v1.3. SMR2 reduction of 0.56% and overall 2SE reduction 3.82%.

Site Recommendations

- Continued operation of the site, even just to further learning from tweaking the setup.

Headswood



Figure 11.28: Headswood camera view.

Site Setup

Latte Panda single-board Windows PC, linked via Ethernet to an IP camera mounted on the gauging station roof. This provides a lower viewing angle, which has proven prohibitive for distinguishing far bank surface tracers.

Site Challenges

- Latte Panda does not start automatically with power on.
- Initially failed to record repeatably on schedule, so had to be manually triggered. This was resolved with a new Python script.
- Initially not set up to GMT. This issue has been resolved.
- The choice of video codec CV2 (compression) caused pixelation. This was resolved using X264.
- Because it is a Windows-based PC, Microsoft updates were downloaded (using bandwidth) and stored on the very limited internal memory, causing the PC to restart randomly. This was partially resolved.

- When processing the videos, the cableway needs to be "masked out" as the software assumes this is an area with no velocity. This issue remains unresolved.
- Power consumption of the Latte Panda is higher than that of the RPi at Sterling Mills. This issue remains unresolved (would be better suited to mains-powered sites).

Site Results

Overall poor results for this site, predominantly constrained by issues with the hardware and communications to AWS. What results were achieved are over a limited stage range and for the most part exhibit a negative deviation to the rated flow ranging from 0 to 25%. It is believed this is mainly a result of the shallow camera angle, which struggles to pick up tracers nearer the far bank. It may be better understood with refinement of the alpha values comparing past ADCP measurements—does this value change with stage?

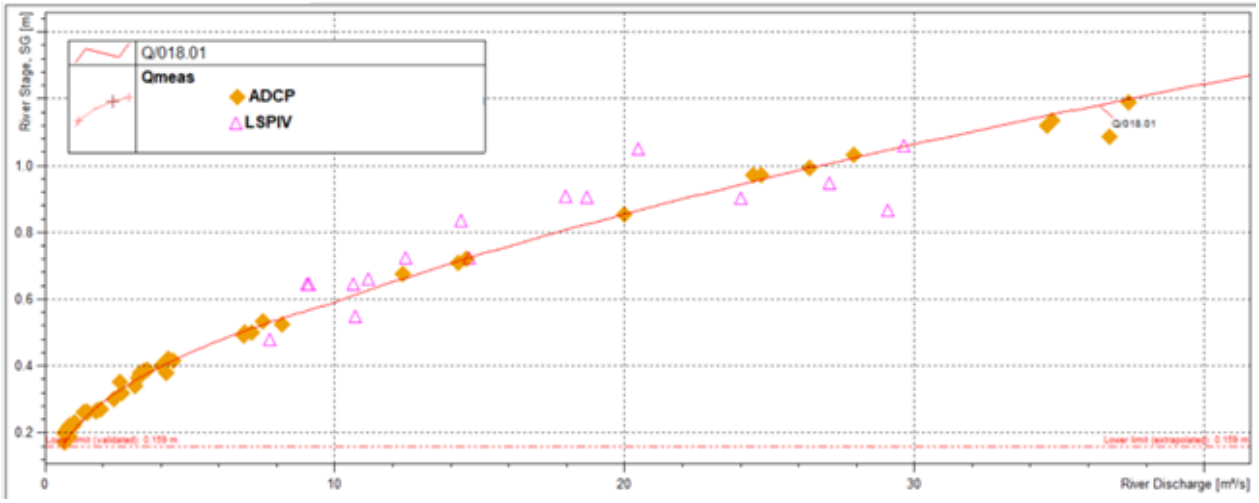


Figure 11.29: Part of Headswood rating and LSPIV/KLT gaugings plotted.

Site Recommendations

- Larger internal storage on the Latte Panda.
- Fix communication issues.
- Mount the camera on a scaffold pole to allow for an elevated angle and orient it slightly further downstream to reduce impact from the cableway and provide a better view of trace material nearer the right bank.
- Alternatively, Headswood, due to its shallower viewing angle, may be a good candidate for experimenting with a different processing algorithm, specifically Space-Time Image Velocimetry (STIV).

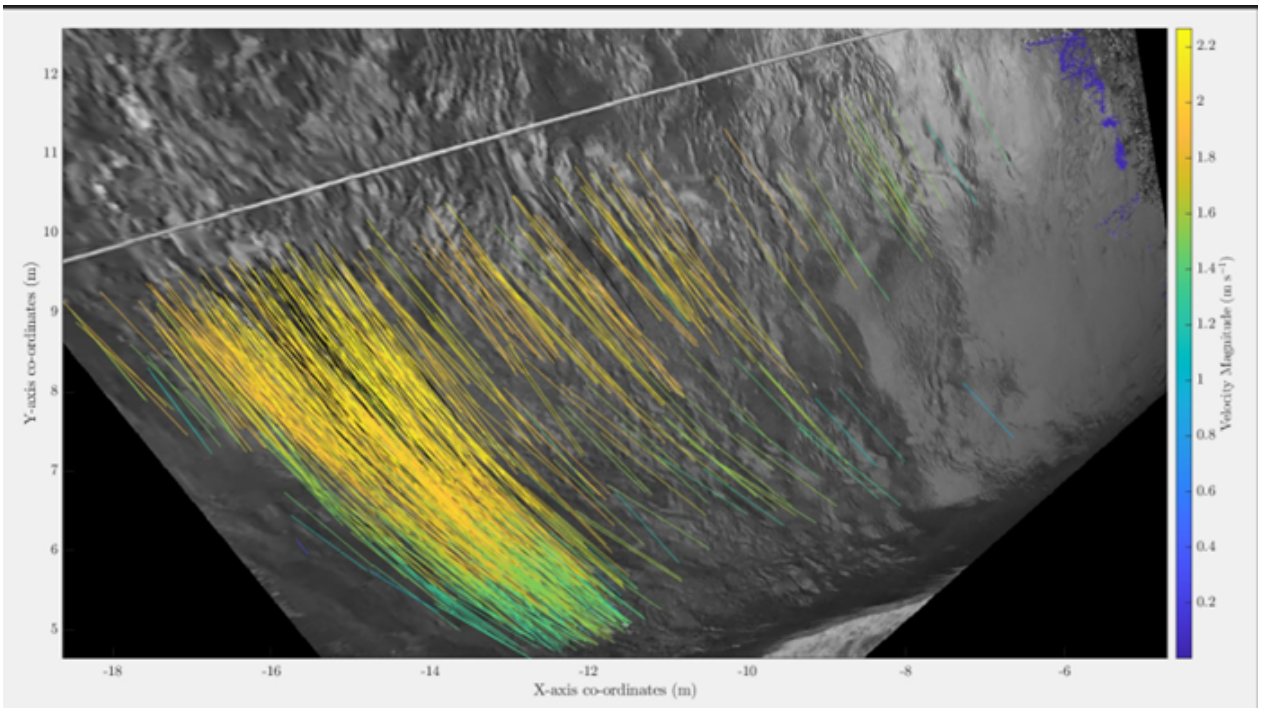


Figure 11.30: KLT vectors.

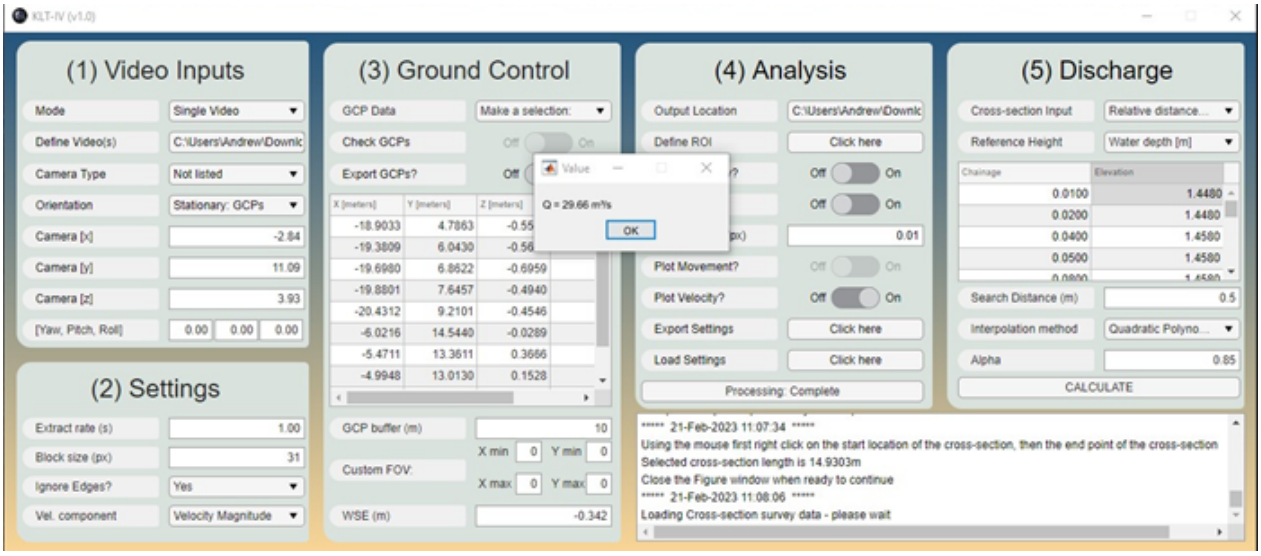


Figure 11.31: Processing and discharge results

Ad-hoc & UAV Deployment

A selection of measurements carried out throughout the year at a variety of sites, including corroborating some of the highest gauged flows on record and one case of a possible significant extension to the rating from the most remote site for hydrometry staff. The ability to capture videos in the field with a mobile phone or UAV quickly and then post-event process them to create supplementary measurements has been very beneficial.

Almondell

One video was acquired by SEPA's drone team at Almondell to coincide with an ADCP measurement. When taken vertically (Nadir), a single distance is required for orthorectifying, in this case, the distance made good from the ADCP.

- ADCP Stage: 0.475m, Q 4.921
- Rated Flow: Q 4.972
- LSPIV: Q 4.990

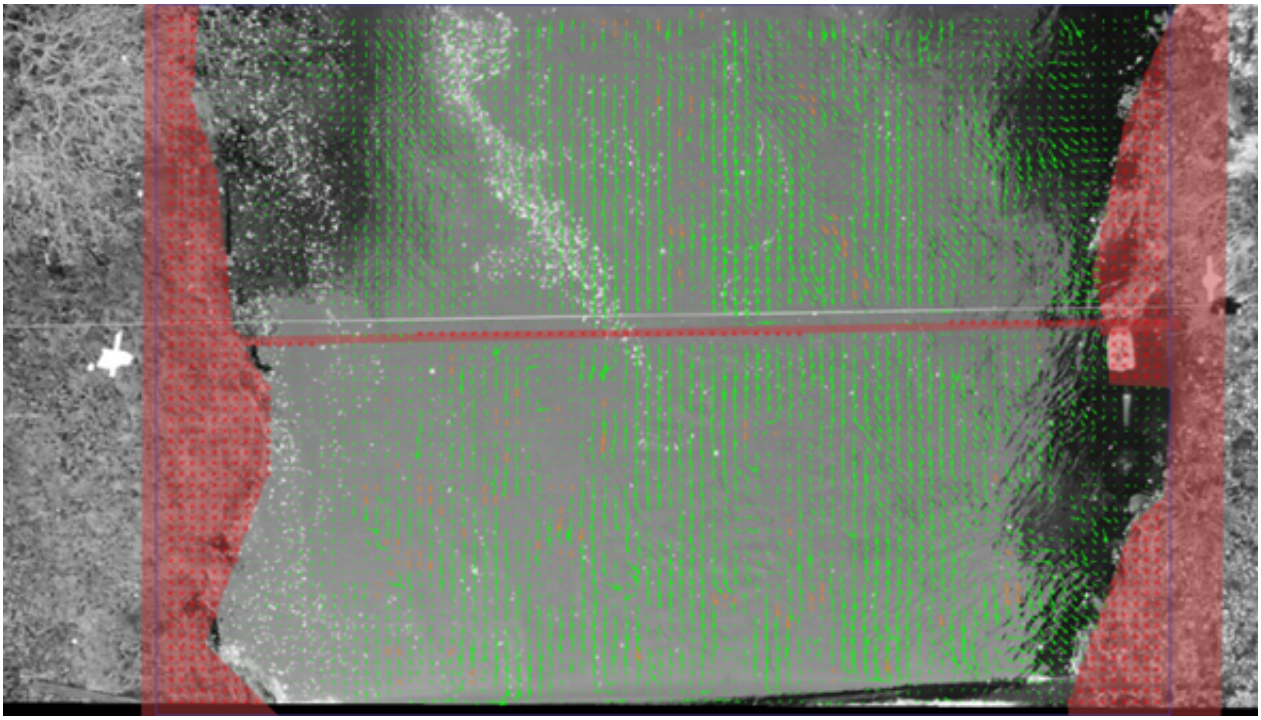


Figure 11.32: PIV Lab mask and vectors.

Cabrach

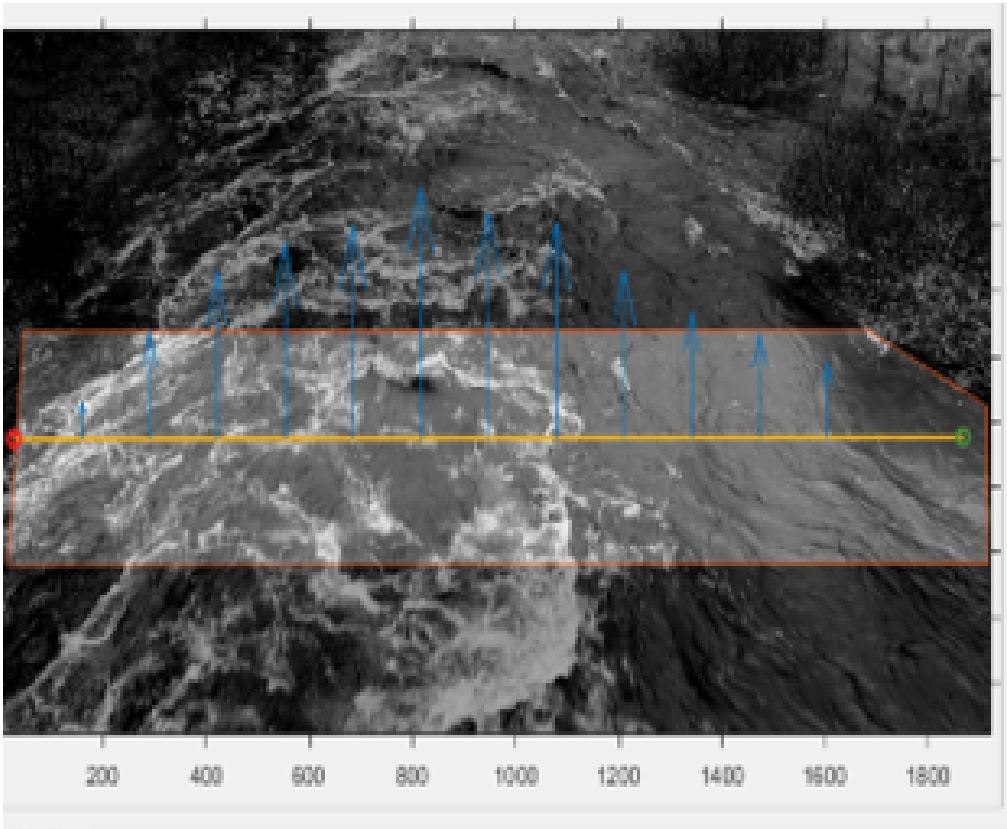
iPhone 30-second video from a downstream bridge, processed in RIVeR, 50mm from the highest ever gauging on record.

- ADCP Stage: 1.900m, Q 59.012
- LSPIV Stage: 1.850m, Q 56.420

No rated flow available at present; these measurements will allow for a rating extension.



(a) View from the bridge at Cabrach.



(b) Transect and velocities.

Figure 11.33: Views showing different aspects: a bridge view and a transect with velocities.

Delnashaugh

iPhone video from the bank, with no known ground control points. Trigonometry was used based on the height of the winch tower on the far bank and the visible portion of a vertical gauge board on the near bank, these were then extrapolated horizontally and distances calculated between them.

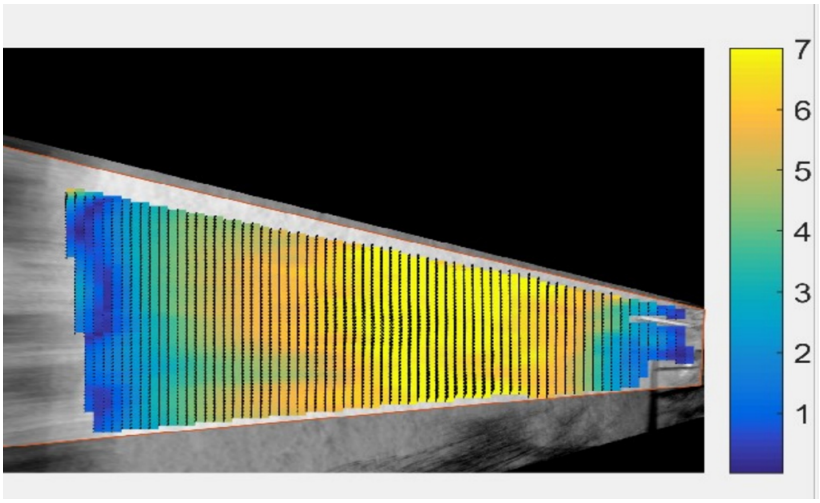
- Current Meter: Stage 3.000m, Q 330.053

- LSPIV: Stage 3.000m, Q 325.37

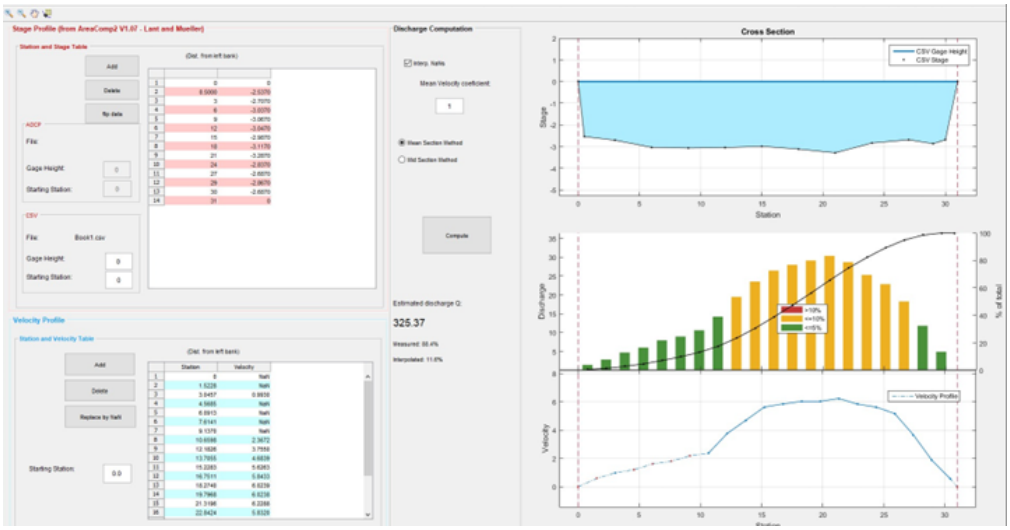
No rated flow available at present; these measurements will allow for a rating extension. Velocities at over 6 meters per second are a challenge for traditional instruments.



(a) Orthorectification in RIVeR (Figure 1)



(b) Orthorectification in RIVeR (Figure 2)



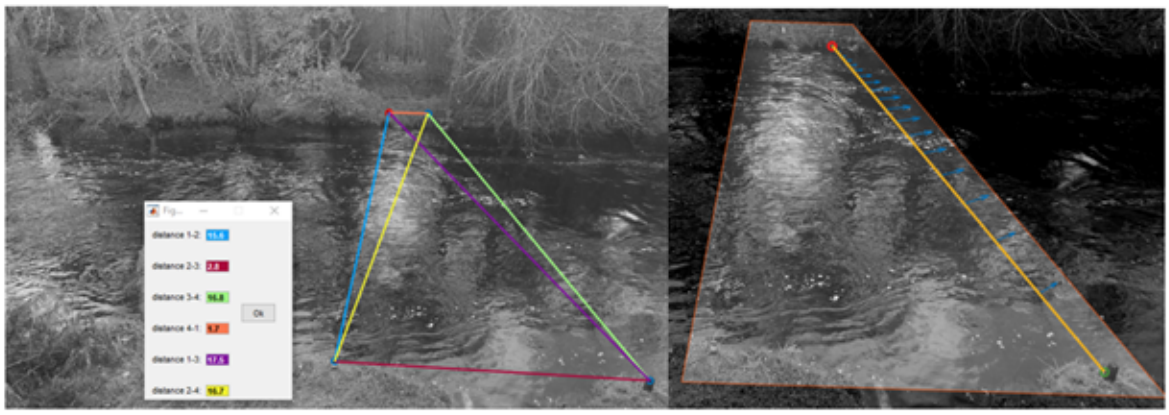
(c) Orthorectification in RIVeR (Figure 3)

Figure 11.34: Orthorectification in RIVeR showing various stages and perspectives.

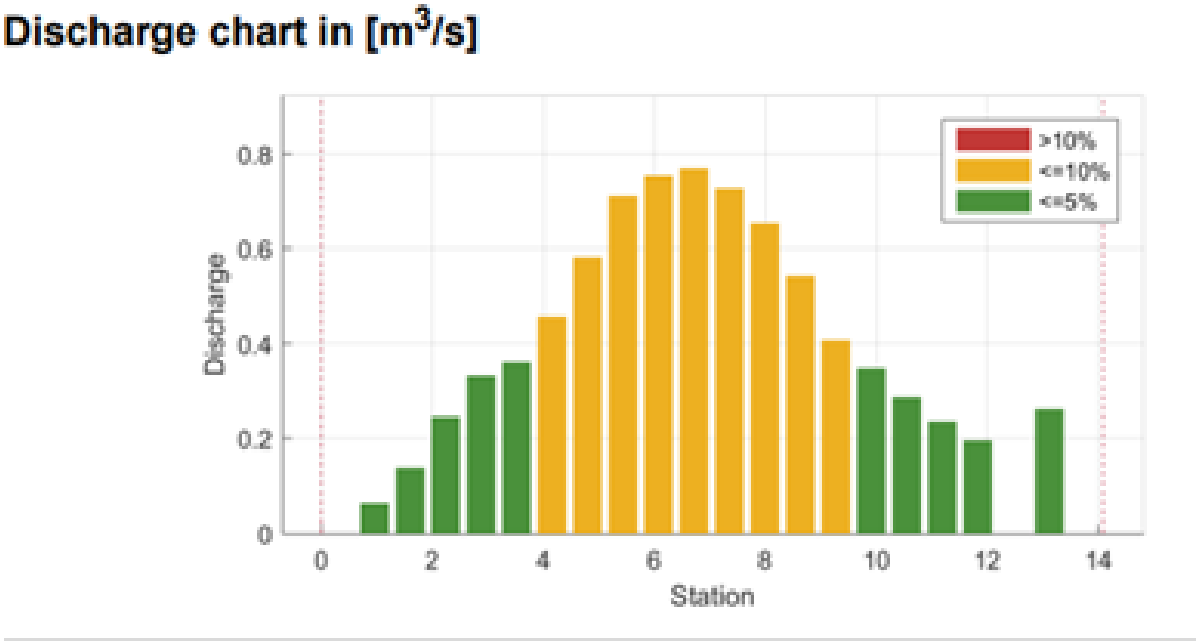
Mill of Tore

Camera from the bank, using surveyed ground control points.

- ADCP stage: 0.905m, Q 6.380
- Rated Flow: Q 6.042
- LSPIV Stage: 0.901m, Q 6.46



(a) A



(b) B

Figure 11.35: Camera from the bank, using surveyed ground control points (A). Discharge Chart for Mill of Tore (B).

Polloch

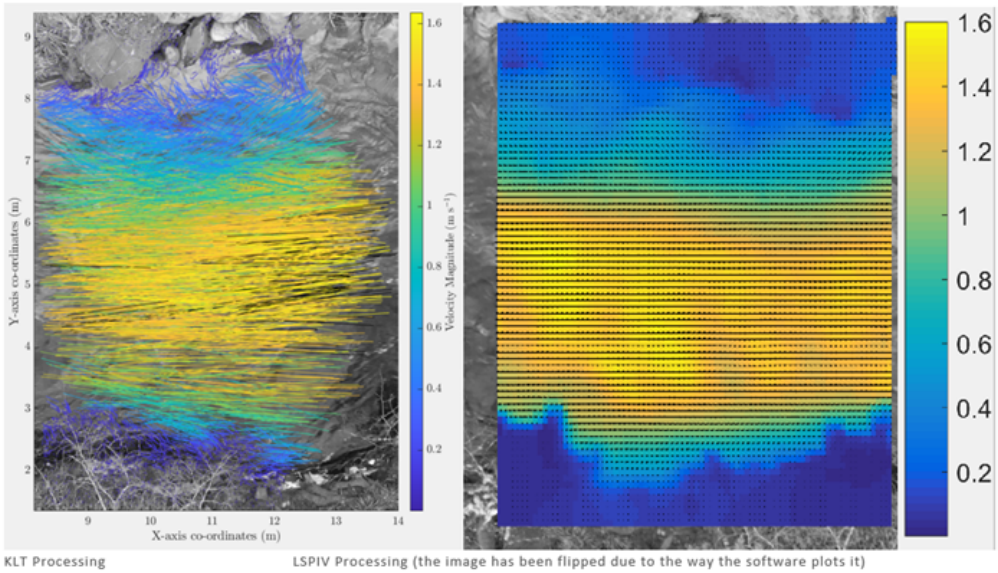


Figure 11.36: KLT-PIV software (KLT) Q3.74 comparison to RIVeR software (LSPIV) Q3.61, M9 Stationary Q3.429

Weisdale

An almost Nadir view from a bridge taken by a member of SEPA staff from the Shetland office. Potential to significantly extend the rating 800mm higher than any previous gauging. Cross-section using a stage-adjusted historic ADCP transect.

- Stage: 1.600m, Q 8.790

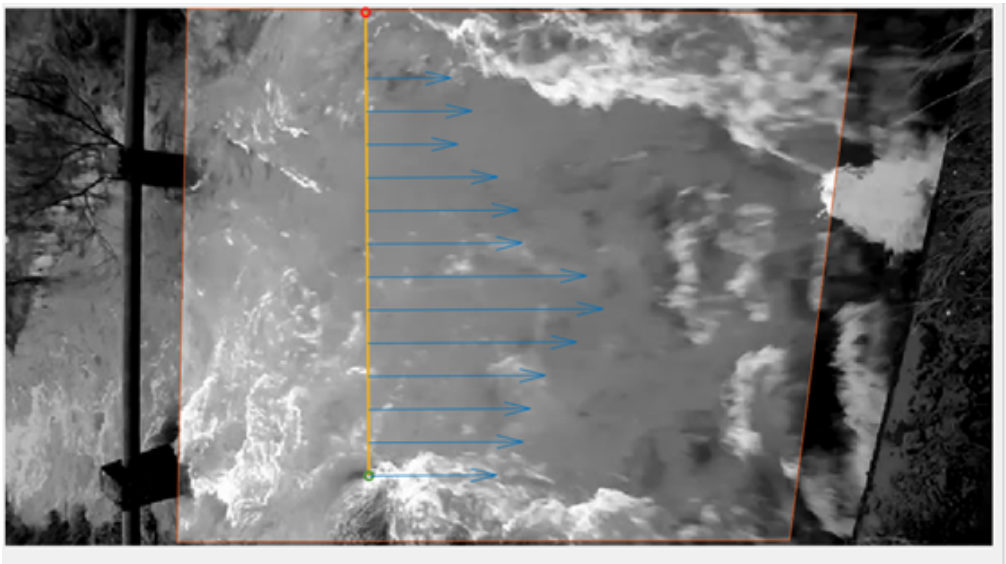


Figure 11.37: Results from STIV for Weisdale. No rated flow available at present, but this measurement may allow for a rating extension.

Conclusions

This project has shown that the use of cameras to obtain videos which can be subsequently processed to provide reliable flow measurements should be an important part of the Hydrometry toolkit in SEPA. A future network incorporating this method should be a mix of fixed cameras (e.g., for sites that can't be accessed due to road flooding at high flows) and UAV / mobile phone deployment. This provides enough flexibility for Hydrometry to tailor the best approach to each unique set of circumstances and allows for a reactive response which is often required.

The use of cameras is particularly well-suited to situations where it is difficult to obtain flow measurements using traditional methods and instruments. Examples include sites where access is impossible at high flows or where the flashy nature of the hydrograph makes it difficult to capture the peak of the event. Fixed cameras also increase our ability to generate flow measurements out of hours and at sites where flying UAVs is not possible, such as near airports. It's also important to recognize that no single method or instrument is optimal in every circumstance, so there will be a role for already established flow measurement techniques used throughout Hydrometry.

Future Recommendations

- Incorporate the application of these techniques into the wider Hydrometry training project (P02 Training Programme).
- Work with the SEPA Drone Steering Group to train pilots in each Hydrometry region and work with a select number of landowners to obtain UAV flight permissions at the site.
- Incorporate the right to fly UAVs for Hydrometry purposes in any new station leases.
- Continue to trial fixed cameras with a focus in 2023 on trailing the camera in development by Sontek. Increased developer support and ease of use with 'plug and play' setups will be key in widening out the use of this technology in Hydrometry.
- Encourage staff to obtain video recordings on their mobile phones as a means of generating flow measurements when other methods aren't suitable.
- Guidance on the use of cameras to capture flows and best practices on processing flows from cameras should be reviewed/produced/disseminated from SEPA's non-acoustic flow measurement group.
- Further testing to be undertaken by the non-acoustic flow measurement group:
  - Use of infrared lights to obtain videos at night.
  - Further trials of different software and guidance on preferred packages.
  - Explore the value of having site-specific alpha values.
  - Further development with Iris loggers to trigger camera capture at predefined stages.
  - Further testing of surface velocimetry methods alongside a range of different gauging methods to better understand their limitations.
- A week of measurements comparing UAV-captured videos and ADCP comparisons is planned in conjunction with UK CEH at a variety of sites, beginning the week of March 27, 2023.

Chapter 12. Appendix C: Further Acknowledgements

For anyone who has been a part of my life throughout the duration of this thesis, it's no secret that this has been one of the hardest things I've ever attempted. When I first applied to Newcastle University in 2014 to study Civil Engineering, no-one would have bet on me reaching this stage and pursuing a PhD. Yet, here we are. This PhD journey has been anything but straightforward—from navigating the "pandemic that shall not be named" to inadvertently diving into a topic that demands *so much* coding and maths (neither of which are my strongest suits!). I wouldn't be where I am today without the unwavering support of those around me, both in life and in this PhD process. My first thank you goes to those who have been there from the beginning, motivating me to keep going even when time was fleeting and progress seemed slow. To my housemates over the years—Alex.C, Matthew.S, Gemma.D, James.L, Josh.G—thank you **so much**. You may not have always realised how much your support meant, but through the lockdowns, the overworking, and the underworking, you were always there, and I am deeply grateful.

This gratitude also extends to all of my friends in Newcastle who have been a big part of my life over the past several years. The list is long, and I've put these names through a randomiser to avoid any complaints about the order: Jack.S, Emma.T, Chris.W, Eve.D, Paul.S, Tom.A, Tom.C, Imogen.A, Martha.S, Nick.S, Maisie.C, Chris.C, Saskia.K, Scott.L, Olly.C, James.G, Harry.H, Becky.M, Aaron.L, Kieran.S, Mike.P, Jack.H, Joe.H, and everyone else who I haven't named individually but who has been there with me—I thank you all.

There are a few names I want to give special recognition to. Julia, you've been a rock throughout. You are quite literally the most consistent, stable friend I could have asked for. Thank you for always checking up on me and pushing me to get this done. Alex, I couldn't mention Julia without mentioning you. The last three years of living together have made me realise just how much I value you. Whether it was providing necessary distractions by 'dragging' me to the pub, or helping me focus and knuckle down over these past few months, you've been a constant support. Finally, Lucy. You entered my life at the perfect time, just in time to witness the chaos of the final push to get this thesis done. I promise there was a time when I wasn't this stressed about it. But rest assured, I'm almost there, and soon you won't have to see me pulling my hair out over coding issues anymore. To the three of you, thank you—I definitely owe you all a drink or three! (Though, once I'm out of the debt that this uni journey has put me in... I'll be good in a few years?).

Finally, I want to acknowledge a few people who have been influential in shaping both who I am and where I am today. Going all the way back to High School, I had two teachers who believed in

my potential so much that they practically (not literally, but you know what I mean) held my hand through an extra year of A-Levels: Rachel and Ben Allsop. I hope you both know how grateful I am for the time you invested in me back then, and I hope you can now see how it has paid off—I owe you both the world. Next, Jaime Amezaga; not only have you been a fantastic lecturer, but you've also been a role model for me throughout my PhD, as well as a friend. You've spent so much time helping me become a better academic and instilling in me the belief that I could get this thesis done (and giving me a much-needed kick up the backside when necessary). The same goes for you, Jean Hall. Thank you both for taking precious time out of your days to meet with me for coffee chats and meetings, even when you didn't have to. Lastly, my work colleagues Abby, Toby, and John. I joined the team in June 2023, towards the end of my PhD, so you've definitely seen me at my worst while trying to balance full-time employment with writing a thesis. You've all helped me manage my time and find balance in my working life—thank you.

To anyone I may have missed in these acknowledgements, please know that I deeply appreciate you and your time. Thank you for being there throughout... now, let's get this thesis submitted!